From Single Cells to Multicellular Organisms - a quantitative analysis

Dagmar Iber

A dissertation submitted to the University of Oxford
In candidature for the degree of
Doctor of Philosophy

St John's College
Oxford

Mathematical Institute
Oxford



Abstract

The evolution and development of multicellular organisms requires cells to differentiate, interact and "collaborate". Our understanding of the molecular mechanisms is still hazy. In this dissertation mathematical modelling is used to integrate available experimental data and to make testable predictions about such mechanisms. The thesis is split into three parts, each of which addresses one of the three challenges: differentiation, adhesion and collaboration.

In the first part, a mathematical model is developed to explain how, in the absence of polarizing cues from the environment, sister cells with identical genomes can follow distinct routes of differentiation. It is shown that difference in cell size, resulting from asymmetric cell division, is sufficient to induce differential cell fate in *Bacillus subtilis*. The model predicts that this effect depends on the allosteric behaviour of a kinase and the low catalytic rate of the corresponding phosphatase; both properties were subsequently confirmed in experiments. During the development of multicellular organisms, differentiation can arise in response to gradients. By example of dorso-ventral patterning it is shown how a shallow maternal gradient can be converted into a sharp pattern.

In the second part, a model for cell adhesion via integrins is developed, and it is shown that, for physiological parameters, binding of a ligand and of a stabilizing factor such as talin are insufficient for ligand-dependent integrin activation, and that a positive signaling feedback is required.

In the final part, antibody affinity maturation is studied as an example for division of labour between collaborating cells. A novel B cell selection mechanism, based on competition for T cell help rather than for antigen, is proposed and shown to reconcile heretofore inexplicable experimental observations. Such a mechanism requires B cells to discriminate among different affinities of binding, and it is further shown that this can be achieved if B cell signaling is initiated by antigen-dependent receptor-inhibitor segregation. The predictions of the model match experimental measurements quantitatively.

Declaration

The work outlined in this dissertation was carried out at the Centre for Mathematical Biology, Mathematical Institute, Oxford over the period October 2003 to September 2006.

Most of the work has been done in collaboration. On chapters 2-4 I collaborated with Iain Campbell, Joanna Clarkson and Michael Yudkin, all at the Department of Biochemistry, Oxford. Chapter 6 reflects collaborative work with Giorgio Gaglia, an undergraduate at the Mathematical Institute. In particular, using my computer code he generated all figures in Chapter 6. Part II of the thesis was developed in close interaction with Iain Campbell at the Department of Biochemistry, Oxford. The work presented in Chapters 11 and 12 was carried out in collaboration with Michael Meyer-Hermann, then at the Centre for Mathematical Biology, Mathematical Institute, Oxford and currently at FIAS, Frankfurt, Germany. Based on my proposals Michael Meyer-Hermann extended his existing code for the germinal centre reaction. The analysis was carried out jointly but the figures in Chapters 11 and 12 were all created by my collaborator. Finally, Chapter 13 reflects collaborative work with Thomas Gruhn and Reinhard Lipowsky, both at the Max-Planck Institute for colloids and interfaces in Golm, Germany.

Most of the text in the thesis has been published (page xii), and I am the main author of these papers. However, because these were joint publications, most of the pieces have received intense attention from my collaborators and have been proof-read in depth. Accordingly, certain small parts of the text which can no longer be identified would have been phrased by my collaborators rather than by me.

This work has not been submitted whole or in part to any other university except for parts of the glossary which are taken from my thesis for the MRes/MSc in Applied and Computational Mathematics (University of Oxford, 2001).

Acknowledgements

Mathematics and the molecular processes that enable life have always exerted a strong fascination on me. Extrapolating from physics, it seemed to me that only quantitative, testable models could lead to a true and integrated understanding of biology. However, when I embarked on my scientific career few examples existed where quantitative models had led to new biological insight. Given the general disrespect for mathematical biology by both biologists and mathematicians, I felt discouraged from pursuing the kind of research that I believed ought to be done. This thesis marks my attempt; the insights that it provides into important biological problems will, I hope, convince the sceptics. It is fair to say that attitudes are changing already, and during the course of my DPhil quantitative biology (in the guise of *Systems Biology*) has become one of the sexy fields in science, with ample funding and great long-term potential; I am delighted to have been here at this moment in its development.

I wish to thank all those who encouraged me to take this step when a career in mathematical biology still looked comparatively bleak, and who supported me when there was as yet no more than a dream of what could be done. In particular, I wish to thank St John's College for offering me a Junior Research Fellowship which provided the grounds for unrestricted intellectual development. These fellowships are meant to give young researchers the opportunity to develop their own unique research program. In my case, I believe that the research described in this thesis could not and would not have been done without this generous support, simply because conservative funding programs would have doubted the potential of the ideas. Here I also have to thank the Mathematical Institute for awarding me one of their few EPSRC DTA studentships - irrespective of my not being trained as a mathematician and despite my having done a PhD before - in biology!

Collaborators are at the heart of any cross-disciplinary research program. I have been very fortunate to meet Iain Campbell at St John's College. His help, encouragement, criticism and support have been invaluable in developing this research program. It is impossible to list his numerous positive influences on my development, but I have to thank him, in particular, for drawing my attention to the sporulation project. The sporulation project involved a very close interaction between theory and experiment, and I wish to thank Joanna Clarkson and Michael Yudkin for a very productive collaboration and many inspiring discussions.

I am equally grateful to my other collaborators, Thomas Gruhn, Reinhard Lipowsky, and Michael Meyer-Hermann, and for the opportunity to supervise two gifted students, Giorgio Gaglia and Kimiya Minoukadeh. I also enjoyed many interesting discussions with colleagues; here I wish to name Kristy Downing in particular.

During the course of my work I have received a great deal of help and friendly support from members of the Mathematical Institute, St John's College and elsewhere. Here I have to mention Brent Doran on whose mathematical knowledge I could always rely when mine was exhausted; in particular I wish to thank him for pointing me to the method of resultants.

Last but not least, I wish to thank my supervisor, Philip Maini, for giving a trained biochemist the opportunity to join his group, and for the help, freedom, tolerance, and friendly environment that I experienced during my DPhil. I am also grateful for his thorough proofreading of my thesis; even when little of it lies within his own area of interest, his experienced eye shines through.

Contents

Abstract i

Declaration ii

Acknowledgements iii

xii

Abbreviations xiii

1 Introduction 1
- 1.1 Cell differentiation by differential gene expression . . . 2
- 1.2 Development of multicellular organisms from a single cell . . . 4
- 1.3 Compartmentalisation by cell cohesion . . . 5
- 1.4 Cell-cell communication . . . 5
- 1.5 Defence . . . 6
- 1.6 Aim of the study . . . 8

Part I: Developmental Biology - Cell differentiation i

2 Introduction to cell differentiation 11
- 2.1 The regulation of the transcription factor σ^F . . . 11
- 2.2 Models for compartment-specific σ^F activation . . . 13
- 2.3 Scope of the study . . . 14

3 A quantitative model for cell differentiation 16
- 3.1 Construction of the mathematical model . . . 16
  - 3.1.1 Principles of the model setup . . . 16
  - 3.1.2 SpoIIAB is an allosteric protein . . . 17
  - 3.1.3 Defining the regulatory network that controls σ^F activity . . . 21
  - 3.1.4 Parameter determination . . . 22
- 3.2 Verification of the model by comparison to *in vitro* data . . . 35
  - 3.2.1 The model quantitatively reproduces experimental results of σ^F·AB sensitivity to variations in AA and IIE. . . . 35
  - 3.2.2 The robustness of the mathematical model to variations in parameters. 36
  - 3.2.3 Predictions of the effect of AB·ADP·AA complex formation. . . . 37
- 3.3 Application of the model to the sporulating cell *in vivo* . . . 38
- 3.4 The mechanism behind compartment-specific gene transcription . . . 41

3.4.1 Accumulation of IIE (in association with its substrate AA-P) at the septum is sufficient to induce σ^F release in the prespore. 42
3.4.2 Formation of the σ^F-RNA polymerase holoenzyme 43
3.4.3 AB allostery enables high sensitivity to IIE 44
3.5 Economic efficiency 46
3.6 Evaluation of alternative models for σ^F activation 46
3.7 Phenotypes of mutants 55
3.8 Robustness 56
3.8.1 Robustness to variations in protein expression rates 56
3.8.2 Robustness to stochastic fluctuations after septation. 63
3.8.3 Critical parameters that determine the behaviour of the regulatory network 64
3.9 Tables 66

4 Mathematical analysis of the sporulation model 68
4.1 The Model 70
4.2 Results 73
4.2.1 A numerical bifurcation analysis of the model 73
4.2.2 Phase Plane analysis 74
4.2.3 AB·ADP·AA complex formation leads to hysteresis 78
4.2.4 AB allostery is necessary for the high sensitivity 80
4.2.5 The impact of inversely proportional affinities on the sensitivity of an allosteric protein 81
4.3 Conclusion 84

5 Discussion of the Sporulation Model 88

6 Cell differentiation in multicellular organisms 94
6.1 Introduction 94
6.2 A model for dorso-ventral morphogen patterning 97
6.3 Ligand is transported to the midline by LST 99
6.4 Determinants of the timing of peak formation 101
6.5 Abrupt increase of the ligand concentration 105
6.6 The width of the signaling peak 109
6.7 Discussion 111

Part II: Cell adhesion i

7 Introduction 117

8 A model for integrin activation 121
8.1 Ligand engagement 122
8.2 A stabilizing factor 125
8.3 The need for a positive feedback 127
8.3.1 A positive feedback that is based on the integrin-ligand pair 127
8.3.2 A positive feedback loop based on a regulatory network can enable ligand-dependent integrin activation 128

9 Discussion 131

Part III: Immunology - Antibody affinity maturation i

10 Introduction **133**
10.1 The basic principles of selection in the immune system 134
10.2 A place to meet 135
10.3 The mechanism of B cell selection 137
10.4 The mechanism of affinity discrimination 139
10.5 Scope of the study 139

11 A model for B cell selection **143**
11.1 *In silico* germinal centre simulations 143
11.2 Antibody representation 144
11.3 Cell movement 144
11.4 Cell types 145
11.4.1 FDC 145
11.4.2 Centroblasts 146
11.4.3 Centrocytes 146
11.4.4 T cells 148
11.4.5 Output cells 148
11.5 Diffusion of molecular signals and soluble antibodies 148
11.6 Initial configuration 149
11.7 Simulations and analysis of the results 150

12 Results from the GC simulation **154**
12.1 Competition for binding sites on FDC 154
12.2 A CC refractory time 155
12.3 Competition for antigen. 159
12.4 The impact of antigen masking by competing antibodies 160
12.5 Competition for T cell help 164
12.6 Conclusion 171

13 Affinity-dependent B cell signaling **174**
13.1 Overview 174
13.2 The spatial arrangement of B cell receptors 178
13.2.1 IgM cluster size distribution 179
13.2.2 The impact of ring formation on IgM cluster organization 182
13.2.3 The impact of co-receptors on IgM clustering 182
13.2.4 Igα/Igβ co-clustering 183
13.3 B cell activation by soluble monomeric antigen 185
13.3.1 The affinity and concentration dependency of antigen binding to pre-formed BCR clusters 186
13.3.2 Comparison of model predictions with experimental data 189
13.4 Surface-bound antigen at high density 191
13.4.1 Derivation of the equilibrium distribution of receptors and inhibitors 192
13.4.2 The model captures experimental results 195
13.5 What is the immunon? - Lessons from polymeric antigen 198
13.6 Conclusion 201

14 Discussion **206**
14.1 The mechanism of B cell selection in germinal centres 206
14.2 What makes antibody affinity maturation so efficient? 209
14.3 The role of soluble versus membrane antigen 211
14.4 Experiments to be done 211

15 Conclusion **213**

A Glossary **237**

B Details on calculations **241**
B.1 AA-AB binding in a non-cooperative binding mechanism 241
B.2 The Scatchard plot 241
B.3 Comments on how to estimate the septation-dependent IIE activity change 242
B.4 A simplified and dimensionless version of the Mizutani model 242
B.5 B cell activation by soluble antigen (R. Lipowsky). 244
B.6 The relation of 2- and 3-dimensional affinity constants 246

List of Figures

2.1 Regulation of σ^F release during sporulation. 12
2.2 A model of the σ^F·AB·AA complex. 13

3.1 SpoIIAB is an allosteric protein. 17
3.2 Model for the regulation of σ^F release. 20
3.3 σ^F-SpoIIAB·ADP binding. 27
3.4 SpoIIAB-σ^F binding in the presence of SpoIIAA. 29
3.5 Phosphorylation of AA. 30
3.6 The AA-P-IIE on-rate is low. 32
3.7 The kinetics of AA-P dephosphorylation. 33
3.8 The impact of Mg^{2+} on the kinetics of AA-P dephosphorylation. 34
3.9 The IIE- and AA-dependent dissociation of σ^F·AB complexes. 35
3.10 The time-dependent concentration of the sporulation proteins in the model. 40
3.11 A lower *in vivo* IIE turn-over rate. 41
3.12 A septation-dependent increase in IIE·AA-P is sufficient for σ^F release. . . 43
3.13 Predicted concentrations of RNA polymerase holoenzymes upon septation. . 44
3.14 AB allostery is necessary because AB·ADP binds σ^F with high affinity. . . 45
3.15 AB allostery reduces ATP consumption. 47
3.16 The effect of the transient genetic imbalance. 48
3.17 The role of accelerated degradation of SpoIIAB. 50
3.18 σ^F can be released compartment-specific without an increase in IIE activity. 52
3.19 The effect of IIE overexpression. 54
3.20 The protein concentration dependency of RNA polymerase(σ^F) formation. . 57
3.21 The impact of parallel and random variations in gene expression on σ^F release. 58
3.22 The impact of stochastic variation in gene expression on sporulation efficiency. 62
3.23 The robustness of the regulatory network to stochastic flucuations. 64

4.1 A simplified model of the sporulation network. 69
4.2 A numerical bifurcation analysis. 73
4.3 The a-b-c phase plane. 76
4.4 The a-c phase plane. 77
4.5 The impact of AB·ADP·AA complex formation. 79
4.6 The impact of SpoIIAB allostery. 81
4.7 Sensitivities of different allosteric mechanisms. 83
4.8 The impact of inversely proportional affinities. 84
4.9 The mechanism by which AB allostery ensures ultrasensitivity and hysteresis. 85

6.1 A schematic model of dorsoventral embryonic expression pattern. 96

6.2 An overview of the molecular interactions in the Mizutani model. 97
6.3 Ligand-receptor dynamics. 99
6.4 Ligand is transported into the midline by LST. 100
6.5 The time-dependent evolution of the protein concentrations in the midline. 102
6.6 Numerical estimates of the Sog-Tsg concentration and its curvature in the midline over time. 103
6.7 The time of peak formation. 106
6.8 The spatial distribution. 107
6.9 A two-component carrier complex is necessary for abrupt peak formation. . 109
6.10 Parameter dependencies of the model behaviour. 110

7.1 A simple model of integrin activation. 118
7.2 Four possible mechanisms for integrin activation. 120

8.1 Ligand engagement is not sufficient for integrin activation. 123
8.2 A stabilizing factor is not sufficient for ligand-dependent integrin activation. 127
8.3 A positive feedback enables ligand-dependent integrin activation. 130

10.1 A simple model of the germinal centre reaction. 136
10.2 A model for B cell activation. 141

11.1 GC kinetics in simulation and experiment. 151

12.1 Competition for FDC sites is too weak for affinity maturation. 156
12.2 A limitation of centrocyte-FDC interaction permits robust affinity maturation. 157
12.3 An affinity-independent reduction of binding probability reduces the necessary refractory time. 158
12.4 Affinity maturation is not induced by competiton for antigen. 161
12.5 Competition for antigen with fixed antigen threshold. 162
12.6 Competition for antigen with binding probability independent of presented antigen amount. 163
12.7 Antigen masking by soluble antibodies increases competition for antigen in the early phase of GC reaction. 165
12.8 Competition for T cell help allows for robust affinity maturation. 167
12.9 The impact of a prolonged time span before induction of apoptosis by T cells. 168
12.10 Competition for T cell help with reduced unspecific binding probability to FDC. 169
12.11 Combining competition for T cell help with a refractory time. 170

13.1 The segregation model for B cell activation. 175
13.2 B cell activation by soluble antigen 176
13.3 B cell activation by inhibitor expulsion. 177
13.4 Cluster length distribution. 179
13.5 Estimate of diffusion effects on the BCR-BCR binding rate. 181
13.6 Fraction of IgM bound to Igα-Igβ. 184
13.7 Antigen concentration and affinity dependency of B cell activation by soluble monomeric antigen. 188
13.8 Affinity dependent fraction of IgM pairs that interact via Igα/Igβ heterodimers. 190
13.9 Affinity dependent receptor and inhibitor density in the contact zone. . . . 196

List of Tables

3.1 Kinetic rate constants employed in the *in vitro* simulation. 66
3.2 Kinetic rate constants employed in the *in vivo* simulation. 66
3.3 Mutant phenotypes *in vivo* and *in silico*. 67

4.1 Kinetic rate constants and protein concentrations employed in the simplified sporulation model. 72

6.1 Kinetic rate constants and protein concentrations employed in the Mizutani model. 98

11.1 Collection of all parameters of the model for the GC *in silico* simulation. . 153

B.1 Kinetic rate constants and protein concentrations employed in the simplified dimensionless form of the Mizutani model. 244

List of Publications

Below is a list of publications that are based on work presented in this thesis.

1. **Iber D**, Clarkson J, Yudkin M, Campbell ID, The mechanism of cell differentiation in *Bacillus subtilis*, ***Nature*** (2006); 441, 371-374

2. **Iber D**, A computational analysis of the impact of the transient genetic imbalance on compartmentalized gene expression during sporulation in *Bacillus subtilis*, ***J Mol Biol*** (2006); 360, 15-20

3. **Iber D** A quantitative study of the benefits of co-regulation using the *spoIIA* operon as an example, ***Molecular Systems Biology*** (2006); 2, 43

4. **Iber D**, Campbell ID., Integrin activation - the importance of a positive feedback. ***Bulletin of Mathematical Biology*** (2006); 68, 945-956

5. Meyer-Herrmann M, Maini PK, **Iber D**, An analysis of B cell selection mechanisms in germinal centres ***Mathematical Medicine and Biology*** (2006); 23, 255-277.

6. **Iber D**, T. Gruhn, Organization of B cell receptors on the cell membrane, ***IEE Proc Systems Biology***; 153, 401-404

7. **Iber D**, G. Gaglia, B The mechanism of sudden stripe formation during dorso-ventral patterning in Drosophila, ***J. Math Biol***, in press

8. **Iber D**, The role of allostery in the regulation of cell differentiation in Bacillus subtilis, under review with ***PLoS Computational Biology***

9. **Iber D**, Gruhn T, Lipowsky R, Maini PK, B cell activation and affinity discrimination by receptor segregation?, under review with ***Biophysical Journal***

Some of the work has appeared in reviews

- Beale R., **Iber D**. Somatic evolution of antibody genes in 'The Implicit Genome', Editor: L.H. Caporale, Oxford University Press (2006)

- **Iber D**, The mechanistic basis of compartmentalized gene expression in *Bacillus subtilis*. Natural Computing (2005); 4:325-338

Abbreviations

AA SpoIIAA

AB SpoIIAB

Ab antibody

Ag antigen

ADP adenosine diphosphate

AFC antibody forming cell

ATP adenosine triphosphate

BCR B cell receptor

CB centroblast

CC centroccyte

DNA deoxyribonucleic acid

Dpp Decapentaplegic

IIE SpoIIE

FDC follicular dendritic cell

FRET fluorescence resonance energy transfer

GC germinal centre

Ig immunoglobulin

MHC major histocompatibility complex

NMR nuclear magnetic resonance

pMHC peptide-loaded MHC

RNA ribonucleic acid

Sog Short gastrulation

SPR surface plasmon resonance

Tsg Twisted gastrulation

Tld Tolloid

TCR T cell receptor

Chapter 1

Introduction

One of evolution's most important experiments was the creation of multicellular organisms (Gilbert, 2000).

While unicellular organisms are impressively successful in adapting to a variety of different environments, multicellular organisms have many advantages over unicellular organisms because collaboration and division of labour enables them to exploit resources that are difficult to access for single cells. The association of unicellular organisms into colonies is likely to have been an early step in the evolution of multicellular organisms. The formation of truly multicellular organisms then required increasing cell specialization and division of labour and eventually 'led to the complexity and diversity observed in the many types of cells that make up present-day plants and animals, including human beings'[1]. Instead of duplicating each somatic cell, reproduction of multicellular organisms only requires the creation of a single cell, the fertilized egg, from which the offspring develops. The developmental program involves a large number of mitotic cell divisions and subsequent differentiation of cells into many different cell types. In a few cases, such as the mammalian red blood cell, cell differentiation involves loss of genetic material but the majority of cells retain the original genetic information of the fertilized egg and differentiate into different directions by changing their program of gene expression. A major challenge in developmental biology is to understand how different programs of gene expression are induced, a problem that we consider in the first part of this thesis.

[1] quoted from (Cooper, 2000)

1.1 Cell differentiation by differential gene expression

The ability to change the program of gene expression is inherent to all forms of life and enables organisms to adapt to changing environmental conditions and needs. Cell differentiation requires not only a change in gene expression in response to cues from the environment or neighbouring cells but also the maintenance of expression programs once these cues have disappeared. Emerging characteristics of regulatory networks that govern cell differentiation are therefore bistability and hysteresis (Ferrell, 1999; Slepchenko & Terasaki, 2004).

While cell differentiation is much more common in eukaryotes it can also be observed in prokaryotes which provide a paradigm for cell differentiation because they are much easier to study. The principles of gene regulation are the same in prokaryotes and eukaryotes although gene regulation is much more complex in the latter and the packaging of DNA into chromatin provides for additional regulatory potential. This is likely to explain why eukaryotic rather than prokaryotic cells are the building blocks of complex multicellular organisms.

Both in prokaryotes and eukaryotes gene transcription is performed by the RNA polymerase which is recruited to the promotor that precedes genes. The eukaryotic RNA polymerase alone cannot initiate transcription at the promotor and also the prokaryotic RNA polymerase needs to form a holoenzyme with transcription factors to achieve efficient transcription. In prokaryotes so-called σ factors bind to the RNA polymerase and mediate the contact with two conserved hexamers in the -10 and -35 DNA elements of the promoter[2]. Once established, the closed promotor complex melts the DNA duplex around the -10 region and transcription is initiated. After about 9-12 nucleotides of RNA have been synthesized, a conformational change results in the dissociation of the σ factor and leads to a highly processive elongation complex (Borukhov & Nudler, 2003).

Gene transcription can be regulated at various stages. The regulation of the different σ factors enables the control of gene expression because different σ factors direct the RNA

[2]The numbers refer to the distance of these elements from the first transcribed DNA base (+1).

polymerase to different sets of promotors/genes. Moreover, binding of the RNA polymerase holoenzyme to the promotor can be blocked by binding of a repressor to an operator sequence contained within the promotor or can be enhanced by binding of activator proteins to the promotor sequence.

In eukaryotes transcription factors need to assemble at the promotor to enable transcription, and regulatory sequences that are far away from the promotor can still regulate eukaryotic gene expression such that a single promotor can in principle be regulated by an almost unlimited number of regulatory interactions; insulator sequences are required to limit the effects of regulatory sequences. Eucaryotes can co-express or regulate groups of genes by a complex signalling network while prokaryotes, in general, organize such genes in an operon so that all genes are under the control of the same promotor. The pattern of gene expression can be maintained by feedback signalling even once the original cues and influences have disappeared.

Daughter cells of differentiated cells, in general, inherit the specialized character of the cell. The necessary information can be passed on either by cytoplasmic proteins that maintain the feedback signalling or, in eukaryotes, also by the packaging of the chromatin. The latter can involve a variety of mechanisms. Gene regulatory proteins and general chromatin structural components may bind cooperatively to the DNA strand such that the fraction of proteins that is inherited by each DNA strand is sufficient to recruit the full set of proteins from the cytoplasmic pool. Alternatively, the chromatin proteins or the DNA itself may be modified enzymatically. DNA methylation patterns are maintained after cell division by *de novo* DNA methyltransferases which methylate the cytosines in CG (cytosine-guanine) sequences on the newly synthesized strand if the cytosines on the parental strand are methylated. Methylation appears to maintain genes in an inactive state.

Because each cell can 'remember' earlier cues the final expression program is not the consequence of the final environment but is determined by the sequence of cues received over the entire lifespan. Thus the full complexity of the body is specified only gradually

during the development of a multicellular organism.

1.2 Development of multicellular organisms from a single cell

The need to generate the many different cell types of an organism from a single cell poses a challenge in the reproduction of multicellular organisms. Cell division leads to an exact copy of the mother cell (up to randomly occurring mutations), and mechanisms therefore needed to evolve to subject the two daughter cells to a different program of cell differentiation despite their identical content of genetic and, in principle, cellular material including proteins and lipids. The simplest possible guidance factors are environmental cues. In particular, once at least two different cell types have been established the differentiation of further cells can be directed by the influences of these differentiated cells. As studied thoroughly in appropriate model organisms such as the fruit fly *Drosophila* and discussed in the first part of this dissertation, the mother organism can generate such a polarized environment to guide cell differentiation and development in the offspring. Looked at from an evolutionary point of view this is of course only possible once a mother organism has evolved. Therefore mechanisms must have evolved at an earlier evolutionary stage that enabled sister cells to follow different paths of development in the absence of any environmental clues.

Asymmetric cell division is a conserved mechanism that enables different cell fates during development. Dividing the cell at the side rather than at the midline leads to differently-sized daughter cells, and the concentration of molecular components can become imbalanced between the two compartments by use of sophisticated mechanisms and even a transient genetic imbalance can arise in prokaryotes (Frandsen *et al.*, 1999). The mechanism by which cells divide asymmetrically has not yet been elucidated. Prokaryotes and eukaryotes necessarily employ very different mechanisms since the position of the mitotic spindle (which does not exist in prokaryotes) is crucial in eukaryotes (an asymmetric position within the cell leads to daughter cells of unequal size (McCarthy & Goldstein, 2006)). A combination of experimental and theoretical studies of cell division in *E.coli* has recently improved

our understanding of bacterial mid-cell division. The high accuracy by which the mid-plane is defined is achieved by a sophisticated oscillatory mechanism which involves only three proteins MinC, MinD, and MinE (Howard *et al.*, 2001; Meinhardt & de Boer, 2001; Kruse, 2002; Huang *et al.*, 2003; Howard & Kruse, 2005). However, *E.coli* does not divide asymmetrically, and *Bacillus subtilis* employs a slightly different mechanism to define the midplane such that the *E.coli* models cannot be extrapolated to *Bacillus subtilis* (Howard, 2004). Finally, even if cells can divide asymmetrically, how are cell-fate determinants then partitioned unequally? Again, different mechanisms are invoked in different organisms, and in Part I of the dissertation we will study spore formation in *Bacillus subtilis* as an example.

1.3 Compartmentalisation by cell cohesion

Humans are made of approximately 10^{14} cells (Stryer, 1995). These need to organize into compartments and controlled internal environments in which specialized functions can be performed by differentiated cells. The simplest way of binding cells together is to prevent (full) cell detachment after division, and in the green algae *Volvox* and in higher plants cells are indeed connected by cytoplasmic bridges. These are unusual in animals which rely on large extracellular matrix molecules (made of proteins and sugars) which form a loose meshwork that binds the cells together. Multicellular sheets (epithelia) are built by side-to-side attachments between cells. Tight binding between cells is, however, often insufficient; cells need to retain the ability to loosen themselves and to migrate. Such flexibility is achieved by employing proteins whose binding strength can be regulated. The most important class of proteins for the attachment of cells to the extracellular matrix are integrins, and their regulation will be discussed in detail in the second part of the thesis.

1.4 Cell-cell communication

The large advantage of multicellular organisms is their opportunity to divide labour between cells such that each can specialize in a particular function. This enables a multicellular

organism to evolve highly sophisticated means to acquire and process nutrients, to move and defend themselves, to reproduce and to receive and use information, which may even enable it to work out strategies to increase performance. Division of labour between cells requires cells to communicate with each other. This is achieved by production of extracellular signal molecules that bind to cell receptors. In general these receptors are expressed on the cell surface but if the signal molecule is sufficiently small and hydrophobic then it may cross the cell membrane and bind to intracellular receptors. In most cases signalling molecules are secreted and diffuse either only in the local tissue (paracrine signalling) or are transported by the bloodstream (endocrine signalling). In the case of autocrine signalling, signalling molecules can bind back to receptors on the secreting cells. This is an important feedback mechanism during development. In some cases the acquisition of signal molecules requires cell contacts such that the signal molecule can be targeted to a cell as observed in neurological and immunological synapses or in the case of gap junctions.

Independent of its delivery, the mechanical binding of ligand needs to be translated into a chemical or electrical signal. This can be accomplished by ligand induced conformational changes which may either affect the conductivity of ion channels or enable enzymatic reactions, as is the case of G protein coupled receptors. Alternatively, ligand binding can induce receptor clustering which brings together kinases that can autophosphorylate proximal substrate and thus initiate signalling, as observed for EGF receptors (Schlessinger, 2002). By studying integrins (Part II) and the B cell receptor (Part III) we will show that both a conformational change or receptor clustering are not always sufficient to translate the signal and that more intricate mechanisms can be necessary.

1.5 Defence

Organisms, no matter how simple, seem to be liable to invasion by even simpler forms of life that exploit their resources. Multicellular organisms face a high cost in that the loss of only a fraction of their constituents can mean death to the entire organism. On the other hand

they can evolve more elaborate defence strategies by dividing the work. A successful defence requires a reliable discrimination between self and non-self and a subsequent elimination of the non-self. In higher organisms, this task is carried out by the immune system which also serves to supervise the body's cell ensemble and to eliminate misbehaving cells that may otherwise lead to cancer or other problems.

The immune system employs two different strategies to identify non-self and abnormal cells. The innate immune system relies on the quick recognition of common surface patterns of microorganisms while the adaptive immune system is reactive to a wide range of non-self and abnormal pattern but requires days to weeks to raise an effective defence. The innate immune system can act as a first line of defence against most invaders while leaving the complete clearance of the invader (especially of those that escaped by mutating the common surface pattern) to the adaptive immune system. Effectors of the innate immune system are phagocytes which can eliminate the invader by internalization and subsequent digestion and the complement system which leads to the lysis (disintegration) of invader cells.

There are two different types of adaptive immune responses, the humoral and the cellular immune response; they are triggered by different infections. If the infection enters cells (as in the cases of viruses and some bacteria), it is hidden from most monitoring which only considers extracellular parts of the body. Specialised cells, termed T cells, can nevertheless identify the infected cells and kill them thus prohibiting the spreading of the infection. This response is called the cellular immune response.

Invaders which reside outside cells, e.g. swimming in the blood or in the lymph, can be recognised by either components of the innate immune system or by those of the humoral immune response. As already mentioned, the innate immune response can only react against a subset of invaders while the effector cells of the humoral immune response (B lymphocytes) are capable of raising an immune response against almost every foreign compound. The main players of the humoral immune response are the so-called B cells which produce antibodies. Antibodies are proteins that can firmly and specifically bind to the invader.

Binding of the antibody prevents the invader from interacting with other body structures, a process called neutralisation. Further on, antibodies mark the object to which they bind for destruction by either phagocytes or the complement system. In order to only attack the invader and not body cells themselves, it is indispensable that antibodies bind very specifically. In addition, they need to bind very firmly since rash detachment would not allow the destruction of the invader. How B cells collaborate with other cells to manufacture these highly specific proteins with the extraordinary affinity for its target is the subject of the third part of this dissertation.

1.6 Aim of the study

In this thesis a wide range of mathematical modelling techniques are employed in order to explore critical steps in the development and evolution of multicellular organisms, that is cell differentiation (Part I), cell adhesion (Part II), and division of labour by example of the immune system (Part III). In the case of cell differentiation we will first concentrate on the evolutionary problem of how daughter cells can differentiate into two different cell types without any cues from the environment. Sporulation in *Bacillus subtilis* serves as a paradigm for such a process, and in the first part of this thesis we show how asymmetric cell division can trigger two different gene transcription programs in the two compartments. We will then turn to the problem of how maternal cues can guide the developmental patterning process of a multicellular off-spring by example of dorso-ventral patterning during the development of the *Drosophila* embryo.

The development and functioning of multicellular organisms requires the controlled migration and adhesion of cells. Cell adhesion strongly relies on integrins and in the second part of this thesis we develop a mathematical model of integrin regulation to explain these processes.

Multicellular organisms have the great advantage that they can divide labour. The defence system that multicellular organisms had to evolve in order to cope with infectious and much faster reproducing microorganisms and viruses provides a good example. A large fraction of blood cells is devoted to protection from infections and we will concentrate on a small subset that is important in the production of high affinity antibodies, the humoral arm of the immune response. The system is analysed on the cellular and molecular level in order to understand both the selection of single cells for certain tasks as well as the information processing of each cell within the network necessary to evaluate its aptitude for the task.

Part I: Developmental Biology - Cell differentiation

Chapter 2

Introduction to the regulation of cell differentiation in *Bacillus subtilis*

A key question in developmental biology is how two sister cells with identical genomes follow different patterns of gene expression. The sporulation of *Bacillus subtilis* is an exceptionally favourable system for studying this question. Early in sporulation the cell divides asymmetrically into two compartments, a smaller prespore and a larger mother-cell (Fig. 2.1A). These remain attached but initiate different programmes of transcription, using compartment-specific transcription factors (sigma factors) that associate with the RNA polymerase and direct the complex to the relevant gene promotors (Hilbert & Piggot, 2004). The first of these, σ^F, is crucial, since its correct activation is essential for regulating the other sigma factors of sporulation. σ^F is inactive in the pre-divisional cell and the mother-cell where it is trapped in a complex with SpoIIAB, but is activated in the prespore where it associates with the RNA polymerase. While the pathways that lead to σ^F dissociation are well-defined (Fig. 2.1B), it is not clear how σ^F association with the core RNA polymerase is restricted to the prespore (Hilbert & Piggot, 2004).

2.1 The regulation of the transcription factor σ^F

σ^F regulation depends on three other proteins, SpoIIAB (AB), SpoIIAA (AA) and SpoIIE (IIE). AB keeps σ^F in an inactive complex from which it is released upon binding of SpoI-

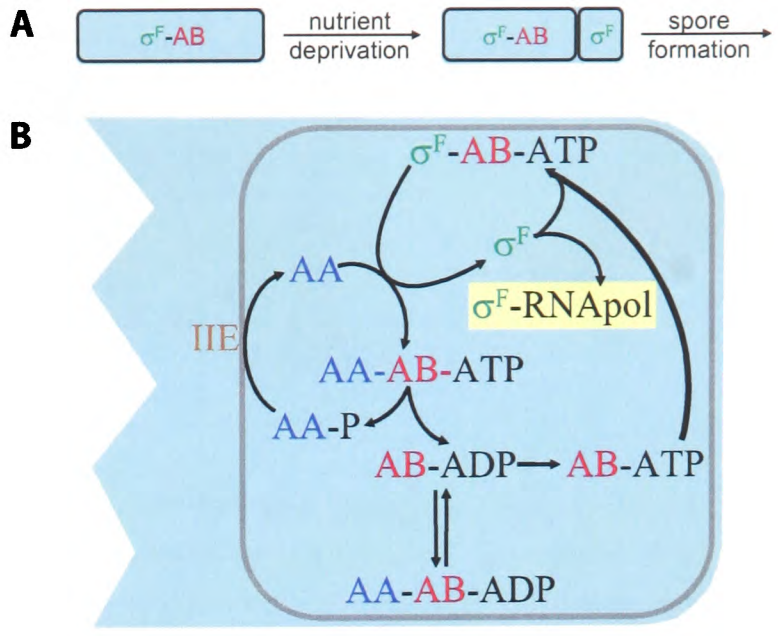


Figure 2.1: **Regulation of σ^F release during sporulation.** **(A)** Nutrient deprivation triggers asymmetric septation; the smaller, prespore compartment develops into a spore. **(B)** Simplified regulatory network that controls σ^F activity in the prespore; for details see text. Figure is courtesy of I.D. Campbell.

IAA (AA). Bound AA is phosphorylated by the kinase AB. This inactivates AA and its reactivation requires dephosphorylation by the phosphatase SpoIIE (IIE). Crystallography has revealed the details of these interactions (Fig. 2.2). One molecule of σ^F binds asymmetrically across the two subunits of the AB dimer (Campbell *et al.*, 2002). The binding of σ^F prevents access of SpoIIAA (hereafter referred to as AA) to one monomer of AB, but allows docking of AA on the other monomer (Ho *et al.*, 2003). Steric and electrostatic clashes are caused by the docking of AA, and σ^F is subsequently displaced from AB (Masuda *et al.*, 2004; Ho *et al.*, 2003). AA binds across the nucleotide-binding pocket of AB, and is phosphorylated when this binding pocket contains ATP, yielding inactive phosphorylated AA (AA-P) and AB·ADP. AB·ADP can either be sequestered in an AA·AB·ADP complex or exchange ADP for ATP. Free AB (in both its ATP and ADP forms) can rebind σ^F, and sustained σ^F release is thus expected to require reactivation of AA-P by SpoIIE-mediated dephosphorylation (Magnin *et al.*, 1997).

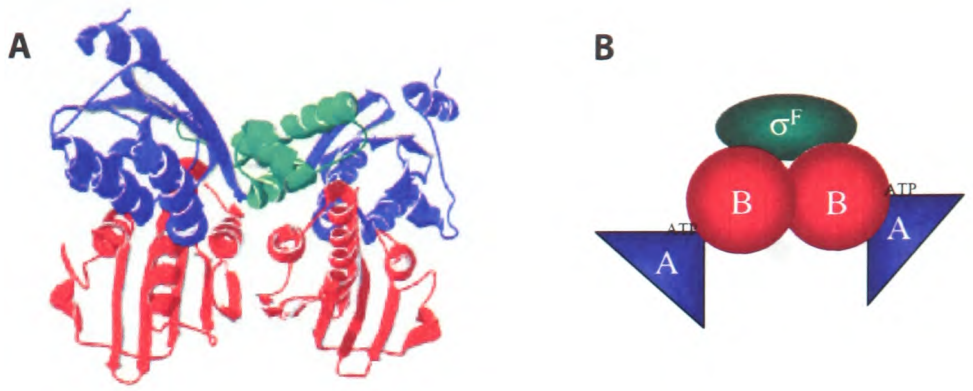


Figure 2.2: **A model of the σ^F·AB·AA complex.** **(A)** A model of the σ^F·AB·AA complex, obtained by superimposing the crystal structure of σ^F in complex with AB·ADP (Campbell *et al.*, 2002) and the structure of AA in complex with AB·ATP (Masuda *et al.*, 2004); note that each AB monomer can bind one AA while σ^F binds to both monomers; the binding sites of AA and σ^F partly overlap so that binding of AA reduces the affinity of σ^F for AB. **(B)** Simplified symbols, representing the component proteins in (A); simple variants of these symbols are used in the complete reaction scheme depicted in Fig. 3.2. Figure is courtesy of J. Clarkson and I.D. Campbell.

2.2 Models for compartment-specific σ^F activation

As σ^F-holoenzyme appears in the prespore and not in the mother-cell, the attack of AA on the σ^F·AB·ATP complex must be compartment-specific. Although this specificity is crucial to the success of sporulation, its mechanism is not clear. One suggestion is that, since the volume of the mother cell is at least four-fold greater than that of the prespore, IIE, which is displayed only on the asymmetric septum, will have higher phosphatase activity in the smaller compartment, leading to a greater concentration of AA in the prespore than in the mother cell (Duncan *et al.*, 1995). However, compartment-specific σ^F activation is still observed when IIE cannot accumulate on the septum (Arigoni *et al.*, 1999), and several other mechanisms have been proposed (Hilbert & Piggot, 2004).

These include effects of the transient genetic imbalance which arises after septation, when only about 30% of the chromosome is initially included in the prespore; the remaining 70% is imported only 10-20 minutes after septum closure (Wu *et al.*, 1998*b*). Given that the origin of replication (ori) is anchored at the poles of the cell, it is always the same fraction of the chromosome that is excluded and this contains the *spoIIA* operon which encodes the genes for SpoIIAA, SpoIIAB, and σ^F. Expression of these proteins in the

prespore is therefore impossible immediately after septation and it has been argued that the rapid degradation of unbound AB (Pan *et al.*, 2001; Dworkin & Losick, 2001) may sufficiently reduce the AB concentration in the prespore such that reassociation of σ^F and AB is prevented. A further proposed result of the genetic imbalance is the degradation and loss of a IIE inhibitor from the prespore, which would further accelerate σ^F release (Frandsen *et al.*, 1999). The nature of such an inhibitor is, however, elusive, and while the concentration of IIE on the septum and the initial exclusion of *spoIIAB* from the prespore have both been shown to be important for successful sporulation, interference with either one of them does not abolish sporulation (Dworkin & Losick, 2001; Arigoni *et al.*, 1999).

No model yet explains how these small and transient differences act together to maintain the release of σ^F for at least 1h. Moreover, without a quantitative analysis it is unclear whether these processes are sufficient for the initiation of sporulation or whether other, still unidentified, factors play a role (Hilbert & Piggot, 2004). Another quantitative difficulty involves the binding of σ^F to the core RNA polymerase. In the pre-divisional cell nearly all the RNA polymerase is in the form of σ^A-holoenzyme; thus the formation of σ^F-holoenzyme requires σ^F to compete with σ^A. But the affinity of core RNA polymerase for σ^A is 25-fold greater than for σ^F, and the maximum concentration of σ^F is only about two-fold greater than that of σ^A (Lord *et al.*, 1999). So how can σ^F-holoenzyme be formed in the prespore?

2.3 Scope of the study

The scope of this study is to explain how the compartment-specific formation of σ^F-holoenzyme is achieved. We employ a combination of experimental and mathematical modelling tools and derive the regulatory circuit that controls σ^F release. The quantitative model identifies the difference in volume between the two cell types as the primary trigger for determining cell fate. It shows that this effect depends on the allosteric behaviour of a key protein kinase and on a low rate of dephosphorylation by the corresponding phosphatase; both predicted effects are confirmed experimentally. In a mathematical analysis of

a simplified version of the detailed model we further show how allostery enables ultrasensitivity, bistability and hysteresis in this small protein network.

The value of any mathematical model depends critically on the accuracy of the parameters used. This study has benefited greatly from the close interaction of theory and experiments and the large body of data available from the literature. The resulting model accounts for numerous published results and correctly predicts the phenotype of essentially all mutants for which the biochemical effect of the mutation is known.

The high accuracy of the model enabled us to reveal a number of further, sophisticated features of the regulatory system that optimise its ability to regulate the initiation of sporulation. For example, it is extremely efficient in its use of ATP because formation of AB·ADP·AA complexes prevents σ^F from re-binding to AB after dissociation of σ^F·AB·ATP. Several mechanisms are employed to control the ratios of σ^F and its regulatory proteins as well as the timing of septation; as a result the system is highly robust to stochastic fluctuations in gene expression, while remaining very sensitive to small changes in the concentration of IIE and AA-P. Moreover, spontaneous initiation of sporulation is prevented by keeping the concentrations of σ^F and its regulators low in the vegetative cell. The model also makes predictions about a number of features whose role had been unclear, including the accelerated degradation of AB (Arigoni *et al.*, 1999; Pan *et al.*, 2001; Dworkin & Losick, 2001), the transient genetic asymmetry (Frandsen *et al.*, 1999; Dworkin & Losick, 2001) and the pre-septational AB·ADP·AA complex formation (King *et al.*, 1999; Carniol *et al.*, 2004).

Chapter 3

A quantitative model for the regulation of cell differentiation in *Bacillus subtilis*

3.1 Construction of the mathematical model

3.1.1 Principles of the model setup

Based on the scheme depicted in Figure 2.1B, the mathematical model was obtained by translating the interactions into sets of ordinary differential equations (ODEs). Thus the interaction $X \rightleftarrows Y \rightarrow Z$ would translate into the following set

$$\begin{aligned} \dot{X} &= k_{YX}Y - k_{XY}X \\ \dot{Y} &= k_{XY}X - (k_{YX} + k_{YZ})Y \\ \dot{Z} &= k_{YZ}Y \end{aligned}$$

where the dot denotes time derivative and k_{ij} is the reaction rate constant from i to j. Once good estimates had been obtained for all the reaction rate constants this set of stiff, non-linear ODEs was solved using the Matlab solver ode15s, which uses an implicit linear multistep algorithm (1^{st} order with an error of the order of $(\Delta t)^5$, where Δt is the time step). The reaction rates k_{ij} were based on the literature or on new experimental data that was obtained by Joanna Clarkson in the laboratory of Michael Yudkin in the Biochemistry Department in Oxford.

3.1.2 SpoIIAB is an allosteric protein

The first result from estimating the reaction rate constants based on published and new data was the insight that AB is an allosteric protein (see Fig. 3.1A for an explanation of allostery). Early hints to the allosteric behaviour of AB came from the failure to fit fluorescence quenching data on AB-AA binding with the non-cooperative binding mechanism of published models (Fig. 3.1B). Thus when 1 μM AB-F97W, a fluorescent derivative of AB (Clarkson *et al.*, 2004*c*), was mixed with different AA concentrations, less than an equimolar AA concentration was needed to quench half the fluorescence (Fig. 3.1 B, circles). The effect was even stronger with the lower affinity AA mutant, AA-S58A, (Fig. 3.1 B, squares). A non-cooperative binding mechanism considers only one AB conformation, that is only one site of the reaction scheme (either balls or squares) in Figure 3.1A, and accordingly

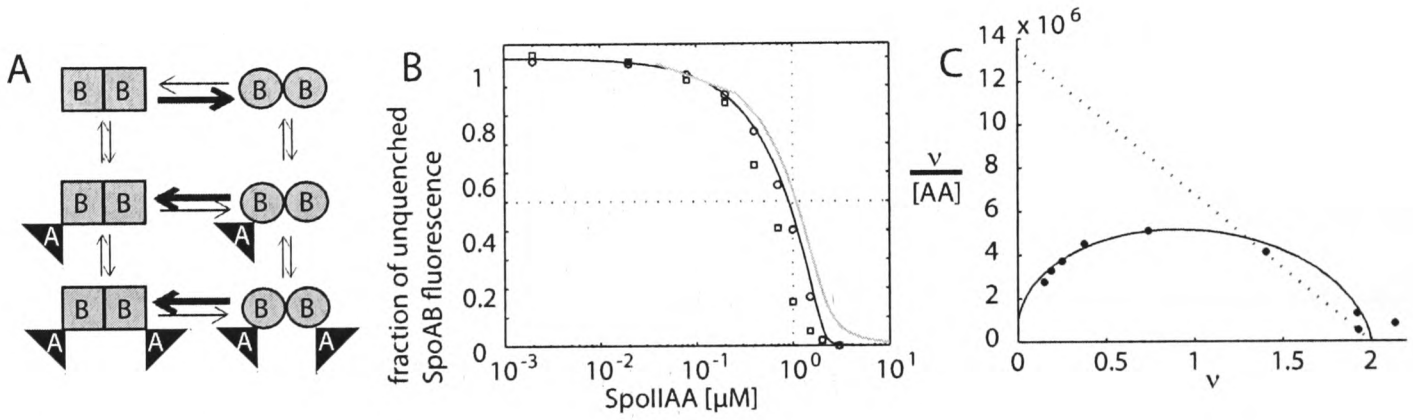


Figure 3.1: **SpoIIAB is an allosteric protein. (A)** AA can bind to either of the two binding sites on the dimeric kinase AB. In the absence of AA, AB exists predominantly in its low affinity conformation (balls). Binding of the first AA shifts the equilibrium to the high affinity conformation such that binding of the second AA is facilitated. **(B)** Fraction of AB (1 μM total) unbound as a function of the concentration of AA, as determined by fluorescence quenching experiments with fluorescent mutant AB-F97W and wildtype AA (○) in the presence of 100 μM ADP or the non-phosphorylatable mutant A58S (□) in the presence of 100 μM ATP (Clarkson *et al.*, 2004*c*). The points show previously unpublished experimental results; the line represents the binding curve expected from the kinetic constants employed in the mathematical model based on Figure 3.2 (which includes allostery of AB). **(C)** Scatchard plot obtained by determining the fraction of bound AB (ν) when 4μM AA-S58A is mixed with different concentrations of AB (0.1-20 μM). The points show previously unpublished experimental results; the lines represent the predicted Scatchard plot based on the assumption that AB is an allosteric protein (continuous line) or non-allosteric (dotted) with an affinity for AA-S58A·AB 3.7 times less than for AB·AA (Table B.1). For details see text. Note that a 1.3-fold higher AB concentration than measured had to be used to keep $\nu \leq 2$.

AB quenching can only be achieved by direct binding of AA to an AB monomer with the consequence that at least an equimolar AA concentration would be required to quench half of the fluorescence of the AB dimers. This is also apparent from the theoretical prediction of the curve for an AB-AA association constant $K = 40$ nM (Magnin *et al.*, 1997) (Fig. 3.1 B, grey line); for details on the calculation see Appendix B.1.

A cooperative binding mechanism on the other hand can fit the experimental data (Fig. 3.1B, black line). This binding mechanism is described mathematically by translation of the scheme in Fig. 3.1A into a set of ordinary differential equations (ODEs). As can be seen from Fig. 3.1A the model comprises 7 variables and 14 reactions which are governed by 8 different kinetic rate constants given in Table B.1 (for their derivation see below). In order to fit the binding data we have to assume that the fluorescence is quenched both when AA is bound and when AB is in its high affinity conformation (squares in Fig. 3.1A). A facilitated conformational change of AB into the high affinity conformation upon binding of the first AA then results in quenching of the fluorescence on the second non-bound monomer. Note that the fit between model and experiment could be further improved if the bias towards the high affinity conformation when one AA is bound was slightly higher than estimated by surface plasmon resonance (SPR).

A Scatchard analysis confirmed the allosteric behaviour of AB (Fig. 3.1 C). In a Scatchard plot the fraction of bound AB ν over the concentration of AA is plotted versus ν. In the case of a non-cooperative binding mechanism one obtains a straight line with slope $-K_s = -\frac{[AA][AB]}{[AB \cdot AA]}$ and an intersection at $\frac{n}{K_s}$ with the vertical axis ($\nu = 0$) (Fig. 3.1 C, dotted line), where n is the number of independent binding sites on AB. In the case of a positive cooperative binding mechanism, on the other hand, the curve is concave-down (Fig. 3.1 C, solid line); see Appendix B.2 for an explanation.

In order to determine the shape of the experimental Scatchard plot for AA-AB binding Joanna Clarkson determined the concentration-dependent fraction of AA that was bound to AB, ν, using SPR as has been described before (Magnin *et al.*, 1997). The concentration

of free AA in solution was determined with the use of AB as a reporter immobilised on the sensor chip. A standard curve of AA concentration against response units was produced with known concentrations of AA. The amount of free AA in AB·AA mixtures was then determined by comparison with this standard curve. The amount of bound AA was calculated from the total concentration of AA in the mixture. The experiment had to be carried out with the AA-S58A mutant to avoid AA phosphorylation by trace amounts of ATP. The mutant's slightly lower affinity for AB (Magnin *et al.*, 1997) was an advantage because the effects of positive cooperativity are therefore observable already at higher concentrations of free AA; this allowed us to measure a full Scatchard plot within the range of sensitivity of the equipment which modelling predicts would not have been possible for the wildtype. Note that the AA/AB ratio is apparently overestimated by a factor of about 1.3, presumably because of systematic errors in the determination of protein concentrations, and these probably explain the $\nu > 2$ result.

A further experimental finding in favour of AB allostery is that SPR binding kinetics obtained with AB bound to the sensor chip are better fitted by an allosteric model (see below). Consistent with the hypothesis that AB is an allosteric protein, crystallographic structures of AB in complex with either σ^F or AA (Campbell *et al.*, 2002; Masuda *et al.*, 2004) have shown it to be a flexible molecule. However, conformational changes that could account for the differences in the allosteric states are not visible on comparing the crystal structures of the AA-bound and the σ^F-bound forms. Since it is possible that this result might be due to constraints imposed on the AB molecule by crystallisation, Joanna Clarkson and Michael Yudkin have studied conformational changes in solution by the use of steady-state fluorescence and FRET (Clarkson and Yudkin, submitted for publication). The results reveal that AB can adopt alternative conformations that are not visible in the crystal structures, which could correspond to the different forms described here.

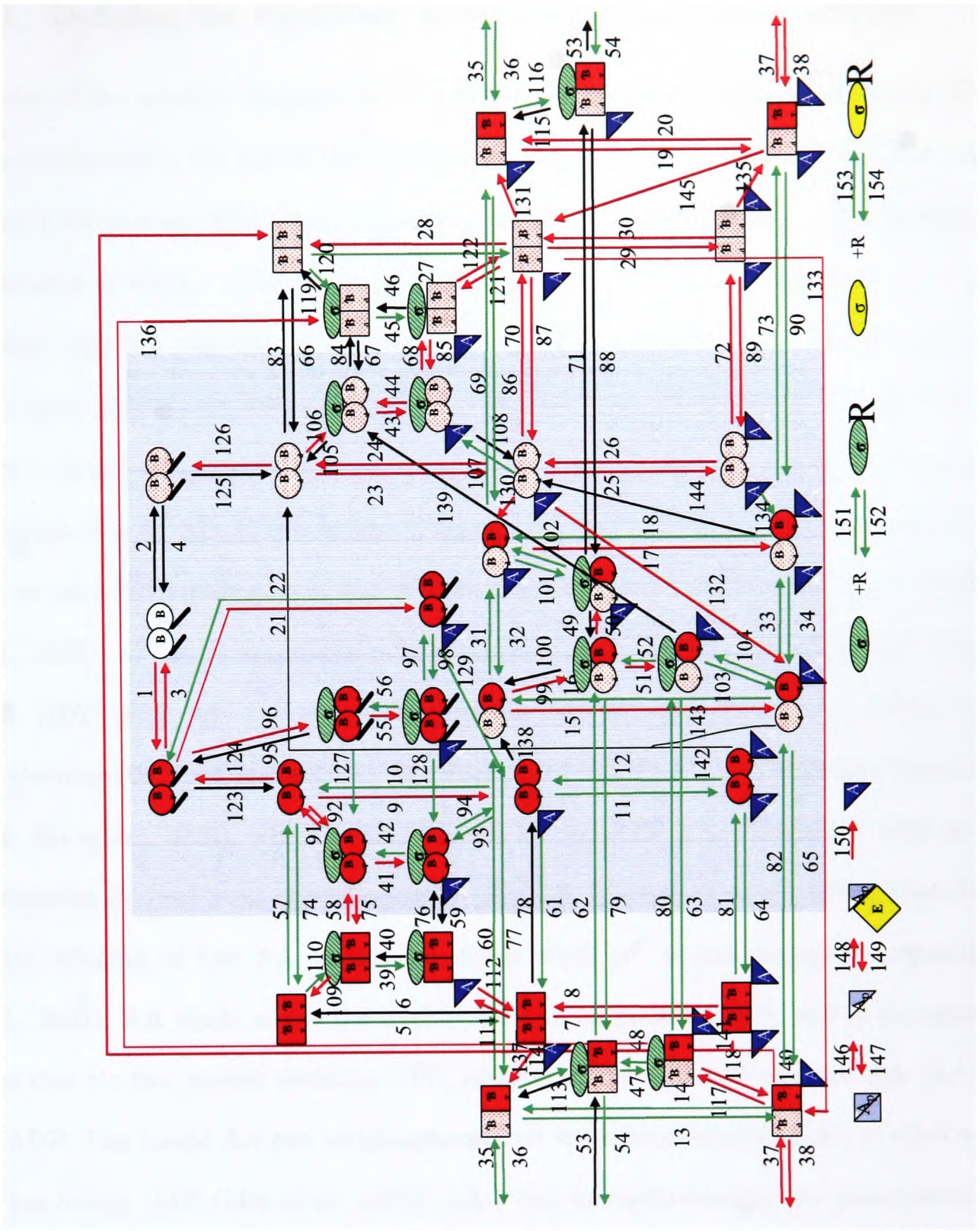


Figure 3.2: **Model for the regulation of σ^F release.** The symbols represent simple variants of those in Figure 2.2B. B refers to SpoIIAB (red squares and circles), A to SpoIIAA (blue triangles), E to SpoIIE (yellow square) and R to the RNA polymerase core enzyme; σ^F is depicted as a green oval, σ^A as a yellow oval. The SpoIIAB conformation that binds SpoIIAA with low affinity (tense state (Fersht, 1998)) is depicted as circles and the high affinity (relaxed (Fersht, 1998)) state as squares. ATP-bound SpoIIAB is depicted as a filled icon, ADP-bound SpoIIAB as a dotted icon, and nucleotide-free SpoIIAB as a white icon. Green arrows represent reactions to which the model is insensitive, red arrows those to which the model is highly sensitive, black arrows those that are considered neither sensitive nor insensitive. See section 3.2.2 for details.

3.1.3 Defining the regulatory network that controls σ^F activity

Because of the positive cooperative of AB-AA binding the number of reactions that need to be considered in the model increases considerably as a comparison of the basic model in Figure 2.1B and our final model scheme in Figure 3.2 demonstrates. The shaded part of the scheme in Figure 3.2 summarizes the interactions of one AB conformer and therefore includes only the well-known reactions that have been reviewed extensively (see Hilbert and Piggot (2004) and references therein). In brief, the binding of σ^F to AB·ATP (arrow 91/92 - all following numbers in round brackets refer to reactions in Fig. 3.2) leads to the formation of a σ^F·AB·ATP complex (Duncan & Losick, 1993). σ^F in this complex cannot bind to core RNA polymerase and is thus termed inactive (Duncan & Losick, 1993; Min *et al.*, 1993). σ^F binds asymmetrically across the two subunits of the AB dimer (Campbell *et al.*, 2002) (Fig. 2.2) and is rapidly displaced (93/94) (Clarkson *et al.*, 2004*a*) by steric and electrostatic clashes caused by the docking of SpoIIAA (AA) (41/42) (Masuda *et al.*, 2004; Ho *et al.*, 2003), which initially forms σ^F·AB·ATP·AA. Consistent with structural information derived from crystallography (Fig 2.2; (Campbell *et al.*, 2002; Masuda *et al.*, 2004)), binding of two AA to the AB dimer while σ^F is still bound is impossible (Ho *et al.*, 2003). AA binds across the nucleotide-binding pocket of AB, and is phosphorylated when this binding pocket contains ATP, yielding inactive phosphorylated AA (AA-P) and AB·ADP. The bound AA can be phosphorylated either immediately (138) or after a further AA has bound (142) (Min *et al.*, 1993). AA-P can be reactivated by the phosphatase action of IIE (146-150; (Duncan *et al.*, 1995; Arigoni *et al.*, 1996)). AB·ADP can either bind AA (23-26), or bind σ^F (105/106), or exchange ADP for ATP (1-4; 123-126) (Magnin *et al.*, 1997). ADP-ATP exchange involves the opening of a "lid" (Clarkson *et al.*, 2004*c*) and is overall a rather slow process. Binding of AA (21/22) or σ^F (95/96) accelerates lid closure (127-129). ADP-ATP exchange is also possible when AA is bound to AB·ADP (130-135). Finally, dimers with two different nucleotides form (15-18, 31-34, 49-52, 99-104, 139, 144) when only one AB monomer phosphorylates AA (138), when only one monomer exchanges

nucleotides (130, 132) or when a mixture of ADP and ATP leads to the formation of mixed forms during nucleotide exchange. The last of these reactions is not considered in the main model as this path has substantial impact only under very special *in vitro* conditions (e.g. Fig. 3.5) that we will discuss.

Given the allosteric behaviour of AB, the scheme had to be extended to include a second conformation of AB (non-shaded part) as well as interconversions between AB states (57-90). This leads to a duplication of almost all the interactions mentioned so far, and the total model comprises 50 dependent variables, each of which is described by one ordinary differential equation. In the diagram, the conformation that binds AA with low affinity and σ^F with higher affinity is depicted as circles, and the other state as squares. As is usual for descriptions of allosteric proteins (e.g. Fersht, 1998) these two states may be referred to as the tense (T) and the relaxed (R) state respectively.

3.1.4 Parameter determination

Lack of quantitative data and experimental detail have often restricted the predictive power of mathematical models. This study has greatly benefited from the large amount of published experimental information and the availability of a well-established *in vitro* system (Yudkin & Clarkson, 2005). Values for essentially all the key parameters could thus be determined experimentally. The more than 150 reactions included in the scheme are characterized by 25 different rate constants (Tables B.1 & 3.2). This small number of rate constants is sufficient because it is assumed that the kinetic constants of one AB monomer are not affected by ADP, ATP or AA being bound to the other monomer other than through a change in the relative concentration of the R and T states.

The 21 kinetic rate constants for the *in vitro* model (Table B.1) can be grouped into those characterising nucleotide binding (Fig. 3.2 reactions 1-4) and exchange (123-135), the AB-AA interaction (5-56), the interconversion between the R and the T state (57-90), the AB-σ^F interaction (91-122), and finally the phosphorylation (136-145) and dephosphorylation (146-150) of AA. The values of many of these parameters have already been published.

However, most of the on- and off-rates have been determined by SPR; this technique requires the proteins analysed to be attached to a sensor chip, which may alter their behaviour. Fluorescence quenching experiments do not have this shortcoming, and a re-analysis of important kinetic parameters was carried out by fluorescence spectroscopy with the help of fluorescent mutants (Clarkson *et al.*, 2004*a*; Clarkson *et al.*, 2004*c*). Constants that had been determined on the assumption that AB is not an allosteric protein were refined to fit the model shown in Figure 3.2.

Nucleotide binding

AB binds its binding partners AA and σ^F with notable affinity only if bound to nucleotides (Clarkson *et al.*, 2001). The affinity of AB for ATP and ADP has been determined to be $K_D \sim 200$ μM (Lord *et al.*, 1996). Assuming that the on-rate (1, 2) for this interaction is in the range found for other associations between proteins and small ligands (10^7 $M^{-1}s^{-1}$ (Fersht, 1998)) we use 2×10^3 s^{-1} for the off-rate (3, 4). Nucleotides can only bind and dissociate while the AB nucleotide binding pocket is not covered by a "lid" (Campbell *et al.*, 2002; Clarkson *et al.*, 2004*c*). From the measured low affinity for nucleotides we can conclude that the lid remains predominantly open when the open form of AB is mixed with nucleotides. Lid closure is induced by binding partners of AB (Clarkson *et al.*, 2004*c*) as is discussed below.

AB-AA binding constants

The interaction of AB and AA (5-56) has been studied in detail. The rate constants for the formation of the AB·AA complex in the presence of ADP (23-38) can be determined by SPR following the protocol established by Magnin *et al* (1997). These measurements can be carried out with either AB or AA bound to the sensor chip. However, AA-interactions with both AB monomers will occur only when AB is bound to the chip, since the spacing of chip-bound AA is unlikely to be appropriate for AB to bind to two molecules of AA. For the monomeric interaction when AA is chip-bound a total of 15 experiments were pooled

from Shu *et al* (2004) together with other unpublished results from this laboratory. The on- and off-rates were determined as $k^*_{on} = 1.6 \times 10^5$ $M^{-1}s^{-1}$ ($\pm 2.1 \times 10^5$ standard deviation) and $k^*_{off} = 6.85 \times 10^{-3}$ s^{-1} ($\pm 4 \times 10^{-3}$ standard deviation) respectively. Here the off-rate will correspond to the high affinity state, since upon binding of AA, AB will undergo a conformational change to the high affinity form.

To facilitate the fitting of the binding of two AA molecules to one chip-bound AB molecule by means of the Biacore software we exploited the fact that one conformation of the AB and AB·AA_2 dimers is particularly favoured; we thus simplified the binding reaction to a 3-step mechanism involving an initial binding of one AA to the AB dimer (in the low affinity state), a subsequent conformational switch and the binding of a second AA to AB·AA in the high affinity state. Fitting of SPR data with this 3-step mechanism was substantially improved over that with a single step (non-allosteric) model, with the average χ^2 value of the fit being reduced by approximately 10-fold. (In contrast fitting was not improved by the 3-step mechanism when AA was bound to the chip.) The estimates obtained from 5 unpublished experiments for the on- and off-rates of the two binding steps were $k_{on1} = 1.1 \times 10^6$ $M^{-1}s^{-1}$ ($\pm$ 10^6 standard deviation), $k_{on2} = 4 \times 10^4$ $M^{-1}s^{-1}$ ($\pm 2.9 \times 10^4$ standard deviation), $k_{off1} = 2.4$ s^{-1} (± 2.2 standard deviation), $k_{off2} = 8.4 \times 10^{-3}$ s^{-1} ($\pm 1.7 \times 10^{-3}$ standard deviation). The conformational change occurs at 7.4 s^{-1} (± 5.6 standard deviation) and 2 s^{-1} (± 1 standard deviation) towards the high and low affinity states respectively. The affinity of the second bound AA will probably have been underestimated by SPR since attachment of AB to the grid is likely to obscure at least one binding site. Equally the AA-AB on-rate will have been underestimated when AA is fixed to the grid. This may be due to alterations of AA on attachment to the grid. We therefore used an intermediate value $k_{on1} = 8 \times 10^5$ $M^{-1}s^{-1}$ as the general AA-AB on-rate in our simulations, and 7.4×10^{-3} s^{-1} as the off-rate in the high affinity state, which is the average value of all measurements made. k_{off1} was used as determined by SPR above. It should be noted that our simulations are a better fit to the kinetics that are obtained by fluorescence quenching experiments if

we use a higher AA-AB on-rate ($\sim 4 \times 10^6$ $M^{-1}s^{-1}$).

The binding constants in the presence of ATP (5-22) are more difficult to measure since AB·ATP·AA complexes are not stable because of phosphorylation of AA under these conditions. SPR measurements of the interaction of AB with the AA-S58A mutant of AA, which cannot be phosphorylated by AB, revealed a higher affinity in the presence of ATP than in the presence of ADP (Magnin *et al.*, 1997). However, the affinity of the AA-S58A mutant in the presence of ADP is lower than for the wild type, which prevents us from directly using the values that have been determined for this mutant. Thus according to the Scatchard plot (Fig. 3.1C) the affinity of each AB monomer for AA-S58A is 3.7-fold lower than for the wild type, and according to published SPR data (which was analysed with a one-step instead of an allosteric three-step mechanism) the affinity is 62-fold lower (Magnin *et al.*, 1997). On remeasuring the affinities by SPR in 15 independent experiments and analysing the data with a 1-step mechanism we found an approximately 10-fold lower affinity for AA-S58A than for wild-type AA (e.g. $K_d = 481$ nM for AA-S58A compared to $K_d \sim 40$ nM for the wild type (Magnin *et al.*, 1997)). This is in good agreement with our estimate from the Scatchard plot.

For the reasons just explained, for the wild type we could not use the off-rate obtained with AA-S58A in the presence of ATP. However, we note that two independent studies find the affinity in the presence of ATP to be 5.2-fold (Magnin *et al.*, 1997) and 8.8-fold (Shu *et al.*, 2004) higher than in the presence of ADP. We therefore used 0.001 s^{-1} for the second off-rate, a value that is 7.4-times lower than the one used in the presence of ADP. In practice, the control coefficient for this reaction is low (-0.03 - Table B.1), so that this rate has relatively little impact on the behaviour of the system *in vivo*.

In the absence of nucleotides AA-AB binding is weak and NMR experiments (Clarkson *et al.*, 2001) suggest a value for K_d of around 1 mM; this value was calculated by comparing the intensities of the resonances obtained for free and bound AA at fixed concentrations of AA and AB. We therefore neglect this reaction in the main model and consider it only

in one *in vitro* experiment aimed at measuring such interactions (Fig. 3.5). Our NMR experiments reveal a similar low affinity between AB and phosphorylated AA (unpublished data), which is also neglected in the model.

While, according to structural information, there are clashes between AA and σ^F when both are bound to AB (Campbell *et al.*, 2002; Masuda *et al.*, 2004) biochemical data suggest that these clashes mainly affect the σ^F·AB interaction (Clarkson *et al.*, 2004*a*). We therefore assume that the presence of σ^F does not affect the AB·AA affinity (39-56).

Rates for AB conformational changes

The SPR experiments on AB-AA binding provide the only rates available for the interconversion between R- and T-states, and we used 2 s^{-1} as the rate for the unfavoured direction throughout (74-90). In order to fit AA-AB binding as measured in fluorescence quenching experiments (Fig. 3.1) the conformational change towards the favoured state had to be taken to be higher than estimated by SPR, and we used 30 s^{-1}. A likely explanation for the lower value found in SPR measurements is that fixation to the chip impairs AB conformational changes. In the two symmetrical states (unbound or fully bound by ligand) the favoured direction (58-74) must be attained at a much higher rate in order to fit Figure 3.1B. The lowest possible rate is 5×10^3 s^{-1}, and 5×10^4 s^{-1} is used in the model for all other states. Higher rates do not alter the predictions of the simulation.

σ^F-AB binding

The next group of constants for which SPR data have been published (Magnin *et al.*, 1997; Ho *et al.*, 2003) are those that characterize the σ^F-AB interaction (100-122). According to published SPR measurements the affinities are very similar in the presence of ATP and ADP (K_d=12-14 nM and K_d= 31 nM respectively (Magnin *et al.*, 1997; Ho *et al.*, 2003)). This stands in apparent contradiction to data from fluorescence quenching measurements (Fig. 3.3) which suggest both a lower on-rate and a lower affinity of binding in the presence of ADP (Shu *et al.*, 2004). Our unpublished SPR binding results confirm that the association

is much slower in the presence of ADP, although fitting of the data with the Biacore software had led to the estimate of a high on-rate. This discrepancy can be accounted for by the use of a one-step mechanism to fit the SPR data. However, while a one-step mechanism provides a good fit for the kinetics of σ^F-AB binding in the presence of ATP (Fig. 3.3B),

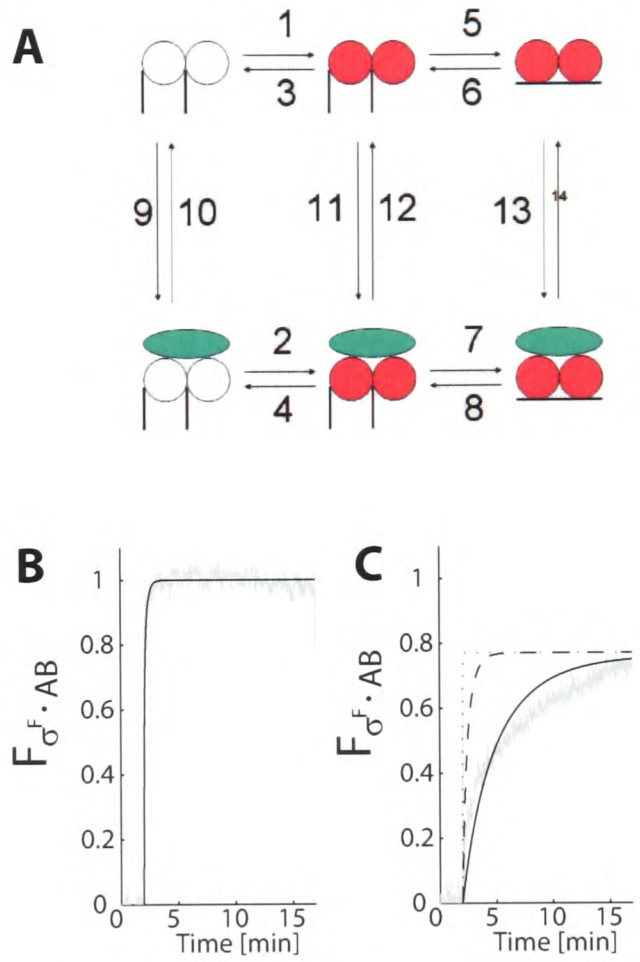


Figure 3.3: **σ^F-SpoIIAB binding.** **(A)** A model for σ^F-SpoIIAB binding. The symbols represent simple variants of those in Figure 2.2B. Circles represent AB monomers that bind nucleotides if filled; the lines indicate the conformation of the "ATP lid". The green ovals represent σ^F. **(B)** Kinetics of σ^F-SpoIIAB·ATP binding. The grey line gives the experimental output from the recorder when 1.3 μM σ^F and 1 μM AB were mixed in the presence of 100 μM ATP. The black line represents the predicted binding curves for a one-step mechanism, that is all rate constants in panel A are set to zero apart from $k_{11} = 4 \times 10^5$ $M^{-1}s^{-1}$ and $k_{12} = 5 \times 10^{-5}$ s^{-1} which are the rate constants as determined by SPR. **(C)** Kinetics of σ^F-SpoIIAB·ADP binding. The grey line is the experimental output from the recorder when 1.3 μM σ^F and 1 μM AB were mixed in the presence of 100 μM ADP. The broken lines represent the predicted binding curves for a one-step mechanism (all rate constants except rates 11 and 12 are zero) if either the on-rate is lowered ($k_{11} = 2.7 \times 10^4$ $M^{-1}s^{-1}$ - dashed line) or the off-rate is increased ($k_{12} = 0.08$ s^{-1} - dotted line) as compared to the rates in the presence of ATP. The solid line represents the prediction for the multistep mechanism. We use rates of binding of nucleotide (rates 1-4) and σ^F (9-14) as determined before; however, σ^F binding is weak in the absence of nucleotides (Clarkson *et al.*, 2001) such that $k_{10} = 4 \times 10^3$ s^{-1}. Moreover we use $k_7 = 30$ s^{-1}, $k_8 = 10^{-5}$ s^{-1} for the lid closing and opening rates in the presence of σ^F.

it does not in the presence of ADP (compare dashed and dotted lines with experimental curves in Fig. 3.3C). We find that the σ^F binding curve in the presence of ADP can only be reproduced by a multistep mechanism that takes into account the details of nucleotide binding as depicted in Figure 3.3A. Thus we have to assume that binding of σ^F results in slow lid closure and opening ($k_7 \sim 30$ s^{-1}, $k_8 \sim 5 \times 10^{-4}$ s^{-1} in Fig. 3.3A). The closing of the lid is important for σ^F binding because the affinity between σ^F and nucleotide-free AB is very low. In the case of ATP binding σ^F-mediated lid closure must be rapid ($k_7 \sim 10^4$ s^{-1} in Fig. 3.3A). Both SPR and fluorescence spectroscopy therefore agree that, as long as the lid is shut, the affinity between nucleotide-bound AB and σ^F is high, irrespective of the nucleotide bound. When the lid is open, however, σ^F binding is very slow in the presence of ADP.

During the dissociation of phosphorylated AA and the change of AB·ADP to the tense conformation (especially if AA dissociates stepwise from AB·ADP·AA$_2$) the lid has time to open. AB·ADP and AB·ADP·AA will therefore generally bind σ^F with a low on-rate, but will show a high affinity once the lid is shut (as will apply upon rebinding). In order to capture these two behaviours without having to introduce many more states to describe the lid opening process in detail, we use the same affinity for both the σ^F-AB·ADP and σ^F-AB·ATP interaction but a 100-fold lower rate for both the on- and off-rates for σ^F-AB·ADP binding.

Since in the absence of AA, AB is predominantly in the tense state, the above-determined rate constants for the σ^F-AB interaction reflect the binding of AB only in its tense state. Because binding of AA biases the equilibrium to the relaxed conformation we can obtain an estimate of the affinities in the relaxed state by incubating σ^F·AB with AA. The kinetics of AA-dependent σ^F release in the presence of ATP can be fitted only by an σ^F-AB off-rate that is about 100 times higher than in the tense conformation (compare Fig. 3.4A with Fig. 3.4B). Accordingly the off-rate in the relaxed conformation was set to 0.4 s^{-1}, which corresponds to a micromolar K$_d$. That the affinity of σ^F for AB is lower in the presence of

AA has been noted previously (Clarkson *et al.*, 2004*a*).

AA phosphorylation rates

The phosphorylation of AA (136-145) exhibits a biphasic time course (Fig. 3.5) (Najafi *et al.*, 1997; Magnin *et al.*, 1997). The initial rate is equal to the AA phosphorylation rate, and the subsequent reduction in rate is due to the sequestering of AA and AB in AB·ADP·AA complexes. The phosphorylation rate of AA can thus be estimated from the initial slope of the biphasic phosphorylation reaction as 0.013 s^{-1}, a value that is close to previous estimates (Ho *et al.*, 2003; Shu *et al.*, 2004). ATP hydrolysis will be much slower than AA phosphorylation and was therefore ignored.

Nucleotide exchange

AB·ATP can be restored by nucleotide exchange, which requires the opening and closing of a "lid" (Clarkson *et al.*, 2004*c*). The rates for lid opening and closure (123-135) can be estimated from the data on AA-dependent σ^F release. In order to reproduce the kinetics of σ^F·AB re-formation after AA addition we require a lid opening rate of 0.02 s^{-1}. This is much smaller than the value (1 s^{-1}) that was estimated previously (Clarkson *et al.*, 2004*c*),

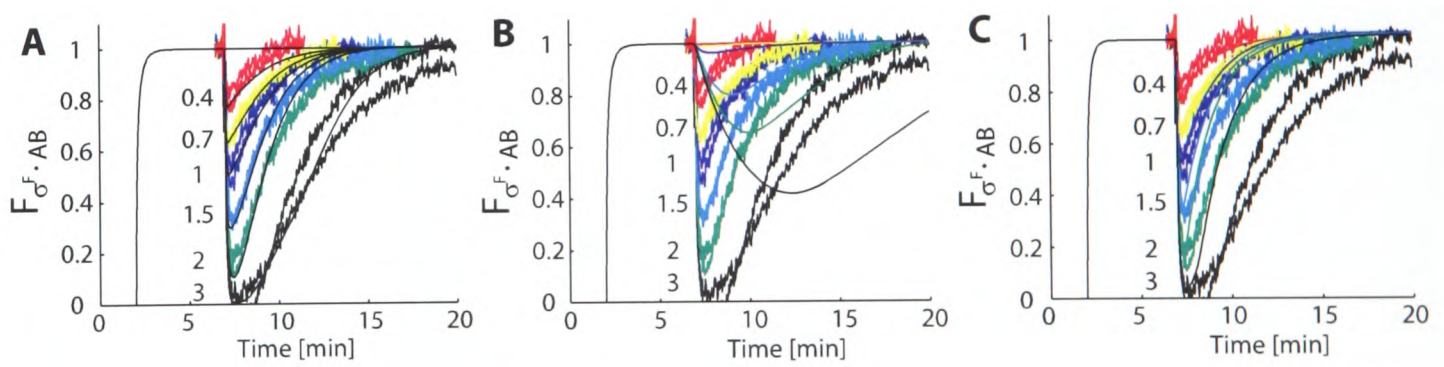


Figure 3.4: **SpoIIAB-σ^F binding in the presence of SpoIIAA.** Measured (recorder output) and predicted (smooth lines) σ^F release from AB·ATP upon addition of AA; on the vertical axis we record the fraction of σ^F in σ^F·AB complexes. The different lines show the predictions for different concentrations of AA. The measured values are for 0.4 (red); 0.7 (yellow); 1 (blue); 1.5 (cyan); 2 (green); 3 (black) μM AA when 1.3 μM σ^F and 1 μM AB were mixed in the presence of 100 μM ATP. **(A)** The predictions are made using the parameters given in Table B.1. **(B)** The predictions are made on the assumption that the SpoIIAB-σ^F affinity was the same in the tense and the relaxed state. **(C)** The predictions are made on the assumption that the lid opening rate was 1 s^{-1}.

but for a rate as high as 1 s^{-1}, re-formation of σ^F·AB is too fast (compare Fig. 3.4A with Fig. S3.4C). The previous estimate of 1 s^{-1} was based on a simple steady-state model, while we see from this more elaborate model that the lid opening rate in particular affects the kinetics of the reaction. Finally, in order to obtain a sufficient (1000-fold) bias to the open form to justify the low affinity for nucleotides, we use 0.001 s^{-1} as the closing rate; rates up to 100 s^{-1} do not change the predictions of the model. We note that such low rates are in agreement with observations of GTPases in the absence of nucleotide exchange factors. Dissociation constants can then be as low as 10^{-5} s^{-1} (Klebe *et al.*, 1995). Nucleotide exchange factors induce a conformational change in two loop regions to allow dissociation of GDP and accelerate the rate of exchange with GTP to rates of 10 s^{-1} (Klebe *et al.*, 1995; Vetter & Wittinghofer, 2001).

The rate of AA-P production when AB·ADP·AA complexes have already formed is much higher than the rate of dissociation of the AB·ADP·AA complex (Fig. 3.5). ADP-ATP exchange must therefore be possible while AA is bound to AB·ADP (130-135) - though at a reduced rate. Modelling of the steady-state rate of phosphorylation (Fig. 3.5) requires a ADP-ATP exchange rate for AB·AA of 1.2×10^{-3} s^{-1}.

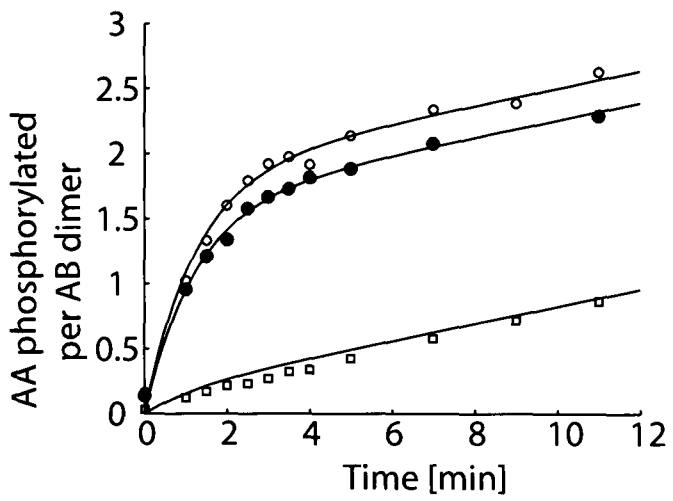


Figure 3.5: **Phosphorylation of AA.** Phosphorylation of AA by AB when AB is directly incubated with 40 μM AA and 100 μM ATP (○) or pre-incubated for 5 minutes with either 5 μM ADP (●) or 5 μM ADP and 40 μM AA (□). The symbols show the experimental results (Clarkson *et al.*, 2004*c*), normalised by the factor 1.3 to take account of inaccuracies in the protein determination (see main text). The lines show the predictions of the mathematical model.

We can further conclude from the measured rate of AA phosphorylation that AA facilitates the closing of the lid (128, 129). AA-dependent lid closure has a notable effect *in vitro* when AB is pre-incubated for 5 minutes with 5μM ADP before addition of 100 μM ATP. If the preincubation is carried out in the presence of AA then the biphasic phosphorylation time course can be directly transformed into a linear time course with the lower phosphorylation rate throughout (Fig. 3.5 □); by contrast, pre-incubation with 5μM ADP alone has only a minor effect (Fig. 3.5 •). From these results it can be concluded that while ADP-AB binding is weak (Lord *et al.*, 1996) it can be facilitated by AA, which itself binds weakly to AB when no nucleotide is bound (Clarkson *et al.*, 2001). The small effect seen when adding 5μM ADP is the result of mixed dimers that bind one ADP and one ATP. These yield only one instead of two phosphates before being captured in AB·ADP·AA complexes, whose production can be further stimulated if one AA binds to the ADP-bound monomer while another AA is phosphorylated on the other monomer. We conclude that in order to form AA·AB·ATP complexes as rapidly as observed after ATP addition AA must facilitate lid closure; we use 10^4 s^{-1} as the AA-dependent lid closing rate to capture the kinetics in Fig. 3.5. This is the same rate as we found above for the σ^F-dependent lid closing rate in the presence of ATP. The same high values for both rates follows from the need to exceed the respective dissociation rates of more than 10^3 s^{-1}. Whilst all these states need to be included in order to model the results shown in Fig. 3.5 we can simplify our general model by neglecting the AA bound state without nucleotides, and we can then lower our AA-dependent lid closing rate to 10 s^{-1}; however, we note that higher rates do not alter the model predictions.

The affinity of IIE·AA-P and the rate of dephosphorylation

Dephosphorylation of AA-P (150) *in vitro* with IIE domain III has been reported to proceed at 0.085 s^{-1} (Lucet *et al.*, 2000). However, when repeating the measurements we found that these experiments underestimated the rate of the reaction, presumably because the results were not fitted directly with a Michaelis-Menten model. Our new data show that failure

to fit the data with a Michaelis-Menten model results in a large error because the reaction proceeds very fast and the velocities estimated after 10 minutes do not represent maximum reaction velocities. When we fit the reactions with a Michaelis-Menten model we obtain the lowest least-square deviations from the experimental data with 6×10^4 $M^{-1}s^{-1}$ for the IIE-AA-P on-rate (148), 0.58 s^{-1} for the off-rate (149), and 0.75 s^{-1} for the catalytic rate (150). This on-rate is very low, especially given the small sizes of the two proteins, but a higher on-rate worsens the fit of the data considerably (compare solid and dotted lines in Fig. 3.6). It has previously been shown that AA-P dimerizes (146, 147)) (Clarkson *et al.*, 2003), and using analytic ultracentrifugation we have determined the affinity constant as $K_d = 3.7 \pm 2.1\mu$M (unpublished data, for methods see Clarkson et al., 2003). Affinities are difficult to measure accurately in the lower range, but even if we use $K_d = 10\mu$M as a conservative estimate (10^5 $M^{-1}s^{-1}$ for the on-rate (146), 1 s^{-1} for the off-rate (147)) we find higher rate constants for the IIE-AA-P interaction, e.g. 10^5 $M^{-1}s^{-1}$ for the IIE-AA-P on-rate (148), 0.58 s^{-1} for the off-rate (149), and 1.25 s^{-1} for the catalytic rate (Fig. 3.7). We

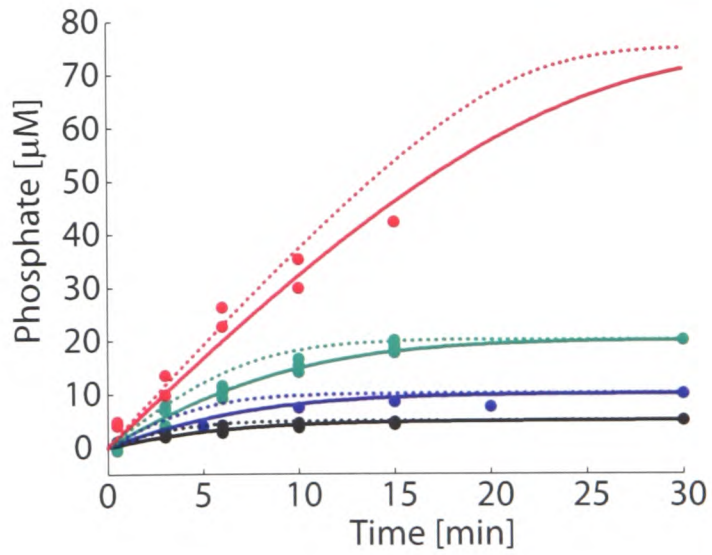


Figure 3.6: **The AA-P-IIE on-rate is low.** Accumulation of phosphate when 5μM (black), 10μM (blue), 20μM (green), or 75μM (red) of AA-P are mixed with 100 nM IIE in 2.5 mM Mn^{2+}. The circles represent measured values. Given that our assays for the determination of protein concentrations are more accurate than the assay for the phosphate concentration, all curves were scaled before fitting the model so that no point would exceed the maximal substrate concentration. The lines represent the fit of the Michaelis-Menten type model (Fig. 3.7A) with $k_{on} = 6 \times 10^4$ $M^{-1}s^{-1}$, $k_{off} = 0.58$ s^{-1} and $k_{cat} = 0.75$ s^{-1} (solid lines), or $k_{on} = 6 \times 10^5$ $M^{-1}s^{-1}$, $k_{off} = 5.8$ s^{-1} and $k_{cat} = 0.75$ s^{-1} (dotted lines).

use these parameter values and include AA-P dimerization with the above rate constants in the model. We conclude that the affinity of the IIE-AA-P interaction is remarkably low ($K_d \sim 5 - 10\mu$M) as confirmed by measurements under different salt conditions. Thus if we use magnesium instead of manganese we obtain the same affinity but an almost 150-fold lower reaction rate ($k_{cat} = 0.0087$ s^{-1}) (Fig. 3.8).

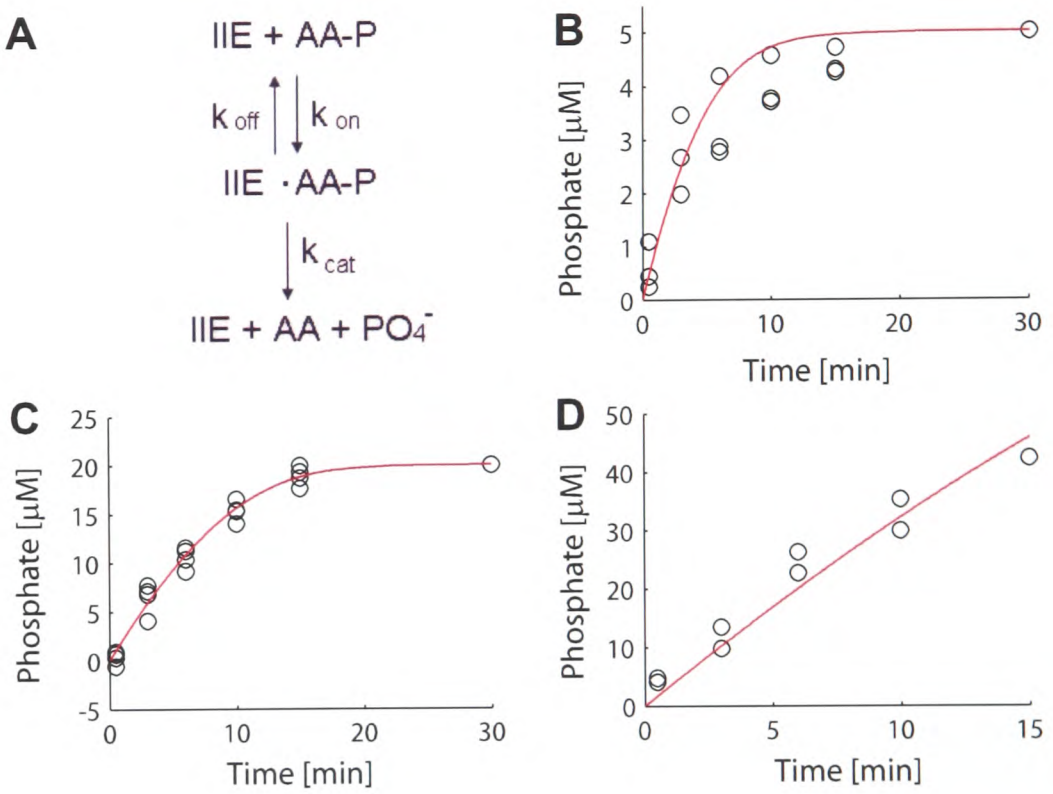


Figure 3.7: **The kinetics of AA-P dephosphorylation.** **(A)** A scheme of the dephosphorylation reaction. The complex between IIE and AA-P is formed at rate k_{on} and dissociates at rate k_{off}. AA and phosphate are formed at rate k_{cat}. **(B-D)** Accumulation of phosphate when **(B)** 5, **(C)** 20, or **(D)** 75 μM AA-P are mixed with 100 nM IIE in 2.5 mM Mn^{2+}. The circles represent measured values that are scaled as in Fig. 3.6. The lines represent results from a Michaelis-Menten type model as depicted in **(A)** with the kinetic rate constants that gave the smallest least squares deviation, that is, $k_{on} = 9.3 \times 10^4$ M^{-1}s^{-1}, $k_{off} = 0.58$ s^{-1} and $k_{cat} = 1.26$ s^{-1}. The rate constants for AA-P dimerization are $k_{on} = 10^5$ M^{-1}s^{-1}, $k_{off} = 1$ s^{-1}.

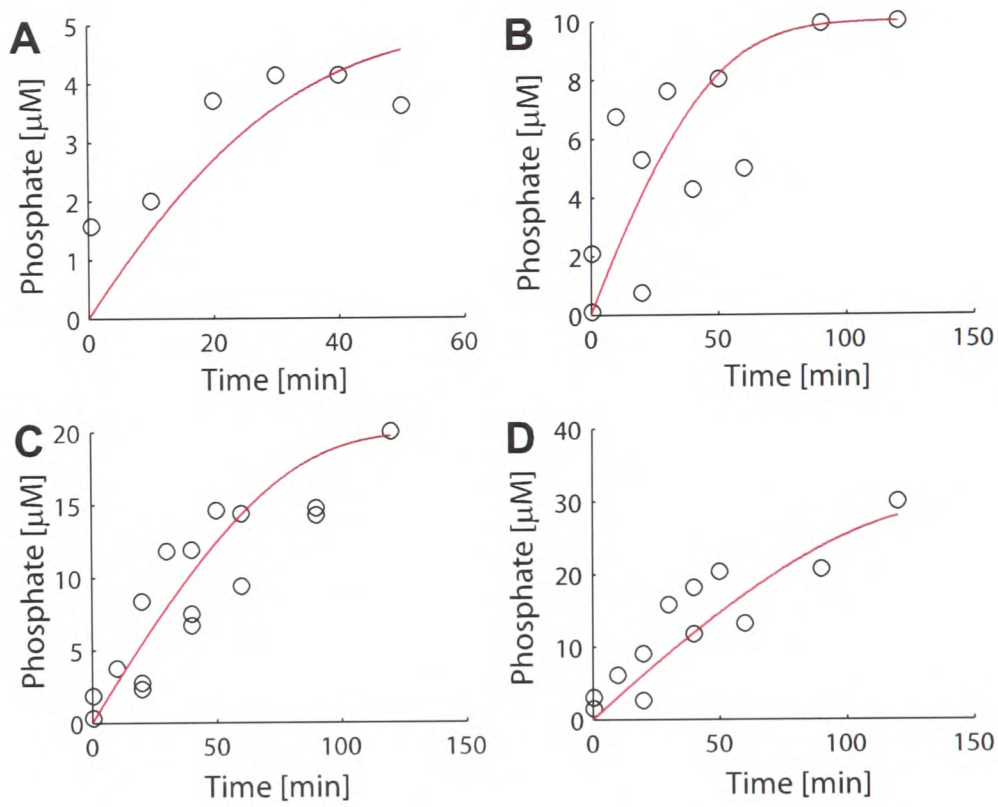


Figure 3.8: **The impact of Mg^{2+} on the kinetics of AA-P dephosphorylation.** Accumulation of phosphate when **(A)** 5, **(B)** 10, **(C)** 20, or **(D)** 30 μM AA-P are mixed with 1μM IIE in 1 mM Mg^{2+} and 0.1 mM Mn^{2+}. The circles represent measured values that are scaled as discussed in Fig. 3.6. The lines represent results from a Michaelis-Menten type model as depicted in Figure 3.7A with the kinetic rate constants that gave the smallest least squares deviation, that is, $k_{on} = 9.3 \times 10^4$ $M^{-1}s^{-1}$, $k_{off} = 0.58$ s^{-1} and $k_{cat} = 0.0087$ s^{-1}. The rate constants for AA-P dimerization are $k_{on} = 10^5$ $M^{-1}s^{-1}$, $k_{off} = 1$ s^{-1}.

3.2 Verification of the model by comparison to *in vitro* data

3.2.1 The model quantitatively reproduces experimental results of σ^F·AB sensitivity to variations in AA and IIE.

With all the kinetic parameters determined we first sought to reproduce biochemical *in vitro* results (shown as blue circles in Fig. 3.9A) which revealed that σ^F·AB·ATP complexes are highly sensitive to changes in IIE activity (Clarkson *et al.*, 2004*b*), thus lending support to

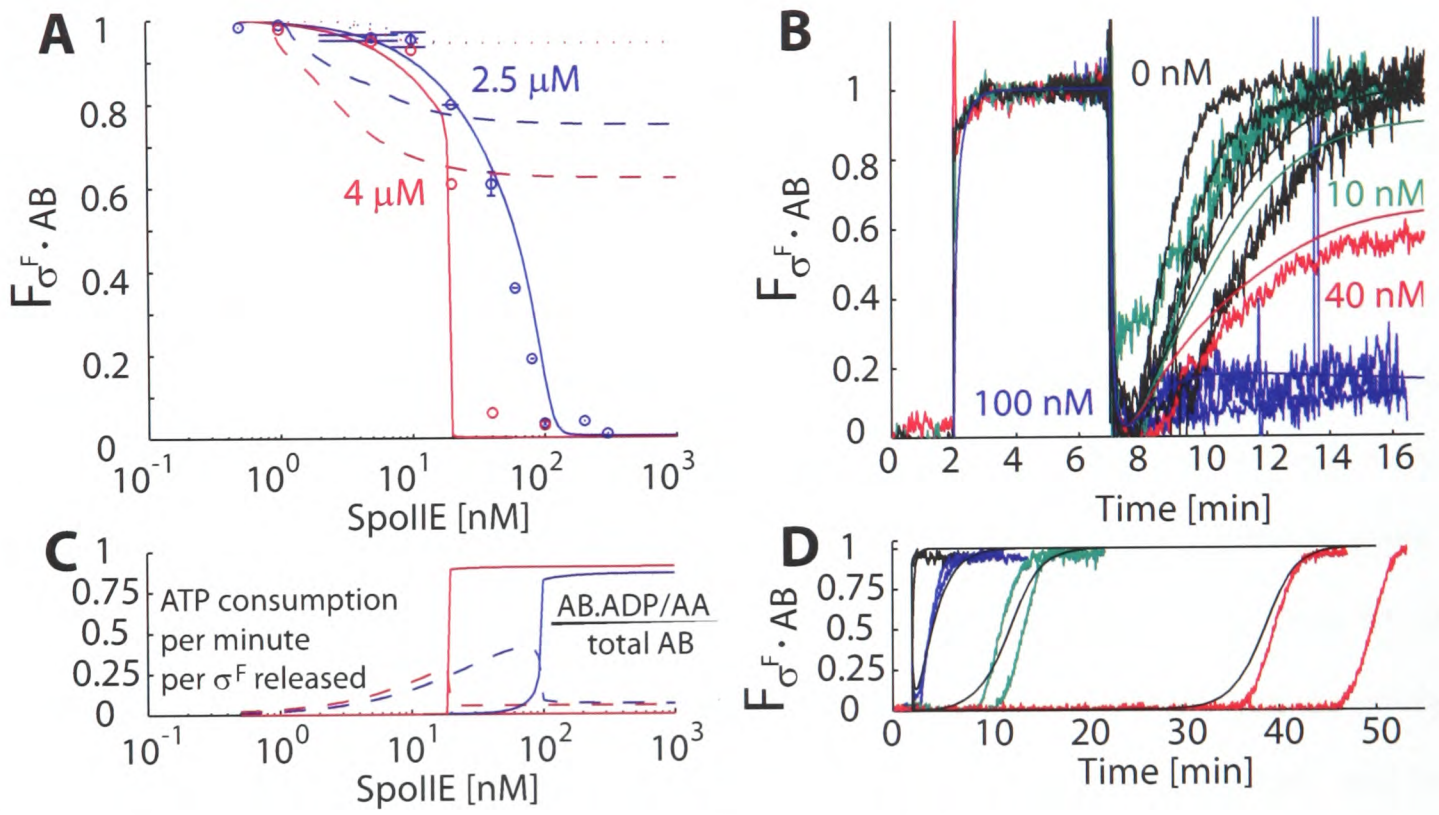


Figure 3.9: **The dissociation of σ^F·AB complexes is sensitive to changes in the concentration of IIE and AA.** **(A)** Steady state after IIE-dependent dissociation of σ^F·AB·ATP (1.3μM σ^F, 1μM AB dimer) in the presence of 2.5μM (blue) or 4μM (red) AA. Circles represent experimental results. Continuous lines show the predictions of the mathematical model based on the interactions shown in Figure 3.2, which includes the formation of the AB·ADP·AA complex. Broken lines show simulations based on the assumption that the formation of such a complex is impossible (dotted lines) or that there is no AB allostery (dashed lines). **(B)** Kinetics of IIE-dependent dissociation of σ^F·AB·ATP (1.3μM σ^F, 1μM AB dimer) in the presence of 2.5μM AA, in the absence of IIE (black lines) or with 10 (green), 40 (red) or 100 (blue) nM IIE. Experimental results are shown as output from a recorder. Note that three experiments were run in the absence of IIE. The smooth continuous lines show simulations from the mathematical model. **(C)** Simulations of the proportion of AB sequestered into AB·ADP·AA complexes (continuous lines) and ATP consumption per minute per σ^F released (dashed lines) in the presence of 2.5μM (blue) or 4μM (red) AA. **(D)** σ^F·AB complex formation on mixing of 1 μM AB and 1.3 μM σ^F with no (grey), 2 μM (blue), 4 μM (green), or 6 μM (red) AA. Experimental results (two for each concentration of AA) are shown as output from a recorder; the black lines show simulations from the mathematical model at the same concentrations of AA. All the experimental results are taken from Clarkson et al, 2004b.

the hypothesis that the septation-dependent increase in IIE activity may lead to σ^F release in the prespore (Duncan *et al.*, 1995). As long as AB allostery was included (compare dashed and continuous curves in Fig. 3.9A) the high sensitivity of σ^F·AB·ATP complexes to changes in IIE activity could be reproduced quantitatively. Moreover, the complexes were predicted to be sensitive to changes in the AA concentration, and this could be confirmed by experiments (compare 2.5 μM and 4 μM curves in Fig. 3.9A). The model also captured the kinetics of σ^F·AB complex formation upon addition of ATP, the dissociation of the complex upon addition of AA and the effect of IIE on re-formation of the complex (Fig. 3.9B). The considerable variation in the experimental time courses (compare the three black curves for IIE=0 nM in Fig. 3.9B) may be due to the high sensitivity of the kinetics to concentration. Comparison with the results in Fig. 3.4A suggests that the slower recovery rate found in the simulation is the more realistic one. The values for the steady-state dissociation of the complex are more robust, and the standard deviations between three independent experiments, as indicated by error bars in Figure 3.9A, are generally small. In both cases the modelling results are within the experimental range. The close fit of simulation and experiment, despite inherent experimental errors in the parameters including protein concentration, can be attributed to the robustness of the model (see below) and to the fact that the constants for the various on- and off-rates were all derived from similar experimental protocols.

3.2.2 The robustness of the mathematical model to variations in parameters.

The regulatory network can be regarded as robust if small changes in the parameter values lead to only small changes in the response. Given the availability of experimental data, the sensitivity of the model to variations in the kinetic parameters can be assessed by determining the deviation Δ_j of the simulation values s_i from the N experimental equilibrium results e_i (Fig. 3.9A) in response to a change in the kinetic parameter value k_j as

$$\Delta_j = \sqrt{\frac{1}{N}\sum_{i=1}^{N}\left(\frac{s_i - e_i}{e_i}\right)^2}. \tag{3.1}$$

Those reactions j for which Δ_j did not increase by more than 1% when k_j was either set to zero or varied between 10^{-3} and 10^6 in multiples of 10, are plotted as green arrows in Figure 3.2. Those for which even a small (10-fold) change in the parameter led to an increase in Δ_j by more than 1% are depicted as red arrows. Inspection of Figure 3.2 shows that about half of all reactions have little impact on the overall dynamics of the system. Those parameters that do affect the dynamics of the model are the key reaction pathways. These include the formation and AA-dependent dissolution of σ^F·AB complexes, phosphorylation and dephosphorylation of AA, as well as those reactions that lead to ADP-ATP exchange.

3.2.3 Predictions of the effect of AB·ADP·AA complex formation.

AB·ADP·AA complex formation coincides with σ^F release from the σ^F·AB·ATP complex (compare Figs. 3.9A and C) and is important for the high sensitivity of σ^F release to changes in the AA concentration (Fig. 3.9A compare solid and dotted lines). The formation of AB·ADP·AA complexes also minimizes the need for cycling between AA and AA-P (Magnin *et al.*, 1997) and associated ATP consumption. Thus, the ATP consumption per minute per σ^F released does not increase monotonically with increasing IIE concentrations, but reaches a minimum (Fig. 3.9C, dashed line) when sufficient unbound AA is available to sequester AB in AB·ADP·AA complexes (Fig. 3.9C, solid line).

The AA-dependent trapping of AB·ADP in AB·ADP·AA complexes can be observed experimentally in the form of an increasing delay in σ^F·AB complex re-formation when equimolar concentrations of AB and σ^F are mixed with increasing molar ratios of AA (Fig. 3.9D). The model reveals that the non-linear increase in the delay times with increasing AA concentrations reflects the non-linear AA-dependence of AB·ADP·AA complex formation. It should be noted that the extent to which this delay increases with increasing AA concentration would be smaller if the AA-AB·ADP affinity were lower. The small difference

between experiment and model predictions can be accounted for by the high sensitivity of the speed of σ^F-AB rebinding to the protein concentration which resulted in rather large deviations in experiments (as the black curves in Figure 3.9B demonstrate); the parameters relevant to σ^F-AB rebinding were based on the experiments in Fig. 3.4A since these had been measured most carefully once the high sensitivity to small changes in the protein concentrations had been realized.

3.3 Application of the model to the sporulating cell *in vivo*

With a model that reproduces the *in vitro* data quantitatively we are now in a position to investigate the physiological situation. Relatively few alterations have to be made to the model to take account of the differences between the *in vitro* and *in vivo* conditions. The membrane location of IIE in the cell does not need to be considered explicitly in the model since, given the dimensions of the forespore, spatial concentration gradients on the timescale of the reactions would be expected to be negligible. A change has, however, to be made to the ATP and protein concentrations, which are higher *in vivo* at the time of septation than in the *in vitro* experiments. The ATP concentration was set to 1 mM because the lower end of the experimentally reported ATP concentration range (0.85 mM to 3 mM) for vegetative *B. subtilis* (Jolliffe *et al.*, 1981; Guffanti *et al.*, 1987; Hecker *et al.*, 1988) is likely to apply to the starving sporulating condition. The ADP concentration was set to 100 μM, which is a tenth of the ATP concentration.

The concentrations of the four sporulation proteins have been determined in three independent experiments (Magnin *et al.*, 1997; Lord *et al.*, 1999; Lucet *et al.*, 1999). We note that the two later publications find substantially higher protein concentrations, a difference that can be accounted for by the more accurate techniques that were used. We therefore base our estimates on this later work; however, we note that for expression rates that are half as high comparable results are obtained. Starting without protein expression at time -120 minutes we used an expression rate of 6×10^{-9} M s^{-1} for AA and AB, and 2×10^{-9}

M s^{-1} for σ^F and IIE, and obtain the protein concentrations that are found experimentally after 120 minutes, the presumed time of septation (Fig. 3.10A). We note that according to the experimental data the expression rates are not constant but increase with time (Magnin *et al.*, 1997; Lord *et al.*, 1999; Lucet *et al.*, 1999). Our simplification of using constant expression rates may therefore overestimate the protein concentration at early times of the expression process. This will not affect our predictions of the mechanism of septation-dependent σ^F release since only the protein concentrations at the time of septation affect this mechanism. We may, however, underestimate the robustness of the mechanism, because the lower expression levels of IIE at early times and the higher expression rate of IIE after septation will protect against premature activation of σ^F. Similarly, our predictions of ATP consumption before septation will be affected by the exact expression dynamics and be valid only qualitatively. However, in the important time period, after septation, the predictions of the model are unlikely to be much affected by our uncertainty about the exact expression rates, especially since the transient genetic imbalance (Frandsen *et al.*, 1999) and repression of Spo0A (Arabolaza *et al.*, 2003) largely inhibit the expression of sporulation proteins in the prespore.

Septation (a 4-fold increase in IIE and associated AA-P) was introduced after 120 minutes (Magnin *et al.*, 1997; Lord *et al.*, 1999; Lucet *et al.*, 1999) unless otherwise stated. The transient genetic imbalance, which arises upon septum formation and which results in the prespore lacking the *spoIIA* operon for 10-20 minutes after septation (Frandsen *et al.*, 1999; Dworkin & Losick, 2001), was modelled by prohibiting expression of AA, AB and σ^F for 15 minutes after septation. The emergence of unphosphorylated AA (Fig. 3.10B) further leads to repression of *spoIIE* and the *spoIIA* operon via inactivation of Spo0A (Arabolaza *et al.*, 2003). We assume that the genes are repressed once the concentration of unphosphorylated AA exceeds 1 μM. Note that in agreement with experimental observations (Arigoni *et al.*, 1996; Magnin *et al.*, 1997; King *et al.*, 1999; Carniol *et al.*, 2004) a substantial amount of AA (about 15% of the total, that is about 5 μM AA) is unphosphorylated even before

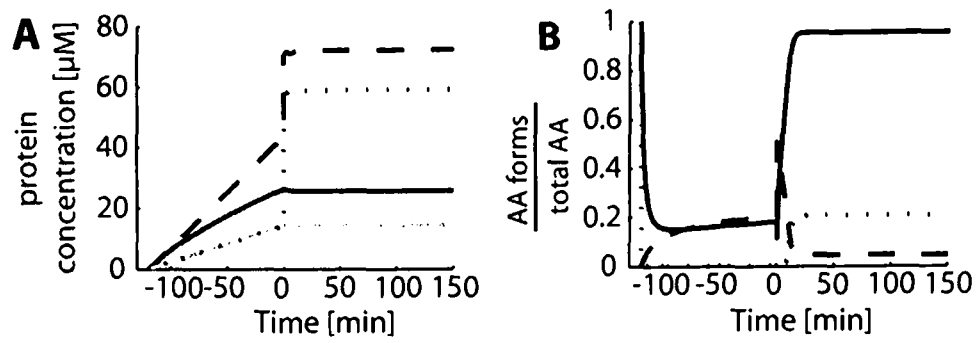


Figure 3.10: **The time-dependent concentration of the sporulation proteins in the model.** **(A)** Increase in the concentration of sporulation proteins during sporulation (AA- dashed; AB - continuous black; IIE - dotted; σ^F - grey). **(B)** Fraction of AA that is unphosphorylated (solid line), unbound and unphosphorylated (dotted line) or bound in IIE·AA-P complexes (dashed line). In both panels, sporulation-dependent protein expression is started at -120 minutes; a four-fold increase in IIE and associated AA-P (to simulate the effect of asymmetric septation) is introduced at t=0.

septation (Fig. 3.10B). However, the unphosphorylated AA is mainly bound to AB and therefore does not repress the *spoIIA* operon (Fig. 3.10B, dotted line).

An amino-acid sequence in the extreme C-terminus of AB markedly increases the AB degradation rate *in vivo* (Pan *et al.*, 2001). In the simulations unbound AB was therefore associated with a degradation rate of 4.1×10^{-4} s^{-1}, which gives rise to the experimentally observed half-life of about 28 minutes (Pan *et al.*, 2001).

The only rate constant that needs to be altered from the *in vitro* model is the IIE phosphatase rate, which experiments suggest is lower *in vivo* (Feucht *et al.*, 2002). Modelling predicts that in order to avoid septation-independent release of σ^F while still permitting septation-dependent release, the phosphorylation rate needs to be reduced by 75- to 150-fold (3.11A). It has previously been noted that the phosphatase rate is substantially higher in the presence of Mn^{2+} (Schroeter *et al.*, 1999), and indeed for a physiological salt concentration (1 mM Mg^{2+}, 0.1 mM Mn^{2+} (Eisenstadt *et al.*, 1973; Kehres & Maguire, 2003)) we find that the phosphatase rate is almost 150-fold lower (0.0087 s^{-1}, Fig. 3.11B) as discussed in section 3.1.4 and shown in Figure 3.8. Further alterations to the IIE environment or an unknown IIE inhibitor (King *et al.*, 1999; Feucht *et al.*, 2002) are not necessary.

Under physiological conditions the RNA polymerase and the general transcription factor

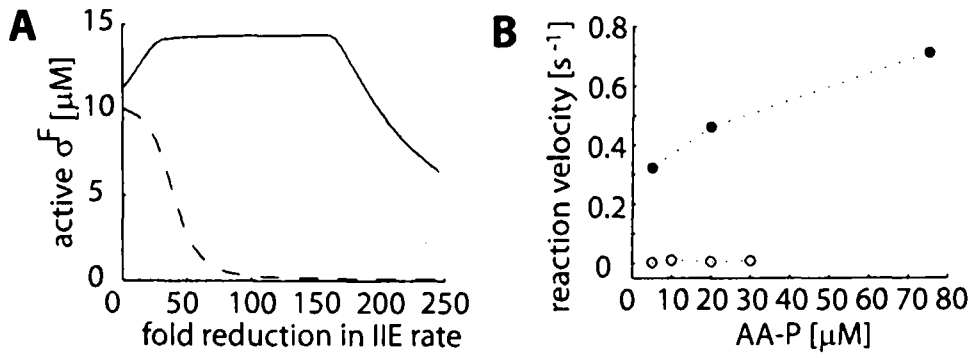


Figure 3.11: **A lower *in vivo* IIE turn-over rate.** **(A)** Predicted concentration of AB-free (active) σ^F before (dashes) and after (continuous line) septation, dependent on how much lower the IIE phosphatase rate is *in vivo* than under *in vitro* conditions. **(B)** Velocity of the IIE reaction as a function of the concentration of its substrate AA-P in 2.5 mM Mn^{2+} (filled circles) or 1 mM Mg^{2+}, 0.1 mM Mn^{2+} (open circles).

σ^A also need to be taken into account. The affinity between the core RNA polymerase and σ^F has been measured to be 560 nM (Lord *et al.*, 1999); the transcription factor σ^A competes with σ^F and binds the polymerase with a 25-fold higher affinity (22.5 nM) (Lord *et al.*, 1999). We assumed a normal protein on-rate of 10^6 M^{-1} s^{-1} for both transcription factors and adjusted the off-rates to reproduce the affinity constants. The cellular concentrations of σ^A and the core RNA polymerase have both been determined as $\sim 7.5\mu$M (Lord *et al.*, 1999).

3.4 IIE accumulation on the septum, AB allostery and a short half-life enable compartment-specific gene transcription

While septal accumulation of IIE (Duncan *et al.*, 1995) and a short half-life of unbound AB (Pan *et al.*, 2001) have been established experimentally as key components of the mechanism that enables prespore-specific σ^F release, it is unclear how they contribute and whether they are sufficient given that the IIE activity increase in the prespore is small and that the half-life of unbound AB strongly exceeds the time scale on which σ^F is activated. Moreover, how released σ^F can displace σ^A on the RNA polymerase despite the (unfavourable) competition of σ^F with the transcription factor σ^A (Lord *et al.*, 1999) has so far been a paradox.

We will show in section 3.4.1 that septal accumulation of IIE is sufficient because IIE accumulates on the septum together with its substrate AA-P and AB allostery enables

an exceptional high sensitivity to such small changes in AA production (section 3.4.3 and Chapter 4). Accelerated degradation of unbound AB is important to tune the protein concentrations in a way that small changes can act as a trigger without rendering the regulatory network vulnerable to fluctuations in protein expression (sections 3.6-3.8). The relative affinities of the RNA polymerase for σ^F and σ^A are shown to be optimized to allow for a coexistence of both holoenzymes (section 3.4.2). Other proposed mechanisms such as the removal of a IIE inhibitor or effects of the transient genetic imbalance are shown to be not necessary (section 3.6).

3.4.1 Accumulation of IIE (in association with its substrate AA-P) at the septum is sufficient to induce σ^F release in the prespore.

Contrary to previous suggestions, the model demonstrates that septal accumulation of IIE is sufficient to induce σ^F release in the prespore; it is not necessary to increase the IIE phosphatase rate in the prespore (for example by the removal of an inhibitor). As AA production is equal to the phosphatase rate multiplied by the concentration of IIE·AA-P complexes, it is sufficient to increase the substrate and enzyme concentrations by accumulation on the septum (Fig. 3.12A). Substrate and enzyme increase together when IIE accumulates on the septum because, owing to a low phosphatase rate and the slightly higher total AA concentration relative to the IIE concentration in the cell, 60% of all IIE is associated with AA-P before septation (Fig. 3.12B).

An increase in either the IIE activity or AA-P concentration alone is insufficient even if the phosphatase rate is set to the highest physiological possible value (Fig. 3.12A). It is therefore necessary for IIE to be present before septation, since that is the only way in which septal accumulation of IIE could also increase the AA concentration in the prespore. In fact asymmetric septation appears to require the presence of a significant IIE concentration (Barák & Youngman, 1996; Khvorova *et al.*, 1998; Feucht *et al.*, 1999; Ben-Yehuda & Losick, 2002).

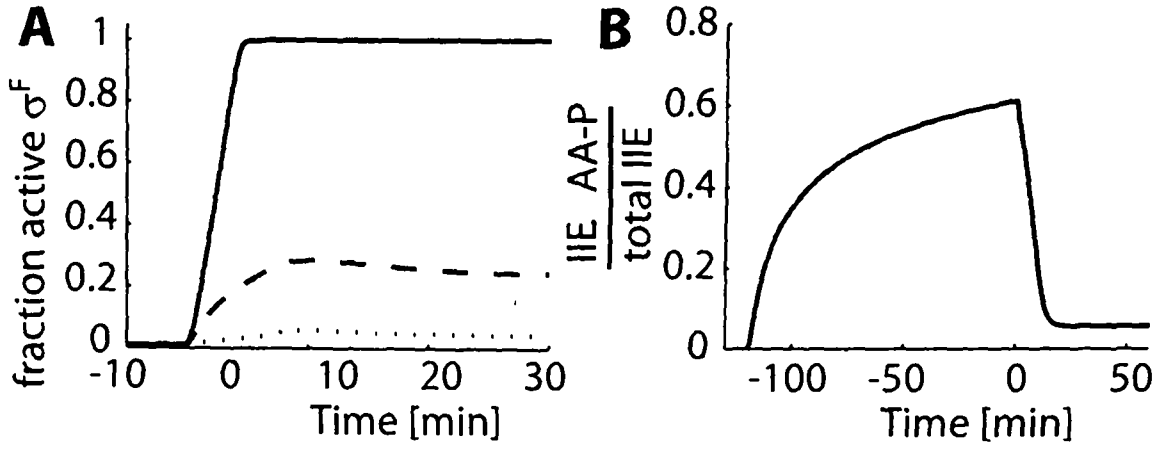


Figure 3.12: **Simulations showing that a septation-dependent increase in IIE·AA-P is sufficient for σ^F release.** **(A)** σ^F release in response to a 4-fold increase in IIE alone (dashes) in AA-P alone (dotted), or in IIE and AA-P (continuous line) imposed at t=0. **(B)** Time-dependent fraction of IIE in IIE·AA-P complexes. In both panels, septation was induced at t=0 (see text).

3.4.2 Formation of the σ^F-RNA polymerase holoenzyme

Prespore-specific σ^F release is only a first step to differential gene expression. In order to direct gene expression σ^F needs to bind to the RNA polymerase, from where it needs to displace σ^A. The mechanism of the latter has so far been unclear given the (unfavourable) competition of σ^F with σ^A (σ^A binds to the polymerase with a 25-fold higher affinity (560 nM and 22.5 nM for σ^F and σ^A respectively), but it is only slightly less abundant ($\sim 7.5\mu$M) than released σ^F (Lord *et al.*, 1999)). As the core RNA polymerase concentration is comparatively high ($\sim 7.5\mu$M), the mathematical model predicts that micromolar concentrations of σ^F·RNApol holoenzyme can form spontaneously in response to asymmetric septation, and that these complexes co-exist with micromolar concentrations of σ^A·RNApol holoenzyme (Fig. 3.13A). This result mimics the known situation in the sporulating cell, where both σ^A-holoenzyme and σ^F-holoenzyme are active (Fujita & Sadaie, 1998). If core RNA polymerase had the same affinity for σ^F as it has for σ^A, formation of σ^F-holoenzyme would not require a septation-dependent increase in IIE activity (Fig. 3.13B). There would then be a risk that σ^F-specific transcription could occur in the predivisional cell once the concentrations of the sporulation proteins had increased sufficiently to permit the formation of micromolar concentrations of σ^F-holoenzyme but before they had triggered septation.

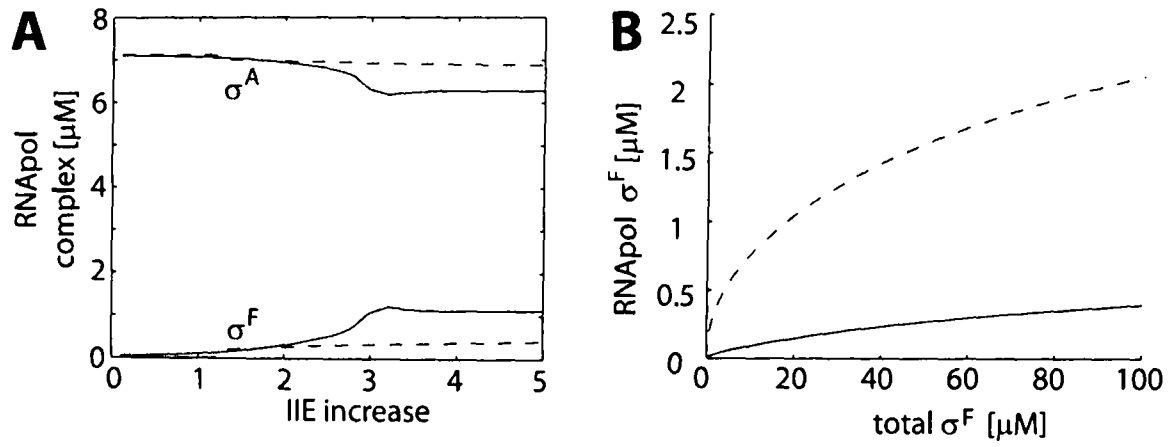


Figure 3.13: **Predicted concentrations of RNA polymerase holoenzymes upon septation.** **(A)** RNA polymerase holoenzyme formed with σ^F (lower curves) or σ^A (upper curves) as a function of an increase in IIE (including IIE complexed with AA-P) relative to the other sporulation proteins after 120 minutes of protein expression if AB is either allosteric (continuous lines) or not (broken lines)). **(B)** Predicted preseptational σ^F·RNApol concentration when the sporulation proteins increase in parallel, with parameters as given in tables B.1, 3.2 (continuous line) or with $k_{off}(\sigma^F\cdot\text{RNApol}) = 0.02\ s^{-1}$ (dashes). On the horizontal axis, the concentration of σ^F is representative of σ^F, AA, AB and IIE.

Figure 3.13A further shows that IIE (and the AA-P bound to it) needs to increase by at least three-fold in order to ensure the formation of micromolar σ^F·RNApol concentrations. Given the difference in volume between the two compartments, accumulation of IIE on the septum will result in at least a 2.5-fold increase (see Appendix B.3). However, as discussed in Appendix B.3, a 4-fold increase is a more realistic description of the sporulating cell and is therefore used in all the simulations presented here.

3.4.3 AB allostery enables high sensitivity to IIE

AB allostery is the key to the high sensitivity to changes in the IIE·AA-P concentration (Fig. 3.13). σ^F·AB complexes are stable at low AA concentration but, through allostery of AB, they become rapidly dissociated once the AA concentration reaches a critical threshold after septation. This effect is achieved by having different AA and σ^F affinities for the two AB conformations. The conformation that is stable in the absence of AA has a low affinity for AA and a high affinity for σ^F while the conformation that is stable in the presence of AA has a high affinity for AA and a low affinity for σ^F. Once a critical AA concentration is exceeded AA binding results in rapid σ^F dissociation and prevents the formation of σ^F·AB

complexes.

Allostery is necessary because σ^F binds with similar affinity to both AB forms, AB·ADP and AB·ATP (Magnin *et al.*, 1997). As a result σ^F can efficiently rebind AB that still has ADP in its binding pocket. Unless AA binding reduced the σ^F·AB affinity σ^F would always outcompete AA in binding because a large fraction of AA becomes inactivated through phosphorylation when releasing σ^F from its complex with AB·ATP. Accordingly, AA-dependent dissolution of σ^F·AB·ADP is important (Fig. 3.2, note the red arrows), and if we alter the simulation in such a way that the σ^F·AB affinity is reduced selectively in the presence of ADP, σ^F is released in response to septation even without AB allostery (Fig. 3.14).

We conclude that allostery is particularly important in controlling the fate of AB·ADP and in facilitating AA-dependent σ^F release. This observation can be confirmed in a smaller mechanistic model that can be studied with analytical tools (Chapter 4).

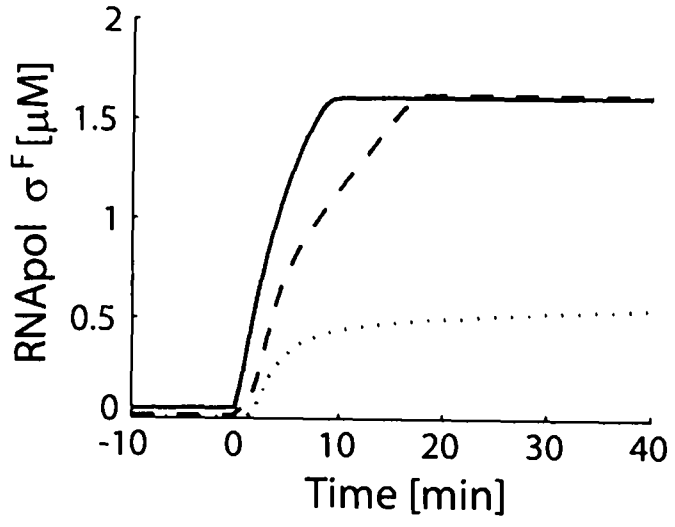


Figure 3.14: **AB allostery is necessary because AB·ADP binds σ^F with high affinity.** The simulations show the effect of a four-fold increase at t=0 min of IIE, together with its associated AA-P, on formation of RNApol(σ^F) holoenzyme assuming that AB is allosteric (continuous line) or not allosteric (broken lines). The σ^F·AB·ADP affinity is reduced by 100-fold in the case of the dashed line.

3.5 Economic efficiency

AB allostery also reduces the consumption of ATP during sporulation (Fig. 3.15C) by favouring the formation of AB·ADP·AA complexes (Fig. 3.15B) once σ^F·RNApol holoenzyme is formed (Fig. 3.15A). If the simulation is altered so as to prohibit the formation of these complexes, AB accumulates instead in AB·ATP·AA complexes; but the consumption of ATP is then greatly increased (Fig. 3.15C). Observing that in the case of the wild type about one ATP is consumed in order to release one σ^F for 10 minutes and that successful sporulation requires micromolar concentrations of free σ^F, we estimate that the wild type uses about 10 μmols per litre cell volume (each cell has a volume of about 10^{-16} litre (Nakano & Kawabata, 2000)) during sporulation. Without the formation of the AB·ADP·AA complex the usage would be more than 100 times higher ($\sim$ 1 mmol per litre). Considering that the cellular ATP concentration is about 1 mM (Jolliffe *et al.*, 1981; Guffanti *et al.*, 1987; Hecker *et al.*, 1988) such a difference would be substantial. We conclude that, for σ^F·RNApol holoenzyme to be formed and to persist without excessive waste of ATP, the (allosterically-enhanced) formation of AB·ADP·AA complexes is important. These complexes play an important role in acting as a sink for AB after the increase in IIE (and associated AA-P) that occurs in the prespore at asymmetric septation. The avoidance of "ATP wastage" can be expected to be particularly important once nutrients are scarce, as is the case at the onset of sporulation. The regulatory network that controls σ^F release appears therefore to be optimized to limit ATP wastage.

3.6 Evaluation of alternative models for σ^F activation

A number of further mechanisms have been proposed to explain compartmentalized activation of σ^F, especially because σ^F activation is still restricted to the prespore even when IIE is prevented from accumulating on the septum (Arigoni *et al.*, 1999). Two prominent suggestions are based on possible effects of the transient genetic imbalance (Frandsen *et al.*, 1999). The transient genetic imbalance arises because about 70% of the chromosome (in-

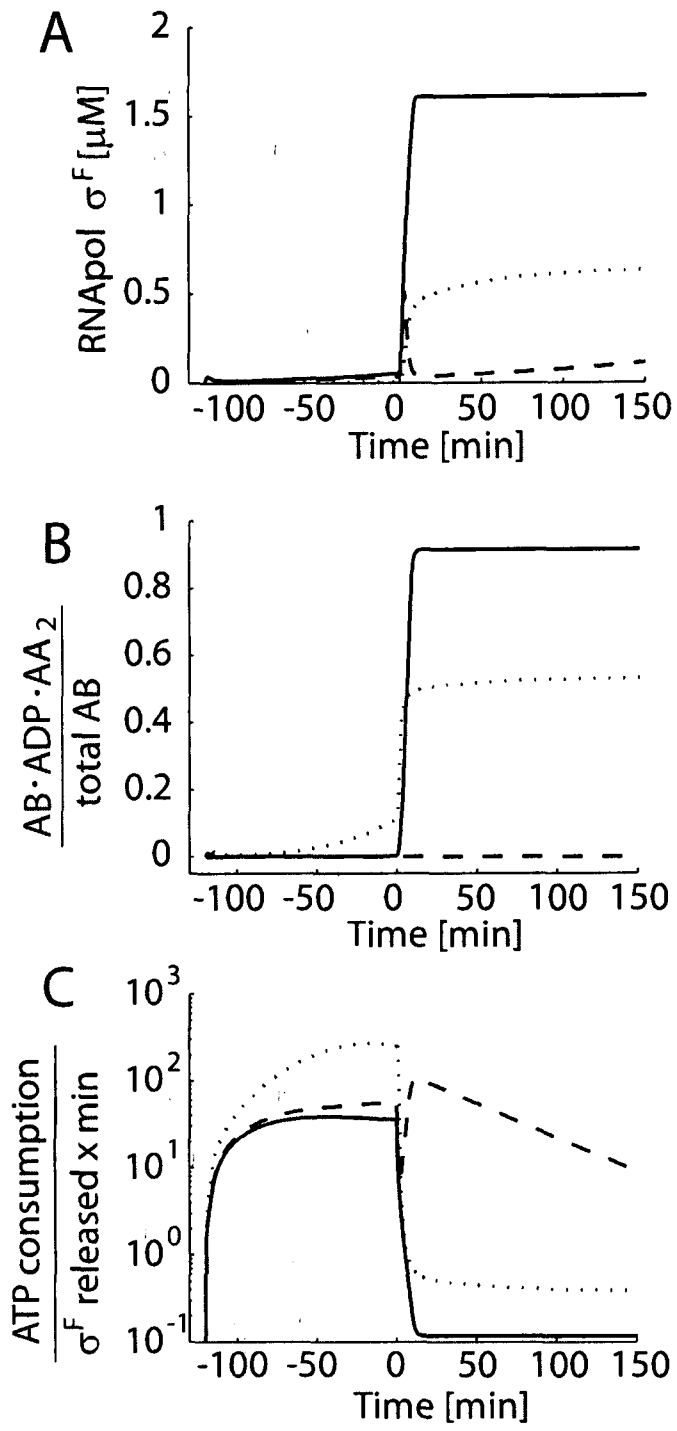


Figure 3.15: **AB allostery reduces ATP consumption.** The simulations show the effect of a four-fold increase at t=0 min of IIE, together with its associated AA-P, on **(A)** formation of RNApol(σ^F) holoenzyme, **(B)** fraction of AB in AA_2·AB·ADP complexes, **(C)** ATP consumption per minute per σ^F released, assuming that AB is allosteric (continuous line) or not allosteric (dotted), or that AB·ADP cannot bind AA (dashes).

cluding the *spoIIA* operon on which AB is coded) is initially excluded from the forespore and is imported only 10-20 minutes after septum closure (Wu *et al.*, 1998*a*). As a result AB cannot be expressed in the prespore immediately after septation (Dworkin & Losick, 2001), and it has been proposed that the accelerated degradation of unbound AB (Pan *et al.*, 2001) results in a net decrease in AB concentration in the prespore and in the prespore-specific

release of σ^F (Dworkin & Losick, 2001). A further proposed result of the genetic imbalance is the degradation and loss of an elusive IIE inhibitor from the prespore, which would further accelerate σ^F release (Frandsen *et al.*, 1999).

The transient genetic imbalance is too brief to affect σ^F release via AB degradation

In agreement with experimental observations (Dworkin & Losick, 2001), micromolar concentrations of σ^F·RNA polymerase holoenzyme still form when there is no transient genetic imbalance, that is when all proteins are continuously expressed in the prespore (Fig. 3.16A). Equally, the additional exclusion of the *spoIIE* gene from the prespore for the first 10-20 minutes after septation does not affect the phenotype either *in vivo* (Dworkin & Losick, 2001) or *in silico* (Table 3.3). The simulation further reveals that under physiological conditions the difference in the AB concentration is marginal in the presence or absence of the transient genetic imbalance (Fig. 3.16B). We therefore conclude that the time span for which the transient genetic imbalance exists (10 – 20 minutes) is too short to substantially affect σ^F release in the prespore.

The physiological role of the transient genetic imbalance remains unclear. One possibility is that it exerts a protective role in the mother cell which may be important because,

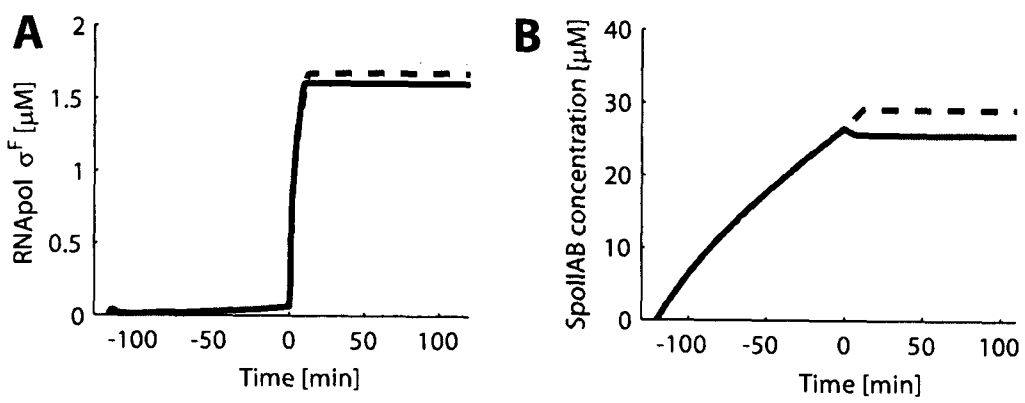


Figure 3.16: **The effect of the transient genetic imbalance.** **(A)** The predicted concentration of σ^F·RNApolymerase holoenzyme, and **(B)** the predicted SpoIIAB concentration assuming that with (solid line) and without (dashed line) a transient genetic imbalance. The concentration of IIE, together with its associated AA-P, was increased by four-fold at t=0 min to model the effect of septation.

contrary to what is assumed in the simulation, the rate of IIE expression is not constant but increases sharply before septation (Lucet *et al.*, 1999). As a consequence the ratio between the expression of IIE and the *spoIIA* genes increases also in the mother cell. Such continuing increase in the *spoIIE*/*spoIIA* expression ratio until after septation could, in principle, eventually trigger σ^F release also in the mother cell, and the availability of two *spoIIA* copies (as a result of the transient genetic imbalance) may be important to compensate for this. A short transient genetic imbalance can be expected to be sufficient in this case because once σ^F has been activated in the prespore the developmental fate of the mother cell is sealed by crisscross activation of transcription factors in the two compartments (Losick & Stragier, 1992).

The role of SpoIIAB degradation

Although the AB half-life is too long for AB degradation to enable rapid σ^F release after septation, simulation (Fig. 3.17A) and experiments (Pan *et al.*, 2001) agree that degradation of AB is necessary for successful sporulation. The quantitative model further reveals that AB degradation substantially reduces the AB concentration before septation (Fig. 3.17 B). If the AB expression rate is lowered in the AB degradation mutant to an extent that the wildtype protein concentration is regained then septation-dependent σ^F release is obtained (Fig. 3.17A, B - red lines). AB degradation thus appears to be necessary in order to tune the AB to AA ratio *before* rather than after septation.

Experiments support the prediction of the model that AB is expressed at a much higher level than AA, and that a substantial fraction of AB is already degraded before septation (Magnin *et al.*, 1997). Thus the ratio of AB monomers to AA is initially much larger than one but decreases towards one over the 90-120 minutes until the septum forms (Fig. 3.17C). While the experimentally observed AB/AA ratios greater than one could, in principle, be accounted for by limitations in the accuracy of the method, the method, even if inaccurate, should still be self-consistent and therefore give a constant AB/AA ratio.

The time-dependent concentrations of the sporulation proteins have been measured in

three independent biochemical studies (Magnin *et al.*, 1997; Lucet *et al.*, 1999; Lord *et al.*, 1999), which, however, do not fully agree. We have so far followed the two later experimental works whose measurements at the time point of septation can be approximated by the constant expression rates 6×10^{-9} M s^{-1} for AA and the AB dimer, and 2×10^{-9} M s^{-1} for σ^F and IIE. These rate constants imply that AB monomers are expressed at higher (twice as high) levels compared to AA (Fig. 3.17A, B). This is at odds with the widely accepted hypothesis that AB and AA are translationally coupled and therefore expressed at exactly the same level (Fort & Piggot, 1984). We note, however, that septation-dependent σ^F release is still possible when AA and AB *monomers* are expressed at 6×10^{-9} M s^{-1} as long as the σ^F and IIE expression rates are halved (10^{-9} M s^{-1}). At the time of septation there are then $\sim 44\mu M$ AA, $\sim 13\mu M$ AB dimer and $\sim 7\mu M$ σ^F and IIE. AB degradation is therefore important no matter what the exact expression rates are.

The model predicts that degradation of AB before septation is important in order to tune the relative protein concentrations. It is unclear why such an energetically costly mechanism

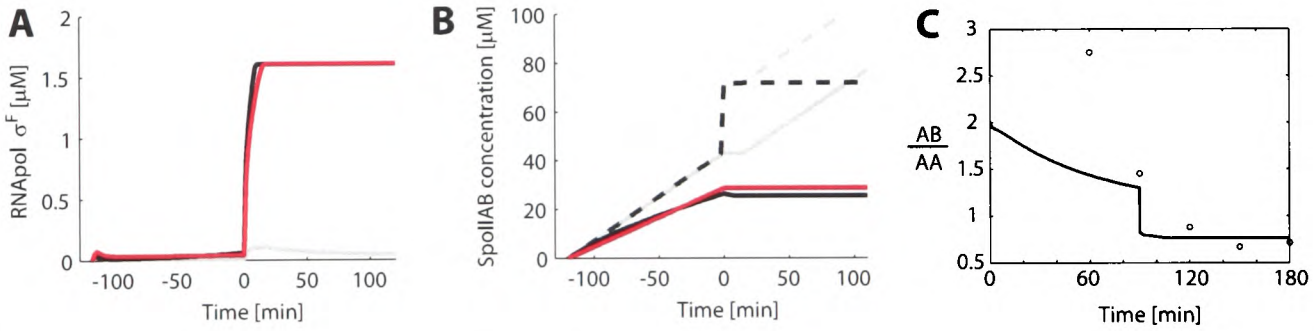


Figure 3.17: **The role of accelerated degradation of SpoIIAB. (A)** The predicted concentration of σ^F·RNApolymerase holoenzyme, and **(B)** the predicted concentrations of SpoIIAA (dashed lines) and SpoIIAB (solid lines) assuming that AB has a half-life of 28 minutes (black lines), or AB is stable (grey lines), or AB is stable and has an expression rate two thirds of what is common for the wildtype (red lines) while the AA expression rate is identical to that of the wild type (black lines). The continued expression of the sporulation proteins in the absence of AB degradation (grey lines) after septation ($t = 0$) is due to the lack of free unphosphorylated AA that would repress *spoIIA*. The concentration of IIE, together with its associated AA-P, was increased by four-fold at t=0 min to model the effect of septation. **(C)** The ratio of AB monomers to AA in experiments (balls) and simulation (line) assuming that the septum forms after 90 minutes; $t = 0$ corresponds to the activation of Spo0A, that is to t=-120 minutes in (A, B). The experimental values were obtained by reading off the values from Figure 2 in Magnin et al (1997).

is employed. One explanation is that AB degradation is important in the mother cell; this would explain the loss of AB after septum formation, which has been found consistently in two independent studies (Magnin *et al.*, 1997; Lucet *et al.*, 1999), and which is too strong to be the result of degradation in the smaller prespore alone. Another possible explanation is the increased robustness when the expression of AA and AB is co-regulated as discussed in section 3.8.1. More experiments that provide further and more accurate data on the cellular protein concentrations are clearly needed to fully understand the role of the operon structure and of AB degradation.

σ^F release without an increase in the IIE activity

The central role of a septation-induced increase in IIE activity has been questioned by experiments which revealed that σ^F release was still restricted to the prespore even if IIE remained homogeneously distributed upon septation (Arigoni *et al.*, 1999). Accumulation of IIE on the septum was prevented in these experiments by expressing only the soluble, homogeneously distributed, phosphatase domain of IIE, without the membrane anchor (IIEΔmem). Importantly, however, σ^F-dependent transcription was observed only with a substantial delay of about 1 hour. Successful sporulation requires that σ^F is released within 10 minutes after septation (Hilbert & Piggot, 2004) and the sporulation efficiency was therefore reduced for this mutant.

The delayed formation of σ^F·RNA polymerase complexes can be reproduced in the simulation (Fig. 3.18A), and is a consequence of the continuous loss of AB in the prespore (Fig. 3.18B). The dependency on AB degradation explains why σ^F release is delayed so much. Because σ^F release now requires loss of AB from the prespore, it is important that AB is not expressed in this compartment, explaining why the transient genetic imbalance is important in IIEΔmem mutants. Accordingly, experiments and simulations agree that mutants in which both IIE accumulation, and the transient genetic imbalance, are abolished are unable to form spores (Fig. 3.18D).

A similar conclusion can be drawn from division mutants. In these mutants, both a

septation-dependent increase in IIE and the block in the AB expression are impossible. Accordingly these mutants fail to form spores, and the simulation predicts that σ^F·RNA polymerase complexes do not form within the timespan required for successful sporulation (Table 3.3). Simultaneous IIE overexpression results in σ^F-dependent transcription, though with a considerable delay (Arigoni *et al.*, 1999). Such delayed formation of micromolar concentrations of RNApol·σ^F complexes is also observed *in silico.*

We conclude that the observation that σ^F can be also released without the septation-dependent increase in IIE activity does not imply that IIE is not the physiological trigger of compartmentalized σ^F release. Since mutants in which both IIE accumulation and the transient genetic imbalance are abolished are effectively spo$^-$, we can further conclude that additional mechanisms that can enable compartment-specific σ^F release seem not to exist.

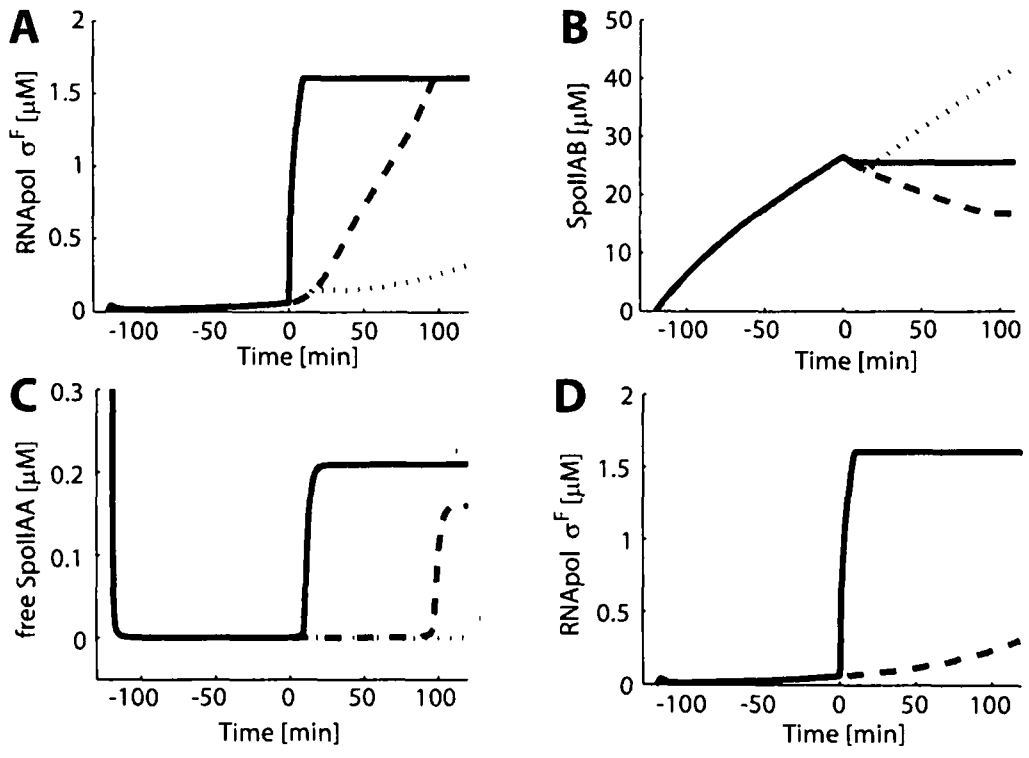


Figure 3.18: **σ^F can be released compartment-specific without an increase in IIE activity.** **(A)** The predicted concentration of σ^F·RNApolymerase holoenzyme, **(B)** the predicted concentrations of SpoIIAB, and **(C)** the predicted fraction of AA that is unbound and unphosphorylate assuming that the concentration of IIE, together with its associated AA-P, either increases by four-fold at t=0 min (solid line), or does not increase (dotted line), or IIE neither increases nor is *spoIIA* transported into the prespore after septation (dashed line). **(D)** The predicted concentration of σ^F·RNApolymerase holoenzyme assuming that the concentration of IIE, together with its associated AA-P, either increases by four-fold at t=0 min (solid line) or IIE neither increases nor is there a transient genetic imbalance (dashed line).

The simulations hint to an additional important detail of the regulatory mechanism. Whilst expression of the *spoIIA* genes is repressed in the wildtype prespore because of the emergence of unphosphorylated AA (Arabolaza *et al.*, 2003), the AA concentration is too low to explain the block in the IIEΔmem mutant (Fig. 3.18C). Moreover, the simulation suggests that in the mutant only the *spoIIA* genes are repressed but not *spoIIE* (Fig. 3.18A). The simulation therefore predicts that the septal location of IIE is necessary for the transfer of the chromosome into the prespore.

This proposition is in agreement with the experimental observation that although septation is rapid, spore engulfment takes more time, and the structure of the septum (which needs to permit DNA translocation) is severely altered in the mutant (Arigoni *et al.*, 1999). Moreover, a mutant that co-expresses a phosphatase deficient version of IIE on the membrane with the soluble phosphatase domain leads to a lower rather than a higher sporulation efficiency (Arigoni *et al.*, 1999). This observation is in good agreement with the notion that IIE facilitates transfer of *spoIIA* into the prespore but is difficult to explain otherwise.

Is there a IIE inhibitor?

It has been suggested that the transient genetic imbalance may also support compartmentalized activation of σ^F by the prespore-specific depletion of an elusive IIE-inhibitor (Frandsen *et al.*, 1999). The idea that IIE is regulated by a IIE inhibitor has received support from the observation that a IIE mutation that does not give rise to an altered phosphatase rate *in vitro* leads to premature σ^F release *in vivo* (Feucht *et al.*, 2002) as well as from IIE overexpression experiments (Arigoni *et al.*, 1996).

Although we find a low IIE turn-over rate under *in vivo* conditions (Fig. 3.8) this is not the result of a IIE inhibitor but of the physiological salt conditions ($\sim$ 1mM Mg^{2+}, and 0.1 mM Mn^{2+} (Eisenstadt *et al.*, 1973)) which reduce the activity of serine phosphatases (Schroeter *et al.*, 1999). Moreover, a septation-dependent increase of the IIE turn-over rate (as may be achieved by the removal of a IIE inhibitor) is not required for compartment-specific σ^F release (Fig. 3.19).

While the simulation therefore does not support a role for a IIE inhibitor in σ^F regulation under physiological conditions, we note that the premature transcription of σ^F-dependent genes in response to overexpression of IIE (Arigoni *et al.*, 1996) can only be reproduced if these genes are either already transcribed at an intermediate RNApol·σ^F concentration ($\sim$ 0.3 μM instead of 1 μM), or if the IIE activity increases (Fig. 3.19). An increase in the IIE concentration alone is insufficient to give rise to micromolar RNApol·σ^F concentrations because the substrate of the phosphatase is limiting as well, and no substrate-saturation of the enzyme is achieved if only the concentration of the enzyme is increased.

In light of our previous finding that the salt conditions are responsible for the low phosphatase rate the existence of a IIE inhibitor is very unlikely because an inhibitor would only further reduce the IIE turn-over rate and its removal would not lead to an increase beyond the low salt-dependent rate. The apparent increase in the IIE activity in response to IIE overexpression and to the reported mutation must therefore result from an activating process, such as the formation of IIE aggregates, which may process the substrate more efficiently.

We conclude that mechanisms other than the septation-dependent IIE activity increase

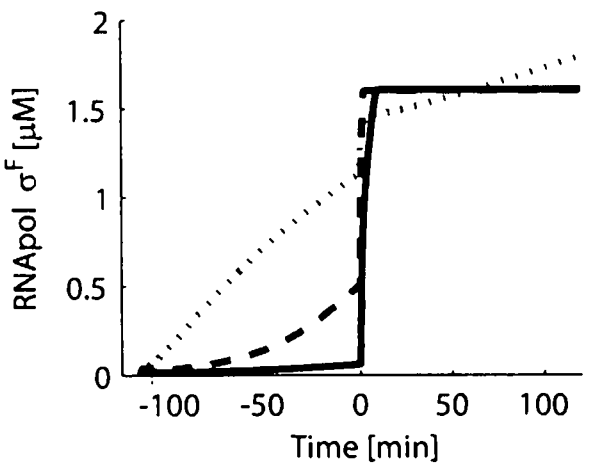


Figure 3.19: **The effect of IIE overexpression.** The predicted concentration of σ^F·RNApolymerase holoenzyme assuming that IIE is expressed at its normal rate (solid line), at a five-fold increased rate (dashed line), or at a five-fold increased rate in conjunction with a five-fold increased turn-over rate (dotted line). The concentration of IIE, together with its associated AA-P, was increased by four-fold at t=0 min to model the effect of septation.

in the smaller prespore are unlikely to play an important role in the compartment-specific activation of σ^F, and that the elusive IIE inhibitor most likely does not exist. Given the intriguing arrangement of the sporulation genes, it will be interesting to learn of other roles for the transient genetic imbalance. More experiments, which also address the different protein concentrations in mother cell and prespore, will be important in that endeavour.

3.7 Phenotypes of mutants

Given that all parameters of the model are based on good experimental data we have tested whether our model correctly predicts the phenotype of mutants. Table 3.3 shows that for those mutants for which the biochemical effect of the mutation is known the simulation succeeds in predicting the physiological effect very well. The predictions of the model for those mutants whose cell division, transient genetic imbalance, AB degradation, and IIE localisation or expression had been affected have been discussed in detail in the previous section. In the following we discuss those mutantions that affect the interactions of AB and AA, and the phosphorylation and dephosphorylation of AA.

The AAL61A and the AAL90A mutations both prohibit spore formation. The AAL61A mutation results in slower AA dephosphorylation and a 10-fold lower AB·ADP·AA affinity (Lee *et al.*, 2001). According to the simulation, a 10-fold lower affinity has no impact, but even a three-fold reduction in the phosphatase rate prohibits the formation of micromolar RNApol·σ^F concentrations on the relevant time scale of several hours.

The AAL90A mutation on the other hand increases the phosphorylation rate by three-fold and decreases the AB·ADP·AA affinity by at least 100-fold (Lee *et al.*, 2001). While the increase in the phosphorylation rate has no notable effect in the model, a 10^4 lower AB·ADP·AA affinity will prohibit rapid RNApol·σ^F formation. If (as unpublished experiments suggest) the AB·ATP·AA affinity is also affected, then even a smaller reduction in affinity will affect RNApol·σ^F formation.

The AAS58A mutant cannot be phosphorylated, and this mutation induces RNApol·σ^F

complex formation even in division mutants (Diederich *et al.*, 1994; King *et al.*, 1999; Carniol *et al.*, 2004). While the lower AB·ADP·AA affinity (Magnin *et al.*, 1997) has no effect in the simulation, the inability to phosphorylate AAS58A is sufficient to enable strong RNApol·σ^F complex formation (as long as AAS58A does not repress *spo0A* too early, since otherwise insufficient protein is produced to form enough RNApol·σ^F). The lower σ^F·AB affinity further increases the concentration of active σ^F.

AB-R105A induces premature σ^F activity *in vivo* (Ho *et al.*, 2003; Shu *et al.*, 2004). It has a higher catalytic rate than the wild type, but a much lower ADP-ATP exchange rate (Shu *et al.*, 2004). Assuming that the ADP-ATP exchange rate is limited by a reduced lid opening rate, the model correctly simulates the phenotype of this mutant.

3.8 Robustness

Biological networks need to be organized a way that they are sensitive to regulatory input but robust to the small variations that may arise from changes in environmental conditions or from stochastic fluctuations within the cell. As shown in the following, the sporulation network meets both conditions to an impressive degree.

3.8.1 Robustness to variations in protein expression rates

During the vegetative phase, the concentrations of σ^F, AA, AB, and IIE are too low to allow sufficient σ^F·RNApol formation to drive prespore development (Fig. 3.20). This efficiently protects the cell from premature σ^F activation. The triggering of differential gene expression requires the formation of IIE·AA-P complexes, and therefore the expression of AA and IIE, prior to septation. In order to avoid premature σ^F activation all sporulation proteins (σ^F, AA, AB and IIE) need to be expressed in parallel (Fig. 3.21A). Given the low numbers of proteins expressed, the process is inherently stochastic, and variations in the environmental conditions can further affect the global protein expression rates. It is therefore important to investigate the robustness of the network to such fluctuations.

The analysis reveals that as long as the protein expression rates for all four sporulation

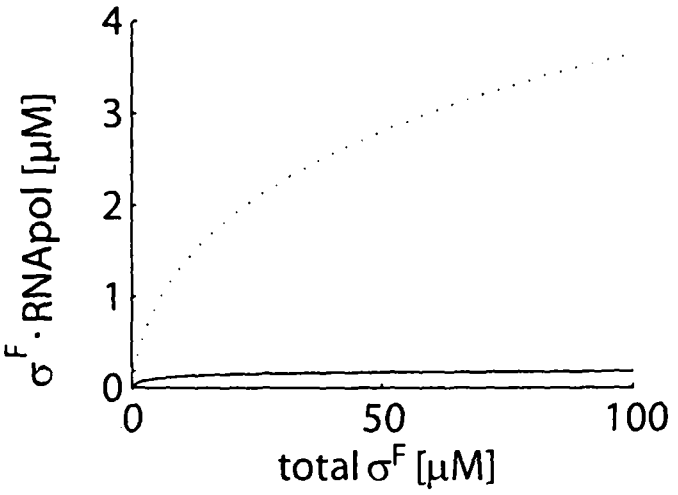


Figure 3.20: **The protein concentration dependency of σ^F·RNA polymerase holoenzyme formation.** Concentration of σ^F·RNA polymerase holoenzyme as a function of the reference protein concentrations (as exemplified by the σ^F concentration). The relative concentration of IIE (and the associated AA-P) was either increased by four-fold (dotted line) or left unchanged (continuous line).

proteins are increased in parallel, that is by a common factor as denoted on the horizontal axis in Figure 3.21B, the sporulation efficiency is not affected by stochastic variation in gene expression; only a minimal expression rate is required to provide sufficient σ^F for binding to the RNA polymerase (Fig. 3.21B, grey lines). While the genes for AA, AB and σ^F are organized in an operon (*spoIIA*), IIE is expressed separately from a distant locus (*spoIIE*) (Fig. 3.21A). Accordingly, in the cell the expression of IIE may vary independently from AA, AB and σ^F. The simulation reveals that an independent increase of up to 2.5-fold in the expression of *spoIIA*-encoded proteins can still be tolerated; for higher *spoIIA*/*spoIIE* ratios the relative activity of the phosphatase becomes too weak (Fig. 3.21B, black lines). An even higher independent increase in the expression of the *spoIIA* genes can be tolerated if we assume that the expression of the *spoIIA* and *spoIIE* genes is at least weakly correlated such that a large increase in the expression of the *spoIIA* genes is accompanied by at least a small increase in the expression of the *spoIIE* genes (Fig. 3.21C). Such a correlation is not unexpected considering that variations in gene expression are the result of both intrinsic and extrinsic noise. The latter, which reflects cell-to-cell variation in the concentration of other molecular species such as the RNA polymerase, will affect all genes similarly. We can conclude that the independent regulation of the *spoIIA* and *spoIIE* genes is unlikely to

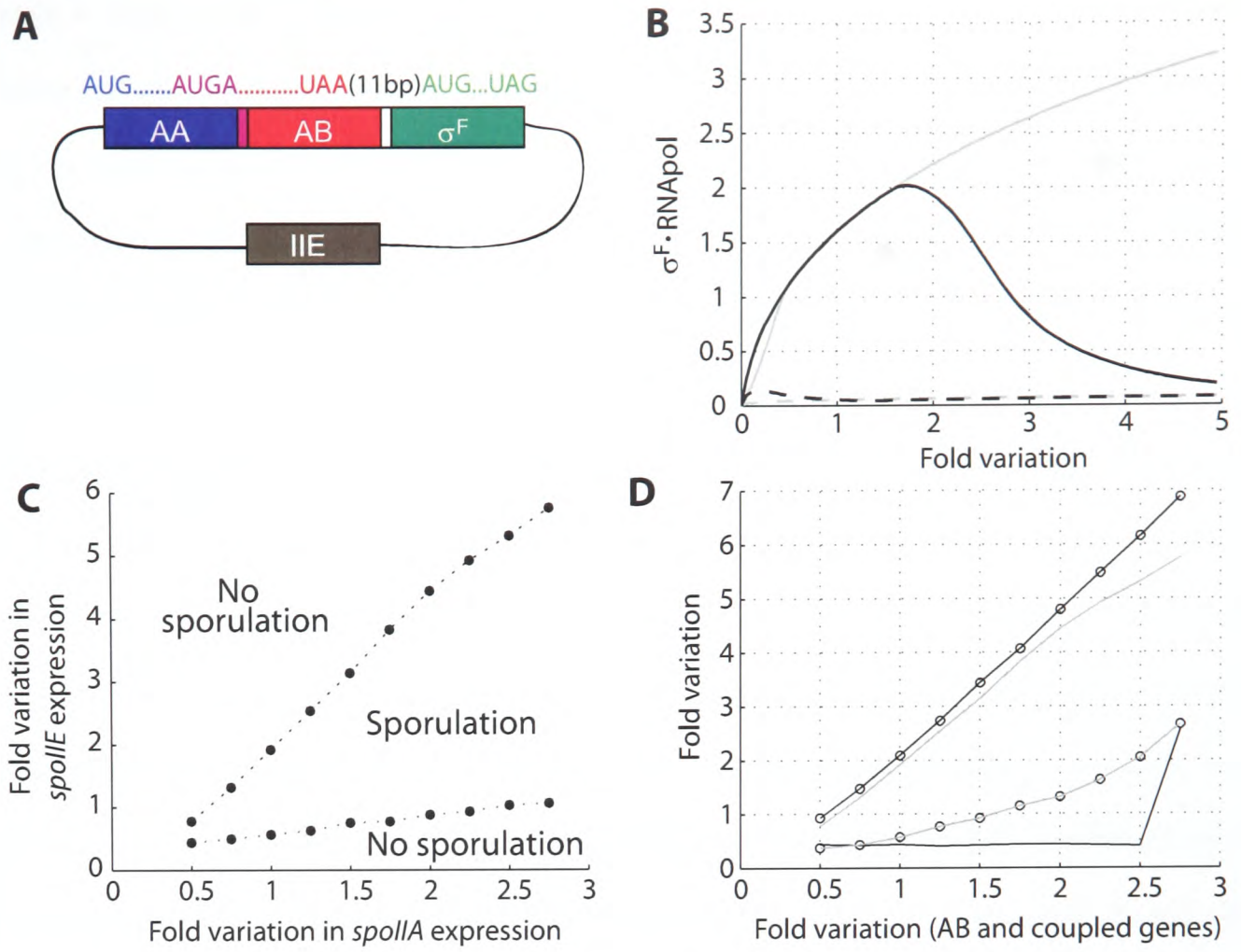


Figure 3.21: **The impact of parallel and random variations in the expression of *spoIIE* and *spoIIA* genes on σ^F release. (A)** The *spoIIA* operon comprises the genes for SpoIIAA, SpoIIAB, and σ^F. The genes for SpoIIAA and SpoIIAB overlap; the genes for SpoIIAB and σ^F are separated by 11 basepairs. **(B)** The regulatory network is robust to parallel variations in gene expression. The predicted concentration of σ^F·RNApolymerase holoenzyme before (dashed lines) and after (continuous lines) septum formation if either all (grey lines) or all protein expression rates except for the one of SpoIIE (black lines) were increased by the factor on the horizontal axis compared to the standard reference rates ($6 \times 10^{-9} Ms^{-1}$ for SpoIIAA and SpoIIAB dimers and $2 \times 10^{-9} Ms^{-1}$ for σ^F and SpoIIE). **(C, D)** The expression rate combinations for which septation-dependent σ^F release is possible (between the lines) or not (outside the area marked by lines). **(C)** The impact of differential regulation of *spoIIE* and *spoIIA* expression. The vertical and horizontal axes indicate the fold variation in the *spoIIE* and *spoIIA* expression rates respectively, compared to the standard reference rates. **(D)** The impact of differential regulation of the expression of genes encoded in the *spoIIA* operon. The vertical axis indicates the fold variation in the expression of AA (circles), σ^F (black lines), or AA and σ^F (grey lines). The horizontal axis indicates the fold variation in the expression of SpoIIAB and of any other protein whose expression is coupled to the one of SpoIIAB (which are those genes in the *spoIIA* operon not reported on the vertical axis). The sudden jump observed at a high SpoIIAB to σ^F ratio (lower black line) is the consequence of impaired σ^F release when the relative SpoIIAB concentration is too high.

generate a major risk of failed sporulation. Separation of the *spoIIA* and *spoIIE* genes on the bacterial chromosome, on the other hand, has benefits because it ensures that, upon septation, each compartment retains one copy of *spoIIE* while initially (for the first $10-20$ minutes) two copies of *spoIIA* are in the mother cell but none in the prespore (Frandsen *et al.*, 1999). This initial transient genetic imbalance may protect the mother cell from a relative increase of *spoIIE* to *spoIIA* gene products as is discussed in section 3.6.

Although the genes in the *spoIIA* operon are co-transcribed into a single mRNA, constant expression ratios are only obtained if translation is perfectly coupled as well. Coupled translation is achieved when two genes are translated by the same ribosome. Reinitiation of translation at a nearby start codon after termination at the upstream gene is possible because ribosome dissociation from the mRNA is a slow and energy-dependent process (McCarthy & Gualerzi, 1990). There is currently no direct experimental evidence for coupled translation of the *spoIIA* operon. Coupling can, however, be postulated based on the arrangement of genes (Fort & Piggot, 1984). The first two genes in the *spoIIA* operon (encoding AA and AB) overlap by four basepairs, while the genes for AB and σ^F are interspaced by 11 basepairs (Fig. 3.21A); coupled translation has been documented for intercistronic distances of more than 60 basepairs (McCarthy & Gualerzi, 1990). The efficiency of reinitiation depends on the distance as well as the strength of the Shine-Dalgarno sequence (McCarthy & Gualerzi, 1990; Adhin & van Duin, 1990) which is, in general, located 5-13 basepairs upstream of a start codon and which binds to the homologous 3' end of the 16S rRNA, a component of the 30S ribosomal subunit. Moreover, the secondary structure of the mRNA can affect lateral diffusion of the ribosomes (Adhin & van Duin, 1990).

According to the protein expression data for the *spoIIA* operon it appears that the last gene in the operon, σ^F, is expressed at much lower levels than are AA and AB, while AB monomers may be expressed at equal or up to 3-times higher levels compared to AA (Magnin *et al.*, 1997; Lucet *et al.*, 1999; Lord *et al.*, 1999). The weaker expression of a downstream gene (as is the case for σ^F) can, in general, be accounted for by a weaker ribosomal binding

site which is removed far enough from the termination codon of the upstream cistron that a considerable fraction of ribosomes dissociate from the mRNA before translation can be reinitiated (McCarthy & Gualerzi, 1990). It should be noted that while the transcriptional and translational coupling will reduce the noise in the relative AB to σ^F expression levels the unbinding of ribosomes is necessarily a stochastic process and will therefore add a (low level) of noise. The stronger expression of a downstream gene (as may be the case for AB relative to AA) can, in general, only be observed if a strong initiation sequence for the downstream gene is occluded by mRNA secondary structure which is melted by the ribosome that transcribes the upstream gene (McCarthy & Gualerzi, 1990). Such a condition does not seem to be met by the gene for AB, and more accurate expression data will be necessary to establish whether more AB than AA is expressed.

The impact of different degrees of translational coupling between the genes in the *spoIIA* operon can be assessed by analyising the effect of varying the expression levels of the genes in the *spoIIA* operon independently of each other. We find that the network is already sensitive to low levels of variation if the expression of AB and AA is no longer co-regulated, (Fig. 3.21D, grey lines and circles). Thus if the AA expression rate remains fixed and the AB expression rate increases by 60% (corresponding to the factor 1.6 on the horizontal axis in Fig. 3.21D), then sporulation is predicted to fail; 60% variation from the mean is a noise level observed in bacterial (*E. coli*) expression systems (Elowitz *et al.*, 2002). On the other hand, if the expression of AA and AB remains co-regulated but σ^F expression is regulated independently, the network is rather robust to variations in gene expression as long as the expression of AB is increased more than the expression of σ^F and the overall σ^F concentration remains high enough to form micromolar concentrations of the holoenzyme (Fig. 3.21D, black lines). The transcriptional coupling together with a strong translational coupling of AA and AB therefore substantially increases the robustness of the network to fluctuations in gene expression. Stochastic variations in the relative rate of σ^F translation, on the other hand, is not as detrimental as long as the translation efficiency for σ^F is lower

than for AA and AB, as can be achieved by a weaker ribosomal binding site and the resulting (stochastic) dissociation of ribosomes. An advantage of preferential dissociation of the ribosomes before translating the gene for σ^F is that the bacterium saves the energy that would otherwise be required to translate, and subsequently degrade, unnecessary (harmful) copies of σ^F. Considering that σ^F comprises 255 amino acids and linkage of each amino acid requires the equivalent of 4 ATPs, the energy gained by not translating and degrading 10 μM σ^F corresponds to more than 10 mM ATP, which is a considerable amount considering that the bacterial ATP concentration is 1-3 mM (Jolliffe *et al.*, 1981; Guffanti *et al.*, 1987; Hecker *et al.*, 1988) and sporulation is a response to starvation, that is, energy deprivation. Coupled translation of AA and AB and decoupled translation of σ^F therefore ensure maximal robustness to stochastic variations while being economical in that no more σ^F is expressed than is required in the network.

The particular organisation of the sporulation genes thus appears to increase the sporulation efficiency. This effect can be quantified. For this we assume that the gene expression levels in the cell population follow a normal distribution with variance η around the mean value. Given the complex regulation pattern of gene expression, gene expression levels are unlikely to be distributed exactly normally. A normal distribution is, however, still likely to provide an approximation no worse than what could be obtained with a detailed model of the regulatory process in the absence of sufficient data to determine all required parameter values (Swain, 2004). Sporulation efficiency is determined as the fraction of simulation runs for which the concentration of $\sigma^F \cdot$ RNA polymerase holoenzyme does not exceed 0.4 μM before septation and exceeds one micromolar after septation. For each condition the mean sporulation efficiency and standard deviation are calculated from 100 independent runs that are carried out 10 times. In each run the protein expression rates were set randomly such that overall the respective distributions of the protein expression rates were obtained. Determination of the sporulation efficiency for $\eta \in [0, 1]$ shows that as long as the sporulation genes are translationally coupled, even high variances hardly affect the sporulation

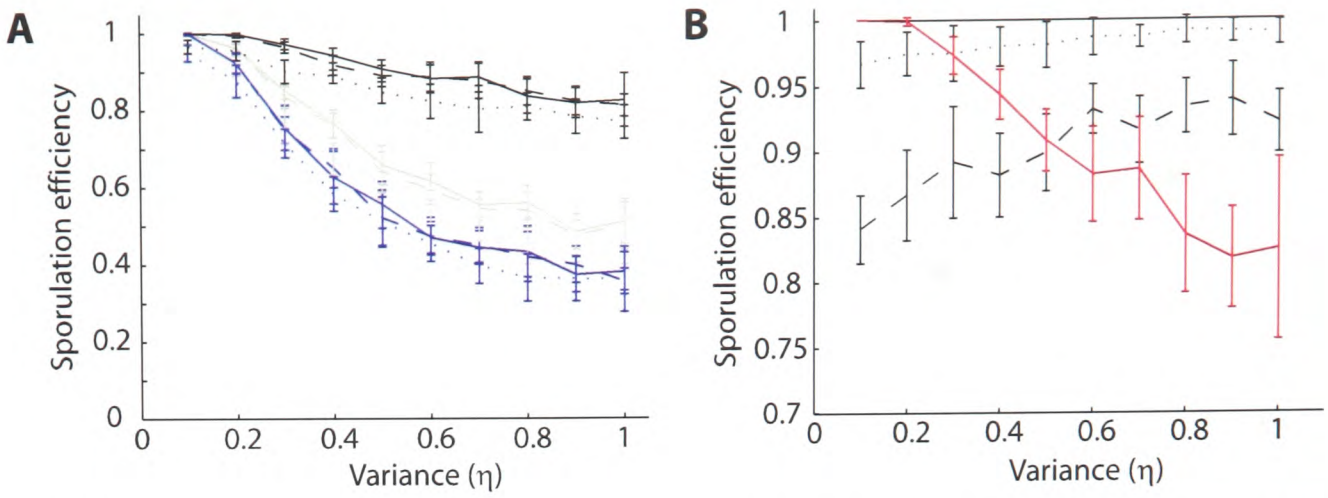


Figure 3.22: **The impact of stochastic variation in gene expression on sporulation efficiency. (A)** The fraction of successful sporulation events (as defined in the text) dependent on the variance in gene expression if expression of the *spoIIA* genes is coupled (black lines), the expression of SpoIIAB and σ^F is coupled (grey lines), or the expression of AA and σ^F is coupled (blue lines). SpoIIE is expressed throughout at the standard rate of 2×10^{-9} M^{-1} s^{-1}. The broken lines show the effect of an additional independent normal variation in the rate of σ^F expression with $\eta_S = 0.1$ (dashed lines) or $\eta_S = 0.3$ (dotted lines) from the coupled rates. If σ^F is one of the coupled rates then σ^F expression is varied both together with its coupling partner and additionally independently to reflect the additive levels of noise acting at the initiation of translation and the re-initiation/dissociation step. **(B)** The fraction of successful sporulation events (as defined in the text) dependent on the variance in gene expression if expression of the *spoIIA* and *spoIIE* genes is coupled (to assess the benefits of correlated expression), and an additional noise term η_E is added to the expression of *spoIIE* with $\eta_E = 0.1$ (black continuous line), $\eta_E = 0.3$ (dotted line), or $\eta_E = 0.6$ (dashed line); η_E assesses the effects of independent promotors and spatial heterogeneity in the concentration of transcription and translation factors. The red line is identical to the continuous black line in panel A (noise in coupled *spoIIA* expression, SpoIIE expressed at 2×10^{-9} M^{-1} s^{-1}). Mean and standard deviation are based on 10 times 100 independent runs.

efficiency (Fig. 3.22A, black lines). The sporulation efficiency is even higher at high noise level, η, if *spoIIE* expression co-varies with *spoIIA* expression, at least weakly (Fig. 3.22B). A lengthening of the transcription time, (that is a delay in septation) when transcription levels are too low to generate sufficient σ^F until septation will further increase robustness to fluctuations in the rate of protein expression. Such a dependency of the time point of septation on the protein (and in particular the SpoIIE) concentration is in agreement with experiments (Khvorova *et al.*, 1998; Ben-Yehuda & Losick, 2002) and might explain the large variance in the delay between the onset of sporulation and septation that is observed under different sporulation conditions. Low levels of additional stochastic noise in σ^F ex-

pression (broken lines), as may arise because of the stochastic dissociation of ribosomes, also has rather little impact and confirms that the weak coupling of AB and σ^F translation does not substantially reduce sporulation efficiency. If, on the other hand, *spoIIAB* is removed from the operon and controlled independently by the same promotor then the sporulation efficiency drops rapidly (Fig. 3.22A, blue lines). This is in good quantitative agreement with experiments which find that the sporulation efficiency drops to $40-80\%$ of wildtype levels (Dworkin & Losick, 2001), especially when considering that $\eta \sim [0.3, 0.6]$ for these expression levels (Elowitz *et al.*, 2002). If *AA* is moved instead, then the effect is reduced (Joanna Clarkson, personal communication) as also predicted by the model (Fig. 3.22A, grey lines).

It should be noted that the drop in sporulation efficiency has previously been accounted for by the loss of the transient genetic imbalance when *spoIIAB* is moved to a chromosomal position close to the origin of replication (Dworkin & Losick, 2001). The transient lack of AB expression in the prespore together with accelerated degradation of unbound AB (Pan *et al.*, 2001) had been suggested to enable σ^F release (Dworkin & Losick, 2001). However, as shown in section 3.6, the transient genetic imbalance does not affect σ^F release on the timescale on which it persists, and the stochastic effects are therefore a much more likely explanation for the observed phenotype of the mutants.

We conclude that the protection from stochastic variation in the expression rates of the *spoIIA* proteins substantially increases viability. This demonstrates the optimized character of gene regulation and suggests that co-regulation of genes can serve to optimize cellular network dynamics in spite of the inherent noise in all biological processes.

3.8.2 Robustness to stochastic fluctuations after septation.

Because the volume of each bacterium is small ($\sim 10^{-15}$l) the total number of protein molecules is still small at the time of septation. We therefore also analysed a stochastic version of the model. If we start the model with the protein concentrations that are used in the deterministic model at the time of septation and increase the concentration of IIE

and IIE-bound AA-P four-fold as in the deterministic model, we, however, find a similar behaviour in both the stochastic and the deterministic models (Fig. 3.23A) and little variance between individual runs in the stochastic simulation. The main difference between the stochastic and the deterministic models is the brief delay and subsequently faster formation of RNApol·σ^F complexes. Larger differences will be apparent only when analysing mutants where protein concentrations are further reduced. There they may explain the intermediate sporulation efficiencies. The simulations were carried out with Matlab Simbiology using the stochastic simulation algorithm SSA, which is equivalent to solving the chemical Master equation for the system.

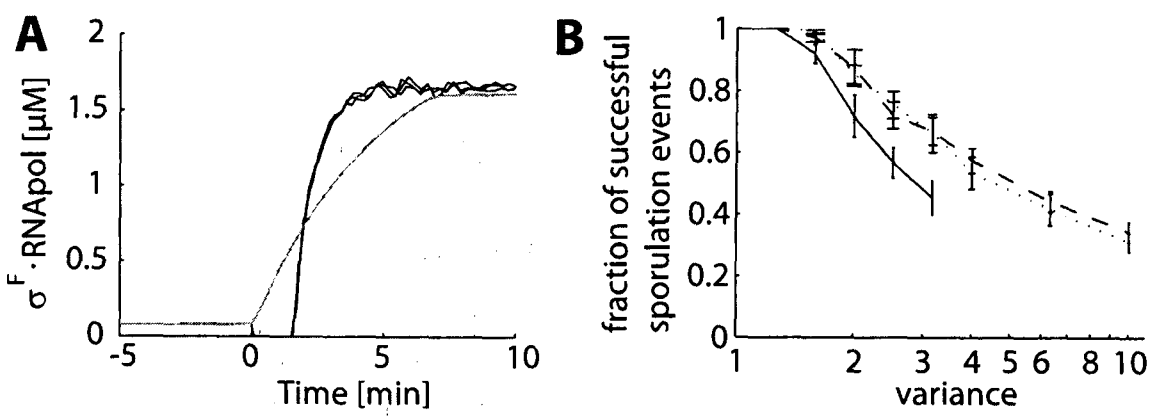


Figure 3.23: **The robustness of the regulatory network to stochastic flucuations. (A)** Predicted concentration of RNApol·σ^F in a deterministic (grey line) and in stochastic (black lines) simulations of the model. **(B)** Fraction of successful sporulation events if either all binding rates (dashed), all enzymatic rates (dotted), all binding and enzymatic rates (solid) are varied randomly by the factor given on the horizontal axis. Standard deviations are based on 10 sets of 100 runs each. In each run kinetic parameters were varied randomly within the set range; successful sporulation events are defined as those with a concentration of RNApol·σ^F holoenzyme less than 0.4 μM without, and greater than 1 μM with, a 4-fold increase in IIE (and associated AA-P).

3.8.3 Critical parameters that determine the behaviour of the regulatory network

The additional robustness of the network to random changes in values of kinetic parameters and enzymatic rates (Fig. 3.23B) justifies our approach of using the kinetic parameters that were determined from *in vitro* experiments. It should be noted that differences between *in vitro* and *in vivo* conditions will, in general, lead to only small changes, and most reaction rates can be changed by an even greater margin than suggested by Fig. 3.23B. Which

reactions have the greatest impact on the model behaviour can be analysed by means of control coefficients, as previously suggested for the analysis of signaling networks by Lee and co-workers (Lee *et al.*, 2003). Control coefficients can be used to quantify the relative change in a model variable in response to (small) relative changes in a parameter value k_i. Here they were determined from

$$C_i^{[\sigma^F \cdot RNApol]} = \frac{\delta[\sigma^F \cdot RNApol]}{[\sigma^F \cdot RNApol]} \frac{k_i}{\delta k_i}, \tag{3.2}$$

allowing the impact of parameter perturbations on the concentration of σ^F·RNApol complexes to be ascertained. To understand the relative impact of the different interactions we studied the 25 independent rate constants listed in Tables B.1 and 3.2. Control coefficients were obtained by numerical determination of the response to a change of the rate constants of all steps by 0.01% at the steady state before septation. Smaller relative changes of the rate constants did not lead to a significant improvement of the control coefficient values. We used 15 μM σ^F, 30 μM AA, 22.5 μM AB, and 15 μM IIE for the concentrations of the sporulation proteins before septation, which reflect the experimentally observed ratios between them and are within the experimental concentration range (Magnin *et al.*, 1997; Lord *et al.*, 1999; Lucet *et al.*, 1999). As required by the summation theorem for concentration control (Heinrich & Rapoport, 1974) the control coefficients sum to zero. Several reactions exert strong control ($|C_i^{[\sigma^F \cdot RNApol]}| \geq 1$), most notably AA phosphorylation and dephosphorylation, but the reactions responsible for lid opening and the binding of the transcription factors also have a strong effect (Tables B.1, 3.2).

3.9 Tables

Table 3.1: **Kinetic rate constants employed in the *in vitro* simulation.** The determination of control coefficients $C_j^{[\sigma^F \cdot RNApol]}$ is described in section 3.8.3. The units of the kinetic rate constants are either s^{-1} or M^{-1} s^{-1}, dependent on whether the rate constant is used in a first-order or second-order reaction. References to a particular figure show that a parameter value was derived from results presented in that figure rather than from previously published results. Numerical references refer to the following papers: [1] (Magnin *et al.*, 1997), [2] (Shu *et al.*, 2004), [3] (Ho *et al.*, 2003), [4] (Lord *et al.*, 1996), [5] (Clarkson *et al.*, 2003).

rates	$C_j^{[\sigma^F \cdot RNApol]}$	**simulation value**	**exp value**	**Ref**
AA-AB on-rate	2×10^{-4}	8×10^5	$1.1 \pm 1 \times 10^6$ $1.6 \pm 2.1 \times 10^5$	SPR SPR
AA-AB off-rate (T-state)	-0.13	2.4	2.4 ± 2.2	SPR
AA-AB·ADP off-rate (R-state)	-0.03	7.4×10^{-3}	$8.4 \pm 1.7 \times 10^{-3}$ $6.85 \pm 4 \times 10^{-3}$	SPR SPR
AA-AB·ATP off-rate (R-state)	0.03	10^{-3}	5.2× lower than ADP 8.8× lower than ADP	[1] [2]
σ^F-AB on-rate	-0.71	4×10^5	4×10^5 3.1×10^5	[1] [3]
σ^F-AB (tense state) off-rate	0.23	5×10^{-3}	5.5×10^{-3} 3.8×10^{-3}	[1] [3]
σ^F-AB· (relaxed state) off-rate	0.22	0.4		Fig. S3.4A
AB conformational change	4×10^{-3}	5×10^4		Fig. S3.1
AB conformational change	0.12	30	7.4 ± 5.6	SPR, Fig. S3.1
AB conformational change	-0.12	2	2 ± 1	SPR
lid opening	-0.66	0.02		Fig. S3.4B
lid closure	3×10^{-4}	10^{-3}	lid predominantly open	[4]
nucleotide-AB on-rate	-0.03	10^7	$K_D \sim 200$ μM	[4]
nucleotide-AB off-rate	0.03	2×10^3	$K_D \sim 200$ μM	[4]
ATP-ADP exchange for AB·AA	-7×10^{-3}	1.2×10^{-3}	2×10^{-3}	Fig. 3c, [2]
AA phosphorylation	-1.23	0.013	0.01-0.013	Fig. 3c , [2, 3]
AA-P·IIE on-rate	0.93	10^5	9×10^4	Figs. S3.6, S3.7
AA-P·IIE off-rate	-0.91	0.58	0.58	Figs. S3.6, S3.7
AA-P dimer on-rate	-0.34	10^5	$K_d = 3.7 \pm 2.1 \mu$M	[5]
AA-P dimer off-rate	0.34	1	$K_d = 3.7 \pm 2.1 \mu$M	[5]
AA dephosphorylation	see Table 3.2	1.25	1.26	Fig. S3.7

Table 3.2: **Kinetic rate constants employed in the *in vivo* simulation.** The determination of control coefficients $C_j^{[\sigma^F \cdot RNApol]}$ is described in section 3.8.3.

rates	$C_j^{[\sigma^F \cdot RNApol]}$	**simulation value**	**exp value**	**Ref**
AA dephosphorylation	2.26	0.0087	0.0087	Fig. S3.8
σ-RNApol on-rate	0.34	10^6	normal protein on-rate	(Lord *et al.*, 1999)
σ^F-RNApol off-rate	-0.8	0.55	K_d=561 nM	(Lord *et al.*, 1999)
σ^A-RNApol off-rate	0.46	0.02	K_d=22.5 nM	(Lord *et al.*, 1999)
AB degradation	n/a	4.1×10^{-4}	$t_{1/2}$ = 28 minutes	(Pan *et al.*, 2001)

Table 3.3: **Mutant phenotypes *in vivo* and *in silico*.**

Mutant	**Phenotype**	**Ref.**	**Alteration to Simulation**	**Simulation results**
amyE::spoIIAB	No effect on transcription; 40 % decrease in sporulation efficiency	(Dworkin & Losick, 2001)	continuous AB expression	same kinetics as wt, slightly higher RNApol(σ^F) level
amyE::spoIIAB spoIIAC at various positions, no spoIIE	no transcription of σ^F-dependent genes, Spo$^-$	(Frandsen *et al.*, 1999)	continuous AB expression while σ^F transcription either continues after septation or does not no IIE expression	after 500 minutes still less than 0.1μM RNApol(σ^F) under all conditions
IIEΔmem	$\sim 40 - 60'$ delay in transcription; $\sim$ 20% sporulation efficiency	(Arigoni *et al.*, 1999)	no IIE increase upon septation; no *spoIIA* expression after septation	$\sim$ 60 minutes delay until micromolar RNApol(σ^F) concentration
amyE::spoIIAB & IIEΔmem	Spo-; 0.8% sporulation efficiency	(Dworkin & Losick, 2001)	continuous AB expression; no IIE increase upon septation	4 hours delay until micromolar RNApol(σ^F) concentration reached
Division mutants (divC, div355)	no septum formation, no transcription of σ^F-dependent genes although unphosphorylated AA accumulates, Spo$^-$	(King *et al.*, 1999)	no IIE increase, continuous expression of all sporulation proteins without any rate increase	no formation of μM RNApol(σ^F) unless AB degradation continues at high rate; unphosph AA level as in wt before septation
IIE overexpression divC	no septum formation, max transcription of σ^F-dependent genes after 4h rather than 2h in wt	(Arigoni *et al.*, 1999)	higher IIE expression rate, no septation-dependent increase	micromolar RNApol(σ^F) complexes after 4h instead of 2h of protein expression; unphosphorylated AA level high
IIE overexpression	Earlier activation of σ^F (after 60$'$ instead of 90$'$, that is 30% earlier than wt)	(Arigoni *et al.*, 1996)	higher IIE expression rate, everything else normal	earlier formation of RNApol(σ^F) (after $\sim 80'$ instead of 120$'$, that is 30% earlier than wt)
spoIIE at 283^o	no effect	(Frandsen *et al.*, 1999)	no IIE production for 15$'$ after septation	no effect, unless IIEΔmem
IIAB-S139stop	stable AB, Spo$^-$	(Pan *et al.*, 2001)	AB degradation set to zero	less than 0.1 μM RNApol(σ^F)
SpoIIAAL61A	Spo$^-$, slower dephosphorylation; 10-fold lower AB·ADP·AA affinity	(Lee *et al.*, 2001)	at least 3-fold lower dephosphorylation rate	less than 1 μM RNApol(σ^F) for at least 4 hours after septation
SpoIIAAL90A	Spo$^-$, 3-fold faster phosphorylation; at least 100-fold lower AB·ADP·AA affinity	(Lee *et al.*, 2001)	AB·ADP·AA affinity reduced 10^4-fold	micromolar RNApol(σ^F) concentration only 8 hours after septation
SpoIIAAS58A	strong σ^F dependent transcription, also on div355 background	(Diederich *et al.*, 1994) (Magnin *et al.*, 1997) (Carniol *et al.*, 2004)	phosphorylation rate set to zero, no SpoIIAA regulation of *spoIIA*	faster RNApol(σ^F) formation than wt
SpoIIABR105A	premature σ^F release, cell lysis, faster phosphorylation rate, slower ADP-ATP exchange	(Ho *et al.*, 2003) (Shu *et al.*, 2004)	5-fold lower lid-opening rate	premature σ^F release

Chapter 4

Mathematical analysis of a simplified version of the model in Chapter 3

The detailed quantitative model revealed that allostery is responsible for the exceptional sensitivity of this small signaling network. The mechanism by which allostery enables non-linear responses is well-understood (Fersht, 1998; Changeux & Edelstein, 2005) and has been documented in many regulatory proteins (Rousseau & Schymkowitz, 2005) that control a wide range of signal transduction pathways and physiological responses, including adhesion (Arnaout *et al.*, 2005), bacterial chemotaxis (Bray *et al.*, 1998) and transcription (Courey, 2001). According to the MWC-model that was proposed by Monod, Wyman and Changeux in 1965 to describe the binding characteristics of allosteric proteins, allosteric proteins assume at least two different conformations that bind ligand with different affinities (Monod *et al.*, 1965; Changeux & Edelstein, 2005). In the absence of ligand the protein is mainly in the low-affinity conformation (referred to as the tense state) and ligand binding stabilizes the high affinity conformation (referred to as the relaxed state) so that the binding of a second ligand is facilitated. As a consequence ligand binding is disfavoured at low ligand concentrations but ligand occupation increases steeply once the ligand concentration sufficiently increases.

While allostery enhances the sensitivity of biological networks, the impact of a dimer is comparably small and alone cannot explain the high sensitivity of the network that

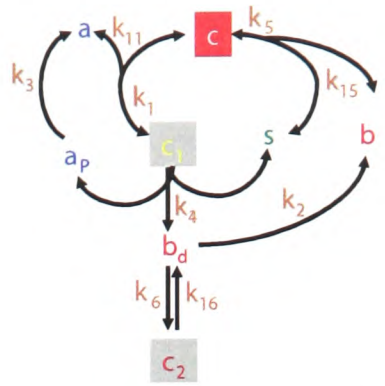


Figure 4.1: **A simplified model of the sporulation network.** The model corresponds to the simple model shown in Fig. 2.1B. s refers to σ^F, a to AA, a_p to AA-P, b to AB·ATP, b_d to AB·ADP, c to σ^F·AB·ATP, and c_1 to σ^F·AB·ATP·AA. The rate constants are summarized in Table 4.1.

controls the activity of σ^F. While the sensitivity of biological signaling networks can be further increased in long cascades (Goldbeter & Koshland, 1981; Heinrich *et al.*, 2002), the sporulation network is too small and other effects must therefore be responsible for the observed ultrasensitivity.

The allosteric protein employed in the sporulation network is unusual in that it not only binds its substrate AA allosterically, but also the affinity of the second ligand, σ^F, is affected by the conformation of the kinase. In the absence of AA, AB is in a conformation that binds AA with low and σ^F with high affinity. AA binding stabilizes the second AB conformation which binds AA with high and σ^F with low affinity. Allostery therefore facilitates AA-dependent release of σ^F. The regulatory mechanism is complicated further by the formation of long-lived $AB \cdot ADP \cdot AA$ complexes that prevent the reformation of $\sigma^F \cdot AB$. Complexes in which the two subunits of AB bind different nucleotides also play an important role in the detailed model.

In order to investigate the impact of these unusual properties and to delineate the mechanism by which the ultrasensitivity is achieved we analyse a simple version of the previously developed model (Figure 4.1). The mathematical analysis reveals that the cooperative binding of two ligands to the kinase with converse affinities is sufficient to generate both the exceptional high sensitivity of the regulatory system as well as bistability and hysteresis; substrate-dependent sequestration of the kinase also leads to bistability and hysteresis.

4.1 The Model

The detailed model of the sporulation network comprises about 50 dependent variables and 150 reactions (Fig. 3.2). The complexity of the model prevents an in-depth analysis of the impact of AB allostery on the network behaviour. We therefore consider a very much simplified model of the regulatory network (Fig. 4.1) that considers only eight key components: σ^F (s), AB·ATP (b), AB·ADP (b_d), σ^F·AB·ATP (c), σ^F·AB·ATP·AA (c_1), AB·ADP·AA (c_2), AA (a), AA-P (a_p). The scheme in Figure 4.1 can be translated, using the law of mass action, into the following set of eight differential equations

$$\dot{c} = k_{11}c_1 + k_5 bs - l_1 ac \tag{4.1}$$

$$\dot{b} = k_2 b_d - k_5 bs \tag{4.2}$$

$$\dot{b_d} = k_4 c_1 + k_{16} c_2 - (k_6 a + k_2) b_d \tag{4.3}$$

$$\dot{c_1} = l_1 ac - (k_{11} + k_4) c_1 \tag{4.4}$$

$$\dot{c_2} = k_6 a b_d - k_{16} c_2 \tag{4.5}$$

$$\dot{a_p} = k_4 c_1 - k_3 a_p \tag{4.6}$$

$$\dot{s} = k_4 c_1 - k_5 bs \tag{4.7}$$

$$\dot{a} = k_{11}c_1 + k_{16}c_2 + k_3 a_p - (k_6 b_d + l_1 c)a \tag{4.8}$$

The dot refers to the time derivative (e.g. $\dot{c} = \frac{dc}{dt}$) such that equations (4.1-4.8) model the dynamics of c, b, b_d, c_1, c_2, a_p, s, a respectively. Thus, binding of AA (a) to σ^F·AB·ATP (c) at rate k_1 leads to the formation of σ^F·AB·ATP·AA (c_1) which either unbinds a at rate k_{11} or binds s at rate k_4. In the cell, unbinding of σ^F permits the binding of a second AA. This step is neglected here in order to keep the model simple, and it is instead assumed that unbinding of s coincides with the phosphorylation of the bound a. It should be noted that the mere binding of a second a would not notably affect the dynamics, and the effect of the full allosteric binding mechanism (for instance with respect to hysteresis) is discussed in detail in section 4.2.5. Phosphorylated a can be reactivated at rate k_3; k_3 reflects the

product of the turn-over rate and the concentration of the phosphatase SpoIIE. AB·ADP (b_d) either binds a at rate k_6 to form AB·ADP·AA (c_2) or exchanges ADP for ATP at rate k_2 to form b. b and s can rebind at rate k_5 to form c.

As compared to the detailed model (Fig. 3.2) this model makes several important simplifications. The most important one is that only binding of one AA per AB is considered. The impact of allostery can nonetheless be explored since its main effect and importance in the detailed model was to facilitate AA-dependent σ^F release. This effect can be captured by the choice of the parameter value for k_4. Thus, without allostery, k_4 would correspond to the normal σ^F·AB off-rate which is so small (5.5×10^{-3} s^{-1}) that the back-reaction from c to b and s is not included here ($k_{15} = 0$ - note that the impact of a non-zero rate will, however, be analysed at a later stage). The allosteric conformational change increases the σ^F-AB off-rate such that $k_4 = 0.4$ s^{-1}, and the impact of such a difference in k_4 can be studied. Direct rebinding of σ^F after its release from σ^F·AB·ATP·AA is ignored in the simple model since we know from the detailed model that in the presence of sufficient AA to release σ^F the neglected binding of the second AA and phosphorylation of AA are more efficient than the rebinding reaction. Equally we neglect binding of σ^F to AB·ADP because the quantitative model demonstrates that this interaction is disfavoured, because of the inefficient and slow σ^F-dependent closure of the nucleotide-"lid" in the presence of ADP (Section 3.1.4) and because of the efficient AA-dependent release of σ^F from σ^F·AB complexes when sufficient AA is available to bind AB (Fig. 3.14). Another important simplification concerns the phosphatase SpoIIE which is not modelled explicitly, but which is assumed to be sufficiently scarce compared to SpoIIAA-P that the phosphatase turn-over rate rather than the SpoIIE-SpoIIAA-P binding reaction is rate-limiting. In fact the IIE concentration is about 15 μM at the time of septation (Lucet *et al.*, 1999) and the IIE-AA-P on-rate has been estimated as $10^5 M^{-1}s^{-1}$ (Section 3.1.4) such that the effective rate at which AA-P becomes bound by IIE is $10^5 M^{-1}s^{-1} \times 15 \times 10^{-6} M = 1.5$ while the *in vivo* phosphatase rate has been estimated as 0.0087 s^{-1} (Section 3.1.4), which is two orders of

Table 4.1: **Kinetic rate constants and protein concentrations employed in the simplified sporulation model (4.1-4.8).**

parameter	functional significance	simulation value
k_1	AB·ATP-AA on-rate	8×10^5 M^{-1} s^{-1}
k_{11}	AB·ATP-AA off-rate	0.001 s^{-1}
k_2	ADP-ATP exchange rate	0.02 s^{-1}
k_3	effective rate of AA-P dephosphorylation	0.003 s^{-1}
k_4	σ^F−AB·AA off-rate	0.4 s^{-1}
k_5	σ^F−AB on-rate	4×10^5 M^{-1} s^{-1}
k_6	AB·ADP-AA on-rate	8×10^5 M^{-1} s^{-1}
k_{16}	AB·ADP-AA off-rate	0.0074 s^{-1}
a_T	total AA concentration	30μM
b_T	total AB concentration	25μM
s_T	total σ^F concentration	15μM

magnitude lower. Accordingly, in the detailed quantitative model about 60% of all SpoIIE is bound by SpoIIAA-P at the time of septation such that this is a reasonable assumption. Asymmetric septation results in a sudden increase of the IIE concentration in the prespore by at least 2.5-fold (Appendix B.3). Since we are interested only in the effect of this sudden septation-dependent increase in the IIE activity in the prespore we can neglect protein expression and degradation which do not play a role on this timescale. Accordingly the total concentrations of σ^F, AB and AA are conserved, and there are only five independent variables in the model since we have

$$s_T = s+c+c_1 = \text{const}, \qquad b_T = b+b_d+c+c_1+c_2 = \text{const}, \qquad a_T = a+a_p+c_1+c_2 = \text{const}. \tag{4.9}$$

When solving the model we can use the parameter values that we estimated before for the detailed model (Tables B.1, 3.2). The value for k_4, the maximal rate of AA-dependent σ^F·AB·ATP dissociation, has been discussed above. We further have $k_5 = 4\times10^5\text{M}^{-1}\text{s}^{-1}$ for the σ^F-AB·ATP on-rate. k_2 represents the rate limiting steps in the AB ADP-ATP exchange reaction which we have estimated as 0.02 s^{-1} (Section 3.1.4). As discussed above the phosphatase reaction rather than IIE-AA-P binding is rate limiting in AA phosphorylation, and this rate has been estimated as 0.0087 s^{-1}. However, since only 60% of all IIE is bound to its substrate this rate would be an overestimate for k_3, and $k_3 = 0.003\text{s}^{-1}$ would be a more realistic estimate for the pre-septational situation. Any increase in IIE and AA-P is

assumed to translate into a direct increase in k_3, the rate at which AA-P is turned over, since enzyme is the limiting factor and the more enzyme that is available to bind and process the substrate the higher the turn-over rate. The concentration of SpoIIAB and σ^F at the time of septation have been measured as $b_T \sim 25 \times 10^{-6}$ M and $s_T \sim 15 \times 10^{-6}$ M (Ho *et al.*, 2003; Lucet *et al.*, 1999; Lord *et al.*, 1999). The SpoIIAA concentration is about twice the concentration of SpoIIAB at the time of septation (Magnin *et al.*, 1997). However, given that in the model binding of only one AA per AB is considered we are using $a_T = 30 \times 10^{-6}$ M.

4.2 Results

4.2.1 A numerical bifurcation analysis of the model

σ^F is sensitive to very small changes in IIE activity, and indeed also in this simple model σ^F·AB·ATP complexes dissolve in response to a small change in k_3, and the sensitive range lies within the physiological range for k_3 (Fig. 4.2A). As in the detailed model this high

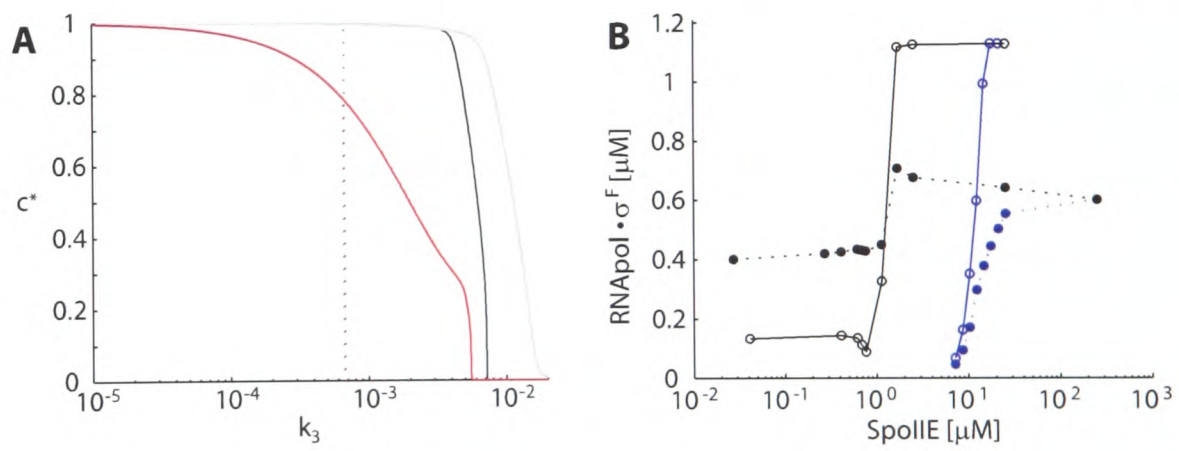


Figure 4.2: **A numerical bifurcation analysis. (A)** The steady state value of c dependent on the bifurcation parameter k_3 if k_3 is increased (solid lines) or decreased (dotted lines) for parameters as in Table B.1 (black lines), with $k_6 = 0$ s^{-1} (grey line) or $k_4 = 5.5 \times 10^{-3}$ s^{-1} (red lines). Note that the two grey lines overlay. **(B)** A bifurcation diagram for the detailed quantitative model that is described in Chapter 3: the concentration of RNApol·σ^F holoenzyme is reported 15 minutes after the concentration of SpoIIE (and any bound substrate AA-P) is either increased (blue lines) or decreased (black lines) to the concentration that is indicated on the horizontal axis; initially, before the first run, the simulation is run for 2 hours in the pre-septational mode as described in Chapter 3. The continuous line represents simulations when AB·ADP can bind to its normal binding partners; the broken line represents the case when it cannot. The bullets mark the simulated SpoIIE concentrations.

sensitivity is the result of AB allostery and the facilitated AA-dependent dissolution of σ^F that it enables. Thus if the rate of σ^F unbinding from the σ^F·AB·ATP·AA complex is as low as is the case for the σ^F·AB·ATP complex (that is $k_4 = 5.5 \times 10^{-3}$ s^{-1} instead of $k_4 = 0.4$ s^{-1}) then a 100-fold increase in k_3 is required to dissolve σ^F (Fig. 4.2A, red lines).

From the numerical solution we further notice that the dynamical system exhibits hysteresis, that is, its state not only depends on the current values of the parameters but also on their previous values. Thus when k_3 is either increased or decreased the dynamical system changes between the lower and the higher steady state value for c at two different k_3-values (Fig. 4.2A, note the two different places at which the switch occurs). As a consequence the septation-dependent switch is robust to fluctuations in k_3 because the steady state value of c will remain close to zero even if k_3 is subsequently slightly reduced. Hysteresis is obtained in this model although we consider binding of only one AA and it requires AB·ADP·AA complex (c_2) formation (Fig. 4.2A, grey line). Hysteresis with respect to changes in the concentration of SpoIIE (and any bound substrate AA-P) is also obtained in the detailed model (Fig. 4.2B, solid lines). Unlike in the small model, however, the hysteretic behaviour is also observed without AB·ADP·AA complex formation (Fig. 4.2B, broken lines). We conclude that the overall behaviour of the small model captures that of the detailed model, and we will come back to this small but important deviation at a later stage.

4.2.2 Phase Plane analysis

In order to understand how AB allostery and AB·ADP·AA complex (c_2) formation contribute to the exceptional sensitivity and hysteresis of the signaling network it is helpful to analyse the steady states of the dynamical system in some more detail. Because of (4.9) we can use $b_d = b_T - c - c_1 - c_2$, $a_p = a_T - a - c_1 - c_2$, and $s = s_T - c - c_1$. Using these relations we then find for the c_1- and c_2-nullclines

$$\dot{c_1} = 0 \Leftrightarrow c_1 = \frac{k_1 a c}{k_{11} + k_4} = L_1 a c; \qquad L_1 = \frac{k_1}{k_{11} + k_4} \tag{4.10}$$

$$\dot{c_2} = 0 \Leftrightarrow c_2 = \frac{k_6 b_d a}{k_{16}} = \frac{k_6 a (b_T - b - c - c_1 - c_2)}{k_{16}} = \frac{k_6 a (b_T - b - c - c_1)}{k_{16} + k_6 a}. \tag{4.11}$$

The steady states, by definition, are in the subspace determined by $\dot{c_1} = 0$, $\dot{c_2} = 0$, and it will suffice to study this subspace to see the hysteretic effect. We can determine the functional form of the a-, b-, and c-nullclines in the a, b, c-parametrized subspace by inserting the above expressions into (4.1), (4.2), and (4.8) to obtain

$$\dot{a} = k_3\left(a_T - a\left(1 + L_1c + \frac{(b_T - b - c(1 + L_1a))}{L_3 + a}\right)\right) - k_4L_1ac \tag{4.12}$$

$$\dot{b} = k_2(b_T - b - c(1 + L_1a))\frac{L_3}{a + L_3} - k_5b(s_T - c(1 + L_1a)); \qquad L_3 = \frac{k_{16}}{k_6} \tag{4.13}$$

$$\dot{c} = k_5b(s_T - c(1 + L_1a)) - k_4L_1ac, \tag{4.14}$$

and by setting the time derivatives to zero such that

$$\dot{b} = 0 \Leftrightarrow c = \frac{bk_5s_T(a + L_3) - k_2L_3(b_T - b)}{(1 + L_1a)(bk_5(L_3 + a) - k_2L_3)} \tag{4.15}$$

$$\dot{c} = 0 \Leftrightarrow c = \frac{k_5bs_T}{bk_5(1 + L_1a) + k_4L_1a} \tag{4.16}$$

$$\dot{a} = 0 \Leftrightarrow c = \frac{k_3(a_T - a - \frac{a}{a+L_3}(b_T - b))}{L_1a(k_3\frac{L_3}{a+L_3} + k_4) - k_3\frac{a}{a+L_3}}. \tag{4.17}$$

According to equation 4.16 the c-value of the c-nullcline approaches its maximal value s_T as a goes to zero, and it goes to zero when b goes to zero and a is greater than zero, as well as when a takes large values (Fig. 4.4, yellow plane). The shape of the b-nullcline is more complicated. As for the c-nullcline it goes to zero for large a. However, for small a, c attains values greater than s_T (which lie outside the physiological domain) if b is either very small or close to its maximal value b_T. The maximal values of c are attained at the extremes $b = 0$ and $b = b_T$, and c therefore decreases as b is taking intermediate values. In particular, as b decreases from b_T the value of c becomes negative when the nominator of the nullcline turns negative ($bk_5 - k_2(\frac{b_T - b}{s_T}) < 0$, for $a = 0$) while the denominator is still positive ($bk_5 - k_2 > 0$, for $a = 0$). This will happen while $\frac{k_2}{k_5} < b < \frac{k_2}{k_5}\frac{b_T}{s_T + \frac{k_2}{k_5}}$. Once $b < \frac{k_2}{k_5}$ the c-value becomes positive again, and there is therefore a discontinuity in c at $b = \frac{k_2}{k_5} = 0.05\mu\text{M}$, $\frac{b}{b_T} = 0.002$, for $a = 0$. A plot of the nullcline confirms this analysis (Fig. 4.4, blue plane). Finally, for the a-nullcline we see that $c \to \infty$ as $a \to 0$ because of the factor a in the denominator, and $c < 0$ as $a \to a_T$; the impact of b is very small (Fig. 4.4,

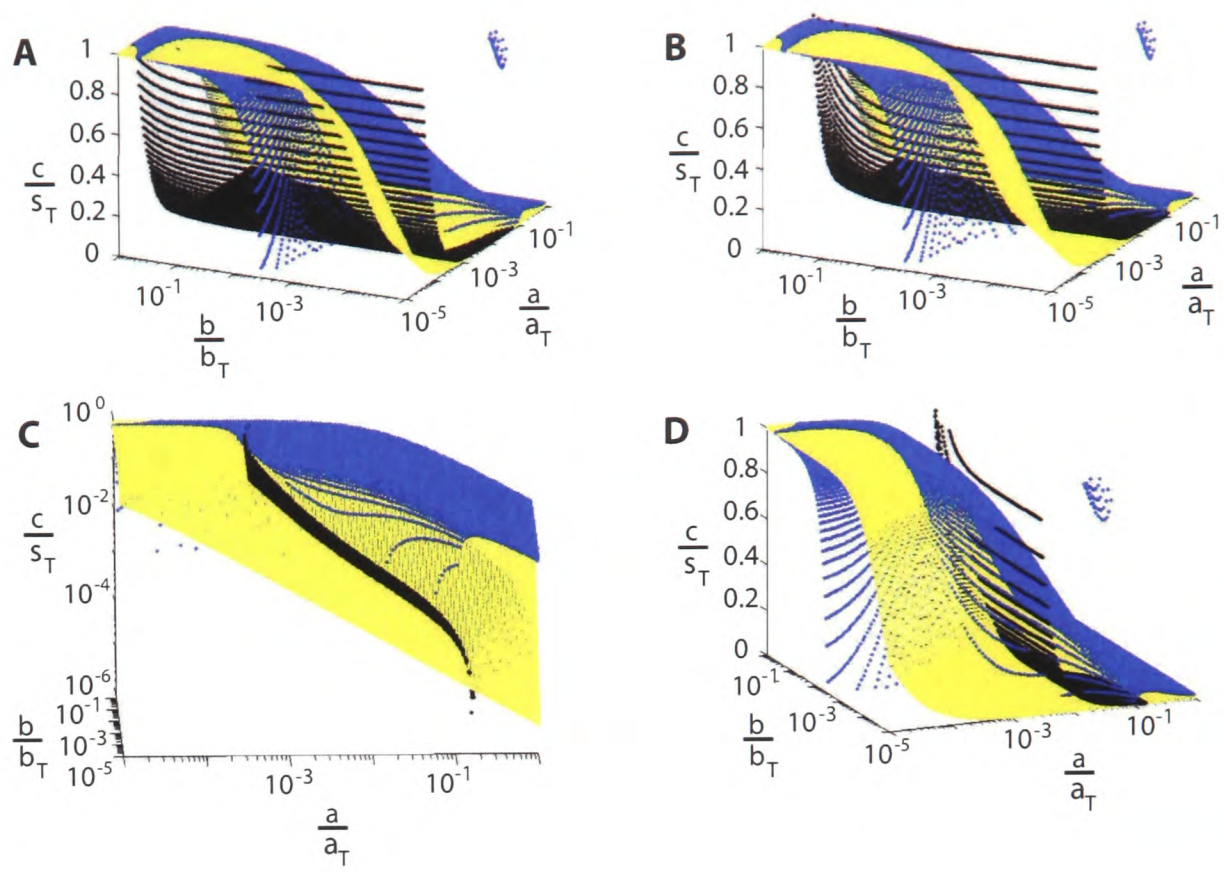


Figure 4.3: **The a-b-c phase plane.** The nullclines $\dot{a} = 0$ (black), $\dot{b} = 0$ (blue) and $\dot{c} = 0$ (yellow) are shown in the physiologically meaningful subset of the a-b-c plane when all other variables are in the steady state and **(A)** $k_3 = 0.0005\ \mathrm{s}^{-1}$, **(B,C)** $k_3 = 0.005\ \mathrm{s}^{-1}$, and **(D)** $k_3 = 0.05\ \mathrm{s}^{-1}$.

black plane). k_3 determines how fast c goes to infinity as a goes to zero.

Since the a-nullcline shows little dependency on b and attains all physiological c-values while the intersection between the b- and c-nullclines is a continuous curve the three nullclines must intersect at least once within the physiological domain. That the intersection between the b- and c-nullclines is a continuous curve follows from the shape of the nullclines discussed above as well as from the algebraic equation that is obtained when the expression for the b-nullcline, $b = \frac{k_2(b_T - c(1+L_1 a))\frac{L_3}{a+L_3}}{k_2\frac{L_3}{a+L_3} + k_5(s_T - c(1+L_1 a))}$, is inserted into the expression for the c-nullcline which yields a second-order polynomial in c. For large k_3 the c-value of the a-nullcline increases already for smaller a-values, and accordingly the intersection will happen for comparably large a and small c. For small k_3, on the other hand, the increase in the c-value comes late, and the a-nullcline will intersect the intersection of the other two nullclines only for large c-values. Inspection of the plot of the three nullclines for three

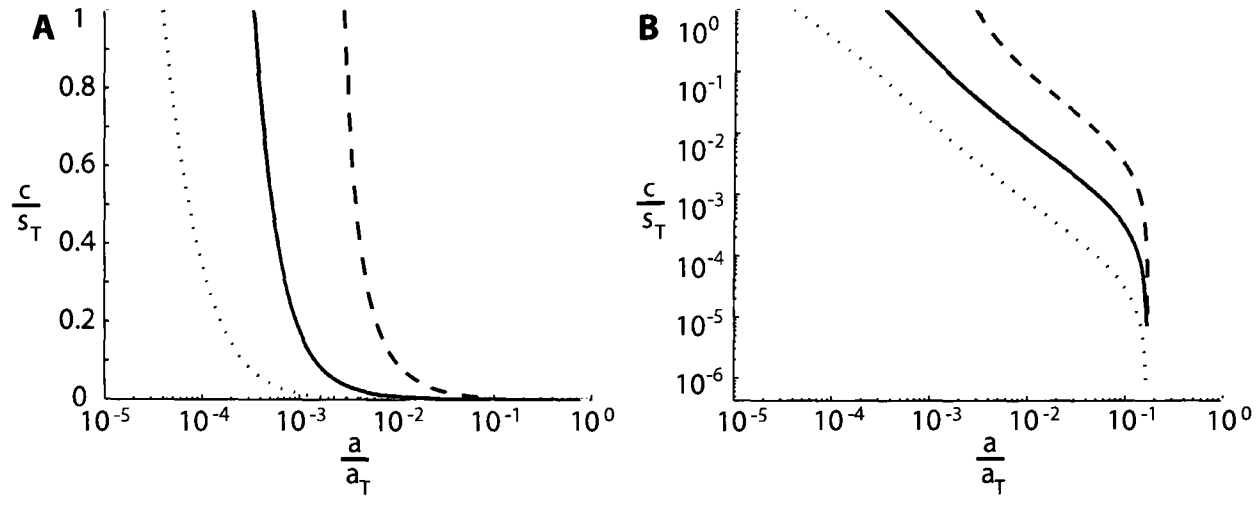


Figure 4.4: **The a-c phase plane.** The nullclines $\dot{a} = 0$ (black lines) and $\dot{c} = 0$ (grey line) are shown in the physiologically meaningful subset of the a-c plane when all other variables are in the steady state and $k_3 = 0.0005$ s^{-1} (dotted line), $k_3 = 0.005$ s^{-1} (continuous line), or $k_3 = 0.05$ s^{-1} (dashed line). Panel A and B show the same plot with linearly and logarithmically scaled vertical axis respectively.

different values of k_3 confirms this (Fig. 4.3 A,D), and further shows that there are three intersections for intermediate values (Fig. 4.3 B,C).

The intersections are, however, difficult to see in the 3-dimensional plot, and since we are particularly interested in how the steady state values of a and c depend on each other, it is sensible to inspect the $a - c$ phase plane. This can be constructed by inserting the expression for the b-nullcline, $b = \frac{k_2(b_T - c(1+L_1 a))\frac{L_3}{a+L_3}}{k_2\frac{L_3}{a+L_3} + k_5(s_T - c(1+L_1 a))}$, in the above equations for a and c, and we obtain

$$\dot{c} = 0 \Leftrightarrow c = \frac{-p_1 \pm \sqrt{p_1^2 - 4q_1}}{2} \tag{4.18}$$

$$\dot{a} = 0 \Leftrightarrow c = \frac{-p_2 \pm \sqrt{p_2^2 - 4q_2}}{2} \tag{4.19}$$

where

$$p_1 = -\frac{k_4 L_1 a(k_2 L_3 + k_5 s_T(a + L_3)) + k_5 k_2 L_3(1 + L_1 a)(b_T + s_T)}{k_5(1 + L_1 a)(k_4 L_1 a(a + L_3) + k_2 L_3(1 + L_1 a))} \tag{4.20}$$

$$q_1 = \frac{k_2 L_3 b_T s_T}{(1 + L_1 a)(k_4 L_1 a(a + L_3) + k_2 L_3(1 + L_1 a))} \tag{4.21}$$

$$p_2 = -\frac{k_3(a_T - a(1 + \frac{b_T + s_T}{a+L3}))k_5(1 + L_1 a)(a + L_3) + k_2 L_3 L_1 a(k_4 + k_3)}{(k_4 L_1 a + k_3 a(L_1 - \frac{1+L_1 a}{a+L_3}))k_5(1 + L_1 a)(a + L_3)} \tag{4.22}$$

$$q_2 = \frac{k_3((a_T - a(1 + \frac{b_T}{a+L3}))k_5 s_T(a + L_3) + k_2 L_3(a_T - a))}{(k_4 L_1 a + k_3 a(L_1 - \frac{1+L_1 a}{a+L_3}))k_5(1 + L_1 a)(a + L_3)}. \tag{4.23}$$

In the physiological range ($a, b, c \in [0, 1]$) there is one nullcline for each variable (Fig. 4.4). The a-nullcline intersects with the c-nullcline either once or three times, depending on the value of k_3. The intersections of the nullclines correspond to steady states. The k_3-dependent steady state values can, in principle, be determined by making use of the method of resultants (Section 13.3.1). Calculating the steady state values involves, however, the determination of the roots of a polynomial of degree 11 in a which is only possible by use of numerical methods and which cannot be expected to yield any further insight.

The local stability of the steady states can be derived from the sign of the time derivatives of the variables in arbitrarily small neighborhoods of the steady state. From such an analysis we see that the two outer steady states are stable while the inner steady state is unstable. This dynamical system therefore shows bistability and hysteresis as seen in the numerical bifurcation analysis.

4.2.3 AB·ADP·AA complex formation leads to hysteresis

We can now investigate the impact of AB·ADP·AA complex formation. Without AB·ADP·AA complex formation the equation for the c-nullcline remains the same as above (4.16) but the expressions for the nullclines of a and b simplify to

$$\dot{a} = 0 \Leftrightarrow c = k_3 \frac{a_T - a}{L_1 a(k_4 + k_3)} \tag{4.24}$$

$$\dot{b} = 0 \Leftrightarrow b = \frac{k_2(b_T - c(1 + L_1 a))}{k_2 + k_5(s_T - c(1 + L_1 a))}. \tag{4.25}$$

Inserting this new equation for b into equation (4.16) we obtain for the c-nullcline

$$\dot{c} = 0 \Leftrightarrow c = \frac{-p_3 \pm \sqrt{p_3^2 - 4q_3}}{2} \tag{4.26}$$

where p_3 and q_3 are identical to p_1 and q_1 except that the L_3-containing terms are missing, such that

$$p_3 = -\frac{k_4 L_1 a(k_2 + k_5 s_T) + k_5 k_2(1 + L_1 a)(b_T + s_T)}{k_5(1 + L_1 a)(k_4 L_1 a + k_2(1 + L_1 a))} \tag{4.27}$$

$$q_3 = \frac{k_2 b_T s_T}{(1 + L_1 a)(k_4 L_1 a + k_2(1 + L_1 a))}. \tag{4.28}$$

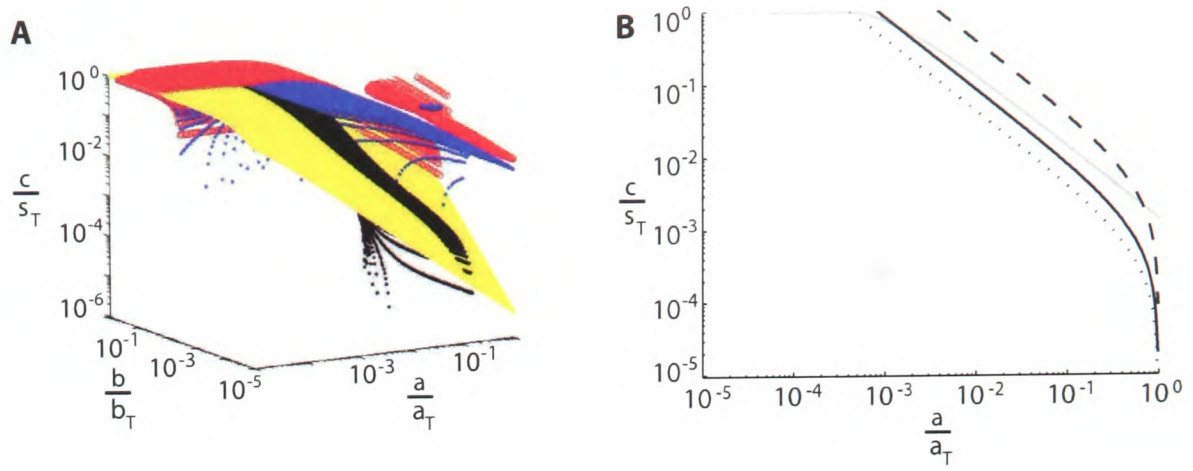


Figure 4.5: **The impact of AB·ADP·AA complex formation.** **(A)** The nullclines $\dot{a} = 0$ (black), $\dot{b} = 0$ (blue and red) and $\dot{c} = 0$ (yellow) are shown in the physiologically meaningful subset of the a-b-c plane when all other variables are in the steady state and $k_3 = 0.005$. The blue plane marks the nullcline $\dot{b} = 0$ for the standard model, and the red plane marks the same nullcline when AB·ADP·AA complex formation (c_2) is ignored. **(B)** The nullclines $\dot{a} = 0$ (black lines) and $\dot{c} = 0$ (grey line) are shown in the a-c plane for the model without AB·ADP·AA complex formation (c_2); all other variables are in the steady state and $k_3 = 0.005$ (dotted line), $k_3 = 0.01$ (continuous line), and $k_3 = 0.05$ (dashed line).

A plot of the nullclines reveals that there is only one steady state for all values of k_3 (Fig. 4.5). The system is therefore no longer bistable and there is no hysteresis in the absence of AB·ADP·AA complex formation. Comparison of the plots with and without c_2 formation reveals that it is mainly the shallower slope of the c-nullcline with respect to $\frac{a}{a_T}$ that removes bistability. It is therefore the change in the equation for the b-nullcline that is crucial. One may therefore be tempted to alter the equation for the dynamics of b in a way to achieve the same form for the b-nullcline also without c_2 formation. A further term for c_1 formation from direct binding of b, s and a does indeed achieve this:

$$\dot{b} = k_2 b_d - k_5 b s \frac{a + L_4}{L_4}, \tag{4.29}$$

$$\dot{b} = 0 \Leftrightarrow b = \frac{k_2 L_4 (b_T - c - c_1)}{k_2 L_4 + k_5 (s_T - c - c_1)(a + L_4)}; \tag{4.30}$$

here L_4 is a constant. However, such an extra term for the formation of c_1 also alters the equations for c_1 and a, and as a numerical bifurcation analysis of such a modified model demonstrates, this alteration does not produce hysteresis. This is not surprising since only AB·ADP·AA complexes can act as a storage device that can "suck" up AA;

AB·ATP·AA complexes, on the other hand, also dissolve by phosphorylation of AA and are therefore much more unstable. Hysteretic behaviour emerges because the "inactive" AB·ADP·AA complexes persist at a lower phosphatase activity than that at which they originally form, simply because once formed less AA goes through cycles of phosphorylation and dephosphorylation and as a consequence less IIE activity is required to achieve a sufficient concentration of free AA to maintain AB·ADP·AA complexes and to keep AB and σ^F apart.

4.2.4 AB allostery is necessary for the high sensitivity

As a consequence of AB allostery, binding of AA modulates the affinity of binding for both AA and σ^F. In this much simplified model which considers binding of only one AA, the main effect of AB allostery is captured by using a much higher rate for σ^F-AB·AA unbinding than for σ^F-AB dissociation ($k_4 >> k_{15}$), that is the AA-favoured conformation of AB binds σ^F with lower affinity. Different affinities for AA, on the other hand, are not as important, and we only use the AB·ATP-AA off-rate, k_{11}, that reflects the conformation of AB which binds AA with high affinity; the low-affinity conformation is ignored here. We have so far neglected σ^F-AB dissociation but in order to study the impact of different σ^F-AB affinities, we now have to include the back-reaction (k_{15}), and we obtain instead of equations 4.1 and 4.2

$$\dot{c} = k_{11}c_1 + k_5bs - (l_1a + k_{15})c \tag{4.31}$$

$$\dot{b} = k_2b_d - k_5bs + k_{15}c. \tag{4.32}$$

This leads to a small change in the equations for p_1 and p_2 that determine the $c-$ nullcline in the a-c plane in that the k_4L_1a factor is expanded to $k_4L_1a + k_{15}$ such that now

$$p_1 = -\frac{(k_4L_1a + k_{15})(k_2L_3 + k_5s_T(a + L_3)) + k_5k_2L_3(1 + L_1a)(b_T + s_T)}{k_5(1 + L_1a)(k_4L_1a + k_{15})(a + L_3) + k_2L_3(1 + L_1a))} \tag{4.33}$$

$$q_1 = \frac{k_2L_3b_Ts_T}{(1 + L_1a)(k_4L_1a + k_{15})(a + L_3) + k_2L_3(1 + L_1a))}. \tag{4.34}$$

The impact on the a-nullcline is very small and therefore ignored.

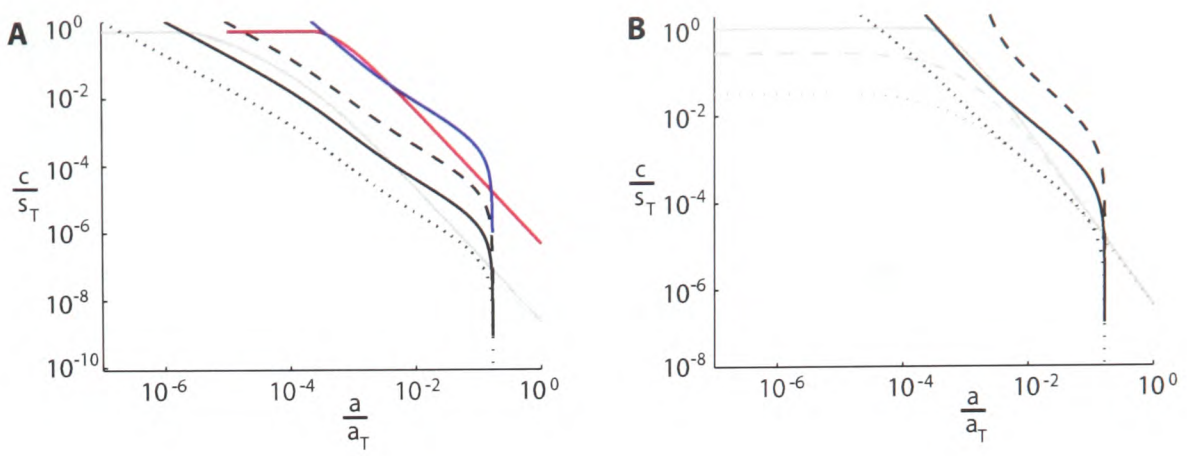


Figure 4.6: **The impact of SpoIIAB allostery. (A)** The nullclines $\dot{a} = 0$ (black and blue lines) and $\dot{c} = 0$ (grey and red lines) are shown in the physiologically meaningful subset of the a-c plane when all other variables are in the steady state and $k_3 = 0.0005$ s^{-1} (dotted line), $k_3 = 0.005$ s^{-1} (continuous lines), and $k_3 = 0.05$ s^{-1} (dashed line). The blue and red line represent the standard case $k_4 = 0.4$ s^{-1} while the black and grey curves illustrate the change for $k_4 = 0.001$ s^{-1}. **(B)** The nullclines $\dot{a} = 0$ (black lines) and $\dot{c} = 0$ (grey lines) are shown in the a-c plane when all other variables are in the steady state and $k_3 = 0.0005$ s^{-1} (dotted black line), $k_3 = 0.005$ s^{-1} (continuous black line), $k_3 = 0.05$ s^{-1} (dashed black line), and $k_{15} = 0.001$ s^{-1} (continuous grey line), $k_{15} = 0.1$ s^{-1} (dashed grey line), $k_{15} = 1$ s^{-1} (dotted grey line). Note that the impact of k_{15} on the a-nullcline is very small such that we used $k_{15} = 0$ for the a-nullclines. Equally k_3 does not affect the c-nullclines.

We can now explore the effects of allostery by investigating the impact of different relative values for k_4 and k_{15}. We find that if k_4 is lowered from 0.4 s^{-1} to 10^{-3} s^{-1} the shape of the c-nullcline changes (compare the red and grey lines in Figure 4.6A). As a consequence the outer steady state $c \sim 1$ remains stable for lower c-values such that the sharp transition from c-values close to one to c-values close to zero is lost. Accordingly the network is less sensitive to changes in k_3 as can also be seen in the numerical bifurcation diagram in Figure 4.2. If, on the other hand, k_{15} is increased from its low value to values close to 1 then little c forms even at low k_3. From this we see that AB allostery and the change in σ^F·AB affinity is essential for the high sensitivity to changes in IIE activity.

4.2.5 The impact of inversely proportional affinities on the sensitivity of an allosteric protein

We now consider the allosteric part of the network separately (depicted in Figure 4.9A) in order to delineate to what extent inversely proportional affinities increase the sensitivity of the allosteric mechanism to changes in the ligand concentration. In the MWC model

only one ligand is considered and the following cycle conditions between the equilibrium constants (as defined in Figure 4.9A) are imposed

$$\frac{L_0}{L_1} = \frac{K_t}{K_r} = \frac{M_0}{M_1}; \qquad L_i = \frac{T_i}{R_i}, \tag{4.35}$$

as a result of which the equilibrium of each interaction can be determined independently because the equilibria with other complexes in the network do not factor in. The fraction of occupied enzyme sites, Y_A^{MWC}, can then be expressed by the simple formula (Fersht, 1998)

$$Y_A^{MWC} = \frac{\alpha(1+\alpha) + L_0 c\alpha(1+c\alpha)}{(1+\alpha)^2 + L_0(1+c\alpha)^2}, \qquad \alpha = \frac{a}{K_r}; \quad c = \frac{K_r}{K_t}, \tag{4.36}$$

where a refers to the concentration of free ligand (AA). If we extend the model to include the second ligand σ^F as depicted in Figure 4.9A, then following the MWC modeling approach we need to impose the additional cycle condition

$$\frac{L_1}{M_1} = \frac{K_s}{K_p}. \tag{4.37}$$

Comparison with experimental data suggests that binding of σ^F does not substantially affect the conformational equilibrium of AB (Section 3.1.4), and we therefore set $M_0 = L_0$ and $M_1 = L_1$ such that $K_s = K_p$ (Eq 4.37). The fraction of enzyme sites occupied by AA can then be expressed as

$$Y_A = \frac{\alpha(1+\alpha+\beta) + L_0 c\alpha(1+c\alpha+\beta d)}{(1+\alpha)^2 + L_0(1+c\alpha)^2 + \beta(1+2\alpha+L_0 d(1+2\alpha c))}, \qquad \beta = \frac{s}{K_p}; \quad d = \frac{K_p}{K_s} = 1 \tag{4.38}$$

while the fraction of enzyme sites occupied by σ^F is given by

$$Y_S = \frac{\beta(1+2\alpha+L_0 d(1+2\alpha c))}{(1+\alpha)^2 + L_0(1+c\alpha)^2 + \beta(1+2\alpha+L_0 d(1+2\alpha c))} \tag{4.39}$$

where s refers to the concentration of free σ^F. We can rewrite Eq. 4.36 as $Y_A^{MWC} = \frac{af(a)}{af(a)+g(a)}$, Eq. 4.38 as $Y_A = \frac{af(a)+sav}{af(a)+g(a)+s(av+w)}$ and Eq. 4.39 as $1 - Y_S = \frac{af(a)+g(a)}{af(a)+g(a)+s(av+w)}$, where f and g are functions of a while v and w are constant expressions that neither depend on a nor s. For $s = 0$ and/or $a = 0$, $Y_A^{MWC}(a) = Y_A(a,s)$ and for $a \to \infty$ and s finite, $Y_A(a,s), Y_A^{MWC}(a) \to 1$. For $a > 0$, $s > 0$ we have $Y_A^{MWC}(a) > Y_A(a,s)$. Binding of the

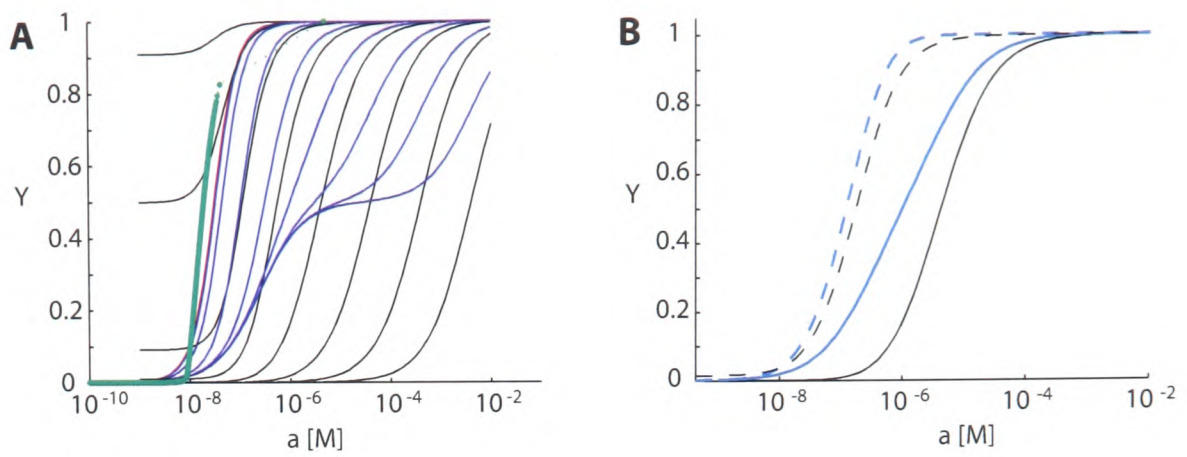


Figure 4.7: **Sensitivities of different allosteric mechanisms.** **(A)** The fraction of AB sites not occupied by σ^F, $1 - Y_S$, according to Eq. 4.39 (black curves) or occupied by AA according to Eq. 4.36 (red curve) or according to Eq. 4.38 (blue curves) dependent on the concentration of free AA, a. The concentration of s was increased by factors of 10 from 10^{-9} M to 10^{-2} M; curves to the left were obtained at the lowest and curves on the right at the highest concentration of s. $L_0 = 10^3$, $K_t = 10^{-6}$M and $K_r = 10^{-9}$M, , $K_s = 10^{-8}$, $K_p = K_s$. For comparison, the green line gives the fraction of free σ^F, $\frac{c+c_1}{s_T}$, at different concentrations of free AA, a, according to the model described by Eqs. 4.1-4.8 with parameters as given in Table B.1. **(B)** The fraction of AB sites not occupied by σ^F, $1 - Y_S$, according to Eq. 4.39 (black curves) or occupied by AA according to Eq. 4.38 (blue curves) dependent on the concentration of free AA, a. $s = 10^{-5}$ M, $L_0 = 10^3$, $K_t = 10^{-6}$M and $K_r = 10^{-9}$M, $K_s = 10^{-9}$. The continuous lines were obtained with $K_p = 10^{-9}$ M, the broken line with $K_p = 10^{-6}$ M.

second ligand, σ^F, therefore reduces the sensitivity to changes in a as can also be seen from a plot of Y_A^{MWC}, Y_A and Y_S (Fig. 4.7A).

Such simple formula as given in (4.38) and (4.39) can no longer be found when the above cycle relations cease to hold as is the case for the inversely proportional affinity case studied here. In that case the network as displayed in Figure 4.9A needs to be translated into a set of ordinary differential equations and solved numerically. We use the same AB-AA equilibrium constants as before and set all on-rates to 10^6 $M^{-1}s^{-1}$. Although we still use $M_0 = L_0$ and $M_1 = L_1$, for the σ^F·AB affinities we now have $K_s \gg K_p$ while the opposite is true if the σ^F·AB affinities correlate in strength with the AB·AA affinities, that is if the conformation that binds AA weakly also binds σ^F weakly and *vice versa.* Comparison of the sensitivities of an allosteric protein that binds two ligands with inversely proportional affinities with one that obeys the cycle conditions of the MWC model (Eqs. 4.35, 4.37) shows that inversely proportional affinities do indeed increase the sensitivity to changes in the concentration of

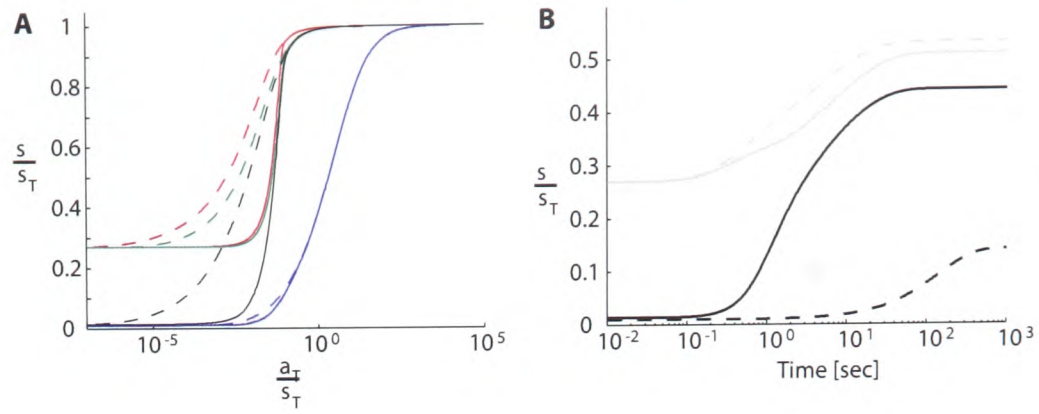


Figure 4.8: **The impact if two ligands bind the different conformations of an allosteric protein with inversely proportional affinities. (A)** The fraction of free σ^F, $\frac{s}{s_T}$, dependent on the relative AA to σ^F concentration, $\frac{a_T}{s_T}$, if a_T is either increased (solid lines) or decreased (broken lines); the off-rates are set to $ks_{11} = kp_{11} = 0.001\ s^{-1}$ (blue lines), $ks_{11} = kp_{11} = 1\ s^{-1}$ (red lines), $ks_{11} = 0.001\ s^{-1}$, $kp_{11} = 1\ s^{-1}$ (black lines), $ks_{11} = 1\ s^{-1}$, $kp_{11} = 0.001\ s^{-1}$ (green lines). **(B)** The kinetics of σ^F release if $ks_{11} = kp_{11} = 0.001\ s^{-1}$ (black broken line), $ks_{11} = kp_{11} = 1\ s^{-1}$ (grey broken line), $ks_{11} = 0.001\ s^{-1}$, $kp_{11} = 1\ s^{-1}$ (black continuous line), $ks_{11} = 1\ s^{-1}$, $kp_{11} = 0.001\ s^{-1}$ (grey continuous line). All protein concentrations were 10μM unless specified otherwise.

a (Figs. 4.7B, 4.8A). The speed at which σ^F·AB complexes dissolve in response to addition of AA is much higher when the σ^F affinity for the AB conformation that binds AA with high affinity is low (Fig. 4.8B). Correlated affinities increase the sensitivity in the same way as inversely proportional affinities but result in substantial "background" σ^F release at low AA concentrations (Fig. 4.8A). Finally, the numerical bifurcation diagram provides evidence for hysteresis with respect to the total AA concentration as bifurcation parameter (Fig. 4.8A). This explains the hysteretic behaviour of the detailed model which is observed with respect to changes in the concentration of IIE (and bound AA-P) also in the absence of AB·ADP·AA complex formation (Fig. 4.2B).

4.3 Conclusion

The analysis of the simple model reveals how an ultrasensitive switch can be generated from a single allosteric protein with only two subunits. According to the well-established theory on allostery, dimeric proteins can enable only limited sensitivity because the Hill coefficient can be no larger than two (Fersht, 1998). This limitation is overcome by a combination of two sophisticated mechanisms: the allosteric protein binds two ligands with inversely

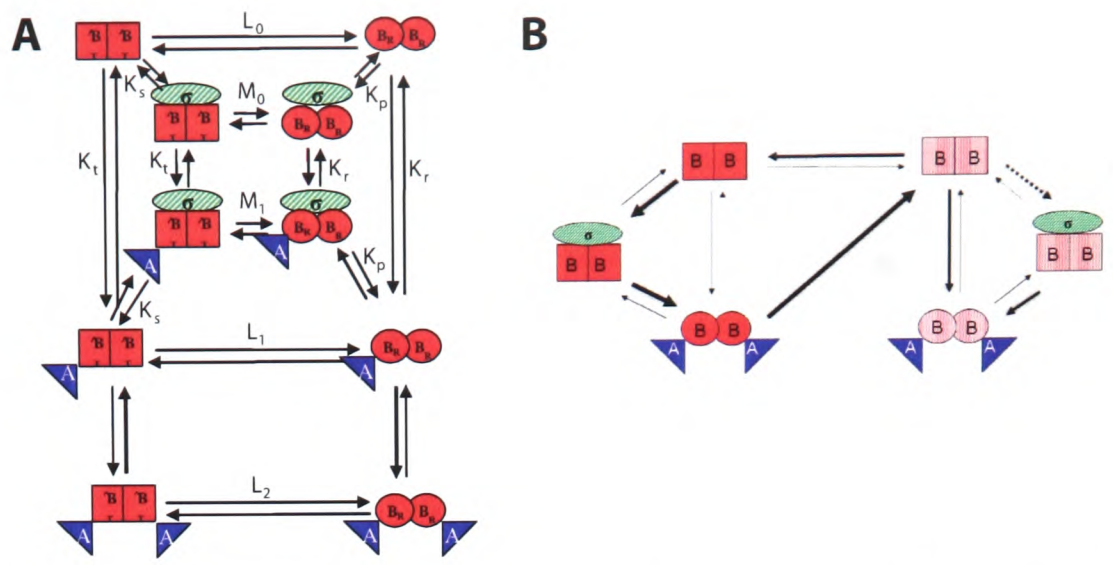


Figure 4.9: **The mechanism by which AB allostery ensures ultrasensitivity and hysteresis. (A)** The allosteric kinase AB binds two ligands with inversely proportional affinities in its two conformations. Thus one AB conformation binds AA (blue triangle) with high and σ^F (green oval) with low affinity (relaxed state, depicted as balls), and one conformation binds AA with low and σ^F with high affinity (tense state, depicted as squares). In the absence of AA most AB is in its tense conformation (squares) and binding of σ^F is strong. Upon binding of AA the conformational equilibrium is shifted to the relaxed conformation (balls) and σ^F is displaced rapidly. Binding of a second AA prevents the rebinding of σ^F. **(B)** The key paths in the regulation of σ^F activity. Unbound AB is mainly in the tense conformation (squares) where it is bound firmly by σ^F. Binding of AA shifts the AB conformation to the relaxed state (balls) and results in rapid displacement of σ^F. In its ATP-bound form (dark red), AB phosphorylates AA. ADP-bound AB (light red) can either rebind σ^F or AA, or exchange ADP for ATP. In the presence of sufficient AA, σ^F is displaced rapidly from AB·ADP.

proportional affinities in its two conformations, and the allosteric protein can be sequestered in an inactive form (Fig. 4.9). The inversely proportional affinities enable the switch-like displacement of the transcription factor σ^F in response to the septation-dependent increase in the competing ligand AA, while the sequestration reaction ensures that σ^F is kept off and does not rebind AB.

While the main mechanistic details were revealed already by the detailed model (Section 3.4.3), the value of an additional analysis of a much simplified model is that it can confirm that these mechanisms are sufficient to explain the observed network behaviour. A detailed model alone rapidly becomes intractable to visualize and "as complex as the problem that it seeks to solve" such that key mechanisms are difficult to discern, especially for those who have not built and extensively analysed the model themselves; there is then a risk

that phenomena which are hidden in the complex model structure may be overlooked even when they play an important role. A simple model, on the other hand, has, in general, little predictive or explanatory power, because the experimental validation is difficult and limitations of simple models are difficult to gauge. Although model predictions can of course be compared to experimental observations, it is, in general, next to impossible to judge whether observed deviations are the consequence of the simplicity of the model, which necessarily leads to inaccuracies, or whether these are significant and also of qualitative importance. When derived from a detailed model, however, the limits of the model's validity can be set out in detail and its applicability, for instance to certain mutant data sets, can therefore be judged. The combination of a detailed quantitative model and a subsequent mathematical analysis of a much simpler model that focuses on the key steps identified by the detailed model therefore constitutes a powerful approach to understanding the dynamics of complex biological networks.

So far most mathematical models in molecular biology are simplistic, and sketchy, and often focus on the qualitative analysis of the steady state behaviour of dynamical biological systems. This is done with the hope that such analysis can unravel general properties of the network for different parts of the parameter space and therefore bypass the need to know parameter values in detail. The limitations of this approach are illustrated by another recently published model (Igoshin *et al.*, 2006) of the same sporulation network. Although based on the same sets of published data, it fails to predict AB allostery, and does not resolve the long-standing question about the significance of AB·ADP·AA complex formation and the role of a structural 'lid' in AB. Their model predicts that AB·ADP·AA complex formation may be essential to achieve hysteretic behaviour; however, our quantitative model reveals that, because of AB allostery, hysteresis can be obtained without AB·ADP·AA complex formation (Figs. 4.2B, 4.8A). If the model of Igoshin and co-workers had been sufficiently quantitative to assess the impact of their proposed evolutionary alternative of a lower catalytic rate they probably would not have questioned our argument that

AB·ADP·AA complex formation is important for limiting ATP consumption. Our detailed quantitative model immediately reveals that AB·ATP·AA complexes are not turned over sufficiently rapidly and σ^F will be freed prematurely if the kinase rate is lower.

It might be argued that a simple, sketchy model could have revealed a number of properties that the quantitative model exposes if important quantitative aspects such as the time scales of the different processes had been respected. For instance, while the assumption of quasistationarity for the ADP-ATP exchange reaction greatly facilitates the analysis, evaluation of kinetic data suggests that this assumption is not valid because the exchange reaction does not proceed substantially faster than other processes such as AB·ADP·AA complex formation. Neglect of this important kinetic interplay explains why the model misses the importance of the AB lid which also leads to a questionable interpretation of the R105 mutant data (Ho *et al.*, 2003; Carniol *et al.*, 2004; Shu *et al.*, 2004). Comparison of model predictions with mutant data did not reveal the inadequacy of the model because of the widely recognised problem that a wide range of sufficiently complicated but very different models can generate a similar qualitative response. This stresses the importance of *quantitative* modelling (and quantitative experimentation) to advance our understanding in molecular biology - much as it did in physics. As Richard Feynman notes (Feynman, 2006) "One might also say that the development of the physical sciences to their present form has depended to a large extent on the emphasis which has been placed on the making of quantitative observations. Only with quantitative observations can one arrive at quantitative relationships which are the heart of physics."

Chapter 5

Discussion

Complex biological networks are difficult to understand from verbal descriptions, and mathematical modelling is a promising tool to integrate the available information. However, realistic models cannot be built without quantitative experimental data. The system studied here offered several unusual advantages in that the entire regulatory network could be reconstituted *in vitro* and specific fluorescence probes were available to study all relevant interactions. This enabled realistic values for all kinetic parameters that affect the model to be estimated from experiments, and allowed the derivation of a very detailed model of the process that reproduced the experimental data quantitatively. In applying the model to the physiological situation the phosphatase rate of IIE, which we showed exhibits a lower rate *in vivo* than *in vitro*, was the only parameter that had to be changed.

We began with a simple, basic circuit from published schemes but this rapidly grew into a large network after mathematical modelling predicted that AB is an allosteric protein. Here the combination of theory and experiment became particularly fruitful because theoretical predictions led to new experiments and analysis. Some rate constants, such as the phosphorylation rate and the σ^F·AB·ADP binding rates, which had been estimated from previous experiments using simple models, also needed to be re-evaluated as the regulatory scheme became more complex. Once the rate and binding constants had been determined, the time-dependent variation in the system variables (e.g. concentrations of the pathway components and their complexes) could be analysed by translating the interactions into a

set of ordinary differential equations, which could be solved numerically. Comparison of the model predictions with data derived *in vitro* confirmed that the model was realistic and a perturbation study revealed that the model is robust to variations in the kinetic parameter values which justified a direct application of the model to the physiological situation.

Extrapolation of the model to the physiological situation enabled us to evaluate many effects that had been associated with the regulation of σ^F release in the prespore and to integrate them into a mechanistic picture of the regulatory process. We conclude that cell size determines cell fate. Thus IIE accumulation on the asymmetrically placed septum is sufficient to trigger σ^F release in the smaller prespore because IIE association with its substrate AA-P maximises AA production in the prespore while AB allostery generates the required sensitivity. Alternative mechanisms such as a block in AB expression or the removal of an (elusive) IIE inhibitor, possibly through a transient genetic imbalance, are unlikely to be of physiological relevance. The critical importance of AB allostery, the low phosphatase rate and the simultaneous accumulation of IIE and its substrate AA-P as well as the need to render septation dependent on the protein (and in particular IIE) concentration would probably have remained unnoticed without mathematical modelling. To the contrary it had already been reasoned that the release of the product AA from IIE was inhibited before septation (King *et al.*, 1999).

While asymmetric cell division, and the resulting difference between the two compartments, is an elegant mechanism for achieving compartmentalized gene expression, other symmetry-breaking mechanisms must exist to induce compartmentalized gene expression in those sporulating bacteria, such as *Sporosarcina ureae*, that divide symmetrically during sporulation (Zhang *et al.*, 1997). A deeper insight into such alternative mechanisms will be of great interest.

The regulatory system that leads to compartmentalized gene expression in *B. subtilis* is optimized to the needs of the organism in many ways. It is tuned to ensure both high sensitivity to stimuli and robustness to random fluctuations. First of all the effect of the

septation-induced difference in the ratio of surface area to volume is maximized between the two compartments by concentrating the phosphatase IIE on the asymmetric septum, that is on the common interface. Given the small size of the bacterium, a homogeneous distribution of IIE on the surfaces of both compartments would have led to only a small change in the relative phosphatase activities. Association of IIE and AA-P ensures a simultaneous increase in concentration of both enzyme and substrate in the prespore, which in turn ensures the strong increase in AA production that leads to σ^F release. Secondly, the protein concentrations are tuned such that minute changes in IIE and AA can tip the balance while robustness to fluctuations in gene expression is ensured by coupled expression combined with protein degradation. Thirdly, the previously unnoticed allosteric behaviour of the AB dimer enables bistability, hysteresis, and an exceptionally high sensitivity to changes in IIE and AA. Fourthly, the formation of AB·ADP·AA complexes after septation serves as a sophisticated mechanism for preventing σ^F from rebinding to the released AB, thus providing rapid and prolonged σ^F release while minimizing cycling and associated wastage of ATP. AB·ADP·AA complexes thus serve to remove AB (AB sink (Lee *et al.*, 2000; Lee *et al.*, 2001)) rather than AA (AA sink (Carniol *et al.*, 2004)). Finally, the relative affinities of the transcription factors σ^F and σ^A for the core RNA polymerase are tuned to prevent premature activation whilst enabling the system to be triggered by small perturbations. Interestingly, σ^A·RNApol holoenzyme remains present when σ^F·RNApol emerges in such a way that general transcription programs can still be carried out.

The network exhibits an impressive robustness to stochastic fluctuations despite its exceptional sensitivity to input. Robustness to fluctuations in gene expression appears to be achieved by a sophisticated arrangement of genes which probably ensures that the expression of AA and AB is coupled while the expression of σ^F is lower than that of AB (Fort & Piggot, 1984). The need to couple the expressions of AB and AA is likely to resolve the paradox of why degradation of unbound AB is necessary for sporulation although the AB half-life ($\sim$ 28 minutes) strongly exceeds the time scale on which σ^F needs to be released

($\sim$ 10 minutes) (Pan *et al.*, 2001; Hilbert & Piggot, 2004). Degradation of unbound AB will sufficiently lower the AB concentration *before* septation such that small changes in the AA concentration can trigger σ^F release upon septation. A IIE dependency of septation may further ensure that sufficient protein has been expressed such that septation can trigger the formation of micromolar σ^F·RNApol holoenzyme concentrations. Overall, the robustness of the regulatory circuit to alterations in concentration and values of kinetic parameters is such that the process can be deregulated only by mutation.

The regulatory network is impressive in that an ultrasensitive switch is generated from a single allosteric protein with only two subunits. According to the well-established theory on allostery, dimeric proteins can enable only limited sensitivity because the Hill coefficient can be no larger than two (Fersht, 1998). This limitation is overcome by a combination of two sophisticated mechanisms: the allosteric protein binds two ligands with inversely proportional affinities in its two conformations, and the allosteric protein can be sequestered in an inactive form (Fig. 4.9). The inversely proportional affinities enable the switch-like displacement of the transcription factor σ^F in response to the septation-dependent increase in the competing ligand AA, while the sequestration reaction ensures that σ^F is kept off and does not rebind AB.

Early studies of the basis of sensitivity in biological systems led to the discovery that a higher sensitivity could be gained when the converting enzymes were saturated (Goldbeter & Koshland, 1981). In metabolic pathways this can be achieved by high substrate concentrations relative to the enzyme concentration. In signaling networks the substrate is in general a protein, and substrate and enzyme concentrations are therefore rather comparable. Near enzyme saturation can, however, still be achieved by virtue of a low Michaelis-Menten constant and a low turn-over rate. This is indeed an important feature of this regulatory network. The detailed model of the regulatory network predicts that for the experimentally determined IIE·AA-P equilibrium constant and phosphatase activity $\sim$ 60% of all IIE is bound by its substrate at the cellular protein concentrations that have been estimated at the

time point of septation. Here it should be noted that a relatively low affinity ($K_d \sim 5\mu$M) is sufficient because the protein concentrations exceed this value. Whilst an accumulation of AA-P on the septum has so far not been observed in published fluorescence studies this is not too surprising considering that antibodies that are specific for AA-P, but not for AA, can be expected to fail to bind to IIE-bound AA-P, and antibodies that are specific for AA will label all cellular AA; the model predicts that not more than 20% of all AA is bound to IIE apart from a short timespan immediately after septation when the fraction reaches 50%. Experiments will therefore need to be repeated specifically to access this crucial timespan.

When enzymes are fully saturated by substrate any increase in the enzyme concentration translates immediately into an increase in the turnover rate. Here enzyme saturation has a second important effect in that IIE·AA-P complex formation leads to the accumulation of both enzyme and substrate on the septum which is crucial because both concentrations are limiting. As well as being a protein and therefore of limited concentration, the substrate concentration cannot be saturating before septation because the substrate can only be expressed in its unphosphorylated form. The formation of the substrate therefore involves AB binding, and this would result in premature σ^F release if the concentration was much higher. The concerted increase in both the enzyme and the substrate concentrations and the particular allosteric mechanism therefore markedly increase the sensitivity under conditions that are characteristic of signaling networks but which fail to yield ultasensitivity in the simple model originally studied by Goldbeter and Koshland (Goldbeter & Koshland, 1984).

Earlier work by Goldbeter and Koshland revealed that cycles of phosphorylation and dephosphorylation (as employed in the σ^F network) can increase the sensitivity of networks (Goldbeter & Koshland, 1981). In the σ^F network phosphorylation of AA serves a further purpose in that it increases the robustness of the network. Because of AA phosphorylation, the concentrations of both AA and IIE need to increase in order to liberate σ^F for a sufficiently long time to trigger the spore-specific genetic programs. Since the expression of these two proteins is not linked, sufficiently large random parallel increases in these two

proteins relative to the AB concentration are unlikely to occur other than by septation. This increases the robustness of the mechanism to stochastic fluctuations in gene expression.

Bistability and hysteresis are important to achieve reliable cell fate decisions and these are therefore emerging characteristics of regulatory networks that govern cell differentiation (Ferrell, 1999; Xiong & Ferrell, 2003; Slepchenko & Terasaki, 2004). A condition for bistability is the existence of some non-linearity that leads to a kind of "vicious cycle" which locks a response in one of the possible steady states (Ferrell & Xiong, 2001). This can be obtained in many different ways (Ferrell & Xiong, 2001; Angeli *et al.*, 2004), and it is achieved here by the co-operative binding of AA as well as by the self-enforcing formation of AB·ADP·AA complexes. Remarkably, the network that controls σ^F activity is small in size (4 proteins) and highly sensitive. The same network topology can also be found in other bacterial signaling pathways such as the general stress response of gram-positive bacteria (Chen *et al.*, 2003), and mitochondria have proteins with homology to AB (Machius *et al.*, 2001; Steussy *et al.*, 2001). This simple network architecture is therefore likely to represent a rather widely used mechanism to obtain robust bistability and ultrasensitivity in small protein networks. It will be interesting to see whether similar network architectures are also employed in higher organisms, especially in their mitochondria.

Chapter 6

Cell differentiation during the development of multicellular organisms

6.1 Introduction

During the development of a multicellular organism cells assume different fates in a position- and time-dependent manner. Cell fate is determined in response to cell signaling which can be triggered either by cell-cell interactions or by binding of signaling molecules, so called morphogens, whose concentration differs in time and space. More than half a century ago spatial gradients of morphogens were suggested to be established by diffusion (Turing, 1952). The role of diffusion has subsequently been questioned because strong receptor binding impedes morphogen diffusion and thus the establishment of a gradient (Kerszberg & Wolpert, 1998). However, this effect can be alleviated by ligand internalization and degradation (Lander *et al.*, 2002; Merkin & Sleeman, 2005), and the comparison of model predictions to experimental data strongly suggests a role for diffusion in generating these patterns, if in a different way than envisaged by Turing more than fifty years ago. Alternative mechanisms that are based on cell-to-cell transfer of morphogens (Kerszberg & Wolpert, 1998) are not in agreement with experimental observations (Lander *et al.*, 2002). Similarly there is no experimental evidence in support of a 'signaling gradient' that might arise if cells integrated receptor occupation over time (Kerszberg & Wolpert, 1998). Hence morphogen distribution by diffusion is the most plausible mechanism.

The formation of a gradient is the simplest of all possible patterns and is intensively studied in the context of anterior-posterior (Houchmandzadeh *et al.*, 2002; Gregor *et al.*, 2005) as well as wing patterning (Lander *et al.*, 2002). The specification of the dorso-ventral axis in the *Drosophila* embryo involves a more complicated pattern in that strong signaling is induced abruptly in a small domain around the dorsal midline (Dorfman & Shilo, 2001; Ross *et al.*, 2001) (Fig. 6.1). Although the signaling network is complicated and only known in parts, mathematical models can make important contributions because spatial effects are difficult to comprehend by verbal models alone. Experimental techniques are available to challenge model predictions, and this has permitted the development of increasingly realistic mathematical models for this important biological phenomenon.

The morphogen Decapentaplegic (Dpp), which triggers signaling in a sharp domain around the dorsal midline is expressed almost in the entire dorsal half of the embryo (St Johnston & Gelbart, 1987; Ray *et al.*, 1991) and its receptor Thickveins (Tkv) is expressed everywhere, even in the ventral part of the embryo. Mechanisms must therefore exist that concentrate the ligand in the dorsal midline. Three further proteins Sog (Short gastrulation), Tsg (Twisted gastrulation) and Tld (Tolloid), which differ in their expression pattern (Fig. 6.1), have been shown to play crucial roles in the process (Shimmi & O'Connor, 2003; De Robertis & Kuroda, 2004; Yamamoto & Oelgeschlager, 2004). Sog is expressed only in the ventral part (Francois *et al.*, 1994; Srinivasan *et al.*, 2002), and it has been proposed that it acts as a carrier protein for Dpp by preventing its capture by receptors and by diffusing with the ligand to the midline where Tld-dependent degradation of Sog (Shimmi & O'Connor, 2003) releases the ligand and enables receptor binding (Holley *et al.*, 1995; Marques *et al.*, 1997). Tsg expression follows a similar pattern as Dpp, and Tsg needs to bind to Sog in order to enable Sog to bind to Dpp (Ross *et al.*, 2001; Shimmi & O'Connor, 2003).

Mizutani and co-workers have recently shown that these protein interactions (Fig. 6.2) and dynamics are sufficient to give rise to the sudden formation of receptor-ligand com-

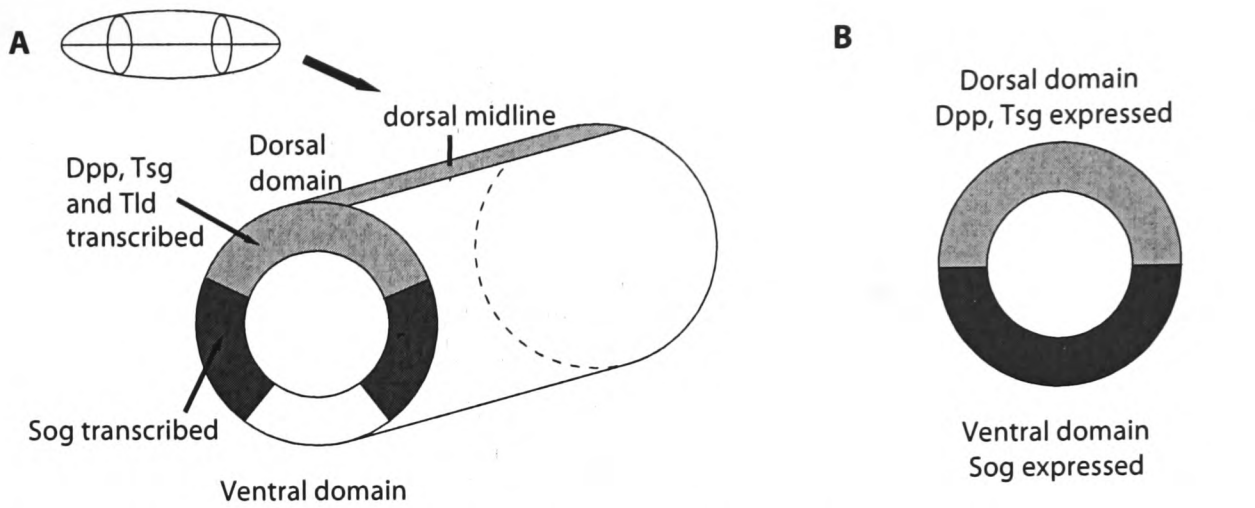


Figure 6.1: **A schematic model of dorsoventral embryonic expression pattern. (A)** Dpp, Tsg and Tld are expressed in the dorsal part (shaded in light grey), Sog is expressed in a region between the dorsal and ventral part (shaded in dark grey); the ventral part is depicted in white and the midline is marked as a light grey stripe. **(B)** For simplicity, in the simulation the dorsal genes are assumed to be expressed in the entire upper half of the embryo while Sog is expressed in the entire lower half of the embryo.

plexes in the midline (Mizutani *et al.*, 2005). While model and experiments agree remarkably well, the numerical studies are insufficient to understand the underlying mechanism. Consequently, it remains unclear which parameters determine the timing of the event and the strength of the response. We therefore sought to analyse the Mizutani model in more detail.

We will first review the Mizutani model and illustrate key properties of the dynamics of the system with numerical results. We then derive and analyse a dimensionless and simplified version of the Mizutani model. We define the mechanism that gives rise to the observed dynamics, and we determine the parameter values that affect the timing and width of the peak. Moreover, we show that the behaviour of the model is very sensitive to small variations in some parameter values, including the receptor concentration, the ligand degradation rate and the carrier diffusion and cleavage rates. The analysis is confirmed by numerical studies of the model.

6.2 A model for dorso-ventral morphogen patterning

Mizutani and co-workers (Mizutani *et al.*, 2005) have proposed the reaction scheme that is depicted in Figure 6.2 as the core that drives Dpp concentration in the midline, and this scheme translates into the following following set of reaction-diffusion equations

$$\begin{aligned}
\frac{\partial[L]}{\partial t} &= D_L\frac{\partial^2[L]}{\partial x^2} - k_{on}[L](R_0-[LR]) + k_{off}[LR] \\
&\quad -j_{on}[L][ST] + (j_{off}+\tau)[LST] + V_L(x) && (6.1)\\
\frac{\partial[LR]}{\partial t} &= k_{on}[L](R_0-[LR]) - (k_{off}+k_{deg})[LR] && (6.2)\\
\frac{\partial[S]}{\partial t} &= D_S\frac{\partial^2[S]}{\partial x^2} - n_{on}[S][T] + n_{off}[ST] + V_S(x) && (6.3)\\
\frac{\partial[ST]}{\partial t} &= D_{ST}\frac{\partial^2[ST]}{\partial x^2} + n_{on}[S][T] - n_{off}[ST] \\
&\quad -j_{on}[L][ST] + j_{off}[LST] && (6.4)\\
\frac{\partial[T]}{\partial t} &= D_T\frac{\partial^2[T]}{\partial x^2} - n_{on}[S][T] + n_{off}[ST] + \tau[LST] + V_T(x) && (6.5)\\
\frac{\partial[LST]}{\partial t} &= D_{LST}\frac{\partial^2[LST]}{\partial x^2} + j_{on}[L][ST] - (j_{off}+\tau)[LST], && (6.6)
\end{aligned}$$

where [ ] denotes the concentration of a component; the parameter values are summarized in Table 6.1. L refers to the morphogen that binds to the receptor R; the concentration of the receptor is assumed to be constant ($R_0 = 3\mu M$). Binding to the receptor results in ligand degradation at rate k_{deg} which is a novel feature of the Mizutani model as compared to earlier models (Eldar *et al.*, 2002; Shimmi *et al.*, 2005). The degradation rate of receptor-bound

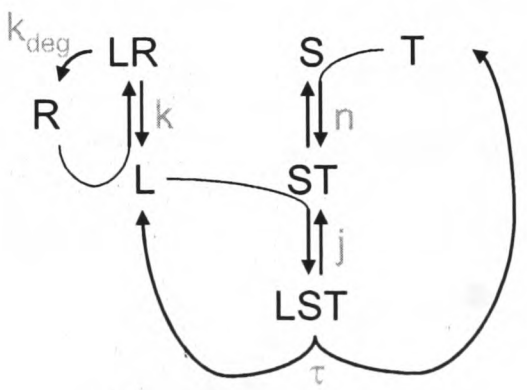


Figure 6.2: **An overview of the molecular interactions that are considered by Mizutani and co-workers (2005).** Ligand, L, can either bind receptor, R, to form ligand-receptor complexes, LR, or Sog-Tsg complexes, ST, to generate ligand-Sog-Tsg complexes, Tsg. Receptor-bound ligand is degraded at rate k_{deg}, and Sog in ligand-Sog-Tsg complexe is cleaved at rate τ.

Table 6.1: **Kinetic rate constants and protein concentrations as used by Mizutani and co-workers for their model (equations 6.1-6.6).**

parameter	functional significance	simulation value
k_{on}	ligand-receptor on-rate	$0.4\mu\text{M}^{-1}\ \text{s}^{-1}$
k_{off}	ligand-receptor off-rate	$4 \times 10^{-6}\ \text{s}^{-1}$
n_{on}	Sog-Tsg on-rate	$4\mu\text{M}^{-1}\ \text{s}^{-1}$
n_{off}	Sog-Tsg off-rate	$4 \times 10^{-5}\ \text{s}^{-1}$
j_{on}	ligand-Sog/Tsg on-rate	$95\mu\text{M}^{-1}\ \text{s}^{-1}$
j_{off}	ligand-Sog/Tsg off-rate	$4 \times 10^{-6}\ \text{s}^{-1}$
k_{deg}	degradation rate of ligand-receptor complexes	$5 \times 10^{-4}\ \text{s}^{-1}$
τ	degradation rate of Sog in LST complexes	$0.54\ \text{s}^{-1}$
V_S	expression rate of Sog	$80\ \text{nM s}^{-1}$
V_T	expression rate of Tsg	$4\ \text{nM s}^{-1}$
V_L	expression rate of ligand	$1\ \text{nM s}^{-1}$
$D_L, D_S, D_{ST}, D_{LST}$	diffusion constants	$85\mu\text{m}^2\ \text{s}^{-1}$
R_0	total receptor concentration	$3\mu\text{M}$

ligand, LR, $k_{deg} = 5 \times 10^{-4} s^{-1}$ is based on experiments (Mizutani *et al.*, 2005). Ligand also binds to a complex, ST, formed of Sog, S, and Tsg, T. The affinity of ligand both for the receptor ($k_{on} = 0.4\mu M^{-1}s^{-1}, k_{off} = 4 \times 10^{-6}s^{-1}$) and for the Sog-Tsg complex is very high ($j_{on} = 95\mu M^{-1}s^{-1}, j_{off} = 4 \times 10^{-6}s^{-1}$). This can be justified with the dimeric nature of the ligand which permits rebinding and thus reduces the off-rate; similarly Sog has four potential binding sites for the ligand. A similar argument has to be used to justify the high affinity between Sog and Tsg ($n_{on} = 4\mu M^{-1}s^{-1}, n_{off} = 4 \times 10^{-5}s^{-1}$). The carrier protein Sog $[S]$ is only expressed in the ventral half ($V_S(x) = 80nMs^{-1}$ for $x \in \mathcal{V}$, $V_S(x) = 0$ for $x \in \mathcal{D}$) while Tsg and Dpp are only expressed in the dorsal half ($V_T(x) = 4nMs^{-1}, V_L(x) = 1nMs^{-1}$ for $x \in \mathcal{D}$ and $V_T(x) = V_L(x) = 0$ for $x \in \mathcal{V}$). The degradation rate of Dpp-bound Sog has not yet been determined by experiments and in order to keep the model simple, Mizutani and co-workers assume the Tolloid activity to be constant and use a first-order rate constant for the degradation term ($\tau = 0.54s^{-1}$). All components except for the receptors that are membrane-bound diffuse at $D_L = D_S = D_{ST} = D_{LST} = 85\mu m^2 s^{-1}$.

The equations are solved on a 1-dimensional domain of length $C = 550\mu\text{m}$ with periodic boundary conditions. The domain represents the circumference of the embryo; given that the pattern is homogeneous along the anterior-posterior axis one dimension is sufficient to study the mechanism. We note a symmetry around the midline and therefore set $x = 0$ in

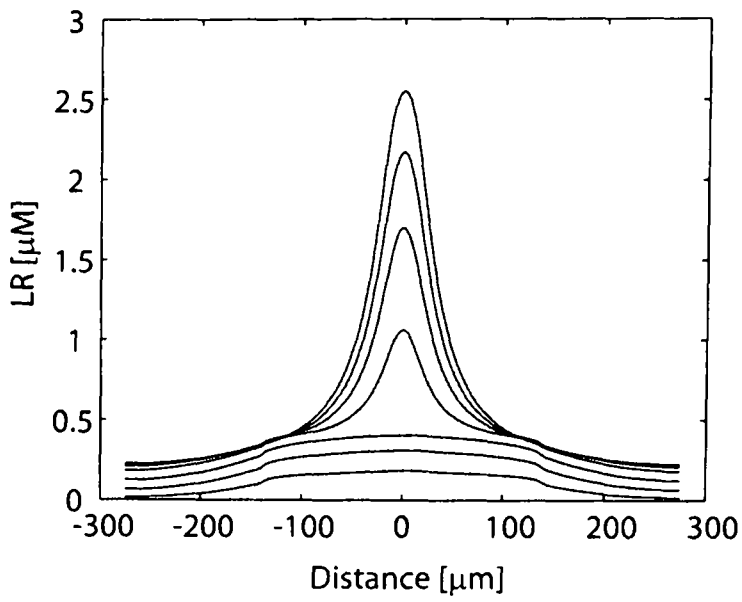


Figure 6.3: **Ligand-receptor dynamics.** Ligand-receptor profiles as calculated from equations 6.1-6.6 are given at 300 second intervals starting at 5 minutes (lowest curve) for the parameter values that are given in the text. The figure is essentially the same as Figure 4 in Mizutani et al., 2005.

the midline such that the dorsal and ventral half are defined by

$$\begin{aligned} \mathcal{D} &= \left[-\frac{C}{4}, \frac{C}{4}\right] \\ \mathcal{V} &= \left[-\frac{C}{2}, -\frac{C}{4}\right] \bigcap \left[\frac{C}{4}, \frac{C}{2}\right] \end{aligned} \tag{6.7}$$

respectively (Fig. 6.1B).

6.3 Ligand is transported to the midline by LST

The key property of the Mizutani model is the sudden formation of the peak of ligand-receptor complexes in the midline (Fig. 6.3). More than ten years ago Ferguson and co-workers suggested that ligand is transported to the midline by ligand-Sog-Tsg complexes (Holley *et al.*, 1995). Comparison of the total concentration of ligand in the midline with ligand expression and ligand transport rates shows that in the Mizutani model this mechanism is indeed responsible for the rapid increase in the ligand concentration once the signaling peak begins to form (Fig. 6.4). Thus once the peak forms (after about 1000 seconds) the ligand concentration in the midline increases more than can be achieved by ligand expression alone (compare dotted and dashed lines in Fig. 6.4a); ligand diffusion without carrier binding is negligible because of the high affinity of ligand-receptor binding.

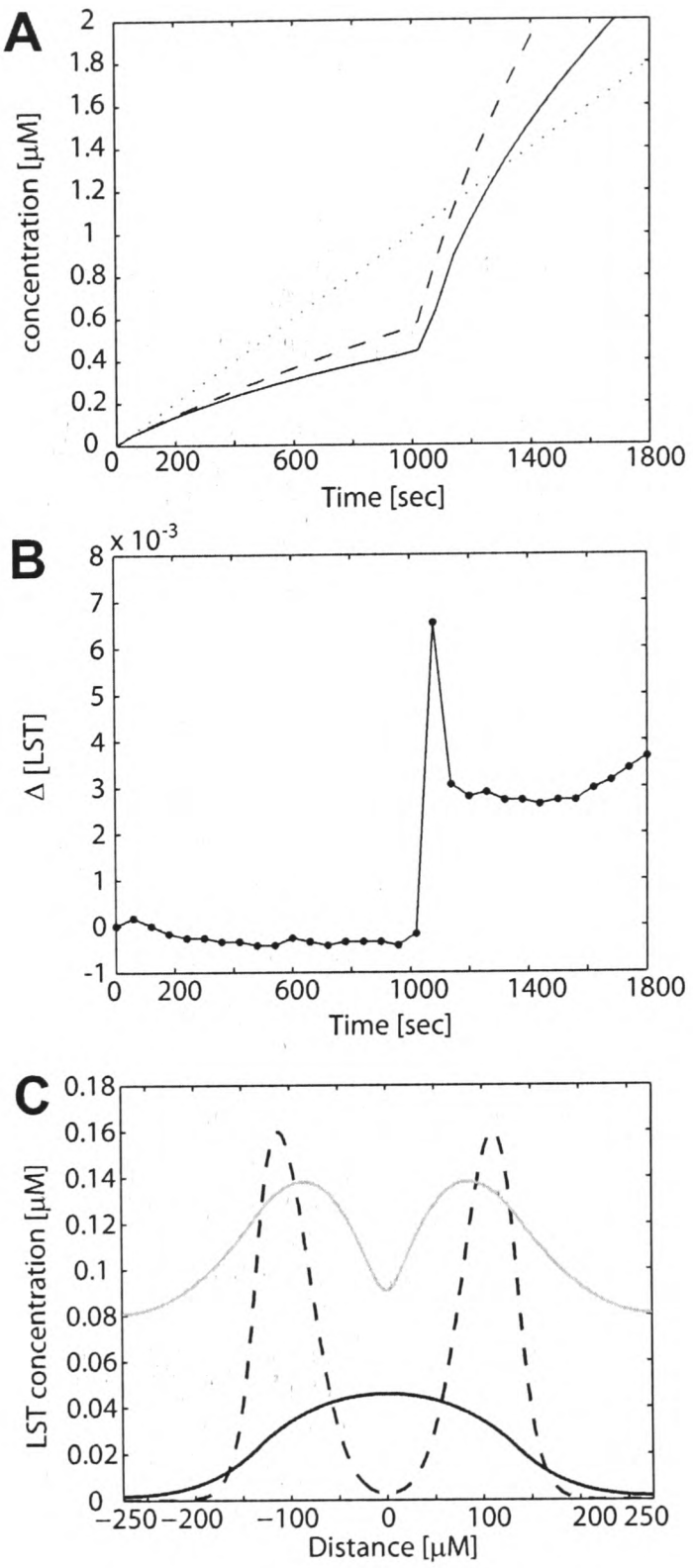


Figure 6.4: **Ligand is transported into the midline by LST. (a)** The total concentration of ligand in the midline for parameters as given in the text (solid line) or if $k_{deg} = 0$ (dashed line), and the total concentration of ligand achieved by expression (dotted line) in the midline over time. **(b)** The curvature of LST, $\Delta[LST]$, inverts twice. $\Delta[LST]$ was approximated by a central difference scheme 5 μm away from the midline. **(c)** The spatial distribution of $[LST]$ after 12 seconds (dashed line), 300 seconds (black line), and 1080 seconds (grey line). The curve at 12 seconds is magnified by 100-fold in order to facilitate comparison.

Interestingly, before the signaling peak emerges ligand is transported out of the midline by *LST* complexes (the solid line has a smaller slope than the dotted line in Fig. 6.4a). The initial increase in the ligand concentration is therefore solely the result of ligand expression in the dorsal domain and is diminished rather than enhanced by *LST*-dependent diffusive transport (Fig. 6.4). This effect has so far been ignored but is a consequence of the curvature of the *LST* curve which is initially negative ($\frac{\partial^2[LST]}{\partial x^2} < 0$) and which inverts only once the signaling peak forms (Fig. 6.4b,c). According to Fick's second law

$$\frac{\partial c}{\partial t} = D\frac{\partial^2 c}{\partial x^2}, \tag{6.8}$$

such that the concentration of a diffusive species c increases because of diffusive transport only if the curvature of c is positive ($\frac{\partial^2 c}{\partial x^2} > 0$). It should be noted that we have $\frac{\partial^2[LST]}{\partial x^2} > 0$ also at the very onset of the reaction. However, the morphogen concentration is still too low to enable this to lead to a notable increase of the morphogen concentration in the midline (Fig. 6.4). In the intermediate time regime, when the curvature of the *LST* function is negative ($\frac{\partial^2[LST]}{\partial x^2} < 0$), we note that receptor-dependent ligand degradation has a substantial effect (Fig. 6.4a, compare curves with and without degradation). We conclude that the total amount of ligand in the midline is initially limited both by degradation and by outward diffusion. After about 1000 seconds the LST gradient suddenly inverts and ligand is transported to the midline by diffusion leading to the abrupt formation of the signaling peak.

6.4 Determinants of the timing of peak formation

Figure 6.5 shows that the sudden increase of ligand-receptor complexes in the midline after about 1000 seconds coincides with a sudden loss in ligand-carrier complexes. The loss in the ligand-carrier concentration (grey, continuous line) is preceded by a sudden drop in the carrier concentration (black, continuous line) which itself is preceded by a drop in the Sog concentration (black, dotted line) and a simultaneous increase in Tsg (black, dashed line). The sudden loss in Sog from the midline is the consequence of Tolloid-dependent cleavage

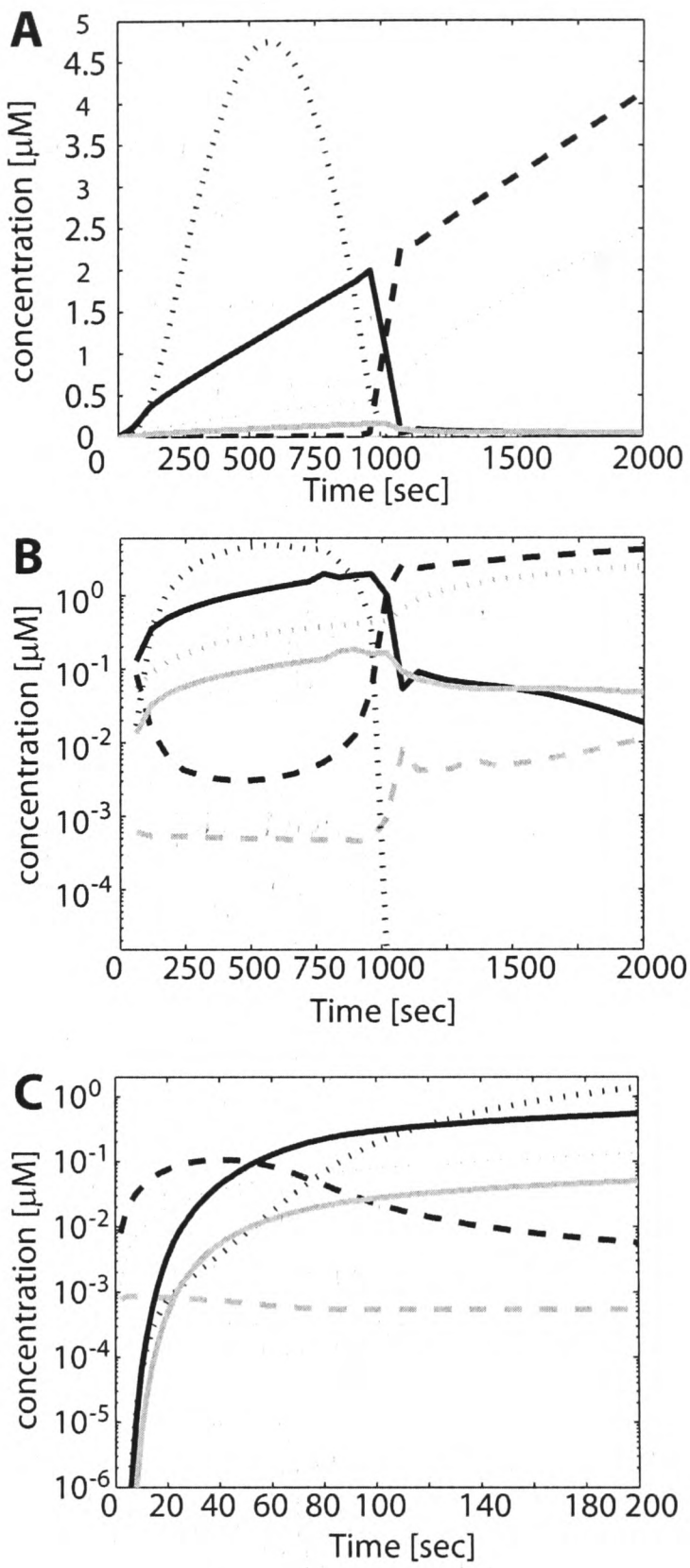


Figure 6.5: **The time-dependent evolution of the protein concentrations in the midline.** The dynamics of L (dashed grey line), LR (dotted grey line), LST (solid grey line), S (dotted black line), ST (solid black line), and T (dashed black line) in the midline as calculated from (6.1-6.6). (A-C) differ only in the scaling of the axes.

of Dpp-bound Sog in the midline. There is a net loss of Sog once the cleavage rate of Sog

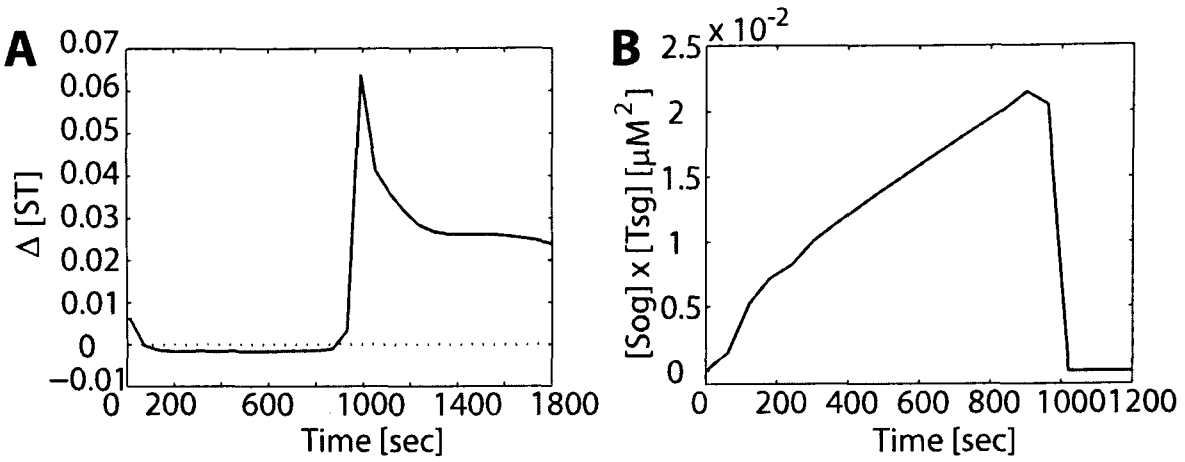


Figure 6.6: **Numerical estimates of the Sog-Tsg concentration and its curvature in the midline over time.** **(A)** The curvature of the Sog-Tsg curve in the midline over time. $\Delta[ST]$ was approximated by a central difference scheme 5 μm away from the midline. **(B)** The product of the Sog and Tsg concentrations in the midline over time.

($\tau[LST]$) exceeds the rate of Sog production. From equations 6.3, 6.4, 6.6 we have

$$\frac{\partial[S]}{\partial t}+\frac{\partial[ST]}{\partial t}+\frac{\partial[LST]}{\partial t}=V_S(x)-\tau[LST]+D_S\frac{\partial^2[S]}{\partial x^2}+D_{ST}\frac{\partial^2[ST]}{\partial x^2}+D_{LST}\frac{\partial^2[LST]}{\partial x^2}, \quad (6.9)$$

such that at the unique turning point where $\frac{\partial[S]}{\partial t}+\frac{\partial[ST]}{\partial t}+\frac{\partial[LST]}{\partial t}=0$

$$[LST]=\frac{V_S}{\tau}\sim 0.15\mu M, \quad (6.10)$$

if we neglect the diffusion terms. This can be justified because diffusion is fast relative to the other processes and the gradients are therefore shallow on the relevant time scale (before the turning point is reached) as confirmed by numerical simulations (Figs. 6.4B, 6.6A). The level of Sog-containing complexes will therefore decrease in the midline once the critical LST concentration $[LST]_c=\frac{V_S}{\tau}\sim 0.15\mu$M is attained in the midline.

The corresponding critical time point can be estimated by solving the differential equation for $[LST]$. Equation 6.6 can be simplified by observing that $j_{off}\ll\tau$, and by again neglecting the diffusion terms to obtain

$$\frac{\partial[LST]}{\partial t}\approx j_{on}[L][ST]-\tau[LST]. \quad (6.11)$$

The numerical solution reveals that before the turning point is reached the ligand concentration is very much constant while the concentration of ST increases linearly (Fig. 6.5A, B).

That the ligand concentration is about constant on the relevant time scale follows because the ligand binding reactions are fast compared to ligand production as long as little receptor is occupied. As a consequence a low stable ligand concentration will be attained quickly. This can be confirmed analytically by using regular perturbation methods and a scaling argument (Appendix B.4). The kinetics of $[ST]$ are estimated in the following. Noting that the off-rates and the diffusion term are very small on the relevant timescale and neglecting these terms, we obtain from equation 6.4

$$\frac{\partial[ST]}{\partial t} \approx n_{on}[S][T] - j_{on}[L][ST]. \tag{6.12}$$

The numerical solution shows that also the product of $[S]$ and $[T]$ increases about linearly before the turning point (Fig. 6.6B), and we can therefore write $[S][T] \approx \frac{\partial[S][T]}{\partial t}t = ct$ where c is a constant such that

$$\frac{\partial[ST]}{\partial t} \approx n_{on}ct - j_{on}[L][ST]. \tag{6.13}$$

We can then solve equation 6.15 to obtain

$$[ST] \approx \frac{n_{on}c}{j_{on}L}\left(t - \frac{1}{(j_{on}L)}\right) + const = \frac{n_{on}c}{j_{on}L}t \tag{6.14}$$

because $[ST] = 0$ at $t = 0$. Since we assume that c and L are constant, we have

$$\frac{\partial[ST]}{\partial t} \approx \frac{n_{on}c}{j_{on}L} = const. \tag{6.15}$$

We can then rewrite equation 6.11 as

$$\frac{\partial[LST]}{\partial t} \approx j_{on}[L]\frac{\partial[ST]}{\partial t}t - \tau[LST]. \tag{6.16}$$

and obtain

$$[LST] \approx \frac{j_{on}L\frac{\partial[ST]}{\partial t}}{\tau}\left(t - \frac{1}{\tau}\right) + const = \frac{n_{on}\frac{\partial[S][T]}{\partial t}}{\tau}t \tag{6.17}$$

because $[LST] = 0$ at $t = 0$. For the critical time we then have

$$t_c = \frac{\tau[LST]_c}{n_{on}\frac{\partial[S][T]}{\partial t}} = \frac{V_S}{n_{on}\frac{\partial[S][T]}{\partial t}}. \tag{6.18}$$

There is no simple way of approximating $\frac{\partial[S][T]}{\partial t}$, but the numerical solution reveals that $\frac{\partial[S][T]}{\partial t} \sim 2.1 \times 10^{-5} \mu M^2 \text{ s}^{-1}$ (Fig. 6.6B). We then have

$$t_c \sim \frac{80nMs^{-1}}{4\mu Ms^{-1} \times 2.1 \times 10^{-5}\mu M^2 s^{-1}} \sim 950s. \tag{6.19}$$

The numerical simulation of the model confirms the value of t_c as well as the dependency of t_c on V_S, although the slope is slightly underestimated because of our linear approximations (Fig. 6.7 B). We cannot determine how $\frac{\partial[S][T]}{\partial t}$ depends on the parameter values but we note from the numerical solution that there is also a linear dependency between t_c and R_0 and V_L (Fig. 6.7). We conclude that the time at which the critical LST concentration is attained depends on the concentration of free ligand and therefore on the concentration of receptors as well as on the Sog and ligand expression rates.

6.5 The mechanistic basis of the abrupt increase of the ligand concentration in the midline

We have concluded in section 6.3 from the numerical analysis of the model that the sudden formation of receptor-ligand complexes in the midline is enabled by a sudden influx of ligand. This influx is the consequence of an inversion in the curvature of the LST graph. From Figure 6.4b we see that the gradient inverts twice. Initially LST forms preferentially at the boundary of the ventral and dorsal domain where sufficient Sog, Tsg, and ligand are available and accordingly minima form at the midline of the ventral and dorsal domains (Fig. 6.8a,b). Because of the high level of Sog expression and fast diffusion, Sog becomes distributed almost homogeneously throughout. Accordingly LST forms in the entire dorsal domain and diffuses into the ventral domain such that the maximum is now attained in the dorsal midline and the minimum in the ventral midline (Fig. 6.8c). This explains the first inversion of the LST curvature.

In the following we define the mechanism and the parameter dependency of the second gradient inversion that enables abrupt peak formation. If we rewrite equation 6.6 to obtain

$$D_{LST}\frac{\partial^2[LST]}{\partial x^2} = -j_{on}[L][ST] + (j_{off} + \tau)[LST] + \frac{\partial[LST]}{\partial t} \tag{6.20}$$

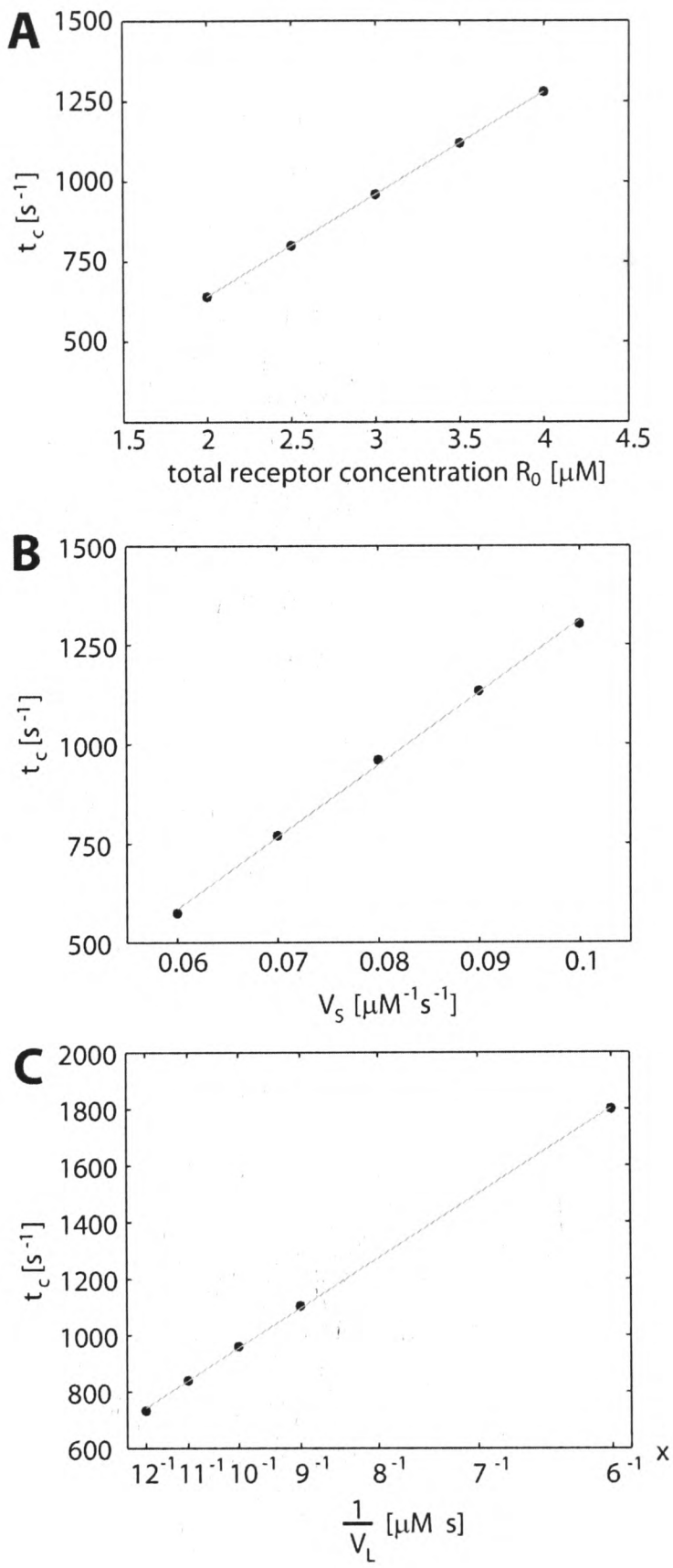


Figure 6.7: **The time of peak formation.** The critical time t_c dependent on **(A)** the receptor concentration, R_0 **(B)** the Sog production rate, V_S, and **(C)** the inverse of the Dpp production rate, V_L. The dots represent the times at which $[ST] + [LST]$ is maximal in the simulation, and the lines represent linear least square fits to the data points. We find (A) $t_c = 320R_0$, (B) $t_c = -508 + 1.82 \times 10^4 V_S$, and (C) $t_c = -319 + 1.27\frac{1}{V_L}$.

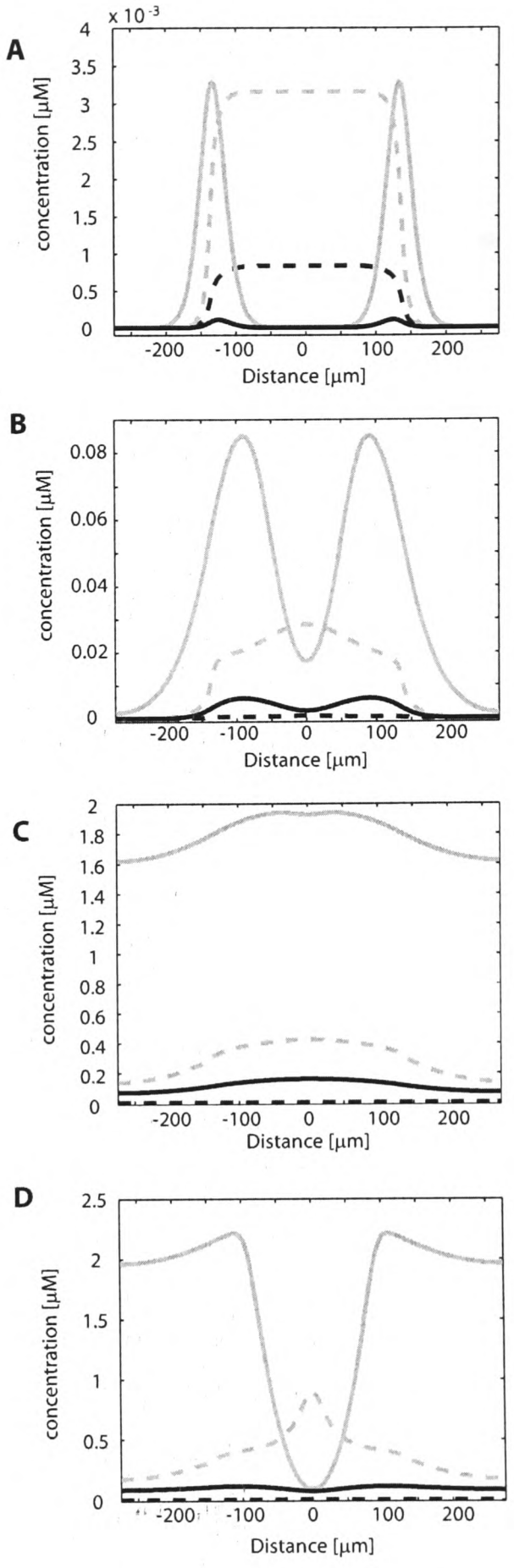


Figure 6.8: **The spatial distribution.** The spatial distribution of L (black, dashed line), LR (grey dashed line), ST (grey continuous line), and LST (black continuous line) after **(a)** 4 seconds **(b)** 30 seconds, **(c)** 900 seconds **(d)** 1080 seconds.

we see that before the formation of the signaling peak we have $D_{LST}\frac{\partial^2[LST]}{\partial x^2} < 0$ because $[LST] \ll [ST]$. A negative curvature of $[LST]$ leads to LST efflux from the midline and this reduces the concentration of LST in the midline. At $t = t_c$, $[LST] = [LST]_c$ is attained and the ventral production and diffusion of Sog is no longer sufficient to replenish cleaved Sog. Because LST achieves its maximum in the midline, $[LST] = [LST]_c$ is attained there first. As a consequence ST decreases rapidly in the midline (Fig. 6.5). According to (6.20) the curvature of LST inverts once

$$j_{on}[L][ST] < (j_{off} + \tau)[LST] + \frac{\partial[LST]}{\partial t}. \tag{6.21}$$

LST then flows into rather than out of the midline where Tolloid cleaves the complex and releases the ligand. We conclude that the sudden loss of Sog from the midline leads to the sudden accumulation of ligand and the formation of the signaling peak.

In order to achieve the sudden formation of the full signaling peak it is important that the LST gradient inverts only once sufficient ligand is available to rapidly fill the receptors. This delay is achieved by a two-component carrier. The carrier concentration is limited by the Tsg expression rate while the time point of gradient inversion is determined by the Sog expression rate. In the case of a one-component carrier the concentration of the carrier cannot be efficiently limited because a lower carrier expression rate results in an even earlier inversion of the gradient for the ligand-carrier complex and therefore in an even earlier formation of the signaling peak. This can be seen when modifying the Mizutani model such that the equations (6.3-6.5) for Sog, Tsg and Sog-Tsg are replaced by a new equation for a carrier that can bind the ligand directly. If, for simplicity, we continue to refer to this carrier as ST and to the formed complex as LST although Tsg is not contained we obtain as an additional equation to equations 6.1, 6.2, 6.6

$$\frac{\partial[ST]}{\partial t} = D_{ST}\frac{\partial^2[ST]}{\partial x^2} - j_{on}[L][ST] + j_{off}[LST] + V_S^*. \tag{6.22}$$

Figure 6.9 shows that with a one-component carrier the peak forms early. While the time at which the peak reaches its maximum can be delayed by reducing the expression

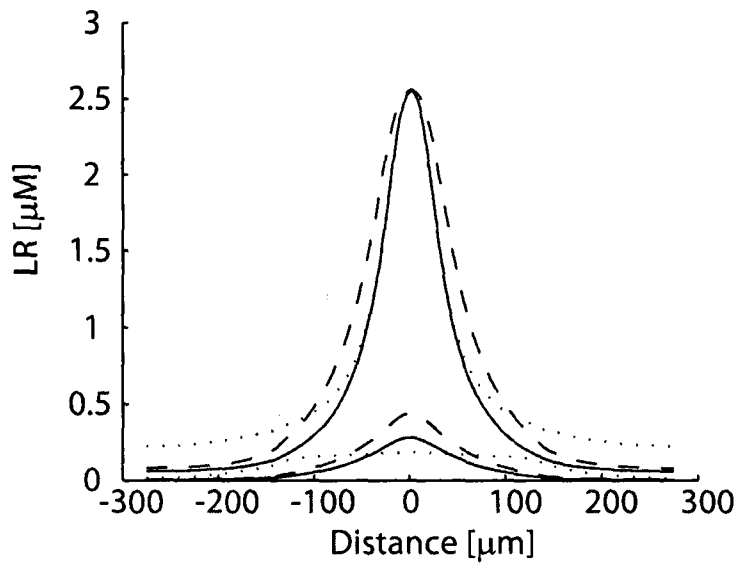


Figure 6.9: **A two-component carrier complex is necessary for abrupt peak formation.** The signaling peaks where obtained by solving either equations 6.1-6.6 (dotted line), or equations 6.1, 6.2, 6.6, 6.22 with $V_S^* = V_S$ (solid line) or $V_S^* = 0.5V_S$ (dashed line). The lower set of peaks is obtained after 300 seconds, and the other set of peaks is obtained after 1500 seconds for the solid line and after 2100 seconds for the other two conditions.

rate of the carrier, this will lead to an even earlier inversion of the ligand-carrier gradient and therefore to an even earlier onset of peak formation.

Since the transport of LST is important for the sudden formation of the peak, the diffusion coefficient can be expected to affect the formation of the signaling peak. As numerical studies confirm, a minimal value for the LST diffusion coefficient in the range employed in the Mizutani model is indeed required in order to obtain the rapid formation of a signaling peak (Fig. 6.10a). Larger values do not affect the signaling peak because transport is limited by the gradient.

Similarly, based on (6.21) the model can be predicted to be very sensitive to τ. For values larger or smaller than order 1 gradient inversion happens either too late or too early. In both cases a peak will not form as indeed confirmed by numerical simulation (Fig. 6.10b).

6.6 The width of the signaling peak

The width of the signaling peak is determined by the gradient of the LST curve. The steeper the LST gradient the smaller is the domain in which ligand accumulates and ligand-receptor

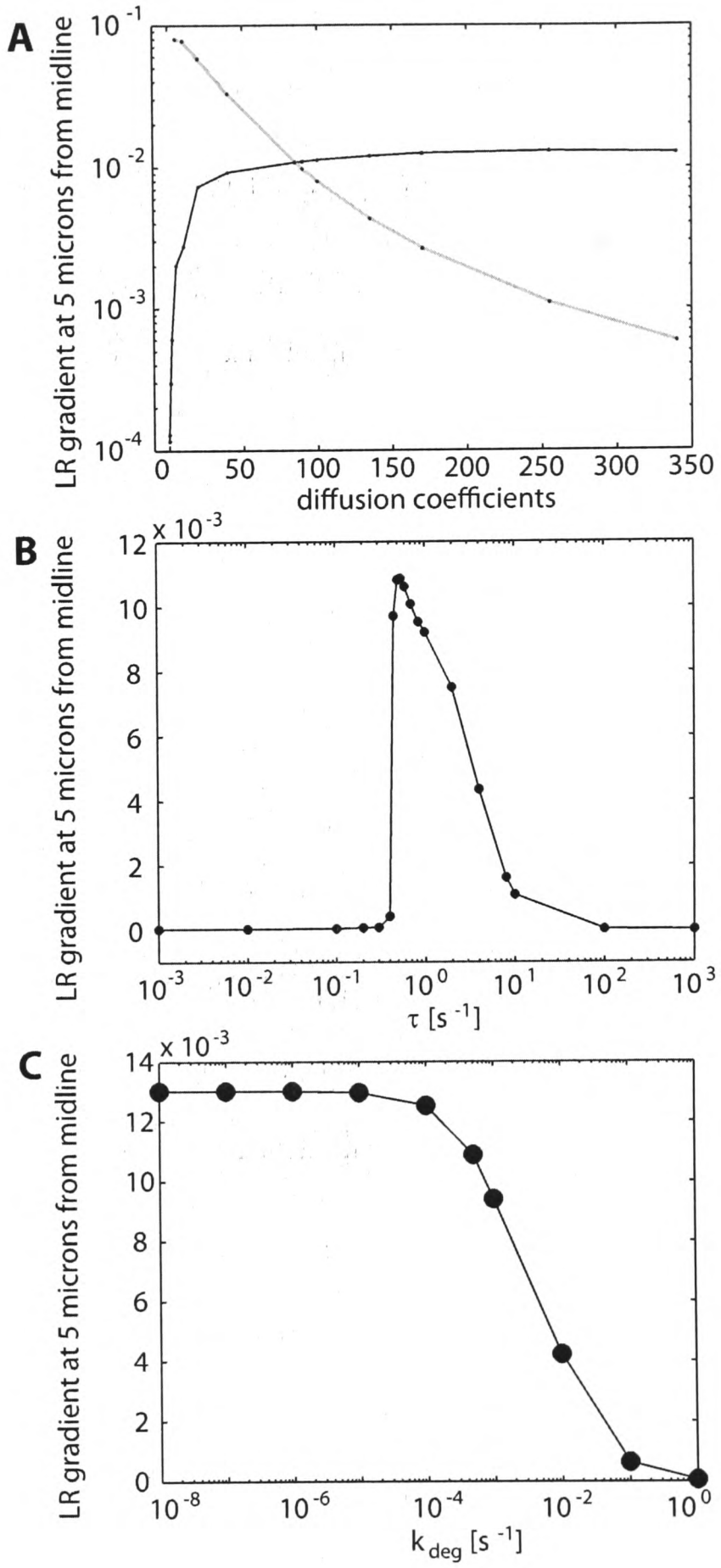


Figure 6.10: **Parameter dependencies of the model behaviour.** LR gradient at 5 μm from the midline if **(A)** D_{LST} (black line), D_{ST} (grey line), **(B)** τ, or **(C)** k_{deg} are varied. Stripe formation in the midline requires an LR gradient of about 0.01. Dots indicate the analysed parameter values.

complexes form. A high degradation rate limits the amount of free ligand and therefore LST formation. Consequently the LST gradient is not as steep and the peak widens. Thus raising k_{deg} from 10^{-8} per second to 1 per second we note that the peak widens once k_{deg} exceeds 10^{-4} per second until the formation of a signaling peak becomes impossible altogether (Fig. 6.10c). The timing of peak formation is, on the other hand, not affected (Fig. 6.4a). The form of the LST curve is affected also by the distribution of ST. Accordingly, a larger Sog-Tsg diffusion coefficient results in peak widening (Fig. 6.10a) because the carrier is distributed more widely.

6.7 Discussion

We conclude from the detailed analysis of the Mizutani model that the sudden formation of ligand-receptor complexes in the midline is the consequence of a chain reaction that is started when the rate of cleavage of ligand-carrier complexes in the midline exceeds the rate of Sog replenishment by ventral expression and diffusion. The rapid net loss of Sog at the midline lowers the concentration of Dpp-Sog-Tsg at the midline. This in turn results in the inversion of the Dpp-Sog-Tsg gradient. This inversion enables Dpp-Sog-Tsg diffusion into the midline which leads to a rapid increase in the ligand concentration in the midline. Because the concentration of Sog is limited by Tolloid-dependent cleavage, the free ligand binds preferentially to receptors which results in the rapid formation of the signaling peak.

Our detailed analysis of the Mizutani model has led to the important mechanistic insight that the sudden formation of the signaling peak is the consequence of the inversion of the gradient formed by Dpp-Sog-Tsg complexes. Whilst a prominent role of Dpp-Sog-Tsg complexes in the transport of ligand to the midline had been proposed before (Holley *et al.*, 1995), previous discussions did not consider a change in the direction of the flux of Dpp-Sog-Tsg complexes. Only because Dpp-Sog-Tsg complexes initially diffuse out of the midline can the signaling peak form abruptly. Moreover, we propose a novel role for the Tsg protein which at first sight appeared to serve a rather redundant function in the model proposed

by Mizutani and co-workers. According to our analysis, Tsg is necessary to delay gradient inversion such that, once the gradient inverts, sufficient ligand is available to rapidly fill the receptors in the midline. In the case of a one-component carrier the final ligand-receptor peak would be similar in shape but the peak would no longer form abruptly. In a previous model (Eldar *et al.*, 2002) which, however, is based on a number of unrealistic assumptions - in particular in view of recent data - a different role, namely the selection between the two ligands Dpp and Scw, had been proposed.

Our analysis identifies a number of parameter values to which the simulation is highly sensitive. Thus the time of peak formation sensitively depends on the relative rates of Sog and Dpp production and on the total receptor concentration. This result is in good agreement with the observation that mutants which are heterozygous for both the *sog* and *dpp* genes have a much higher viability than mutants that are heterozygous only in *dpp* (Francois *et al.*, 1994). Whether the time of peak formation is affected in the heterozygotes has not been reported. Regulatory processes will need to exist to control the receptor concentration as well as the ratio of these expression rates, which will be subject to stochastic fluctuations (Kaern *et al.*, 2005).

Even more interesting, perhaps, is our observation that the simulation is highly sensitive to even small variations in τ, the rate of Tolloid-dependent cleavage of Sog in Dpp-Sog-Tsg complexes. This sensitivity is a considerable weakness of the model since the Tolloid-dependent cleavage has been modelled only phenomenologically. In reality Tolloid is expressed alongside the other proteins and there is some evidence that the activity of Tolloid is regulated (Yamamoto & Oelgeschlager, 2004). As a consequence the rate of Tolloid-dependent cleavage of Sog is unlikely to be constant. Similarly, the peak width is very sensitive to the receptor-dependent ligand degradation rate which can be affected by many physiological processes.

The high sensitivity of the Mizutani model to small changes in a number of parameter values suggests that important details that stabilize the regulatory network have been ne-

glected. These may include ligand heterodimers (Shimmi *et al.*, 2005), intracellular signaling networks (Wang & Ferguson, 2005), and further protein interactions. Further refined models that build on the Mizutani model are clearly needed to fully understand the mechanistic basis of dorsoventral patterning.

Part II: Cell adhesion

Chapter 7

Introduction

Cell adhesion and migration are fundamental requirements for the working of multicellular organisms. Because of the complexity of the process, which involves a large number of proteins, a detailed understanding is lacking, and even very basic mechanistic details about key components are still elusive. In particular the initial step of receptor-mediated adhesion is badly understood because the receptors themselves are large, complicated proteins.

An important class of cell adhesion receptors are integrins, large membrane-spanning heterodimeric proteins which participate in a wide-range of biological interactions, including development, tissue repair, angiogenesis, inflammation and hemostasis (Horwitz & Webb, 2003). Their name derives from their ability to link the extracellular and intracellular skeletons (Tamkun *et al.*, 1986). Integrins are key components of focal adhesions, dynamic multi-protein complexes that are involved in the regulation of cell adhesion and migration. Focal adhesions (Zamir & Geiger, 2001) provide a physical link between integrins and the actin cytoskeleton as well as sites for signal transduction into the cell interior. Information about identified interactions and players in these complexes is ever-increasing but our overall understanding of how the ensemble works remains relatively poor.

According to the current model of integrin activation, ligand binding shifts the equilibrium between different integrin conformations to the active one (Hynes, 2002). The two extreme conformations of this allosteric protein are a bent or 'closed' conformation which represents the low affinity state for ligand and an 'open' conformation that will bind with

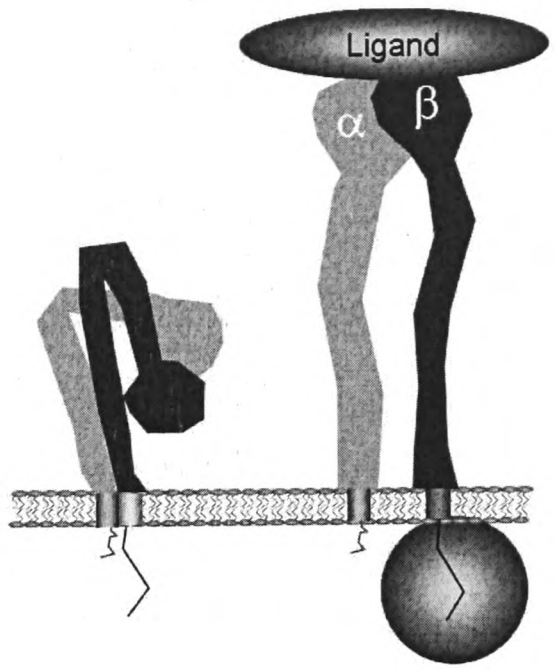


Figure 7.1: **A simple model of integrin activation.** Integrins are transmembrane proteins and exist in either a closed (LHS) or open conformation (RHS); the open, high affinity form, in which the intracellular part of the α- and β chains are separated, can be stabilized by binding of extracellular ligand (oval) or intracellular proteins (ball). The open conformation triggers downstream signaling and is termed active.

high affinity to ligand (Fig. 7.1). Conformational changes in the extracellular domain affect the cytoplasmic tails, which are separated in the open conformation but not in the closed conformation. Separation of the cytoplasmic domains promotes their interaction with cytoskeletal and signal transduction molecules, and thus the activation of integrins and downstream signaling. The conformational equilibrium can be influenced both by ligand binding to the extracellular domain (outside-in signaling) and by binding of cytoplasmic proteins to the separated cytoplasmic domains (inside-out signaling). Talin, a large intracellular protein that binds integrin cytoplasmic tails and the actin cytoskeleton, is, for example, essential for integrin activation (Campbell & Ginsberg, 2004). As well as changes in affinity induced by structural changes, integrins can also modulate their avidity by clustering, thus changing the valency of their interactions with ligand (Carman & Springer, 2003).

Previous theoretical studies have addressed the mechanism of integrin clustering (Ward & Hammer, 1994; Irvine *et al.*, 2002) but they have not yet explored whether ligand binding

is sufficient or if other factors such as clustering are necessary for integrin activation. In principle, ligand-dependent integrin activation can be enabled by any of the four different mechanisms depicted in Figure 7.2. A) Extracellular ligand alone is sufficient to activate integrins and other factors are only important for downstream signaling (Fig. 7.2A); B) Ligand-dependent integrin activation requires the binding of an intracellular stabilizing factor that interacts with and stabilizes the on state (Fig. 7.2B); C) A positive feedback, provided either by integrin-ligand pairs themselves or by self-interactions, is important (Li *et al.*, 2003)) (Fig. 7.2C); D) A positive feedback that increases the activity of an intracellular stabilizing factor is required (Fig. 7.2D). The latter would need to be based on a larger intracellular signaling network.

In Chapter 8 mathematical modelling is used to evaluate the physiological potential of these mechanisms. The analysis suggests that, at least for some physiological conditions, binding of ligand (even if it is preclustered) and/or a stabilizing factor (Fig. 7.2A, B) is insufficient for ligand-dependent integrin activation; a positive feedback (Fig. 7.2C, D) is required which results in the further stabilization of the active conformation. Integrin clustering is a likely consequence of such a positive feedback.

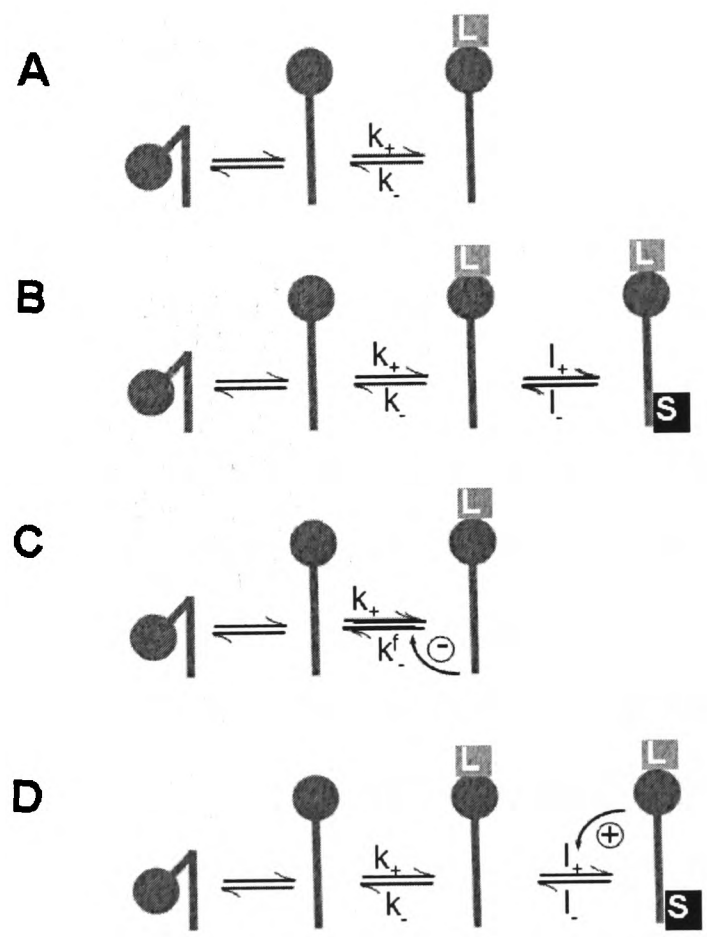


Figure 7.2: **Four possible mechanisms for integrin activation.** **(A)** Ligand-binding is sufficient for integrin activation; other factors are only important for downstream signaling events. **(B)** A stabilizing factor (such as talin) is necessary in addition to ligand binding. **(C)** A ligand induced positive feedback (based for instance on integrin self-interaction) induces integrin activation. **(D)** A positive feedback involving further signaling molecules is necessary for integrin activation. The symbols represent simple variants of those in Figure 7.1. L refers to ligand, S to a stabilizing factor. The rate constants correspond to those used in the models discussed in Section 8.

Chapter 8

A model for integrin activation

Broadly speaking, integrins can be taken to exist in one of two states, a closed low affinity or an open high affinity conformation. In the absence of ligand the equilibrium is biased towards the inactive, low affinity conformation (Tadokoro *et al.*, 2003). Binding of ligand (L) stabilizes the active, high affinity conformation. Under physiological conditions integrin activation therefore requires ligand binding and accordingly the physiological relevance of the mechanisms depicted in Figure 7.2 can be evaluated by analysing the extent to which they promote ligand binding. While the relationship between ligand binding and cellular action in response to integrin activation is unlikely to be linear we will show that the mechanisms differ substantially in the level to which they promote integrin-ligand binding such that they can be readily classified as 'non-supportive' or 'activating'. The analysis can be greatly simplified if we determine the fraction of ligands bound by integrins rather than the fraction of integrins bound to ligands. In this case, integrins in the closed, low affinity conformation do not have to be considered explicitly. We will assume that there is a constant number of unbound integrins in the high affinity conformation since any integrin that binds to ligand can be replaced rapidly from the integrins in the low affinity conformation by conformational changes. While ligand binding will eventually deplete the pool of unbound integrins, this does not need to be included in an analysis of mechanisms for integrin signal initiation: if integrin-ligand binding occurs to a level that integrin depletion becomes relevant the activation mechanism can be considered successful independently of

the exact final number of integrin-ligand complexes.

Under physiological conditions, the ligand is expected to be sufficiently dense that spatial details and diffusion constraints can be neglected in the initial steps of focal adhesion assembly. Transport of integrins from parts of the cell that are not in contact with the substrate is not relevant for the initial activation of cell adhesion signaling cascades and is not considered in this model.

The model follows the binding of single integrins to ligands; the probability of integrin-ligand complex formation can be calculated by solving the appropriate master equation. The master equation is a gain-loss equation for the probabilities of the separate states with n integrin-ligand complexes (van Kampen, 1992), from which the macroscopic kinetic equation can be derived when the density fluctuations are negligible. In order to decide which of the four mechanisms depicted in Figure 7.2 is sufficient for ligand-dependent integrin activation, the fraction of ligand bound by integrin is determined for each case.

8.1 Ligand engagement is not sufficient for integrin activation

According to the first mechanism (Fig. 7.2A), ligand-dependent integrin activation does not require any further supporting processes and interactions. The master equation for the formation of i integrin-ligand complexes is thus given as

$$\dot{p}_i = k_-(i+1)p_{i+1} + k_+(L-i+1)p_{i-1} - (k_- i + k_+(L-i))p_i, \qquad i \in (0, L) \qquad (8.1)$$

with $p_i = 0$ if $i \notin (0, L)$. p_i is the probability that i (open) integrins are bound to a ligand with L sites. k_+, k_- refer respectively to the on- and off-rates of the integrins. The on-rate includes the density of integrins which are taken to be constant (see previous section). The first two terms in (8.1) represent the gains of state i due to the transition from other states, that is, due to unbinding of an integrin from a complex with $i+1$ integrins (first term) or the binding to a complex with $i-1$ integrins (second term). The bracketed term is the loss

due to transitions from i into other states either by unbinding or binding of an integrin.

For the steady state ($\dot{p}_i = 0$) we obtain

$$p_i^* = \frac{\binom{L}{i}\left(\frac{k_+}{k_-}\right)^i}{(1+\frac{k_+}{k_-})^L}, \qquad i \in (0, L). \tag{8.2}$$

The steady state is stable because $\sum_i \dot{p}_i = 0$ and $p_i \geq 0$. Since the sum of all p_i is bounded and no p_i can become negative, no p_i can grow exponentially, and the linear system must be globally stable. $\sum_i \dot{p}_i = 0$ is an immediate consequence of the requirement that the sum of all probabilities is one (and therefore constant), but also follows from adding all differential equations and noting that the coefficients add to zero. Starting with $p_i \geq 0$, p_i cannot take negative values because when $p_i = 0$, $\dot{p}_i > 0$ and p_i cannot decrease further.

The expectation value for the number of integrins bound to a given ligand with L binding sites is given by $< I_b >= \sum_{i=0}^{L} i p_i$. Integrin activation therefore requires $p_i \gg p_0$ $(i > 0)$ and thus $\frac{k_+}{k_-} \geq 1$ (Fig. 8.1), which corresponds to a high on- and low off-rate. This is because the probability of i bound integrins is proportional to the ith power of $\frac{k_+}{k_-}$ and only for $\frac{k_+}{k_-} > 1$ does this probability increase with increasing i, that is with increasing numbers of integrins bound.

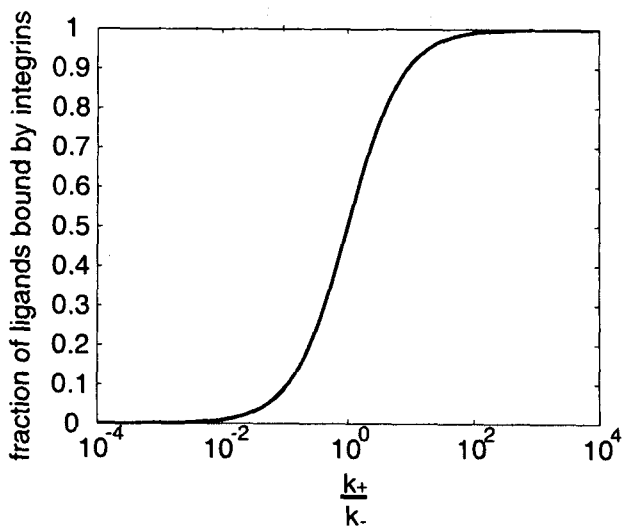


Figure 8.1: **Ligand engagement is not sufficient for integrin activation.** The integrin saturation of the ligand, $\frac{<I_b>}{L}$, is plotted against the integrin-ligand association constant $K_a = \frac{k_+}{k_-}$; L=10. As discussed in the text, experimental data suggest that $\frac{k_+}{k_-} \ll 1$ such that the fraction of activated integrins would be very small.

$k_- \sim 1\ s^{-1}$ has been established experimentally (Vitte *et al.*, 2004); the 2-dimensional on-rate is more difficult to determine and has to be calculated from the 2-dimensional dissociation constant which itself is difficult to measure and is often obtained via its 3-dimensional counterpart ($K_D^{3d} \sim 6 \times 10^{-8}$ M for the high affinity conformation (Faull *et al.*, 1993; Suehiro *et al.*, 1997) and $K_D^{3d} > 1\mu$M for the low affinity conformation (Faull *et al.*, 1993)). It is generally assumed that the two dissociation constants are linearly related such that $K_D^{2d} = \eta K_D^{3d}$. The value of the conversion factor η is, however, still a matter of debate (Moy *et al.*, 1999), since theoretical estimates are not in complete agreement with the latest experimental results. According to theoretical estimates for a protein complex that spans a distance d, $\eta = dN_A$, where N_A is the Avogardo constant (Bell, 1978). Accordingly for $d = 20$ nm, $\eta = 1.2 \times 10^{19} m^{-2}\ M^{-1}$. Studies employing protein-coated beads report $\eta = 8 \times 10^{24} m^{-2}\ M^{-1}$ (Moy *et al.*, 1999) and $\eta = 10^{22} m^{-2}\ M^{-1}$ (Kuo & Lauffenburger, 1993). The lower η value is corroborated by measurements of the 2-dimensional dissociation constant for the LFA-3/CD2 adhesion pair that were carried out using cells instead of beads (Dustin *et al.*, 1996). While there are experimental difficulties involved in obtaining an exact measurement of this parameter, the discrepancy between the theoretical and experimental estimates may well reflect a lower affinity of integrins when membrane bound, possibly due to steric constraints which will have a profound impact on this allosteric protein. We will therefore follow Moy and co-workers (1999) who used $\eta = 10^{22} m^{-2}\ M^{-1}$ rather than their own estimate for converting integrin dissociation constants. For $\eta = 10^{22} m^{-2}\ M^{-1}$ we find $k_{on} \sim 2 \times 10^{-3} \mu m^2\ s^{-1}$. In order to determine the frequency of integrin-ligand bond formation the density of open integrins needs to be taken into consideration. The average total (closed and open) integrin density on the cell surface has been estimated as $\rho \sim 1 - 3 \times 10^2 \mu m^{-2}$ (Wiseman *et al.*, 2004). At least in some cells (e.g. platelets) more than 95% of all integrins are in the closed inactive conformation in the absence of ligand (Tadokoro *et al.*, 2003); the density of integrin in the open conformation is therefore small ($\rho_o < 10 \mu m^{-2}$). Given that $k_+ = k_{on} \rho_o$ this implies, using the experimental estimate for η,

that $k_+ \sim 10^{-1} - 10^{-2}$ s^{-1} such that $\frac{k_+}{k_-} \ll 1$, which is insufficient to drive integrin activation. A larger k_+ can be achieved if a larger fraction of integrins is in the open conformation already in the absence of ligand. However, this leads to ligand-independent integrin activation. We can conclude that for experimentally determined parameters the model predicts that ligand-dependent integrin activation will not occur without further supporting interactions.

8.2 A stabilizing factor is not sufficient for ligand-dependent integrin activation

Proteins that bind and stabilize the active integrin conformation have been suggested to be important for integrin activation (Fig. 7.2B). The master equation derived in the previous section can be extended to include such factors that stabilize integrin-ligand binding. While talin is an excellent candidate for such a protein (and we will therefore call this factor talin in the following), the analysis is kept sufficiently general such that it could be extended to any cytoplasmic protein that prolongs the open active conformation by binding to the active integrin.

Much as in the case of integrins, talins can be considered to exist in two forms of different activity. Cytoplasmic talin is inactivated by self-interactions and only the 'open' conformation can bind to the membrane (PIP2), integrins and other proteins. Therefore we can again simplify the model by only considering the open active form, whose concentration can again be taken to be constant, since any open talin bound to integrins can be expected to be rapidly replenished from the pool of closed talins. Given the low abundance of both open talin and integrin, complexes of the two are taken to be absent in the absence of ligand. The gains and losses of the state with i integrins and t talins bound can again be translated into the linear master equation

$$\begin{aligned}\dot{p}_{i,t} &= k_-(i+1-t)p_{i+1,t} + k_-^*(t+1)p_{i+1,t+1} \\ &+k_+(L-i+1)p_{i-1,t} \\ &+l_-(t+1)p_{i,t+1} + l_+(i-t+1)p_{i,t-1} \\ &-(k_-(i-t) + k_-^* t + k_+(L-i) + l_+(i-t) + l_- t)p_{i,t}\end{aligned} \tag{8.3}$$

with $p_{i,t} = 0$ if $t > i$; $t, i < 0$; $t, i > L$. Here $p_{i,t}$ is the probability that i (open) integrins and t (open) talins are bound to the ligand with L sites. $p_{i,t} = 0$ if $t > i$ reflects the fact that talins can only attach to the ligand indirectly by binding to integrins. k_+, k_-, l_+, l_- refer to the on- and off-rates of the integrins and talins respectively. The on-rates include the density of integrin and talin which are taken to be constant (see above). k_-^* refers to the integrin off-rate when talin is bound ($k_-^* \leq k_-$).

For the steady state ($\dot{p}_{i,t} = 0$) we obtain from (8.3)

$$p_{i,t} = \frac{\binom{L}{t}\binom{L-t}{i-t} a^{L-i} b^{i-t}}{\sum_{i=0,t=0}^{i=L,t=L} \binom{L}{t}\binom{L-t}{i-t} a^{L-i} b^{i-t}} \tag{8.4}$$

with $a = \frac{k_-(k_-^*+l_-)+l_+k_-^*}{l_+k_+}$, $b = \frac{k_-^*+l_-}{l_+}$ for $i \geq t$ and $p_{i,t} = 0$ for $i < t$. From an argument similar to that given above it follows that this steady state is stable. The expectation value for the number of integrins and talins bound to a given ligand with L binding sites is given by $< I_b >= \sum_{i=0}^{L} i \sum_{t=0}^{L} p_{i,t}$ and $< T_b >= \sum_{t=0}^{L} t \sum_{i=0}^{L} p_{i,t}$ respectively. For strong ligand binding in the absence of talin binding ($p_{L,0} \gg p_{0,0}$) we require $b > a$ and we recover the condition $k_+ \gg k_-$ found in the previous section. If talin binds the condition becomes $\sum_{t=0}^{t=L} p_{L,t} \gg p_{0,0}$ and thus $a < b + 1$. This condition can be met if either $a < b$ or $a < 1$. Assuming that the integrin-ligand off-rate in the presence of talin is very small ($k_-^* \ll 1$), $a < b$ still requires $k_- < k_+$ (high integrin-ligand affinity) which we have found above to disagree with experimental estimates. The condition $a < 1$ can be met if either $k_- \ll k_+$ or if $k_- > k_+$ and $l_- \ll l_+$, that is integrin activation would be possible despite a low

integrin-ligand affinity if the integrin-talin affinity were sufficient high (Fig. 8.2). However, such high integrin-talin affinity would also lead to integrin activation in the absence of ligand binding. We can therefore conclude that a stabilizing factor alone is not sufficient for ligand-dependent integrin activation.

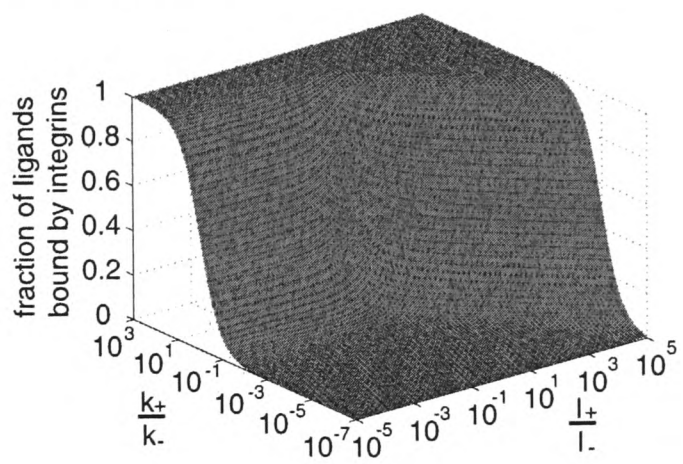


Figure 8.2: **A stabilizing factor is not sufficient for ligand-dependent integrin activation.** The fraction of ligand bound by integrin, $\frac{<I_b>}{L}$, is plotted against the integrin-ligand association constant $K_a = \frac{k_+}{k_-}$ and the integrin-talin association constant $K_a = \frac{l_+}{l_-}$ for $k_-^* = 0$; L=10. For experimental estimates of these association constants the activated fraction is small.

8.3 A positive-feedback is required for ligand-dependent integrin activation

The remaining two mechanisms in Fig. 7.2 both involve a positive feedback. Here, Figure 7.2C considers a feedback mechanism that only involves the integrin-ligand pair itself while according to Figure 7.2D a larger network would be necessary. Both mechanisms are analysed below.

8.3.1 A positive feedback that is based on the integrin-ligand pair

A positive feedback only involving the integrin-ligand pair (Fig. 7.2C) could either be enabled by integrin-integrin interactions in the open form (Li *et al.*, 2003) or by a ligand-induced conformational change that leads to a higher affinity of binding. In both cases this positive feedback ought to be triggered once a certain (small) number of integrins is engaged in close proximity. Such interaction can thus be captured in the model by replacing k_- with

k_-^f in (8.1) and setting $k_-^f = \frac{k_-^o}{(1+\frac{k_c i^n}{(i+K)^n})}$, where k_-^o refers to the integrin-ligand off-rate in the absence of a positive feed-back. k_c determines the strength with which the feedback reduces the integrin-ligand off-rate, and K and n limit the effect of integrin-integrin interactions to local interactions. The model does not contain any spatial information and it is thus assumed that integrins either bind to pre-clustered ligand, or preferentially in the vicinity of other bound integrins. Note that the assumption that ligand-integrin interactions are short-lived in the absence of integrin-integrin interaction will lead to such preferential binding in the vicinity of bound integrins. For the steady state ($\dot{p}_i = 0$) we then obtain from (8.1)

$$p_i = \frac{\binom{L}{i}\left(\frac{k_+}{k_-}\right)^i \prod_{j=0}^{i}\left(1+\frac{k_c j^n}{(j+K)^n}\right)}{\sum_{l=0}^{L}\binom{L}{l}\left(\frac{k_+}{k_-}\right)^l \prod_{j=0}^{l}(1+\frac{k_c j^n}{(j+K)^n})}. \tag{8.5}$$

Given that K and n need to be chosen such that only local integrin-integrin interactions reduce the ligand-integrin off-rate, we, in general, have $i >> K$, and for sufficiently large k_c (and i) (8.5) can be approximated by

$$p_i = \frac{\binom{L}{i}\left(\frac{k_+ k_c}{k_-}\right)^i}{\sum_{l=0}^{L}\binom{L}{l}\left(\frac{k_+ k_c}{k_-}\right)^l}. \tag{8.6}$$

Equations (8.6) and (8.2) are similar and only differ in the factor k_c. The same argument thus applies such that $k_c \gg \frac{k_-}{k_+} \sim 10^2 - 10^3$ is required to enable ligand-dependent integrin activation (Fig 8.1). In the analysis of (8.2), $\frac{k_\pm}{k_-}$ was determined for the high affinity integrin-ligand interaction and a further ligand-induced affinity increase by 100-1000 fold is impossible. Integrin-integrin interactions sufficiently strong to reduce the high affinity dissociation constant by a further factor of $10^2 - 10^3$ are also unlikely. Thus a feedback loop only involving integrins is unlikely to drive ligand-dependent integrin activation.

8.3.2 A positive feedback loop based on a regulatory network can enable ligand-dependent integrin activation

The last mechanism (Fig. 7.2D) to be analysed is one that considers a regulatory network that mediates the positive feedback. This mechanism involves a stabilizing factor whose

activity is increased in response to ligand binding. Such positive feedback has indeed been reported in the form that ligand-bound integrins as well as talins trigger an increase in PIP2, which in turn increases the recruitment of talin to the membrane, and thereby talin-integrin complex formation (l_+) (Garcia-Alvarez *et al.*, 2003; Martel *et al.*, 2001). The talin density on the membrane will thus be very small when integrins are inactive and increase when ligands increase the integrin activity. This positive feedback can be incorporated into the model as

$$l_+ = l_c \frac{(t+1)^n}{(t+1)^n + K^n}, \tag{8.7}$$

such that the talin on-rate, l_+, depends on the number of talins in the integrin-ligand complex with K being the Hill constant, n the Hill coefficient and l_c some proportionality factor. While many other formulations of such feedback are possible, this saturation form captures the likely talin dependence of the membrane PIP2 concentration, which will be low below a certain talin threshold and eventually become saturated.

The steady state for $p_{i,t}$ is now more difficult to derive but the numerical solution shows that such positive feedback indeed enables ligand-induced integrin activation as long as $K/L \ll 1$ (Fig. 8.3). Note that, as in the case of integrin-integrin interactions, ligand-dependent integrin activation requires the proportionality factor l_c to be of order $10^2 - 10^3$. In case of talin recruitment this is reasonable since local PIP2 production may lead to a 100-1000 fold increase in the local membrane talin density. A ligand-independent increase in l_+, due to a signaling dependent increase in a factor that stabilizes the open integrin conformation, will also lead to integrin activation. This is likely to provide the mechanistic basis for inside-out signaling.

We thus conclude that ligand-dependent integrin activation requires $k_- \gg k_+$, $l_- \gg l_+$ in the resting, and $k_- \ll k_+$, $l_- \ll l_+$ in the active state. The first condition is met by the binding of the stabilizing factor which reduces k_-, and the second condition is enabled by a positive feedback that leads to an increase in l_+ in the presence of ligand.

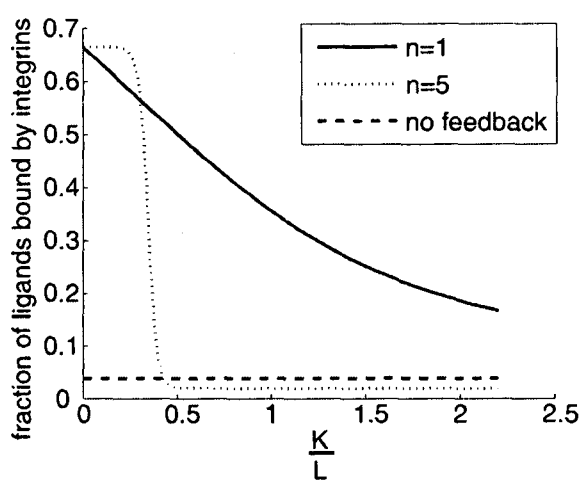


Figure 8.3: **A positive feedback enables ligand-dependent integrin activation.** The fraction of ligand bound by integrin, $\frac{<I_b>}{L}$, is plotted in the absence (- -) or presence of a talin feedback regulation against the Hill constant K (Eq. 8.7) normalized by the number of binding sites L for different Hill coefficients. Parameters were set to $L = 10$, $k_+ = 0.1$, $l_c = 10^2$, $k_- = 5$, $k_-^* = 10^{-3}$, $l_- = 1$. It can be seen that as long as positive feedback is initiated upon binding of few integrins (small $\frac{K}{L}$), a large active integrin fraction is obtained.

Chapter 9

Discussion

The analysis of possible mechanisms for integrin activation suggests that a positive feedback is required for ligand-dependent integrin activation. Thus the ligand-integrin affinity appears to be too low to stabilize the active integrin conformation in the absence of a further stabilizing factor such as talin. To ensure that ligand-independent integrin activation by such a stabilizing factor alone is impossible a positive feedback that upregulates the stabilizing factor upon ligand binding is required.

This conclusion strongly depends on the order of magnitude of the conversion factor η between the 2- and 3-dimensional dissociation constants and further careful measurements of this parameter will be important. While ligand-dependent integrin activation would be possible in the absence of further stabilizing interactions if the theoretical rather than the experimental estimates for η were correct (that is if η were 1000 times smaller), available experimental information is very much in favour of the experimental estimate that has been used in this study. In addition to the argument already given (see above) further experimental observations corroborate the notion that the physiological integrin-ligand affinity is tuned such that integrin activation depends on supporting factors. Thus mutations in the β-tail that disrupt the talin-integrin interaction markedly reduce the fraction of active integrins (Tadokoro *et al.*, 2003). This reduction can be overcome by binding of an antibody that stabilizes the high affinity conformation (Tadokoro *et al.*, 2003) which is in agreement with the model prediction that a higher ligand-integrin affinity can enable talin-independent

integrin activation. With integrin activation balanced on a knife-edge small changes in the affinity, density and conformational bias of integrins can have a large impact on the cell's adhesiveness and motility - as is observed in experiments (Palecek *et al.*, 1997).

An advantage of a positive feedback regulation is the regulatory potential. Signaling processes can affect the positive feedback, providing a basis for inside-out signaling. It is likely that the observed integrin clustering is a result of such a positive feedback mechanism; a local increase in the density of a stabilizing factor will facilitate the formation of further integrin-ligand bonds in the vicinity of existing ones. Clustering would then result from a process that enables long-lived integrin-ligand interactions but is not of itself essential. The concept that ligand binding and clustering are independent processes is in agreement with the observation in *Drosophila* that integrins can still bind to the extracellular matrix in the absence of talin but fail to cluster (Brown *et al.*, 2002).

The feedback loop that is considered in the current model only comprises a stabilizing factor (such as talin) and a way of increasing the concentration of the stabilizing factor, such as by PIP2 formation. Many more players are known to be involved and understanding their relative contributions will be important. Here, the role of PIPKIγ will be of special interest. While PIPKIγ produces PIP2 and thus increases talin recruitment to the membrane, PIPKIγ itself is recruited to the membrane by talin (Di Paolo *et al.*, 2002) and competes with the integrin β tail for talin binding (de Pereda *et al.*, 2005). Integrin activation leads to FAK activation and a FAK-enhanced Src-mediated phosphorylation of PIPKIγ further increases its affinity for talin (Ling *et al.*, 2002; Arias-Salgado *et al.*, 2003). PIPKIγ therefore appears to play an important role both in integrin activation and the turnover of focal contacts. A combination of modelling and experiment, of the sort described here, is expected to shed more light on this complex regulatory network.

Part III: Immunology - Antibody affinity maturation

Chapter 10

Introduction

Proteins evolve by the iterative alternation of mutation and selection over evolutionary time. Yet in a matter of days, the vertebrate immune system generates novel antibodies with high affinity for cognate antigen. This is accomplished by somatic mutation of a diverse pool of antibody genes and clonal selection of high-affinity antibody producing B cells - a process of somatic rather than the familiar germ-line evolution.

Targeting of mutations increases the fraction of effective mutations, that is of mutations that alter the binding characteristics to the antigen at hand (Jolly *et al.*, 1996). However, in the immune system, much as in evolutionary biology, the great majority of all effective mutations are unfavorable. Such mutations may not only lead to loss of antigen specificity, but worse still may engender significant affinity to an autoantigen. On-going selection is therefore essential both to eliminate self-reactivity and to select pathogen-specific antibodies that have acquired affinity enhancing mutations (MacLennan *et al.*, 2000). While in the case of adaptive genome evolution selective forces derive from challenges from the external environment across generations, this cannot apply to a somatic evolution process. Rather, selective forces must originate from within the organism. The immune system thus did not only have to evolve an elaborate mutation mechanism to generate variation in antibody genes but also an anatomic framework and a signaling infrastructure to enable selection of high affinity variants.

10.1 The basic principles of selection in the immune system

The selective forces applied to the B cell are similar to those experienced at the whole organism level. For natural selection to drive genome evolution, entities must be able to produce similar offspring with variations in individual characteristics that affect the fitness of the offspring - that is its reproductive success. Likewise in the immune system, selection cannot act directly on antibodies (which cannot reproduce) but must act on B cells, which express the rearranged and possibly mutated antibody gene as B cell receptor (BCR). B cells increase their proliferative rate upon stimulation by antigen via their BCRs but low affinity as well as self-reactive B cells are ultimately doomed to death by apoptosis. While apoptosis of autoreactive clones is crucial to guard against autoimmunity, apoptosis of low affinity B cells increases the stringency of selection (Takahashi *et al.*, 1999; Takahashi *et al.*, 2001). The reproductive success of B cell clones is thus represented by their ability both to proliferate and to avoid apoptotic death.

In order to survive and proliferate, B cells need to pass a two-step selection process during which they first acquire antigen and subsequently present fragments of this antigen to T helper cells (MacLennan, 1994). The first step is dependent on BCR recognition of antigen, and thus serves to demonstrate binding capabilities of the BCR. The second step of recruiting T cell help requires B cells to internalize BCR-bound antigen and target the antigen to specialized compartments (the MIIC) where the antigen is proteolytically processed into shortened peptides (Clark *et al.*, 2004). These peptides are subsequently loaded onto MHC class II molecules and transported to the B cell surface. Antigen specific T helper cells can recognize the peptide-MHC molecules (pMHC) and rescue the pMHC-presenting B cells from apoptosis. While antigen presentation by "professional" cells (which also provide co-stimulation) is likely to reduce the risk for B cells to acquire self-reactivity, it seems to be the requirement for B cell-T cell interaction which mainly helps guard against auto-immunity. This is because self-reactive T cells are eliminated during their development in the thymus (Palmer, 2003) and should thus not be available in the periphery.

10.2 A place to meet

Antibody affinity maturation requires multiple interactions between antigen, B cells and T cells. Usually antigen and antigen-specific B and T lymphocytes are scarce at the onset of an infection and thus it is insufficient to rely on chance encounters. The immune system solves this problem of first contact by concentrating antigen in local lymph nodes through which lymphocytes pass. After a proliferative burst in primary foci, a small number of B cells and T cells enter primary follicles and seed germinal centres (GCs) (MacLennan *et al.*, 1997). These GCs are microenvironments for antibody affinity maturation and greatly facilitate B cell selection and survival by increasing the number of B cell-antigen and B cell-T cell encounters. It should be noted that affinity maturation can, however, also be observed in the absence of GC reactions, though not with the same efficiency (Matsumoto *et al.*, 1996).

The GC reaction is complex, as shown by Figure 10.1, and a full review can be found in MacLennan, 1994. Briefly, GCs are initially seeded by a small number of blasting B cells, that bind the antigen with at least low affinity (Kroese *et al.*, 1987; Jacob *et al.*, 1991; Liu *et al.*, 1991*a*). Once the primary follicles are filled with proliferating B cells, the B cell blasts differentiate into so-called centroblasts (CB) (Liu *et al.*, 1991*a*). CB are thought to express activation-induced cytidine deaminase (AID) and thus to hypermutate their antibody genes before they differentiate into centrocytes (CC). CC increase the expression of surface immunoglobulin and are selected upon their BCR's affinity for antigen. Importantly, B cell selection relies on the rescue of high affinity clones rather than on the active elimination of low affinity clones. Thus CC are prone to apoptosis (Liu & Arpin, 1997) and will die rapidly unless they are rescued by follicular dendritic cells (FDCs), which provide temporary survival signals to antigen-specific CC (Tew *et al.*, 1997; Kosco-Vilbois, 2003); GCs formed in the absence of FDCs fail to support affinity maturation and rapidly regress (Koni & Flavell, 1999). While FDCs retain antigen in the form of immune complexes (composed of antigen, antibodies and complement) (MacLennan, 1994) it is currently controversial whether antigen trapped on FDCs as opposed to soluble antigen is critical in the selection process

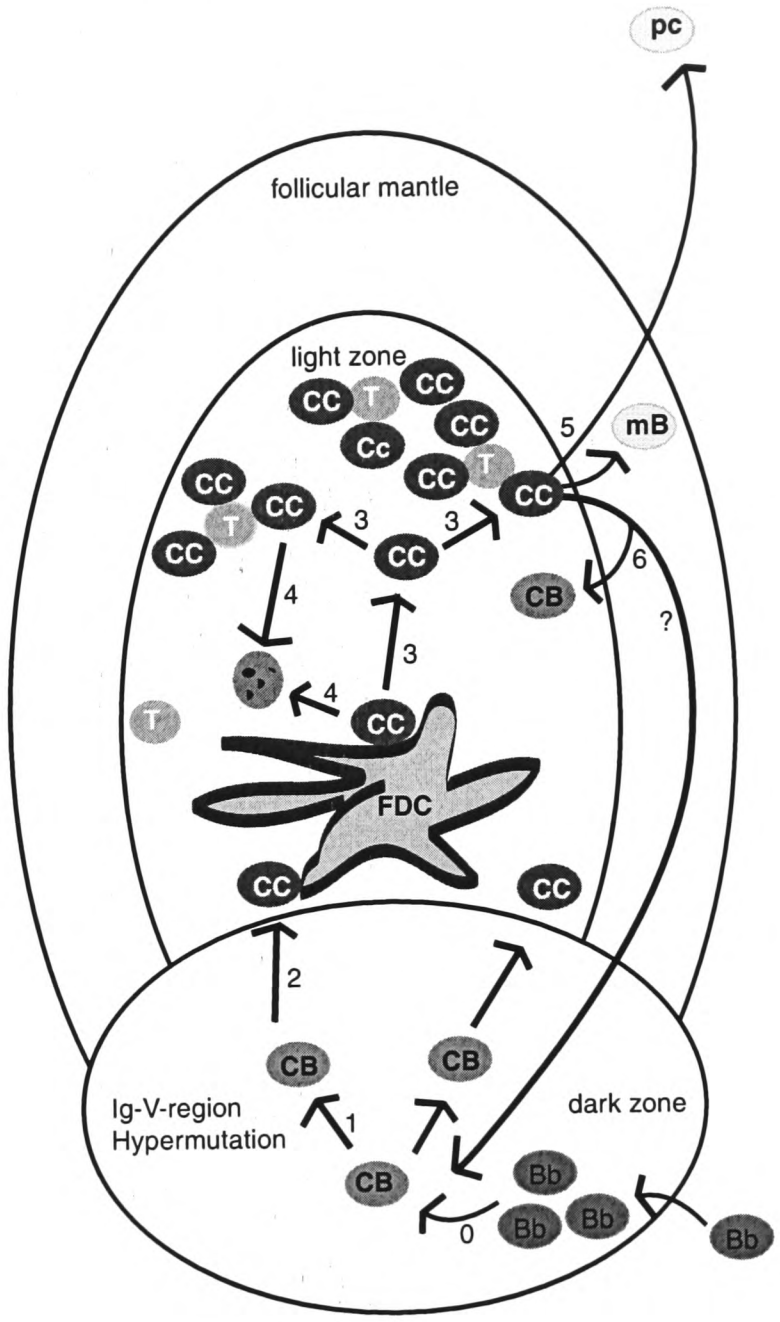


Figure 10.1: **A simple model of the germinal centre reaction.** A small number of B blasts (Bb) initially seeds the GC reaction and exponentially expands before differentiating (0) into centroblasts (CB). Due to the rapid proliferation, this area is densely packed with centroblasts and appears dark in the light microscope, thus leading to its name dark zone. The rapidly proliferating centroblasts (CB) are characterized by a low expression of surface immunoglobulin and the expression of AID which allows them to hypermutate their antibody genes (1). Centroblasts differentiate (2) into centrocytes (CC) which constitute the light zone. Centrocytes upregulate the expression of surface immunoglobulin and are selected according to their affinity for antigen. Selection involves antigen acquisition from follicular dendritic cells (FDC) and subsequent presentation of antigen fragments in the form of peptide-MHCs to T cells (T) (3). Failure to either acquire antigen or to find T cell help results in B cell apoptosis (4). Selected B cells on the other hand either leave the GC reaction to become memory B cells (mB) or plasma cells (pc) (5), or back-differentiate into centroblasts thus enabling several rounds of mutation and selection (6). The recycled centroblasts most likely stay in the light zone but migration back to the former dark zone has not been ruled out experimentally, and this route is therefore marked by a question mark.

(Haberman & Shlomchik, 2003; Kosco-Vilbois, 2003). In a final selection step B cells need to present the acquired antigen to antigen-specific T cells (Liu *et al.*, 1991*a*; Arpin *et al.*, 1995) which most probably have entered the GCs together with the antigen specific B cells (MacLennan *et al.*, 2000). Non-selected CC undergo apoptosis and are quickly engulfed by macrophages; selected CC may leave the GC reaction to become memory or plasma cells (Liu *et al.*, 1997). Back-differentiation of selected CC into CB enables a B cell clone to go through multiple rounds of mutation and selection (MacLennan *et al.*, 2000; Kepler & Perelson, 1993).

10.3 The mechanism of B cell selection

For affinity to increase during the course of the GC reaction the affinity threshold for selection needs to increase, i.e. a higher affinity must be required for survival as selection proceeds over time. The extent of increase required for survival appears to be determined by clonal competition within the B cell population. Accordingly, low affinity B cell clones can persist when competition with high affinity B cell clones is reduced (Dal Porto *et al.*, 2002; Shih *et al.*, 2002).

Principally, B cell clones might compete for antigen or for T cell help - or both. Older models have particularly stressed the role of B cell competition for scarce antigen (Siskind & Benacerraf, 1969) and suggest that antigen removal during the immune response as well as emerging serum antibodies would lead to a gradual increase of the affinity threshold (Tarlinton & Smith, 2000; Iber & Maini, 2002). However, affinity maturation is hardly compromised by alterations in the initial amount of antigen deposited on FDCs (Haberman & Shlomchik, 2003; Manser, 2004) or by lack of secreted antibodies (Hannum *et al.*, 2000). Competition for antigen thus appears inadequate to explain B cell selection for all the conditions under which it occurs.

The alternative model of a clonal competition for binding sites instead of antigen (Kesmir & De Boer, 2003) requires affinity maturation to strictly depend on antigen being encoun-

tered membrane-bound, which is the subject of controversy (Haberman & Shlomchik, 2003). Also, antigen localization would have to be restricted to a small number of places within the large dendritic network. Despite many electron microscopy studies, such localization restriction has not yet been reported.

Without competition for access to antigen or FDCs, higher affinity B cell clones could be favoured on the level of antigen binding, either because of differential signaling of B cells in response to different affinities of binding (Kouskoff *et al.*, 1998) or because high affinity B cells require fewer encounters with the FDC to establish an immunological synapse and to extract antigen (Batista *et al.*, 2001). Here, immunological synapse refers to the supramolecular segregation of proteins in lymphoid cell-cell contact zones (Kupfer & Kupfer, 2003), which enable long-term signaling and effector functions (Huppa *et al.*, 2003).

Finally, T cell help may be competitive. *In vitro* assays show that higher affinity B cells are more able to recruit T cell help (Batista & Neuberger, 1998), which may be crucial in the GC environment, where T cells constitute only $5 - 10\%$ of the GC cell population (Kelsoe, 1996*a*). Given that T cell responsiveness to antigen-challenged B cells correlates with binding affinity (Batista & Neuberger, 1998), it is conceivable that the BCR binding affinity is translated into a cellular signal that affects the ability of B cells to recruit T cell help. One way B cell signaling strength may affect T cell responsiveness is an enhanced presentation of pMHC (Harding & Unanue, 1990; Grakoui *et al.*, 1999), which may be enabled by an improved targeting of antigen to the processing compartments. Targeting to and accession of the processing compartments requires signaling through Igα, Syk (as well as downstream effectors) (Clark *et al.*, 2003). The degree of Igα and Syk phosphorylation is affinity-dependent (Kouskoff *et al.*, 1998) thus suggesting a link between BCR affinity and the level of pMHC presentation on the B cell surface.

10.4 The mechanism of affinity discrimination

The mechanism by which B cells discriminate between a wide range of binding affinities ($K_a \sim 10^4 - 10^{10}$ M^{-1}) (Batista & Neuberger, 2000) is elusive as is the mechanism by which the mechanical binding of antigen is translated into a cellular signal (Reth *et al.*, 2000). Receptor clustering has long been recognised to be essential for B cell activation (Seed, 1995) and it has been proposed that clustering of receptors results in cross-activation of the kinases that are bound by each receptor. Clustering is necessary because the autoactivating Src-family kinases and Syk, which are bound to the resting BCR (Yamanashi *et al.*, 1991; Clark *et al.*, 1992; Hutchcroft *et al.*, 1992), phosphorylate substrate in trans but not in cis on the same receptor (Sotirellis *et al.*, 1995). Receptor clustering alone is however unlikely to result in B cell activation since the resting BCR is not only bound by Src-family kinases and Syk but also by SHP-1, a key phosphatase (Pani *et al.*, 1995). Given that phosphatases exhibit in general a 10-100 times higher activity than the kinases (Reth & Wienands, 2004), even at closest proximity the kinase efficiency will remain minute compared to the phosphatase efficiency. Reth and co-workers have taken the effect of inhibitors into account and propose that the BCR exists on the B cell surface as an oligomeric complex and that antigen binding distorts the complex, resulting in the exposure of residues that lead to a relocation of the receptor to a different membrane environment where the NADPH oxidase resides (Reth *et al.*, 2000; Reth, 2002). NADPH oxidases produce H_2O_2, which inhibits phosphatases (Lee *et al.*, 1998). This inhibition would then lead to B cell activation. Both the distortion of the BCR complex as well as its antigen-induced colocalisation with NADPH oxidase remain to be shown.

10.5 Scope of the study

The failure of experiments to define the B cell selection mechanism and to explain how B cells are activated by antigen binding in an affinity-dependent manner can largely be attributed to major experimental difficulties that are associated with the investigation of such complex

systems. In order to delineate the mechanism of B cell selection I collaborated with Michael Meyer-Hermann (FIAS, University of Frankfurt, Germany) to extend a previously described agent-based model for GC reactions (Meyer-Hermann, 2002*a*) and to investigate the effects of each of the discussed potential selection mechanisms separately. Experimental data were available to define most parameter values; those for which data were not available were studied in detail to exclude the possibility that qualitatively different results could emerge from a different (but still physiological) set of parameters.

The simulations reveal that both a competition for access to FDCs as well as a competition for antigen (even in the presence of antibodies) does not enable affinity maturation to the experimentally observed degree. On the other hand, both slow CC-FDC interactions and competition for T cell help can drive affinity maturation - especially when the acquisition of antigen and survival signals from the FDCs are uncompetitive. Both selection mechanisms enable affinity maturation over a wide range of antigen densities and possibly even if antigen is encountered in soluble form. One or both of these are likely to be the physiological mechanism of B cell selection. Experiments are suggested to test this unexpected result.

Both mechanisms require B cells to discriminate between the affinities of binding in the first step. Different lines of evidence suggest that receptor clustering plays a role in B cell activation, but the organisation of B cell receptors on the cell membrane has not yet been resolved. Integrating available experimental information by use of techniques from statistical physics suggests that for physiological parameters BCRs mainly polymerize into small open chains. The polymerization would depend on the receptor density, and accordingly, the cluster size would be strongly reduced at the receptor densities that are generally observed for anergic MD4 B cells (Goodnow *et al.*, 1988; Goodnow *et al.*, 1991). The failure to form BCR clusters may explain the unresponsiveness of anergic B cells to immunogenic reagents unless these are highly cross-linking.

Based on the BCR organization that is predicted by the model I show in a further

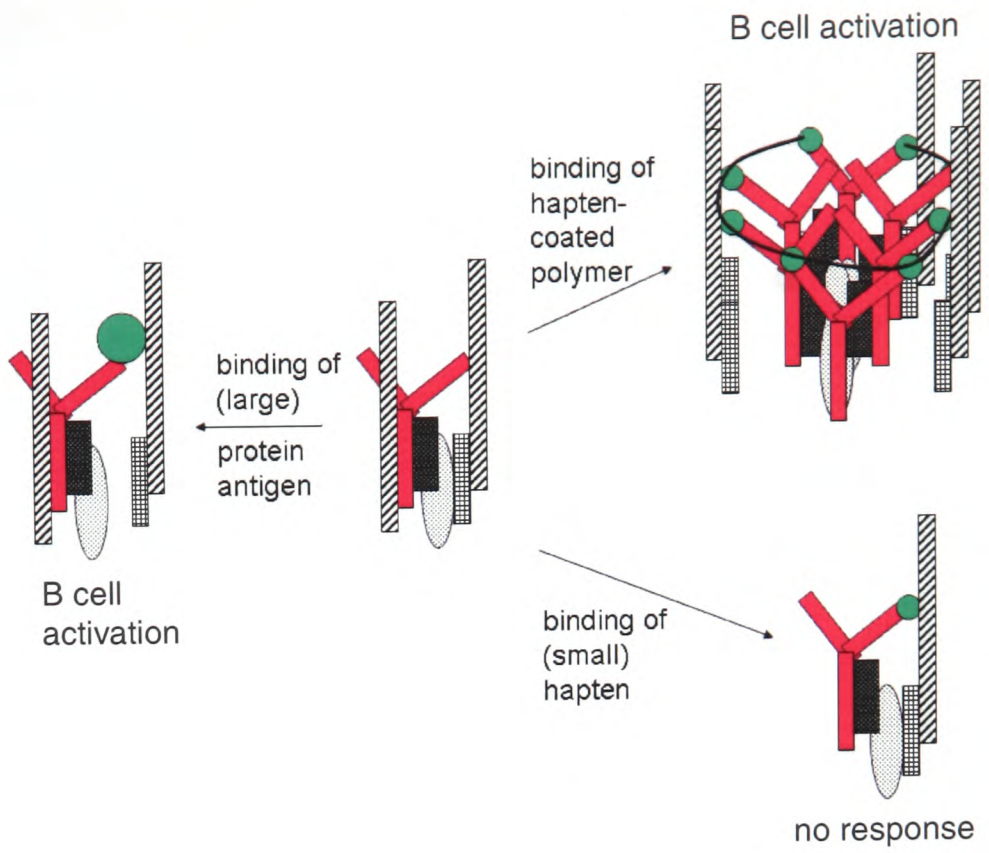


Figure 10.2: **A model for B cell activation.** In the absence of antigen, inhibitors inactivate BCR-bound kinases (middle). While binding of (large) protein antigens can separate inhibitors and kinases to a sufficient extent to trigger B cell signaling (LHS) binding of haptens is insufficient to block access for inhibitors to the BCRs (bottom). Binding of hapten-coated polymers (top) stabilizes the pre-formed BCR clusters from whose interior inhibitors are excluded, thus enabling B cell activation. Inhibitors are depicted as striped rectangle, Ig-α/Ig-β as black rectangle, kinases as ovals and the phosphatase as checkered rectangle.

step that differential B cell signaling can be explained with an antigen-induced separation of receptors and inhibitors (Fig. 10.2, left). This mechanism is reminiscent of the one suggested for T cells (Davis & van der Merwe, 2006) with the important difference that in the T cell contact zone segregation can be achieved by size while a different mechanism is required for B cells because the BCR-antigen complex is of similar length as the inhibitory co-receptors. The model, which makes use of concepts from statistical mechanics, is shown to reproduce available data quantitatively and to provide explanations for a number of previously counterintuitive experimental observations. Moreover, the unresponsiveness of B cells to haptens can be understood in light of the segregation concept by noting that a sufficient antigen size is necessary to separate BCRs and inhibitors (Fig. 10.2, bottom);

attachment of the hapten to a larger carrier protein can circumvent the problem and lead to B cell activation (Fig. 10.2, top).

In a final part the model is used to solve the long-standing question about the nature of the 'immunon' (Dintzis *et al.*, 1976; Vogelstein *et al.*, 1982).

Chapter 11

A model for B cell selection during the GC reaction

11.1 *In silico* germinal centre simulations

In collaboration with Michael Meyer-Hermann I employed *in silico* simulations of the GC reaction to analyse the B cell selection mechanisms. The simulations were performed using a previously described stochastic hybrid agent-based model (Meyer-Hermann, 2002*a*; Meyer-Hermann & Maini, 2005) which we extended to test the different selection mechanisms. The basic idea was to rebuild a GC *in silico* and to study how its spatial organization, dynamics and output depend on the assumptions that are made on the comprised cells and their interactions. The GC is represented by a regular lattice whose nodes represent cells. With the exception of pre-plasma and memory cells the GC cells are confined to the area of the GC as defined by the mantle zone. The cell-lattice is supplemented by a second grid for soluble signals. These satisfy reaction-diffusion equations which are solved numerically. Given that the analysis of three-dimensional models leads to similar results (Meyer-Hermann & Beyer, 2002) we restrict our analysis to two dimensions in order to gain better statistics because of substantially shorter computation times. We include CB, CC, FDCs and output cells such as plasma and memory cells in all our simulations and study the effect of T helper cells on CC selection in an additional set of simulations. The different cell types are encoded in the simulation by defining differently sized objects that are associated with distinct sets of rules which reflect their biological properties. The rules

determine the cellular dynamics by defining motility, cell-cell interactions, cell-cycle times, cellular lifetimes and similar properties. A comprehensive list of these properties is given below. Despite the complexity of the GC reaction only a limited set of parameters is required to respect commonly accepted GC properties and to capture available quantitative experimental data. Reasonable estimates can be obtained for most of the parameters (Table 11.1), and the few exceptions are studied in detail. While most of the experimental data stems from lymph nodes of mice or rats the model applies to all GCs that exhibit similar GC morphology and cell dynamics.

11.2 Antibody representation

In order to analyse B cell affinity maturation we need to define the affinity and thus quality of antibodies. Antibodies are represented in a four-dimensional shape space (Perelson & Oster, 1979). The antigen defines the position of the optimal antibody (maximum affinity) in the shape space. The distance d_{ab} of an arbitrary antibody to this optimal clone is calculated as a 1-norm in the shape space and is assumed to be a measure for its affinity to the antigen K_{ab}. The latter is calculated as a Gaussian function with the distance as argument and a width of $\Gamma = 2.8$ mutations such that

$$K_{ab} = \exp -\frac{d_{ab}^2}{\Gamma^2}. \tag{11.1}$$

The power and the width of the affinity function have been estimated based on experimental data which relate the number of mutations in GC reactions to the increase in affinity (Meyer-Hermann *et al.*, 2001).

11.3 Cell movement

In agreement with recent two-photon imaging data collected *in vivo* from mice lymph nodes (Miller *et al.*, 2002) cells are assumed to perform an undirected and active movement. Unless stated otherwise, every cell is attributed to a single node. All cell states include a mean speed v_{cell}, a polarity $\vec{p}_{cell}$ and a persistence time Δt_{cell}, where *cell* denotes the different

cell types. The probability of displacement of a cell to a next (unoccupied) neighbour node is determined by v_{cell}. The direction of movement is set by $\vec{p}_{cell}$, and the polarity changes with a rate according to Δt_{cell}. The new polarity is chosen randomly, i.e. without any memory effect. The values of these motility parameters are taken from experiment (Miller *et al.*, 2002) and are given in Table 11.1. Note that while these are the best data available they were not obtained for GC reactions and the values may therefore not be accurate for GC cells. The actual movement of the cells may be less than expected from v_{cell} when contact inhibition by other cells suppresses the movement.

11.4 Cell types

The following list provides a comprehensive description of all cells and their specificities. All parameters without explicitly given value are of importance for the selection process and are discussed in Chapter 12.

11.4.1 FDC

The soma of each FDC is represented as a single lattice node. Each FDC is assumed to have four (two per space dimension) dendrites. Every dendrite is attached to the soma and extends to neighbouring nodes. Given that dendrites are flexible the lattice nodes to which dendrites are attributed are not exclusive, i.e. other cells can move onto these nodes. This is not possible for other cell types or the FDC soma. FDCs are assumed to produce a differentiation signal for CBs with a rate r_{signal} (see below). In order to reduce computational effort FDCs are assumed to be immobile. This is a reasonable approximation because the interaction frequency with centrocytes is dominantly determined by the typical distance between FDC binding sites and CCs. This corresponds to the density of the FDC network which is determined by the number of FDCs, N_{FDC}, and the length of the dendrites, d_{FDC}. A suitable quantity to measure the density of the FDC network is the number of nodes, X_{FDC}, from which access to FDC sites is possible in the GC area, where

$$X_{FDC} = \frac{6DN_{FDC}d_{FDC}}{\Delta x}, \tag{11.2}$$

and D is the dimension, $\Delta x = 10\mu$m the resolution of the lattice (chosen as the average B cell diameter). The physiological range is $48 \leq X_{FDC} \leq 144$; this corresponds to 100 FDCs per GC (Kesmir & De Boer, 1999) ($N_{FDC} = 4$ in the two-dimensional simulation) with a total length of dendrites of each FDC $2Dd_{FDC} = 40 - 120\mu$m. The number of FDCs in two dimensions is calculated by comparing the FDC density of a spherical GC in three dimensions to the FDC density in a GC slice of thickness $\Delta x = 10\mu$m.

11.4.2 Centroblasts

CBs are a subpopulation of B cells in the GC. CBs divide with a cycle time of 6 hours (Liu *et al.*, 1991*b*) and, owing to somatic hypermutation, acquire in each cell division non-silent mutations with probability 0.5 (Nossal, 1992). Mutations are modelled by a jump to a next neighbour in the shape space (in an arbitrary direction); wider jumps are excluded. The transcription factors for susceptibility to apoptosis are already up-regulated in CBs (Klein *et al.*, 2003) but we assume CBs not to be affected by these. Equally, CBs are assumed not to interact with FDCs or T cells, thus neglecting possible rescue mechanisms acting directly on CBs. CBs differentiate to CCs at rate r_{diff} once the local concentration of differentiation signal (which is produced by FDCs and diffuses over the lattice) exceeds a threshold value. Given that neither the exact signal nor its threshold concentration are known the signal production rate by FDC is given in units of this threshold. Because of their larger size we expect CBs to move at a lower mean speed than naive B cells and we estimate the speed by use of Stokes' friction law (which predicts that the speed scales with the inverse ratio of the radii of CBs and naive B cells) to be $v_{CB} = 1.5\mu$m/min and Δt_{CB}=2min.

11.4.3 Centrocytes

CCs differentiate from CBs and neither divide nor mutate. CCs are in an activated state of apoptosis and they have a lifetime of 10 hours (Liu *et al.*, 1994), within which they need to receive a rescue signal to avoid death. Dead CCs are rapidly removed from the lattice assuming a fast clearance of apoptotic bodies. The exact nature of the rescue signal depends

on the selection mechanism. CCs can be in one of the following states: unselected, in contact with FDC, selected by FDC, in contact with T cell, selected. Thus the subpopulation of CCs is rather heterogeneous (Klein *et al.*, 2003).

Unselected CCs need to find one of the X_{FDC} sites. Once they have access to an FDC site, they try to bind the antigen. The binding probability is proportional to the antibody-antigen affinity. In the standard configuration unsuccessful CCs have to wait for 6 minutes before they can try binding again. This short refractory time ensures independence of the binding process from the time resolution in the simulations. Experimental data is not available to define this refractory time and this parameter is therefore explored in detail in section 12.2. Successful CCs switch to the state in contact with FDC and are rescued from apoptosis. The CC remains bound to the FDC for two hours (Lindhout *et al.*, 1995). During this time the rescue signals are thought to be provided by the FDC and the CCs turn into the state selected by FDC. Note that the FDCs are assumed to only provide rescue signals; negative selection of unsuccessful CCs via FasL-Fas (Verbeke *et al.*, 1999) or other pathways is neglected.

How CCs are selected depends on the details of the selection mechanism and is discussed in detail in Chapter 12.

Selected CCs further differentiate within 7 hours to pre-plasma cells or memory cells (both summarised as output cells in the following), or, alternatively, they recycle back to CBs. No data yet exists to relate the relative receptor quality of the CC to its probability of entering either differentiation path. In fact, available experimental data (Han *et al.*, 1995) can be reproduced by assuming that this probability does not depend on receptor quality (Meyer-Hermann *et al.*, 2001) and as in Meyer-Hermann et al (2001) we therefore assume that selected CCs recycle with probability 0.8 and differentiate to output cells with probability 0.2.

CC motility characteristics are assumed to be identical to those of naive B cells (Miller *et al.*, 2002) and to be the same in all states, i.e. $v_{CC} = 5\mu$m/min and Δt_{CC}=2min.

11.4.4 T cells

T cells are only included in one set of simulations in which they are part of the selection process of CC. As the relative amount of specific and unspecific T cells is not known, only T cells that are specific for the antigen are included, such that all N_{TC} T cells will be able to interact with CCs selected by FDC. Consequently, the number of included T cells may underestimate the total number of T cells present in the GC. The error introduced by this simplification is restricted to spatial effects of T cells, which can be assumed to be small in view of the comparably small total number of T cells in GCs. When T cells interact with CC that have encountered antigen on FDC they develop a polarity towards the CC. If more than one CC selected by FDC simultaneously interact with a T cell, the T cell is assumed to polarize towards the CC with highest affinity to the antigen. Without CC the polarity of the T cell is random. The T cell motility characteristics are $v_{TC} = 10.8\mu$m/min and Δt_{TC}=2min (Miller *et al.*, 2002).

11.4.5 Output cells

Pre-plasma cells and memory B cells are collected in a cell pool denoted by output cells. These cells are assumed to have the same motility characteristics as CCs. In contrast to CCs, output cells can leave the GC environment when reaching the border of the GC. These cells may be thought of as crossing the mantle zone and entering the marginal zone. The total number of output cells produced will be taken as a measure of GC success independent of their presence in the GC at the end of the reaction.

11.5 Diffusion of molecular signals and soluble antibodies

The model includes diffusing CB differentiation signals as well as soluble antibodies. The discretised diffusion equation is solved on the square lattice with Dirichlet boundary conditions and with constant diffusion coefficient using the Crank-Nicholson Θ-method. Dirichlet boundary conditions are imposed because due to diffusion out of the GC the effective concentration will be zero on the boundary. Note that the diffusion coefficients $D_{diff} = 200\mu\text{m}^2/\text{hr}$

and $D_{ab} = 2000\mu\text{m}^2/\text{hr}$ are chosen to be very small in order to respect the high cell density in GC that act as obstacles for free diffusion of molecules. However, the results are robust against different choices. In one selection mechanism antigen masking by antibodies is considered. Antibodies (b) are produced by output cells at some rate r_{ab}, diffuse on the lattice, and locally bind to antigen (a) on FDCs to form immune complexes (c) according to the rate equation

$$\frac{dc}{dt} = k_+ a(t) b(t) - k_- c(t). \tag{11.3}$$

While the affinity of the secreted antibodies will increase during the course of the immune response, we simplified the simulation by using binding rates characteristic of high affinity antibodies, e.g. $k_+ = 10^6\ \text{M}^{-1}\text{s}^{-1}$ and $k_- = 10^{-3}\text{s}^{-1}$ (Batista & Neuberger, 1998; Fersht, 1998). This simplification is appropriate as we show that even under such conditions antibody production at a physiological rate does not sufficiently increase affinity maturation. The total amount of antigen and antibody is conserved in the antibody-antigen binding reaction, but the concentration of antigen will nonetheless decrease because it is consumed by CCs that bind to FDC, and antibodies are produced by output cells. Equation 11.3 is solved using a simple Euler method at every node.

11.6 Initial configuration

The GC reaction is seeded by a small number of B blasts that expand rapidly and fill the GC with about 10^4 B cells before somatic hypermutation starts and enables the evolution of higher affinity antibodies. In general a small number of clones dominate the reaction after this expansion. We start the GC simulation after this expansion phase with 1100 CBs (which correspond to the 10^4 B cells in three dimensions) that stem from three different low affinity clones (binding probability 0.04). The antibodies of these clones all have a distance of 5 mutations to the optimal clone in the shape space; that is, they require a minimum of 5 mutations to gain the optimal affinity. However, most sequences of mutations will not follow such optimal antibody affinity evolution path. In fact we observe about 9 mutations

in most output cells, which is in agreement with experimental data (Kuppers *et al.*, 1993). The CBs are distributed randomly within the GC. We assume a polarised morphology of the GC in the sense that the FDCs are placed at arbitrary nodes on 2/3 of the total GC volume (Camacho *et al.*, 1998). If T cells are included then they are distributed randomly within the GC.

11.7 Simulations and analysis of the results

In order to achieve comparability between the different selection mechanisms, two parameters that affect CB to CC differentiation were varied within physiological limits, while all other parameters were kept constant throughout all simulations (see Table 11.1), such that the experimentally determined GC kinetics and dark zone duration were reproduced. These two GC characteristics were chosen since both are well established by experiments and variations of these strongly affect the output of the reaction (Meyer-Hermann, 2002*a*).

We assume the differentiation of CB to CC to be initiated by an FDC-derived signal. A signal for CB to CC differentiation has not yet been identified experimentally. However, this mechanism - unlike other mechanisms - gives rise to the experimentally observed GC zoning (Meyer-Hermann & Maini, 2005), and a realistic GC morphology is important for a realistic investigation of selection mechanisms. Beyond the effects stemming from the spatial organisation of the GC, this parameter does not affect B cell selection. The differentiation signal production rate per FDC, r_{signal}, widely determines the persistence of the dark zone and is adjusted such that the dark zone vanishes between days 8 and 9 (~200 hours - solid line in panel D in the figures in Chapter 12) after immunization (Kuppers *et al.*, 1993).

The second adjusted parameter, the duration of CB-CC differentiation, Δt_{diff}, governs the total population dynamics and is chosen such that GC kinetic data (Liu *et al.*, 1991*b*; Hollowood & Macartney, 1992) are reproduced with sufficient accuracy (Fig. 11.1A). The deviation η from the experimental data is calculated according to

$$\eta = \frac{\sum_{i=1}^{N}(x_{exp}(t_i) - \frac{n(t_i)}{n_{max}})^2}{(N-1)x_{exp}(t_i)^2}, \tag{11.4}$$

where N is the number of experimental values, t_i denotes the time in the reaction at which the value is taken, $n(t_i)$ is the corresponding volume in the simulation, and n_{max} is the peak population averaged over all 50 simulations. We find acceptable GC kinetics when η is smaller than 0.3 (Fig. 11.1B). Note that Δt_{diff} must be less than 7 hours since CBs are found in the light zone as CCs within 6-7 hours (Liu *et al.*, 1991*b*). A minimal value is not known.

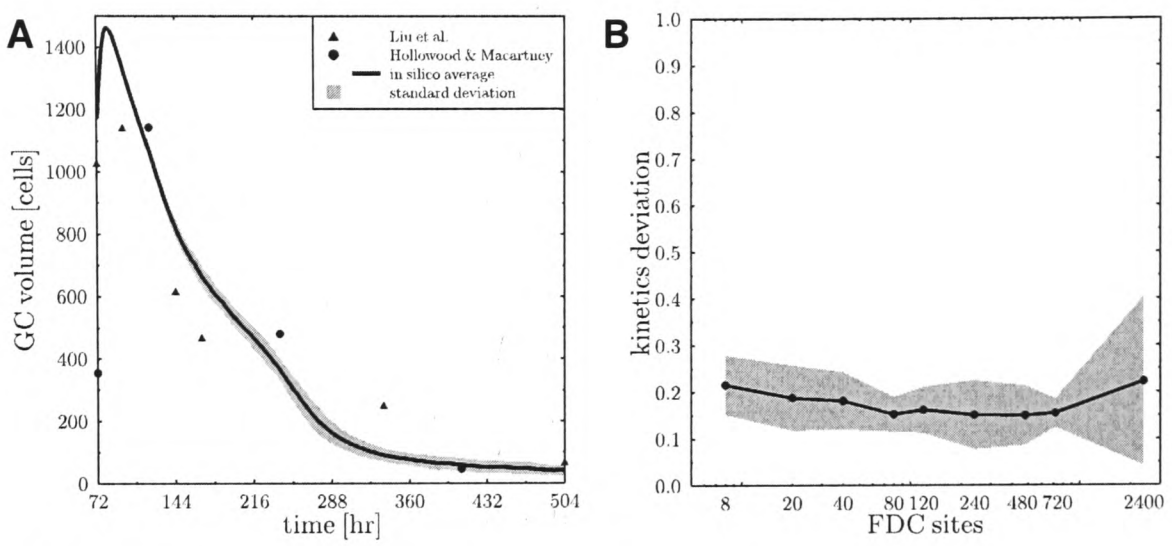


Figure 11.1: **GC kinetics in simulation and experiment.** **(A)** GC kinetics (line) and one standard deviation (shading) taken from 50 simulations with site competition as selection mechanism ($X_{FDC} = 80$, Section 12.1). Dots and triangles represent data read off from published experiments (Liu *et al.*, 1991*b*; Hollowood & Macartney, 1992). **(B)** Deviation η (see Eq. 11.4) of simulations from experimental GC kinetics.

The GC reaction is expected to end after 21 days. Given that the simulation was tuned to reproduce the GC kinetics, the cell number within the GC decreases below 100 cells after 300-400 hours for all analysed selection mechanisms (dotted line in panel D in the figures in Chapter 12). The final cell numbers at day 21 vary for different selection regimes between almost zero and less than 100 (dashed dotted line in panel D in the figures in Chapter 12).

There are further characteristics of GC reactions to which the simulation was not fitted, but which had to be reproduced by the simulation in order to ensure the model's physiological relevance. Thus the ratio of CCs to CBs at day 12 after immunization needs to be larger than 2 in order to agree with the experimental observation that CCs greatly outnumber

CBs during the GC reaction (MacLennan *et al.*, 1990) and the ratio q_6^{12} of produced output cells (i.e. pre-plasma and memory B cells) at day 12 to day 6 after immunization should be the order of 6 (Han *et al.*, 1995) (dotted line in panel B in the figures in Chapter 12). The factor q_6^{12} can be interpreted as a measure for the steepness of the output production.

Unless stated otherwise all simulations remain in agreement with the aforementioned experimental constraints. The selection mechanisms that rescue CCs from apoptosis have to rely on some affinity dependent competition between different CCs to achieve affinity maturation. Therefore, the success of a GC reaction is measured by the affinity of the output cells averaged over all cells produced during the reaction (in panel A in the figures in Chapter 12). This quantity is an indicator of the entire GC reaction and is not restricted to arbitrary time points of the reaction. The total number of output cells produced is monitored since a stable population will need to be formed to enable robust antibody production.

Table 11.1: **Parameter Values.** The parameters are classified in the two categories *fixed* and variable. *Fixed* parameters remain unchanged throughout all simulations presented in this work. *Variable* parameters have been varied according to the selection process under consideration. If a value is stated then this is the value employed in all selection scenarios where this parameter is fixed. Symbols correspond to the ones used in the text.

Parameter and reference	symbol	value	type	references
Lattice constant	Δx	$10\mu m$	fixed	
Lattice dimension	D	2	fixed	
Radius of reaction volume		$220\mu m$	fixed	
Shape space dimension		4	fixed	(Perelson & Oster, 1979; Lapedes & Farber, 2001)
Width of Gaussian affinity weight function		2.8	fixed	(Meyer-Hermann *et al.*, 2001; Meyer-Hermann, 2002*a*)
Duration of optimization phase		$48hr$	fixed	(Jacob *et al.*, 1993; Pascual *et al.*, 1994; Meyer-Hermann, 2002*a*)
Number of seeder clones		3	fixed	(Kroese *et al.*, 1987; Liu *et al.*, 1991*b*; Jacob *et al.*, 1991; Kuppers *et al.*, 1993)
CB velocity	v_{CB}	$1.5\mu m/min$	fixed	(Miller *et al.*, 2002; Wei *et al.*, 2003)
CB persistence time	Δt_{CB}	$2min$	fixed	(Miller *et al.*, 2002; Meyer-Hermann & Maini, 2005)
Cell cycle time of CB		$9hr$	fixed	(Liu *et al.*, 1991*b*)
Mutation probability of CB		0.5	fixed	(Berek & Milstein, 1987; Nossal, 1992)
Duration of CB differentiation to CC	$1/r_{\mathrm{diff}}$		variable	(Liu *et al.*, 1991*b*; Meyer-Hermann, 2002*b*)
CC velocity	v_{CC}	$5\mu m/min$	fixed	(Miller *et al.*, 2002; Wei *et al.*, 2003)
CC persistence time	Δt_{CC}	$2min$	fixed	(Miller *et al.*, 2002; Meyer-Hermann & Maini, 2005)
Duration of FDC-CC contact		$2hr$	fixed	(van Eijk & de Groot, 1999)
CC refractory time	$\Delta t_{\mathrm{delay}}$	$6min$	variable	
Duration of differentiation of selected CC		$7hr$	fixed	(Meyer-Hermann, 2002*a*)
Probability of recycling for selected CC		0.8	fixed	(Han *et al.*, 1995; Meyer-Hermann *et al.*, 2001)
CC lifetime		$10hr$	fixed	(Liu *et al.*, 1994)
Number of T cells	N_{TC}	10	variable	(Kelsoe, 1996*b*)
T cell velocity	v_{TC}	$10.8\mu m/min$	fixed	(Miller *et al.*, 2002; Wei *et al.*, 2003)
T cell persistence time	Δt_{TC}	$2min$	fixed	(Miller *et al.*, 2002; Meyer-Hermann & Maini, 2005)
Duration of CC-T cell interaction before apoptosis	Δt_{apop}	$2.1hr$	variable	
Duration of CC-T cell interaction before selection	$\Delta t_{\mathrm{rescue}}$	$2.0hr$	variable	
Number of FDCs	N_{FDC}	10	variable	
Length of FDC dendrites	d_{FDC}	$10\mu m$	variable	
Rate of differentiation signal production by FDCs	r_{signal}		variable	(Meyer-Hermann, 2002*a*)
Diffusion constant of signal molecules in tissue		$200\mu m^2/hr$	fixed	(Meyer-Hermann, 2002*a*)
Number of antigen portions per FDC site	N_{ag}	0	variable	
Antigen threshold for maximum binding probability	Θ_{ag}	$= N_{\mathrm{ag}}$	variable	
Antibody production by output cells		$0M/(hr\,cell)$	variable	(Randall *et al.*, 1992)
Immune complex association rate	k_+	$10^6/(Ms)$	fixed	(Batista & Neuberger, 1998; Fersht, 1998)
Immune complex dissociation rate	k_-	$10^{-3}/s$	fixed	(Batista & Neuberger, 1998; Fersht, 1998)

Chapter 12

Results from the GC simulation

12.1 Competition for binding sites on FDC allows for moderate affinity maturation

According to the simplest of all suggested models, B cells are selected in a competition for access to antigen and/or survival factors that are provided by the FDC. Accordingly, the number of FDC sites X_{FDC} (see Eq. 11.2) on which antigen is presented would be the limiting factor for which different clones would compete. As described in Chapter 11.2 we assume that CC bind antigen held on FDC with a probability proportional to the affinity of the antibody. CC selected by FDC do not need any further steps to be positively selected and thus are already selected CC. Given that no further limiting resources are considered in this very simple model, CC that have been selected by FDC (e.g. CC selected by FDC in the language of the model, see Chapter 11) do not need any further steps to be positively selected and can follow the differentiation paths of successfully selected CC.

By variation of the site number X_{FDC} the simulation indeed reveals that affinity maturation is enforced when the number of FDC sites is low (Fig. 12.1A). Affinity maturation can be observed for a physiological number of FDC sites ($48 \leq X_{FDC} \leq 144$ - see Eq. 11.2); the extent of the process (less than 50% high affinity output cells) is however rather low compared to other selection mechanisms investigated here and not robust to changes in the number of accessible sites. The GC characteristics are reproduced *in silico* (Fig. 12.1C, D). Importantly the two characteristics to which the simulation is not fitted, the CC to CB ratio

at day 12, as well as the output ratio at day 12 to day 6, are in agreement with experimental data for the entire physiological range (Fig. 12.1B). The duration of CB-CC differentiation Δt_{diff}, which decreases from 7 hours to 1 hour with increasing site numbers (Fig. 12.1C), remains within its expected range for the physiological FDC site numbers. Short CB to CC differentiation times had to be employed in order to reproduce the experimentally observed GC kinetics (Fig. 11.1) because the selection method is not stringent enough to reduce the volume of the GC reaction considerably. We conclude that whilst B cell competition for access to FDC can give rise to the observed GC kinetics and properties, affinity maturation is relatively poor and not robust against small variations in the number of binding sites.

12.2 Limiting the interactions with FDC by introducing a refractory time results in strong affinity maturation.

If CC can reinitiate binding to FDC every 6 minutes (as assumed in our analysis of site competition) then the total number of encounters is considerable during a CC lifetime of 10 hours. Any mechanism that limits the total number of encounters will lower the probability of a successful interaction within a CC's lifetime and will favour higher affinity clones because they have a higher chance of binding successfully in an early attempt. We therefore speculate that an increase in the refractory time (Δt_{delay} - the time during which B cells that failed to bind during a previous contact with a FDC are unable to bind again) will increase the selection pressure.

By increasing the refractory time from 6 minutes to 4 hours we find that a refractory time as low as 0.5 hours is sufficient to induce affinity maturation of extent similar to that with site competition but for a wide range of FDC site numbers. Thus at $X_{FDC} = 120$, when competition for antigen presenting FDC sites is weak, affinity maturation reaches a level previously only seen at low ($X_{FDC} = 40$) site numbers (compare full lines in Figs. 12.1A and 12.2A). A refractory time of 4 hours leads to rather efficient affinity maturation (60-70% of all output cells are of high affinity) while allowing an even better reproduction of the other GC characteristics (kinetics, dark zone duration, ratio of CC to CB at day 12

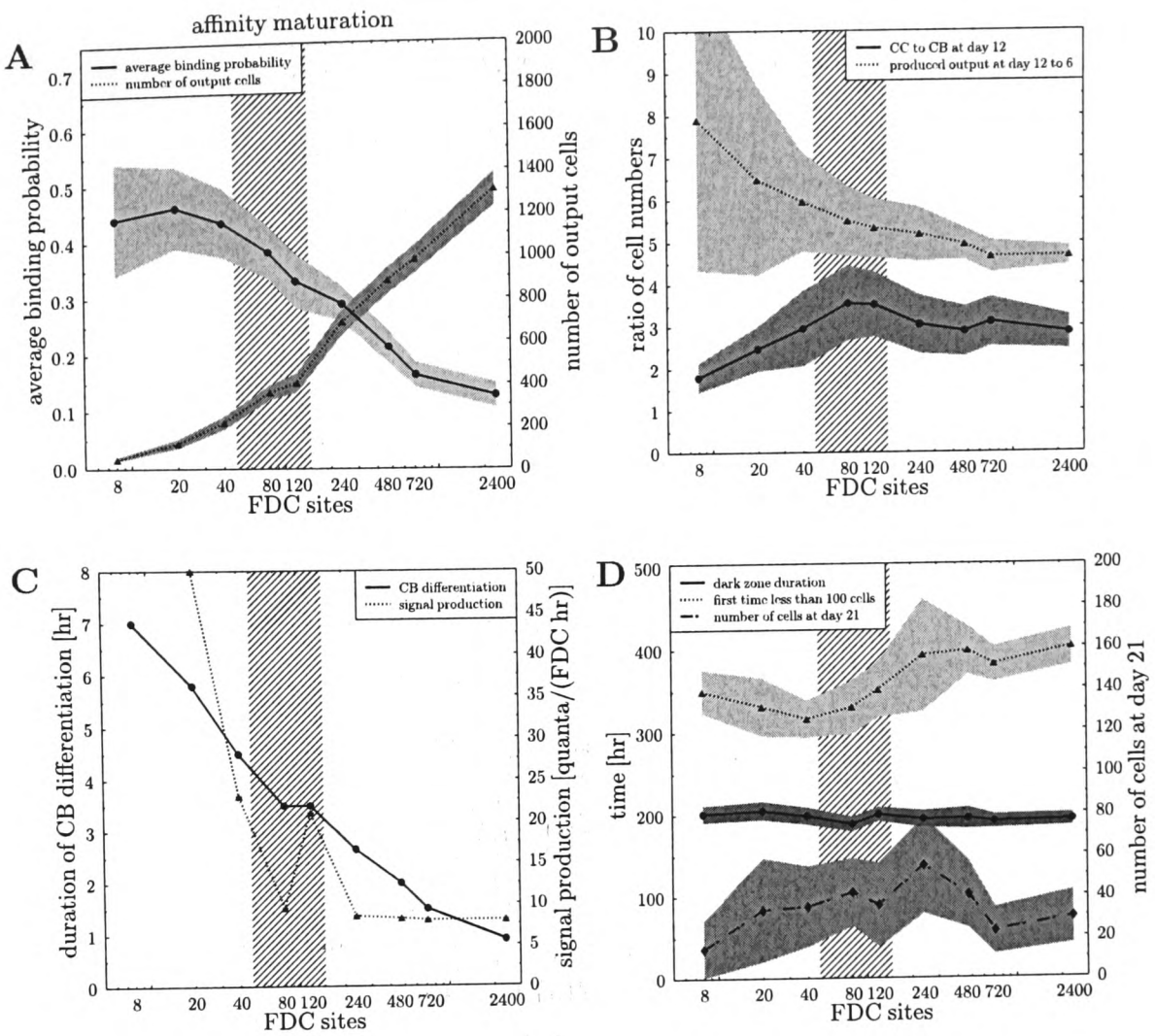


Figure 12.1: **Competition for FDC sites is too weak for affinity maturation.** *In silico* GC experiments with different numbers of FDC sites. Vertical bars indicate the physiological range. **(A)** Extent of affinity maturation (measured as average binding probability and number of output cells), **(B)** CC/CB ratio at day 12 of the reaction (continuous line), and the ratio q_6^{12} of number of output cells at day 12 to 6 (dotted line), **(C)** parameter values for the duration of CB differentiation (solid line) and the FDC signal production rate, r_{signal} (note that the jumps in the per FDC production rate of the differentiation signal correspond to a change in the number of FDC in the simulation), **(D)** dark zone persistence (solid line), time when the total GC population drops below 100 cells for the first time (dotted line), number of cells remaining after 21 days (dash-dotted line). The shaded area denotes one standard deviation in 50 simulations.

and output ratio at day 12 to day 6 (Fig. 12.2C-E)) than competition for FDC sites (Figs. 11.1B, 12.1C, D).

Given that the binding probability depends on both the affinity dependent binding probability per encounter as well as the number of encounters per CC lifetime, affinity maturation can also be fostered by reducing the binding probability per encounter by a certain factor for all affinities (Fig. 12.3). However, the effect is smaller than in the case of

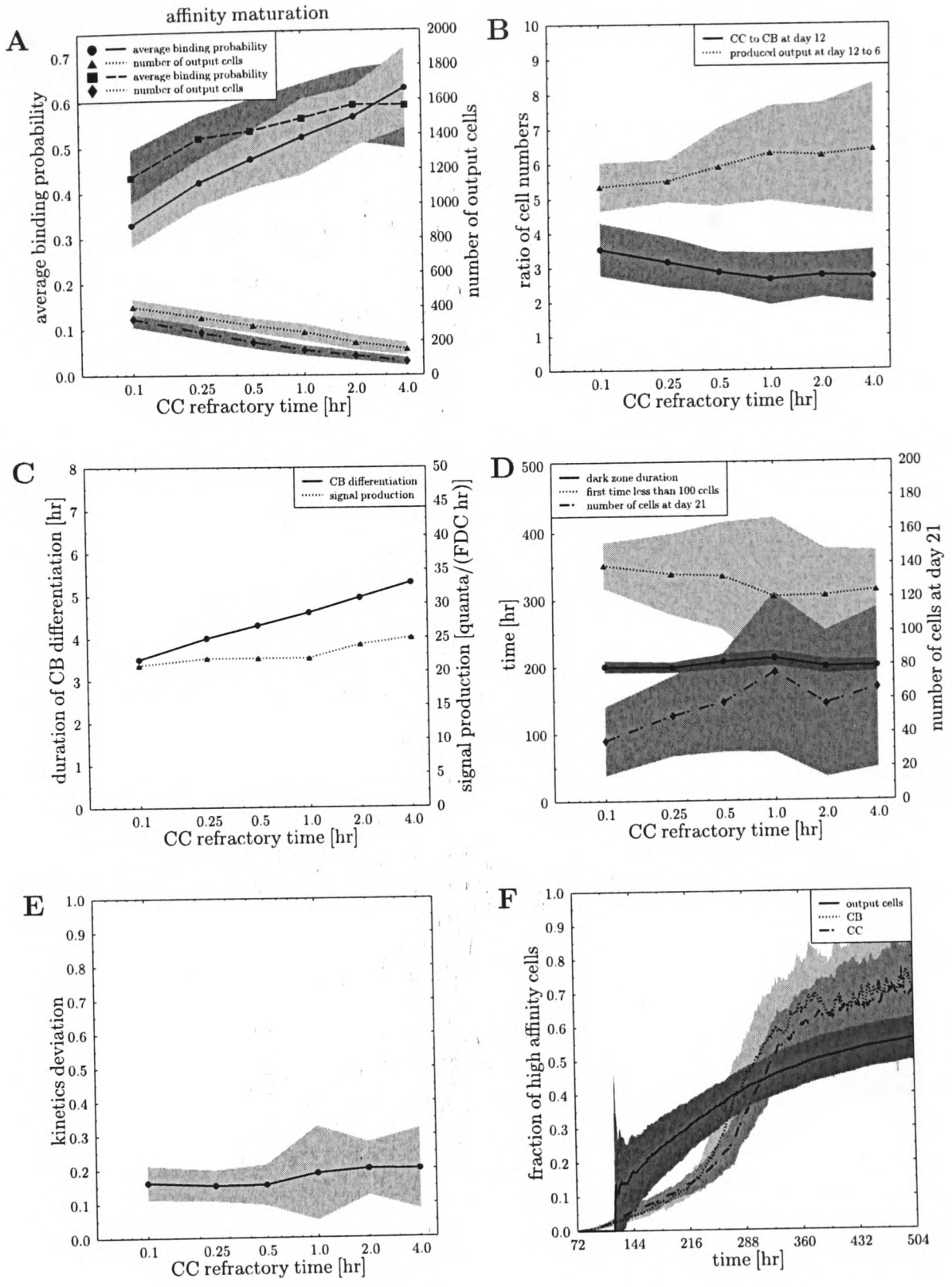


Figure 12.2: **A limitation of centrocyte-FDC interaction allows for robust affinity maturation.** *In silico* GC experiments with 10 FDC and 120 FDC sites, and for different refractory times of CC after FDC encounters. **(A)** Extent of affinity maturation (measured as average binding probability and number of output cells) when the probability that an optimal clone binds to antigen presented on FDC is 1 (solid line) or 0.5 (dotted line). **(B)** CC/CB ratio at day 12 of the reaction (continuous line), and the ratio q_6^{12} of number of output cells at day 12 to 6 (dotted line), **(C)** parameter values for the duration of CB differentiation (solid line) and the FDC signal production rate, r_{signal}, **(D)** dark zone persistence (solid line), time when the total GC population drops below 100 cells for the first time (dotted line), number of cells remaining after 21 days (dash-dotted line). The shaded area denotes one standard deviation in 50 simulations. **(E)** Deviation η from experimental GC kinetics. **(F)** The fraction of high affinity cells (defined as cells with antigen binding probability of more than 0.3) over time shown for CB, CC, and output cells separately averaged for simulations with a refractory time of 2 hours.

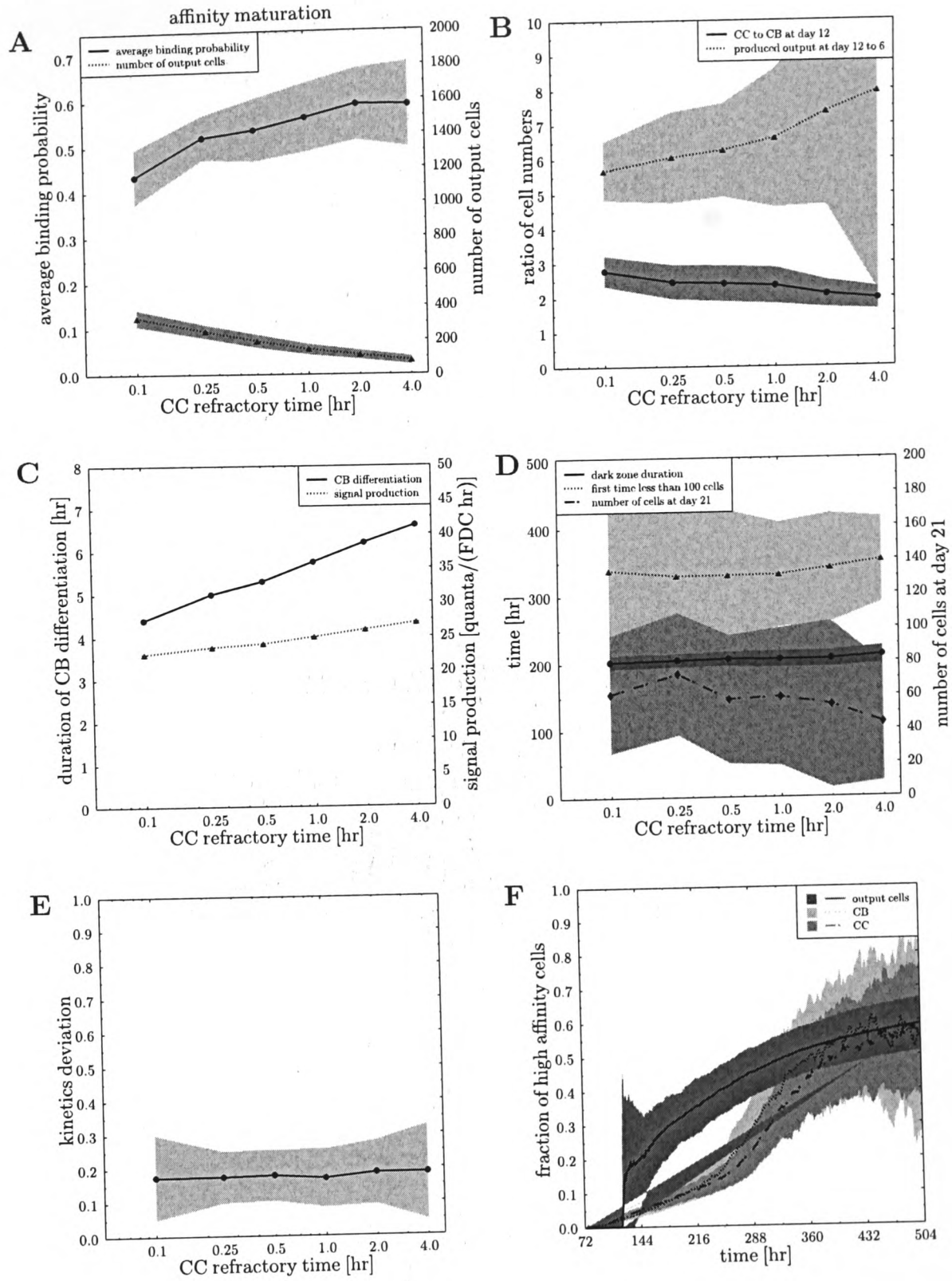


Figure 12.3: **An affinity-independent reduction of binding probability reduces the necessary refractory time.** *In silico* GC experiments with 10 FDC and 120 FDC sites, and for different refractory times of CC after FDC encounters. The simulations differ from those presented in Fig. 12.2 by an additional affinity-unspecific reduction of the binding probability of the optimal clone from 1 to 0.5. The regime of good affinity maturation is shifted to shorter refractory times. **(A)** Extent of affinity maturation (measured as average binding probability and number of output cells), **(B)** CC/CB ratio at day 12 of the reaction (continuous line), and the ratio q_6^{12} of number of output cells at day 12 to 6 (dotted line), **(C)** parameter values for the duration of CB differentiation (solid line) and the per FDC signal production rate, τ_{signal}, **(D)** dark zone persistence (solid line), time when the total GC population drops below 100 cells for the first time (dotted line), number of cells remaining after 21 days (dash-dotted line). The shaded area denotes one standard deviation in 50 simulations. **(E)** Deviation η from experimental GC kinetics. **(F)** The fraction of high affinity cells (defined as cells with antigen binding probability of more than 0.3) over time shown for CB, CC, and output cells separately averaged for simulations with a refractory time of 2 hours.

an increased CC refractory time since such a general reduction in the binding probability also strongly reduces the selection probability for high affinity clones. These are little affected by a reduction in the number of encounters since they will bind with high probability on their first or second trial. A combination of both effects can however reduce the refractory time required to gain good affinity maturation to more reasonable physiological values (Fig. 12.2A, dotted line).

The agreement with general GC properties, the efficient affinity maturation and the robustness to variations in the antigen presenting FDC site number, make this a candidate mechanism for B cell selection *in vivo*.

12.3 Competition for antigen presented on FDC fails to improve affinity maturation and is not robust.

In the two previous scenarios antigen is presented by FDC on a limited number of sites where it is available in limitless supply.. However, it has been proposed that antigen is widely spread but that the total amount is limiting such that antigen consumption can drive affinity maturation (Sidman & Unanue, 1975). Using a sufficiently dense FDC network ($X_{FDC} = 120$) to avoid site competition, we can study this selection mechanism *in silico* by homogeneously distributing a number of antigen portions, N_{ag}, on all FDC sites and by removing one portion from each site on which CC have successfully interacted with the FDC. The binding probability is expected to decrease with decreasing amounts of antigen remaining on the FDC sites. As a simple approximation we assume a linear decrease of the CC-binding probability for antigen amounts below some threshold θ_{ag}. For larger antigen amounts the binding probability is constant and solely determined by the antibody-antigen affinity. This assumption corresponds to a saturation of the binding probability when antigen is abundant.

While the selection pressure indeed increases over time as a result of this (Fig. 12.4F), the extent of affinity maturation is rather worse than for site competition alone (compare Fig. 12.1A for $X_{FDC} = 120$ and Fig. 12.4A). This is due to the initial abundance of antigen

and the inferred low selection pressure which in turn results in the production of a large number of low affinity output cells before antigen consumption can increase the selection pressure (compare Figs. 12.4F and 12.2F).

If the size of the removed antigen portions per CC-FDC interaction is constant, antigen consumption is insufficient to increase the selection pressure in the case of large initial antigen densities (more than 80 antigen portions per FDC site, compare Figs. 12.4A and 12.1A); at lower antigen density, antigen is rapidly consumed and the GC reaction declines early, before high affinity clones are found (Fig. 12.4A). In the case of antigen consumption proportional to the level of presented antigen a scenario comparable to antigen masking by antibodies arises (see section 12.4). Experiments have revealed a high robustness to variations in the initial antigen density (Hannum *et al.*, 2000; Vora *et al.*, 1997). If in the simulation the antigen-threshold to the maximum binding probability θ_{ag} is fixed and not scaled with the amount of initially deposited antigen ($\theta_{ag} = N_{ag}$), then such robustness can be observed on a low level (see Figs. 12.5 and 12.6). It should be noted that successful affinity maturation at lower antigen densities results from a reduced binding probability for all affinities (as discussed in the previous section) such that the observed robustness is the result of two different mechanisms acting in different antigen density ranges. We conclude that *in silico* antigen consumption does not improve affinity maturation over site competition alone. At low antigen densities the general properties of the GC reaction can no longer be reproduced. Affinity maturation is therefore unlikely to be driven by antigen consumption even when combined with site competition.

12.4 The impact of antigen masking by competing antibodies

Plasma cells outside the GC produce antibodies at rates of up to $r_{\mathrm{ab}} = 2 \times 10^3$ antibody molecules per second (Randall *et al.*, 1992). These antibodies may mask antigen in the GCs and thereby increase the selection pressure on B cells and simultaneously provide a feedback mechanism that enables a robustness towards alterations in the initial antigen

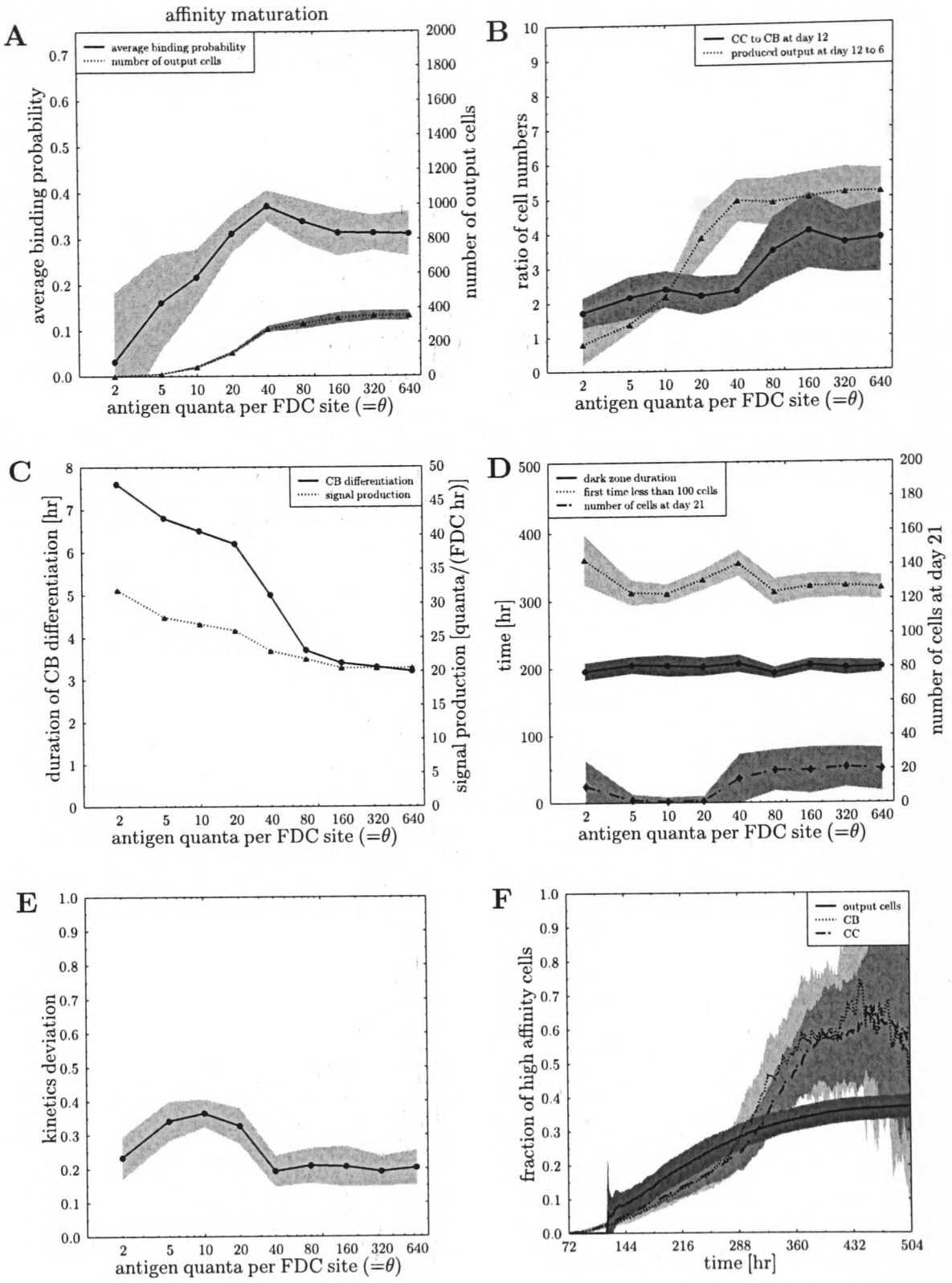


Figure 12.4: **Affinity maturation is not induced by competition for antigen.** *In silico* GC experiments with 10 FDC. θ_{ag} is set to the initial amount of antigen per FDC site in each simulation. **(A)** Extent of affinity maturation (measured as average binding probability and number of output cells), **(B)** CC/CB ratio at day 12 of the reaction (continuous line), and the ratio q_6^{12} of number of output cells at day 12 to 6 (dotted line), **(C)** parameter values for the duration of CB differentiation (solid line) and the per FDC signal production rate, r_{signal}, **(D)** dark zone persistence (solid line), time when the total GC population drops below 100 cells for the first time (dotted line), number of cells remaining after 21 days (dash-dotted line). The shaded area denotes one standard deviation in 50 simulations. **(E)** Deviation η from experimental GC kinetics. **(F)** The fraction of high affinity cells (defined as cells with antigen binding probability of more than 0.3) over time in simulations with 40 antigen portions per FDC shown for CB, CC, and output cells.

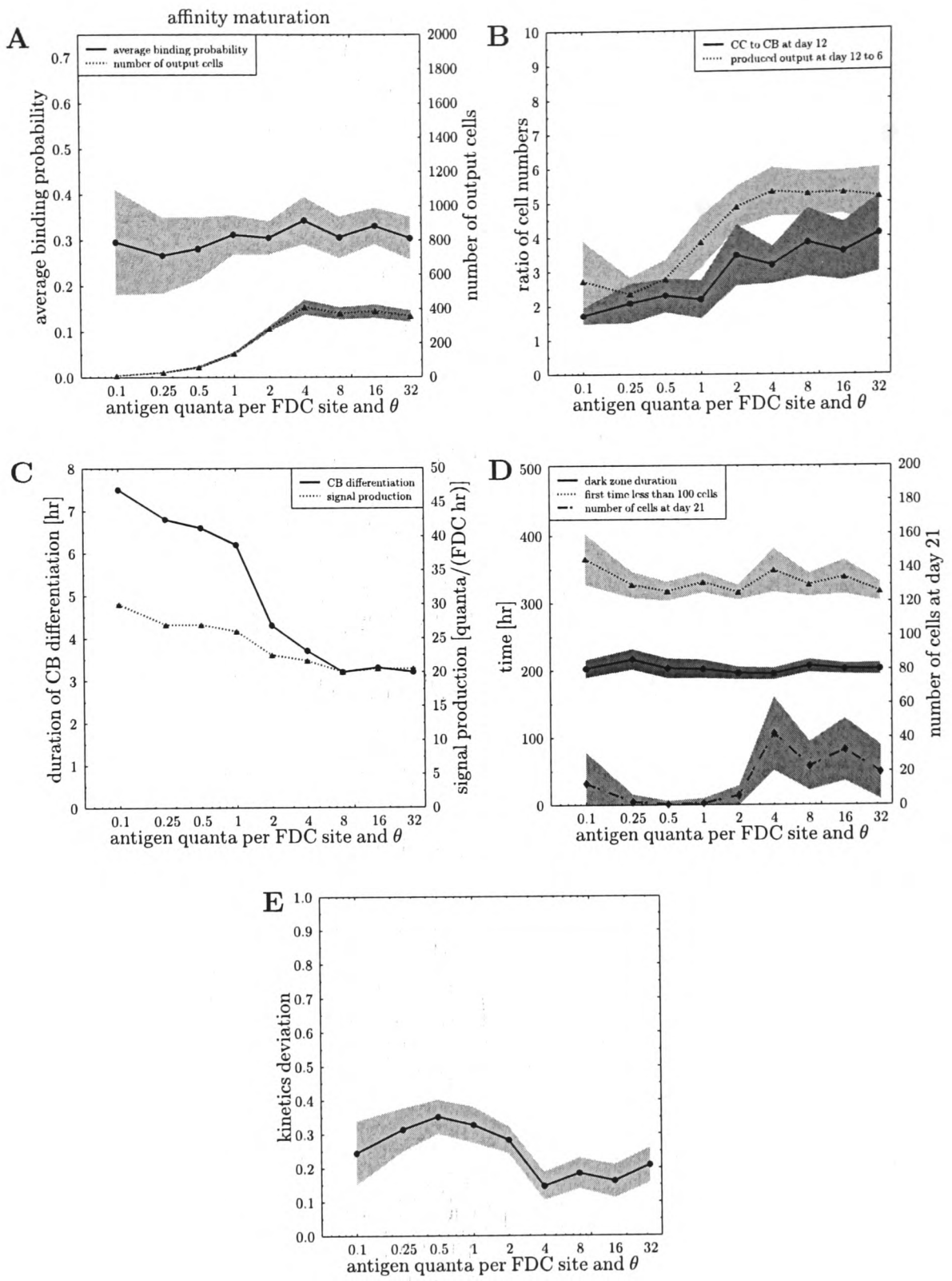


Figure 12.5: **Competition for antigen with fixed antigen threshold.** The simulations are run as in Fig. 12.4 but with $\theta = 20$ fixed independent of the amount of initial antigen. A clear transition is observed between two classes of results: If antigen is limiting, affinity maturation is poor and the whole GC reaction is disrupted too early. If antigen is abundant, selection pressure is too weak to increase affinity maturation with respect to competition for antigen sites. **(A)** Extent of affinity maturation (measured as average binding probability and number of output cells), **(B)** CC/CB ratio at day 12 of the reaction (continuous line), and the ratio q_6^{12} of number of output cells at day 12 to 6 (dotted line), **(C)** parameter values for the duration of CB differentiation (solid line) and the per FDC signal production rate, r_{signal}, **(D)** dark zone persistence (solid line), time when the total GC population drops below 100 cells for the first time (dotted line), number of cells remaining after 21 days (dash-dotted line). The shaded area denotes one standard deviation in 50 simulations. **(E)** Deviation η from experimental GC kinetics.

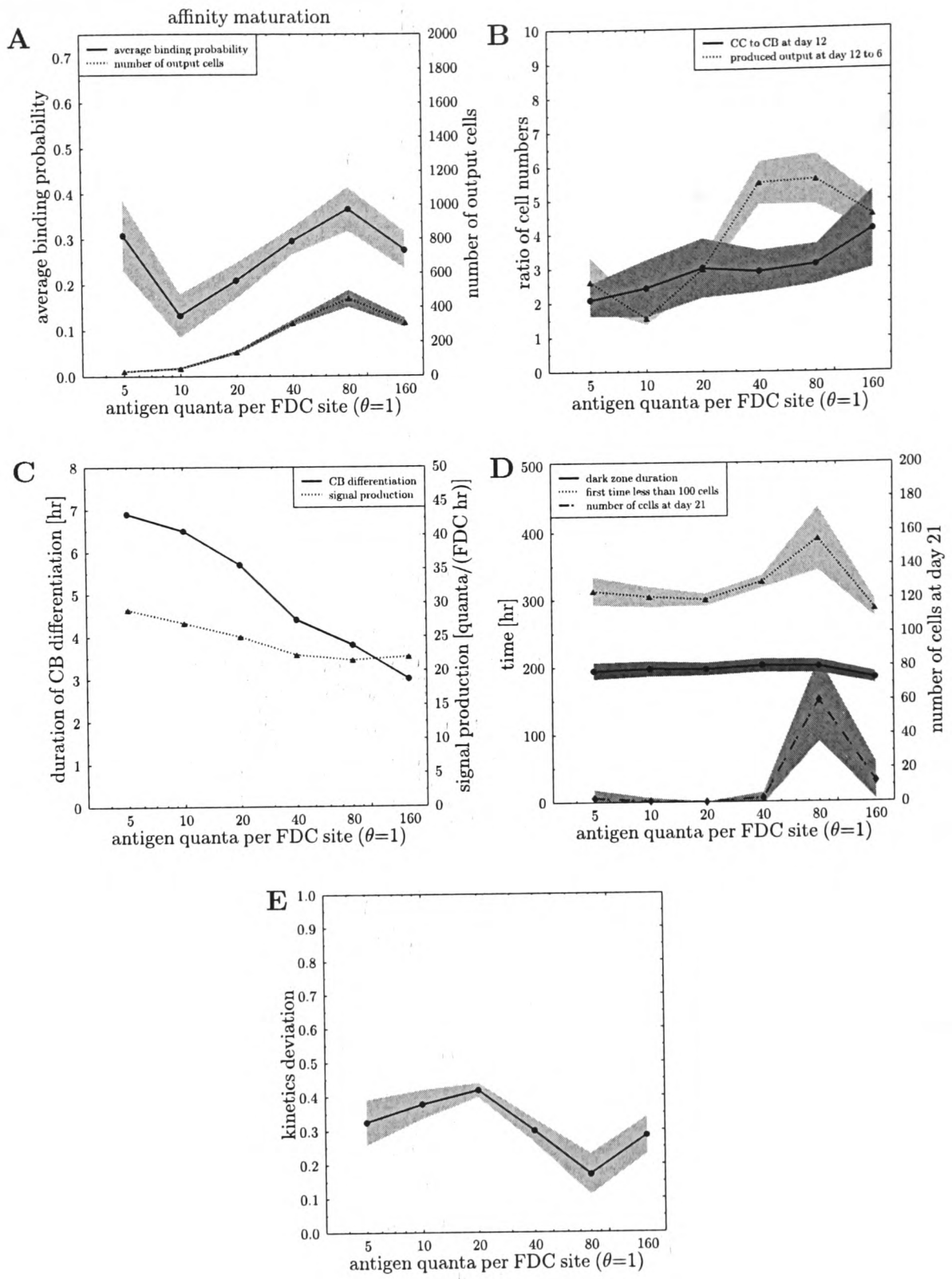


Figure 12.6: **Competition for antigen with binding probability independent of presented antigen amount.** The same as in Fig. 12.4 with $\theta = 1$. The amount of antigen necessary to reproduce the correct GC kinetics is even higher as compared to a dynamic binding probability. **(A)** Extent of affinity maturation (measured as average binding probability and number of output cells), **(B)** CC/CB ratio at day 12 of the reaction (continuous line), and the ratio q_6^{12} of number of output cells at day 12 to 6 (dotted line), **(C)** parameter values for the duration of CB differentiation (solid line) and the per FDC signal production rate, r_{signal}, **(D)** dark zone persistence (solid line), time when the total GC population drops below 100 cells for the first time (dotted line), number of cells remaining after 21 days (dash-dotted line). The shaded area denotes one standard deviation in 50 simulations. **(E)** Deviation η from experimental GC kinetics.

density (Vora *et al.*, 1997; Tarlinton & Smith, 2000; Iber & Maini, 2002). Assuming that plasma cells produce high affinity antibodies in the GC at a rate of $r_{ab} = 10^2$ per output cell (thus overestimating a realistic production of soluble antibody in GCs), we find that the above considerations hold true: A physiological GC kinetic can be obtained for antigen amounts between 20 and 200 antigen portions per FDC site. A small improvement in affinity maturation is observed relative to site and antigen competition alone (Fig. 12.7A). As before, affinity maturation approaches the site competition value for 120 sites when antigen is abundant (Fig. 12.7A and Fig. 12.1A).

The effect of strong antibody production is an early reduction in free antigen, and thus an early increase in the selection pressure (Fig. 12.7F). For example, in the case of 40 antigen portions per FDC site (i.e. for optimal affinity maturation) only 25% of the antigen is used during the GC reaction, but free antigen is kept in the limiting regime throughout the reaction (Fig. 12.7F). In that way the inefficient time course of affinity maturation found in the case of antigen consumption without soluble antibodies (Fig. 12.4F) is restored.

While antigen masking leads to the correct kinetics and a small improvement of affinity maturation, the number of produced output cells is low (Fig. 12.7A), the ratio of CC to CB is rather small, and $q_6^{12} \ll 6$ (Fig. 12.7B). We conclude that antigen masking resolves some of the problems in the antigen competition scenario, but some major GC properties are still not reproduced. In addition this mechanism is not robust to a substantial (10-fold) decrease in the antibody production rate, which is more realistic than the rate assumed in the present *in silico* experiment.

12.5 Competition for T cell help

Interactions between antigen specific CC and T cells are necessary for CC survival and differentiation (de Vinuesa *et al.*, 2000). Given that T cells only constitute $5 - 10\%$ of the GC cell population (Kelsoe, 1996*a*) this interaction may be competitive. While T cells can bind to several B cells simultaneously, they can only polarize to one (Kupfer *et al.*, 1994),

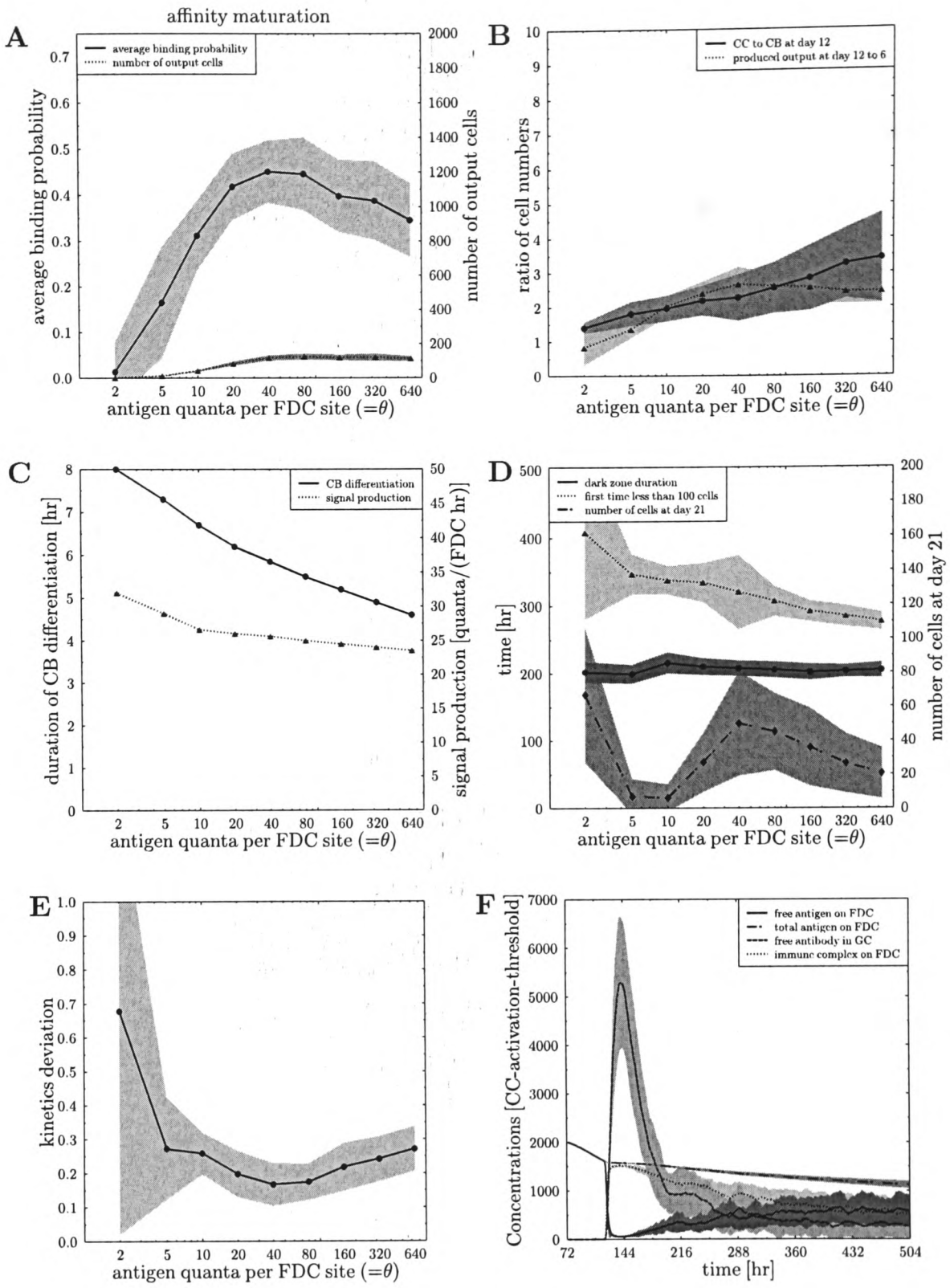
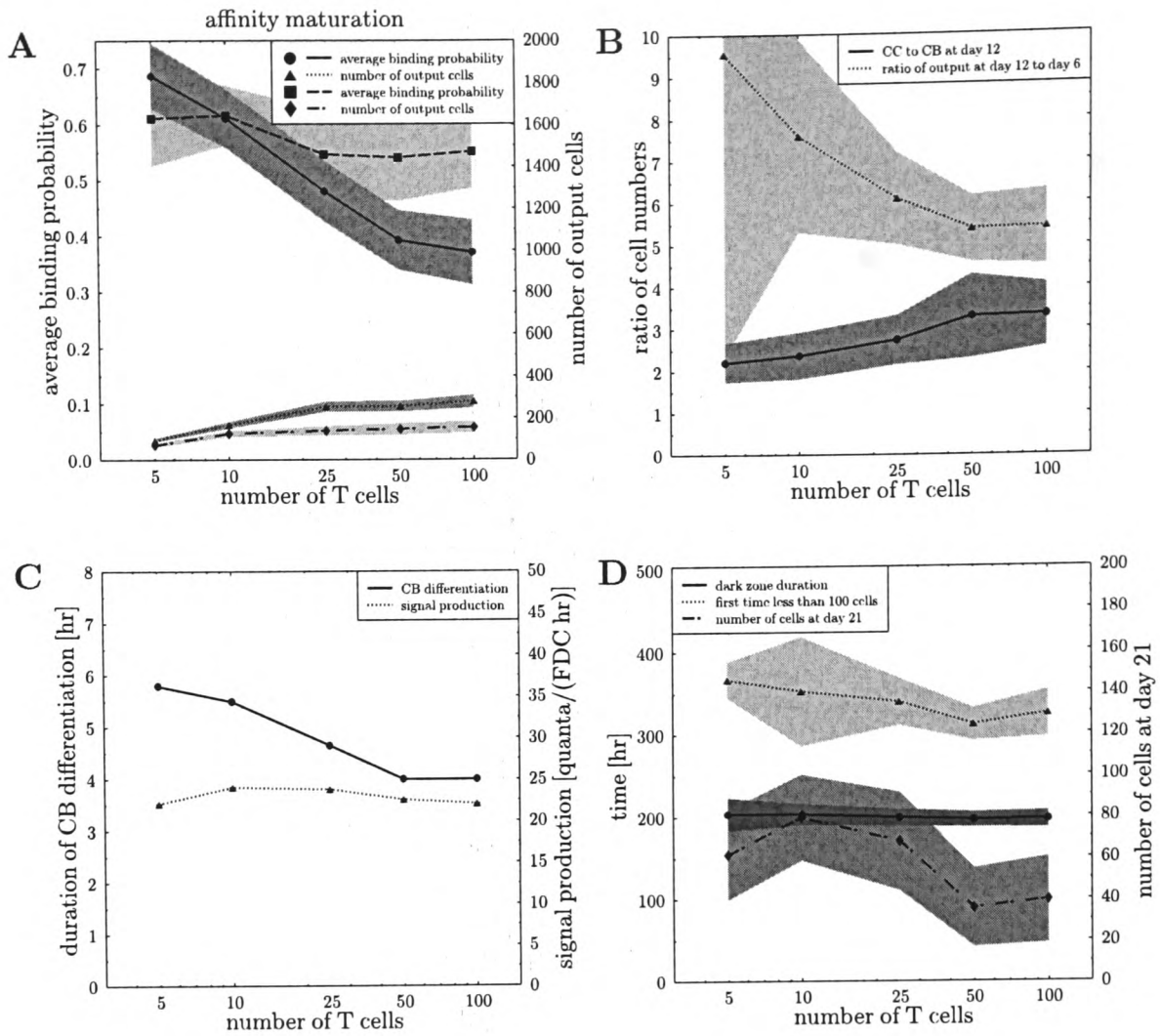


Figure 12.7: **Antigen masking by soluble antibodies increases competition for antigen in the early phase of GC reaction.** *In silico* GC experiments as in Fig. 12.4 but with each output cell producing $r_{\mathrm{ab}} = 10^2$ antibodies per second. **(A)** Extent of affinity maturation (measured as average binding probability and number of output cells), **(B)** CC/CB ratio at day 12 of the reaction (continuous line), and the ratio q_6^{12} of number of output cells at day 12 to 6 (dotted line), **(C)** parameter values for the duration of CB differentiation (solid line) and the per FDC signal production rate, r_{signal}, **(D)** dark zone persistence (solid line), time when the total GC population drops below 100 cells for the first time (dotted line), number of cells remaining after 21 days (dash-dotted line). The shaded area denotes one standard deviation in 50 simulations. **(E)** Deviation η from experimental GC kinetics. **(F)** The time course of free antigen on FDC, soluble antibody, and immune complexes for an example experiment with 40 antigen quanta per FDC site. Soluble antibody induces an early reduction of free antigen and thereby increases competition.

which we assume to be the CC that has previously bound antigen with highest affinity. In our simulation, polarization has to be maintained for a minimum time (Δt_{rescue}) to rescue a B cell. Cells that bind to T cells for longer than Δt_{apop} and do not receive rescue signals for at least Δt_{rescue} are doomed to apoptosis. Note that all CC need to be selected by FDC before they can compete for T cell help.

We find that the extent of affinity maturation is only slightly enhanced as compared to site competition alone ($X_{\mathrm{FDC}} = 120$ sites) if $5 - 10\%$ of all GC cells are antigen-specific T cells (50-100 T cells per GC) to which antigen-presenting CC can bind (Fig. 12.8A). However, given that each antigen-specific T cell only recognizes a certain antigen epitope and different CC will process the antigen differently and therefore present different epitopes, only a small fraction of GC T cells will be reactive to a given CC. The simulation reveals that affinity maturation is strongest (60-70% of all output cells are of high affinity) when only about $0.5 - 1\%$ of all GC cells (5-10 T cells per GC in the 2-dimensional simulation) can rescue a given antigen presenting CC (Fig. 12.8A). The GC characteristics are reproduced (Fig. 12.8B-E). The mechanism is robust to large variations in antigen availability and will still work when antigen is encountered in soluble form since the simulations were performed in a regime where antigen acquisition and interactions with FDC are uncompetitive.

The time span Δt_{apop} for which CC can survive while binding to T cells without receiving rescue signals has a major impact on the level of affinity maturation (Fig. 12.9A). Thus a small increase in Δt_{apop} from 2.1 to 4 hours already reduces affinity maturation to a level comparable to site competition. A combination of T cell competition with a general reduction of the binding probability to 50% of its value (see above) has no major effect on the result (Fig. 12.10). However, a combination of competition for T cell help with a longer CC refractory time makes affinity maturation more robust against changes in the T cell density (Fig. 12.11).



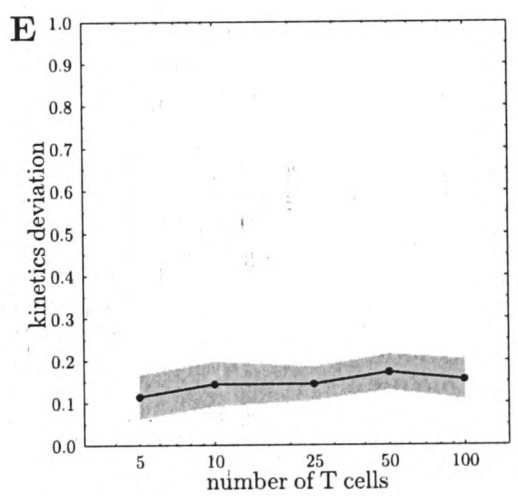


Figure 12.8: **Competition for T cell help allows for robust affinity maturation.** *In silico* GC experiments with 10 FDC and 120 FDC sites. Neither antigen nor antibody is included explicitly. The number of T cells is varied, where $\Delta t_{\text{rescue}} = 2$ hours and $\Delta t_{\text{apop}} = 2.1$ hours. **(A)** Extent of affinity maturation (measured as average binding probability and number of output cells). Combining competition for T cell help with a CC refractory time of 0.5 hours and a reduction of the binding probability to 0.5 leads to more robust affinity maturation (squares and diamonds). **(B)** CC/CB ratio at day 12 of the reaction (continuous line), and the ratio q_6^{12} of number of output cells at day 12 to 6 (dotted line), **(C)** parameter values for the duration of CB differentiation (solid line) and the per FDC signal production rate, r_{signal}, **(D)** dark zone persistence (solid line), time when the total GC population drops below 100 cells for the first time (dotted line), number of cells remaining after 21 days (dash-dotted line). The shaded area denotes one standard deviation in 50 simulations. **(E)** Deviation η from experimental GC kinetics.

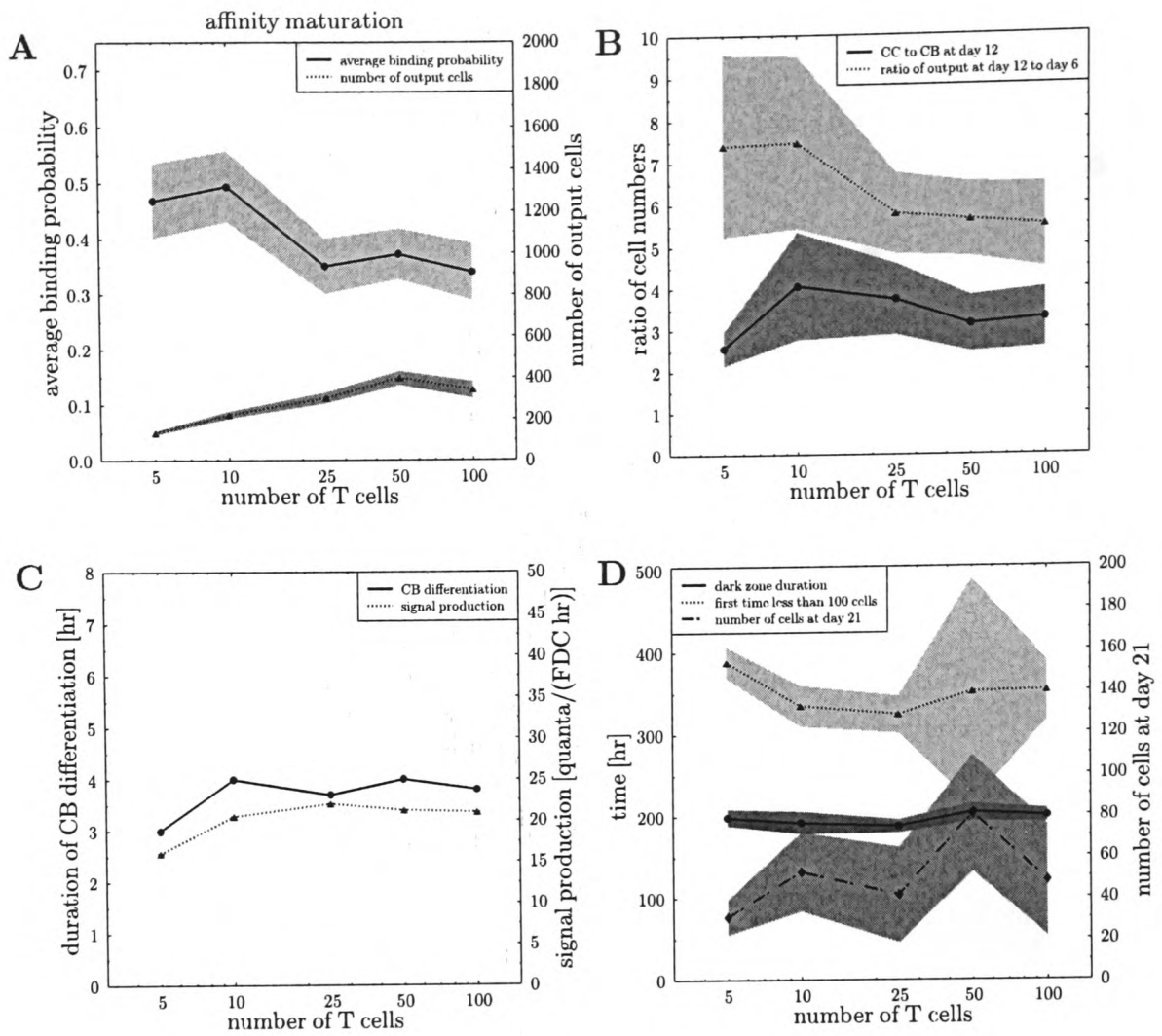


Figure 12.9: **The impact of a prolonged time span before induction of apoptosis by T cells.** *In silico* GC experiments with 10 FDC and 120 FDC sites. Neither antigen nor antibody is included explicitly. The number of T cells is varied, where $\Delta t_{\text{rescue}} = 2$ hours and $\Delta t_{\text{apop}} = 4$ hours (instead of 2.1 hours in Fig. 12.8). Affinity maturation is considerably reduced. **(A)** Extent of affinity maturation (measured as average binding probability and number of output cells). **(B)** CC/CB ratio at day 12 of the reaction (continuous line), and the ratio q_6^{12} of number of output cells at day 12 to 6 (dotted line), **(C)** parameter values for the duration of CB differentiation (solid line) and the per FDC signal production rate, r_{signal}, **(D)** dark zone persistence (solid line), time when the total GC population drops below 100 cells for the first time (dotted line), number of cells remaining after 21 days (dash-dotted line). The shaded area denotes one standard deviation in 50 simulations. **(E)** Deviation η from experimental GC kinetics.

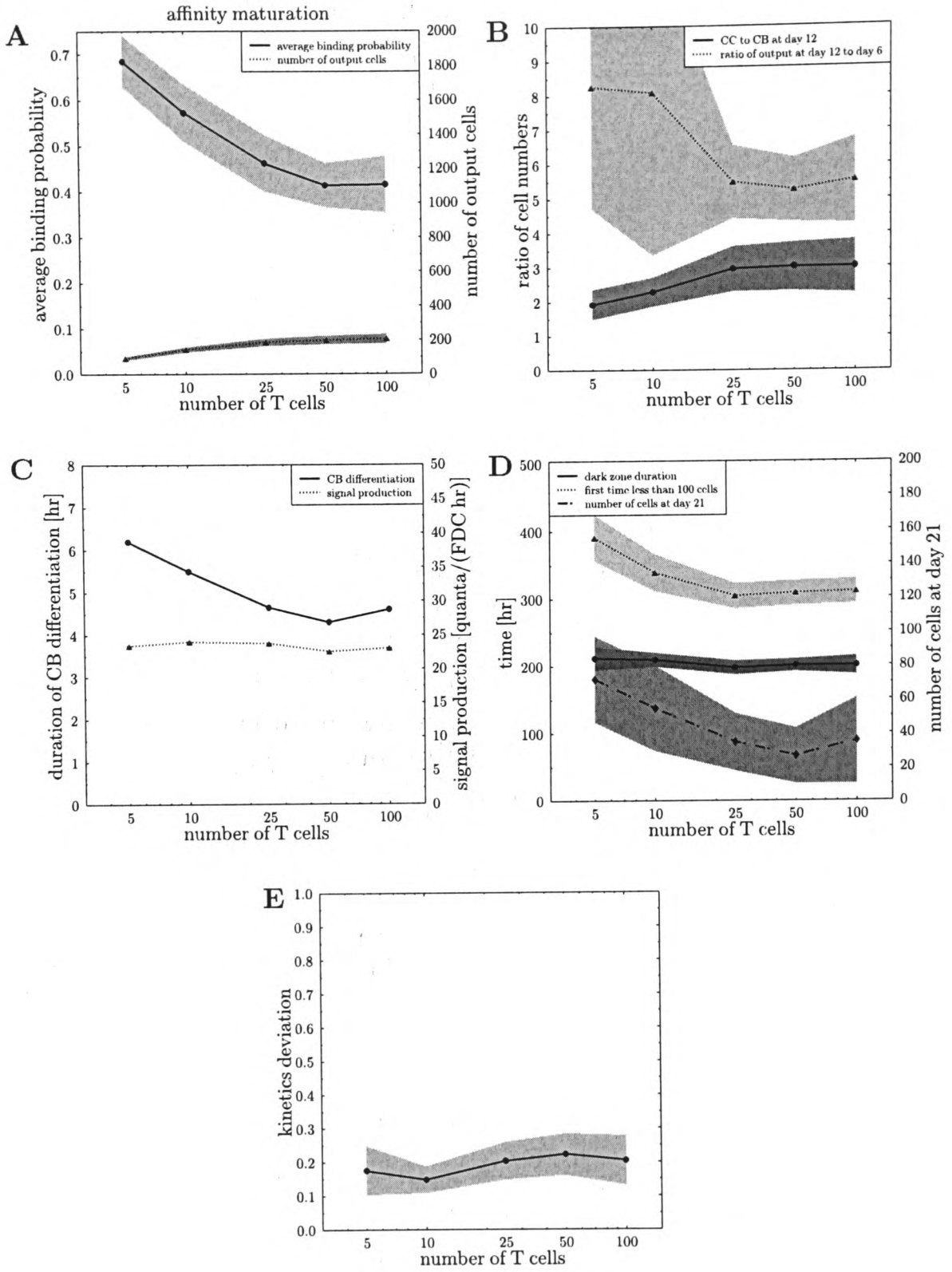


Figure 12.10: **Competition for T cell help with reduced unspecific binding probability to FDC.** *In silico* GC experiments with 10 FDC and 120 FDC sites. Neither antigen nor antibody is included explicitly. The number of T cells is varied, where $\Delta t_{\text{rescue}} = 2$ hours and $\Delta t_{\text{apop}} = 2.1$ hours. In addition to Fig. 12.8 the binding probability of the optimial CC to FDC has been reduced from 1 to 0.5. The latter slightly increases affinity maturation when T cell help is non-limiting and leaves the results unchanged when T cell help is limiting. **(A)** Extent of affinity maturation (measured as average binding probability and number of output cells). **(B)** CC/CB ratio at day 12 of the reaction (continuous line), and the ratio q_6^{12} of number of output cells at day 12 to 6 (dotted line), **(C)** parameter values for the duration of CB differentiation (solid line) and the per FDC signal production rate, r_{signal}, **(D)** dark zone persistence (solid line), time when the total GC population drops below 100 cells for the first time (dotted line), number of cells remaining after 21 days (dash-dotted line). The shaded area denotes one standard deviation in 50 simulations. **(E)** Deviation η from experimental GC kinetics.

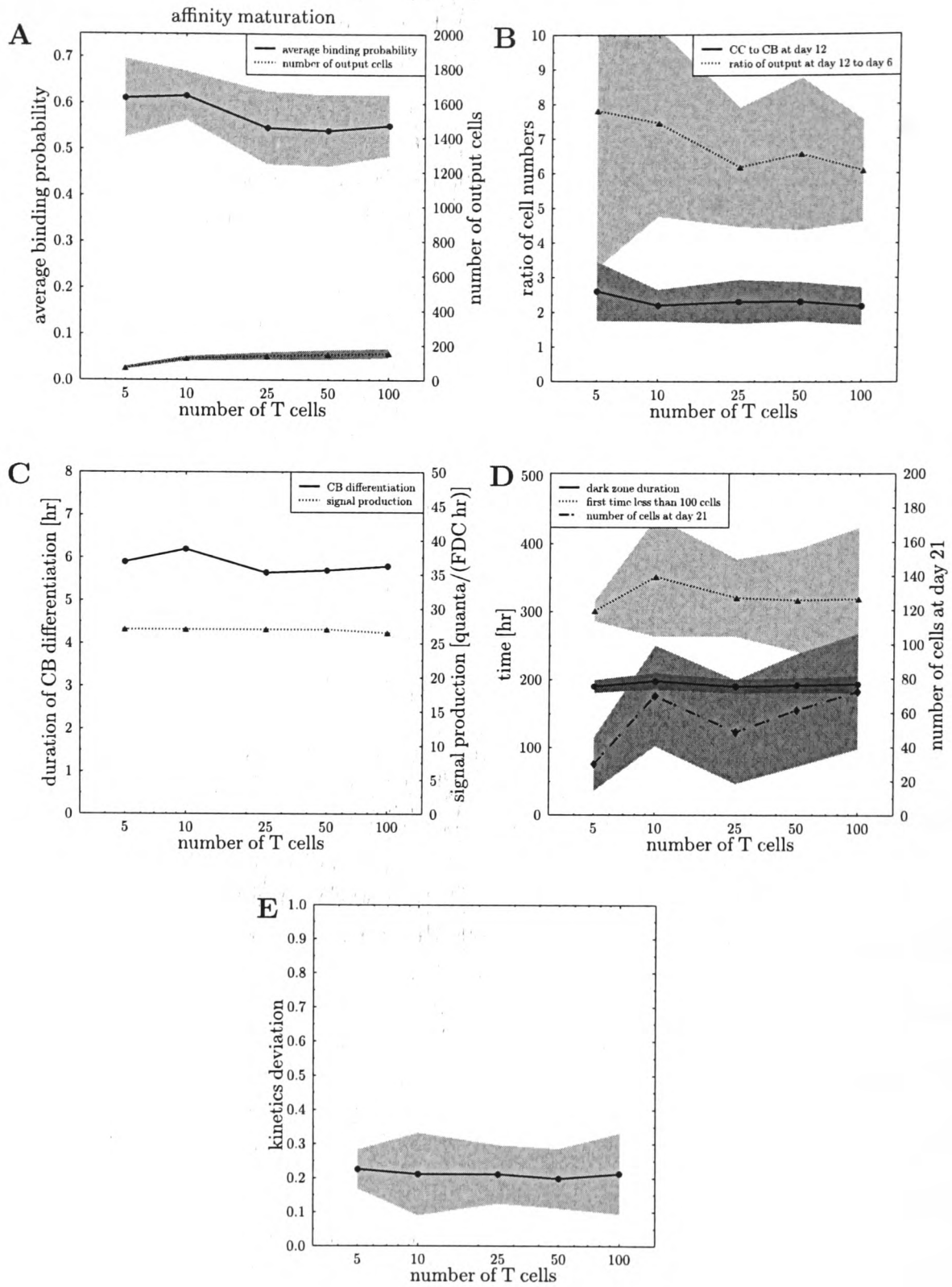


Figure 12.11: **Combining competition for T cell help with a refractory time.** *In silico* GC experiments with 10 FDC and 120 FDC sites. Neither antigen nor antibody is included explicitly. The number of T cells is varied, where $\Delta t_{\text{rescue}} = 2$ hours and $\Delta t_{\text{apop}} = 2.1$ hours. The refractory time is set to 0.5 hours and the binding probability of the optimial CC to FDC to 0.5. Combining competition of T cell help with a CC refractory time increases the range of acceptable affinity maturation. **(A)** Extent of affinity maturation (measured as average binding probability and number of output cells). **(B)** CC/CB ratio at day 12 of the reaction (continuous line), and the ratio q_6^{12} of number of output cells at day 12 to 6 (dotted line), **(C)** parameter values for the duration of CB differentiation (solid line) and the per FDC signal production rate, r_{signal}, **(D)** dark zone persistence (solid line), time when the total GC population drops below 100 cells for the first time (dotted line), number of cells remaining after 21 days (dash-dotted line). The shaded area denotes one standard deviation in 50 simulations. **(E)** Deviation η from experimental GC kinetics.

12.6 Conclusion

The systematic comparison of different B cell selection mechanisms in GC reactions presented here reveals current models of B cell selection (competition for access to FDC or antigen) to be incompatible with available experimental information. We propose two novel mechanisms, a refractory time between CC-FDC engagements as well as competition for T cell help. Both mechanisms enable strong affinity maturation *in silico* while reproducing all available experimental information on GC dynamics. In agreement with experiments (Vora *et al.*, 1997; Hannum *et al.*, 2000), the mechanisms are robust to variations in the amount of initially deposited antigen. As competition for antigen held on FDC is assumed to be non-limiting in both mechanisms, it is likely that these mechanisms also work with soluble antigen which would be in agreement with results from recent experiments that call into question the concept that antigen presentation by FDC is essential (Hannum *et al.*, 2000; Haberman & Shlomchik, 2003). However, in the present simulations an FDC-independent pre-selection of CC with soluble antigen has not been tested.

Competition for access to FDC or antigen does not provide a sufficient selection pressure to enable a high level of affinity maturation in the simulation. While antigen consumption does lead to an increase in the selection pressure, this increase comes too late so that many low affinity output cells have already been produced and the remaining cell numbers are insufficient for successful affinity maturation. Moreover, for low antigen densities the GC reaction ends prematurely since antigen consumption then removes too much antigen. While antigen masking by emerging antibodies can, in principle, increase the selection pressure earlier, the antibody production rate would need to be unphysiologically high. Even then the available data on GCs could not be reproduced and, in addition, affinity maturation is not as strong as that produced by the alternative mechanism. Given that evolution tends to optimise performance, this latter limitation may also be interpreted as an argument against these mechanisms.

In an earlier work I concluded from an ODE model that antibody masking can drive

affinity maturation (Iber & Maini, 2002). The apparent discrepancy can be accounted for by the use of only two affinity levels, low and high affinity. Accordingly, the model revealed that maximal affinity maturation is achieved when high affinity clones leave the GC early (and produce antibodies). This, however, obviously only works for a two-step process. In a multistep process (as realistic and modelled here) loss of high affinity clones in the early phase will hamper the entire affinity maturation process which requires several rounds of mutation and selection.

At first sight, less than 200 output cells (that is less than 8000 cells in three dimensions) may seem low. Given the efficient expansion of output cells the success of an immune response can, however, be expected to primarily depend on the size of the high affinity fraction; this is therefore a physiologically realistic result. Note that the level of affinity maturation that is achieved in the simulations (60-70% of all output cells are of high affinity) is in qualitative agreement with the experimentally observed domination of high affinity clones (Smith *et al.*, 1997). We had to restrict ourselves to two-dimensional simulations to generate the results with sufficient statistics, which prevents us from a quantitative comparison of this result.

The model is based on available GC kinetics and cell motility data (see Chapter 11) and the parameters have been evaluated carefully using data from mice and rat lymph nodes (see Table 11.1). We did not find any experimentally uncertain parameter which would change our results qualitatively. The only critical assumption is the shape space concept combined with a smooth affinity function. Changes of the width Γ of the function for the affinity dependent selection probability in the shape space has important consequences for GC development. For small variations of the width all the constraints that the experimental findings impose can be respected by a corresponding adaption of other parameters. However, this becomes impossible when the width is altered substantially. Such sensitivity is not a weakness of the model but most likely a realistic feature; affinity maturation and the germinal centre reaction can be expected to be sensitive to the rate at which affin-

ity enhancing or decreasing mutations appear. While the suitability of the shape space concept for antigen-antibody affinity may be questioned, insufficient molecular information on antigen-antibody interaction is currently available to allow a more accurate model of mutation-dependent increases in antibody-antigen affinity.

Autoreactive B cells have not been considered in the present simulations because under normal circumstances they are not positively selected by T cells and are therefore eliminated by apoptosis similar to other antigen-unspecific CC. We therefore assumed autoreactive B cells to be part of the pool of low affinity BC that emerge from the seeder cells by disadvantageous mutations. This may shift the proportion of advantageous and disadvantageous mutations. However, we believe that this approximation remains within the error introduced by the shape space concept itself which most likely will inaccurately reproduce this proportion.

We conclude that a combination of T cell competition together with slow CC-FDC interactions and a sub-optimal binding probability of high affinity clones can drive B cell selection in GCs under the experimentally established conditions. Further insight into GC dynamics and affinity maturation should be gained by combining the powerful predictions of these agent based simulations with the latest imaging techniques.

Chapter 13

The mechanistic basis of affinity-dependent B cell signaling

13.1 Overview

The first step in the selection of B cells is the activation of B cells by antigen which leads to antigen extraction and presentation to T cells (Batista *et al.*, 2001; Iber, 2005). Despite intense efforts no model for B cell activation yet exists that agrees with the relevant experimental observations (see section 10.4). I propose that B cell activation is the result of an antigen-induced spatial separation of receptors and inhibitors (Fig. 13.1).

That B cells are activated once the key inhibitors are silenced has been shown in various experiments. Thus an increased reactivity of B cells has been observed when an inhibitory receptor (CD22) was ligated in a way to prevent its coaggregation with the BCR (Doody *et al.*, 1995). Moreover, the attenuation of the effects of phosphatases has been found to trigger B cell signaling. Thus reconstitution of the early B cell signaling circuit comprising a single-chain BCR, Syk and BLNK in Drosophila Schneider S2 cells results in autoactivation if the phosphatase SHP-1 is not co-expressed (Rolli *et al.*, 2002); co-expression of SHP-1 prevents autoactivation. Similarly, pervanadate, which inhibits phosphatases by oxidation, elicits B cell signaling without any need for antigen binding (Wienands *et al.*, 1996).

In this chapter it is shown that within this novel framework the concentration and affinity dependency of B cell signaling can be predicted quantitatively and several so far counterintuitive experimental observations can be explained. The BCR is unique in that

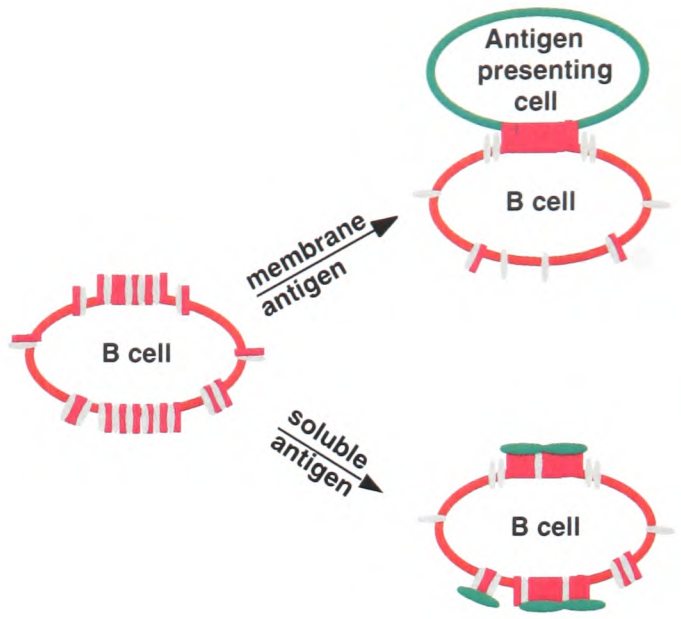


Figure 13.1: **The segregation model for B cell activation.** Antigen binding leads to the segregation of receptors (red stickers) and inhibitor (grey stickers) thus enabling B cell signal initiation.

it can be activated by a large number of different ligands (antigens) that may bind with very different affinities (Kouskoff *et al.*, 1998; Batista & Neuberger, 1998). Moreover, the antigen can be encountered in many different forms, i.e. soluble, on surfaces, monomeric or polymeric. All these ways of displaying antigen have been studied *in vitro*, and I will show that the results obtained under these very different conditions can all be understood within this novel framework. Finally, the correlation of receptor downregulation and B cell unresponsiveness (which is observed in anergic MD4 B cells (Goodnow *et al.*, 1988; Goodnow *et al.*, 1991)) as well as the nature of the immunon and other observations with haptens can be understood in this framework.

While it is relatively straightforward to imagine how polymeric antigen may induce local segregation structures (a problem that we will turn to at the end of this chapter) this is not as easy to accomplish with monomeric antigen (Batista & Neuberger, 1998), the problem that we will consider first. It is likely that the organisation of BCRs into pre-formed clusters plays an important role but while experiments suggest their existence (Schamel & Reth, 2000) little is known about their exact size and structure. We therefore first develop a simple mathematical model in section 13.2.2 based on physiological parameters which predicts that,

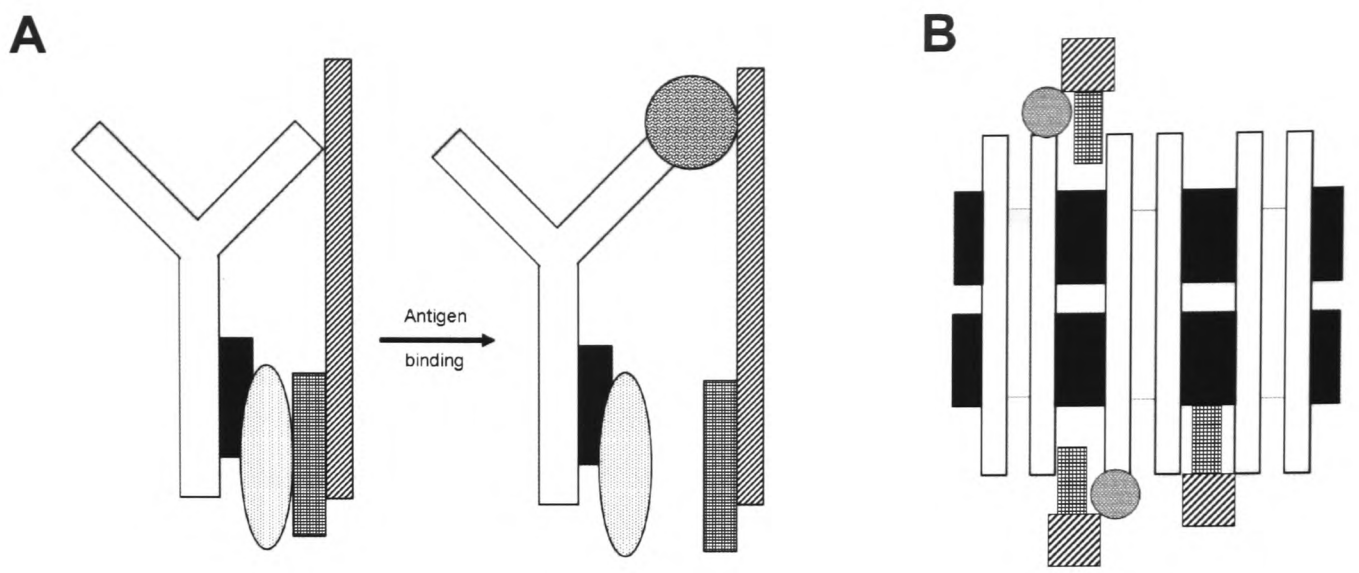


Figure 13.2: **B cell activation by soluble antigen (A)** Antigen of sufficient size separates inhibitors from BCRs. **(B)** Binding of soluble or membrane antigen to pre-formed BCR clusters can efficiently protect BCR-bound kinases from inhibitory interactions (discussed in Section 13.3). Engagement of at least three neighbouring receptors by antigen is sufficient to initiate B cell signaling (RHS) even if the cluster partial dissociates and opens on the LHS such that inhibitors can intercalate. The Y-shaped elements represent receptors, the balls antigens; inhibitors are depicted by the striped rectangles, Ig-α/Ig-β as black rectangles, kinases as ovals and the phosphatase as checkered rectangles.

according to the information available from experiments, BCRs most likely polymerize into small open chains. In such a configuration, soluble antigen of sufficient size can, in principle, block access of inhibitory co-receptors to the BCR-bound kinases (Fig. 13.2). Inhibition of inhibitors has been shown before to result in spontaneous B cell signaling (see above). In agreement with earlier work (Vogelstein *et al.*, 1982) the model predicts that a tenth of all receptors need to be engaged by soluble antigen to trigger a response, and it reproduces available experimental data on the affinity and concentration dependency of B cell signaling quantitatively (Section 13.3).

Artificial antigen-covered surfaces have been studied as a model for membrane antigen (Batista & Neuberger, 2000). These eliminate potential effects of additional proteins such as integrins. Unlike in the case of mobile antigen, inhibitory receptors can be expelled from

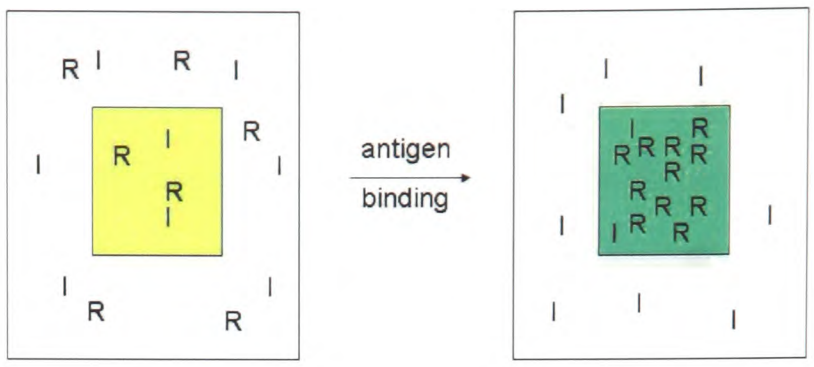


Figure 13.3: **B cell activation by inhibitor expulsion.** Antigen, if immobilized on a surface (as is discussed in Section 13.4), can lead to molecular crowding in the contact zone (shaded area) which then results in inhibitor (I) expulsion and receptor (R) activation.

the contact zone by molecular crowding (Fig. 13.3). The assumption that antigen binding results in receptor-inhibitor segregation is supported by experiments. Thus macroscopic segregation structures have been observed to evolve in the B cell contact zone upon encounter of membrane-tethered antigen (Batista *et al.*, 2001; Iber, 2005). The generated pattern (which is generally referred to as immunological synapse (Kupfer & Kupfer, 2003)) is characterized by an accumulation of activating proteins such as BCR, Syk and PLCγ in the contact zone, while proteins with a known inhibitory function (CD22,C45, Fc receptor, SHP-1) are excluded (Batista *et al.*, 2001; Iber, 2005). Receptor-inhibitor segregation has so far not been studied in response to soluble antigen, but a patching of the BCR has been reported (Schreiner & Unanue, 1976).

While both the mature B cell synapse as well as large caps in response to soluble reagents are the result of active transport processes (De Petris, 1974; Ryan *et al.*, 1974), IgM accumulation in the contact zone as well as the formation of small BCR patches in response to soluble reagents can still be observed when active transport processes are inhibited (Ryan *et al.*, 1974; Iber, 2005). The initial cluster formation thus appears to be driven by passive processes and may then trigger signaling and thereby the subsequent active reorganisations, thus determining the extent of capping in response to soluble antigen and the structure of the mature synapse in response to membrane antigen.

Accordingly we can use concepts from statistical mechanics to predict the affinity-

dependent spatial segregation of receptors and inhibitors in the contact zone (Section 13.4). The predicted distributions correlate quantitatively with the degree of B cell activation observed in experiments. Even more importantly the model explains the previously counter-intuitive observation that antigen arrayed on a smaller particle triggers maximal B cell activation already at a lower affinity.

An extension of this model in section 13.5 makes predictions on the structure of the immunon that has been elusive for the past 30 years (Dintzis *et al.*, 1976).

13.2 The organization of the B cell receptor on the cell membrane

The spatial arrangement of B cell receptors and inhibitors is likely to be of great importance in B cell signaling, and it is of particular importance in the context of our model. Only indirect information is, however, available from experiments (Matsuuchi & Gold, 2001). In the following we therefore develop a mathematical model to synthesize the available information and to derive a likely structure of the BCR arrangements on the B cell membrane.

Experiments suggest that IgMs interact with each other and form small clusters (Matsuuchi & Gold, 2001). Whilst only one side of the helix appears to mediate direct IgM-IgM interactions, the other side has been found to be responsible for interactions with Igα/Igβ (Matsuuchi & Gold, 2001) which are here assumed to also lead to IgM-IgM interactions, though in the form IgM-Igα/Igβ-Igα/IgβIgM. Each IgM is thus assumed to interact non-covalently with two other IgMs. It is currently unclear how Igα/Igβ binds to IgM (Matsuuchi & Gold, 2001) because each IgM can in principle bind to either one or two Igα/Igβ heterodimers. However, given that IgM can only get to the surface when Igα/Igβ covers the polar helix surface and the ratio of IgM to Igα/Igβ is 1:1 (Schamel & Reth, 2000) each Igα/Igβ must either cover both binding sites or each Igα/Igβ binds only one binding site per IgM but binds to two IgMs. It is likely that, if geometrically possible, both forms exist. In an IgM pair, however, each Igα/Igβ is most likely to be shared between two IgM because each IgM pair is then bridged by two instead of three non-covalent bonds and no

self-interactions between Igα/Igβ heterodimers are required. Moreover, such a configuration is in agreement with FRET experiments which show that Igα chains are not in close proximity to each other (Tolar *et al.*, 2005) as would be the case if the heterodimers interacted with each other. Because of the lower number of non-covalent bonds, the direct interaction between two IgMs is likely to be stronger than the interaction via Igα/Igβ, and the IgM polymer will break preferentially at the Igα/Igβ interaction.

13.2.1 IgM cluster size distribution

In order to facilitate the analysis we will initially ignore the details of the IgM-IgM interaction and instead consider IgM monomers that can each interact with two other IgM monomers directly, with equal binding probability p. If, in a first step, we also ignore any ring formation then, according to (Flory, 1953; van der Gucht, 2004), we can estimate the cluster length distribution as

$$c(n) = \varrho(1-p)^2 p^{n-1} \tag{13.1}$$

where $c(n)$ is the density (number per area) of clusters of length n, ϱ is the total IgM density (IgM per area), and p is the probability of forming a bond between two monomers. The

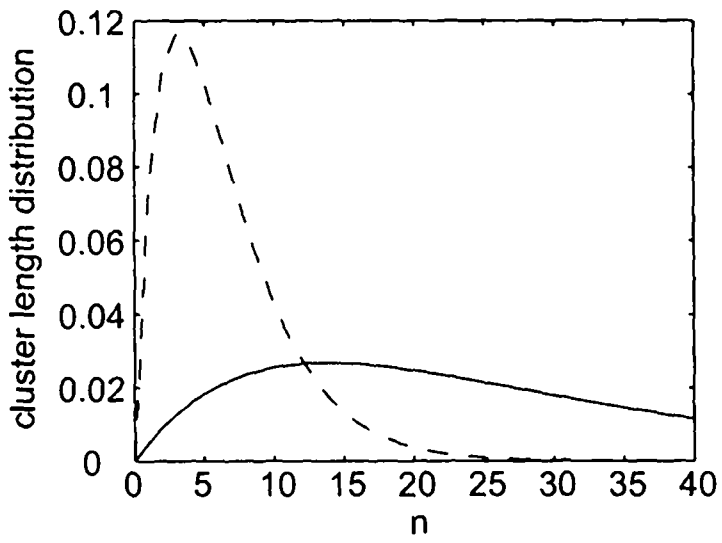


Figure 13.4: **Cluster length distribution.** The cluster length distribution $c(n)$ weighted by the length n and normalized with the IgM density ϱ, $\frac{nc(n)}{\varrho}$, dependent on the cluster length n for binding probabilities $p = 0.93$ (continuous line) or $p = 0.73$ (broken line).

number density, $< n >$, of clusters follows as

$$< n >= \frac{\sum_{n=1}^{\infty} nc(n)}{\sum_{n=1}^{\infty} c(n)} = \frac{\varrho(1-p)^2 \sum_{n=1}^{\infty} np^{n-1}}{\varrho(1-p)^2 \sum_{n=1}^{\infty} p^{n-1}} = \frac{\frac{1}{(1-p)^2}}{\frac{1}{1-p}} = \frac{1}{1-p}, \tag{13.2}$$

and $nc(n)$ attains a maximum at $n = -\frac{1}{ln(p)}$, which is the polymer length into which the majority of monomers organizes. A plot of the $nc(n)$ curve for two different values of p is shown in Figure 13.4.

The binding probability p can be related to the binding constant K (van der Gucht, 2004) by observing that the total density of all bonds is given as $[B] = p\varrho$ and the density of all free sites on the monomers is $[F] = 2(1-p)\varrho$ such that

$$K = \frac{k_+}{k_-} = \frac{[B]}{[F]^2} = \frac{p\varrho}{(2(1-p)\varrho)^2} = \frac{p}{4(1-p)^2\varrho}. \tag{13.3}$$

Three-dimensional protein-protein on-rates are in the range $10^6 - 10^7$ M^{-1}; the two-dimensiona counterpart can therefore be expected to be of the order $k_{on} \in [0.1 - 1]$ μm^2 (using $K_d^{2d} = \eta K_d^{3d}$ and $\eta = 1.2 \times 10^{19} m^{-2} M^{-1}$ (Bell *et al.*, 1984; Moy *et al.*, 1999)). Due to diffusion limitations we in general expect $k_+ \neq k_{on}$. According to Keizer (Keizer, 1982) the effect of diffusion limitations on the two-dimensional on-rate can be estimated as

$$k_+ = \frac{4\pi D k_{on}}{k_{on} K_0(\sqrt{\frac{k_+\varrho}{D}}d) + 4\pi D} \tag{13.4}$$

where $K_0(x)$ is the zero-order modified Bessel function of the second kind. $D \sim 0.1$ $\frac{\mu m^2}{s}$ represents the TCR-based estimate for the diffusion constant (Favier *et al.*, 2001), and $d \sim 0.02$ μm the lateral distance on which receptors can interact. The implicit equation 13.4 can be solved numerically (Fig. 13.5); this shows that for $k_{on} \in [0.1 - 1]$ μm^2 s^{-1} and $\varrho \in [50, 500]$ μm^{-2}, $k_+ \sim 0.1$ μm^2 s^{-1}. In order to determine $< n >$ we need to estimate the physiological values of the employed parameters. The approximate IgM density on B cell surfaces is $\varrho = 500 \mu m^{-2}$. While the affinity for BCR-BCR interactions has not yet been determined it is likely to be rather low (as observed for self-interactions between other large membrane proteins (Li *et al.*, 2003)) such that the off-rate k_- will be high ($k_- \sim 1$ s^{-1}) and $K \sim 0.1$ μm^2.

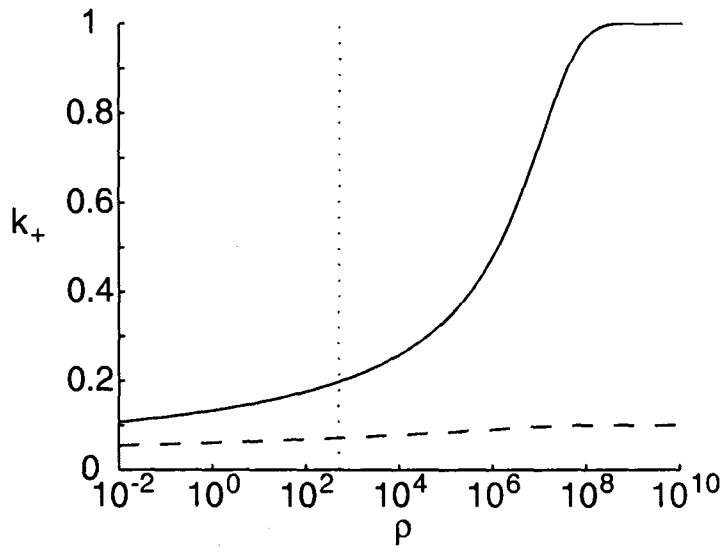


Figure 13.5: **Estimate of diffusion effects on the BCR-BCR binding rate.** Receptor density-(ϱ) dependent on-rate (k_+) if the on-rate without limitations is either $k_{on} = 1$ (solid line) or $k_{on} = 0.1$ (dashed line). The dotted line marks the estimated BCR density on the B cell surface.

For sufficiently large ϱ it follows from (13.3) that $p = 1 - (4K\varrho)^{-0.5} = 1 - (4 \times 0.1 \times 500)^{-0.5} = 0.93$ (van der Gucht, 2004). Accordingly the number density of IgM clusters on the B cell surface in the absence of any ring formation would be $< n >= \frac{1}{1-p} \approx 2\sqrt{K\varrho} = 14.3$ and the distribution peaks at $n = -\frac{1}{ln(p)} = 13.8$ (Fig. 13.4). At lower IgM density p is much smaller and has to be determined from $p = 1 + \frac{1}{8\rho K} - \sqrt{(1 + \frac{1}{8\rho K})^2 - 1}$. If IgM is reduced to 5% of its normal density then for $K = 0.1\ \mu m^2$, $p = 1 + \frac{1}{20} - \sqrt{(1 + \frac{1}{20})^2 - 1} = 0.73$ such that $< n >= 3.7$ and the distribution peaks at $n = -\frac{1}{ln(p)} = 3.2$ (Fig. 13.4). The chains therefore shorten at lower receptor density approximately with the square root of ϱ.

A reduction in IgM density has been observed for anergic MD4 B cells that are specific for hen egg lysozyme (Goodnow *et al.*, 1988; Goodnow *et al.*, 1991). Anergic B cells are characterized by a lower responsiveness towards an immunogenic antigen challenge and arise when B cells are exposed to a relatively weak, co-stimulatory-deficient antigenic stimulus for sufficiently long time (Goodnow *et al.*, 1988; Goodnow *et al.*, 1991; Goodnow, 1996). The basis of their unresponsiveness is so far not understood because proteins important for BCR-induced signal transduction such as Syk, Lyn, CD45, and SHP-1 are expressed at a normal level and with normal basal activity (Weintraub *et al.*, 2000). The reduced IgM density may explain their unresponsiveness if IgM clustering is indeed crucial for B cell

signal initiation.

13.2.2 The impact of ring formation on IgM cluster organization

So far we have neglected any ring formation but IgM clusters on the B cell membrane have been suggested to form similar structures as secreted IgM which would include the formation of closed rings (Matsuuchi & Gold, 2001). We can extend the above model to include ring formation, and we obtain for the length distribution of closed chains

$$c_c(n) = \varrho(1-p)^2 p^{n-1} p_r \tag{13.5}$$

and for the length distribution of open chains

$$c_o(n) = \varrho(1-p)^2 p^{n-1}(1-p_r) \tag{13.6}$$

where p_r is the probability that a chain closes into a ring. For small n, p_r can be expected to be very low. Experimental data is, however, not available to judge whether (and if, how) p_r depends on n at larger polymer length. We therefore only consider the simplest case, that p_r does not depend on n. We note by comparison with (13.2) that in this case the formation of rings does not affect the number density $< n >$ of clusters which is given by

$$< n >= \frac{\sum_{n=1}^{\infty} n(c_c(n) + c_o(n))}{\sum_{n=1}^{\infty} c_c(n) + c_o(n)} = \frac{1}{1-p}. \tag{13.7}$$

The probability p_r with which a chain closes therefore only determines the fraction, F, of chains that are closed as can be seen from

$$F = \frac{\sum_{n=1}^{\infty} c_c(n)}{\sum_{n=1}^{\infty} c_c(n) + c_o(n)} = \frac{\sum_{n=1}^{\infty} \varrho(1-p)^2 p^{n-1} p_r}{\sum_{n=1}^{\infty} \varrho(1-p)^2 p^{n-1}} = p_r. \tag{13.8}$$

13.2.3 The impact of co-receptors on IgM clustering

We have so far neglected co-receptors that have been found to interact with the resting BCR. For example CD22, an inhibitory receptor, has been noted to interact with membrane IgM both at the receptor stem as well as at the "arms" (Zhang & Varki, 2004). If CD22 binds to the arms it is unlikely to affect BCR clustering. In case it interacts with the stem it

may either intercalate and become integrated into the polymer or it may block interactions between IgMs and thus prohibit IgM clustering. If CD22 blocks receptor interactions it may do so either only on one or on both sites. Given that ring formation does not affect the number density $< n >$, we neglect ring formation in the following and modify Eq 13.1 to

$$c(n) = \varrho(1 - p(1 - p_I)^i)^2(p(1 - p_I)^i)^{n-1} \tag{13.9}$$

where p_I is the probability for an inhibitor to bind to an IgM site and i is the number of inhibitor interaction sites per IgM. The number density in the presence of co-receptors follows as

$$< n >= \frac{\sum_{n=1}^{\infty} nc(n)}{\sum_{n=1}^{\infty} c(n)} = \frac{1}{1 - p(1 - p_I)^i}. \tag{13.10}$$

We therefore see that for $p_I \rightarrow 1$ the cluster size will be reduced substantially. Experiments find that 15% of all IgM are bound by CD22 (Zhang & Varki, 2004), and $(1 - p_I)^i = 0.85$ is therefore a reasonable estimate; other co-receptors that bind with a lower probability will make up for the fraction of CD22 that binds to the antibody arms. For parameter values as used before we then have $< n >= \frac{1}{1-p(1-p_I)^i} = 4.8$. We conclude that the model predicts IgM clusters of similar size as found in experiments if the IgM-IgM affinity is about K=0.1 μm^2.

If the receptor density is reduced then the ratio of inhibitor to IgM increases and so will the fraction of IgM that is bound by inhibitor. As a consequence the cluster size will shrink even further.

13.2.4 Igα/Igβ co-clustering

Antigen-bound IgMs translate antigen binding into cellular signaling via Igα/Igβ and co-precipitation studies show that each IgM binds on average one Igα/Igβ complex (Schamel & Reth, 2000). It has been found in experiments that a large fraction of IgMs (50 – 80%) on anergic B cells does not firmly interact with Igα/Igβ (Vilen *et al.*, 1999). We can use our modelling approach to judge whether this is a consequence of IgM downregulation.

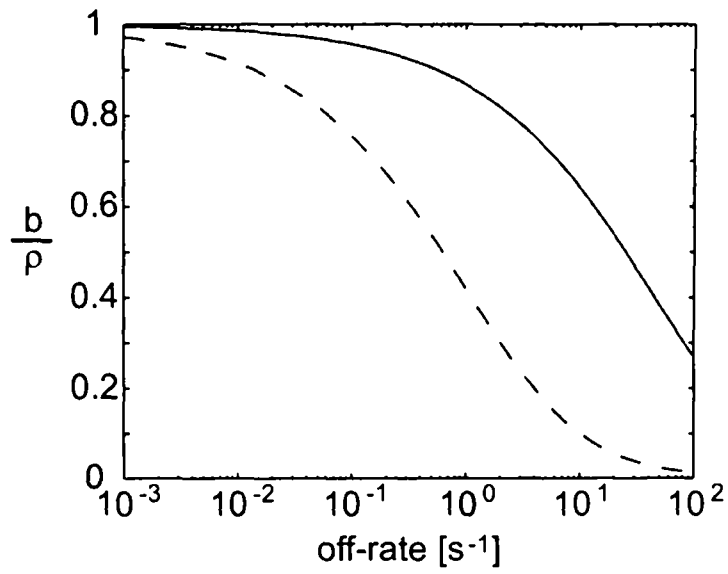


Figure 13.6: **Fraction of IgM bound to Igα-Igβ.** Fraction of IgM bound to Igα-Igβ ($\frac{b}{\varrho}$) dependent on the off-rate l_- of the interaction if the IgM density is normal ($\varrho = 500\mu\text{m}^{-2}$ - continuous line) or reduced to 5% ($\varrho = 25\mu\text{m}^{-2}$ - broken line).

Monomeric interactions between IgM (m) and Igα/Igβ (a) can be modelled as

$$\dot{b} = l_+ma - l_-b \tag{13.11}$$

where b denotes the density of IgM-Igα/Igβ complexes, and l_+ and l_- are the rate constants for the binding and unbinding reactions respectively. Since IgMs and Igα/Igβ are transported together to the cell surface (Hombach *et al.*, 1990), the total Igα/Igβ density is taken to be equal to the receptor density, ϱ. We can then rewrite (13.11) as

$$\frac{\dot{b}}{\varrho} = l_+(1 - \frac{b}{\varrho})^2 - l_-\frac{b}{\varrho}. \tag{13.12}$$

In equilibrium ($\frac{\dot{b}}{\varrho} = 0$) we then have

$$\frac{b}{\varrho} = 1 + \frac{K_d}{2\varrho} - \sqrt{(1 + \frac{K_d}{2\varrho})^2 - 1} \tag{13.13}$$

where we set $K_d = \frac{l_-}{l_+}$. For the forward rate constant the estimate by Keizer can be used again such that $l_+ = k_+ = 0.1\mu\text{m}^2\text{s}^{-1}$ (Fig. 13.5). No experimental estimate exists for the off-rate but plotting $\frac{b}{\varrho}$ against the off-rate l_- reveals that, as long as the receptor density is high ($\varrho = 500\mu\text{m}^{-2}$), for the physiological low-affinity range ($l_- \sim 1\ \text{s}^{-1}$), $\frac{b}{\varrho} > 0.8$ (Fig. 13.6, continuous line), which means that more than 80% of all monomeric IgM is bound by

Igα/Igβ. The physiological figure may even be higher if conformational constraints in the IgM polymer further reduce IgM-Igα/Igβ unbinding. For $\varrho = 25\mu\text{m}^{-2}$, on the other hand, we find that, in agreement with experiments (Vilen *et al.*, 1999), less than 50% of all IgM is bound by Igα/Igβ, and, given that at lower IgM density there is substantially less IgM polymer formation, further constraints are unlikely to increase this figure.

A reduction in the IgM density therefore reduces both IgM-IgM and IgM-Igα/Igβ interactions. The latter not only reduces the number of signaling proteins in the vicinity of the receptor but also reduces the fraction of IgM which can interact with other IgMs on both sides; this will further reduce IgM clustering, below the value estimated in the previous section. If, as we argue below, BCR clustering is important for B cell signaling then these two effects together may explain the experimentally observed lower responsiveness of anergic B cells.

13.3 B cell activation by soluble monomeric antigen

Following the above analysis we will assume IgMs to be organized into small open polymeric chains on the cell surface which comprise Igα/Igβ and which are limited in size by binding of inhibitory co-receptors that will downregulate any spontaneous antigen-independent B cell activation. Inhibitory receptors can interact with IgM not only at the stem but also at the arms, and according to our model, soluble antigen of sufficient size blocks the latter interaction (by increasing the distance between inhibitory receptor and the antibody arm) and thereby access of inhibitory receptors to the BCR bound kinases (Fig. 13.2A). In the absence of inhibitors the BCR is activated spontaneously (Wienands *et al.*, 1996; Rolli *et al.*, 2002). BCR signaling is generally assumed to be initiated by autophosphorylation of Src-kinases at the Ig-α/Ig-β heterodimer and therefore at least one cluster with two neighbouring, fully protected Ig-α/Ig-β will need to form in order to initiate B cell signaling (Fig. 13.2B). The activation of a very small number of Ig-α/Ig-β pair(s) can be expected to be sufficient for a B cell response because T cells are very sensitive to even very low

densities of peptide-MHC complexes. Moreover, B cell signaling can be "stabilized" by signaling-dependent inhibitor inactivation (possibly by activation of the NADPH oxidase) and downstream signals can be amplified by feedback loops (Reth & Brummer, 2004). A maximal response can be expected to be attained once essentially all receptors are bound by antigen. B cell responsiveness should therefore correlate with the extent of antigen binding. In the following we estimate the affinity and concentration dependency of antigen binding to pre-formed BCR clusters and compare the predictions of the model to experimental data.

13.3.1 The affinity and concentration dependency of antigen binding to pre-formed BCR clusters

The probabilities P_1^{eq} and P_2^{eq} that in equilibrium a randomly chosen receptor is occupied by one or two bound antigens respectively can be determined as (Appendix B.5)

$$P_1^{\mathrm{eq}} = 2K_a\, c/(1+K_a\, c)^2\,, \tag{13.14}$$

$$P_2^{\mathrm{eq}} = (K_a\, c)^2/(1+K_a\, c)^2\,, \tag{13.15}$$

which depend only on the equilibrium association constant

$$K_a \equiv k_{\mathrm{on}}/k_{\mathrm{off}}\,. \tag{13.16}$$

and the antigen concentration

$$c = (N_L - (P_1^{\mathrm{eq}} + 2P_2^{\mathrm{eq}})N_R))/V\,, \tag{13.17}$$

where N_L denotes the total number of antigens, N_R the total number of B cell receptors and V the total volume. Using the substitution $z = P_1^{\mathrm{eq}} + 2P_2^{\mathrm{eq}}$ or the method of resultants (Eisenbud, 1995) Eqs. 13.14, 13.15, 13.17 can be solved exactly for P_1^{eq}, P_2^{eq}. The method of resultants can be used to determine the intersection of two polynomials in two variables also when the problem cannot be simplified by appropriate substitutions. Because of its general applicability the technique will be discussed and used here.

The idea of the technique is as follows. Consider two polynomials in two variables, $f(x,y)$, $g(x,y)$. We want to find the set of pairs (x,y) such that $f(x,y) = 0$, $g(x,y) = 0$.

Think of $f(x,y)$ and $g(x,y)$ as polynomials in x with coefficients that are polynomials in y. For any given value in x, $f(x,y)$ and $g(x,y)$ both equal zero if and only if as polynomials in y, $F(y)$ and $G(y)$, they have a common root. The method of resultants enables us to determine these values of x for which this holds. Two polynomials $F(y)$, $G(y)$ have common root $R(y) = y - \alpha$ if and only if

$$F(y) = R(y)F_1(y) \qquad deg(F_1(y)) < deg(F(y)) \tag{13.18}$$

$$G(y) = R(y)G_1(y) \qquad deg(G_1(y)) < deg(G(y)). \tag{13.19}$$

But then $F(y)G_1(y) = G(y)F_1(y)$. This implies that there is a linear dependency, in the vector space of polynomials in y, amongst $F(y), yF(y), y^2F(y), ..., y^{deg(G_1(y))}F(y)$, and $G(y)$, $yG(y)$, $y^2G(y)$, ..., $y^{deg(F_1(y))}G(y)$. This can be interpreted as a $deg(F) + deg(G)$ square matrix with vanishing determinant.

In our case we have, by combining Eq. 13.17 with Eq. 13.14 and Eq. 13.15, and by setting $x = P_1^{eq}$, $y = P_2^{eq}$ and $l = \frac{N_L}{V}$, $r = \frac{N_R}{V}$,

$$\begin{aligned} f(x,y) &= K^2r^2x^3 - 2Kr(1 + K(l - 2ry))x^2 + ((1 + K(l - 2ry))^2 + 2Kr)x \\ &\quad -2K(l - 2ry) \end{aligned} \tag{13.20}$$

$$\begin{aligned} g(x,y) &= K^2r^2(y-1)x^2 + Kr(-2y(1 + K(l - 2ry)) + 2K(l - 2ry))x \\ &\quad +y(1 + K(l - 2ry))^2 - K^2(l - 2ry)^2. \end{aligned} \tag{13.21}$$

Rewriting the polynomials as $f(x,y) = \sum_{i=0}^{i=3} a_i(y)x^i$, $g(x,y) = \sum_{i=0}^{i=3} r_i(y)x^i$ we obtain for the matrix

$$S = \begin{pmatrix} a_0 & a_1 & a_2 & a_3 & 0 \\ 0 & a_0 & a_1 & a_2 & a_3 \\ b_0 & b_1 & b_2 & 0 & 0 \\ 0 & b_0 & b_1 & b_2 & 0 \\ 0 & 0 & b_0 & b_1 & b_2 \end{pmatrix} \tag{13.22}$$

We obtain as determinant

$$\det(S) = K^4r^4(-4K^2r^2y^2 + ((1 + Kl)^2 + 4Kr(1 + Kr))y - K^2r^2l^2) = 0. \tag{13.23}$$

The zeros of this polynomial of degree 2 can be determined exactly, yielding two solutions for y. Only one of the two solutions is, however, in the range between zero and one, and

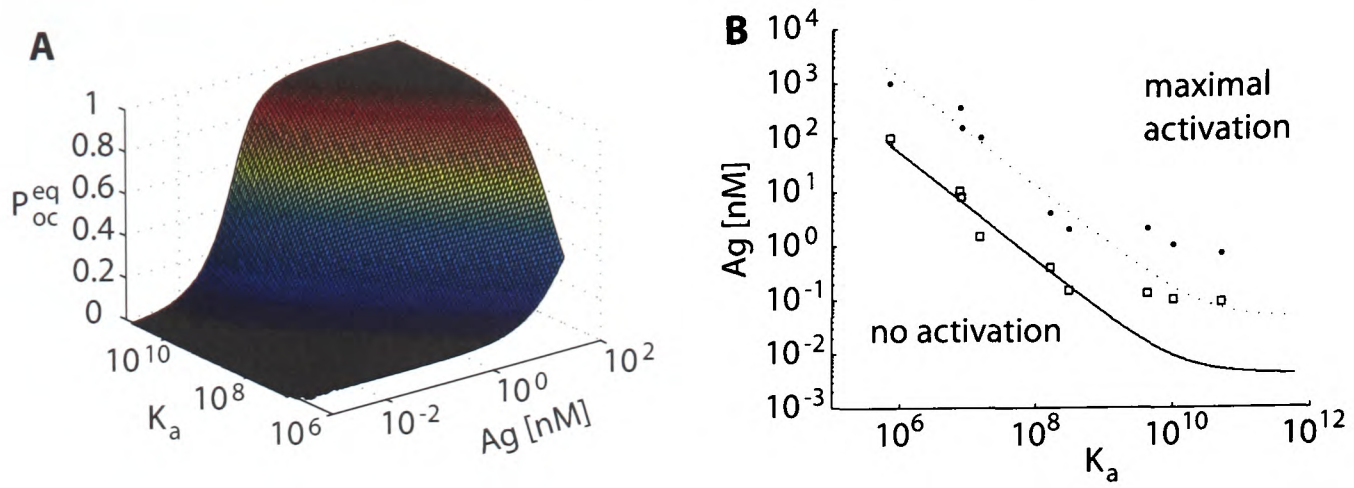


Figure 13.7: **Antigen concentration and affinity dependency of B cell activation by soluble monomeric antigen. (A)** Fraction of BCRs bound by antigens in equilibrium, $P_{\mathrm{OC}}^{\mathrm{eq}}$, for different antigen concentrations, Ag, and affinities, K_a. **(B)** Antigen concentration-affinity phase plane. The lower graph (solid line) marks the antigen concentration and affinity pairs at which 10% of all BCRs are bound by antigen, and separates the regions where B cell activation is possible (above the graph) from where it is not (below the graph). Above the higher graph (dotted line), which marks the antigen concentration and affinity pairs at which 80% of all BCRs are bound by antigen, B cells are maximally activated while in between the two graphs affinity discrimination is possible. The symbols represent the experimentally determined thresholds (squares) and ceilings (dots) for B cell activation and have been read off from published experimental work (Batista & Neuberger, 1998).

this is our solution for P_2^{eq}. By inserting P_2^{eq} either in equation 13.14 or equation 13.15 we find P_1^{eq}, and we obtain as unique solution between zero and one

$$P_1^{\mathrm{eq}} = \frac{K(l-2rP_2^{\mathrm{eq}})(P_2^{\mathrm{eq}}-1)+P_2^{\mathrm{eq}}+\sqrt{P_2^{\mathrm{eq}}}}{Kr(P_2^{\mathrm{eq}}-1)}, \tag{13.24}$$

$$P_2^{\mathrm{eq}} = \frac{p-\sqrt{p^2-4q}}{2}, \tag{13.25}$$

where

$$p=\frac{(1+Kl)^2+4Kr(1+Kr)}{4K^2r^2}, \quad q=\frac{l^2}{4r^2}. \tag{13.26}$$

The occupation probability P_{OC} for a single binding site is given by $P_{\mathrm{OC}} = \frac{1}{2}P_1 + P_2$. The equilibrium occupation probability $P_{\mathrm{OC}}^{\mathrm{eq}} = \frac{1}{2}P_1^{\mathrm{eq}} + P_2^{\mathrm{eq}}$, which is equivalent to the fraction of receptors that is bound by antigen in equilibrium, is plotted in Figure 13.7 for varying antigen concentration and affinity.

13.3.2 Comparison of model predictions with experimental data

Experiments carried out to determine the antigen concentration and affinity dependency of B cell reactivity showed that B cells can discriminate between a wide range of binding affinities ($K_a^{3d} \in [10^6, 5 \times 10^{10}]$ M^{-1}) and antigen concentrations (0.1-100 nM); at higher antigen concentrations unspecific responses can be observed which can be accounted for by fluid phase uptake (Batista & Neuberger, 1998). The experiments used 10^5 B cells each carrying an estimated 5×10^4 BCRs ($N_R = 5 \times 10^9$) in a reaction volume $V = 2 \times 10^{-4}$ l. The analysed antigen concentration range of 0.1-100 nM corresponds to about $N_L = [10^{10}, 10^{13}]$ antigens per experiment.

The range in which the model predicts the fraction of antigen-bound receptors to vary can be seen to correlate with the experimentally observed concentration dependent range of affinity discrimination (Fig. 13.7). The discrimination range (e.g. the distance between the two curves in Fig. 13.7B) is independent of the exact antigen concentration as is also observed in the corresponding experiments (Batista & Neuberger, 1998). While the model predicts that the affinity threshold could fall below $K_a = 10^5$ M if the antigen concentration was sufficiently high, this prediction cannot be tested in experiments because antigen concentrations that exceed 100 nM lead to unspecific responses.

The quantitative analysis further reveals that the experimentally observed thresholds and ceilings for a B cell response to antigen correspond to a certain occupation of receptors by antigen. Thus a response is observed when 10% of the BCRs are engaged by antigen (and 0.2% are engaged by two antigens), and a maximal response is obtained when about 80% of the BCRs are engaged by antigen (25% are engaged by two antigens). The threshold occupation of 10% is in good agreement with a previous estimate made in a different experimental system (Vogelstein *et al.*, 1982), and can therefore be considered as independent of the particular details of the system studied.

The predicted threshold occupation required for B cell activation depends on the total number of IgM pairs that interact via the Igα/Igβ heterodimer, and therefore on the total

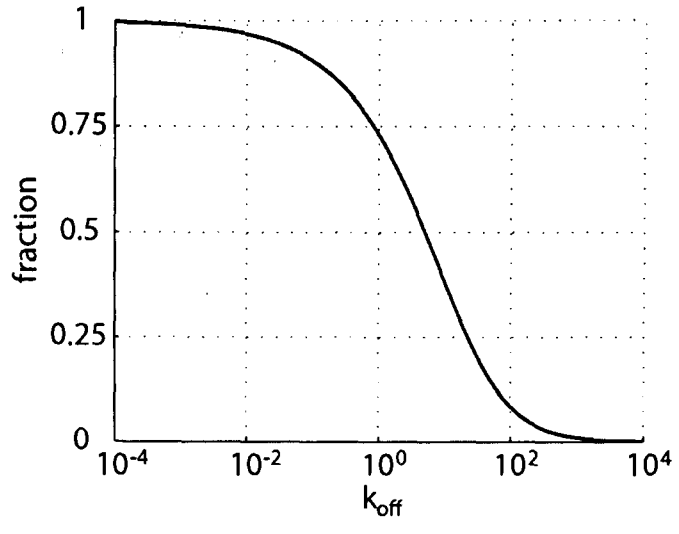


Figure 13.8: **Affinity dependent fraction F of IgM pairs that interact via Igα/Igβ heterodimers.** The fraction, $F = \frac{D}{T}$, was determined from $\frac{dD}{dt} = k_{on}(T-D)^2 - k_{off}D = 0$ where D denotes the density of IgM pairs that interact via Igα/Igβ heterodimers, $T = 100\mu m^{-2}$ is used for the total density of IgM-IgM pairs, $k_{on} = 0.1\mu$m s^{-1} is the apparent on-rate for the IgM_2-IgM_2 interactions via Igα/Igβ heterodimers; this rate represents the standard 2-dimensional on-rate and takes diffusion limitations into account (Keizer, 1982). That IgM pairs, which interact via Igα/Igβ heterodimers, require two non-covalent interactions is, however, neglected. k_{off} is the off-rate.

receptor number and the fraction of IgM pairs that are formed via the Igα/Igβ heterodimer. The affinity of the IgM-Igα/Igβ interaction is unknown but BCR clusters have been estimated to comprise about 5-6 receptors on average (Schamel & Reth, 2000) which would suggest that at most two thirds of all IgM interact with other IgMs via the Igα/Igβ heterodimer if we assume that the direct IgM-IgM interaction is stronger as discussed above. This corresponds to a low IgM-Igα/Igβ affinity ($k_{off} \sim 1 - 10$ s^{-1} - Fig. 13.8) as is realistic for such interaction. For a cell with 5×10^4 receptors an antigen occupation of 10% then gives rise to an expected number of $5 \times 10^4 \times 0.1^2 \times \frac{2}{3} \times \frac{1}{2} \times \frac{1}{2} \sim 80$ IgM-IgM pairs that share two Igα/Igβ heterodimers and where both IgM are bound by at least one antigen on the appropriate side. In a further $5 \times 10^4 \times 0.002 \times \frac{2}{3} \times \frac{1}{2} \sim 33$ IgM-IgM pairs at least one IgM is bound by two antigens. A total number of about 120 protected IgM pairs per cell may appear high for a threshold value. However, antigen processing may be inefficient such that this number of antigen-bound receptors may be required to generate a sufficient number of pMHC to activate the T cell. Moreover, we note that the number of clusters in

which two neighbouring IgM-IgM pairs are both protected by antigen binding is no larger than $5 \times 10^4 \times 0.1^4 \times \frac{1}{2} \times \frac{1}{6} \sim 0.4$. Whether such local clustering of protected receptors is necessary for B cell activation or whether the low density of isolated protected IgM pairs is sufficient cannot be judged from current experimental data. Both alternative explanations are, however, within a realistic physiological range, and more experiments will be required to distinguish between these two possibilities.

The difference between modelling and experimental results at high affinities can be accounted for by the different read-outs in model and experiments. While the model predicts the level of B cell activation (and thus signaling) the experiments determine the level of B-cell dependent T cell activation, i.e., the level of antigen presentation by B cells. At high affinity only few antigens are required to occupy 10% of all receptors (and activate the B cell) but the total available antigen amount is then too low for successful antigen presentation to T cells. The low experimental ceiling of 80% occupation observed in experiments can be accounted for by the saturation of antigen presentation to T cells.

We conclude that the model predictions are in agreement with available experimental results. This model therefore demonstrates that (and how) soluble, monomeric antigen can trigger B cell activation. Measurements of the extent of phosphorylation of proximal signaling proteins such as Syk in response to different antigen concentrations and affinities will be important in order to test the model predictions with more accurate B-cell-specific (and T-cell independent) affinity thresholds and ceilings.

13.4 Surface-bound antigen at high density - a grand canonical ensemble description

As a model for membrane antigen, experiments have been carried out with antigen being either displayed on small particles (beads) or tethered on plastic surfaces (Batista & Neuberger, 2000). This experimental system is ideal to test the hypothesis that B cell activation is elicited by receptor-inhibitor segregation with surface antigen since detailed data on the affinity dependence of B cell responsiveness are available and due to the artifi-

cial way in which the antigen is displayed interactions between other cell surface molecules (such as integrins) do not affect the conclusions. Antigen-dependent B cell signaling can thus be assumed to be mainly triggered by the BCR itself and not by early integrin binding, which may otherwise activate cellular transport processes. Moreover, given the high antigen density, kinetic constraints in establishing a stable contact zone (Bell, 1978) can be ignored.

The immobilization of antigen on a surface by a chemical linkage will result in two differences as compared to soluble or cell membrane-bound antigen. First of all because the spacing between antigen is fixed and random, BCRs are unlikely to engage both binding sites. Secondly, given the fixed spacing, pre-formed BCR clusters (Schamel & Reth, 2000) are unlikely to remain intact and protection from inhibitors will therefore require a macroscopic separation of receptors and inhibitors, that is, the expulsion of the inhibitors from the contact zone. Molecular crowding may drive such an expulsion (Fig. 13.3), in which case B cell responsiveness should correlate with the equilibrium number of receptors and inhibitors in the contact zone.

13.4.1 Derivation of the equilibrium distribution of receptors and inhibitors

The patterning of surface receptors has been studied in great detail for the T cell synapse (Qi *et al.*, 2001; Burroughs & Wulfing, 2002; Lee *et al.*, 2002; Weikl & Lipowsky, 2004) using a variety of methods, including systems of partial differential equations (Qi *et al.*, 2001; Burroughs & Wulfing, 2002) as well as a lattice gas and grand-canonical description (Weikl & Lipowsky, 2004). The affinity dependent equilibrium number of B cell receptors (BCRs) and inhibitors in the contact zone can best be estimated with the help of statistical mechanics, and in particular by employing the grand canonical ensemble. We define Λ_b as the maximal number of proteins that can be accommodated in the contact zone (where the receptor can interact with antigen) and Λ_{ub} as the maximal number of proteins that can be accommodated on the remaining part of the B cell (where such interactions are impossible). The B cell surface can thus be modelled as a lattice with $\Lambda = \Lambda_b + \Lambda_{ub}$ lattice sites. Each

lattice site can either be free or occupied by either a receptor or an inhibitor; sites that are occupied by other B cell surface proteins count as empty. If a receptor occupies one of the Λ_b lattice sites in the contact zone then it binds antigen with a binding energy of magnitude $U_R > 0$, an inhibitor binds with a binding energy of magnitude $U_I > 0$. The contact zone with the target cell is thus modelled as an affinity field of the size of the contact zone which attracts the BCR (and possibly also the inhibitor). Direct interactions between BCR and inhibitor are ignored in this model up to sterical exclusion.

In the grand canonical ensemble (Guénault, 1995) the probability that N_R^b receptors are bound in the contact zone is proportional to $\exp[(\mu_R + U_R)N_R^b/kT]$, and the probability that N_R^{ub} receptors reside outside the contact zone is proportional to $\exp[\mu_R N_R^{ub}/kT]$; k is the Boltzmann factor and μ_j refers to the chemical potential of the component j. Accordingly, the probability that N_R^b receptors are bound in the contact zone while N_R^{ub} receptors reside outside the contact zone is proportional to the product of these two terms, $W(N_R^b, N_R^{ub}) = \exp[(\mu_R + U_R)N_R^b/kT]\exp[\mu_R N_R^{ub}/kT]$. The probability that in addition there are N_I^b inhibitors in and N_I^{ub} inhibitors outside the contact zone is proportional to

$$\prod_j W(N_j^b, N_j^{ub}) = \prod_j \exp[(\mu_j + U_j)N_j^b/kT]\exp[\mu_j N_j^{ub}/kT] \tag{13.27}$$

with $j = R, I$. The grand canonical partition function of the whole system is the sum over all configurations weighted with the corresponding functions $W(N_j^b, N_j^{ub})$

$$Z = \prod_j \sum_{N_j^b, N_j^{ub}} \Omega(N_R^b, N_R^{ub}, N_I^b, N_I^{ub}) W(N_j^b, N_j^{ub}), \tag{13.28}$$

where $N_j^b \in [0, \Lambda_b]$; $N_j^{ub} \in [0, \Lambda_{ub}]$ and $\Omega(N_R^b, N_R^{ub}, N_I^b, N_I^{ub})$ is the number of ways the $N_R^b, N_R^{ub}, N_I^b, N_I^{ub}$ particles can be arranged on the lattice. Note that Z is calculated from the product of the sum of all receptor and inhibitor configurations because only this will lead to the inclusion of all possible combinations. For illustration consider the difference between $\prod_{j=1}^2 \sum_{i=1}^2 a_{ij} = (a_{11} + a_{21})(a_{12} + a_{22}) = a_{11}a_{12} + a_{11}a_{22} + a_{21}a_{12} + a_{21}a_{22}$ and $\sum_{i=1}^2 \prod_{j=1}^2 a_{ij} = a_{11}a_{12} + a_{21}a_{22}$. Combining Eqs. 13.27 and 13.28 we obtain the standard

representation of the grand canonical partition function as

$$Z = \prod_j \sum_{N_j^b, N_j^{ub}} \Omega(N_R^b, N_R^{ub}, N_I^b, N_I^{ub}) \exp(\mu_j N_j^b/kT) \exp(U_j N_j^b/kT) \exp(\mu_j N_j^{ub}/kT) \tag{13.29}$$

with $j = R, I$; $N_j^b \in [0, \Lambda_b]$; $N_j^{ub} \in [0, \Lambda_{ub}]$; $\Omega(N_R^b, N_R^{ub}, N_I^b, N_I^{ub})$ is the number of ways the N_R^b receptors and N_I^b inhibitors can be distributed inside and the N_R^{ub} receptors and N_I^{ub} inhibitors can be arranged outside the contact zone. k is the Boltzmann factor and μ_j refers to the chemical potential of the component j. Eq. 13.29 can be rewritten as

$$Z = (1 + \zeta_R \exp(U_R/kT) + \zeta_I \exp(U_I/kT))^{\Lambda_b} (1 + \zeta_R + \zeta_I)^{\Lambda_{ub}}, \tag{13.30}$$

where we used $\zeta_j = \exp(\mu_j/kT)$ to simplify the notation. Since lattice sites must either be free or occupied (by one receptor or one inhibitor) the derivation of Eq. 13.30 from Eq. 13.29 follows a similar route as used for Fermi-Dirac gases (Guénault, 1995); by multiplying out both Eqs. 13.29 and 13.30 it can be seen that both notations for Z add all possible microstates, that is the contributions of all possible combinations of unoccupied, receptor-occupied and inhibitor-occupied sites.

Again by using standard techniques (Guénault, 1995) averages can be expressed in terms of Z and its derivatives. Thus the mean density of bound receptors can be determined as

$$< N_R^b >= Z^{-1} \prod_j \sum_{N_j^b, N_j^{ub}} N_R^b W(N_j^b, N_j^{ub}) \Omega(N_R^b, N_R^{ub}, N_I^b, N_I^{ub}) = kT Z^{-1} \partial Z/\partial U_R. \tag{13.31}$$

Using Eqs. 13.30 and 13.31 one has $\bar{n}_R^b = \frac{\bar{N}_R^b}{\Lambda_b} = \frac{kT \partial \ln Z}{\Lambda_b \partial U_R} = \frac{\zeta_R \exp(U_R/kT)}{1+\zeta_R \exp(U_R/kT)+\zeta_I \exp(U_I/kT)}$ and similarly $\bar{n}_I^b = \frac{\bar{N}_I^b}{\Lambda_b} = \frac{kT \partial \ln Z}{\Lambda_b \partial U_I} = \frac{\zeta_I \exp(U_I/kT)}{1+\zeta_R \exp(U_R/kT)+\zeta_I \exp(U_I/kT)}$. The ratio of receptor to inhibitor in the contact zone is then given as

$$\nu = \frac{\bar{n}_R^b}{\bar{n}_I^b} = \frac{\zeta_R \exp(U_R/kT)}{\zeta_I \exp(U_I/kT)}. \tag{13.32}$$

While the B cell receptor is internalized and downregulated at later stages of the response, the receptor number can be regarded as conserved at the onset of the response and ζ_j can therefore be determined by inverting the equations for the average density of BCRs and

inhibitors, $\bar{n}_R$ and $\bar{n}_I$ respectively, which follow in a way analogous to the derivation of $\bar{n}_R^b$ as

$$\bar{n}_j = \frac{\bar{N}_j}{\Lambda} = \frac{kT\partial \ln Z}{\Lambda \partial \mu_j} = \omega_b \frac{\zeta_j \exp(U_j/kT)}{1 + \zeta_R \exp(U_R/kT) + \zeta_I \exp(U_I/kT)} + (1-\omega_b)\frac{\zeta_j}{1+\zeta_R+\zeta_I} \tag{13.33}$$

where $\omega_b = \frac{\Lambda_b}{\Lambda}$ was used. Basic algebraic manipulations yield a forth-order polynomial for ν, whose positive, real roots are plotted in Figure 13.9 dependent on the BCR-antigen binding energies U_R for different contact zone sizes ω_b; the inhibitor binding energy in the contact zone was set to zero ($U_I = 0$); a higher inhibitor binding energy would shift the curve to the right.

13.4.2 The model captures experimental results

Most importantly, the model captures the experimentally observed (Batista & Neuberger, 2000) but so far counter-intuitive sensitivity of the receptor-inhibitor ratio to the size of the contact zone ω_b (Fig. 13.9). The size of the contact zone will be different if antigen is either presented on a plate or a small particle. In the case of the plate the contact zone size will only be restricted by cell volume and membrane stiffness constraints, which prevent the formation of a flat cell geometry ($\omega_b \simeq 0.5$), such that the maximal contact zone size observed with antigen-displaying cells will not exceed 1% of the cell surface ($\omega_b = 0.01$) (Delon *et al.*, 1998). The employed particles measure only 4.5 μm and 2.8 μm in diameter compared to antigen-displaying cells which measure between 10 and 50 μm in diameter (Batista & Neuberger, 2000). We therefore assume that the contact zone with beads is 5-fold smaller than the contact zone with a plate; note that this exact value does not affect the qualitative observation described below.

The model reveals that for sufficiently large BCR-antigen binding energies U_R the receptor to inhibitor density ν is larger in a smaller contact zone. Importantly, this property is also independent of the exact values of the two binding energies U_I, the binding energy with which inhibitors bind in the contact zone, and U_R, which will depend on whether or

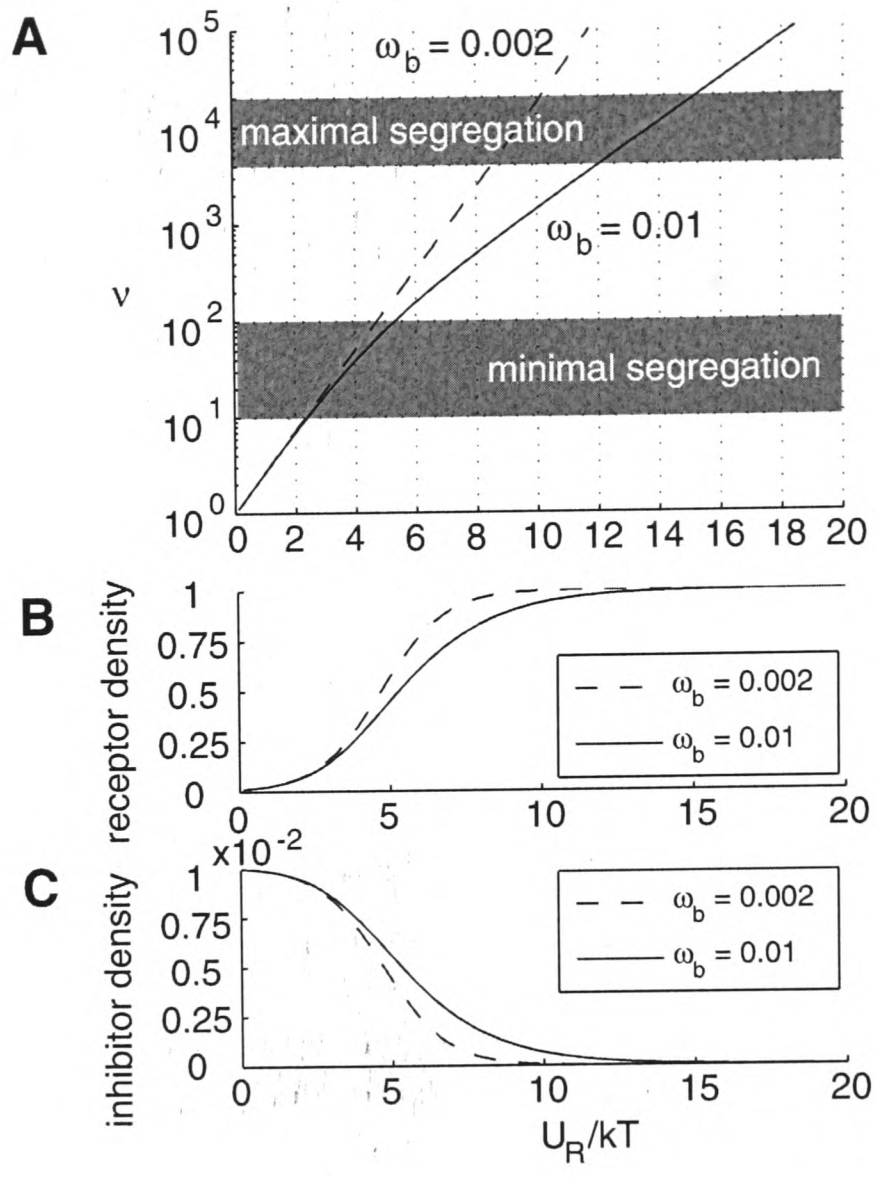


Figure 13.9: **Affinity dependent receptor and inhibitor density in the contact zone.** Affinity dependent **(A)** receptor/inhibitor ratio ν, **(B)** receptor density, and **(C)** inhibitor density in the contact zone. The overall receptor and inhibitor density was set to $\bar{n}_R = \bar{n}_I = 0.01$; the contact zone size to $w_b = 0.01$ $(-)$ and $w_b = 0.002$ $(- -)$.

not both arms of the BCRs can bind to antigen that is fixed on a bead. (Given the random spacing of immobilized antigen on the beads most BCRs can be expected to only bind one antigen at a time. Binding of two antigens by a small fraction of BCRs will lead to a small increase of the average affinity.) Alternative models of B cell activation that do not rely on inhibitor expulsion predict a smaller rather than a higher reactivity to a smaller antigen-covered particle because the number of engaged BCRs is smaller under such conditions. However, the total number of engaged receptors is in any case a weak measure of the binding quality since this can also be increased by the binding of several particles to a single B

cell. The level of B cell activation indeed depends on the concentration of the beads (and not only on the density of the immobilized antigen) (Batista & Neuberger, 2000).

Our model also reproduces the experimentally determined affinity threshold and ceiling of the B cell response to surface antigen (Batista & Neuberger, 1998; Batista & Neuberger, 2000; Batista *et al.*, 2001). The affinity threshold is defined as the binding energy that needs to be exceeded for antigen binding to elicit B cell signaling. B cell responsiveness then increases with increasing affinity until the affinity ceiling is reached.

The affinity threshold can be estimated from the observation that phosphatases exhibit in general 10-1000 times higher catalytic rates than kinases (Fischer *et al.*, 1991), and B cell activation will therefore require a comparable increase in the density of receptors (which are bound by autocatalytic kinases) relative to the inhibitors. The model predicts this threshold binding energy to be about 2-4 kT (Fig. 13.9A, intersection with lower shaded area) which corresponds to the experimental threshold affinity of about $K_D = 10^{-5} - 10^{-6}$ M (Batista & Neuberger, 2000). Note that the 3-dimensional dissociation constant can be calculated from the binding energy as $K_D^{3d} = \frac{\rho_R}{\eta} \exp(-\frac{U}{kT})$ with $\rho_R = 500\mu m^{-2}$ being the approximate BCR density on the cell membrane and $\eta = 1.2 \times 10^7 \mu m^{-2} M^{-1}$ being the conversion factor between the 2-dimensional and the 3-dimensional dissociation constant ($K_D^{2d} = \eta K_D^{3d}$) (for details see Appendix B.6).

According to our model of B cell activation the affinity ceiling will be attained once maximal segregation of receptors and inhibitors has been achieved. For a high, non-limiting antigen density in the contact zone (as characteristic for the *in vitro* experiments (Batista & Neuberger, 2000)), this corresponds to an exclusion of inhibitors from the Λ_b lattice sites. (At lower antigen density the Λ_b and Λ_{ub} lattice sites are no longer spatially separated and an exclusion from the Λ_b lattice sites thus does not automatically correspond to an inhibitor-receptor segregation, explaining the high sensitivity to a high antigen density that is observed in the experiments (Batista & Neuberger, 2000)). Cell-cell contact zones similar to those of B cells and antigen-displaying cells have been found to span about 1% of the

B cell surface ($\omega_b = 0.01$) (Delon *et al.*, 1998). Given that the BCRs cover about 1% of the B cell surface (Bell, 1988) (and together with co-receptors a slightly larger fraction of the cell surface) maximal receptor-inhibitor segregation will be achieved once almost all receptors accumulate in the contact zone and the receptor to inhibitor ratio approaches 5×10^4 (Fig. 13.9A, intersection with upper shaded area).

The corresponding binding energy ceiling is $U_R \sim 15 - 16$ kT which corresponds to $K_D \sim 2 \times 10^{-11}$ M, the affinity ceiling noted in experiments for antigen displayed on a large surface (Batista & Neuberger, 2000). Reducing the contact zone size to a fifth ($\omega_b = 0.002$) reduces the ceiling to $U_R \sim 8$ kT, which corresponds to $K_D \sim 10^{-8}$ M, the maximal affinity at which a differential response could be observed when antigen was displayed at high antigen density on small particles (beads) (Batista & Neuberger, 2000).

We conclude that a model which relates BCR activation to the extent of receptor-inhibitor segregation captures the sensitivity to the mode of antigen presentation (plate versus bead) in terms of the different contact zone sizes independently of the exact choice of the two parameters U_R and U_I (which depend on the correct value for η), and reproduces the experimentally observed affinity thresholds and ceilings in terms of receptor to inhibitor ratios for the employed (and physiological justifiable) parameter values.

13.5 What is the immunon? - Lessons from polymeric antigen

Early efforts to understand how antigen binding is translated into a cellular signal made use of polymeric rather than monomeric antigen. By using hapten-covered polymers, total numbers and spacing could be controlled and it was concluded that at least 10-20 (Vogelstein *et al.*, 1982) (7-15 in a later re-analysis (Sulzer & Perelson, 1997)) hapten groups from the *same* polymer needed to bind to the BCR in order to trigger a B cell. This requirement was explained by invoking the 'immunon', the conformation to which the BCRs would change once a sufficient number was engaged by the same polymer (Dintzis *et al.*, 1976; Vogelstein *et al.*, 1982). However, a structural change has remained elusive and no model yet explains

why this number of receptors would need to be engaged to trigger such conformational change.

How does this experimental observation fit with our model of B cell activation? We have shown above that in the framework of the model monomeric antigen can also activate B cells. However, the monomeric antigen in that case was a protein while the polymers are covered by haptens which alone can only bind but not trigger a B cell. According to the segregation concept this is due to the size which is insufficient to separate receptors and inhibitors. So why would hapten-covered polymers then activate although the polymers are much too thin to sufficiently increase the distance between receptors and inhibitors? As is illustrated in Figure 10.2, inhibitors could be separated from receptor-bound kinases if the polymers stabilized a closed ring conformation of the receptor cluster. According to section 13.2.2 this would require that the hapten-covered polymers increase the ring closure rate k_r (corresponding to the ring closure probability p_r) to form closed rings that prevent inhibitors from accessing kinases that locate to the inner core of the cluster. Moreover the closed ring structure would need to be maintained for a sufficiently long time to enable cross-phosphorylation between kinases and downstream signaling which could then lead to the permanent inactivation of the inhibitors, possibly by activation of the NADPH oxidase as discussed above.

Assuming that BCR rings close at rate k_r and open by IgM-IgM unbinding at rate k_- we can estimate p_r by determining the steady state of its evolution (or Markov or Master) equation

$$\frac{dp_r}{dt} = k_r(1 - p_r) - nk_-p_r = 0 \qquad \Rightarrow \qquad p_r = \frac{k_r}{k_r + k_-}. \tag{13.34}$$

Since low affinity haptens can also activate B cells a reduction of the IgM-IgM off-rate, k_-, by binding of the hapten-covered polymer seems not to be essential for B cell activation. Accordingly, we use $k_- = 1\ \mathrm{s}^{-1}$ as in section 13.2.1. n denotes the average length of the polymer, and reflects the fact that unbinding at any IgM-IgM bond will open the polymer. The rate of ring closure, k_r, in the absence of hapten-coated polymers has not been defined

experimentally, and we therefore use the standard diffusion-limited on-rate $k_r = k_+ = 0.1$ s^{-1} as derived in section 13.2.1. We then predict that in the absence of hapten-coated polymers about 2% of all BCR polymers (assuming $n = 5$, Section 13.2.3) are closed. The polymer-dependent increase in the ring closure rate is not easy to estimate because little is known about the flexibility of the IgM suprapolymer. The only available indication is the increase in the size of the volume in which reactions between the two ends of the chain become possible. Thus the minimal spacing between haptens on the activating polymers is 10 nm (Dintzis *et al.*, 1976) while the receptors are unlikely to bind on distances longer than 1 nm. The polymer therefore has a much wider reach than the receptors and the volume in which binding reactions are possible therefore increases. Given that the volume scales with the cube of the radius this would imply a possible increase in the reaction rate by 10^3-fold such that $k_r = k_+ = 0.1$ s^{-1} in the absence of the hapten-coated polymer and $k_r \sim 100$ s^{-1}. For such high ring closure rate almost all BCR clusters will be closed ($p_r \sim 1$).

For B cell activation the kinetics of the process will, of course, also be of importance since if the rings open (and then re-close) before the BCRs have been activated and nearby inhibitors have been inactivated then insertion of inhibitors could interfere with B cell activation. This constraint may explain the experimentally observed requirement that one polymer must engage about 7-15 BCR sites in order to activate a B cell (Sulzer & Perelson, 1997). Thus, considering that BCR clusters will comprise about 5 IgMs (see section 13.2.3), engagement of 7-15 BCR sites by a polymer will greatly reduce the ring opening rate. In the absence of polymers any spontaneously formed closed rings will disintegrate at a rate of 5 s^{-1}. Binding of a polymer in such a way that the polymer winds around the cluster and at least one receptor binds the polymer twice will strongly reduce the rate at which inhibitors gain access since now several bonds need to be broken before the ring opens up for inhibitors.

The number of receptors that are bound by one polymer can be affected by the concentration and length of the polymer, as well as the spacing of hapten groups. Dependent

on the spacing of hapten groups, polymers may either form many large loops when binding BCRs or rather long trains, where segments of the polymer attach tightly to the surface. Correlation of experimental data with theoretical models suggests that B cell signaling requires that the loop length is limited (Perelson & Wiegel, 1981) and our model explains this with the need to tightly link BCRs in the cluster.

The inhibitory effect of short polymers (Dintzis *et al.*, 1982) can be explained with the failure to link an entire cluster together such that the ring closure rate is too slow to enable B cell signaling. While several polymers could in principle bind in an overlapping manner diffusion effects will favour smaller entities and the non-uniform polymer length in experiments will make overlapping binding even more difficult.

Finally, at high concentrations several polymers may bind to the same cluster, which leads to an effect similar to that predicted for the case where the polymers are too short. At low polymer concentrations the ligand becomes depleted (Vogelstein *et al.*, 1982; Sulzer & Perelson, 1997).

13.6 Conclusion

I propose that antigen-induced receptor inhibitor segregation triggers B cell activation and gives rise to the experimentally observed affinity and antigen density/concentration dependency of B cell signaling. According to this novel concept, B cells discriminate between different affinities of binding based on the extent to which inhibitor-free receptor-antigen complexes form. This activation mechanism therefore does not require any conformational changes to explain antigen-dependent B cell activation. This is an important difference from the activation mechanism for other well-studied membrane receptors (such as G-protein-linked receptors or enzyme-linked receptors including the EGF receptor, PDGF receptor, and integrins) which are activated upon ligand induced structural changes; in the case of enzyme-linked receptors, the conformational change is in general followed by receptor oligomerization (Burgess *et al.*, 2003; Kim *et al.*, 2004).

The model is based on quantitative data and captures the affinity thresholds and ceilings for both surface and soluble antigen. One of the previously counter-intuitive observations which the model can explain is that smaller particles (which form a smaller contact zone with the B cell) trigger full B cell activation at a lower affinity (Batista & Neuberger, 2000). The explanation that inhibitors are expelled from the smaller contact zone at a lower affinity does not depend on the exact choice of the parameter values. This is important since, although all employed parameter values are derived from the experimental literature, their accuracy remains limited by the accuracy of the available experimental methods. Alternative models of B cell activation which relate activity to the extent of IgM engagement and not to the extent of IgM separation from inhibitors cannot explain this result. Such models would predict that a smaller contact zone triggers less B cell signaling because less IgM is engaged by antigen; binding of several small particles should still not trigger a stronger response than large particles.

The segregation concept also addresses the long ongoing dispute of whether soluble monomeric antigen can trigger a B cell response or whether B cells are triggered by aggregates. Our model shows how soluble monomeric antigen of sufficient size can elicit a response by separating receptor and inhibitors. In this it is important that BCRs are pre-clustered (Schamel & Reth, 2000) as the interactions of at least two protected Ig-α/Ig-β will be necessary for B cell activation, and in our model this level of protection is only achieved when three neighbouring receptors bind antigen (Fig. 13.2A, B). The importance of Ig-α/Ig-β co-clustering is demonstrated by experiments in which about 15% of all IgM are mutated in a way that they could not bind Ig-α/Ig-β; this affects signal transduction by Ig-α/Ig-β-bound IgM (Vilen *et al.*, 2002). The need for pre-clustering may also explain how a point mutation in the constant region of an Ig-light chain can prohibit BCR signaling (Sun *et al.*, 2002); the point mutation was characterized to introduce a hydrophobic patch which may affect receptor aggregation.

The need for receptor clustering to trigger B cell signaling also provides an explanation

as to how IgM downregulation can render MD4 B cells anergic. Given that the pre-clustering of the BCR is isotype-specific (Schamel & Reth, 2000) a reduction in the IgM density will preclude IgM cluster formation. In the absence of BCR clusters there are no neighbouring, protected Ig-α/Ig-β and antigen-triggered B cell activation becomes impossible. That tolerance can be broken by membrane antigen (Hartley *et al.*, 1991) and cross-linking substances can be explained with the higher local IgM density (30-fold in experiments with lipid bilayers (Carrasco *et al.*, 2004)) and the enforced cluster formation, respectively. Anergic B cells have been found to express IgM dissociated from Ig-α/Ig-β (Vilen *et al.*, 1999; Vilen *et al.*, 2002) which modelling suggests is a consequence of less IgM clustering which destabilizes the BCR. Control of B cell reactivity on the level of receptor densities is an elegant mechanism as it is simple and prevents any difficult signal integration at later steps. Moreover, IgM downregulation by a block in transport from the endoplasmic reticulum (Bell & Goodnow, 1994) is a rapid process that can also be quickly reversed. It should, however, be noted that anergic B cells that are specific for single-stranded DNA have been found to express almost normal IgM levels (Erikson *et al.*, 1991; Benschop *et al.*, 2001). There must therefore exist alternative ways to induce IgM destabilization when IgM is expressed at almost normal levels.

Small antigenic compounds - so-called haptens - fail to induce a B cell response although they can still bind the receptor; linkage of the hapten to a larger carrier restores the ability to trigger a B cell response. Why antigen size matters has so far been a conundrum but can now be understood in terms of receptor segregation which will only be achieved if the antigen exceeds a certain size. Small protein antigens, such as hen egg lysozyme, will introduce a sufficient separation ($\sim$ 2nm (Fiedler *et al.*, 1998)) to initiate BCR signaling. However, because of the instability of BCR clusters, inhibition of the inhibitors by subsequent chemical modifications can be expected to be required in order to maintain the active state. Inactivation of phosphatases can be achieved by reactive oxygen species such as H_2O_2 which oxidizes the cysteines of phosphatases (Reth, 2002). H_2O_2 is produced by

NADPH oxidase which is activated by PI3K which itself is activated by the (BCR-bound) Src kinases (Vlahos *et al.*, 1995). A role for H_2O_2 in lymphocyte signaling has recently be reported for both T cells (Kwon *et al.*, 2005) and B cells (Singh *et al.*, 2005). The need for inhibitor inhibition provides an explanation for the experimental observation that a response to soluble antigen requires a signaling competent BCR while a response to particulated antigen, where inhibitors can be pushed out, does not (Batista & Neuberger, 2000). A response to particulated antigen on the other hand requires that tight IgM clusters can form and therefore that the antigen density on the particle is sufficiently high. Reduction of the antigen density in experiments indeed prohibits B cell activation, even at high affinity.

The segregation concept also resolves the long-standing paradoxes which emerged from experiments with hapten-coated polymers that led to the immunon concept (Dintzis *et al.*, 1976; Vogelstein *et al.*, 1982). In this novel framework the immunon can be interpreted as a cluster of BCR that is stabilized by binding to a single polymer in a way that all receptors are bound and at least one receptor is bound twice. All receptors need to be bound by a single polymer because only this can sufficiently increase the ring closure rate and, probably even more importantly, lower its opening rate. This stabilization of the cluster is proposed to be important to prevent access of inhibitors to the kinases; inhibitor exclusion for a sufficient time can enable B cell activation by kinase autophosphorylation. Experiments could test the prediction that stable BCR clusters trigger B cell signaling by altering the site that mediates the BCR-BCR interaction in a way that the affinity is increased. An increase in the affinity should result in antigen-independent B cell activation.

We conclude that B cell activation by receptor-inhibitor segregation can explain several previously counter-intuitive features of B cell biology while capturing and explaining available *in vitro* results. The model also provides an explanation for why haptens can elicit a B cell response only when bound to a larger carrier protein. Several experiments support the hypothesis that receptor-inhibitor segregation triggers B cell activation; more intricate experiments will be necessary to obtain direct evidence and to assess its role in B cell affinity

discrimination.

Chapter 14

Discussion

In this third part of the thesis a novel framework has been developed to explain affinity-dependent B cell activation and selection in germinal centres. This has been necessitated by our thorough computational analysis of the germinal centre reaction which revealed that current models of B cell selection, which are all based on a competition for (or access to) antigen held on FDCs, are not in agreement with available experimental data. In light of our studies I suggest that B cells are selected in a competition for T cell help. Such a mechanism requires B cells to be able to discriminate between different affinities of binding, and I also provide an explanation of how this can be achieved. Altogether I propose the following comprehensive model of the molecular events that lead to the selection of high affinity B cells.

14.1 The mechanism of B cell selection in germinal centres

During the selection process B cells first acquire antigen in a non-competitive manner. The efficiency of antigen processing then depends on the affinity of binding, such that high affinity B cells will present peptide-MHC complexes at a higher density, and this will give them a higher chance of being rescued by T helper cells. In the following I discuss the molecular details of this process.

How the mechanical binding of antigen to the B cell receptor is translated into a chemical signal has long been a conundrum. I propose that activation is achieved by an antigen-

induced receptor-inhibitor segregation. For this to be possible either the antigen or the receptor needs to be pre-clustered. Experiments suggest that most receptors are indeed pre-clustered (Schamel & Reth, 2000), and our mathematical analysis further suggests that these clusters are of polymeric structure with 5-6 receptors per polymer. Given the arrangement of IgMs in this polymer, two sides of the IgM-bound Igα/Igβ heterodimer can be expected to be protected from interactions with phosphatases that are bound to inhibitory co-receptors (Fig. 13.2). Antigen binding can increase the distance between IgM and inhibitory receptors on the other two sides. Inhibition of inhibitors has been shown to result in spontaneous B cell activation (Wienands *et al.*, 1996; Rolli *et al.*, 2002), and it is therefore conceivable that this physical separation is sufficient for B cell signal initiation. If the antigen is pre-clustered, either in a soluble aggregate or on a surface, then inhibitors can be excluded by molecular crowding. For this it is important that the antigen is sufficiently dense and that the contact zone is sufficiently small such that segregation is efficient. Both aspects indeed determine the strength of the B cell response in experiments (Batista & Neuberger, 2000).

The affinity of binding determines the fraction of B cell receptors that are protected from the action of inhibitors in our model. Experiments demonstrate that antigen, which has been bound by signaling-active receptors, will be presented more efficiently to T cells (Aluvihare *et al.*, 1997). Accordingly, the higher fraction of signaling-active B cell receptors would directly translate into a higher presentation efficiency, that is a higher density of peptide-bound MHC complexes. On the molecular level the higher presentation efficiency is likely to reflect more efficient targeting of internalized antigen-bound receptors to a compartment that is rich in newly expressed MHC class II (MIIC) (Clark *et al.*, 2003). The targeting to such a compartment increases the efficiency with which antigenic peptides are presented to T cells on MHC class II complexes (pMHC) because circulating MHC class II complexes are already loaded with competing peptides, and this reduces presentation efficiency for the new peptide (Harding & Unanue, 1990). Here it is interesting to note that the efficient delivery of antigen-bound IgM relies, in particular, on signaling through Syk and Igα (Clark

et al., 2003), whose degree of phosphorylation has been shown to depend on the affinity of antigen binding (Kouskoff *et al.*, 1998). In order to retain the affinity-dependency it is of crucial importance that signal activation happens locally and does not spread to non-protected receptors; otherwise all receptors would be activated and targeted once at least one receptor becomes activated. The later re-organisations of receptors and the cytoskeleton must therefore serve other purposes such as the exchange of further information, for instance by co-receptor engagement, which may modulate the response.

In a final step B cells need to recruit T cell help. Given that there are only very few T cells in each GC (5-10% (Kelsoe, 1996*b*)) of which only a fraction will be specific for a given peptide, several CCs can be expected to bind to a single T cell. These will enter a competition for the attraction of the microtubule organizing centre (MTOC) since the reorientation of the MTOC is required for the secretion of survival factors such as interleukin (IL)-4 (Kupfer *et al.*, 1991) and only the B cell that faces the MTOC receives cytokines and enters mitosis (Kupfer *et al.*, 1994). The reorientation of the MTOC is dependent on and directed towards the site of TCR signaling (Sedwick *et al.*, 1999). T cell responsiveness depends on the number of pMHC that are presented on the B cell surface (Harding & Unanue, 1990; Grakoui *et al.*, 1999), and, when interacting with several B cells, T cells polarize to the B cell with the highest density of specific pMHC (Depoil *et al.*, 2005). As discussed above, I propose that a higher affinity of interaction results in increased pMHC presentation, as a consequence of which the highest affinity CC interacting with a T cell has the highest chance of being rescued. At low BCR affinity, affinity-dependent CD86 expression on the B cell (Kouskoff *et al.*, 1998) may further amplify the difference between B cells as co-engagement of CD28 by CD86 amplifies TCR signaling (Michel *et al.*, 2001), enables MTOC reorientation also under less favorable conditions (Sedwick *et al.*, 1999) and triggers IL2 production close to the contact zone (Reichert *et al.*, 2001). Rescue by T cells takes several hours (Kupfer *et al.*, 1994) such that the polarization will need to be maintained over longer times, which again most likely favours the highest affinity B cell

that presents the most pMHC.

The ability of T cells to confer both death and survival signals is likely to enhance the efficiency of B cell selection. The example of the cytokine IL4 and Fas (a receptor of the tumour necrosis factor (TNF) receptor family, which is triggered upon binding of Fas ligand (FasL) expressed on T cells (van Eijk *et al.*, 2001)) illustrates how survival may be restricted to high affinity B cells while all others are killed by the T cell. While IL4 is targeted to one B cell at a time, Fas-FasL complexes are likely to form in each contact zone. IL4 (synergistically with BCR cross-linking) rescues B cells from Fas-dependent apoptosis (Foote *et al.*, 1996; Rothstein *et al.*, 2000) such that Fas-FasL interactions will only negatively select low affinity B cells, which do not receive IL4. Indeed, in Fas-deficient lpr mice and in transgenic mice that overexpress Bcl-x, a suppressor of Fas mediated apoptosis, low affinity B cells persist in the GC reaction and the selection of high-affinity B cells is impaired (Takahashi *et al.*, 1999; Takahashi *et al.*, 2001).

T cells not only select/rescue B cells, they also subsequently direct B cell proliferation and differentiation. A key regulatory protein is CD40 ligand (CD40L), which engages CD40 on the B cell and supports survival (although it does not protect from Fas-mediated apoptosis), promotes proliferation, and directs CC differentiation (Arpin *et al.*, 1995; Liu *et al.*, 1997; Bishop & Hostager, 2003). Accordingly, germinal centres are abrogated upon addition of anti-CD40L antibody (Han *et al.*, 1995).

14.2 What makes antibody affinity maturation so efficient?

Antibodies evolve new binding specificities in a matter of days. Several features enable such efficiency. First of all, the detrimental nature of the increased mutation rate is limited by targeting of mutations to those regions of the antibody (complementarity-determining regions (CDRs) in the V-region) that mediate contact with the antigen; this limits the number of mutations that may disrupt other essential structural elements of the antibody - a cause for a large proportion of detrimental mutations in other proteins. The affinity

of antibody binding is altered both by direct changes in the binding site as well as by mutations that lie more distant and alter the conformation of the binding site. While some single mutations can increase an antibody's affinity by tenfold, affinity maturation is the result of several additive changes; high-affinity antibodies harbor on average six to eight mutations (Berek *et al.*, 1991). Considering that in protein engineering approximately six to eight appropriately targeted mutations are required to alter binding specificity (Scrutton *et al.*, 1990), the optimized character of antibody affinity maturation becomes clear.

While the multiple rounds of mutation and selection enable a stepwise affinity maturation process, which strongly facilitates the generation of high affinity antibodies (Kepler & Perelson, 1993), analysis of fitness landscapes in evolutionary biology suggests that a potential danger of such a stepwise evolution process is trapping in local optima (Kauffman, 1993). The parallel but spatially separate evolution of many GC reactions in the follicle (each seeded by few B blasts) avoids trapping all lineages of B cells in what may prove to be an unfavourable local optima that lacks paths to high affinity antibodies.

The combination of an evaluation of BCR affinity in absolute terms together with a second competitive step to compare the relative affinity between different B cell clones within the GC reaction will ensure a higher robustness to variations in antigen concentration. While B cell responsiveness depends on both affinity and concentration, affinity discrimination is still possible at antigen concentrations that would be so high as to permit an intraclonal competition for antigen. At very high antigen concentration antibody affinity maturation becomes impossible because B cells either die or are tolerized (Pulendran *et al.*, 1995*a*; Pulendran *et al.*, 1995*b*). Our model agrees that at high antigen abundance affinity discrimination becomes impossible if antigen is encountered in soluble form, as is the case in these experiments. However, under such condition it will probably be the unspecific fluid phase antigen uptake (Batista & Neuberger, 1998) which renders the process entirely affinity-independent. Contrary to the suggestion of earlier models antigen consumption (Sidman & Unanue, 1975) or masking by emerging antibodies (Tarlinton & Smith, 2000;

Iber & Maini, 2002) cannot provide the experimentally observed robustness (Vora *et al.*, 1997; Hannum *et al.*, 2000) to variations in antigen concentration.

B cells must not only be selected for their ability to produce high-affinity antibodies, there also must be a mechanism that guards against emerging auto-reactivity. This challenge is met by the second key feature of the selection strategy, that B cell selection depends not only on the acquisition of antigen but also on T cell help. The requirement for T cell help therefore also assures that those B cells that alter their binding specificity in a way that they recognize and acquire self-antigen will not be selected.

14.3 The role of soluble versus membrane antigen

The possible roles of soluble or membrane antigen for B cell antibody affinity maturation are currently controversial (Haberman & Shlomchik, 2003). On the one hand, displaying antigen on a large surface considerably reduces the affinity threshold (without lowering the ceiling), which is likely to be important especially at the onset of an immune response (Batista & Neuberger, 2000). On the other hand, affinity maturation has also been observed when membrane deposition of antigen was not detectable (Matsumoto *et al.*, 1996; Hannum *et al.*, 2000), and even when the formation of immune complexes, which reduce the threshold for B cell activation, was also not possible (Hannum *et al.*, 2000). However, this is only true for large (but not low) doses of injected antigen suggesting that membrane presentation of antigen on FDCs is important for an early and efficient onset of the immune response.

14.4 Experiments to be done

Although the ideas that B cells are activated by antigen-dependent receptor-inhibitor segregation and that high affinity B cells are selected in a competition for T cell help are attractive they suffer one important shortcoming - lack of experimental evidence. More experiments that test the segregation concept and which investigate the role of clonal competition for either antigen or T cell help are needed. It will be of particular importance

to test whether an increased number of T cells in a GC relaxes selection and consequently blunts affinity maturation as suggested by the hypothesis of a clonal competition for T cell help. Moreover, the duration of low affinity CC-FDC interactions needs to be measured in order to find out about a potential refractory time. Combined with details on the affinity and antigen density (concentration) dependent interaction of B cells with either antigen presenting cells or T cells as well as further work on B cell signaling initiation, this may help to eventually resolve how high affinity B cells are preferentially selected.

Chapter 15

Conclusion

The recent data explosion in the biological sciences has given birth to a new field called 'Systems Biology', which is concerned with the integration of the available molecular information into a coherent framework in order to reveal the principles and details of biological information processing. With the creation of this new field both new technical opportunities and mathematical challenges have emerged. The formulation of quantitative models offers the exciting opportunity to inform experiments with quantitative predictions and to understand nonlinear cellular behaviours which are difficult to grasp by experiments and verbal reasoning alone. On the other hand quantitative predictions are only possible if the model contains a sufficient level of detail. As a consequence mathematical models in systems biology tend to include a large number of variables, reactions and parameters, even if they only describe the smallest biological module amenable to a quantitative analysis, as illustrated by the sporulation model in Part I of this thesis which requires about 50 variables to describe the dynamics of 4 proteins. While the parameters can be defined by experiments (or can be expected to be so soon for most problems), a general criticism of such an approach remains that a model that is as complicated as the underlying process can not be expected to yield new insights or deeper understanding. However, as also illustrated by the sporulation project, with a realistic model at hand simulations can reveal interdependencies and causalities that would have been difficult if not impossible to define in experiments. A simple model that includes only the interactions that are of major importance will, in

general, not be sufficiently accurate to predict small effects (as that of the accumulation of IIE on the asymmetrically placed septum - Part I) and may also not be reliable when investigating the effects of mutants because neglected parts of the model may suddenly become important under such conditions. The thorough analysis of simple models can, however, have explanatory power as demonstrated in the case of the sporulation model. To do so it is important that the simple model is realistic and that its range of validity is known. This will rarely be the case unless it is based on a detailed, validated model. Simple models also provide a good starting point to understand the general behaviour of a system, especially if it exhibits complex spatial-temporal dynamics. However, very often the main benefit of such models is that they force one "to think clearly" (May, 2004) rather than that they reveal features that could not have been revealed without the help of mathematics.

The routine generation of large models, possibly also by experiments themselves, poses several challenges, one of which is the understanding of the underlying principles that determine the architecture of signaling pathways. Very often this requires insights into the mechanistic basis of robustness and sensitivity which can in general only be obtained by an exploration of the parameter space. Such exploration is daunting if not computationally impossible with the large parameter spaces employed in recent models. Current studies therefore restrict the exploration of the parameter space to 1-parameter perturbations which is, generally speaking, unsatisfactory.

A compromise between large, detailed and small, mathematically tractable models may be the reduction of the large model to smaller submodels whenever a specific question allows the neglect of certain parts of the model. The question could then be studied in detail in the smaller subsystem and predictions could subsequently be tested in the larger model before subjected to an experimental analysis. However, unlike in the case of modules, the definition of these submodels will no longer be guided by biological insight but rather mathematical studies will need to define these submodels, for instance based on different time scales which themselves may depend on the population of certain states of the system. The development

of new techniques to define such subsystems routinely may be of great help. However, even such subsystems are unlikely to reduce to two or three equations and it will therefore be important to improve mathematical techniques to enable an efficient stability analysis in more than two or three dimensions.

While the methods that are employed in systems biology appear to be no different from (if not simpler than) those routinely used in mathematical biology, this field represents an entirely new paradigm in theoretical biology. While the predictive power has led to a dramatic increase in the acceptance of quantitative methods in molecular biology the difficulties in comprehensively analysing the models with mathematical methods has made the field less popular with mathematicians. This thesis illustrates the interdisciplinary nature of the challenge in that methods from mathematics (differential equations, linear stability analysis, probability), numerical analysis (numerical solution of sets of differential equations, agent-based simulations), and physics (statistical mechanics) are used to explore a wide range of questions on many different aspects of the development and evolution of multicellular organisms. Last but not least, a good knowledge of experimental techniques is important since experiments need to be carried out during the process of model building in order to improve and validate the model during its construction.

By use of these techniques in this thesis, several long-standing questions have been resolved and novel models have been proposed that now await testing by experiments. The thesis is split into three parts which address different aspects of the development and evolution of multicellular organisms, their development and evolution from a single cell, the basis of cohesion and migration, and the division of labour between billions of specialized cells by example of the humoral immune response.

The first part of the thesis has provided us with an understanding of how asymmetric cell division can be translated into two different routes of cell differentiation, a basic requirement when generating a multicellular organism from a single cell. It is impressive that small volume differences as found in the bacterium can be sufficient to reliably trig-

ger compartment-specific gene expression, and it will be interesting to learn about the mechanism by which asymmetric cell division translates into differential gene expression in eukaryotic single-celled organisms, the origin of all multicellular organisms. Self-renewing stem cells also employ asymmetric cell division but here extrinsic cues such as hormones and local interactions between stem cells and their neighboring cells play an important role. How the first step, the asymmetric division of the cell, is directed is so far unknown. Whilst intuitively it may appear simpler to divide asymmetrically than to divide symmetrically, it is not sufficient for cell division planes to be positioned randomly, and while a simple oscillating mechanism can determine the cell middle (Howard *et al.*, 2001; Meinhardt & de Boer, 2001; Kruse, 2002; Huang *et al.*, 2003; Howard & Kruse, 2005) it is currently unclear which simple mechanism could mark the poles (Howard, 2004). The mechanisms that enable asymmetric cell division in prokaryotes and eukaryotes are necessarily very different, and more experimental information will be required before real progress can be made on the latter.

Whilst in each generation multicellular organisms develop from a single cell, this process becomes simpler once the first multicellular organism has evolved because the mother organism can provide cues that direct cell differentiation in the offspring. Understanding the cues that direct the development of complex organisms such as flies, worms and humans is a difficult task. Even simple patterns that are created by morphogen gradients are only understood in a rudimentary fashion but the combination of mathematical modeling with experiments shows great promise in this area (Lander *et al.*, 2002; Kruse *et al.*, 2004; Mizutani *et al.*, 2005). Because of the combination of spatial and temporal effects it will be of particular importance to subject realistic detailed models to a thorough mathematical analysis in order to understand the underlying mechanism of an observed and modelled biological behaviour as is illustrated in Chapter 6.

An important difference between loose colonies and multicellular organisms is the cohesion of cells. This shapes the organism into a well-defined form and thereby enables

cell specialization and a division of labour. While many components that are involved in adhesion and migration have been determined in experiments our understanding of the molecular properties of the involved proteins (such as integrins and their binding partners) as well as of the signaling processes that integrate cues from many sources is very limited. Mathematical modelling can guide experiments by ruling out hypotheses and by stating constraints based on the quantitative information that is available, as described in Chapter 8. Eventually, continual updating of models with new experimental information can be expected to lead to a quantitative understanding of this complex process. Such quantitative models can be expected to be of great help in medical applications as deregulated cell adhesion and migration is at the heart of many diseases and responses to them, including tissue repair, angiogenesis, inflammation and hemostasis (Horwitz & Webb, 2003).

Any process in a multicellular organism is the result of cellular cooperation and division of labour. The adaptive immune response that is discussed in Chapters 10-14 provides a particularly good example as it is an almost self-contained system which illustrates both the evolution of function in a living organism as well as the degree of division of labour up to the death of "useless" cells by apoptosis. As illustrated, quantitative tools can be of great use in investigating processes that are too complex to be dissected in experiments. However, without experimental validation such models lack predictive power and therefore provide only limited insights. The simulations described in Chapters 11-12 suggest a number of feasible experiments. It is now important that these experiments are carried out and that the experimental results are fed back into the simulation. Only then will the simulation become a truly useful tool in informing experimentalists which experiments to do to obtain informative results despite the limitation that in experiments the entire system can never be dissected and controlled at once.

The thesis illustrates how different techniques have to be used dependent on the scale of the problem and the quantitative details known. It also illustrates how quickly models become rather philosophical when quantitative data is not known. Whilst providing inter-

esting conceptual insights, all models on the immunological project will require much more quantitative information before they can provide a comprehensive mechanistic picture of the processes involved. Because of the many different aspects studied the thesis also illustrates how very different biological processes (integrin and B cell activation for example) can be described by very similar mathematical tools. As a result of this it can be hoped that quantitative studies will also lead to an exchange of ideas and concepts between such otherwise disparate biological disciplines.

Systems Biology is a very young discipline with enormous potential. An integrative understanding of biology will not be possible without quantitative methods - but quantitative methods will also be of no use unless they are used by people who understand both the quantitative aspects and the biology. Intense collaborations between scientists from all branches in the natural sciences will be important. Biologists will need to be trained so that they appreciate the potential and limitations of quantitative methods and are prepared to also publish their raw data, hopefully in a (still-to-be-created) database. Similarly, mathematicians, physicists, computer scientists, and engineers will need to be prepared for the meaningful analysis of large models. Currently we would still fail to understand even if given a CD rom that contained a complete quantitative description of all the processes that make up a human.

Bibliography

Adhin, M. R. & van Duin, J. (1990). Scanning model for translational reinitiation in eubacteria. *J Mol Biol,* **213** (4), 811–818.

Aluvihare, V., Khamlichi, A., Williams, G., Adorini, L. & Neuberger, M. (1997). Acceleration of intracellular targeting of antigen by the B-cell antigen receptor: importance depends on the nature of the antigen-antibody interaction. *EMBO J,* **16**, 3553–62.

Angeli, D., Ferrell, J. E. J. & Sontag, E. D. (2004). Detection of multistability, bifurcations, and hysteresis in a large class of biological positive-feedback systems. *Proc Natl Acad Sci U S A,* **101** (7), 1822–1827.

Arabolaza, A. L., Nakamura, A., Pedrido, M. E., Martelotto, L., Orsaria, L. & Grau, R. R. (2003). Characterization of a novel inhibitory feedback of the anti-anti-sigma SpoIIAA on Spo0A activation during development in *Bacillus subtilis. Mol Microbiol,* **47**, 1251–1263.

Arias-Salgado, E. G., Lizano, S., Sarkar, S., Brugge, J. S., Ginsberg, M. H. & Shattil, S. J. (2003). Src kinase activation by direct interaction with the integrin beta cytoplasmic domain. *Proc Natl Acad Sci U S A,* **100** (23), 13298–13302.

Arigoni, F., Duncan, L., Alper, S., Losick, R. & Stragier, P. (1996). SpoIIE governs the phosphorylation state of a protein regulating transcription factor σ^F during sporulation in *Bacillus subtilis. Proc Natl Acad Sci U S A,* **93**, 3238–3242.

Arigoni, F., Guérout-Fleury, A. M., Barák, I. & Stragier, P. (1999). The SpoIIE phosphatase, the sporulation septum and the establishment of forespore-specific transcription in *Bacillus subtilis*: a reassessment. *Mol Microbiol,* **31**, 1407–1415.

Arnaout, M. A., Mahalingam, B. & Xiong, J.-P. (2005). Integrin structure, allostery, and bidirectional signaling. *Annu Rev Cell Dev Biol,* **21**, 381–410.

Arpin, C., Dechanet, J., Kooten, C. V., Merville, P., Grouard, G., Briere, F., Banchereau, J. & Liu, Y. (1995). Generation of memory B cells and plasma cells in vitro. *Science,* **268**, 720–722.

Barák, I. & Youngman, P. (1996). SpoIIE mutants of Bacillus subtilis comprise two distinct phenotypic classes consistent with a dual functional role for the SpoIIE protein. *J Bacteriol,* **178** (16), 4984–4989.

Batista, F., Iber, D. & Neuberger, M. (2001). B cells aquire antigen from target cells after synapse formation. *Nature,* **411**, 489–494.

Batista, F. & Neuberger, M. (1998). Affinity dependencs of the B cell response to antigen: a threshold, a ceiling and the importance of off-rate. *Immunity,* **8**, 751–759.

Batista, F. & Neuberger, M. (2000). B cells extract and present immobilized antigen: implications for affinity discrimination. *EMBO,* **19**, 513–520.

Bell, G. (1978). Models for the specific adhesion of cells to cells. *Science,* **200**, 618–627.

Bell, G. (1988). *in Physical basis of cell-cell adhesion*, p. 227. CRC Press, Boca Raton.

Bell, G. I., Dembo, M. & Bongrand, P. (1984). Cell adhesion. Competition between non-specific repulsion and specific bonding. *Biophys J,* **45** (6), 1051–1064.

Bell, S. & Goodnow, C. (1994). A selective defect in IgM antigen receptor synthesis and transport causes loss of cell surface IgM expression on tolerant B lymphocytes. *EMBO J,* **13**, 816–826.

Ben-Yehuda, S. & Losick, R. (2002). Asymmetric cell division in B. subtilis involves a spiral-like intermediate of the cytokinetic protein FtsZ. *Cell,* **109** (2), 257–266.

Benschop, R. J., Aviszus, K., Zhang, X., Manser, T., Cambier, J. C. & Wysocki, L. J. (2001). Activation and anergy in bone marrow B cells of a novel immunoglobulin transgenic mouse that is both hapten specific and autoreactive. *Immunity,* **14** (1), 33–43.

Berek, C., Berger, A. & Apel, M. (1991). Maturation of the immune response in germinal centers. *Cell,* **67**, 1121–1129.

Berek, C. & Milstein, C. (1987). Mutation drift and repertoire shift in the maturation of the immune response. *Immunol Rev,* **96**, 23–41.

Bishop, G. A. & Hostager, B. S. (2003). The CD40-CD154 interaction in B cell-T cell liaisons. *Cytokine Growth Factor Rev,* **14** (3-4), 297–309.

Borukhov, S. & Nudler, E. (2003). RNA polymerase holoenzyme: structure, function and biological implications. *Curr Opin Microbiol,* **6** (2), 93–100.

Bray, D., Levin, M. D. & Morton-Firth, C. J. (1998). Receptor clustering as a cellular mechanism to control sensitivity. *Nature,* **393** (6680), 85–88.

Brown, N. H., Gregory, S. L., Rickoll, W. L., Fessler, L. I., Prout, M., White, R. A. H. & Fristrom, J. W. (2002). Talin is essential for integrin function in Drosophila. *Dev Cell,* **3** (4), 569–579.

Burgess, A. W., Cho, H.-S., Eigenbrot, C., Ferguson, K. M., Garrett, T. P. J., Leahy, D. J., Lemmon, M. A., Sliwkowski, M. X., Ward, C. W. & Yokoyama, S. (2003). An open-and-shut case? Recent insights into the activation of EGF/ErbB receptors. *Mol Cell,* **12** (3), 541–552.

Burroughs, N. & Wulfing, C. (2002). Differential segregation in a cell-cell contact interface: the dynamics of the immunological synapse. *Biophys. J.* **83**, 1784–96.

Camacho, S., Kosco-Vilbois, M. & Berek, C. (1998). The dynamic structure of the germinal center. *Immunol Today,* **19**, 511–4.

Campbell, E. A., Masuda, S., Sun, J. L., Muzzin, O., Olson, C. A., Wang, S. & Darst, S. A. (2002). Crystal structure of the *Bacillus stearothermophilus* anti-sigma factor SpoIIAB with the sporulation sigma factor σ^F. *Cell,* **108** (6), 795–807.

Campbell, I. D. & Ginsberg, M. H. (2004). The talin-tail interaction places integrin activation on FERM ground. *Trends Biochem Sci,* **29** (8), 429–435.

Carman, C. V. & Springer, T. A. (2003). Integrin avidity regulation: are changes in affinity and conformation underemphasized. *Curr Opin Cell Biol,* **15** (5), 547–556.

Carniol, K., Eichenberger, P. & Losick, R. (2004). A threshold mechanism governing activation of the developmental regulatory protein σ^F in *Bacillus subtilis*. *J Biol Chem,* **279** (15), 14860–14870.

Carrasco, Y. R., Fleire, S. J., Cameron, T., Dustin, M. L. & Batista, F. D. (2004). LFA-1/ICAM-1 interaction lowers the threshold of B cell activation by facilitating B cell adhesion and synapse formation. *Immunity,* **20** (5), 589–599.

Changeux, J.-P. & Edelstein, S. J. (2005). Allosteric mechanisms of signal transduction. *Science,* **308** (5727), 1424–1428.

Chen, C.-C., Lewis, R. J., Harris, R., Yudkin, M. D. & Delumeau, O. (2003). A supramolecular complex in the environmental stress signalling pathway of Bacillus subtilis. *Mol Microbiol,* **49** (6), 1657–1669.

Clark, M., Campbell, K., Kazlauskas, A., Johnson, S., Hertz, M., Potter, T., Pleiman, C. & Cambier, J. (1992). The B cell antigen receptor complex: association of Ig-alpha and Ig-beta with distinct cytoplasmic effectors. *Science,* **258**, 123–6.

Clark, M. R., Massenburg, D., Siemasko, K., Hou, P. & Zhang, M. (2004). B-cell antigen receptor signaling requirements for targeting antigen to the MHC class II presentation pathway. *Curr Opin Immunol,* **16** (3), 382–387.

Clark, M. R., Massenburg, D., Zhang, M. & Siemasko, K. (2003). Molecular mechanisms of B cell antigen receptor trafficking. *Ann N Y Acad Sci,* **987**, 26–37.

Clarkson, J., Campbell, I. D. & Yudkin, M. D. (2001). NMR studies of the interactions of SpoIIAA with its partner proteins that regulate sporulation in *Bacillus subtilis*. *J Mol Biol,* **314** (3), 359–364.

Clarkson, J., Campbell, I. D. & Yudkin, M. D. (2003). Phosphorylation induces subtle structural changes in SpoIIAA, a key regulator of sporulation. *Biochem J,* **372** (Pt 1), 113–119.

Clarkson, J., Campbell, I. D. & Yudkin, M. D. (2004*a*). Physical evidence for the induced release of the *Bacillus subtilis* transcription factor, σ^F, from its inhibitory complex. *J Mol Biol,* **340** (2), 203–209.

Clarkson, J., Campbell, I. D. & Yudkin, M. D. (2004*b*). Efficient regulation of σ^F, the first sporulation-specific sigma factor in *B.subtilis*. *J Mol Biol,* **342**, 1187–1195.

Clarkson, J., Shu, J.-C., Harris, D. A., Campbell, I. D. & Yudkin, M. D. (2004*c*). Fluorescence and kinetic analysis of the SpoIIAB phosphorylation reaction, a key regulator of sporulation in *Bacillus subtilis*. *Biochemistry,* **43** (11), 3120–3128.

Cooper, G. M. (2000). *The Cell - A Molecular Approach.* SINAUER ASSOCIATES, INC., Publishers.

Courey, A. J. (2001). Cooperativity in transcriptional control. *Curr Biol,* **11** (7), 250–252.

Dal Porto, J. M., Haberman, A. M., Kelsoe, G. & Shlomchik, M. J. (2002). Very low affinity B cells form germinal centers, become memory B cells, and participate in secondary immune responses when higher affinity competition is reduced. *J Exp Med,* **195** (9), 1215–1221.

Davis, S. J. & van der Merwe, P. A. (2006). The kinetic-segregation model: TCR triggering and beyond. *Nat Immunol,* **7** (8), 803–809.

de Pereda, J. M., Wegener, K. L., Santelli, E., Bate, N., Ginsberg, M. H., Critchley, D. R., Campbell, I. D. & Liddington, R. C. (2005). Structural basis for phosphatidylinositol phosphate kinase type Igamma binding to talin at focal adhesions. *J Biol Chem,* **280** (9), 8381–8386.

De Petris, S. (1974). Inhibition and reversal of capping by cytochalasin B, vinblastine and colchicine. *Nature,* **250** (461), 54–56.

De Robertis, E. M. & Kuroda, H. (2004). Dorsal-ventral patterning and neural induction in Xenopus embryos. *Annu Rev Cell Dev Biol,* **20**, 285–308.

de Vinuesa, C., Cook, M., Ball, J., Drew, M., Sunners, Y., Cascalho, M., Wabl, M., Klaus, G. & MacLennan, I. (2000). Germinal centers without T cells. *J. Exp. Med.* **191**, 485–493.

Delon, J., Bercivici, N., Raposo, G., Liblau, R. & Trautmann, A. (1998). Antigen-dependent and -independent Ca^{2+} responses triggered in T cells by dentritic cells compared with B cells. *J. Exp. Med,* **188**, 1473–1484.

Depoil, D., Zaru, R., Guiraud, M., Chauveau, A., Harriague, J., Bismuth, G., Utzny, C., Muller, S. & Valitutti, S. (2005). Immunological synapses are versatile structures enabling selective T cell polarization. *Immunity,* **22** (2), 185–194.

Di Paolo, G., Pellegrini, L., Letinic, K., Cestra, G., Zoncu, R., Voronov, S., Chang, S., Guo, J., Wenk, M. R. & De Camilli, P. (2002). Recruitment and regulation of phosphatidylinositol phosphate kinase type 1 gamma by the FERM domain of talin. *Nature,* **420** (6911), 85–89.

Diederich, B., Wilkinson, J. F., Magnin, T., Najafi, M., Erringston, J. & Yudkin, M. D. (1994). Role of interactions between SpoIIAA and SpoIIAB in regulating cell-specific transcription factor sigma F of Bacillus subtilis. *Genes Dev,* **8** (21), 2653–2663.

Dintzis, H. M., Dintzis, R. Z. & Vogelstein, B. (1976). Molecular determinants of immunogenicity: the immunon model of immune response. *Proc Natl Acad Sci U S A,* **73** (10), 3671–3675.

Dintzis, R. Z., Vogelstein, B. & Dintzis, H. M. (1982). Specific cellular stimulation in the primary immune response: experimental test of a quantized model. *Proc Natl Acad Sci U S A,* **79** (3), 884–888.

Doody, G., Justement, L., Delibrias, C., Matthews, R., Lin, J., Thomas, M. & Fearon, D. (1995). A role in B cell activation for CD22 and the protein tyrosine phosphatase SHP. *Science,* **269**, 242–244.

Dorfman, R. & Shilo, B. Z. (2001). Biphasic activation of the BMP pathway patterns the Drosophila embryonic dorsal region. *Development,* **128** (6), 965–972.

Duncan, L., Alper, S., Arigoni, F., Losick, R. & Stragier, P. (1995). Activation of cell-specific transcription by a serine phosphatase at the site of asymmetric division. *Science,* **270**, 641–644.

Duncan, L. & Losick, R. (1993). SpoIIAB is an anti-sigma factor that binds to and inhibits transcription by regulatory protein σ^F from *Bacillus subtilis. Proc Natl Acad Sci U S A,* **90** (6), 2325–2329.

Dustin, M. L., Ferguson, L. M., Chan, P. Y., Springer, T. A. & Golan, D. E. (1996). Visualization of CD2 interaction with LFA-3 and determination of the two-dimensional dissociation constant for adhesion receptors in a contact area. *J Cell Biol,* **132** (3), 465–474.

Dworkin, J. & Losick, R. (2001). Differential gene expression governed by chromosomal spatial asymmetry. *Cell,* **107**, 339–346.

Eisenbud, D. (1995). *Commutative Algebra with a View Toward Algebraic Geometry.* Springer-Verlag, New York.

Eisenstadt, E., Fisher, S., Der, C. L. & Silver, S. (1973). Manganese transport in Bacillus subtilis W23 during growth and sporulation. *J Bacteriol,* **113** (3), 1363–1372.

Eldar, A., Dorfman, R., Weiss, D., Ashe, H., Shilo, B.-Z. & Barkai, N. (2002). Robustness of the BMP morphogen gradient in Drosophila embryonic patterning. *Nature,* **419** (6904), 304–308.

Elowitz, M. B., Levine, A. J., Siggia, E. D. & Swain, P. S. (2002). Stochastic gene expression in a single cell. *Science,* **297** (5584), 1183–1186.

Erikson, J., Radic, M. Z., Camper, S. A., Hardy, R. R., Carmack, C. & Weigert, M. (1991). Expression of anti-DNA immunoglobulin transgenes in non-autoimmune mice. *Nature,* **349** (6307), 331–334.

Faull, R. J., Kovach, N. L., Harlan, J. M. & Ginsberg, M. H. (1993). Affinity modulation of integrin alpha 5 beta 1: regulation of the functional response by soluble fibronectin. *J Cell Biol,* **121** (1), 155–162.

Favier, B., Burroughs, N., Wedderburn, L. & Valitutti, S. (2001). TCR dynamics on the surface of living cells. *Int. Immunol.* **13**, 1525–1532.

Ferrell, J. E. J. (1999). Building a cellular switch: more lessons from a good egg. *Bioessays,* **21** (10), 866–870.

Ferrell, J. E. J. & Xiong, W. (2001). Bistability in cell signaling: How to make continuous processes discontinuous, and reversible processes irreversible. *Chaos,* **11** (1), 227–236.

Fersht, A. (1998). *Structure and Mechanism in Protein Science: Guide to enzyme catalysis and protein folding.* W.H. Freeman, New York.

Feucht, A., Abbotts, L. & Errington, J. (2002). The cell differentiation protein SpoIIE contains a regulatory site that controls its phosphatase activity in response to asymmetric septation. *Mol Microbiol,* **45**, 1119–1130.

Feucht, A., Daniel, R. A. & Errington, J. (1999). Characterization of a morphological checkpoint coupling cell-specific transcription to septation in Bacillus subtilis. *Mol Microbiol,* **33** (5), 1015–1026.

Feynman, R. (2006). *The Feynman Lectures of Physics - Definitive Edition.* Pearson Addison Weasley.

Fiedler, W., Borchers, C., Macht, M., Deininger, S. O. & Przybylski, M. (1998). Molecular characterization of a conformational epitope of hen egg white lysozyme by differential chemical modification of immune complexes and mass spectrometric peptide mapping. *Bioconjug Chem,* **9** (2), 236–241.

Fischer, E. H., Charbonneau, H. & Tonks, N. K. (1991). Protein tyrosine phosphatases: a diverse family of intracellular and transmembrane enzymes. *Science,* **253** (5018), 401–406.

Flory, P. (1953). *Principles of polymer chemistry.* Cornell University Press.

Foote, L. C., Howard, R. G., Marshak-Rothstein, A. & Rothstein, T. L. (1996). IL-4 induces Fas resistance in B cells. *J Immunol,* **157** (7), 2749–2753.

Fort, P. & Piggot, P. J. (1984). Nucleotide sequence of sporulation locus *spoIIA* in *Bacillus subtilis. J Gen Microbiol,* **130**, 2147–2153.

Francois, V., Solloway, M., O'Neill, J. W., Emery, J. & Bier, E. (1994). Dorsal-ventral patterning of the Drosophila embryo depends on a putative negative growth factor encoded by the short gastrulation gene. *Genes Dev,* **8** (21), 2602–2616.

Frandsen, N., Barák, I., Karmazyn-Campelli, C. & Stragier, P. (1999). Transient gene asymmetry during sporulation and establishment of cell specificity in *Bacillus subtilis. Genes Dev,* **13**, 394–399.

Fujita, M. & Sadaie, Y. (1998). Rapid isolation of RNA polymerase from sporulating cells of *Bacillus subtilis. Gene,* **221** (2), 185–190.

Garcia-Alvarez, B., de Pereda, J. M., Calderwood, D. A., Ulmer, T. S., Critchley, D., Campbell, I. D., Ginsberg, M. H. & Liddington, R. C. (2003). Structural determinants of integrin recognition by talin. *Mol Cell,* **11** (1), 49–58.

Gilbert, S. F. (2000). *Developmental Biology.* SINAUER ASSOCIATES, INC., Publishers.

Goldbeter, A. & Koshland, D. E. J. (1981). An amplified sensitivity arising from covalent modification in biological systems. *Proc Natl Acad Sci U S A,* **78** (11), 6840–6844.

Goldbeter, A. & Koshland, D. E. J. (1984). Ultrasensitivity in biochemical systems controlled by covalent modification. Interplay between zero-order and multistep effects. *J Biol Chem,* **259** (23), 14441–14447.

Goodnow, C. (1996). Balancing immunity and tolerance: deleting and tuning lymphocyte repertoires. *Proc Natl Acad Sci U S A,* **93**, 2264–71.

Goodnow, C., Brink, R. & Adams, E. (1991). Breakdown of self-tolerance in anergic b lymphocytes. *Nature,* **352**, 532–536.

Goodnow, C. C., Crosbie, J., Adelstein, S., Lavoie, T. B., Smith-Gill, S. J., Brink, R. A., Pritchard-Briscoe, H., Wotherspoon, J. S., Loblay, R. H., Raphael, K., Trent, R. J. & Basten, A. (1988). Altered immunoglobulin expression and functional silencing of self-reactive B lymphocytes in transgenic mice. *Nature,* **334** (6184), 676–682.

Grakoui, A., Bromley, S., Sumen, C., Davis, M., Shaw, A., Allen, P. & Dustin, M. (1999). The immunological synapse: a molecular machine controlling T cell activation. *Science,* **285**, 221–227.

Gregor, T., Bialek, W., de Ruyter van Steveninck, R. R., Tank, D. W. & Wieschaus, E. F. (2005). Diffusion and scaling during early embryonic pattern formation. *Proc Natl Acad Sci U S A,* **102** (51), 18403–18407.

Guénault, T. (1995). *Statistical Physics.* Kluwer Academic Publishers.

Guffanti, A. A., Clejan, S., Falk, L. H., Hicks, D. B. & Krulwich, T. A. (1987). Isolation and characterization of uncoupler-resistant mutants of *Bacillus subtilis*. *J Bacteriol,* **169** (10), 4469–4478.

Haberman, A. & Shlomchik, M. (2003). Reassessing the function of immune-complex retention by follicular dendritic cells. *Nat Rev Immunol,* **3**, 757–764.

Han, S., Hathcock, K., Zheng, B., Kepler, T. B., Hodes, R. & Kelsoe, G. (1995). Cellular interaction in germinal centers. Roles of CD40 ligand and B7-2 in established germinal centers. *J Immunol,* **155** (2), 556–567.

Hannum, L., Haberman, A., Anderson, S. & Shlomchik, M. (2000). Germinal center initiation, variable gene region hypermutation, and mutant B cell selection without detectable immune complexes on follicular dendritic cells. *J. Exp. Med.* **192**, 931–942.

Harding, C. V. & Unanue, E. R. (1990). Quantitation of antigen-presenting cell MHC class II/peptide complexes necessary for T-cell stimulation. *Nature,* **346** (6284), 574–576.

Hartley, S., Crosbie, J., Brink, R., Kantor, A., Basten, A. & Goodnow, C. (1991). Elimination from peripheral lymphoid tissues of self-reactive b lymphocytes recognizing membrane-bound antigens. *Nature,* **353**, 765–9.

Hecker, M., Heim, C., Volker, U. & Wolfel, L. (1988). Induction of stress proteins by sodium chloride treatment in *Bacillus subtilis*. *Arch Microbiol,* **150** (6), 564–566.

Heinrich, R., Neel, B. G. & Rapoport, T. A. (2002). Mathematical models of protein kinase signal transduction. *Mol Cell,* **9** (5), 957–970.

Heinrich, R. & Rapoport, T. A. (1974). A linear steady-state treatment of enzymatic chains. General properties, control and effector strength. *Eur J Biochem,* **42** (1), 89–95.

Hilbert, D. W. & Piggot, P. J. (2004). Compartmentalization of gene expression during *Bacillus subtilis* spore formation. *Microbiol Mol Biol Rev,* **68** (2), 234–262.

Ho, M. S., Carniol, K. & Losick, R. (2003). Evidence in support of a docking model for the release of the transcription factor σ^F from the antisigma factor SpoIIAB in *Bacillus subtilis*. *J Biol Chem,* **278**, 20898–20905.

Holley, S. A., Jackson, P. D., Sasai, Y., Lu, B., De Robertis, E. M., Hoffmann, F. M. & Ferguson, E. L. (1995). A conserved system for dorsal-ventral patterning in insects and vertebrates involving sog and chordin. *Nature,* **376** (6537), 249–253.

Hollowood, K. & Macartney, J. (1992). Cell kinetics of the germinal center reaction–a stathmokinetic study. *Eur J Immunol,* **22** (1), 261–266.

Hombach, J., Tsubata, T., Leclercq, L., Stappert, H. & Reth, M. (1990). Molecular components of the B-cell antigen receptor complex of the IgM class. *Nature,* **343** (6260), 760–762.

Horwitz, R. & Webb, D. (2003). Cell migration. *Curr Biol,* **13** (19), 756–759.

Houchmandzadeh, B., Wieschaus, E. & Leibler, S. (2002). Establishment of developmental precision and proportions in the early Drosophila embryo. *Nature,* **415** (6873), 798–802.

Howard, M. (2004). A mechanism for polar protein localization in bacteria. *J Mol Biol,* **335** (2), 655–663.

Howard, M. & Kruse, K. (2005). Cellular organization by self-organization: mechanisms and models for Min protein dynamics. *J Cell Biol,* **168** (4), 533–536.

Howard, M., Rutenberg, A. D. & de Vet, S. (2001). Dynamic compartmentalization of bacteria: accurate division in E. coli. *Phys Rev Lett,* **87** (27 Pt 1), 278102.

Huang, K. C., Meir, Y. & Wingreen, N. S. (2003). Dynamic structures in Escherichia coli: spontaneous formation of MinE rings and MinD polar zones. *Proc Natl Acad Sci U S A,* **100** (22), 12724–12728.

Huppa, J. B., Gleimer, M., Sumen, C. & Davis, M. M. (2003). Continuous T cell receptor signaling required for synapse maintenance and full effector potential. *Nat Immunol,* **4** (8), 749–755.

Hutchcroft, J., Harrison, M. & Geahlen, R. (1992). Association of the 72-kDa protein-tyrosine kinase PTK72 with the B cell antigen receptor. *J Biol Chem,* **267**, 8613–8619.

Hynes, R. O. (2002). Integrins: bidirectional, allosteric signaling machines. *Cell,* **110** (6), 673–687.

Iber, D. (2005). Formation of the B cell synapse: retention or recruitment? *Cell Mol Life Sci,* **62** (2), 206–213.

Iber, D. & Maini, P. (2002). A mathematical model of germinal centre kinetics and affinity maturation. *J. Theor. Biol,* **219**, 153–175.

Igoshin, O. A., Price, C. W. & Savageau, M. A. (2006). Signalling network with a bistable hysteretic switch controls developmental activation of the sigma transcription factor in Bacillus subtilis. *Mol Microbiol,* **61** (1), 165–184.

Illing, N. & Errington, J. (1991). Genetic regulation of morphogenesis in *Bacillus subtilis*: roles of σ^E and σ^F in prespore engulfment. *J Bacteriol,* **173** (10), 3159–3169.

Irvine, D. J., Hue, K.-A., Mayes, A. M. & Griffith, L. G. (2002). Simulations of cell-surface integrin binding to nanoscale-clustered adhesion ligands. *Biophys J,* **82** (1 Pt 1), 120–132.

Jacob, J., Kassir, R. & Kelsoe, G. (1991). In situ studies of the primary immune response to (4-hydroxy-3-nitrophenyl)acetyl. I. the architecture and dynamics of responding cell populations. *J. Exp. Med.* **173**, 1165–1175.

Jacob, J., Przylepa, J., Miller, C. & Kelsoe, G. (1993). In situ studies of the primary immune response to (4-hydroxy-3-nitrophenyl)acetyl. III. the kinetics of V region mutation and selection in germinal center B cells. *J. Exp. Med.* **178**, 1293–1307.

Janeway, C. & Travers, P. (1997). *Immunology. The Immune System in Health and Disease.* Garland Publisher.

Jolliffe, L. K., Doyle, R. J. & Streips, U. N. (1981). The energized membrane and cellular autolysis in *Bacillus subtilis. Cell,* **25** (3), 753–763.

Jolly, C. J., Wagner, S. D., Rada, C., Klix, N., Milstein, C. & Neuberger, M. S. (1996). The targeting of somatic hypermutation. *Semin Immunol,* **8** (3), 159–168.

Kaern, M., Elston, T. C., Blake, W. J. & Collins, J. J. (2005). Stochasticity in gene expression: from theories to phenotypes. *Nat Rev Genet,* **6** (6), 451–464.

Kauffman, S. (1993). *The Origins of Order.* Oxford University Press.

Kehres, D. G. & Maguire, M. E. (2003). Emerging themes in manganese transport, biochemistry and pathogenesis in bacteria. *FEMS Microbiol Rev,* **27** (2-3), 263–290.

Keizer, J. (1982). Nonequilibrium statistical thermodynamics and the effect of diffusion on chemical reaction rates. *J. Phys. Chem.* **86**, 5052–5067.

Kelsoe, G. (1996*a*). The germinal center: a crucible for lymphocyte selection. *Semin. Immunol.* **8**, 179ff.

Kelsoe, G. (1996*b*). The germinal center: a crucible for lymphocyte selection. *Semin Immunol,* **8** (3), 179–184.

Kepler, T. & Perelson, A. (1993). Somatic hypermutation in B cells: an optimal control treatment. *J. Theor. Biol.* **164**, 37–64.

Kerszberg, M. & Wolpert, L. (1998). Mechanisms for positional signalling by morphogen transport: a theoretical study. *J Theor Biol,* **191** (1), 103–114.

Kesmir, C. & De Boer, R. J. (1999). A mathematical model on germinal center kinetics and termination. *J Immunol,* **163** (5), 2463–2469.

Kesmir, C. & De Boer, R. J. (2003). A spatial model of germinal center reactions: cellular adhesion based sorting of B cells results in efficient affinity maturation. *J Theor Biol,* **222** (1), 9–22.

Khvorova, A., Zhang, L., Higgins, M. L. & Piggot, P. J. (1998). The spoIIE locus is involved in the Spo0A-dependent switch in the location of FtsZ rings in Bacillus subtilis. *J Bacteriol,* **180** (5), 1256–1260.

Kim, M., Carman, C. V., Yang, W., Salas, A. & Springer, T. A. (2004). The primacy of affinity over clustering in regulation of adhesiveness of the integrin alphaLbeta2. *J Cell Biol,* **167** (6), 1241–1253.

King, N., Dreesen, O., Stragier, P., Pogliano, K. & Losick, R. (1999). Septation, dephosphorylation, and the activation of σ^F during sporulation in *Bacillus subtilis*. *Genes Dev,* **13**, 1156–1167.

Klebe, C., Prinz, H., Wittinghofer, A. & Goody, R. S. (1995). The kinetic mechanism of Ran–nucleotide exchange catalyzed by RCC1. *Biochemistry,* **34** (39), 12543–12552.

Klein, U., Tu, Y., Stolovitzky, G. A., Keller, J. L., Haddad, J. J., Miljkovic, V., Cattoretti, G., Califano, A. & Dalla-Favera, R. (2003). Gene expression dynamics during germinal center transit in B cells. *Ann N Y Acad Sci,* **987**, 166–172.

Koni, P. A. & Flavell, R. A. (1999). Lymph node germinal centers form in the absence of follicular dendritic cell networks. *J Exp Med,* **189** (5), 855–864.

Kosco-Vilbois, M. H. (2003). Are follicular dendritic cells really good for nothing? *Nat Rev Immunol,* **3** (9), 764–769.

Kouskoff, V., Famiglietti, S., Lacaud, G., Lang, P., Rider, J. E., Kay, B. K., Cambier, J. C. & Nemazee, D. (1998). Antigens varying in affinity for the B cell receptor induce differential B lymphocyte responses. *J Exp Med,* **188** (8), 1453–1464.

Kroese, F., Wubena, A., Seijen, H. & Nieuwenhuis, P. (1987). Germinal centers develop oligoclonally. *Eur. J. Immunol.* **17**, 1069–1072.

Kruse, K. (2002). A dynamic model for determining the middle of Escherichia coli. *Biophys J,* **82** (2), 618–627.

Kruse, K., Pantazis, P., Bollenbach, T., Julicher, F. & Gonzalez-Gaitan, M. (2004). Dpp gradient formation by dynamin-dependent endocytosis: receptor trafficking and the diffusion model. *Development,* **131** (19), 4843–4856.

Kuo, S. C. & Lauffenburger, D. A. (1993). Relationship between receptor/ligand binding affinity and adhesion strength. *Biophys J,* **65** (5), 2191–2200.

Kupfer, A. & Kupfer, H. (2003). Imaging immune cell interactions and functions: smacs and the immunological synapse. *Semin Immunol,* **15**, 295–300.

Kupfer, A., Mosmann, T. R. & Kupfer, H. (1991). Polarized expression of cytokines in cell conjugates of helper T cells and splenic B cells. *Proc Natl Acad Sci U S A,* **88** (3), 775–779.

Kupfer, H., Monks, C. R. & Kupfer, A. (1994). Small splenic B cells that bind to antigen-specific T helper (Th) cells and face the site of cytokine production in the Th cells selectively proliferate: immunofluorescence microscopic studies of Th-B antigen-presenting cell interactions. *J Exp Med,* **179** (5), 1507–1515.

Kuppers, R., Zhao, M., Hansmann, M.-L. & Rajewsky, K. (1993). Tracing B cell development in human germinal centres by molecular analysis of singel cells picked from histological sections. *EMBO,* **12**, 4955–4967.

Kwon, J., Qu, C.-K., Maeng, J.-S., Falahati, R., Lee, C. & Williams, M. S. (2005). Receptor-stimulated oxidation of SHP-2 promotes T-cell adhesion through SLP-76-ADAP. *EMBO J,* **24** (13), 2331–2341.

Lander, A. D., Nie, Q. & Wan, F. Y. M. (2002). Do morphogen gradients arise by diffusion? *Dev Cell,* **2** (6), 785–796.

Lapedes, A. & Farber, R. (2001). The geometry of shape space: application to influenza. *J Theor Biol,* **212** (1), 57–69.

Lee, C. S., Clarkson, J., Shu, J. C., Campbell, I. D. & Yudkin, M. D. (2001). *Bacillus subtilis* mutations that alter the pathway of phosphorylation of the anti-anti-σ^F factor SpoIIAA lead to a Spo- phenotype. *Mol Microbiol,* **40** (1), 9–19.

Lee, C. S., Lucet, I. & Yudkin, M. D. (2000). Fate of the SpoIIAB*-ADP liberated after SpoIIAB phosphorylates SpoIIAA of *Bacillus subtilis*. *J Bacteriol,* **182** (21), 6250–6253.

Lee, E., Salic, A., Kruger, R., Heinrich, R. & Kirschner, M. W. (2003). The roles of APC and axin derived from experimental and theoretical analysis of the Wnt pathway. *PLoS Biol,* **1** (1), E10.

Lee, S.-J. E., Hori, Y., Groves, J. T., Dustin, M. L. & Chakraborty, A. K. (2002). Correlation of a dynamic model for immunological synapse formation with effector functions: two pathways to synapse formation. *Trends Immunol,* **23** (10), 492–499.

Lee, S. R., Kwon, K. S., Kim, S. R. & Rhee, S. G. (1998). Reversible inactivation of protein-tyrosine phosphatase 1B in A431 cells stimulated with epidermal growth factor. *J Biol Chem,* **273** (25), 15366–15372.

Li, R., Mitra, N., Gratkowski, H., Vilaire, G., Litvinov, R., Nagasami, C., Weisel, J. W., Lear, J. D., DeGrado, W. F. & Bennett, J. S. (2003). Activation of integrin alphaI-Ibbeta3 by modulation of transmembrane helix associations. *Science,* **300** (5620), 795–798.

Lindhout, E., Lakeman, A. & de Groot, C. (1995). Follicular dendritic cells inhibit apoptosis in human B lymphocytes by a rapid and irreversible blockade of preexisting endonuclease. *J Exp Med,* **181** (6), 1985–1995.

Ling, K., Doughman, R. L., Firestone, A. J., Bunce, M. W. & Anderson, R. A. (2002). Type I gamma phosphatidylinositol phosphate kinase targets and regulates focal adhesions. *Nature,* **420** (6911), 89–93.

Lipowsky, R. & Klumpp, S. (2005). Life is Motion - Multiscale Motility of Molecular Motors. *Physica A,* **352**, 53–112.

Liu, Y., Zhang, J., Chan, E. & MacLennan, I. (1991*a*). Sites of specific B cell activation in primary and secondary responses to T-cell-dependent and T-cell-independent antigens. *Eur J Immunol,* **21**, 2951–2962.

Liu, Y., Zhang, J., Chan, E. & MacLennan, I. (1991*b*). Sites of specific B cell activation in primary and secondary responses to T-cell-dependent and T-cell-independent antigens. *Eur J Immunol,* **21**, 2951–2962.

Liu, Y. J. & Arpin, C. (1997). Germinal center development. *Immunol Rev,* **156**, 111–126.

Liu, Y.-J., Barthelemy, C. & de Bouteiller, O. (1994). The differences in survival and phenotype between centroblasts and centrocytes. *InVivo Immunology,* , 213–218.

Liu, Y. J., de Bouteiller, O. & Fugier-Vivier, I. (1997). Mechanisms of selection and differentiation in germinal centers. *Curr Opin Immunol,* **9** (2), 256–262.

Lord, M., Barillà, D. & Yudkin, M. D. (1999). Replacement of vegetative σ^A by sporulation-specific σ^F as a component of the RNA polymerase holoenzyme in sporulating *Bacillus subtilis*. *J Bacteriol,* **181**, 2346–2350.

Lord, M., Magnin, T. & Yudkin, M. D. (1996). Protein conformational change and nucleotide binding involved in regulation of σ^F in *Bacillus subtilis*. *J Bacteriol.* **178**, 6730–6735.

Losick, R. & Stragier, P. (1992). Crisscross regulation of cell-type-specific gene expression during development in B. subtilis. *Nature,* **355** (6361), 601–604.

Lucet, I., Borriss, R. & Yudkin, M. D. (1999). Purification, kinetic properties, and intracellular concentration of SpoIIE, an integral membrane protein that regulates sporulation in *Bacillus subtilis*. *J Bacteriol,* **181**, 3242–3245.

Lucet, I., Feucht, A., Yudkin, M. D. & Errington, J. (2000). Direct interaction between the cell division protein FtsZ and the cell differentiation protein SpoIIE. *EMBO J,* **19**, 1467–1475.

Machius, M., Chuang, J. L., Wynn, R. M., Tomchick, D. R. & Chuang, D. T. (2001). Structure of rat BCKD kinase: nucleotide-induced domain communication in a mitochondrial protein kinase. *Proc Natl Acad Sci U S A,* **98** (20), 11218–11223.

MacLennan, I. (1994). Germinal centers. *Annu. Rev. Immunol.* **12**, 117–139.

MacLennan, I., de Vinuesa, C. G. & Casamayor-Palleja, M. (2000). B-cell memory and the persistence of antibody responses. *Philos Trans R Soc Lond B Biol Sci.* **355**, 345–350.

MacLennan, I., Liu, Y., Oldfield, S., Zhang, J. & Lane, P. (1990). The evolution of B-cell clones. *Curr Top Microbiol Immunol,* **159**, 37–64.

MacLennan, I. C., Gulbranson-Judge, A., Toellner, K. M., Casamayor-Palleja, M., Chan, E., Sze, D. M., Luther, S. A. & Orbea, H. A. (1997). The changing preference of T and B cells for partners as T-dependent antibody responses develop. *Immunol Rev,* **156**, 53–66.

Magnin, T., Lord, M. & Yudkin, M. D. (1997). Contribution of partner switching and SpoIIAA cycling to regulation of σ^F activity in sporulating *Bacillus subtilis*. *J Bacteriol,* **179**, 3922–3927.

Manser, T. (2004). Textbook germinal centers? *J Immunol,* **172** (6), 3369–3375.

Marques, G., Musacchio, M., Shimell, M. J., Wunnenberg-Stapleton, K., Cho, K. W. & O'Connor, M. B. (1997). Production of a DPP activity gradient in the early Drosophila embryo through the opposing actions of the SOG and TLD proteins. *Cell,* **91** (3), 417–426.

Martel, V., Racaud-Sultan, C., Dupe, S., Marie, C., Paulhe, F., Galmiche, A., Block, M. R. & Albiges-Rizo, C. (2001). Conformation, localization, and integrin binding of talin depend on its interaction with phosphoinositides. *J Biol Chem,* **276** (24), 21217–21227.

Masuda, S., Murakami, K. S., Wang, S., Anders Olson, C., Donigian, J., Leon, F., Darst, S. A. & Campbell, E. A. (2004). Crystal structures of the ADP and ATP bound forms of the *Bacillus* anti-sigma factor SpoIIAB in complex with the anti-anti-sigma SpoIIAA. *J Mol Biol,* **340** (5), 941–956.

Matsumoto, M., Lo, S. F., Carruthers, C. J., Min, J., Mariathasan, S., Huang, G., Plas, D. R., Martin, S. M., Geha, R. S., Nahm, M. H. & Chaplin, D. D. (1996). Affinity maturation without germinal centres in lymphotoxin-alpha-deficient mice. *Nature,* **382** (6590), 462–466.

Matsuuchi, L. & Gold, M. R. (2001). New views of BCR structure and organization. *Curr Opin Immunol,* **13** (3), 270–277.

May, R. M. (2004). Uses and abuses of mathematics in biology. *Science,* **303** (5659), 790–793.

McCarthy, E. K. & Goldstein, B. (2006). Asymmetric spindle positioning. *Curr Opin Cell Biol,* **18** (1), 79–85.

McCarthy, J. E. & Gualerzi, C. (1990). Translational control of prokaryotic gene expression. *Trends Genet,* **6** (3), 78–85.

Meinhardt, H. & de Boer, P. A. (2001). Pattern formation in Escherichia coli: a model for the pole-to-pole oscillations of Min proteins and the localization of the division site. *Proc Natl Acad Sci U S A,* **98** (25), 14202–14207.

Merkin, J. H. & Sleeman, B. D. (2005). On the spread of morphogens. *J Math Biol,* **51** (1), 1–17.

Meyer-Hermann, M. (2002*a*). A mathematical model for the germinal center morphology and affinity maturation. *J Theor Biol,* **216** (3), 273–300.

Meyer-Hermann, M. (2002*b*). Does recycling in germinal centres exist. *Immunol Cell Biol,* **80** (1), 30–35.

Meyer-Hermann, M. & Beyer, T. (2002). Conclusions from two model concepts on germinal center dynamics and morphology. *Dev Immunol,* **9** (4), 203–214.

Meyer-Hermann, M., Deutsch, A. & Or-Guil, M. (2001). Recycling probability and dynamical properties of germinal center reactions. *J Theor Biol,* **210**, 265–285.

Meyer-Hermann, M. E. & Maini, P. K. (2005). Cutting edge: back to "one-way" germinal centers. *J Immunol,* **174** (5), 2489–2493.

Michel, F., Attal-Bonnefoy, G., Mangino, G., Mise-Omata, S. & Acuto, O. (2001). CD28 as a molecular amplifier extending TCR ligation and signaling capabilities. *Immunity,* **15** (6), 935–945.

Miller, M., Wei, S., Parker, I. & Cahalan, M. (2002). Two-photon imaging of lymphocyte motility and antigen response in intact lymph node. *Science,* **296**, 1869–73.

Min, K. T., Hilditch, C. M., Diederich, B., Errington, J. & Yudkin, M. D. (1993). σ^F, the first compartment-specific transcription factor of *B. subtilis*, is regulated by an anti-sigma factor that is also a protein kinase. *Cell,* **74** (4), 735–742.

Mizutani, C. M., Nie, Q., Wan, F. Y. M., Zhang, Y.-T., Vilmos, P., Sousa-Neves, R., Bier, E., Marsh, J. L. & Lander, A. D. (2005). Formation of the BMP activity gradient in the Drosophila embryo. *Dev Cell,* **8** (6), 915–924.

Monod, J., Wyman, J. & Changeux, J. P. (1965). On the nature of allosteric transitions: a plausible model. *J Mol Biol,* **12**, 88–118.

Moy, V. T., Jiao, Y., Hillmann, T., Lehmann, H. & Sano, T. (1999). Adhesion energy of receptor-mediated interaction measured by elastic deformation. *Biophys J,* **76** (3), 1632–1638.

Najafi, S. M. A., Harris, D. A. & Yudkin, M. D. (1997). Properties of the phosphorylation reaction catalyzed by SpoIIAB that help to regulate sporulation of *Bacillus subtilis*. *J Bacteriol,* **179** (17), 5628–5631.

Nakano, S. & Kawabata, Z. (2000). Changes in cell volume of bacteria and heterotrophic nanoflagellates in a hypereutrophic pond. *Hydrobiologia,* **428**, 197–203.

Nossal, G. J. (1992). The molecular and cellular basis of affinity maturation in the antibody response. *Cell,* **68** (1), 1–2.

Palecek, S. P., Loftus, J. C., Ginsberg, M. H., Lauffenburger, D. A. & Horwitz, A. F. (1997). Integrin-ligand binding properties govern cell migration speed through cell-substratum adhesiveness. *Nature,* **385** (6616), 537–540.

Palmer, E. (2003). Negative selection–clearing out the bad apples from the T-cell repertoire. *Nat Rev Immunol,* **3** (5), 383–391.

Pan, Q., Garsin, D. A. & Losick, R. (2001). Self-reinforcing activation of a cell-specific transcription factor by proteolysis of an anti-sigma factor in *B. subtilis*. *Mol Cell,* **8**, 873–883.

Pani, G., Kozlowski, M., Cambier, J., Mills, G. & Siminovitch, K. (1995). Identification of the tyrosine phosphatase PTP1C as a B cell antigen receptor-associated protein involved in the regulation of B cell signaling. *J Exp Med,* **181**, 2077–84.

Pascual, V., Cha, S., Gershwin, M. E., Capra, J. D. & Leung, P. S. (1994). Nucleotide sequence analysis of natural and combinatorial anti-PDC-E2 antibodies in patients with primary biliary cirrhosis. Recapitulating immune selection with molecular biology. *J Immunol,* **152** (5), 2577–2585.

Perelson, A. S. & Oster, G. F. (1979). Theoretical studies of clonal selection: minimal antibody repertoire size and reliability of self-non-self discrimination. *J Theor Biol,* **81** (4), 645–670.

Perelson, A. S. & Wiegel, F. W. (1981). Theoretical considerations of the role of antigen structure in B cell activation. *Fed Proc,* **40** (5), 1479–1483.

Pulendran, B., Kannourakis, G., Nouri, S., Smith, K. G. & Nossal, G. J. (1995*a*). Soluble antigen can cause enhanced apoptosis of germinal-centre B cells. *Nature,* **375** (6529), 331–334.

Pulendran, B., Smith, K. G. & Nossal, G. J. (1995*b*). Soluble antigen can impede affinity maturation and the germinal center reaction but enhance extrafollicular immunoglobulin production. *J Immunol,* **155** (3), 1141–1150.

Qi, S., Groves, J. & Chakraborty, A. (2001). Synaptic pattern formation during cellular recognition. *PNAS,* **98**, 6548–6553.

Randall, T., Parkhouse, R. & Corley, R. (1992). J chain synthesis and secretion of hexameric igm is differentially regulated by lipopolysaccharide and interleukin 5. *Proc Natl Acad Sci U S A,* **89**, 962–966.

Ray, R. P., Arora, K., Nusslein-Volhard, C. & Gelbart, W. M. (1991). The control of cell fate along the dorsal-ventral axis of the Drosophila embryo. *Development,* **113** (1), 35–54.

Reichert, P., Reinhardt, R. L., Ingulli, E. & Jenkins, M. K. (2001). Cutting edge: in vivo identification of TCR redistribution and polarized IL-2 production by naive CD4 T cells. *J Immunol,* **166** (7), 4278–4281.

Reth, M. (2002). Hydrogen peroxide as second messenger in lymphocyte activation. *Nat Immunol,* **3**, 1129–1134.

Reth, M. & Brummer, T. (2004). Feedback regulation of lymphocyte signalling. *Nat Rev Immunol,* **4** (4), 269–277.

Reth, M. & Wienands, J. (2004). *in Molecular Biology of B cells: Structure and Function of B cell antigen receptor complexes*, pp. 161–169. Elsevier Science (USA).

Reth, M., Wienands, J. & Schamel, W. (2000). An unsolved problem of the clonal selection theory and the model of an oligomeric B-cell antigen receptor. *Immunol Rev,* **176**, 10–18.

Rolli, V., Gallwitz, M., Wossning, T., Flemming, A., Schamel, W., Zurn, C. & Reth, M. (2002). Amplification of B cell antigen receptor signaling by a Syk/ITAM positive feedback loop. *Mol Cell,* **10**, 1057–69.

Ross, J. J., Shimmi, O., Vilmos, P., Petryk, A., Kim, H., Gaudenz, K., Hermanson, S., Ekker, S. C., O'Connor, M. B. & Marsh, J. L. (2001). Twisted gastrulation is a conserved extracellular BMP antagonist. *Nature,* **410** (6827), 479–483.

Rothstein, T. L., Zhong, X., Schram, B. R., Negm, R. S., Donohoe, T. J., Cabral, D. S., Foote, L. C. & Schneider, T. J. (2000). Receptor-specific regulation of B-cell susceptibility to Fas-mediated apoptosis and a novel Fas apoptosis inhibitory molecule. *Immunol Rev,* **176**, 116–133.

Rousseau, F. & Schymkowitz, J. (2005). A systems biology perspective on protein structural dynamics and signal transduction. *Curr Opin Struct Biol,* **15** (1), 23–30.

Ryan, G. B., Unanue, E. R. & Karnovsky, M. J. (1974). Inhibition of surface capping of macromolecules by local anaesthetics and tranquillisers. *Nature,* **250** (461), 56–57.

Ryter, A. (1965). Étude morphologique de la sporulation de *Bacillus subtilis*. *Ann Inst Pasteur (Paris),* **108**, 40–60.

Schamel, W. & Reth, M. (2000). Monomeric and oligomeric complexes of the B cell antigen receptor. *Immunity,* **13**, 5–14.

Schlessinger, J. (2002). Ligand-induced, receptor-mediated dimerization and activation of EGF receptor. *Cell,* **110** (6), 669–672.

Schreiner, G. & Unanue, E. (1976). Membrane and cytoplasmic changes in B lymphocytes induced by ligand-surface immunoglobulin interaction. *Adv Immunol,* **24**, 37–165.

Schroeter, R., Schlisio, S., Lucet, I., Yudkin, M. & Borriss, R. (1999). The *Bacillus subtilis* regulator protein SpoIIE shares functional and structural similarities with eukaryotic protein phosphatases 2C. *FEMS Microbiol Lett,* **174** (1), 117–123.

Scrutton, N. S., Berry, A. & Perham, R. N. (1990). Redesign of the coenzyme specificity of a dehydrogenase by protein engineering. *Nature,* **343** (6253), 38–43.

Sedwick, C. E., Morgan, M. M., Jusino, L., Cannon, J. L., Miller, J. & Burkhardt, J. K. (1999). TCR, LFA-1, and CD28 play unique and complementary roles in signaling T cell cytoskeletal reorganization. *J Immunol,* **162** (3), 1367–1375.

Seed, B. (1995). Initiation of signal transduction by receptor aggregation: role of nonreceptor tyrosine kinases. *Semin Immunol,* **7** (1), 3–11.

Shih, T.-A. Y., Meffre, E., Roederer, M. & Nussenzweig, M. C. (2002). Role of BCR affinity in T cell dependent antibody responses in vivo. *Nat Immunol,* **3** (6), 570–575.

Shimmi, O. & O'Connor, M. B. (2003). Physical properties of Tld, Sog, Tsg and Dpp protein interactions are predicted to help create a sharp boundary in Bmp signals during dorsoventral patterning of the Drosophila embryo. *Development,* **130** (19), 4673–4682.

Shimmi, O., Umulis, D., Othmer, H. & O'Connor, M. B. (2005). Facilitated transport of a Dpp/Scw heterodimer by Sog/Tsg leads to robust patterning of the Drosophila blastoderm embryo. *Cell,* **120** (6), 873–886.

Shu, J. C., Clarkson, J. & Yudkin, M. D. (2004). Studies of SpoIIAB mutant proteins elucidate the mechanisms that regulate the developmental transcription factor σ^F in *Bacillus subtilis*. *Biochem J.* **384**, 169–178.

Sidman, C. & Unanue, E. (1975). Receptor-mediated inactivation of early b lymphocytes. *Nature,* **257**, 149–51.

Singh, D. K., Kumar, D., Siddiqui, Z., Basu, S. K., Kumar, V. & Rao, K. V. S. (2005). The strength of receptor signaling is centrally controlled through a cooperative loop between Ca2+ and an oxidant signal. *Cell,* **121** (2), 281–293.

Siskind, G. W. & Benacerraf, B. (1969). Cell selection by antigen in the immune response. *Adv Immunol,* **10**, 1–50.

Slepchenko, B. M. & Terasaki, M. (2004). Bio-switches: what makes them robust? *Curr Opin Genet Dev,* **14** (4), 428–434.

Smith, K. G., Light, A., Nossal, G. J. & Tarlinton, D. M. (1997). The extent of affinity maturation differs between the memory and antibody-forming cell compartments in the primary immune response. *EMBO J,* **16** (11), 2996–3006.

Sotirellis, N., Johnson, T. M., Hibbs, M. L., Stanley, I. J., Stanley, E., Dunn, A. R. & Cheng, H. C. (1995). Autophosphorylation induces autoactivation and a decrease in the Src homology 2 domain accessibility of the Lyn protein kinase. *J Biol Chem,* **270** (50), 29773–29780.

Srinivasan, S., Rashka, K. E. & Bier, E. (2002). Creation of a Sog morphogen gradient in the Drosophila embryo. *Dev Cell,* **2** (1), 91–101.

St Johnston, R. D. & Gelbart, W. M. (1987). Decapentaplegic transcripts are localized along the dorsal-ventral axis of the Drosophila embryo. *EMBO J,* **6** (9), 2785–2791.

Steussy, C. N., Popov, K. M., Bowker-Kinley, M. M., Sloan, R. B. J., Harris, R. A. & Hamilton, J. A. (2001). Structure of pyruvate dehydrogenase kinase. Novel folding pattern for a serine protein kinase. *J Biol Chem,* **276** (40), 37443–37450.

Stryer, L. (1995). *Biochemistry.* W.H. Freeman, New York.

Suehiro, K., Gailit, J. & Plow, E. F. (1997). Fibrinogen is a ligand for integrin alpha5beta1 on endothelial cells. *J Biol Chem,* **272** (8), 5360–5366.

Sulzer, B. & Perelson, A. S. (1997). Immunons revisited: binding of multivalent antigens to B cells. *Mol Immunol,* **34** (1), 63–74.

Sun, T., Clark, M. R. & Storb, U. (2002). A point mutation in the constant region of Ig lambda1 prevents normal B cell development due to defective BCR signaling. *Immunity,* **16** (2), 245–255.

Swain, P. S. (2004). Efficient attenuation of stochasticity in gene expression through post-transcriptional control. *J Mol Biol,* **344** (4), 965–976.

Tadokoro, S., Shattil, S. J., Eto, K., Tai, V., Liddington, R. C., de Pereda, J. M., Ginsberg, M. H. & Calderwood, D. A. (2003). Talin binding to integrin beta tails: a final common step in integrin activation. *Science,* **302** (5642), 103–106.

Takahashi, Y., Cerasoli, D. M., Dal Porto, J. M., Shimoda, M., Freund, R., Fang, W., Telander, D. G., Malvey, E. N., Mueller, D. L., Behrens, T. W. & Kelsoe, G. (1999). Relaxed negative selection in germinal centers and impaired affinity maturation in bcl-xL transgenic mice. *J Exp Med,* **190** (3), 399–410.

Takahashi, Y., Ohta, H. & Takemori, T. (2001). Fas is required for clonal selection in germinal centers and the subsequent establishment of the memory B cell repertoire. *Immunity,* **14** (2), 181–192.

Tamkun, J. W., DeSimone, D. W., Fonda, D., Patel, R. S., Buck, C., Horwitz, A. F. & Hynes, R. O. (1986). Structure of integrin, a glycoprotein involved in the transmembrane linkage between fibronectin and actin. *Cell,* **46** (2), 271–282.

Tarlinton, D. & Smith, K. (2000). Dissecting affinity maturation: a model explaining selection of antibody-forming cells and memory B cells in the germinal centre. *Immunol Today,* **9**, 436–441.

Tew, J. G., Wu, J., Qin, D., Helm, S., Burton, G. F. & Szakal, A. K. (1997). Follicular dendritic cells and presentation of antigen and costimulatory signals to B cells. *Immunol Rev,* **156**, 39–52.

Tolar, P., Sohn, H. W. & Pierce, S. K. (2005). The initiation of antigen-induced B cell antigen receptor signaling viewed in living cells by fluorescence resonance energy transfer. *Nat Immunol,* **6** (11), 1168–1176.

Turing, A. (1952). The chemical basis of morphogenesis. *Phil. Trans. Roy. Soc. Lond,* **B237**, 37–72.

van der Gucht, J. (2004). *Equilibrium polymers in solution and at interfaces.* PhD thesis, Wageningen Universiteit.

van Eijk, M. & de Groot, C. (1999). Germinal center B-cell apoptosis requires both caspase and cathepsin activity. *J. Immunol.* **163**, 2478–2482.

van Eijk, M., Defrance, T., Hennino, A. & de Groot, C. (2001). Death-receptor contribution to the germinal-center reaction. *Trends Immunol,* **22** (12), 677–682.

van Kampen, N. (1992). *Stochastic Processes in physics and chemistry.* Elsevier Science Publishers.

Verbeke, C. S., Wenthe, U. & Zentgraf, H. (1999). Fas ligand expression in the germinal centre. *J Pathol,* **189** (2), 155–160.

Vetter, I. R. & Wittinghofer, A. (2001). The guanine nucleotide-binding switch in three dimensions. *Science,* **294** (5545), 1299–1304.

Vilen, B. J., Burke, K. M., Sleater, M. & Cambier, J. C. (2002). Transmodulation of BCR signaling by transduction-incompetent antigen receptors: implications for impaired signaling in anergic B cells. *J Immunol,* **168** (9), 4344–4351.

Vilen, B. J., Nakamura, T. & Cambier, J. C. (1999). Antigen-stimulated dissociation of BCR mIg from Ig-alpha/Ig-beta: implications for receptor desensitization. *Immunity,* **10** (2), 239–248.

Vitte, J., Benoliel, A.-M., Eymeric, P., Bongrand, P. & Pierres, A. (2004). Beta-1 integrin-mediated adhesion may be initiated by multiple incomplete bonds, thus accounting for the functional importance of receptor clustering. *Biophys J,* **86** (6), 4059–4074.

Vlahos, C. J., Matter, W. F., Brown, R. F., Traynor-Kaplan, A. E., Heyworth, P. G., Prossnitz, E. R., Ye, R. D., Marder, P., Schelm, J. A. & Rothfuss, K. J. (1995). Investigation of neutrophil signal transduction using a specific inhibitor of phosphatidylinositol 3-kinase. *J Immunol,* **154** (5), 2413–2422.

Vogelstein, B., Dintzis, R. Z. & Dintzis, H. M. (1982). Specific cellular stimulation in the primary immune response: a quantized model. *Proc Natl Acad Sci U S A,* **79** (2), 395–399.

Vora, K., Ravetch, J. & Manser, T. (1997). Amplified follicular immune complex deposition in mice lacking the Fc receptor γ-chain does not alter maturation of the B cell response. *J Immunol,* **159**, 2116–2124.

Wang, Y.-C. & Ferguson, E. L. (2005). Spatial bistability of Dpp-receptor interactions during Drosophila dorsal-ventral patterning. *Nature,* **434** (7030), 229–234.

Ward, M. D. & Hammer, D. A. (1994). Focal contact assembly through cytoskeletal polymerization: steady state analysis. *J Math Biol,* **32** (7), 677–704.

Wei, S. H., Parker, I., Miller, M. J. & Cahalan, M. D. (2003). A stochastic view of lymphocyte motility and trafficking within the lymph node. *Immunol Rev,* **195**, 136–159.

Weikl, T. R. & Lipowsky, R. (2004). Pattern formation during T-cell adhesion. *Biophys J,* **87** (6), 3665–3678.

Weintraub, B., Jun, J., Bishop, A., Shokat, K., Thomas, M. & Goodnow, C. (2000). Entry of B cell receptor into signaling domains is inhibited in tolerant B cells. *J Exp Med,* **191**, 1443–8.

Wienands, J., Larbolette, O. & Reth, M. (1996). Evidence for a preformed transducer complex organized by the B cell antigen receptor. *Proc Natl Acad Sci U S A,* **93**, 7865–7870.

Wiseman, P., Brown, C., Webb, D., Hebert, B., Johnson, N., Squier, J., Ellisman, M. & Horwitz, A. (2004). Spatial mapping of integrin interactions and dynamics during cell migration by Image Correlation Microscopy. *J Cell Sci,* **117** (Pt 23), 5521–5534.

Wu, L. J., Feucht, A. & Errington, J. (1998*a*). Prespore-specific gene expression in *Bacillus subtilis* is driven by sequestration of SpoIIE phosphatase to the prespore side of the asymmetric septum. *Genes Dev,* **12** (9), 1371–1380.

Wu, Y., Nadler, M., Brennan, L., Gish, G., Timms, J., Fusaki, N., Jongstra-Bilen, J., Tada, N., Pawson, T., Wither, J., Neel, B. & Hozumi, N. (1998*b*). The B-cell transmembrane protein CD72 binds to and is an in vivo substrate of the protein tyrosine phosphatase SHP-1. *Curr Biol,* **8**, 1009–1017.

Xiong, W. & Ferrell, J. E. J. (2003). A positive-feedback-based bistable 'memory module' that governs a cell fate decision. *Nature,* **426** (6965), 460–465.

Yamamoto, Y. & Oelgeschlager, M. (2004). Regulation of bone morphogenetic proteins in early embryonic development. *Naturwissenschaften,* **91** (11), 519–534.

Yamanashi, Y., Kakiuchi, T., Mizuguchi, J., Yamamoto, T. & K, K. T. (1991). Association of B cell antigen receptor with protein tyrosine kinase Lyn. *Science,* **251**, 192–4.

Yudkin, M. D. & Clarkson, J. (2005). Differential gene expression in genetically identical sister cells: the initiation of sporulation in Bacillus subtilis. *Mol Microbiol,* **56** (3), 578–589.

Zamir, E. & Geiger, B. (2001). Molecular complexity and dynamics of cell-matrix adhesions. *J Cell Sci,* **114** (Pt 20), 3583–3590.

Zhang, L., Higgins, M. L. & Piggot, P. J. (1997). The division during bacterial sporulation is symmetrically located in Sporosarcina ureae. *Mol Microbiol,* **25** (6), 1091–1098.

Zhang, M. & Varki, A. (2004). Cell surface sialic acids do not affect primary CD22 interactions with CD45 and surface IgM nor the rate of constitutive CD22 endocytosis. *Glycobiology,* **14** (11), 939–949.

Appendix A

Glossary

Adaptive immune response is the response of antigen-specific lymphocytes to antigen, including the development of immunological memory. Adaptive immune responses are generated by clonal selection of lymphocytes. Adaptive immune responses are distinct from innate and non-adaptive phases of immunity, which are not mediated by clonal selection of antigen-specific lymphocytes. Adaptive immune responses are also known as **acquired immune responses**

Affinity is the strength of binding of one molecule to another at a single site, such as the binding of a monovalent Fab fragment of antibody to a monovalent antigen.

Affinity maturation refers to the increase in affinity of the antibodies produced during the course of a humoral immune response. It is particularly prominent in secondary and subsequent immunizations.

Allosteric regulation, regulation of a protein's activity by binding of a ligand to a place distant from the active site.

Anergy Anergic B cells are characterized by a lower responsiveness towards an immunogenic antigen challenge and arise when B cells are exposed to a relatively weak, co-stimulatory-deficient antigenic stimulus for sufficiently long time.

anterior, near the front of an animal

Antibody (Ab) is a protein which binds specifically to a particular substance - the antigen. Each antibody molecule has a unique structure, that enables it to bind specifically to its corresponding antigen, but all antibodies have the same overall structure and are known collectively as immunoglobulins. Antibodies are produced by plasma cells in response to infection or immunization, and bind to and neutralize pathogens or prepare them for uptake and destruction by phygocytes.

Antigen (Ag) is any molecule that can bind specifically to an antibody.

antigen receptors, T and B lymphocytes collectively bear on their surface highly diverse antigen receptors capable of recognizing a wide diversity of antigens. Each individual lymphocyte bears receptors of a single antigen specificity.

Antigen presentation describes the display of antigen as peptide fragments bound to MHC molecules on the surface of a cell; all T cells recognize antigen only when it is presented in this way.

Antigen presenting cells are highly specialized cells that can process antigens and display peptide fragments on the cell surface together with molecules required for

lymphocyte activation. The main antigen-presenting cells for T cells are dendritic cells, macrophages, and B cells, whereas the main antigen-presenting cells for B cells are follicular dendritic cells.

Apoptosis, or programmed cell death, is a form of cell death in which the cell activates an internal death program.

B cells or **B lymphocytes**, are one of the two major types of lymphocyte. The antigen receptor on B lymphocytes, sometimes called the B-cell receptor, is a cell-surface immunoglobulin. On activation by antigen, B cells differentiate into cells producing antibody molecules of the same antigen-specificity as this receptor.

cellular selection A cell is said to be selected by antigen when its receptors bind that antigen. If the cell starts to proliferate as a result, this is called clonal selection, and the cell founds a clone; if the cell is killed as a result of binding antigen, this is called negative selection or clonal deletion.

Centroblasts (CB) are large, rapidly dividing cells found in germinal centres, and are the cells in which somatic hypermutation is believed to occur. Antibody-secreting and memory B cells derive from these cells.

Centrocytes (CC) are small, non-proliferating B cells in germinal centres that derive from centroblasts. They may mature into antibody-secreting plasma cells or memory B cells, or may undergo apoptosis, depending on their receptor's interaction with antigen.

cooperative binding, binding of ligand to a multimeric protein with several binding sites makes the binding of the next ligand easier (positive cooperativity) or harder (negative cooperativity).

dorsal, near the rear surface of an animal

Effector cells are lymphocytes that can mediate the removal of pathogens from the body without the need for further differentiation , as distinct from naive lymphocytes, which must proliferate and differentiate before they can mediate effector functions, and memory cells, which must differentiate and often proliferate before they become effector cells.

Follicular dendritic cells (FDC) are found in lymphoid follicles and are cells of uncertain origin with long branching processes that make intimate contact with many different B cells. They have Fc receptors that are not internalized by receptor-mediated endocytosis and thus hold antigen:antibody complexes on the surface for long periods. These cells are crucial in selecting antigen-binding B cells during antibody responses.

Fluorescence resonance energy transfer FRET describes an energy transfer mechanism between two fluorescent molecules. A fluorescent donor is excited at its specific fluorescence excitation wavelength. By a long-range dipole-dipole coupling mechanism, this excited state is then nonradiatively transferred to a second molecule, the acceptor. The donor returns to the electronic ground state (http://en.wikipedia.org/wiki/FRET).

Germinal centres (GC) in secondary lymphoid tissues are sites of intense B-cell proliferation, selection, maturation, and death during antibody responses. Germinal centres form around follicular dendritic cell networks when activated B cells migrate into lymphoid follicles.

Haptens are molecules which can bind antibody but cannot by themselves elicit an immune response. Haptens must be chemically linked to protein carriers to elicit antibody and T-cell responses.

Immune response, the response by a host to an immunogenic challenge. Different types of responses are referred to as innate immune response or as **adaptive/acquired immune response**.

Immunological tolerance, failure of an immunocompetent host to respond to an immunogenic challenge with a specific antigen.

Major histocompatibility complex (MHC), a large, polymorphic genomic region or gene family found in most vertebrates. Major histocompatibility complex molecules bind antigen fragments and present them to T cells to induce an adaptive immune response (see **antigen presentation**).

Plasmablast, a B cell in a lymph node that already shows some features of a plasma cell.

Plasma cells are terminally differentiated B lymphocytes and are the main antibody-secreting cells of the body. They are found in the medulla of the lymph nodes, in splenic red pulp, and in bone marrow.

posterior, near the rear of an animal

Primary focus During T-dependent antibody responses, a primary focus (plural, **primary foci**) of B-cell activation forms in the vicinity of the margin between T and B cell areas of lymphoid tissue. Here, the T and B cells interact and B cells can directly into antibody-forming cells or migrate to lymphoid follicles for further proliferation and differentiation.

Primary follicles Lymphoid tissues contain lymphoid follicles made up of follicular dendritic cells and B lymphocytes. The primary follicles contain resting B lymphocytes and are the site at which germinal centres form when they are entered by activated B cells, forming secondary follicles.

Primary immune response, the adaptive immune response to an initial exposure to antigen.

Primary immunization, also known as priming, generates both the primary immune response and immunological memory.

σ factor In prokaryotes so-called σ factors bind to the RNA polymerase and mediate the contact with the promoter. After about 9-12 nucleotides of RNA have been synthesized, a conformational change results in the dissociation of the σ factor and leads to a highly processive elongation complex (see page 2).

Surface plasmon resonance SPR is a phenomenon which occurs when light is reflected off thin metal films. A fraction of the light energy incident at a sharply defined angle can interact with the delocalised electrons in the metal film (plasmon) thus reducing the reflected light intensity. The precise angle of incidence at which this occurs is determined by a number of factors, but in the commercial BIACORE devices the principal determinant becomes the refractive index close to the backside of the metal film, to which target molecules are immobilised and addressed by ligands in a mobile phase running along a flow cell. If binding occurs to the immobilised target the local refractive index changes, leading to a change in SPR angle, which can be monitored in real-time by detecting changes in the intensity of the reflected light, producing a sensorgram. The rates of change of the SPR signal can be analysed to yield apparent rate constants for the association and dissociation phases of the reaction. The ratio of these values gives the apparent equilibrium constant (affinity). The size of the change in SPR signal is directly proportional to the mass being immobilised and can thus be interpreted crudely in terms of the stoichiometry of the interaction. Signals are easily

obtained from sub-microgram quantities of material. Since the SPR signal depends only on binding to the immobilised template, it is also possible to study binding events from molecules in extracts; i.e. it is not necessary to have highly purified components. (http://www.astbury.leeds.ac.uk/facil/SPR/spr_intro2004.htm)

T cells, or **T lymphocytes**, are a subset of lymphocytes defined by their development in the thymus and by heterodimeric receptors associated with the proteins of the CD3 complex.

Ultrasensitivity, a term which was coined by Goldbeter and Koshland to refer to "an output response that is more sensitive to change in stimulus than the hyperbolic (Michaelis-Menten) equation" (Goldbeter & Koshland, 1981).

ventral, near the forward surface of an animal

The definitions of immunological terms in this Glossary follow by and large those given in (Janeway & Travers, 1997) and the majority have been submitted before as part of the glossary of my thesis for the MRes/MSc in Applied and Computational Mathematics (University of Oxford, 2001). The definition of FRET is a direct quote from Wikipedia (http://en.wikipedia.org/wiki/FRET), and the definition of SPR is a direct quote from the webpage of the Astbury Centre for Structural Molecular Biology in Leeds (http://www.astbury.leeds.ac.uk/facil/SPR/spr_intro2004.htm).

Appendix B

Details on calculations

B.1 AA-AB binding in a non-cooperative binding mechanism

The non-cooperative binding mechanism considers only one AB conformation that is only one site of the reaction scheme (either balls or squares) in Figure 3.1A. A plot of the fraction of free AB sites $\frac{b}{[B_0]}$ versus the total AA concentration a_T can best be obtained by determining the total AA concentration that results in $b = n[AB] + [AB \cdot AA]$ free AB sites if the total AB concentration is $[B_0] = [AB] + [AB \cdot AA] + [AB \cdot AA_2]$ and there are $n = 2$ binding sites for AA; $[x]$ denotes the concentration of x. In equilibrium the total AA concentration $a_T = [AA] + [AB \cdot AA] + 2[AB \cdot AA_2]$ can be expressed in terms of b and the binding constants for the binding of the first ($K_1 = \frac{[AB \cdot AA]}{[AB][AA]}$) and second ($K_2 \frac{[AB \cdot AA_2]}{[AB \cdot AA][AA]}$) AA as

$$\begin{aligned} a_T &= [AA] + [AB \cdot AA] + [AB \cdot AA_2] \\ &= [AA] + K_1[AB][AA] + K_2[AB \cdot AA][AA] \\ &= [AA](1 + K_1[AB](1 + K_2[AA])) \\ &= [AA]\left(1 + K_1 \frac{b}{2 + K1[AA]}(1 + K_2[AA])\right). \end{aligned} \tag{B.1}$$

The concentration of free AA can be expressed dependent on the parameters K_1, K_2, $[B_0]$ and on the variable b by translating the scheme in Figure 3.1A into a set of ODEs, substituting and solving for the equilibrium concentration. We obtain

$$[AA] = 0.5\left(\frac{1}{K_2}\left(\frac{[B_0]}{b} - 1\right) + \sqrt{\left(\frac{1}{K_2}\left(\frac{[B_0]}{b} - 1\right)\right)^2 + \frac{4}{K_1 K_2}\left(2\frac{[B_0]}{b} - 1\right)}\right). \tag{B.2}$$

B.2 The Scatchard plot

If AB has n independent binding sites for AA then the binding can be described by the reaction scheme $AA + AB \rightleftarrows AB \cdot AA$; $K_s = \frac{[AA][AB]}{[AB \cdot AA]}$ where $[AA]$,$[AB]$, and $[AB \cdot AA]$ are the concentrations of unbound AA, AB monomers, and of the complex between AB monomers and AA (AB·AA) respectively. If $[B_0]$ is the total concentration of AB we can write $n[B_0] = [AB] + [AB \cdot AA]$ such that $[AB \cdot AA] = n[B_0][AA]/([AA] + K_s)$, which can be rewritten as $[AB \cdot AA] = n[B_0] - K_s \frac{[AB \cdot AA]}{[AA]}$ or

$$\nu = n - K_s \frac{\nu}{[A]}, \qquad \nu = \frac{[B \cdot A]}{[B_0]}. \tag{B.3}$$

From (B.3) we see that a plot of $\frac{\nu}{[AA]}$ against ν will result in a straight line where K_s is the slope of the graph and $\frac{n}{K_s}$ is the intersection with the vertical axis at $\nu = 0$ (Fig. 3.1C, dotted line).

If the binding sites of AA on AB are not independent as assumed above but interact then the Scatchard plot no longer forms a straight line. In the case of positive cooperativity, binding to the first binding site is more difficult and accordingly at low AA concentrations ν is sublinear small, thus resulting in a bell-shaped curve (Fig. 3.1C, solid line) as also predicted by a model based on the interactions depicted in Figure 3.1A. Both graphs in Figure 3.1C were obtained with off-rates 3.7-fold higher than for wildtype AA (Table B.1) which is in agreement with the lower affinity of AA-A58S for AB described in previous work (Magnin *et al.*, 1997).

B.3 Comments on how to estimate the septation-dependent IIE activity change

Given that IIE accumulates on the septum (together with any AA-P that is bound to it) the number of IIE·AA-P complexes present per unit volume increases in the prespore and decreases in the mother cell. A lower limit for the septation-dependent increase in IIE activity in the prespore can be determined by assuming a) that all the IIE locates, together with its substrate, on to the septum in such a way that its activity is displayed equally on both faces, and b) that the cell is cuboid. Insertion of a septum at a fraction x along the length of the cuboid will give rise to two compartments, with the smaller having an xth of the total volume. If half of all IIE·AA-P is present in the smaller volume then there is an effective $\frac{x}{2}$-fold increase in IIE·AA-P per unit volume of the smaller compartment. Septa form at one-fifth or less of the length of the cell (Illing & Errington, 1991) and the minimal increase in IIE activity is therefore 2.5.

While not all IIE may locate to the septum, each of the other assumptions mentioned above underestimates the probable increase in IIE activity: the total quantity of IIE is slightly greater on the prespore face than on the mother-cell face of the septum (Wu *et al.*, 1998*a*; King *et al.*, 1999); and the prespore is not a cuboid but has rounded ends (Ryter, 1965). Thus, although a 2.5-fold increase in IIE activity is sufficient to ensure the formation of enough σ^F·RNApol to permit transcription in the prespore (Fig. 3.12C), the 4-fold increase that we have assumed throughout this paper is a more realistic representation of the physiological situation.

B.4 A simplified and dimensionless version of the Mizutani model

Below a simplified and dimensionless version of the Mizutani model (equations 6.1-6.6) is derived. We adopt a single-letter code for the dependent variables to simplify the notation, and we use r for the ligand-receptor complex, s for Sog (S), g for Tsg (T), u for the ligand, v for the Sog-Tsg complex (ST), and w for the ligand-Sog-Tsg complex (LST). Moreover, we neglect unbinding of the Sog-Tsg and ligand-Sog-Tsg complexes because the off-rates are much smaller than the other loss rates. By writing $k = k_{on}$, $n = n_{on}$, $j = j_{on}$, and $\delta = k_{deg}$ as well as $D = D_L = D_S = D_T = D_{ST} = D_{LST}$ and $\eta = V_L = \frac{V_T}{4}$ and $\zeta = V_S$ we obtain from (6.1-6.6)

$$\begin{aligned}
\dot{r} &= ku(R_0 - r) - \delta r \\
\dot{s} &= -nsg + \zeta + D\Delta s \\
\dot{g} &= -nsg + \tau w + 4\eta + D\Delta g \\
\dot{u} &= -juv + \tau w + \eta - ku(R_0 - r) + D\Delta u \\
\dot{v} &= nsg - juv + D\Delta v \\
\dot{w} &= juv - \tau w + D\Delta w.
\end{aligned} \tag{B.4}$$

We can make equations (B.4) dimensionless by writing

$$\begin{aligned}
\bar{r} &= \frac{r}{R_0}, \quad \bar{s} = \frac{s}{R_0}, \quad \bar{g} = \frac{g}{R_0}, \quad \bar{u} = \frac{u}{R_0}, \quad \bar{v} = \frac{v}{R_0}, \quad \bar{w} = \frac{w}{R_0}, \\
\bar{t} &= t_0 t, \quad \bar{\tau} = \tau t_0 \quad \epsilon = \frac{1}{jR_0t_0}, \quad \bar{k} = kR_0t_0, \quad \bar{n} = nR_0t_0\epsilon^{\frac{1}{2}}, \\
\bar{x} &= \frac{x}{L}, \quad \bar{D} = \frac{Dt_0}{L^2}, \quad \bar{\eta} = \frac{\eta t_0}{R_0\epsilon} = \eta t_0^2 j, \quad \bar{\zeta} = \frac{\zeta t_0}{R_0\epsilon^{\frac{1}{3}}} \quad \bar{\delta} = \delta\frac{t_0}{\epsilon}.
\end{aligned} \tag{B.5}$$

Applying (B.5) in equations (B.4) gives the dimensionless version of the model as

$$\dot{\bar{r}} = \bar{k}\bar{u}(1 - \bar{r}) - \epsilon\bar{\delta}\bar{r} \tag{B.6}$$

$$\dot{\bar{s}} = -\epsilon^{-\frac{1}{2}}\bar{n}\bar{s}\bar{g} + \epsilon^{\frac{1}{3}}\bar{\zeta} + \bar{D}\Delta\bar{s} \tag{B.7}$$

$$\dot{\bar{g}} = -\epsilon^{-\frac{1}{2}}\bar{n}\bar{s}\bar{g} + \bar{\tau}\bar{w} + 4\epsilon\bar{\eta} + \bar{D}\Delta\bar{g} \tag{B.8}$$

$$\dot{\bar{u}} = -\frac{1}{\epsilon}\bar{u}\bar{v} + \bar{\tau}\bar{w} + \epsilon\bar{\eta} - \bar{k}\bar{u}(1 - \bar{r}) + \bar{D}\Delta u \tag{B.9}$$

$$\dot{\bar{v}} = \epsilon^{-\frac{1}{2}}\bar{n}\bar{s}\bar{g} - \frac{1}{\epsilon}\bar{u}\bar{v} + \bar{D}\Delta\bar{v} \tag{B.10}$$

$$\dot{\bar{w}} = \frac{1}{\epsilon}\bar{u}\bar{v} - \bar{\tau}\bar{w} + \bar{D}\Delta\bar{w}. \tag{B.11}$$

We have $k = k_{on} = 0.4\ \mu M^{-1}s^{-1}$, $j = j_{on} \sim 10^2\mu M^{-1}s^{-1}$, $n = n_{on} = 4\ \mu M^{-1}s^{-1}$, $\delta = 5 \times 10^{-4}s^{-1}$, $R_0 = 3\mu M$, $\eta = V_L(x)$, $\zeta = V_S(x)$ such that

$$\begin{aligned}
\eta &= 10^{-3}\mu M s^{-1}, \quad \zeta = 0 \quad \text{for} \quad x \in \mathcal{D} \\
\zeta &= 0.08\ \mu M s^{-1}, \quad \eta = 0 \quad \text{for} \quad x \in \mathcal{V}.
\end{aligned} \tag{B.12}$$

By setting $t_0 = \sqrt{\frac{1}{\eta j}} \sim 3.2s$, $L = \sqrt{Dt_0} \sim 13\mu m$ (which corresponds to the approximate width of a cell) all parameters apart from ϵ are of order 1. $\epsilon = \frac{1}{jR_0t_0} = \frac{1}{100\times\sqrt{10}\times 3} \sim 0.001$ (Table B.1). For convenience we will drop the bars in the following.

Using regular perturbation methods and a scaling argument it can be shown that $\bar{u} = O(\epsilon)$ while $t < t_c$. Thus since the initial conditions are $u(0) = v(0) = w(0) = r(0) = 0$, we rescale (B.6- B.11) with $u = \epsilon^{\alpha}\tilde{u}, v = \epsilon^{\nu}\tilde{v}, w = \epsilon^{\beta}\bar{w}$, $r = \epsilon^{\rho}\bar{r}$, $g = \epsilon^{\gamma}\tilde{g}$, $s = \epsilon^{\sigma}\tilde{s}$, $t = \epsilon^{\theta}\tilde{t}$ to obtain

$$\epsilon^{\rho-\theta}\dot{\tilde{r}} = k\epsilon^{\alpha}\tilde{u}(1 - \epsilon^{\rho}\tilde{r}) - \epsilon^{\rho+1}\delta\tilde{r} \tag{B.13}$$

$$\epsilon^{\sigma-\theta}\dot{\tilde{s}} = -\epsilon^{-\frac{1}{2}+\sigma+\gamma}n\tilde{s}\tilde{g} + \epsilon^{\frac{1}{3}}\zeta + \epsilon^{\sigma}D\Delta\tilde{s} \tag{B.14}$$

$$\epsilon^{\gamma-\theta}\dot{\tilde{g}} = -\epsilon^{-\frac{1}{2}+\sigma+\gamma}n\tilde{s}\tilde{g} + \tau\tilde{w} + 4\epsilon\eta + \epsilon^{\gamma}D\Delta\tilde{g} \tag{B.15}$$

Table B.1: **Kinetic rate constants and protein concentrations employed in the simplified dimensionless form of the Mizutani model.**

parameter	functional significance	rounded value
k	ligand-receptor on-rate	3.8
$\bar{n}$	Sog-Tsg on-rate	3.9
ϵ	ligand-Sog/Tsg on-rate	0.001
δ	degradation rate of ligand-receptor complexes	1.4
$\bar{\tau}$	degradation rate of Sog in LST complexes	1.7
ζ	expression rate of Sog	0.82
$\bar{\eta}$	expression rate of ligand	1
D	diffusion constant	1.6

$$\epsilon^{\alpha-\theta}\dot{\tilde{u}} = -\epsilon^{\alpha+\nu-1}\tilde{u}\tilde{v} + \epsilon^{\beta}\tau\tilde{w} + \epsilon\eta - \epsilon^{\alpha}\tilde{u}(1-r) + \epsilon^{\alpha}D\Delta u \tag{B.16}$$

$$\epsilon^{\nu-\theta}\dot{\tilde{v}} = -\epsilon^{\alpha+\nu-1}\tilde{u}\tilde{v} + \epsilon^{-\frac{1}{2}+\sigma+\gamma}n\tilde{s}\tilde{g} + D\Delta(\epsilon^{\nu}\tilde{v}) \tag{B.17}$$

$$\epsilon^{\beta-\theta}\dot{\tilde{w}} = \epsilon^{\alpha+\nu-1}\tilde{u}\tilde{v} - \epsilon^{\beta}\tau\tilde{w} + D\Delta(\epsilon^{\beta}\tilde{w}) \tag{B.18}$$

Since formation of v requires expression of s and g the total amount of v is bounded and, if we ignore diffusion for a start $v < \epsilon t$, that is, $\nu > 1 + \theta$; similarly, $\beta > 1 + \theta$. By rewriting equation B.16 as

$$\begin{aligned}\dot{\tilde{u}} &= -\epsilon^{\nu-1+\theta}\tilde{u}\tilde{v} + \epsilon^{\beta-\alpha+\theta}\tau\tilde{w} + \epsilon^{1-\alpha+\theta}\eta - \epsilon^{\theta}\tilde{u}(1-r) \\ &< -\epsilon^{2\theta}\tilde{u}\tilde{v} + \epsilon^{2\theta+1-\alpha}\tau\tilde{w} + \epsilon^{1-\alpha+\theta}\eta - \epsilon^{\theta}\tilde{u}(1-r)\end{aligned}$$

we see that the loss term is always greater than the gain term if $\alpha < 1$. Therefore $u = O(\epsilon)$ until diffusion leads to the transport of ligand into the midline.

B.5 Derivation of the antigen concentration and affinity dependency of B cell activation by soluble monomeric antigen - by Reinhard Lipowsky

In the following, we estimate the affinity and concentration dependence of antigen binding to B-cell receptors and compare the predictions of the model to experimental data. In order to do so, we first calculate the probabilities that a randomly chosen receptor is occupied by one or two bound antigens. Thus, let us consider N_R B-cell receptors which interact with a solution of antigens with concentration c. Each receptor has two binding sites for antigen and can attain three different states corresponding to no, one, and two bound antigens; these states will be denoted by $|0\rangle$, $|1\rangle$, and $|2\rangle$, respectively. This representation automatically ensures that each binding site of the receptors can only be occupied by at most one antigen.

At any moment in time, the ensemble of N_R B-cell receptors can be divided up into N_{R0}, N_{R1}, and N_{R2} receptors without any bound antigen, with one bound antigen, and with two bound antigens, respectively. The probability to find a randomly chosen receptor in state $|i\rangle$ is then given by $P_i \equiv N_{Ri}/N_R$. These probabilities satisfy the normalization condition

$$P_0 + P_1 + P_2 = 1. \tag{B.19}$$

The probabilities P_i change with time t because of adsorption and desorption processes. The simultaneous adsorption or desorption of two antigens are highly unlikely events which can be ignored. The probability P_0 is then decreased by adsorption of one antigen to a receptor in state $|0\rangle$ and increased by desorption of one antigen from a receptor in state $|1\rangle$. The corresponding evolution (or Markov or Master) equation for P_0 has the general form

$$\frac{\partial P_0}{\partial t} = P_1\omega_{10} - P_0\omega_{01} \tag{B.20}$$

with transition rates ω_{10} and ω_{01}. In general, the transition rate ω_{ij} counts the number of transitions from state $|i\rangle$ to state $|j\rangle$ per unit time. In the present case, one has

$$\omega_{10} = k_{\text{off}} \quad \text{and} \quad \omega_{01} = 2\,k_{\text{on}}c \tag{B.21}$$

where k_{on} and k_{off} are the adsorption and desorption rates for a single antigen binding site. The factor 2 in the second equation arises because, in state $|0\rangle$, the receptor has two unoccupied binding sites.

Likewise, the probabilities P_1 and P_2 to find a randomly chosen receptor in state $|1\rangle$ and $|2\rangle$ are governed by the evolution equations

$$\frac{\partial P_1}{\partial t} = P_0\omega_{01} - P_1\omega_{10} + P_2\omega_{21} - P_1\omega_{12} \tag{B.22}$$

and

$$\frac{\partial P_2}{\partial t} = P_1\omega_{12} - P_2\omega_{21}. \tag{B.23}$$

The additional transition rates ω_{12} and ω_{21} are given by

$$\omega_{12} = k_{\text{on}}c \quad \text{and} \quad \omega_{21} = 2\,k_{\text{off}}. \tag{B.24}$$

The factor 2 in the latter equation again arises because the receptor has two occupied binding sites in state $|2\rangle$.

Note that the three evolution equations Eq. B.20, Eq. B.22, and Eq. B.23 are not linearly independent but satisfy $\partial P_1/\partial t = -\partial P_0/\partial t - \partial P_2/\partial t$ which reflects the normalization condition $P_1 + P_2 + P_3 = 1$ as given by Eq. B.19.

The equilibrium state of the system corresponds to a steady state with $\partial P_i/\partial t = 0$. This steady state is characterized by time-independent probabilities P_i^{eq} which satisfy the detailed balance relations $P_i^{\text{eq}}\omega_{ij} = P_j^{\text{eq}}\omega_{ji}$, see, e.g., (Lipowsky & Klumpp, 2005). It then follows from Eq. B.20 that $P_1^{\text{eq}} = (\omega_{01}/\omega_{10})P_0^{\text{eq}}$ and from Eq. B.23 that $P_2^{\text{eq}} = (\omega_{12}/\omega_{21})P_1^{\text{eq}}$. Combining these two relations with the normalization condition Eq. B.19, one obtains the equilibrium probabilities

$$P_0^{\text{eq}} = 1/(1 + K_a\,c)^2\,, \tag{B.25}$$

$$P_1^{\text{eq}} = 2K_a\,c/(1 + K_a\,c)^2\,, \tag{B.26}$$

$$P_2^{\text{eq}} = (K_a\,c)^2/(1 + K_a\,c)^2 \tag{B.27}$$

which depend only only on the antigen concentration c and the equilibrium association constant $K_a \equiv k_{\text{on}}/k_{\text{off}}$.

It is instructive to consider a few special cases of the general solution as given by Eq. B.25, Eq. B.26, and Eq. B.27. In the limit of small antigen concentration c, the probabilites P_1^{eq} and P_2^{eq} vanish as $P_1^{\text{eq}} \approx K_a c$ and $P_2^{\text{eq}} \approx (K_a\,c)^2$. In the limit of large c, the probabilities P_0^{eq} and P_1 vanish as $P_0^{\text{eq}} \approx 1/(K_a\,c)^2$ and $P_1^{\text{eq}} \approx 2/(K_a\,c)$. Finally, if we consider the occupation probability P_{OC} for a single binding site, which is given by $P_{\text{OC}} = \frac{1}{2}\,P_1 + P_2$, and we take c to be constant, we obtain the equilibrium value

$$P_{\text{OC}}^{\text{eq}} = K_a\,c/(1 + K_a\,c). \tag{B.28}$$

The latter relation is equivalent to the classical formula for Langmuir-type adsorption.

B.6 The relation of 2- and 3-dimensional affinity constants

The binding energies U used in the mathematical models can be translated into 3-dimensional affinity constants as $K_D^{3d} = \frac{rho_R}{\eta} \exp -\frac{U}{kT}$, where $\rho_R = 500\mu m^{-2}$ is the approximate BCR density on the cell membrane and $\eta = 1.2 \times 10^7 \mu m^{-2} M^{-1}$ the conversion factor between the 2-dimensional and the 3-dimensional dissociation constant ($K_D^{2d} = \eta K_D^{3d}$). The conversion factor η is still a matter of debate (Moy *et al.*, 1999), since theoretical estimates are not in complete agreement with the latest experimental results. According to theoretical estimates for a protein complex that spans about 20 nm (extracellularly), $\eta = 1.2 \times 10^{19} m^{-2} M^{-1}$ (Bell, 1978). Experiments using beads suggest $\eta = 8 \times 10^{24} m^{-2} M^{-1}$ but this result is considered unlikely to reflect the cellular situation (Moy *et al.*, 1999). An intermediate value of $\eta = 10^{22} m^{-2} M^{-1}$ has been obtained by Kuo and Lauffenburger (Kuo & Lauffenburger, 1993). The discrepancy between the experimental values can be accounted for by general experimental difficulties as well as by differences between the studied systems such as the different degrees by which access to ligand may be restricted. Because of the large size of the BCR and the flexibility of the cell membrane we use the theoretical estimate in this paper.

Vol 441|18 May 2006|doi:10.1038/nature04666

nature

LETTERS

The mechanism of cell differentiation in *Bacillus subtilis*

Dagmar Iber[1], Joanna Clarkson[2], Michael D. Yudkin[2] & Iain D. Campbell[3]

Sporulation in *Bacillus subtilis* serves as a model for the development of two different cell types from a single cell[1]. Although much information has been accumulated about the mechanisms that initiate the developmental programmes[2], important questions remain that can be answered only by quantitative analysis. Here we develop, with the help of existing and new experimental results, a mathematical model that reproduces published *in vitro* experiments and explains how the activation of the key transcription factor is regulated. The model identifies the difference in volume between the two cell types as the primary trigger for determining cell fate. It shows that this effect depends on the allosteric behaviour of a key protein kinase and on a low rate of dephosphorylation by the corresponding phosphatase; both predicted effects are confirmed experimentally.

A key question in developmental biology is how two sister cells with identical genomes follow different patterns of gene expression. The sporulation of *Bacillus subtilis* is an exceptionally favourable system for studying this question. Early in sporulation the cell divides asymmetrically into two compartments, a smaller prespore and a larger mother cell (Fig. 1a). These remain attached but initiate different programmes of transcription, using compartment-specific transcription factors (σ factors)[1]. The first of these, σ^F, is crucial, because its correct activation is essential for regulating the other sigma factors of sporulation. σ^F is inactive in the predivisional cell and the mother cell, but is activated in the prespore. Its regulation depends on three other proteins, SpoIIAB (AB), SpoIIAA (AA) and SpoIIE (IIE). AB is bifunctional: it can form a complex with, and thus inactivate, σ^F, and it can act as a specific protein kinase that phosphorylates AA to AA-P (Supplementary Fig. S1). AA-P is hydrolysed to AA by IIE, a serine phosphatase. AA interacts with the σ^F–AB–ATP complex, releasing σ^F, which then binds to the core RNA polymerase to form the active σ^F holoenzyme[2]. The key reactions are summarized in Fig. 1b.

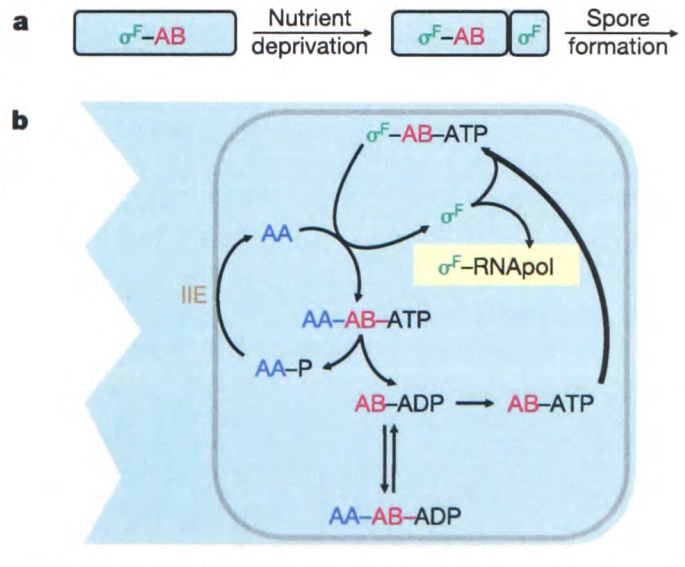


Figure 1 | Regulation of σ^F release during sporulation. **a**, Nutrient deprivation triggers asymmetric septation; the smaller, prespore compartment develops into a spore. **b**, Simplified regulatory network that controls σ^F activity in the prespore; for details see the text. RNApol, RNA polymerase.

As σ^F holoenzyme appears in the prespore and not in the mother cell, the attack of AA on the σ^F–AB–ATP complex must be compartment-specific. Although this specificity is crucial to the success of sporulation, its mechanism is not clear. One suggestion is that, because the volume of the mother cell is at least fourfold that of the prespore, IIE, which is displayed only on the asymmetric septum, will have higher phosphatase activity in the smaller compartment, leading to a greater concentration of AA in the prespore than in the mother cell[3]. However, without a mathematical analysis it is unclear whether such a small difference could account for compartment-specific σ^F activation, and several other mechanisms have been proposed[1]. Another quantitative difficulty involves the binding of σ^F to the core RNA polymerase. In the predivisional cell nearly all the RNA polymerase is in the form of σ^A holoenzyme; the formation of σ^F holoenzyme therefore requires σ^F to compete with σ^A. But the affinity of core RNA polymerase for σ^A is 25-fold that for σ^F, and the maximum concentration of σ^F is only about double that of σ^A (ref. 4), so how can σ^F holoenzyme be formed?

We have now constructed a mathematical model that provides the answer to these two questions and many others. The model was first developed and refined by fitting to numerous *in vitro* experiments (Supplementary Information) before being applied to the situation expected in the living cell. A first success of this rigorous analysis was the insight that AB is an allosteric protein. Positive cooperativity in AB–AA binding, predicted by the model, could be shown experimentally by a Scatchard plot (Fig. 2), obtained by measuring the binding of a non-phosphorylatable derivative of AA (AA-S58A)[5] to

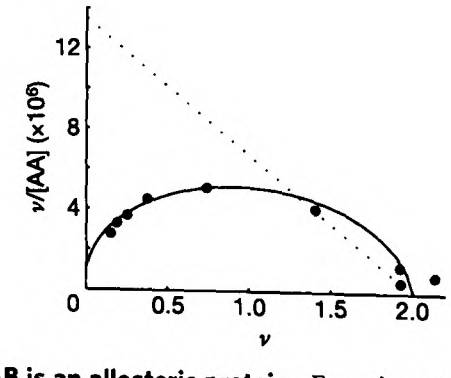


Figure 2 | SpoIIAB is an allosteric protein. Experimental (circles) and predicted Scatchard plot if AB is an allosteric (solid line) or non-allosteric (dotted line) protein; ν is the fraction of AB that has bound AA.

[1]Mathematical Institute, Centre for Mathematical Biology, University of Oxford, Oxford OX1 3LB, UK. [2]Microbiology Unit, Department of Biochemistry, University of Oxford, Oxford OX1 3QU, UK. [3]Department of Biochemistry, University of Oxford, Oxford OX1 3QU, UK.

© 2006 Nature Publishing Group

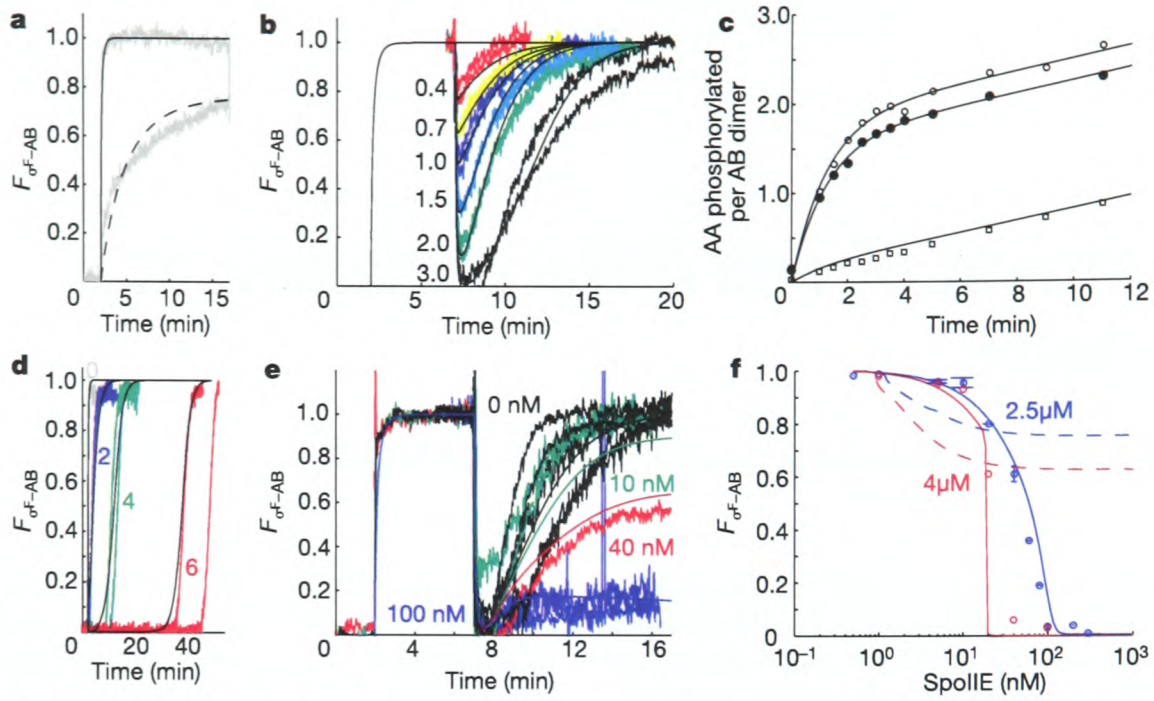


Figure 3 | Verification of the model with *in vitro* data. **a**, Measured (grey recorder output) and predicted (smooth lines) fraction F of σ^F in σ^F–AB complexes when 1.3 μM σ^F and 1 μM AB were mixed in the presence of 100 μM ATP (continuous line) or ADP (dashed line). **b**, Measured (recorder output) and predicted (smooth lines) σ^F release from AB–ATP on addition of AA. Black lines show the predictions for the indicated concentrations of AA. The measured values are for 0.4 μM (red), 0.7 μM (yellow), 1 μM (blue), 1.5 μM (cyan), 2 μM (green) and 3 μM (black), each carried out in duplicate. **c**, Measured (symbols) and predicted (lines) phosphorylation of AA by AB when AB is directly incubated with 40 μM AA and 100 μM ATP (open circles) or preincubated for 5 min with either 5 μM ADP (filled circles) or 5 μM ADP and 40 μM AA (open squares). The kinetics of phosphorylation of AA by AB was followed by measuring the uptake of radioactivity from [γ-^{32}P]ATP into the protein over time, as described previously[9]. The experimental results are normalized by the factor 1.3 to take account of a systematic error in the determination of protein concentrations (see Supplementary Information). **d**, Measured (recorder output) and predicted (black lines) σ^F–AB complex formation on mixing of 1 μM AB and 1.3 μM σ^F with no (grey), 2 μM (blue), 4 μM (green) or 6 μM (red) AA. Measurements were carried out in duplicate. **e**, Measured (recorder output) and predicted (smooth line) kinetics of IIE-dependent dissociation of σ^F–AB–ATP (1.3 μM σ^F,1 μM AB dimer) by 2.5 μM AA, in the absence of IIE (five repeats as black lines) or with 10 nM (duplicates as green lines), 40 nM (red) or 100 nM (duplicates as blue lines) IIE. **f**, Measured (open circles) and predicted (lines) equilibrium fraction of σ^F complexed to AB as a function of different IIE concentrations, in the presence of 2.5 μM (blue) or 4 μM (red) AA, assuming that AB is allosteric (continuous line) or not allosteric with both AA and σ^F binding at high affinity (dashed). Error bars show s.d. from three experiments.

AB by surface plasmon resonance (SPR). We further find that the conformation of AB with high affinity for AA binds σ^F with low affinity and that the conformation with high affinity for σ^F binds AA with low affinity (Supplementary Information); this explains how AA binding to AB can result in the rapid dissociation of σ^F.

Because of AB allostery the different AB conformers and the interconversions between them have to be taken into account, and the simple description above grew into the more realistic regulatory scheme shown in Supplementary Fig. S2. Experimentally determined values were used for all the 25 rate constants (Supplementary Tables 1 and 2) that characterize the more than 150 reactions included in Supplementary Fig. S2.

Over the past few years numerous *in vitro* experiments have yielded much information about interactions between the components of the system[2]. The use of fluorescent derivatives of AB and σ^F has been particularly fruitful in allowing the formation and dissociation of various complexes to be followed in real time[6–9]. Translation of the scheme of Supplementary Fig. S2 into a set of differential equations enabled us to simulate and predict the results of these experiments. As long as AB allostery was included, simulations and results agreed remarkably well for all experiments, for example those in which σ^F–AB complexes were made (Fig. 3a) and challenged (Fig. 3b) with different concentrations of AA. Simulations also gave excellent agreement with experiments in which AA was phosphorylated in the presence of AB, either with or without preincubation with ADP (Fig. 3c). Similarly, there was good agreement between the simulations and results of experiments in which AB and σ^F were mixed in the presence of different concentrations of AA (Fig. 3d). Here the model captured the increasing delay in the formation of the AB–σ^F complex with increasing concentrations of AA. This delay is due to the trapping of AA and AB–ADP in complexes, which are important in the regulation of σ^F (refs 6, 10, 11). The model was highly successful in simulating the results of experiments in which σ^F–AB complexes were incubated with AA in the presence of different concentrations of IIE; the resemblance between experiment and simulation held for both the kinetics (Fig. 3e) and the equilibrium (Fig. 3f) of the process.

The success of the model in simulating *in vitro* experiments gave us confidence to apply it to the situation in the sporulating cell. Given that the model is relatively insensitive (robust) to small perturbations in most parameters (Supplementary Information, Supplementary Tables 1 and 2, and Supplementary Figs S2 and S12), parameter values derived from *in vitro* experiments could be used to model the physiological situation. The only exception was the rate of IIE phosphatase activity. The model predicted that this needed to be 75–150-fold smaller than measured *in vitro* to avoid septation-independent σ^F release (Fig. 4a). Earlier work had suggested that IIE activity might well be much lower in the cell than measured *in vitro*[12], at least partly because of the predominance of Mg^{2+} over Mn^{2+} (ref. 13). We tested this prediction of the model and found that for physiological salt concentrations (1 mM Mg^{2+} and 0.1 mM Mn^{2+} (ref. 14)) the phosphatase rate is indeed almost 150-fold lower than under *in vitro* conditions (2.5 mM Mn^{2+}) (Fig. 4b; Supplementary Information and Supplementary Figs S6–S8).

As a result of the accumulation of IIE on the asymmetrically positioned septum, the concentration of IIE increases in the smaller prespore[3]. To see whether such an increase is sufficient to account for the prespore-specific release of σ^F, we modelled the system with the known intracellular concentrations of the proteins (Supplementary Information and Supplementary Fig. S9) and then studied the effect of a fourfold increase in the IIE concentration (Supplementary Information). The simulation shows that little σ^F is released (Fig. 4c, dashed

© 2006 Nature Publishing Group

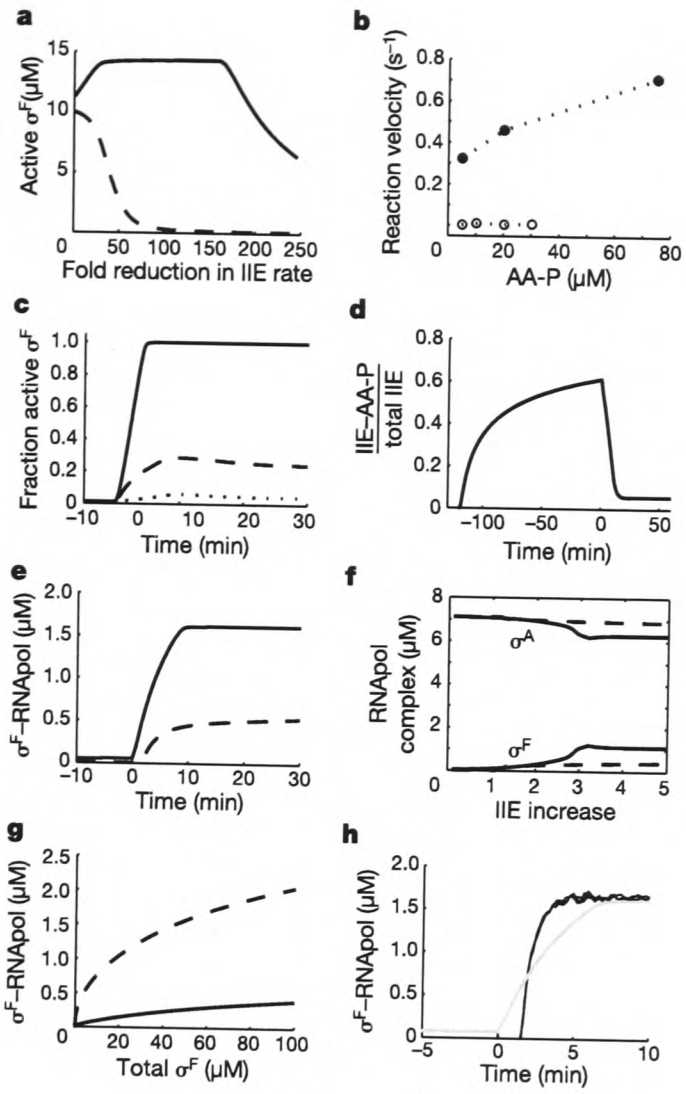


Figure 4 | Mechanism of prespore-specific σ^F-RNA-polymerase holoenzyme formation. **a**, Predicted concentration of AB-free (active) σ^F before (dashed line) and after (continuous line) septation, dependent on how much lower the IIE phosphatase rate is *in vivo* than under *in vitro* conditions. **b**, Velocity of the IIE reaction as a function of the concentration of its substrate AA-P in 2.5 mM Mn^{2+} (filled circles) or 1 mM Mg^{2+} and 0.1 mM Mn^{2+} (open circles). **c**, Predicted σ^F release in response to a fourfold increase in IIE alone (dashed line), AA-P alone (dotted line) or IIE and AA-P (solid line) imposed at $t = 0$. **d**, Predicted fraction of IIE bound by AA-P. **e**, Predicted σ^F–RNApol concentration during sporulation assuming that AB is allosteric (continuous line) or not allosteric with both AA and σ^F binding with high affinity (dashed line). **f**, Predicted concentration of σ^F (lower curves) or σ^A (upper curves) RNA polymerase holoenzyme formed 90 min after septation, as a function of an increase in IIE (including IIE complexed with AA-P) relative to the other sporulation proteins after 120 min of protein expression, assuming that AB is allosteric (continuous lines) or not allosteric with both AA and σ^F binding with high affinity (dashed lines). **g**, Predicted preseptational σ^F–RNApol concentration when the sporulation proteins increase in parallel, with parameters as given in Supplementary Tables 1 and 2 (continuous line) or with $k_{off}(\sigma^F\text{–RNApol}) = 0.02\ s^{-1}$ (dashed line). On the horizontal axis, the concentration of σ^F is representative of σ^F, AA, AB and IIE. **h**, Predicted concentration of σ^F–RNApol in a deterministic simulation (grey line) and in stochastic simulations (black lines) of the model.

line). However, if the increase in IIE is accompanied by an equimolar increase in its substrate, AA-P, almost all the σ^F is rapidly released (Fig. 4c, solid line); an increase in AA-P alone is not sufficient (Fig. 4c, dotted line). For the enzyme/substrate ratios found in the sporulating cell[4,12,15] and the measured phosphatase rate and IIE–AA-P affinity (Supplementary Tables 1 and 2) the model predicts that enzyme and substrate will indeed appear together at the face of the asymmetric septum as the septum is being formed (Fig. 4d). The predicted increases in concentration of these two proteins in the smaller prespore are sufficient to trigger compartment-specific release of σ^F; an increase in IIE phosphatase rate, for example by the removal of an inhibitor, is not required.

The model can also be applied to the competition of σ^F and σ^A for core RNA polymerase. It predicts the rapid formation of micromolar concentrations of σ^F holoenzyme (Fig. 4e) whenever the IIE concentration increases at least threefold over that in the predivisional cell (Fig. 4f). However, σ^F holoenzyme does not wholly supplant σ^A holoenzyme. The simulation mimics the known situation in the sporulating cell, in which both σ^A holoenzyme and σ^F holoenzyme are active[16]. If core RNA polymerase had the same affinity for σ^F as it has for σ^A, formation of σ^F holoenzyme would not require a septation-dependent increase in IIE activity (Fig. 4g). There would then be a risk that σ^F-specific transcription could occur in the predivisional cell once the concentrations of the sporulation proteins had increased sufficiently to permit the formation of micromolar concentrations of σ^F holoenzyme but before they had triggered septation.

The exceptional sensitivity of the model to a small increase in the concentration of AA derives from AB allostery (Fig. 4e, f). AA binding stabilizes the AB conformation that binds σ^F with low affinity; this enables the release of σ^F and prevents σ^F from rebinding once a critical AA concentration has been reached (Supplementary Information and Supplementary Fig. S10). Allostery also reduces the consumption of ATP by favouring the formation of AB–ADP–AA complexes, which reduces cycles of AA phosphorylation and dephosphorylation (Supplementary Information and Supplementary Fig. S11).

The model reveals several further, sophisticated features of the σ^F system that optimize its ability to regulate the initiation of sporulation. For example, several mechanisms are employed to control the ratios of σ^F and its regulatory proteins as well as the timing of septation; as a result the system is highly robust to stochastic fluctuations in gene expression that might arise because of low copy numbers[17] (Fig. 4h; Supplementary Information and Supplementary Fig. S12), but it remains very sensitive to small changes in the concentrations of IIE and AA-P. Moreover, spontaneous initiation of sporulation is prevented by keeping the concentrations of σ^F and its regulators low in the vegetative cell. A detailed account of these features of the model will be published elsewhere, as will its predictions about the role of the transient genetic asymmetry[18,19], AB degradation[20] and preseptational AB–ADP–AA complex formation[21,22].

The value of any mathematical model depends critically on the accuracy of the parameters used. This study has benefited greatly from our knowledge of intracellular concentrations of the relevant components[4,12,15] and from the fact that all the relevant kinetic constants are available from investigations of well-established *in vitro* systems[2]. The resulting model accounts for numerous published results and correctly predicts the phenotype of essentially all mutants for which the biochemical effect of the mutation is known (Supplementary Information and Supplementary Table 3). In addition it has succeeded in predicting two novel features, AB allostery and a very low phosphatase rate *in vivo*, both of which prove to be essential components of the mechanisms that establish differential gene expression in this widely studied model system.

METHODS

Scatchard plot. A Scatchard plot was generated from AB–AA binding data obtained by SPR analysis. For the SPR measurements, concentrations of free AA in solution were determined with the use of AB as a reporter immobilized on the sensor chip. A standard curve of AA concentration against response units was produced with known concentrations of AA. The amount of free AA in AB–AA mixtures was then determined by comparison with this standard curve. The amount of bound AA was calculated from the total concentration of AA in the mixture. For this analysis the non-phosphorylatable mutant AA-S58A was used. Measurements with wild-type AA were also attempted. However, we were unable to obtain reliable data at the very high AB/AA ratios required for some of the measurements because it was not possible to eliminate phosphorylation of the AA by traces of ATP in the mixture.

© 2006 Nature Publishing Group

SPR methods have been described previously[15]. AA–AB mixtures were generated with 4 μM AA and 0.1–20 μM AB. Because of a systematic error in the determination of protein concentrations the results have been scaled by a factor of 1.3 so that $\nu \leq 2$ in Fig. 2.

Fluorescence spectroscopy and enzyme kinetics. Fluorescence spectroscopy and measurements of enzyme kinetics were performed as described previously[6–8]. Some of the results in Fig. 3 are derived from previously published data[6,8].

Numerical methods. The set of stiff ordinary differential equations (ODE) was solved by employing suitable Matlab ODE solvers. The stochastic simulation was performed with Matlab Simbiology using the stochastic simulation algorithm SSA, which is equivalent to solving the chemical Master equation for the system.

Received 19 January; accepted 21 February 2006.

1. Hilbert, D. W. & Piggot, P. J. Compartmentalization of gene expression during *Bacillus subtilis* spore formation. *Microbiol. Mol. Biol. Rev.* **68,** 234–262 (2004).
2. Yudkin, M. D. & Clarkson, J. Differential gene expression in genetically identical sister cells: the initiation of sporulation in *Bacillus subtilis*. *Mol. Microbiol.* **56,** 578–589 (2005).
3. Duncan, L., Alper, S., Arigoni, F., Losick, R. & Stragier, P. Activation of cell-specific transcription by a serine phosphatase at the site of asymmetric division. *Science* **270,** 641–644 (1995).
4. Lord, M., Barillà, D. & Yudkin, M. D. Replacement of vegetative σ^A by sporulation-specific σ^F as a component of the RNA polymerase holoenzyme in sporulating *Bacillus subtilis*. *J. Bacteriol.* **181,** 2346–2350 (1999).
5. Diederich, B. *et al.* Role of interactions between SpoIIAA and SpoIIAB in regulating cell-specific transcription factor σ^F of *Bacillus subtilis*. *Genes Dev.* **8,** 2653–2663 (1994).
6. Clarkson, J., Shu, J.-C., Harris, D. A., Campbell, I. D. & Yudkin, M. D. Fluorescence and kinetic analysis of the SpoIIAB phosphorylation reaction, a key regulator of sporulation in *Bacillus subtilis*. *Biochemistry* **43,** 3120–3128 (2004).
7. Clarkson, J., Campbell, I. D. & Yudkin, M. D. Physical evidence for the induced release of the *Bacillus subtilis* transcription factor, σ^F, from its inhibitory complex. *J. Mol. Biol.* **340,** 203–209 (2004).
8. Clarkson, J., Campbell, I. D. & Yudkin, M. D. Efficient regulation of σ^F, the first sporulation-specific sigma factor in *B. subtilis*. *J. Mol. Biol.* **342,** 1187–1195 (2004).
9. Shu, J.-C., Clarkson, J. & Yudkin, M. D. Studies of SpoIIAB mutant proteins elucidate the mechanisms that regulate the developmental transcription factor σ^F in *Bacillus subtilis*. *Biochem. J.* **384,** 169–178 (2004).
10. Garsin, D. A., Duncan, L., Paskowitz, D. M. & Losick, R. The kinase activity of the antisigma factor SpoIIAB is required for activation as well as inhibition of transcription factor σ^F during sporulation in *Bacillus subtilis*. *J. Mol. Biol.* **284,** 569–578 (1998).
11. Lee, C.-S., Lucet, I. & Yudkin, M. D. Fate of the SpoIIAB*-ADP liberated after SpoIIAB phosphorylates SpoIIAA of *Bacillus subtilis*. *J. Bacteriol.* **182,** 6250–6253 (2000).
12. Lucet, I., Borriss, R. & Yudkin, M. D. Purification, kinetic properties, and intracellular concentration of SpoIIE, an integral membrane protein that regulates sporulation in *Bacillus subtilis*. *J. Bacteriol.* **181,** 3242–3245 (1999).
13. Schroeter, R., Schlisio, S., Lucet, I., Yudkin, M. D. & Borriss, R. The *Bacillus subtilis* regulator protein SpoIIE shares functional and structural similarities with eukaryotic protein phosphatases 2C. *FEMS Microbiol. Lett.* **174,** 117–123 (1999).
14. Eisenstadt, E., Fisher, S., Der, C. L. & Silver, S. Manganese transport in *Bacillus subtilis* W23 during growth and sporulation. *J. Bacteriol.* **113,** 1363–1372 (1973).
15. Magnin, T., Lord, M. & Yudkin, M. D. Contribution of partner switching and SpoIIAA cycling to regulation of σ^F activity in sporulating *Bacillus subtilis*. *J. Bacteriol.* **179,** 3922–3927 (1997).
16. Fujita, M. & Sadaie, Y. Rapid isolation of RNA polymerase from sporulating cells of *Bacillus subtilis*. *Gene* **221,** 185–190 (1998).
17. Kaern, M., Elston, T. C., Blake, W. J. & Collins, J. J. Stochasticity in gene expression: from theories to phenotypes. *Nature Rev. Genet.* **6,** 451–464 (2005).
18. Frandsen, N., Barák, I., Karmazyn-Campelli, C. & Stragier, P. Transient gene asymmetry during sporulation and establishment of cell specificity in *Bacillus subtilis*. *Genes Dev.* **13,** 394–399 (1999).
19. Dworkin, J. & Losick, R. Differential gene expression governed by chromosomal spatial asymmetry. *Cell* **107,** 339–346 (2001).
20. Pan, Q., Garsin, D. A. & Losick, R. Self-reinforcing activation of a cell-specific transcription factor by proteolysis of an anti-sigma factor in *Bacillus subtilis*. *Mol. Cell* **8,** 873–883 (2001).
21. Carniol, K., Eichenberger, P. & Losick, R. A threshold mechanism governing activation of the developmental regulatory protein σ^F in *Bacillus subtilis*. *J. Biol. Chem.* **279,** 14860–14870 (2004).
22. King, N., Dreesen, O., Stragier, P., Pogliano, K. & Losick, R. Septation, dephosphorylation, and the activation of σ^F during sporulation in *Bacillus subtilis*. *Genes Dev.* **13,** 1156–1167 (1999).

Supplementary Information is linked to the online version of the paper at www.nature.com/nature.

Acknowledgements We thank J.-C. Shu for providing unpublished SPR and AA phosphorylation data. This work was supported by the BBSRC UK. D.I. is a Junior Research Fellow at St John's College, Oxford, and is supported by a EPSRC DTA studentship. I.D.C. acknowledges financial support from the Wellcome Trust and the NIH-funded Cell Migration Consortium.

Author Contributions D.I. developed the model and conducted the simulations. J.C. performed the experiments and all the authors contributed to the concepts and writing of the paper.

Author Information Reprints and permissions information is available at npg.nature.com/reprintsandpermissions. The authors declare no competing financial interests. Correspondence and requests for materials should be addressed to D.I. (iber@maths.ox.ac.uk) or M.D.Y. (michael.yudkin@kellogg.ox.ac.uk).

© 2006 Nature Publishing Group

doi:10.1016/j.jmb.2006.05.011 J. Mol. Biol. (2006) 360, 15–20

JMB

Available online at www.sciencedirect.com

SCIENCE DIRECT®

ELSEVIER

COMMUNICATION

A Computational Analysis of the Impact of the Transient Genetic Imbalance on Compartmentalized Gene Expression During Sporulation in *Bacillus subtilis*

Dagmar Iber

Mathematical Institute
Centre for Mathematical Biology, University of Oxford
Oxford, UK

Sporulation in *Bacillus subtilis* serves as paradigm for the development of two different cell types (mother cell and prespore) from a single cell. Differential gene expression is achieved by restricting the activation of the key transcription factor σ^F to the smaller prespore. By use of a combination of mathematical and experimental techniques we have recently shown that the volume difference determines cell fate and that the accumulation of the phosphatase SpoIIE on the asymmetrically placed septum is sufficient for prespore-specific σ^F activation. Since compartmentalized gene expression is still obtained when SpoIIE cannot accumulate on the septum a number of alternative mechanisms have been proposed. These mechanisms focus on the difference in gene content between mother cell and prespore immediately after septation. Here the computational model is employed to show that under physiological conditions the transient genetic imbalance is unlikely to affect the septation-dependent release of σ^F. The duration of the transient genetic imbalance is too short for the degradation of SpoIIAB to have an impact on the release of σ^F. Moreover, the existence of an elusive IIE inhibitor, which has been proposed to become depleted in the prespore because of the transient genetic imbalance, is shown to be inconsistent with available experimental data. We conclude that the volume difference between the two compartments is the main determinant of cell fate.

© 2006 Elsevier Ltd. All rights reserved.

Keywords: sporulation; asymmetric septation; degradation; SpoIIAB; SpoIIE

Spore formation in *Bacillus subtilis* has long served as a paradigm for an important developmental process, the differentiation of two daughter cells into different cell types.[1] Spore formation is induced when nutrient deprivation and high cell densities result in the phosphorylation of the transcription factor Spo0A. Phosphorylated Spo0A upregulates the expression of many genes, including SpoIIAA, SpoIIAB, SpoIIE, and σ^F, and results in the formation of an asymmetrically positioned septum 90–120 min after the new transcription program has been initiated. Asymmetric cell division gives rise to two compartments, the larger mother cell and the smaller prespore. The distinct developmental programs in the two compartments are initiated when the transcription factor σ^F is selectively activated in the smaller prespore but not in the larger mother cell. Once active, σ^F initiates a cascade of events necessary for successful spore formation, both in the prespore and in the mother cell compartment.

A long-standing question concerns the mechanism by which activation of σ^F is restricted to the smaller compartment. With the help of a detailed quantitative model of the protein network that controls σ^F we have recently shown that the difference in cell size is sufficient in order to determine cell fate.[2]

The mechanism by which cell size affects cell fate is elaborate. The network that controls σ^F activity comprises only three other proteins (Figure 1), a kinase (SpoIIAB), which binds and inactivates σ^F, its substrate (SpoIIAA), which can release σ^F from the inhibitory interaction with SpoIIAB at the expense of being phosphorylated and thereby inactivated, and the corresponding phosphatase (SpoIIE), which reactivates SpoIIAA. IIE ("Spo" is omitted from all

E-mail address of the corresponding author: iber@maths.ox.ac.uk

0022-2836/$ - see front matter © 2006 Elsevier Ltd. All rights reserved.

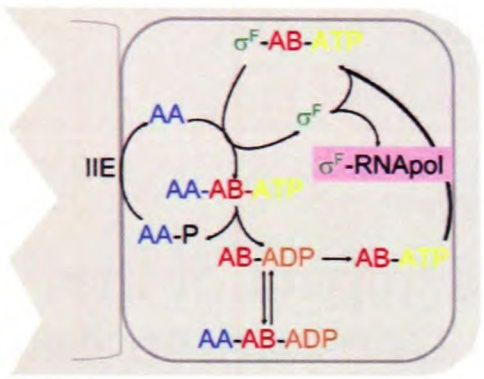


Figure 1. An overview of the interactions in the network that controls σ^F activity in *Bacillus subtilis*. For details see the text. The figure is an adaptation of Figure 1 in Hilbert & Piggot.[1]

protein names hereafter) is a membrane protein and accumulates homogenously on both sides of the septum.[3] Since the volume of the prespore is smaller than that of the mother cell there is a net increase in IIE per volume in the smaller prespore. Moreover, because the phosphatase rate is very low, most IIE accumulates on the septum together with its substrate.[2] As a consequence the total IIE and AA concentrations increase in the smaller compartment. Although small, the resulting increase in unphosphorylated AA is sufficient to release σ^F because the dimeric kinase AB is allosteric and binds its two ligands, σ^F and AA, in its two conformations with converse affinities.[2] Thus in the absence of AA, AB is in the conformation that binds σ^F with high and AA with low affinity. Binding of AA biases AB to its other conformation, which binds σ^F with low and AA with high affinity. The conformational change therefore promotes σ^F dissociation and the binding of a second AA; binding of the second AA blocks further access of σ^F to AB.[4]

A number of further mechanisms have been proposed to explain compartmentalized activation of σ^F, especially since σ^F activation is still restricted to the prespore even when IIE is prevented from accumulating on the septum.[5] Two prominent suggestions are based on possible effects of the transient genetic imbalance.[6] The transient genetic imbalance arises because about 70% of the chromosome (including the *spoIIA* operon on which AB is encoded) is initially excluded from the forespore and is imported only 10–20 min after septum closure.[7] As a result AB cannot be expressed in the prespore immediately after septation,[8] and it has been proposed that the accelerated degradation of unbound AB[9] results in a net decrease in the concentration of AB in the prespore and in the prespore-specific release of σ^F.[8] A further proposed result of the genetic imbalance is the degradation and loss of an elusive IIE inhibitor from the prespore, which would further accelerate σ^F release.[6]

Our computational model was described in detail by Iber *et al.*[2] It accurately predicts essentially all available *in vitro* results as well as the phenotype of those mutants for which the biochemical defect is known. The high level of accuracy of the model's predictions was achieved by the high level of detail that was incorporated in the model and by the accuracy of the parameter values used. The model comprises 50 dependent variables and 150 reactions, and we carried out experiments to determine the kinetic parameters for all reactions if these had not yet been published. The computational model is therefore well suited to assess the relevance of the transient genetic imbalance, of the short half-life of unbound AB, and of a IIE inhibitor for sustained and compartment-specific σ^F release.

As in our previous work we start the simulations of the sporulation reaction without protein. The proteins are expressed at a rate such that the experimentally observed protein concentrations are obtained at the time of septum formation, that is 90–120 min after the initiation of protein expression, dependent on the detailed experimental conditions.[10–12] In the simulation we assume that the protein concentrations increase linearly. While experiments suggest otherwise the data are too inaccurate and in parts contradictory to be modeled exactly. It should be noted that this approximation will not affect our conclusions since for the compartment-specific activation of σ^F only the protein concentrations at the time of septation are relevant, and these match the experimentally observed values. Moreover, the more realistic non-linear expression pattern will further enhance rather than reduce the already remarkable robustness of the regulatory network to perturbations in the protein expression levels before septation[2] because it is IIE whose concentration remains initially particularly low,[11] and the lower relative IIE levels will protect the cell from spontaneous σ^F release. The accumulation of IIE on the septum is modelled as a fourfold increase in the concentration of IIE, together with any AA-P that may be bound. Unbound AB has a half-life of about 28 min[9] and the degradation rate was set accordingly. The transient genetic imbalance is incorporated as a transient block in the expression of the genes in the *spoIIA* operon. Moreover, *spoIIE* and the *spoIIA* operon are repressed by high concentrations of unphosphorylated AA[13], and as before[2] we use a threshold concentration of 1 μM.

The transient genetic imbalance is too brief to affect σ^F release *via* SpoIIAB degradation

We have shown before[2] that, in agreement with experimental studies, a septation-dependent increase of IIE and associated substrate by at least threefold results in abrupt σ^F release and in the formation of micromolar concentrations of σ^F·RNA polymerase holoenzyme in our model (Figure 2(a)). It has been argued that the transient genetic imbalance may play an important role for the regulation of σ^F because it reduces the AB concentration specifically in the prespore.[8] However, in agreement with experimental observations,[8] this abrupt response is still obtained also without a transient genetic imbalance, that is when all proteins are continuously expressed in the

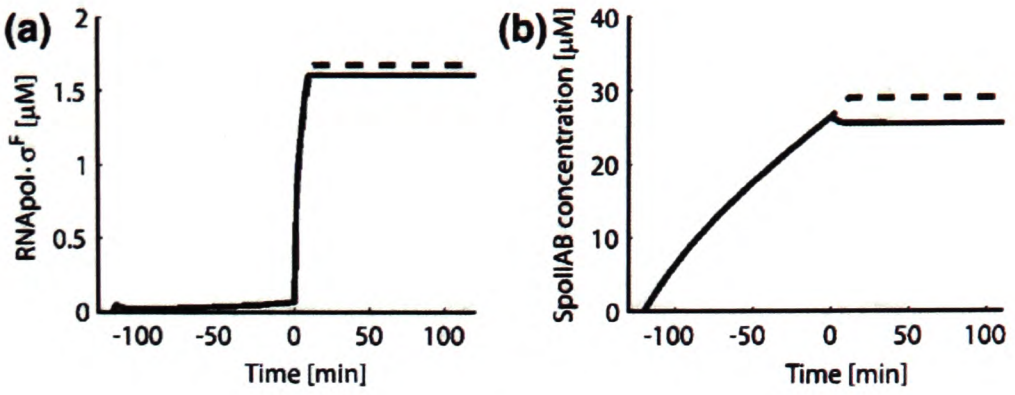


Figure 2. The effect of the transient genetic imbalance. (a) The predicted concentration of σ^F·RNApolymerase holoenzyme, and (b) the predicted SpoIIAB concentration with (continuous line) and without (broken line) a transient genetic imbalance. The concentration of IIE, together with its associated AA-P, was increased by fourfold at $t=0$ min to model the effect of septation.

prespore (Figure 2(a)). Moreover, the simulation reveals that under physiological conditions the difference in the AB concentration is marginal in the presence or absence of the transient genetic imbalance (Figure 2(b)). We conclude that the time span for which the transient genetic imbalance exists (10–20 min) is too short to substantially affect σ^F release in the prespore.

The physiological role of the transient genetic imbalance remains unclear. One possibility is that it exerts a protective role in the mother cell which may be important because, contrary to what is assumed in the simulation, the rate of IIE expression is not constant but increases sharply before septation.[11] As a consequence the ratio between the expression of IIE and the *spoIIA* genes increases also in the mother cell. Such continuing increase in the *spoIIE*/*spoIIA* expression ratio until after septation could, in principle, eventually trigger σ^F release also in the mother cell, and the availability of two *spoIIA* copies (as a result of the transient genetic imbalance) may be important to compensate for this. A short transient genetic imbalance can be expected to be sufficient in this case because once σ^F has been activated in the prespore the developmental fate of the mother cell is sealed by crisscross activation of transcription factors in the two compartments.[14]

The role of SpoIIAB degradation

Although the AB half-life is too long for AB degradation to enable rapid σ^F release after septation, simulation (Figure 3(a)) and experiments[9] agree that degradation of AB is necessary for successful sporulation. The quantitative model further reveals that AB degradation substantially reduces the AB concentration before septation (Figure 3(b)). If the AB expression rate is lowered in the AB degradation mutant to an extent that the wild-type protein concentration is regained then septation-dependent σ^F release is obtained (Figure 3(a) and (b), red lines). AB degradation thus appears to be necessary in order to tune the AB to AA ratio before rather than after septation.

Experiments strongly support the prediction of the model that AB is expressed at a much higher level than AA, and that a substantial fraction of AB is degraded already before septation.[10] Thus the ratio of AB monomers to AA is initially much larger than one but decreases towards one over the 90–120 min until the septum forms (Figure 3(c)). While the experimentally observed AB/AA ratios greater than one could, in principle, be accounted for by limitations in the accuracy of the experimental method, the method, even if inaccurate, should

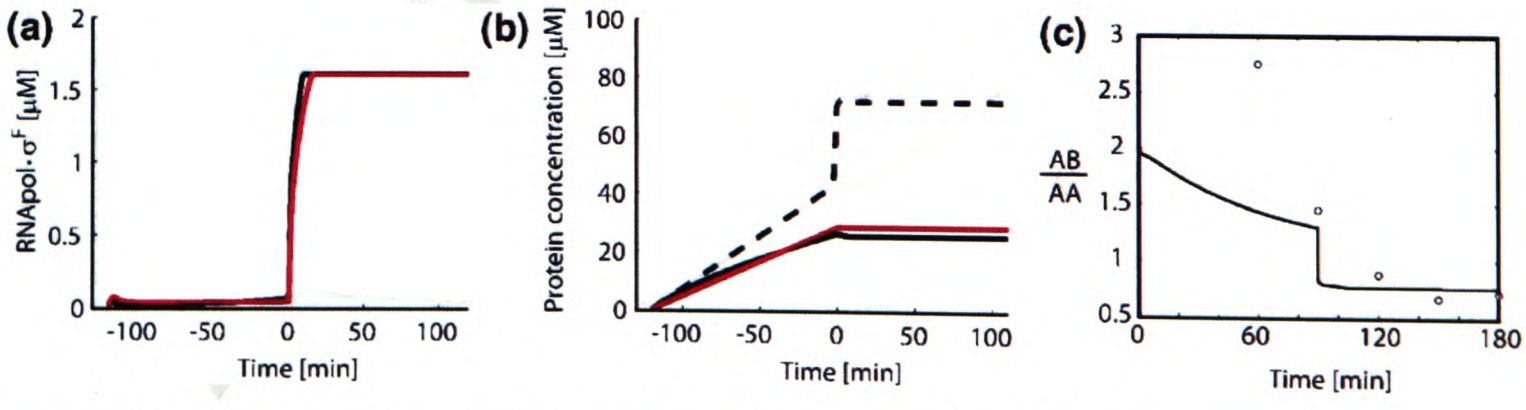


Figure 3. The role of SpoIIAB degradation. (a) The predicted concentration of σ^F·RNApolymerase holoenzyme, and (b) the predicted concentrations of AA (broken lines) and AB (continuous lines) assuming that AB has a half-life of 28 min (black lines), or AB is stable (grey lines), or AB is stable and has an expression rate two thirds of what is common for the wild-type (red lines) while the AA expression rate is identical to that of the wild-type (black lines). The continued expression of the sporulation proteins in the absence of AB degradation (grey lines) after septation ($t=0$) is due to the lack of free unphosphorylated AA that would repress *spoIIA*. The concentration of IIE, together with its associated AA-P, was increased by fourfold at $t=0$ min to model the effect of septation. (c) The ratio of AB monomers to AA in experiments (balls) and simulation (line) assuming that the septum forms after 90 min; $t=0$ corresponds to the activation of Spo0A, that is to $t=-120$ min in (a) and (b). The experimental values were obtained by reading off the values from Figure 2 of Magnin *et al.*[10]

still be self-consistent and therefore give a constant AB/AA ratio. The experiments therefore strongly support the model prediction that a large fraction of AB is degraded already before septum formation.

The time-dependent concentrations of the sporulation proteins have been measured in three independent biochemical studies[10–12] which, however, do not fully agree. Here (as in our previous work[2]) we follow the two later experimental works whose measurements at the time point of septation can be approximated by the constant expression rates 6×10^{-9} M s^{-1} for AA and the AB dimer, and 2×10^{-9} M s^{-1} for σ^F and IIE. These rate constants imply that AB monomers are expressed at higher (twice as high) levels compared to AA (Figure 3(a) and (b)). This is at odds with the widely accepted hypothesis that AB and AA are translationally coupled and therefore expressed at exactly the same level.[15] We note, however, that septation-dependent σ^F release is still possible when AA and AB monomers are expressed at 6×10^{-9} M s^{-1} as long as the σ^F and IIE expression rates are halved (10^{-9} M s^{-1}). At the time of septation there are then ~44 μM AA, ~13 μM AB dimer and ~7 μM σ^F and IIE. AB degradation is therefore important, irrespective of the exact expression rates.

The model predicts that degradation of AB before septation is important in order to tune the relative protein concentrations. It is unclear why such an energetically costly mechanism is employed. One possible explanation is that AB degradation is important in the mother cell; this would explain the loss of AB after septum formation, which has been found consistently in two independent studies,[10,11] and which is too strong to be the result of degradation in the smaller prespore alone. Alternatively, enhanced AB degradation may have evolved to enable the translational coupling of AA and AB expression. More experiments, that provide further and more accurate data on the cellular protein concentrations, are clearly needed to fully understand the role of the operon structure and of AB degradation.

σ^F Release without an increase in the SpoIIE activity

The central role of a septation-induced increase in IIE activity has been questioned by experiments that revealed that σ^F release was still restricted to the prespore even if IIE remained homogeneously distributed upon septation.[5] Accumulation of IIE on the septum was prevented in these experiments by expressing only the soluble, homogeneously distributed, phosphatase domain of IIE, without the membrane anchor (IIEΔmem). Importantly, however, σ^F-dependent transcription was observed only with a substantial delay of about 1 h. Successful sporulation requires that σ^F is released within 10 min after septation,[1] and accordingly the sporulation efficiency was reduced for this mutant.

The delayed formation of σ^F·RNA polymerase complexes can be reproduced in the simulation (Figure 4(a)), and is a consequence of the continuous loss of AB in the prespore (Figure 4(b)). The dependency on AB degradation explains why σ^F release is so much delayed. Because σ^F release now requires loss of AB from the prespore, it is important that AB is not expressed in this compartment, explaining why the transient genetic imbalance is important in IIEΔmem mutants. Accordingly, experiments and simulations agree that mutants in which both IIE accumulation, and the transient genetic imbalance are abolished are unable to form spores (Figure 4(d)).

We conclude that the observation that σ^F can be released also without the septation-dependent increase in IIE activity does not imply that IIE is not the physiological trigger of compartmentalized σ^F

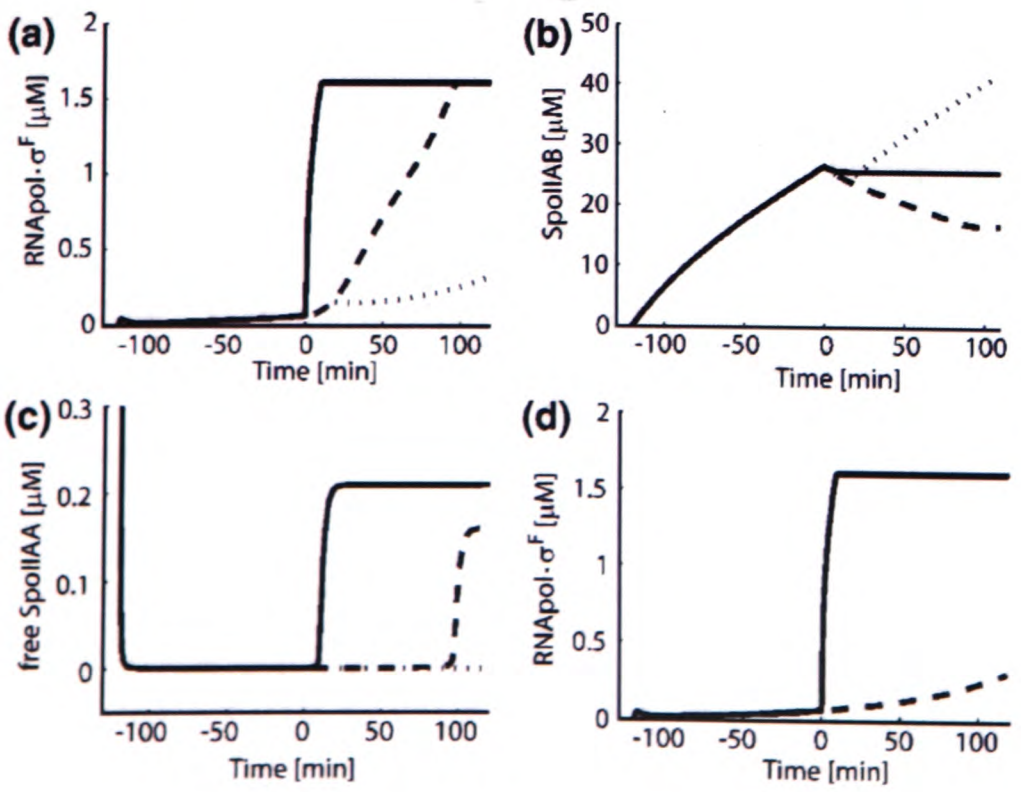


Figure 4. σ^F can be released compartment-specifically without an increase in IIE activity. (a) The predicted concentration of σ^F·RNA-polymerase holoenzyme, and (b) the predicted concentrations of SpoIIAB, and (c) the predicted fraction of AA that is unbound and unphosphorylated assuming that the concentration of IIE, together with its associated AA-P, either increases by fourfold at $t=0$ min (continuous line), or does not increase (dotted line), or neither IIE increases nor is *spoIIA* transported into the prespore after septation (dashed line). (d) The predicted concentration of σ^F·RNApolymerase holoenzyme assuming that the concentration of IIE, together with its associated AA-P, either increases by fourfold at $t=0$ min (continuous line) or neither IIE increases nor is there any genetic imbalance (dashed line).

release. Since mutants in which both IIE accumulation and the transient genetic imbalance are abolished are effectively spo$^-$, we can further conclude that additional mechanisms that can enable compartment-specific σ^F release seem not to exist.

The simulations hint to an additional important detail of the regulatory mechanism. Whilst expression of the *spoIIA* genes is repressed in the wild-type prespore because of the emergence of unphosphorylated AA,[13] the AA concentration is too low to explain the block in the IIEΔmem mutant (Figure 4(c)). Moreover, the simulation suggests that in the mutant only the *spoIIA* genes are repressed but not *spoIIE* (Figure 4(a)). The simulation therefore predicts that the septal location of IIE is necessary for the transfer of the chromosome into the prespore.

This proposition is in agreement with the experimental observation that although septation is rapid, spore engulfment takes more time, and the structure of the septum (which needs to permit DNA translocation) is severely altered in the IIEΔmem mutant.[5] Moreover, a mutant that co-expresses a phosphatase-deficient version of IIE on the membrane with the soluble phosphatase domain leads to a lower rather than a higher sporulation efficiency.[5] This observation is in good agreement with the notion that IIE facilitates transfer of *spoIIA* into the prespore but is difficult to explain otherwise.

Is there a SpoIIE inhibitor?

It has been suggested that the transient genetic imbalance may also support compartmentalized activation of σ^F by the prespore-specific depletion of an elusive IIE-inhibitor.[6] The idea that IIE is regulated by a IIE inhibitor has received support from the observation that a IIE mutation that does not give rise to an altered phosphatase rate *in vitro* leads to premature σ^F release *in vivo*[16] as well as from IIE overexpression experiments.[17]

We have recently shown that the IIE turn-over rate is indeed very low *in vivo*.[2] However, this low rate is not the result of a IIE inhibitor but of the physiological salt conditions ~1 mM Mg^{2+}, and 0.1 mM Mn^{2+})[18] which reduce the activity of serine phosphatases.[2,19] Moreover, a septation-dependent increase of the IIE turn-over rate (as may be achieved by the removal of a IIE inhibitor) is not required for compartment-specific σ^F release.[2]

While the simulation therefore does not support a role of a IIE inhibitor in σ^F regulation under physiological conditions, we note that the premature transcription of σ^F-dependent genes in response to overexpression of IIE[17] can only be reproduced if these genes are either transcribed already at an intermediate σ^F·RNApol concentration (~0.3 μM instead of 1 μM), or if the IIE activity increases (Figure 5). An increase in the IIE concentration alone is insufficient to give rise to micromolar σ^F·RNApol concentrations because the substrate of the phosphatase is limiting as well, and no substrate-saturation of the enzyme is achieved if only the concentration of the enzyme is increased.

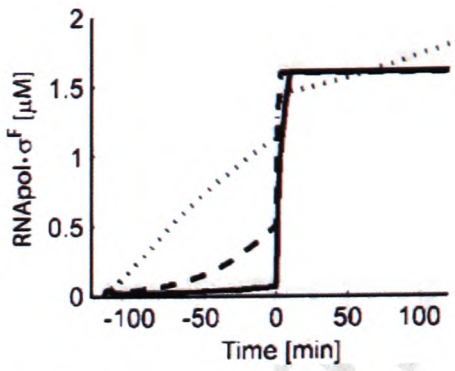


Figure 5. The effect of IIE overexpression. The predicted concentration of σ^F·RNApolymerase holoenzyme assuming that IIE is expressed at its normal rate (continuous line), at a fivefold increased rate (dashed line), or at a fivefold increased rate in conjunction with a fivefold increased turn-over rate (dotted line). The concentration of IIE, together with its associated AA-P, was increased by fourfold at $t=0$ min to model the effect of septation.

In light of our previous finding that the salt conditions are responsible for the low phosphatase rate, the existence of a IIE inhibitor is very unlikely because an inhibitor would only further reduce the IIE turn-over rate and its removal would not lead to an increase beyond the low salt-dependent rate. The apparent increase in the IIE activity in response to IIE overexpression and to the reported mutation must therefore result rather from an activating process, such as the formation of IIE aggregates, which may process the substrate more efficiently.

We conclude that mechanisms other than the septation-dependent IIE activity increase in the smaller prespore are unlikely to play an important role in the compartment-specific activation of σ^F, and that the elusive IIE inhibitor most likely does not exist. Given the intriguing arrangement of the sporulation genes, it will be interesting to learn of other roles for the transient genetic imbalance. More experiments, which also address the different protein concentrations in mother cell and prespore, will be important in that endeavor.

Acknowledgements

I thank Iain D. Campbell, Joanna Clarkson, and Michael D. Yudkin for many valuable discussions, and Joanna Clarkson for comments on the manuscript. The work was supported by a DTA EPSRC studentship as well as by a Junior Research fellowship held at St John's College, University of Oxford.

References

1. Hilbert, D. W. & Piggot, P. J. (2004). Compartmentalization of gene expression during *Bacillus subtilis* spore formation. *Microbiol. Mol. Biol. Rev.* **68**, 234–262.

2. Iber, D., Clarkson, J., Yudkin, M. D. & Campbell, I. D. (2006). The mechanism of cell differentiation in *Bacillus subtilis*. *Nature*, **441**, 371–374.
3. Duncan, L., Alper, S., Arigoni, F., Losick, R. & Stragier, P. (1995). Activation of cell-specific transcription by a serine phosphatase at the site of asymmetric division. *Science*, **270**, 641–644.
4. Ho, M. S., Carniol, K. & Losick, R. (2003). Evidence in support of a docking model for the release of the transcription factor σ^F from the antisigma factor SpoIIAB in *Bacillus subtilis*. *J. Biol. Chem.* **278**, 20898–20905.
5. Arigoni, F., Gu'erout-Fleury, A. M., Bar'ak, I. & Stragier, P. (1999). The SpoIIE phosphatase, the sporulation septum and the establishment of forespore-specific transcription in *Bacillus subtilis*: a reassessment. *Mol. Microbiol.* **31**, 1407–1415.
6. Frandsen, N., Bar'ak, I., Karmazyn-Campelli, C. & Stragier, P. (1999). Transient gene asymmetry during sporulation and establishment of cell specificity in *Bacillus subtilis*. *Genes Dev.* **13**, 394–399.
7. Wu, L. J., Feucht, A. & Errington, J. (1998). Prespore-specific gene expression in *Bacillus subtilis* is driven by sequestration of SpoIIE phosphatase to the prespore side of the asymmetric septum. *Genes Dev.* **12**, 1371–1380.
8. Dworkin, J. & Losick, R. (2001). Differential gene expression governed by chromosomal spatial asymmetry. *Cell*, **107**, 339–346.
9. Pan, Q., Garsin, D. A. & Losick, R. (2001). Self-reinforcing activation of a cell-specific transcription factor by proteolysis of an anti-sigma factor in *B. subtilis*. *Mol. Cell.* **8**, 873–883.
10. Magnin, T., Lord, M. & Yudkin, M. D. (1997). Contribution of partner switching and SpoIIAA cycling to regulation of σ^F activity in sporulating Bacillus subtilis. *J. Bacteriol.* **179**, 3922–3927.
11. Lucet, I., Borriss, R. & Yudkin, M. D. (1999). Purification, kinetic properties, and intracellular concentration of SpoIIE, an integral membrane protein that regulates sporulation in *Bacillus subtilis*. *J. Bacteriol.* **181**, 3242–3245.
12. Lord, M., Barill'a, D. & Yudkin, M. D. (1999). Replacement of vegetative σ^A by sporulationspecific σ^F as a component of the RNA polymerase holoenzyme in sporulating Bacillus subtilis. *J. Bacteriol.* **181**, 2346–2350.
13. Arabolaza, A. L., Nakamura, A., Pedrido, M. E., Martelotto, L., Orsaria, L. *et al.* (2003). Characterization of a novel inhibitory feedback of the anti-anti-sigma SpoIIAA on Spo0A activation during development in *Bacillus subtilis*. *Mol. Microbiol.* **47**, 1251–1263.
14. Losick, R. & Stragier, P. (1992). Crisscross regulation of cell-type-specific gene expression during development in *B. subtilis*. *Nature*, **355**, 601–604.
15. Fort, P. & Piggot, P. J. (1984). Nucleotide sequence of sporulation locus *spoIIA* in *Bacillus subtilis*. *J. Gen. Microbiol.* **130**, 2147–2153.
16. Feucht, A., Abbotts, L. & Errington, J. (2002). The cell differentiation protein SpoIIE contains a regulatory site that controls its phosphatase activity in response to asymmetric septation. *Mol. Microbiol.* **45**, 1119–1130.
17. Arigoni, F., Duncan, L., Alper, S., Losick, R. & Stragier, P. (1996). SpoIIE governs the phosphorylation state of a protein regulating transcription factor σ^F during sporulation in *Bacillus subtilis*. *Proc. Natl Acad. Sci. USA*, **93**, 3238–3242.
18. Eisenstadt, E., Fisher, S., Der, C. L. & Silver, S. (1973). Manganese transport in Bacillus subtilis W23 during growth and sporulation. *J. Bacteriol.* **113**, 1363–1372.
19. Schroeter, R., Schlisio, S., Lucet, I., Yudkin, M. & Borriss, R. (1999). The *Bacillus subtilis* regulator protein SpoIIE shares functional and structural similarities with eukaryotic protein phosphatases 2C. *FEMS Microbiol. Leters*, **174**, 117–123.

Edited by J. Karn

(Received 1 March 2006; received in revised form 25 April 2006; accepted 4 May 2006)
Available online 19 May 2006

Author's personal copy

Molecular Systems Biology (2006) doi:10.1038/msb4100084
© 2006 EMBO and Nature Publishing Group All rights reserved 1744-4292/06
www.molecularsystemsbiology.com
000043

molecular systems biology

REPORT

A quantitative study of the benefits of co-regulation using the *spoIIA* operon as an example

Dagmar Iber*

Mathematical Institute, Centre for Mathematical Biology, University of Oxford, Oxford, UK
* Correspondence: Mathematical Institute, Centre for Mathematical Biology, University of Oxford, 24-29 St. Giles, Oxford OX1 3LB, UK.
Tel.: +44 1865 283875; Fax: +44 1865 273583; E-mail: iber@maths.ox.ac.uk

Received 4.4.06; accepted 7.7.06

The distribution of most genes is not random, and functionally linked genes are often found in clusters. Several theories have been put forward to explain the emergence and persistence of operons in bacteria. Careful analysis of genomic data favours the co-regulation model, where gene organization into operons is driven by the benefits of coordinated gene expression and regulation. Direct evidence that coexpression increases the individual's fitness enough to ensure operon formation and maintenance is, however, still lacking. Here, a previously described quantitative model of the network that controls the transcription factor σ^F during sporulation in *Bacillus subtilis* is employed to quantify the benefits arising from both organization of the sporulation genes into the *spoIIA* operon and from translational coupling. The analysis shows that operon organization, together with translational coupling, is important because of the inherent stochastic nature of gene expression, which skews the ratios between protein concentrations in the absence of co-regulation. The predicted impact of different forms of gene regulation on fitness and survival agrees quantitatively with published sporulation efficiencies.
Molecular Systems Biology 22 August 2006; doi:10.1038/msb4100084
Subject Categories: metabolic and regulatory networks; chromatin & transcription
Keywords: coupled gene expression; noise; operon; signalling networks; sporulation

Introduction

The available genome sequences demonstrate that many genes are clustered on chromosomes according to their function. Genes in bacteria are clustered but can also be organized into operons such that the expression of a group of genes is regulated by the same genetic control element. When operons were first discovered, it was assumed that the benefit of co-transcription led to operon assembly (Jacob and Monod, 1961). Other models have since been proposed, and these belong to one of three classes, the natal model, the Fisher model, or the selfish operon model (Lawrence, 1997). According to the natal model, clustering of genes is the consequence of gene duplication. However, as operons comprise genes that belong to very distant families and the majority of paralogues do not cluster, this model is insufficient to explain operon origin (Lawrence, 1997; Dandekar *et al*, 1998). A recast of the Fisher model, adapted to prokaryotes, proposes that clustering of genes reduces the likelihood that co-adapted genes become separated by recombination. However, this does not explain how operons can emerge, as recombination is as likely to generate clusters as to disrupt them. According to the selfish operon model, operons facilitate the horizontal transfer of functionally related genes (Lawrence and Roth, 1996). The physical proximity of genes thus does not necessarily provide a selective advantage to the individual organism but rather to the gene cluster itself, because it can be efficiently transmitted horizontally as well as vertically. Recent studies have, however, failed to observe the gene cluster pattern predicted by the model, and this strongly suggests that the selfish operon model does not explain the emergence and persistence of operons (Pal and Hurst, 2004; Price *et al*, 2005). So what drives operon assembly?

The idea that co-transcription of genes provides a selective advantage to the individual organism has never been contradicted. It has been questioned only because it remains unclear whether the benefits of co-transcription could be strong enough to drive the assembly of operons by rare recombination events (Lawrence and Roth, 1996; Lawrence, 1997). A genotype that confers higher fitness will dominate in a population with bounded total population size only if selection acts on a timescale that is substantially shorter than the timescale on which recombination and mutation events could negate the benefits.

There are a number of potential selective advantages given by co-transcription. In the case of operons that code for multiprotein complexes, co-transcription enables co-translational folding (Dandekar *et al*, 1998), it limits the half-life of toxic monomers (Pal and Hurst, 2004), and it reduces stochastic differences in gene expression (Swain, 2004). Operons that do

© 2006 EMBO and Nature Publishing Group

not code for interacting proteins may be advantageous because of the co-regulation of protein expression (Price *et al*, 2005). Many examples of this class of operons are associated with metabolic operons (Lawrence and Roth, 1996) where co-regulated expression is likely to optimize the flux and to facilitate the regulation of functions, especially if these are required only under certain environmental conditions, or if complex regulatory structures are employed (Price *et al*, 2005).

Evidence in favour of any of these proposed driving forces has so far largely been obtained from comparative genomics. Here we use a previously derived quantitative model for the network that controls the transcription factor σ^F during sporulation in *Bacillus subtilis* (Iber *et al*, 2006) to quantify the benefits of coexpression. Spore formation in *B. subtilis* is a response to nutrient deprivation at high cell density and involves asymmetric septation and compartment-specific initiation of gene expression (Hilbert and Piggot, 2004). The different gene programs in the larger mother cell and the smaller prespore are both directed by the transcription factor σ^F, which, although only active in the smaller prespore, affects the transcriptional programs across the septum also in the mother cell, a phenomenon that is referred to as criss-cross regulation (Losick and Stragier, 1992). Successful sporulation therefore requires the rapid septation-dependent and prespore-specific activation of σ^F. σ^F is kept inactive by binding to SpoIIAB and is released upon binding of SpoIIAA (Figure 1). SpoIIAA is phosphorylated by SpoIIAB (Min *et al*, 1993) and reactivated by the serine phosphatase SpoIIE (Duncan *et al*, 1995). The balance between kinase and phosphatase activity thus determines whether or not σ^F is released from its inactive complex with SpoIIAB. SpoIIE accumulates on both sides of the asymmetrically positioned septum and therefore has an increased activity in the smaller compartment (Arigoni *et al*, 1995). A quantitative model of the regulatory network predicts that because of the low turnover rate, most SpoIIE is bound by its substrate such that enzyme and substrate increase together in the smaller compartment (Iber *et al*, 2006). According to the model, this combined increase is sufficient to trigger the formation of micromolar concentrations of σ^F holoenzyme in the prespore.

It is obvious from the above that the protein concentration ratio is important. An excess of σ^F or SpoIIAA compared to SpoIIAB will result in free σ^F and σ^F-dependent gene expression, whereas an excess of SpoIIAB will prevent

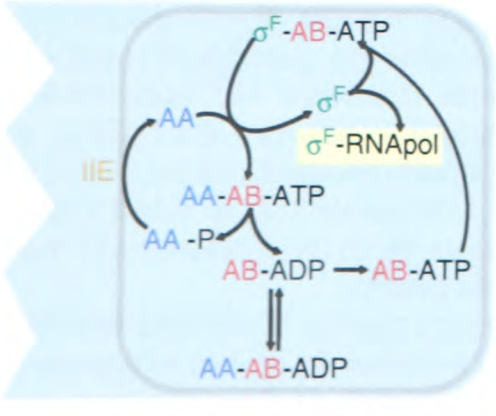


Figure 1 An overview of the interactions in the network that controls σ^F activity in *B. subtilis*. For details, see text. The figure is a reproduction of Figure 1 of Iber *et al* (2006).

SpoIIAA-dependent σ^F release. In the vegetative cell, the sporulation proteins are not detectable, and septation is preceded by 90–120 min of gene expression, dependent on the exact experimental conditions (Magnin *et al*, 1997; Lord *et al*, 1999; Lucet *et al*, 1999). Limiting the stochastic noise inherent in protein expression can be expected to be crucial for avoiding variations in the relative protein concentrations and the resulting sporulation defects. Three of the four proteins in the network are transcribed from genes in the *spoIIA* operon (Figure 2A). These genes are not only co-transcribed into a single mRNA but are also most likely to be coexpressed, as the translation of the three proteins appears to be coupled, at least to some degree. This system therefore offers an excellent opportunity to analyse the influence of transcriptional and translational co-regulation of the sporulation genes on an individual's survival and fitness.

Coupled translation is achieved when two genes are translated by the same ribosome. Reinitiation of translation at a nearby start codon after termination at the upstream gene is possible because ribosome dissociation from the mRNA is a slow and energy-dependent process (McCarthy and Gualerzi, 1990). There is currently no direct experimental evidence for coupled translation of the *spoIIA* operon. Such coupling can, however, be postulated based on the arrangement of genes (Fort and Piggot, 1984). The first two genes in the *spoIIA* operon (encoding SpoIIAA and SpoIIAB) overlap by 4 bp, whereas the genes for SpoIIAB and σ^F are interspaced by 11 bp (Figure 2A); coupled translation has been documented for intercistronic distances of more than 60 bp (McCarthy and Gualerzi, 1990). The majority of genes that are organized in operons are separated by distances comparable to those found in the *spoIIA* operon (Salgado *et al*, 2000), so that the studied system can be considered as representative of operons in general. The efficiency of reinitiation depends on the distance as well as the strength of the Shine–Dalgarno sequence (Adhin and van Duin, 1990; McCarthy and Gualerzi, 1990), which is, in general, located 5–13 bp upstream of a start codon and which binds to the homologous 3′ end of the 16S rRNA, a component of the 30S ribosomal subunit. Moreover, the secondary structure of the mRNA can affect lateral diffusion of the ribosomes (Adhin and van Duin, 1990).

According to the protein expression data for the *spoIIA* operon, it appears that the last gene in the operon which encodes σ^F, is expressed at much lower levels than are *spoIIAA* and *spoIIAB*, whereas SpoIIAB monomers may be expressed at equal or up to three times higher levels compared to SpoIIAA (Magnin *et al*, 1997; Lord *et al*, 1999; Lucet *et al*, 1999). The weaker expression of a downstream gene (as is the case for σ^F) can, in general, be accounted for by a weaker ribosomal binding site, which is removed far enough from the termination codon of the upstream cistron that a considerable fraction of ribosomes dissociate from the mRNA before translation can be reinitiated (McCarthy and Gualerzi, 1990). It should be noted that whereas the transcriptional and translational coupling will reduce the noise in the relative SpoIIAB to σ^F expression levels, the unbinding of ribosomes is necessarily a stochastic process and will therefore add a low level of noise. The stronger expression of a downstream gene (as may be the case for SpoIIAB relative to SpoIIAA) can, in general, only be observed if a strong initiation sequence for the downstream

© 2006 EMBO and Nature Publishing Group

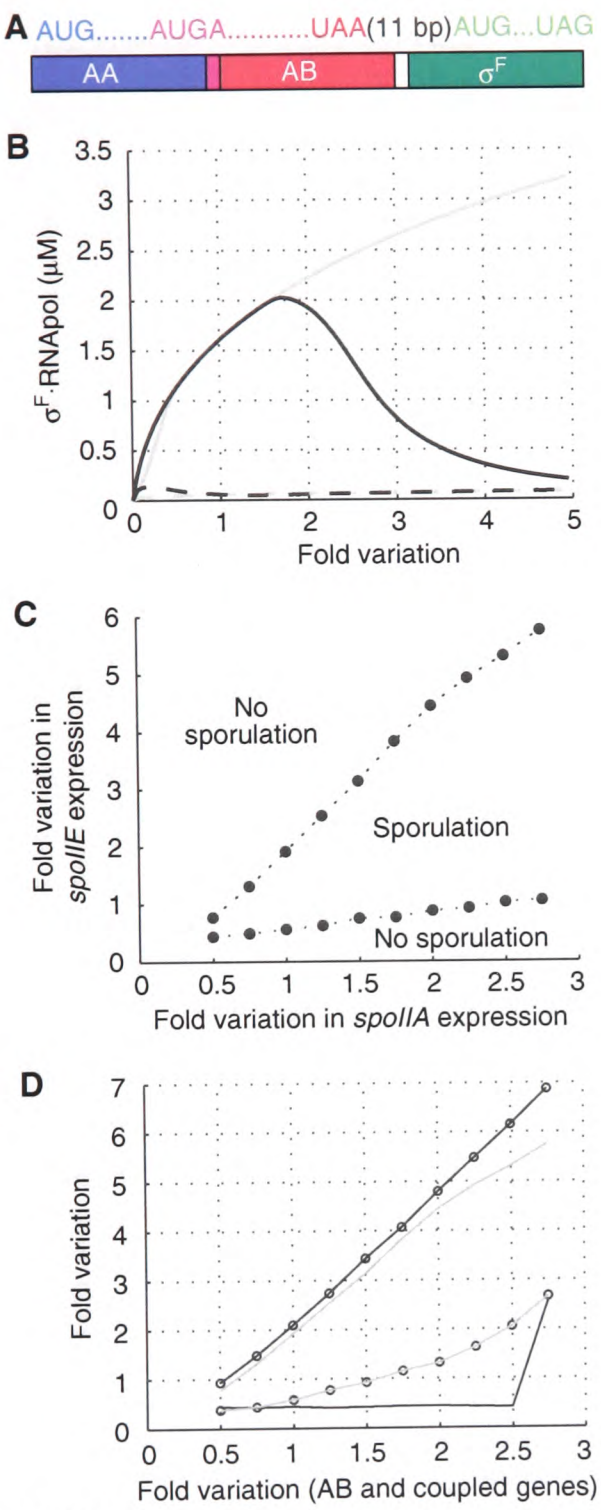


Figure 2 The impact of parallel and random variations in the expression of *spoIIE* and *spoIIA* genes on σ^F release. (**A**) The *spoIIA* operon comprises the genes for SpoIIAA, SpoIIAB, and σ^F. The genes for SpoIIAA and SpoIIAB overlap; the genes for SpoIIAB and σ^F are separated by 11 bp. (**B**) The regulatory network is robust to parallel variations in gene expression. The predicted concentration of σ^F-RNA polymerase holoenzyme before (dashed lines) and after septum formation (continuous lines) if either all (grey lines) or all protein expression rates except that of SpoIIE (black lines) were increased by the factor on the horizontal axis compared to the standard reference rates ($6 \times 10^{-9}\,M\,s^{-1}$ for SpoIIAA and SpoIIAB dimers and $2 \times 10^{-9}\,M\,s^{-1}$ for σ^F and SpoIIE; Iber *et al*, 2006). (C, D) The expression rate combinations for which septation-dependent σ^F release is possible (between the lines) or not possible (outside the area marked by lines). (**C**) The impact of differential regulation of *spoIIE* and *spoIIA* expression. The vertical and horizontal axes indicate the fold variation in the *spoIIE* and *spoIIA* expression rates respectively, compared to the standard reference rates. (**D**) The impact of differential regulation of the expression of genes encoded in the *spoIIA* operon. The vertical axis indicates the fold variation in the expression of SpoIIAA (circles), σ^F (black lines), or SpoIIAA and σ^F (grey lines). The horizontal axis indicates the fold variation in the expression of SpoIIAB and of any other protein whose expression is coupled to that of SpoIIAB (which are those genes in the *spoIIA* operon not reported on the vertical axis). The sudden jump observed at a high SpoIIAB to σ^F ratio (lower black line) is the consequence of impaired σ^F release when the relative SpoIIAB concentration is too high.

gene is occluded by mRNA secondary structure, which is melted by the ribosome that transcribes the upstream gene (McCarthy and Gualerzi, 1990). Such a condition does not seem to be met by the gene for SpoIIAB, and more accurate expression data will be necessary to establish whether more SpoIIAB than SpoIIAA is expressed.

Available expression data can best be captured by an expression rate for SpoIIAB dimers and SpoIIAA of $6 \times 10^{-9}\,M\,s^{-1}$ and $2 \times 10^{-9}\,M\,s^{-1}$ for σ^F and SpoIIE (Iber *et al*, 2006); it should be noted that the simulation yields qualitatively similar results if SpoIIAB monomers and SpoIIAA are expressed at equal rates ($6 \times 10^{-9}\,M\,s^{-1}$), as long as the σ^F and SpoIIE expression rate is then reduced to $10^{-9}\,M\,s^{-1}$ (Iber, 2006). As discussed by Iber (2006), the linear increase in the protein concentration assumed here does not fully match the experimental observations. There are, nonetheless, two good reasons to use a linear model. First of all, the data are too inaccurate and, in parts, contradictory to be modelled exactly. Secondly, the chosen rates correspond to the protein concentrations measured at the time of septation (Magnin *et al*, 1997; Lord *et al*, 1999; Lucet *et al*, 1999), the critical time point to judge sporulation success. This is because, in the cell, the IIE concentration increases more slowly than the other protein concentrations and only increases sharply immediately before septation (Feucht *et al*, 2002). As a consequence, the greatest danger of spontaneous uncompartmentalized activation of σ^F is just before septation, and this risk is fully assessed by the linear expression model. As our analysis focuses mainly at what happens minutes before and after septation, individual fluctuations in the global expression rates during the 2 h preceding septation are not important and the linear protein expression rates used should be considered as an averaged protein expression rate per bacterium.

Our quantitative ordinary differential equation model is very detailed—it comprises 50 dependent variables and 150 kinetic constants to describe the dynamics of only four proteins; the reader is referred to a detailed discussion of the model in Supplementary information of Iber *et al* (2006). Given its high level of detail and accuracy, the model predicts the phenotypes of essentially all mutants for which the biochemical effect is known. We can therefore expect that the predicted sporulation efficiencies in response to changes in parameter values are realistic. In the following, we employ the model to quantify how far different levels of stochastic noise in gene expression, as modulated by different degrees of coupling of protein expression (that is by the coupling of both transcription and translation), affect the sporulation efficiency, that is the survival chances.

Results and discussion

In addressing how variations in the protein expression rates affect the sporulation efficiency we will look at the effect of parallel changes in all protein expression rates as well as at the effects of independent changes that skew the ratios of protein concentrations. As the standard, 'wild-type' protein expression rates, we use $6 \times 10^{-9}\,M\,s^{-1}$ for SpoIIAA and SpoIIAB dimers and $2 \times 10^{-9}\,M\,s^{-1}$ for σ^F and SpoIIE (Iber *et al*, 2006). After 120 min of protein expression, the septum forms and SpoIIE

© 2006 EMBO and Nature Publishing Group

accumulates on both sides of this septum. This is modelled by a four-fold increase in the concentration of SpoIIE, together with its associated substrate (phosphorylated SpoIIAA) in the prespore. As before, we define a successful sporulation event by the requirement that before septation the concentration of σ^F. RNA polymerase holoenzyme does not exceed 0.4 μM, whereas after septation the concentration exceeds 1 μM (Iber *et al*, 2006).

If the protein expression rates are all varied in parallel, that is by a common factor as denoted on the horizontal axis in Figure 2B, we find that the predicted sporulation efficiency is not affected as long as a minimal expression rate is kept to provide sufficient σ^F for binding to the RNA polymerase (Figure 2B, grey lines). If the expression of SpoIIE is kept constant (in order to reflect that this protein is transcribed from a different locus and may therefore vary independently), then an independent 2.5-fold increase in the other sporulation proteins can still be tolerated before the relative activity of the phosphatase becomes too weak (Figure 2B, black lines). An even higher independent increase in the expression of the *spoIIA* genes can be tolerated if we assume that the expression of the *spoIIA* and *spoIIE* genes is at least weakly correlated such that a large increase in the expression of the *spoIIA* genes is accompanied by a small increase in the expression of the *spoIIE* genes (Figure 2C). Such a correlation is not unexpected, considering that variations in gene expression are the result of both intrinsic and extrinsic noise. The latter, which reflects cell-to-cell variation in the concentration of other molecular species such as the RNA polymerase, will affect all genes similarly. We can conclude that the independent regulation of the *spoIIA* and *spoIIE* genes is unlikely to generate a major risk of failed sporulation. Separation of the *spoIIA* and *spoIIE* genes on the bacterial chromosome, on the other hand, has benefits because it ensures that, upon septation, each compartment retains one copy of *spoIIE* while initially (for the first 10–15 min) two copies of *spoIIA* are in the mother cell but none in the prespore (Frandsen *et al*, 1999). This initial transient genetic imbalance may protect the mother cell from a relative increase *of spoIIE* to *spoIIA* gene products (Iber, 2006).

If the expression levels of the genes in the *spoIIA* operon are varied independently of each other, the tolerance of the network to variations in gene expression drops substantially. In particular, if expression of SpoIIAB and SpoIIAA is no longer co-regulated, the network is sensitive to rather small changes (Figure 2D, grey lines and circles). Thus, if the SpoIIAA expression rate remains fixed and the SpoIIAB expression rate increases by 60% (corresponding to the factor 1.6 on the horizontal axis in Figure 2D), then sporulation is predicted to fail; 60% variation from the mean is a noise level observed in bacterial (*Escherichia coli*) expression systems (Elowitz *et al*, 2002). On the other hand, if expression of SpoIIAA and SpoIIAB remains co-regulated but σ^F expression is regulated independently (Figure 2D, black lines), the network is rather robust to variations in gene expression as long as the expression of SpoIIAB is increased more than the expression of σ^F and the overall σ^F concentration remains high enough to form micromolar concentrations of the holoenzyme. The transcriptional coupling together with a strong translational coupling of SpoIIAA and SpoIIAB therefore substantially increases the robustness of the network to fluctuations in gene expression. Stochastic variations in the relative rate of σ^F translation, on the other hand, are not as detrimental as long as the translation efficiency for σ^F is lower than for SpoIIAA and SpoIIAB, as can be achieved by a weaker ribosomal binding site and the resulting (stochastic) dissociation of ribosomes. An advantage of preferential dissociation of the ribosomes before translating the gene for σ^F is that the bacterium saves the energy that would otherwise be required to translate, and subsequently degrade, unnecessary (harmful) copies of σ^F. Considering that σ^F comprises 255 amino acids and linkage of each amino acid requires the equivalent of four ATPs, the energy by not translating and degrading 10 μM σ^F corresponds to more than 10 mM ATP, which is a considerable amount

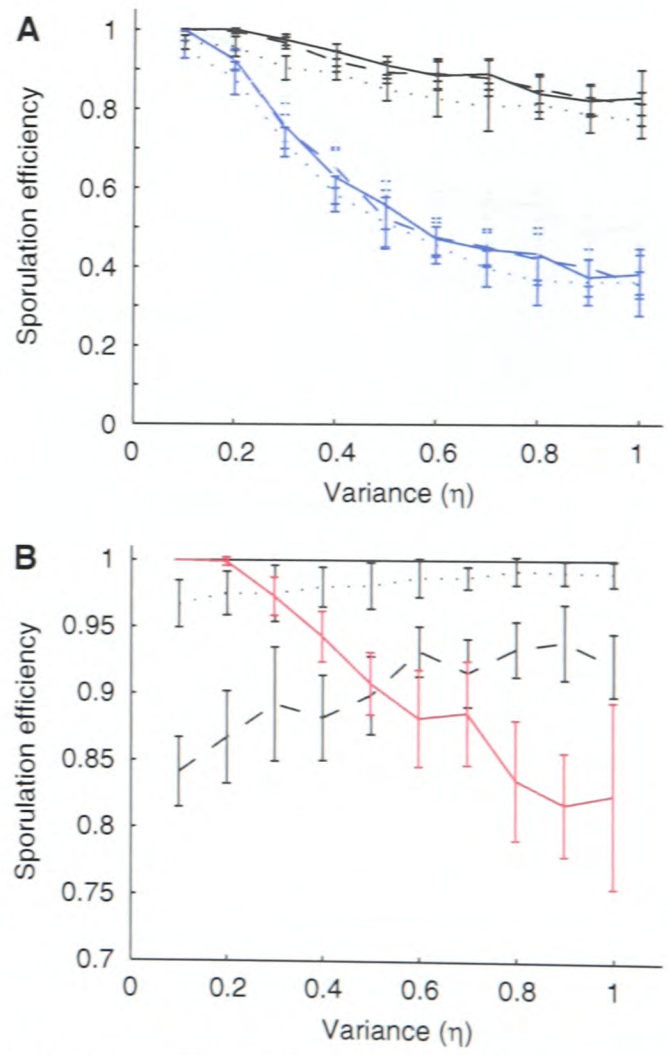


Figure 3 The impact of stochastic variation in gene expression on sporulation efficiency. (**A**) The fraction of successful sporulation events (as defined in the text) dependent on the variance in gene expression if expression of the *spoIIA* genes is either coupled (black lines), the expression of SpoIIAB and σ^F is coupled (grey lines), or the expression of SpoIIAA and σ^F is coupled (blue lines). SpoIIE is expressed throughout at the standard rate of 2×10^{-9} M s^{-1}. The broken lines show the effect of an additional independent normal variation in the rate of σ^F expression with η_S=0.1 (dashed lines) or η_S=0.3 (dotted lines) from the coupled rates. If σ^F is one of the coupled rates, then σ^F expression is varied both together with its coupling partner and additionally independently to reflect the additive levels of noise acting at the initiation of translation and the re-initiation/dissociation step. (**B**) The fraction of successful sporulation events (as defined in the text) dependent on the variance in gene expression if expression of the *spoIIA* and *spoIIE* genes is coupled (to assess the benefits of correlated expression), and an additional noise term η_E is added to the expression *of spoIIE* with η_E=0.1 (black continuous line), η_E=0.3 (dotted line), or η_E=0.6 (dashed line); η_E assesses the effects of independent promoters and spatial heterogeneity in the concentration of transcription and translation factors. The red line is identical to the continuous black line in panel A (noise in coupled *spoIIA* expression, SpoIIE expressed at 2×10^{-9} M s^{-1}). Mean and standard deviation are based on 10 times 100 independent runs.

© 2006 EMBO and Nature Publishing Group

considering that the bacterial ATP concentration is 1–3 mM (Jolliffe *et al*, 1981; Guffanti *et al*, 1987; Hecker *et al*, 1988) and sporulation is a response to starvation, that is energy deprivation.

In a last step, we can now quantify the impact of gene organization on sporulation efficiency, and therefore fitness. For this, we assume that the gene expression levels in the cell population follow a normal distribution with variance η around the mean value. Given the complex regulation pattern of gene expression, gene expression levels are unlikely to be distributed exactly normally. A normal distribution is, however, still likely to provide an approximation no worse than what could be obtained with a detailed model of the regulatory process in the absence of sufficient data to determine all required parameter values (Swain, 2004). Sporulation efficiency is determined as the fraction of simulation runs for which the concentration of σ^F. RNA polymerase holoenzyme does not exceed 0.4 μM before septation and exceeds one micromolar after septation (Iber *et al*, 2006). For each condition, the mean sporulation efficiency and standard deviation are calculated from 100 independent runs that are carried out 10 times. In each run, the protein expression rates were set randomly such that overall the respective distributions of the protein expression rates were obtained. Determination of the sporulation efficiency for $\eta \in [0,1]$ shows that as long as the sporulation genes are translationally coupled, even high variances hardly affect the sporulation efficiency (Figure 3A, black lines). The sporulation efficiency is even higher at high noise level, η, if *spoIIE* expression co-varies with *spoIIA* expression, at least weakly (Figure 3B). A lengthening of the transcription time (that is a delay in septation), when transcription levels are too low to generate sufficient σ^F until septation, will further increase robustness to fluctuations in the rate of protein expression. Such a dependency of the time point of septation on the protein (and in particular the SpoIIE) concentration is in agreement with experiments (Khvorova *et al*, 1998; Ben-Yehuda and Losick, 2002) and might explain the large variance in the delay between the onset of sporulation and septation that is observed under different sporulation conditions. Low levels of additional stochastic noise in σ^F expression (broken lines), as may arise because of the stochastic dissociation of ribosomes, also has rather little impact and confirms that the weak coupling of SpoIIAB and σ^F translation does not substantially reduce sporulation efficiency. If on the other hand, *spoIIAB* is removed from the operon and controlled independently by the same promoter, then the sporulation efficiency drops rapidly (Figure 3A, blue lines). This is in good quantitative agreement with experiments, which find that the sporulation efficiency drops to 40–80% of wild-type levels (Dworkin and Losick, 2001), especially when considering that $\eta \sim [0.3, 0.6]$ for these expression levels (Elowitz *et al*, 2002). If *spoIIAA* is moved instead, then the effect is reduced (J Clarkson, personal communication), as also predicted by the model (Figure 3A, grey lines).

It should be noted that this drop in sporulation efficiency has previously been accounted for by the loss of the transient genetic imbalance when *spoIIAB* is moved to a chromosomal position close to the origin of replication (Dworkin and Losick, 2001). The transient lack of SpoIIAB expression in the prespore together with accelerated degradation of unbound SpoIIAB (Pan *et al*, 2001) had been suggested to enable σ^F release (Dworkin and Losick, 2001). However, we have shown previously that the transient genetic imbalance does not affect σ^F release on the timescale on which it persists (Iber, 2006), and stochastic effects are therefore a much more likely explanation for the observed phenotype of the mutants.

We conclude from the analysis of this well-studied model system that the protection from stochastic variation in the expression rate of interacting proteins can substantially increase viability, and therefore constitutes a driving force for gene clustering and co-regulation. Although the importance of gene dosage had been recognized before (Veitia, 2002), and underexpression and overexpression of protein complex subunits in yeast had been shown to lower fitness (Papp *et al*, 2003), this study reveals that much smaller variances, as can result from stochastic effects, can already have substantial detrimental effects. The detailed analysis of the expression of the sporulation proteins therefore demonstrates the optimized character of gene regulation and suggests that co-regulation of genes serves to optimize cellular network dynamics in spite of the inherent noise in all biological processes.

Supplementary information

Supplementary information is available at the *Molecular Systems Biology* website (www.nature.com/msb).

Acknowledgements

I thank Iain D Campbell, Joanna Clarkson, and Michael D Yudkin for many valuable discussions, and Iain D Campbell for his critical reading of the manuscript. The work was supported by a DTA EPSRC studentship as well as by a Junior Research fellowship held at St John's College, University of Oxford.

References

Adhin MR, van Duin J (1990) Scanning model for translational reinitiation in eubacteria. *J Mol Biol* **213:** 811–818

Arigoni F, Pogliano K, Webb C, Stragier P, Losick R (1995) Localization of protein implicated in establishment of cell type to sites of asymmetric division. *Science* **270:** 637–640

Ben-Yehuda S, Losick R (2002) Asymmetric cell division in *B. subtilis* involves a spirallike intermediate of the cytokinetic protein FtsZ. *Cell* **109:** 257–266

Dandekar T, Snel B, Huynen M, Bork P (1998) Conservation of gene order: a fingerprint of proteins that physically interact. *Trends Biochem Sci* **23:** 324–328

Duncan L, Alper S, Arigoni F, Losick R, Stragier P (1995) Activation of cell-specific transcription by a serine phosphatase at the site of asymmetric division. *Science* **270:** 641–644

Dworkin J, Losick R (2001) Differential gene expression governed by chromosomal spatial asymmetry. *Cell* **107:** 339–346

Elowitz MB, Levine AJ, Siggia ED, Swain PS (2002) Stochastic gene expression in a single cell. *Science* **297:** 1183–1186

Feucht A, Abbotts L, Errington J (2002) The cell differentiation protein SpoIIE contains a regulatory site that controls its phosphatase activity in response to asymmetric septation. *Mol Microbiol* **45:** 1119–1130

© 2006 EMBO and Nature Publishing Group

Fort P, Piggot PJ (1984) Nucleotide sequence of sporulation locus *spoIIA* in *Bacillus subtilis*. *J Gen Microbiol* **130:** 2147–2153

Frandsen N, Barak I, Karmazyn-Campelli C, Stragier P (1999) Transient gene asymmetry during sporulation and establishment of cell specificity in *Bacillus subtilis*. *Genes Dev* **13:** 394–399

Guffanti AA, Clejan S, Falk LH, Hicks DB, Krulwich TA (1987) Isolation and characterization of uncoupler-resistant mutants of *Bacillus subtilis*. *J Bacteriol* **169:** 4469–4478

Hecker M, Heim C, Volker U, Wolfel L (1988) Induction of stress proteins by sodium chloride treatment in *Bacillus subtilis*. *Arch Microbiol* **150:** 564–566

Hilbert DW, Piggot PJ (2004) Compartmentalization of gene expression during *Bacillus subtilis* spore formation. *Microbiol Mol Biol Rev* **68:** 234–262

Iber D (2006) A computational analysis of the impact of the transient genetic imbalance on compartmentalized gene expression during sporulation in *Bacillus subtilis*. *J Mol Biol* **360:** 15–20

Iber D, Clarkson J, Yudkin MD, Campbell ID (2006) The mechanism of cell differentiation in *Bacillus subtilis*. *Nature* **441:** 371–374

Jacob F, Monod J (1961) On the regulation of gene activity. *Cold Spring Harbor Symp Quant Biol* **26:** 193–211

Jolliffe LK, Doyle RJ, Streips UN (1981) The energized membrane and cellular autolysis in *Bacillus subtilis*. *Cell* **25:** 753–763

Khvorova A, Zhang L, Higgins ML, Piggot PJ (1998) The spoIIE locus is involved in the Spo0A-dependent switch in the location of FtsZ rings in *Bacillus subtilis*. *J Bacteriol* **180:** 1256–1260

Lawrence JG (1997) Selfish operons and speciation by gene transfer. *Trends Microbiol* **5:** 355–359

Lawrence JG, Roth JR (1996) Selfish operons: horizontal transfer may drive the evolution of gene clusters. *Genetics* **143:** 1843–1860

Lord M, Barilla D, Yudkin MD (1999) Replacement of vegetative σ^F by sporulation-specific σ^F as a component of the RNA polymerase holoenzyme in sporulating *Bacillus subtilis*. *J Bacteriol* **181:** 2346–2350

Losick R, Stragier P (1992) Crisscross regulation of cell-type-specific gene expression during development in *B. subtilis*. *Nature* **355:** 601–604

Lucet I, Borriss R, Yudkin MD (1999) Purification, kinetic properties, and intracellular concentration of SpoIIE, an integral membrane protein that regulates sporulation in *Bacillus subtilis*. *J Bacteriol* **181:** 3242–3245

Magnin T, Lord M, Yudkin MD (1997) Contribution of partner switching and SpoIIAA cycling to regulation of σ^F activity in sporulating *Bacillus subtilis*. *J Bacteriol* **179:** 3922–3927

McCarthy JE, Gualerzi C (1990) Translational control of prokaryotic gene expression. *Trends Genet* **6:** 78–85

Min KT, Hilditch CM, Diederich B, Errington J, Yudkin MD (1993) σ^F, the first compartment-specific transcription factor of *B. subtilis*, is regulated by an anti-sigma factor that is also a protein kinase. *Cell* **74:** 735–742

Pal C, Hurst LD (2004) Evidence against the selfish operon theory. *Trends Genet* **20:** 232–234

Pan Q, Garsin DA, Losick R (2001) Self-reinforcing activation of a cell-specific transcription factor by proteolysis of an anti-sigma factor in *B. subtilis*. *Mol Cell* **8:** 873–883

Papp B, Pal C, Hurst LD (2003) Dosage sensitivity and the evolution of gene families in yeast. *Nature* **424:** 194–197

Price MN, Huang KH, Arkin AP, Alm EJ (2005) Operon formation is driven by co-regulation and not by horizontal gene transfer. *Genome Res* **15:** 809–819

Salgado H, Moreno-Hagelsieb G, Smith TF, Collado-Vides J (2000) Operons in *Escherichia coli*: genomic analyses and predictions. *Proc Natl Acad Sci USA* **97:** 6652–6657

Swain PS (2004) Efficient attenuation of stochasticity in gene expression through post-transcriptional control. *J Mol Biol* **344:** 965–976

Veitia RA (2002) Exploring the etiology of haploinsufficiency. *BioEssays* **24:** 175–184

© 2006 EMBO and Nature Publishing Group

Bulletin of Mathematical Biology (2006) 68: 945–956
DOI 10.1007/s11538-005-9049-5

ORIGINAL ARTICLE

Integrin Activation—the Importance of a Positive Feedback

Dagmar Iber[a,*], Iain D. Campbell[b]

[a] *Mathematical Institute, Centre for Mathematical Biology, 24–29 St. Giles, Oxford OX1 3LB, UK*
[b] *Department of Biochemistry, University of Oxford, Oxford OX1 3QU, UK*

Received: 5 April 2005 / Accepted: 2 September 2005 / Published online: 13 May 2005
© Society for Mathematical Biology 2006

Abstract Integrins mediate cell adhesion and are essential receptors for the development and functioning of multicellular organisms. Integrin activation is known to require both ligand and talin binding and to correlate with cluster formation but the activation mechanism and precise roles of these processes are not yet resolved. Here mathematical modeling, with known experimental parameters, is used to show that the binding of a stabilizing factor, such as talin, is alone insufficient to enable ligand-dependent integrin activation for all observed conditions; an additional positive feedback is required.

Keywords Talin · Integrin · Receptor activation · Master equation · Positive feedback

1. Introduction

Integrins, large membrane-spanning heterodimeric proteins, were so named for their ability to link the extracellular and intracellular skeletons (Tamkun et al., 1986). As an important class of cell adhesion receptors they participate in a wide range of biological interactions, including development, tissue repair, angiogenesis, inflammation and hemostasis (Horwitz and Webb, 2003). Cell adhesion and detachment as well as controlled actin polymerization inside the cell are of particular importance in cell migration. The speed of cell movement depends on the density of integrins and ligands as well as their affinity of binding (Palecek et al., 1997). Integrins are key components of focal adhesions, dynamic multiprotein complexes that are involved in the regulation of cell adhesion and migration. Focal adhesions (Zamir and Geiger, 2001) provide a physical link between integrins and the actin cytoskeleton as well as sites for signal transduction into the cell

*Corresponding author
E-mail address: iber@maths.ox.ac.uk (Dagmar Iber)

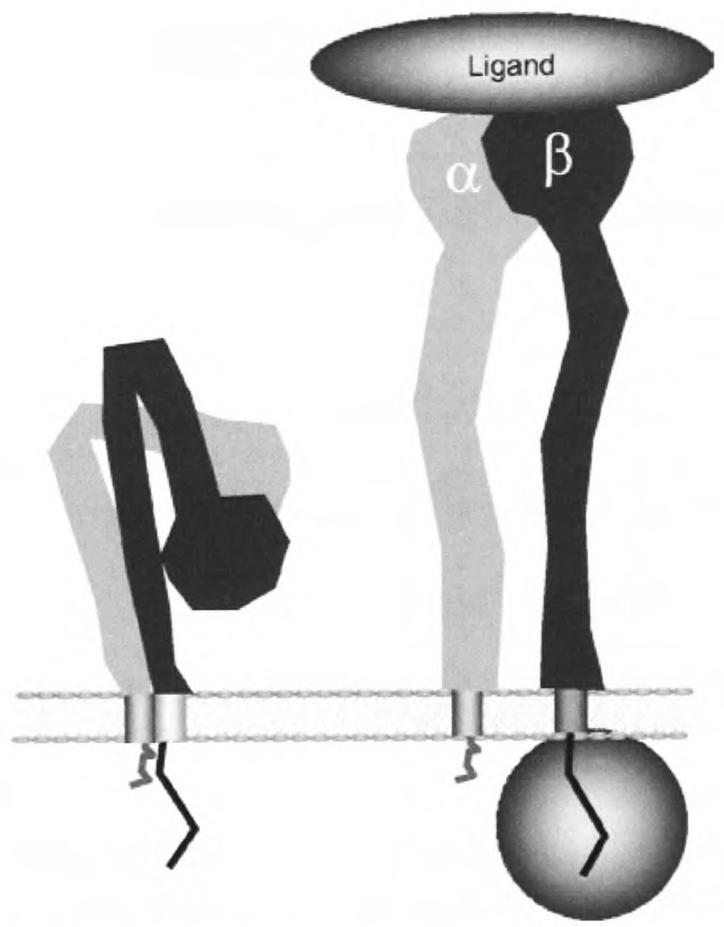


Fig. 1 A simple model of integrin activation. Integrins exist in either a closed (LHS) or open conformation (RHS); the open, high affinity form, can be stabilized by binding of extracellular ligand or intracellular proteins. The open conformation triggers downstream signaling and is termed active.

interior. Information about identified interactions and players in these complexes is ever-increasing but our overall understanding of how the ensemble works remains relatively poor.

According to the current model of integrin activation, ligand binding shifts the equilibrium between different integrin conformations to the active one (Hynes, 2002). The two extreme conformations of this allosteric protein are a bent or "closed" conformation which represents the low affinity state for ligand and an "open" conformation that will bind with high affinity to ligand (Fig. 1). Conformational changes in the extracellular domain affect the cytoplasmic tails, which are separated in the open conformation but not in the closed. Separation of the cytoplasmic domains promotes their interaction with cytoskeletal and signal transduction molecules, and thus the activation of integrins and downstream signaling. The conformational equilibrium can be influenced both by ligand binding to the extracellular domain (outside-in signaling) and by binding of cytoplasmic proteins to the separated cytoplasmic domains (inside-out signaling). Talin, a large intracellular protein that binds integrin cytoplasmic tails and the actin cytoskeleton is, for example, essential for integrin activation (Campbell and Ginsberg, 2004). As well as changes in affinity induced by structural changes, integrins can also modulate their avidity by clustering, thus changing the valency of their interactions with ligand (Carman and Springer, 2003).

Previous theoretical studies have addressed the mechanism of integrin clustering (Ward and Hammer, 1994; Irvine et al., 2002) but they have not yet explored whether ligand binding is sufficient or if other factors such as clustering are

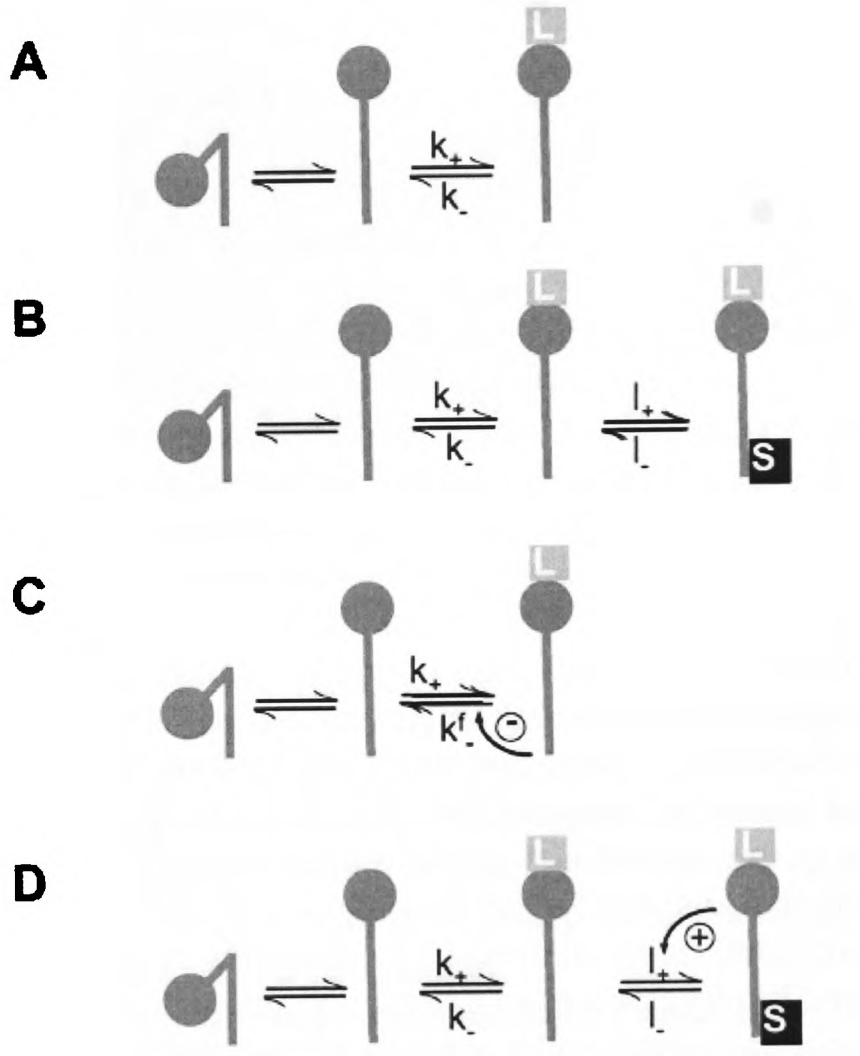


Fig. 2 Four possible mechanisms for integrin activation. (A) Ligand-binding is sufficient for integrin activation, other factors are only important for down-stream signaling events. (B) A stabilizing factor (such as talin) is necessary in addition to ligand binding. (C) A ligand induced positive feedback (based for instance on integrin self-interaction) induces integrin activation. (D) A positive feedback involving further signaling molecules is necessary for integrin activation. The symbols represent simple variants of those in Fig. 1. *L* refers to ligand, *S* to a stabilizing factor. The rate constants correspond to those used in the models.

necessary for integrin activation. In principle, ligand-dependent integrin activation can be enabled by any of the four different mechanisms depicted in Fig. 2. (A) Extracellular ligand alone is sufficient to activate integrins and other factors are only important for downstream signaling (Fig. 2A); (B) Ligand-dependent integrin activation requires the binding of an intracellular stabilizing factor that interacts with and stabilizes the on state (Fig. 2B). (C) A positive feedback, provided either by integrin–ligand pairs themselves or by self-interactions, is important (Li et al., 2003) (Fig. 2C); (D) A positive feedback that increases the activity of an intracellular stabilizing factor is required (Fig. 2D). The latter would need to be based on a larger intracellular signaling network.

Mathematical modeling is used in the following to evaluate the physiological potential of these mechanisms. The analysis suggests that, at least for some physiological conditions, binding of ligand (even if it is preclustered) and/or a stabilizing factor (Fig. 2A,B) are insufficient for ligand-dependent integrin activation; a positive feedback (Fig. 2C,D) is required which results in the further stabilization of the active conformation. Integrin clustering is a likely consequence of such a positive feedback.

2. A model for integrin activation

Overly simplified, integrins can be taken to exist in one of two states, a closed low affinity or an open high affinity conformation. In the absence of ligand the equilibrium is biased towards the inactive, low affinity conformation (Tadokoro et al., 2003). Binding of ligand (L) stabilizes the active, high affinity conformation. Under physiological conditions integrin activation therefore requires ligand binding and accordingly the physiological relevance of the mechanisms depicted in Fig. 2 can be evaluated by analyzing the extent to which they promote ligand binding. While the relationship between ligand binding and cellular action in response to integrin activation is unlikely to be linear we will show that the mechanisms differ substantially in the level to which they promote integrin–ligand binding such that they can be readily classified as "non-supportive" or "activating." The analysis can be greatly simplified if we determine the fraction of ligands bound by integrins rather than the fraction of integrins bound to ligands. In this case, integrins in the closed, low affinity conformation do not have to be considered explicitly. We will assume that there is a constant number of unbound integrins in the high affinity conformation since any integrin that binds to ligand can be replaced rapidly from the integrins in the low affinity conformation by conformational changes. While ligand binding will eventually deplete the pool of unbound integrins, this does not need to be included in an analysis of mechanisms for integrin signal initiation: if integrin–ligand binding occurs to a level that integrin depletion becomes relevant the activation mechanism can be considered successful independently of the exact final number of integrin–ligand complexes.

Under physiological conditions, the ligand is expected to be sufficiently dense that spatial details and diffusion constraints can be neglected in the initial steps of focal adhesion assembly. Transport of integrins from parts of the cell that are not in contact with the substrate is not relevant for the initial activation of cell adhesion signaling cascades and is not considered in this model.

The model follows the binding of single integrins to ligands; the probability of integrin–ligand complex formation can be calculated by solving the appropriate Master equation. The Master equation is a gain–loss equation for the probabilities of the separate states with n integrin–ligand complexes (van Kampen, 1992), from which the macroscopic kinetic equation can be derived when the density fluctuations are negligible. In order to decide which of the four mechanisms depicted in Fig. 2 is sufficient for ligand-dependent integrin activation, the fraction of ligand bound by integrin is determined for each case.

2.1. *Ligand engagement is not sufficient for integrin activation*

According to the first mechanism (Fig. 2A), ligand-dependent integrin activation does not require any further supporting processes and interactions. The Master equation for the formation of i integrin–ligand complexes is thus given as

$$\dot{p}_i = k_-(i+1)p_{i+1} + k_+(L-i+1)p_{i-1} - (k_- i + k_+(L-i))p_i \tag{1}$$

with $p_i = 0$ if $i \notin [0, L]$, where p_i is the probability that i (open) integrins are bound to a ligand with L sites, k_+, k_- refer to the on- and off-rate of the integrins. The on-rates include the density of integrins which are taken to be constant (see previous section). The first two terms in (1) represent the gains of state i due to the transition from other states, that is due to unbinding of an integrin from a complex with $i + 1$ integrins (first term) or the binding to a complex with $i - 1$ integrins (second term). The bracketed term is the loss due to transitions from i into other states either by unbinding or binding of an integrin.

For the steady state ($\dot{p}_i = 0$) we obtain from (1)

$$p_i = \frac{\binom{L}{I}\left(\frac{k_i}{k_-}\right)}{\left(1 + \frac{k_+}{k_-}\right)^L}. \tag{2}$$

The expectation value for the number of integrins bound to a given ligand with L binding sites is given by $\langle I_b \rangle = \sum_{i=0}^{L} i p_i$. Integrin activation therefore requires $p_i \gg p_0 (i > 0)$ and thus $\frac{k_+}{k_-} \gg 1$ (Fig. 3), which corresponds to a high on- and low off-rate. This is because the probability of i bound integrins is proportional to the ith power of $\frac{k_+}{k_-}$ and only for $\frac{k_+}{k_-} > 1$ this probability increases with increasing i, that is with increasing numbers of integrins bound.

$k_- \sim 1\ \mathrm{s}^{-1}$ has been established experimentally (Vitte et al., 2004); the two-dimensional on rate is more difficult to determine and has to be calculated from the two-dimensional dissociation constant which itself is difficult to measure and often obtained via its three-dimensional counterpart $K_D^{3d} \sim 6 \times 10^{-8}$ M for the high affinity conformation (Faull et al., 1993; Suehiro et al., 1997) and $K_D^{3d} > 1\,\mu$M for the low affinity conformation (Faull et al., 1993). It is generally assumed that the two dissociation constants are linearly related such that $K_D^{2d} = \eta K_D^{3d}$, the value of the conversion factor η is, however, still a matter of debate (Moy

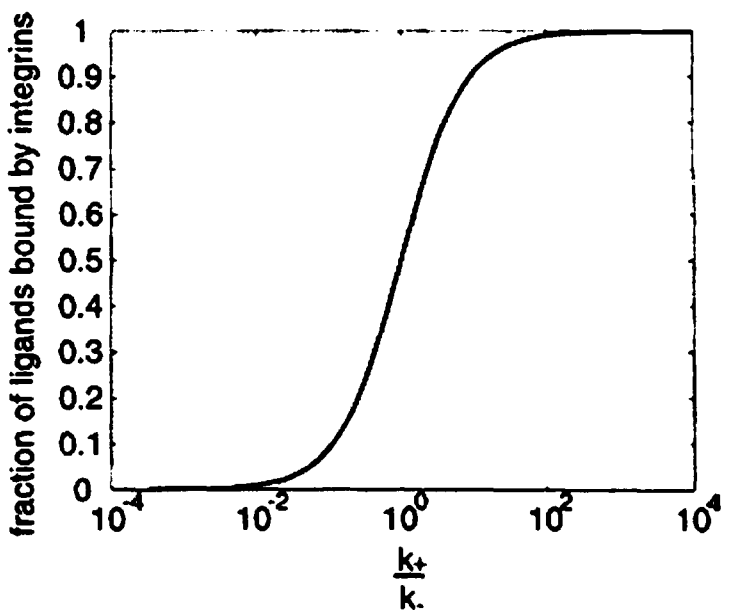


Fig. 3 Ligand engagement is not sufficient for integrin activation. The integrin saturation of the ligand, $\frac{\langle I_b \rangle}{L}$, is plotted against the integrin–ligand association constant $K_a = \frac{k_+}{k_-}$; $L = 10$. As discussed in the text, experimental data suggest that $\frac{k_+}{k_-} \ll 1$ such that the fraction of activated integrins would be very small.

et al., 1999), since theoretical estimates are not in complete agreement with latest experimental results. According to theoretical estimates for a protein complex that spans about 20 nm, $\eta = 1.2 \times 10^{19}\,\mathrm{m}^{-2}\,\mathrm{M}^{-1}$ (Bell, 1978). Studies employing protein-coated beads report $\eta = 8 \times 10^{24}\,\mathrm{m}^{-2}\,\mathrm{M}^{-1}$ (Moy et al., 1999) and $\eta = 10^{22}\,\mathrm{m}^{-2}\,\mathrm{M}^{-1}$ (Kuo and Lauffenburger, 1993). The lower η value is corroborated by measurements of the two-dimensional dissociation constant for the LFA-3/CD2 adhesion pair that were carried out using cells instead of beads (Dustin et al., 1996). While there are experimental difficulties involved in getting an exact measurement of this parameter, the discrepancy between the theoretical and experimental estimates may well reflect a lower affinity of integrins when membrane bound, possibly due to steric constraints which will have a profound impact on this allosteric protein. We will therefore follow Moy et al. (1999) who used $\eta = 10^{22}\,\mathrm{m}^{-2}\,\mathrm{M}^{-1}$ rather than their own estimate for converting integrin dissociation constants. For $\eta = 10^{22}\,\mathrm{m}^{-2}\,\mathrm{M}^{-1}$ we find $k_{\mathrm{on}} \sim 2 \times 10^{-3}\,\mu\mathrm{m}^2\,\mathrm{s}^{-1}$. In order to determine the frequency of integrin–ligand bond formation the density of open integrins needs to be taken into consideration. The average total (closed and open) integrin density on the cell surface has been estimated as $\rho \sim 1\text{–}3 \times 10^2\,\mu\mathrm{m}^{-2}$ (Wiseman et al., 2004). At least in some cells (e.g., platelets) more than 95% of all integrins are in the closed inactive conformation in the absence of ligand (Tadokoro et al., 2003); the density of integrin in the open conformation is therefore small ($\rho_o < 10\,\mu\mathrm{m}^{-2}$). Given that $k_+ = k_{\mathrm{on}}\rho_o$ this implies, using the experimental estimate for η, that $k_+ \sim 10^{-1}$ to $10^{-2}\,\mathrm{s}^{-1}$ such that $\frac{k_+}{k_-} \ll 1$, which is insufficient to drive integrin activation. A larger k_+ can be achieved if a larger fraction of integrins is in the open conformation already in the absence of ligand. However, this leads to ligand-independent integrin activation. We can conclude that for experimentally determined parameters the model predicts that ligand-dependent integrin activation will not occur without further supporting interactions.

2.2. *A stabilizing factor is not sufficient for ligand-dependent integrin activation*

Proteins that bind and stabilize the active integrin conformation have been suggested to be important for integrin activation (Fig. 2B). The Master equation derived in the previous section can be extended to include such factors that stabilize integrin–ligand binding. While talin is an excellent candidate for such a protein (and we will therefore call this factor talin in the following), the analysis is kept general enough such that it could be extended to any cytoplasmic protein that prolongs the open active conformation by binding to the active integrin.

Much as in the case of integrins, talins can be considered to exist in two forms of different activity. Cytoplasmic talin is inactivated by self-interactions and only the "open" conformation can bind to the membrane (PIP2), integrins and other proteins. Therefore, we can again simplify the model by only considering the open active form, whose concentration can again be taken to be constant, since any open talin bound to integrins can be expected to be rapidly replenished from the pool of closed talins. Given the low abundance of both open talin and integrin, complexes of the two are taken to be absent in the absence of ligand. The gains and losses of the state with i integrins and t talins bound can again be translated into the linear

Master equation

$$\begin{aligned}\dot{p}_{i,t} = {} & k_-(i+1-,t)p_{i+1,t} + k_-^*(t+1)p_{i+1,t+1} \\ & + k_+(L-i+1)p_{i+1,t} \\ & + l_-(t+1)p_{i,t+1} + l_+(i-t+1)p_{i,t-1} \\ & - (k_-(i-t) + k_-^* t + k_+(L-i) + l_+(i-t) + l_- t)p_{i,t}\end{aligned} \tag{3}$$

with $p_{i,t} = 0$ if $t > i; t, i < 0; t, i > L$. Here $p_{i,t}$ is the probability that i (open) integrins and t (open) talins are bound to the ligand with L sites, $p_{i,t} = 0$ if $t > i$ reflects the fact that talins can only attach to the ligand indirectly by binding to integrins. k_+, k_-, l_+, l_- refer to the on- and off-rates of the integrins and talins respectively. The on-rates include the density of integrin and talin which are taken to be constant (see above). k_-^* refers to the integrin off-rate when talin is bound ($k_-^* \leq k_-$).

For the steady state ($\dot{p}_{i,t} = 0$) we obtain from (3)

$$p_{i,t} = \frac{\binom{L}{t}\binom{L-t}{i-t} a^{L-i} b^{i-1}}{\sum_{i=0,t=0}^{i=L,t=L} \binom{L}{t}\binom{L-t}{i-t} a^{L-i} b^{i-t}} \tag{4}$$

with $a = \frac{k_-(k_-^*+l_-)+l_+k^*}{l_+k_+}$, $b = \frac{k_-^*+l_-}{l_+}$ for $i \geq t$ and $p_{i,t} = 0$ for $i < t$. The expectation value for the number of integrins and talins bound to a given ligand with L binding sites is given by $\langle I_b \rangle = \sum_{i=0}^{L} i \sum_{t=0}^{L} p_{i,t}$ and $\langle T_b \rangle = \sum_{t=0}^{L} t \sum_{i=0}^{L} p_{i,t}$, respectively. For strong ligand binding in the absence of talin binding $p_{L,0} \gg p_{0,0}$ we require $b > a$ and we recover the condition $k_+ \gg k_-$ found in the previous section. If talin binds the condition becomes $\sum_{t=0}^{t=L} p_{L,t} \gg p_{0,0}$ and thus $a < b + 1$. This condition can be met if either $a < b$ or $a < 1$. Assuming that the integrin–ligand off-rate in the presence of talin is very small ($k_-^* \ll 1$), $a < b$ still requires $k_- < k_+$, (high integrin–ligand affinity) which we have found above to disagree with experimental estimates. The condition $a < 1$ can be met if either $k_- \ll k_+$ or if $k_- > k_+$ and $l_- \ll l_+$, that is integrin activation would be possible despite a low integrin–ligand affinity if the integrin–talin affinity were sufficient high (Fig. 4). However, such high integrin–talin affinity would also lead to integrin activation in the absence of ligand binding. We can therefore conclude that a stabilizing factor alone is not sufficient for ligand-dependent integrin activation.

2.3. A positive-feedback is required for ligand-dependent integrin activation

The remaining two mechanisms in Fig. 2 both involve a positive feedback. Here, Fig. 2C considers a feedback mechanism that only involves the integrin–ligand pair itself while according to Fig. 2D a larger network would be necessary. Both mechanisms are analysed in the following.

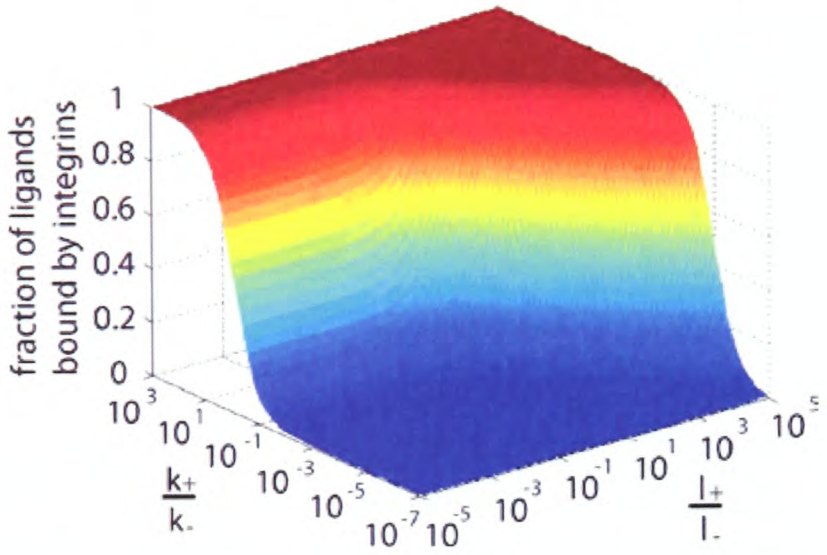


Fig. 4 A stabilizing factor is not sufficient for ligand-dependent integrin activation. The fraction of ligand bound by integrin, $\frac{\langle I_b \rangle}{L}$, is plotted against the integrin–ligand association constant $K_a = \frac{k_+}{k_-}$ and the integrin–talin association constant $K_a = \frac{l_+}{l_-}$ for $k_-^* = 0$; $L = 10$. For experimental estimates of these association constants the activated fraction is small.

2.4. A positive feedback that is based on the integrin–ligand pair

A positive feedback only involving the integrin–ligand pair (Fig. 2C) could either be enabled by integrin–integrin interactions in the open form (Li et al., 2003) or by a ligand-induced conformational change that leads to a higher affinity of binding. In both cases this positive feedback ought to be triggered once a certain (small) number of integrins is engaged in close proximity. Such interaction can thus be captured in the model by replacing k_- with k_-^f in (1) and setting $k_-^f = k_-^o/(1 + \frac{k_c i^n}{(i+K)^n})$, where k_-^o refers to the integrin–ligand off-rate in the absence of a positive feedback, k_c determines the strength with which the feedback reduces the integrin–ligand offrate, and K and n limit the effect of integrin–integrin interactions to local interactions. The model does not contain any spatial information and it is thus assumed that integrins either bind to preclustered ligand, or preferentially in the vicinity of other bound integrins. Note that the assumption that ligand–integrin interactions are short-lived in the absence of integrin–integrin interaction will lead to such preferential binding in the vicinity of bound integrins. For the steady state ($\dot{p}_i = 0$) we then obtain from (1)

$$p_i = \frac{\binom{L}{i}\left(\frac{k_+}{k_-}\right)^i \prod_{j=0}^{i}\left(1 + \frac{k_c j^n}{(j+K)^n}\right)}{\sum_{l=0}^{L}\binom{L}{l}\left(\frac{k_+}{k_-}\right)^l \prod_{j=0}^{l}(1 + \frac{k_c j^n}{(j+K)^n})}. \tag{5}$$

Given that K and n need to be chosen such that only local integrin–integrin interactions reduce the ligand–integrin off-rate, for sufficiently large k_c (5) can be approximated by

$$p_i = \frac{\binom{L}{i}\left(\frac{k_+ k_c}{k_-}\right)^i}{\sum_{l=0}^{L}\binom{L}{l}\left(\frac{k_+ k_c}{k_-}\right)^l} \tag{6}$$

(6) and (2) are similar and only differ in the factor k_c. The same argument thus applies such that $k_c \gg \frac{k_-}{k_+} \sim 10^2$–$10^3$ is required to enable ligand-dependent integrin activation (Fig. 3). In the analysis of (2) $\frac{k_+}{k_-}$ was determined for the high affinity integrin–ligand interaction and a further ligand-induced affinity increase by 100–1000 fold is impossible. Integrin–integrin interactions strong enough to reduce the high affinity dissociation constant by a further factor of 10^2–10^3 are also unlikely. Thus, a feedback loop only involving integrins is unlikely to drive ligand-dependent integrin activation.

2.5. A positive feedback loop based on a regulatory network can enable ligand-dependent integrin activation

The last mechanism (Fig. 2D) to be analyzed is one that considers a regulatory network that mediates the positive feedback. This mechanism involves a stabilizing factor whose activity is increased in response to ligand binding. Such positive feedback has indeed been reported in the form that ligand-bound integrins as well as talins trigger an increase in PIP2, which in turn increases the recruitment of talin to the membrane, and thereby the talin-integrin complex formation (l_+) (Garcia-Alvarez et al., 2003; Martel et al., 2001). The talin density on the membrane will thus be very small when integrins are inactive and increase when ligands increase the integrin activity. This positive feedback can be incorporated into the model as

$$l_+ = l_c \frac{(t+1)^n}{(t+1)^n + K^n}, \tag{7}$$

such that the talin on-rate l_+ depends on the number of talins in the integrin–ligand complex with K being the Hill constant, n the Hill coefficient and l_c some proportionality factor. While many other formulations of such feedback are possible, this saturation form captures the likely talin dependence of the membrane PIP2 concentration, which will be low below a certain talin threshold and eventually become saturated.

The steady state for $p_{i,t}$ is now more difficult to derive but numerical studies show that such positive feedback indeed enables ligand-induced integrin activation as long as $K/L \ll 1$ (Fig. 5). Note that, as before in the case of integrin–integrin interactions, ligand-dependent integrin activation requires the proportionality factor l_c to be of order 10^2–10^3 In case of talin recruitment this is reasonable since local PIP2 production may lead to a 100–1000 fold increase in the local membrane talin density. A ligand-independent increase in l_+, due to a signaling dependent increase in a factor that stabilizes the open integrin conformation, will also lead to integrin activation. This is likely to provide the mechanistic basis for inside-out signaling.

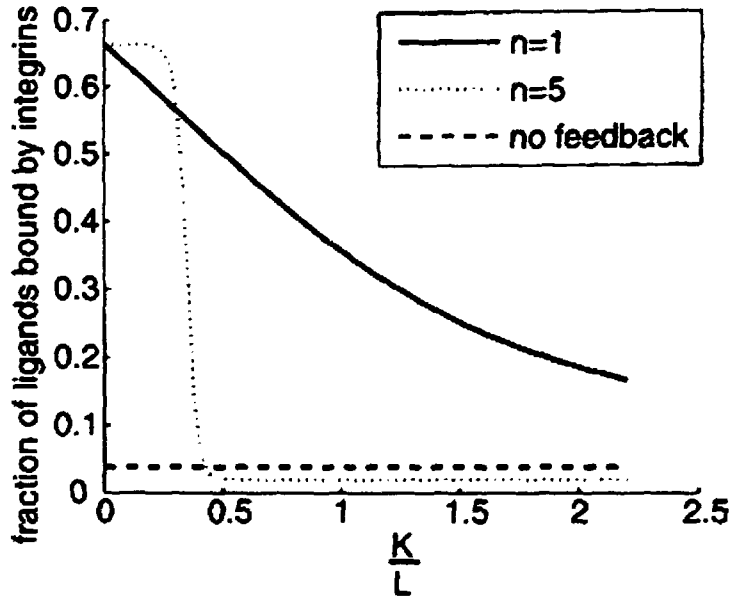


Fig. 5 A positive feedback enables ligand-dependent integrin activation. The fraction of ligand bound by integrin, $\frac{\langle l_b \rangle}{L}$, is plotted in the absence (–) or presence of a talin feedback regulation against the Hill constant K (Eq. 7) normalized by the number of binding sites L for different Hill coefficients $[n = 1(-); n = 5(\cdots)]$. Parameters were set to $L = 10, k_+ = 0.1, l_c = 10^2, k_- = 5, k_-^* = 10^{-3}, l_- = 1$ It can be seen that as long as positive feedback is initiated upon binding of few integrins (small $\frac{K}{L}$), a large active integrin fraction is obtained.

We thus conclude that ligand-dependent integrin activation requires $k_- \gg k_+, l_- \gg l_+$ in the resting and $k_- \ll k_+, l_- \ll l_+$ in the active state. The first condition is met by the binding of the stabilizing factor which reduces k_-, and the second condition is enabled by a positive feedback that leads to an increases in l_+ in the presence of ligand.

3. Conclusion

The analysis of possible mechanisms for integrin activation suggests that a positive feedback is required for ligand-dependent integrin activation. Thus the ligand-integrin affinity appears to be too low to stabilize the active integrin conformation in the absence of a further stabilizing factor such as talin. To ensure that ligand-independent integrin activation by such a stabilizing factor alone is impossible a positive feedback that upregulates the stabilizing factor upon ligand binding is required.

This conclusion strongly depends on the order of magnitude of the conversion factor η between the two- and three-dimensional dissociation constants and further careful measurements of this parameter will be important. While ligand-dependent integrin activation would be possible in the absence of further stabilizing interactions if the theoretical rather than the experimental estimates for η were correct (that is if η were 1000 times smaller), available experimental information is very much in favour of the experimental estimate that has been used in this study. In addition to the argument already given (see above) further experimental observations corroborate the notion that the physiological integrin–ligand affinity is tuned such that integrin activation depends on supporting factors. Thus, mutations in the β-tail that disrupt the talin–integrin interaction markedly reduce the fraction of

active integrins (Tadokoro et al., 2003). This reduction can be overcome by binding of an antibody that stabilizes the high affinity conformation (Tadokoro et al., 2003) which is in agreement with the model prediction that a higher ligand–integrin affinity can enable talin-independent integrin activation. With integrin activation balanced on a knife-edge small changes in the affinity, density and conformational bias of integrins can have a large impact on the cell's adhesiveness and motility—as is observed in experiments (Palecek et al., 1997).

An advantage of a positive feedback regulation is the regulatory potential. Signaling processes can affect the positive feedback, providing a basis for inside-out signaling. It is likely that the observed integrin clustering is a result of such a positive feedback mechanism; a local increase in the density of a stabilizing factor will facilitate the formation of further integrin–ligand bonds in the vicinity of existing ones. Clustering would then result from a process that enables long-lived integrin–ligand interactions but is not of itself essential. The concept that ligand binding and clustering are independent processes is in agreement with the observation in *Drosophila* that integrins can still bind to the extracellular matrix in the absence of talin but fail to cluster (Brown et al., 2002).

The feedback loop that is considered in the current model only comprises a stabilizing factor (such as talin) and a way of increasing the concentration of the stabilizing factor, such as by PIP2 formation. Many more players are known to be involved and understanding their relative contributions will be important. Here, especially the role of PIPKIγ will be of interest. While PIPKIγ produces PIP2 and thus increases talin recruitment to the membrane, PIPKIγ itself is recruited to the membrane by talin (Di Paolo et al., 2002) and competes with the integrin β tail for talin binding (de Pereda et al., 2005). Integrin activation leads to FAK activation and a FAK-enhanced Src-mediated phosphorylation of PIPKIγ further increases its affinity for talin (Ling et al., 2002; Arias-Salgado et al., 2003). PIPKIγ therefore appears to play an important role both in integrin activation and the turnover of focal contacts. A combination of modeling and experiment, of the sort described here, is expected to shed more light on this complex regulatory network.

Acknowledgements

We thank D.A. Calderwood and N.V. Valeyev for discussions. D.I. is a Junior Research Fellow at St John's College, Oxford University and is supported by an EPSRC scholarship. I.D.C acknowledges financial support from the Wellcome Trust and the NIH funded Cell Migration Consortium.

References

Arias-Salgado, E.G., Lizano, S., Sarkar, S., Brugge, J.S., Ginsberg, M.H., Shattil, S.J., 2003. Src kinase activation by direct interaction with the integrin beta cytoplasmic domain. Proc. Natl. Acad Sci. USA 100(23), 13298–13302.

Bell, G., 1978. Models for the specific adhesion of cells to cells. Science 200, 618–627.

Brown, N.H., Gregory, S.L., Rickoll, W.L., Fessler, L.I., Prout, M., White, R.A.H., Fristrom, J.W., 2002. Talin is essential for integrin function in Drosophila. Dev. Cell 3(4), 569–579.

Campbell, I.D., Ginsberg, M.H., 2004. The talin-tail interaction places integrin activation on FERM ground. Trends Biochem. Sci. 29(8), 429–435.

Carman, C.V., Springer, T.A., 2003. Integrin avidity regulation: Are changes in affinity and conformation underemphasized. Curr. Opin. Cell. Biol. 15(5), 547–556.

de Pereda, J.M., Wegener, K.L., Santelli, E., Bate, N., Ginsberg, M.H., Critchley, D.R., Campbell, I.D., Liddington, R.C., 2005. Structural basis for phosphatidylinositol phosphate kinase type Igamma binding to talin at focal adhesions. J. Biol. Chem. 280(9), 8381–8386.

Di Paolo, G., Pellegrini, L., Letinic, K., Cestra, G., Zoncu, R., Voronov, S., Chang, S., Guo, J., Wenk, M.R., De Camilli, P., 2002. Recruitment and regulation of phosphatidylmositol phosphate kinase type 1 gamma by the FERM domain of talin. Nature 420(6911), 85–89.

Dustin, M.L., Ferguson, L.M., Chan, P.Y., Springer, T.A., Golan, D.E., 1996. Visualization of CD2 interaction with LFA-3 and determination of the two-dimensional dissociation constant for adhesion receptors in a contact area. J. Cell Biol. 132(3), 465–474.

Faull, R.J., Kovach, N.L., Harlan, J.M., Ginsberg, M.H., 1993. Affinity modulation of integrin alpha5beta1: Regulation of the functional response by soluble fibronectin. J. Cell Biol. 121(1), 155–162.

Garcia-Alvarez, B., de Pereda, J.M., Calderwood, D.A., Ulmer, T.S., Critchley, D., Campbell, I.D., Ginsberg, M.H., Liddington, R.C., 2003. Structural determinants of integrin recognition by talin. Mol. Cell 11(1), 49–58.

Horwitz, R., Webb, D., 2003. Cell migration. Curr. Biol. 13(19), 756–759.

Hynes, R.O., 2002. Integrins: Bidirectional, allosteric signaling machines. Cell 110(6), 673–687.

Irvine, D.J., Hue, K.-A., Mayes, A.M., Griffith, L.G., 2002. Simulations of cell-surface integrin binding to nanoscale-clustered adhesion ligands. Biophys. J. 82(1 Pt 1), 120–132.

Kuo, S.C., Lauffenburger, D.A., 1993. Relationship between receptor/ligand binding affinity and adhesion strength. Biophys. J. 65(5), 2191–2200.

Li, R., Mitra, N., Gratkowski, H., Vilaire, G., Litvinov, R., Nagasami, C., Weisel, J.W., Lear, J.D., DeGrado, W.F., Bennett, J.S., 2003. Activation of integrin alphaIIbbeta3 by modulation of transmembrane helix associations. Science 300(5620), 795–798.

Ling, K., Doughman, R.L., Firestone, A.J., Bunce, M.W., Anderson, R.A., 2002. Type I gamma phosphatidylinositol phosphate kinase targets and regulates focal adhesions. Nature 420(6911), 89–93.

Martel, V., Racaud-Sultan, C., Dupe, S., Marie, C., Paulhe, F., Galmiche, A., Block, M.R., Albiges-Rizo, C., 2001. Conformation, localization, and integrin binding of talin depend on its interaction with phosphoinositides, J. Biol. Chem. 276(24), 21217–21227.

Moy, V.T., Jiao, Y., Hillman, T., Lehmann, H., Sano, T., 1999. Adhesion energy of receptor-mediated interaction measured by elastic deformation. Biophys. J. 76(3), 1632–1638.

Palecek, S.P., Loftus, J.C., Ginsberg, M.H., Lauffenburger, D.A., Horwitz, A.F., 1997. Integrin–ligand binding properties govern cell migration speed through cell-substratum adhesiveness. Nature 385(6616), 537–540.

Suehiro, K., Gailit, J., Plow, E.F., 1997. Fibrinogen is a ligand for integrin alpha5beta1 on endothelial cells. J. Biol. Chem. 272(8), 5360–5366.

Tadokoro, S., Shattil, S.J., Eto, K., Tai, V., Liddington, R.C., de Pereda, J.M., Ginsberg, M.H., Calderwood, D.A., 2003. Talin binding to integrin beta tails: A final common step in integrin activation. Science 302(5642), 103–106.

Tamkun, J.W., DeSimone, D.W., Fonda, D., Patel, R.S., Buck, C., Horwitz, A.F., Hynes, R.O., 1986. Structure of integrin, a glycoprotein involved in the transmembrane linkage between fibronectin and actin. Cell 46(2), 271–282.

van Kampen, N., 1992. Stochastic Processes in Physics and Chemistry. Elsevier Science Publishers.

Vitte, J., Benoliel A.-M., Eymeric, P., Bongrand, P., Pierres, A., 2004. Beta-1 integrin-mediated adhesion may be initiated by multiple incomplete bonds, thus accounting for the functional importance of receptor clustering. Biophys. J. 86(6), 4059–4074.

Ward, M.D., Hammer, D.A., 1994. Focal contact assembly through cytoskeletal polymerization: Steady state analysis. J. Math. Biol. 32(7), 677–704.

Wiseman, P., Brown, C., Webb, D., Hebert, B., Johnson, N., Squier, J., Ellisman, M., Horwitz, A., 2004. Spatial mapping of integrin interactions and dynamics during cell migration by Image Correlation Microscopy. J. Cell Sci. 117(Pt 23), 5521–5534.

Zamir, E., Geiger, B., 2001. Molecular complexity and dynamics of cell-matrix adhesions. J. Cell Sci. 114(Pt 20), 3583–3590.

Mathematical Medicine and Biology (2006) **23**, 255–277
doi:10.1093/imammb/dql012
Advance Access publication on May 17, 2006

An analysis of B cell selection mechanisms in germinal centres

MICHAEL E. MEYER-HERMANN†
Frankfurt Institute for Advanced Studies (FIAS), Max von Laue Strasse 1, 60438 Frankfurt/Main, Germany and Centre for Mathematical Biology, Mathematical Institute, Oxford, UK

AND

PHILIP K. MAINI AND DAGMAR IBER
Centre for Mathematical Biology, Mathematical Institute, Oxford, UK

[Received on 6 February 2006; revised on 6 April 2006]

Affinity maturation of antibodies during immune responses is achieved by multiple rounds of somatic hypermutation and subsequent preferential selection of those B cells that express B cell receptors with improved binding characteristics for the antigen. The mechanism underlying B cell selection has not yet been defined. By employing an agent-based model, we show that for physiologically reasonable parameter values affinity maturation can be driven by competition for neither binding sites nor antigen—even in the presence of competing secreted antibodies. Within the tested mechanisms, only clonal competition for T cell help or a refractory time for the interaction of centrocytes with follicular dendritic cells is found to enable affinity maturation while generating the experimentally observed germinal centre characteristics and tolerating large variations in the initial antigen density.

Keywords: germinal centre; lymphocytes; B cell selection.

1. Introduction

During the course of an immune response, antibodies evolve that bind with increased affinity to an antigen (Jerne, 1951; Eisen & Siskind, 1964). This phenomenon, termed affinity maturation, is based on multiple rounds of somatic hypermutation targeted to the antibody genes and subsequent selection for increased binding affinity (MacLennan *et al.*, 2000). Both the latter processes are in general confined to germinal centres (GCs) (Jacob *et al.*, 1991b). Selection acts on B cells that express as B cell receptor the rearranged and possibly mutated antibody gene. Recent experiments suggest that B cells are selected in a clonal competition, since low-affinity B cells can persist in the GC reaction when competition is reduced (Dal Porto *et al.*, 2002; Shih *et al.*, 2002). Although the key cellular dynamics of the GC reaction are by now well-characterised (Liu *et al.*, 1991; Hollowood & Macartney, 1992; MacLennan, 1994), the mechanism enabling clonal competition and thus B cell selection has not yet been defined and is the subject of this paper.

GCs are initially seeded by a small number of proliferating B cells that bind the antigen with at least low affinity (Kroese *et al.*, 1987; Jacob *et al.*, 1991a; Liu *et al.*, 1991). After a phase of B cell expansion, somatic hypermutation is initiated in so-called centroblasts (CBs) which are characterised by a low

†Email: m.meyer-hermann@fias.uni-frankfurt.de

© The author 2006. Published by Oxford University Press on behalf of the Institute of Mathematics and its Applications. All rights reserved.

expression of surface immunoglobulin M (IgM). Upon differentiation into so-called centrocytes (CCs), the IgM expression increases and CCs are selected according to the quality of antigen binding. CCs are in a state of activated apoptosis (Liu & Arpin, 1997) and in order to survive, they need to acquire antigen and present it to antigen-specific T cells that most probably have entered the GCs together with the antigen-specific B cells (MacLennan *et al.*, 2000; Aydar *et al.*, 2005).

Whether antigen trapped on follicular dentritic cells (FDCs), as opposed to soluble antigen, is critical in the selection process is currently controversial (Aydar *et al.*, 2005; Haberman & Shlomchik, 2003; Kosco-Vilbois, 2003). Selected CCs differentiate into either memory cells or plasma cells or recycle, i.e. differentiate back into CBs, which enables them to go through multiple rounds of mutation and selection.

Early models of affinity maturation have focused on the selective effect of clonal competition for FDC-presented antigen (Siskind & Benacerraf, 1969). This view has been challenged by the recently observed robustness of affinity maturation towards large variation in the amount of initially deposited antigen (Vora *et al.*, 1997; Hannum *et al.*, 2000; Manser, 2004). Given that secreted antibodies appear to be dispensable for affinity maturation (Hannum *et al.*, 2000), this robustness is unlikely to derive from a competition with emerging serum antibodies (Vora *et al.*, 1997; Tarlinton & Smith, 2000; Iber & Maini, 2002).

The alternative model of a clonal competition for binding sites instead of antigen (Kesmir & De Boer 2003) requires affinity maturation to strictly depend on antigen being encountered membrane bound, which is the subject of controversy (Haberman & Shlomchik, 2003). Also, antigen localisation would have to be restricted to a small number of places within the large dendritic network. Despite many electron microscopy studies, such localisation restriction has not yet been reported.

Without competition for access to antigen or FDCs, higher-affinity B cell clones could be favoured on the level of antigen binding, either because of differential signalling of B cells in response to different affinities of binding (Kouskoff *et al.*, 1998) or because high-affinity B cells require fewer encounters with the FDC to establish an immunological synapse and to extract antigen (Batista *et al.*, 2001; Meyer-Hermann, 2002a). Here, immunological synapse refers to the supramolecular segregation of proteins in lymphoid cell–cell contact zones (Kupfer & Kupfer, 2003), which enable long-term signalling and effector functions (Huppa *et al.*, 2003).

Finally, recruitment of T cell help may be competitive. *In vitro* assays show that higher-affinity B cells are more able to recruit T cell help (Batista & Neuberger, 1998), which may be crucial in the GC environment, where T cells constitute only 5–10% of the GC cell population (Kelsoe, 1996).

While experiments have addressed the various hypotheses, they have not yet succeeded in ruling out any of the above mechanisms. This is largely due to the experimental difficulties that are associated with the investigation of such complex systems. We therefore employed an extended version of a previously described agent-based model for GC reactions (Meyer-Hermann, 2002a; Meyer-Hermann & Maini, 2005b), which allowed us to investigate the impact of each factor separately. Model assumptions are based on experimental data mostly stemming from lymph nodes of mice or rats and the results are robust against physiologically conceivable variations in the parameter values.

We find that both a competition for access to FDCs as well as a competition for antigen (even in the presence of antibodies) does not enable affinity maturation to the experimentally observed degree. On the other hand, both a CC refractory time for interaction with FDCs and competition for T cell help can drive affinity maturation—especially when the acquisition of antigen and survival signals from the FDCs is uncompetitive. Given that both selection mechanisms enable affinity maturation over a wide range of antigen densities, even if antigen is encountered in soluble form, we suggest either one or both of these to be the physiological mechanism of B cell selection. Experiments are suggested to test this unexpected model prediction.

2. Model

2.1 *In silico GC simulations*

We employ *in silico* simulations of the GC reaction to analyse the B cell selection mechanisms. The simulations are performed using a previously described stochastic hybrid agent-based model (Meyer-Hermann, 2002a; Meyer-Hermann & Maini, 2005b), which has been extended to test the different selection mechanisms. The basic idea is to rebuild a GC *in silico* and to study how its spatial organisation, dynamics and output depend on the assumptions that are made about the comprised cells and their interactions. The GC is represented by a lattice whose nodes represent cells. With the exception of preplasma and memory cells, the GC cells are confined to the area of the GC as defined by the mantle zone. The cell-lattice is supplemented by a second grid for soluble signals. These satisfy reaction–diffusion equations which are solved numerically. Given that the analysis of 3D models leads to similar results (Meyer-Hermann & Beyer, 2002), we restrict our analysis to 2D in order to gain better statistics because of substantially shorter computation times. We include CBs, CCs, FDCs and output cells such as plasma and memory cells in all our simulations and study the effect of T helper cells on CC selection in an additional set of simulations. The different cell types are encoded in the simulation by defining differently sized objects that are associated with distinct sets of rules which reflect their biological properties. The rules determine the cellular dynamics by defining motility, cell–cell interactions, cell-cycle times, cellular lifetimes and similar properties. A comprehensive list of these properties is given below. Despite the complexity of the GC reaction, only a limited set of parameters is required to respect commonly accepted GC properties and to capture available quantitative experimental data. Reasonable estimates can be obtained for most of the parameters (Table 1), and the few exceptions are studied in detail. While most of the experimental data stem from lymph nodes of mice or rats, the model applies to all GCs that exhibit similar GC morphology and cell dynamics.

2.2 *Antibody representation*

In order to analyse B cell affinity maturation, we need to define the affinity and thus quality of antibodies. Antibodies are represented in a 4D shape space (Perelson & Oster, 1979). According to the principle of complementarity, the antigen defines the position of the antibody of maximum affinity to it in the shape space. The distance of an arbitrary antibody to this optimal clone is calculated as a one-norm in the shape space (the minimum number of mutations to reach the optimal clone) and is assumed to be a measure for its affinity to the antigen. The latter is calculated as a Gaussian function with the distance as argument and a width of 2.8 mutations. The power and the width of the affinity function are calculated on the basis of experimental data relating the number of mutations in GC reactions to the increase in affinity (for more details, see Meyer-Hermann, 2002a; Meyer-Hermann & Beyer, 2004).

2.3 *Cell motility*

In agreement with recent two-photon imaging data collected *in vivo* from mice lymph nodes (Miller *et al.*, 2002), cells are assumed to perform an undirected and active movement. Unless stated otherwise, every cell is attributed to a single node. All cell states include a mean speed v_{cell}, a polarity $\vec{p}_{\text{cell}}$ and a persistence time Δt_{cell}, where 'cell' denotes the different cell types. The probability of displacement of a cell to a next neighbour node is determined by v_{cell}. The direction of movement is set by $\vec{p}_{\text{cell}}$, and the polarity changes with a rate according to Δt_{cell}. The new polarity is chosen randomly, i.e. without any memory effect. The values of these motility parameters are taken from experiment (Miller *et al.*, 2002) and are given in the subsequent list of cell types and in Table 1. However, the two-photon experiment

TABLE 1 *Collection of all parameters of the model with references to the literature on which the values are based. The parameters are classified in the two categories fixed and variable. Fixed parameters remain unchanged throughout all simulations presented in this work. Variable parameters have been varied according to the selection process under consideration. If a value is stated, then this is the value employed in all selection scenarios where this parameter is fixed. Symbols correspond to the ones used in the text*

Parameter and reference	Symbol	Value	Type	References
Lattice constant	Δx	10 μm	Fixed	
Lattice dimension	D	2	Fixed	
Radius of reaction volume		220 μm	Fixed	
Shape space dimension		4	Fixed	Perelson & Oster (1979), Lapedes & Farber (2001)
Width of Gaussian affinity weight function		2.8	Fixed	Meyer-Hermann *et al.* (2001)
Duration of optimisation phase		48 h	Fixed	Jacob *et al.* (1993), Pascual *et al.* (1994), Meyer-Hermann (2002a)
Number of seeder clones		3	Fixed	Kroese *et al.* (1987)
CB velocity	v_{CB}	1.5 μm/min	Fixed	Miller *et al.* (2002), Wei *et al.* (2003)
CB persistence time	Δt_{CB}	2 min	Fixed	Miller *et al.* (2002), Meyer-Hermann & Maini (2005a)
Cell cycle time of CB		9 h	Fixed	Liu *et al.* (1991)
Mutation probability of CB		0.5	Fixed	Berek & Milstein (1987), Nossal (1992)
Duration of CB differentiation to CC	$1/r_{diff}$		Variable	Liu *et al.* (1991), Meyer-Hermann (2002b)
CC velocity	v_{CC}	5 μm/min	Fixed	Miller *et al.* (2002), Wei *et al.* (2003)
CC persistence time	Δt_{CC}	2 min	Fixed	Miller *et al.* (2002), Meyer-Hermann & Maini (2005a)
Duration of FDC–CC contact		2 h	Fixed	van Eijk *et al.* (2001)
CC refractory time	Δt_{delay}	6 min	Variable	
Duration of differentiation of selected CC		7 h	Fixed	Meyer-Hermann (2002a)
Probability of recycling for selected CC		0.8	Fixed	Han *et al.* (1995b)
Lattice constant	Δx	10 μm	Fixed	Meyer-Hermann *et al.* (2001)
CC lifetime		10 h	Fixed	Liu *et al.* (1994)
Number of T cells	N_{TC}	10	Variable	Kelsoe (1996)
T cell velocity	v_{TC}	10.8 μm/min	Fixed	Miller *et al.* (2002), Wei *et al.* (2003)

Continued . . .

TABLE 1 *Continued*

Parameter and reference	Symbol	Value	Type	References
T cell persistence time	Δt_{TC}	2 min	Fixed	Miller *et al.* (2002), Meyer-Hermann & Maini (2005a)
Duration of CC–T cell interaction before apoptosis	Δt_{apop}	2.1 h	Variable	
Duration of CC–T cell interaction before selection	Δt_{rescue}	2.0 h	Variable	
Number of FDCs	N_{FDC}	10	Variable	
Length of FDC dendrites	d_{FDC}	10 μm	Variable	
Rate of differentiation signal production by FDCs	r_{signal}		Variable	Meyer-Hermann (2002a)
Diffusion constant of signal molecules in tissue		200 $\mu m^2/h$	Fixed	Meyer-Hermann (2002a)
Number of antigen portions per FDC site	N_{ag}	0	Variable	
Antigen threshold for maximum binding probability	Θ_{ag}	$= N_{ag}$	Variable	
Antibody production by output cells		0 M/(h cell)	Variable	Randall *et al.* (1992)
Immune complex association rate	k_+	$10^6/(M s)$	Fixed	Batista & Neuberger (1998), Fersht (1998)
Immune complex dissociation rate	k_-	$10^{-3}/s$	Fixed	Batista & Neuberger (1998), Fersht (1998)

does not necessarily apply to GC reactions, such that this has to be considered as an assumption. Note that the actual movement of the cells may be less than expected from v_{cell} when contact inhibition by other cells suppresses the movement.

2.4 *Cell types*

The following list provides a comprehensive description of all cells and their specificities. All parameters without explicitly given value are of importance for the selection process and are discussed within Section 3.

2.4.1 *Follicular dentritic cell.* The soma of each FDC is represented as a single lattice node. Each FDC is assumed to have four (two per space dimension) dendrites. Every dendrite is attached to the soma and extends to neighbouring nodes. Given that dendrites are flexible, the lattice nodes to which dendrites are attributed are not exclusive, i.e. other cells can move onto these nodes. This is not possible for other cell types or the FDC soma. FDCs are assumed to produce a differentiation signal for CBs with

a rate r_{signal} (see below). In order to reduce computational efforts, FDCs are assumed to be immobile. This is a sufficient approximation because the interaction frequency with CCs is dominantly determined by the typical distance between FDC-binding sites and CCs. This corresponds to the density of the FDC network which is determined by the number of FDCs, N_{FDC}, and the length of the dendrites, d_{FDC}. A suitable quantity to measure the density of the FDC network is the number of nodes, X_{FDC}, from which access to FDC sites is possible in the GC area. We assume access points to be at the position of the dendrites and on all neighbour lattice points. This yields

$$X_{\text{FDC}} = N_{\text{FDC}} \frac{6\text{D}d_{\text{FDC}}}{\Delta x}, \tag{1}$$

with D the dimension of the lattice and $\Delta x = 10$ μm the resolution of the lattice (chosen as the average B cell diameter). The physiological range is $48 \leqslant X_{\text{FDC}} \leqslant 144$; this corresponds to 100 FDCs per GC (Kesmir & De Boer, 1999) ($N_{\text{FDC}} = 4$ in the 2D simulation) with a total length of dendrites of each FDC $2\text{D}d_{\text{FDC}} = 40$–$120$ μm. The FDC number in 2D is calculated by comparing the FDC density of a spherical GC in 3D to the FDC density in a GC slice of thickness $\Delta x = 10$ μm.

2.4.2 *Centroblasts.* CBs are a subpopulation of B cells in the GC. CBs divide with a cycle time of 6 h (Liu *et al.*, 1991) (i.e. 9 h in 2D) and, owing to somatic hypermutation, acquire in each cell division non-silent mutations with probability 0.5 (Nossal, 1992). Mutations are modelled by a jump to a next neighbour in the shape space (in an arbitrary direction); wider jumps are excluded. The transcription factors for susceptibility to apoptosis are already upregulated in CB (Klein *et al.*, 2003). We assume CBs not to be affected by these before they differentiate to CCs. Equally, CBs are assumed not to interact with FDCs or T cells, thus neglecting possible rescue mechanisms acting directly on CBs. CBs differentiate to CCs at rate r_{diff} once the local concentration of differentiation signal (which is produced by FDCs and diffuses over the lattice) exceeds a threshold value. Given that neither the exact signal nor its threshold concentration is known, the signal production rate by FDC is given in units of this threshold. Because of their larger size, we expect CBs to move at a lower mean speed ($v_{\text{CB}} = 1.5$ μm/min and $\Delta t_{\text{CB}} = 2$ min) than measured for naive B cells (Miller *et al.*, 2002). Assuming that the mean speed scales according to Stokes' friction law, i.e. with the inverse ratio of the radii of CBs and naive B cells, we obtain a realistic approximation of real motility properties. This assumption might be wrong in view of observed rather motile large B cells (Gunzer *et al.*, 2004). However, the motility of CBs does not significantly influence the selection mechanisms which are primarily related to the CC motility.

2.4.3 *Centrocytes.* CCs differentiate from CBs and neither divide nor mutate. CCs are in an activated state of apoptosis and they have a lifetime of 10 h (Liu *et al.*, 1994), within which they need to receive a rescue signal to avoid death. Dead CCs are rapidly removed from the lattice assuming a fast clearance of apoptotic bodies. The exact nature of the rescue signal depends on the selection mechanism. CCs can be in one of the following states: 'unselected', 'in contact with FDC', 'selected by FDC', 'in contact with T cell', 'selected'. Thus, the subpopulation of CCs is rather heterogeneous (Klein *et al.*, 2003).

'Unselected' CCs need to find one of the X_{FDC} sites. Once they have access to an FDC site, they try to bind the antigen. The binding probability is proportional to the antibody–antigen affinity. Unsuccessful CCs have to wait for 6 min before they can try binding again. This short refractory time ensures independence of the binding process from the time resolution in the simulations. Note that one investigated selection mechanism consists of a prolongation of this refractory time (see Section 3). Successful CCs switch to the state 'in contact with FDC' and are rescued from apoptosis. The CC remains

bound to the FDC for 2 h (Lindhout *et al.*, 1995). During this time, the rescue signals are thought to be provided by the FDC and the CCs turn into the state 'selected by FDC'. Note that the FDCs are assumed to provide rescue signals and not to negatively select unsuccessful CCs via, e.g. the FasL–Fas pathway (Verbeke *et al.*, 1999).

All investigated selection mechanisms act on CCs and define how CCs in the state 'selected by FDC' reach the state 'selected'. This process is described when the different selection mechanisms are introduced in Section 3.

'Selected' CCs further differentiate within 7 h to pre-plasma cells or memory cells (both summarised as output cells in the following), or, alternatively, they recycle back to CBs. No data yet exist to relate the relative receptor quality of the CC to its probability of entering either differentiation path. In fact, available experimental data (Han *et al.*, 1995b) can be reproduced by assuming that this probability does not depend on receptor quality (Meyer-Hermann *et al.*, 2001) and as in Meyer-Hermann *et al.* (2001), we therefore assume that 'selected' CCs recycle with probability 0.8 and differentiate to output cells with probability 0.2.

CC motility characteristics are assumed to be identical to those of naive B cells (Miller *et al.*, 2002) and to be the same in all states, i.e. $v_{CC} = 5$ μm/min and $\Delta t_{CC} = 2$ min.

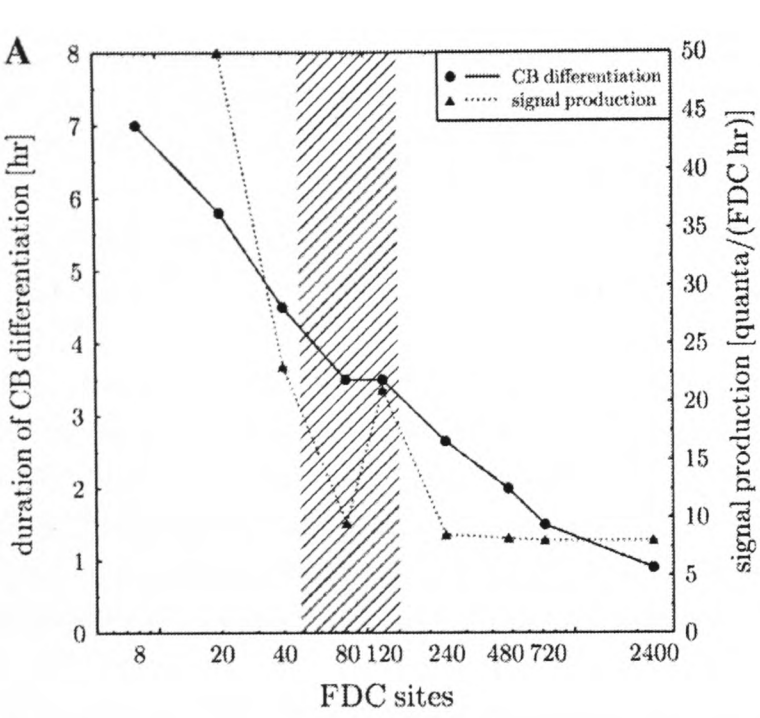
2.4.4 *T cells.* T cells are only included in one set of simulations in which they are part of the selection process of CCs. As the relative amount of specific and unspecific T cells is not known, only T cells that are specific for the antigen are included, such that all N_{TC} T cells will be able to interact with CCs selected by FDC. Consequently, the number of included T cells may underestimate the total number of T cells present in the GC. The error introduced by this simplification is restricted to spatial effects of T cells, which can be assumed to be small in view of the comparably small total number of T cells in GCs. When T cells interact with CCs that have encountered antigen on FDC they develop a polarity towards the CC. If more than one CC selected by FDC simultaneously interact with a T cell, the T cell is assumed to polarise towards the CC with highest affinity to the antigen. Without CC the polarity of the T cell is random. The T cell motility characteristics are $v_{TC} = 10.8$ μm/min and $\Delta t_{TC} = 2$ min (Miller *et al.*, 2002).

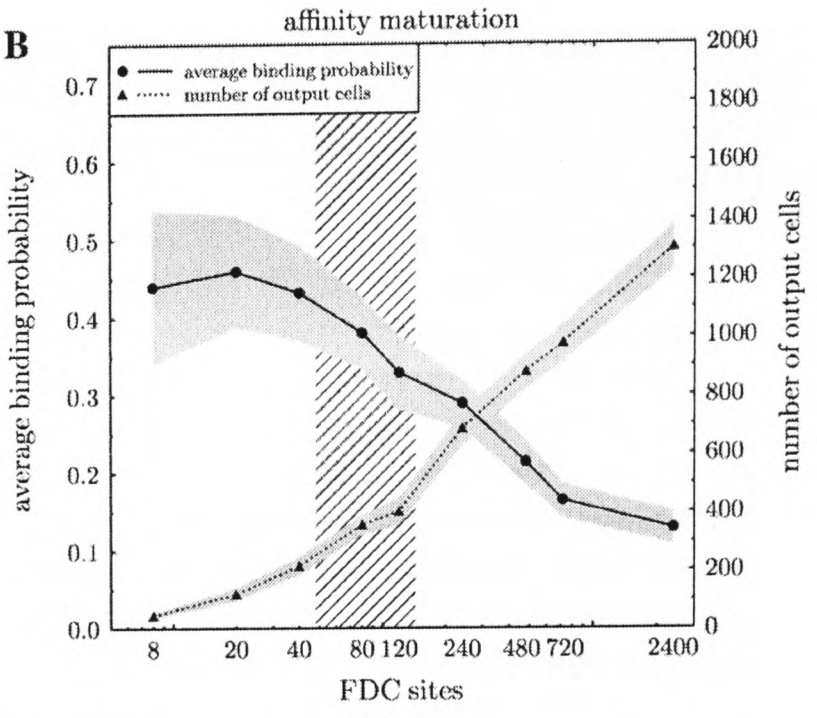
2.4.5 *Output cells.* Pre-plasma cells and memory B cells are collected in a cell pool denoted by output cells. These cells are assumed to have the same motility characteristics as CCs. In contrast to CCs, output cells can leave the GC environment when reaching the border of the GC. These cells may be thought of as crossing the mantle zone and entering the marginal zone. The total number of output cells produced will be taken as a measure of GC success independent of their presence in the GC at the end of the reaction.

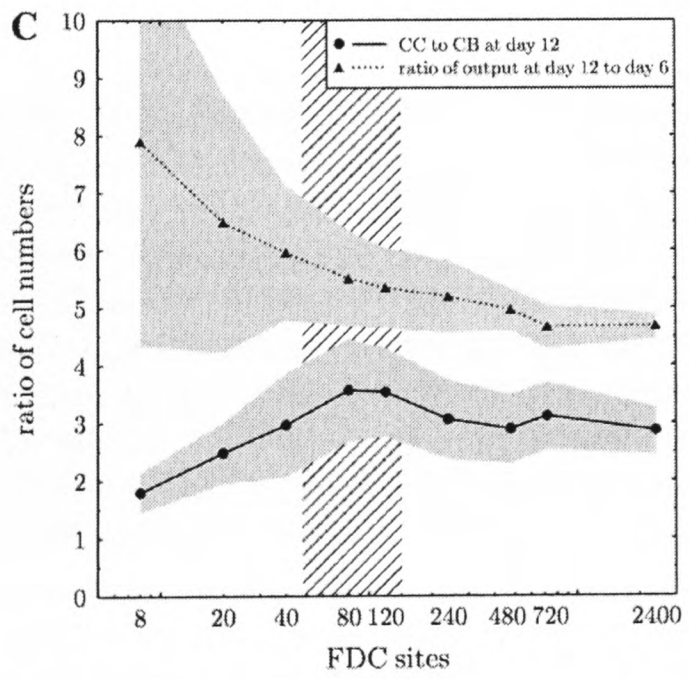
2.5 *Diffusion of molecular signals and soluble antibodies*

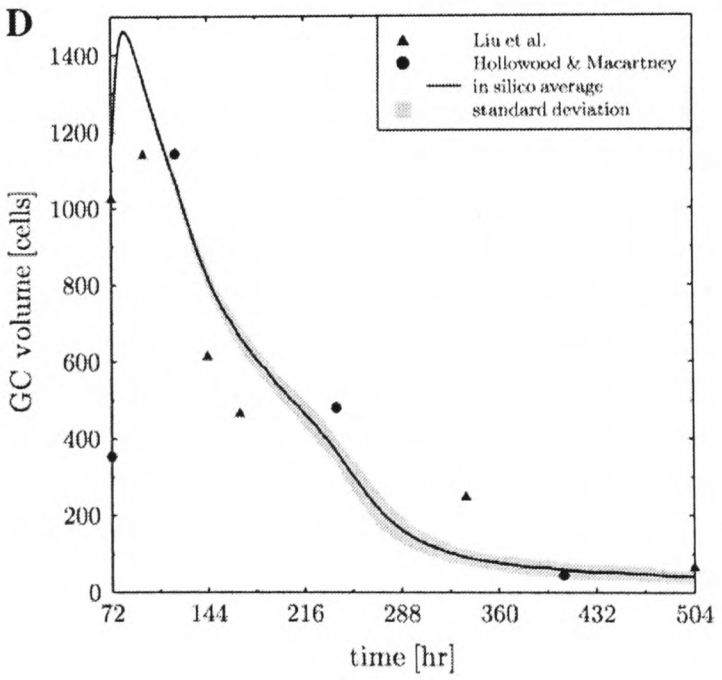
The model includes diffusing CB differentiation signals as well as soluble antibodies. The discretised diffusion equation is solved on the lattice with Dirichlet boundary conditions and with constant diffusion coefficient. Note that the diffusion coefficients $D_{diff} = 200$ μm^2/h and $D_{ab} = 2000$ μm^2/h are chosen to be very small in order to respect the high cell density in GC that acts as obstacles for free diffusion of molecules. However, the results are robust against different choices of parameter values. Numerically, the Crank–Nicholson and the alternating direction implicit method are used in 2D and 3D, respectively.

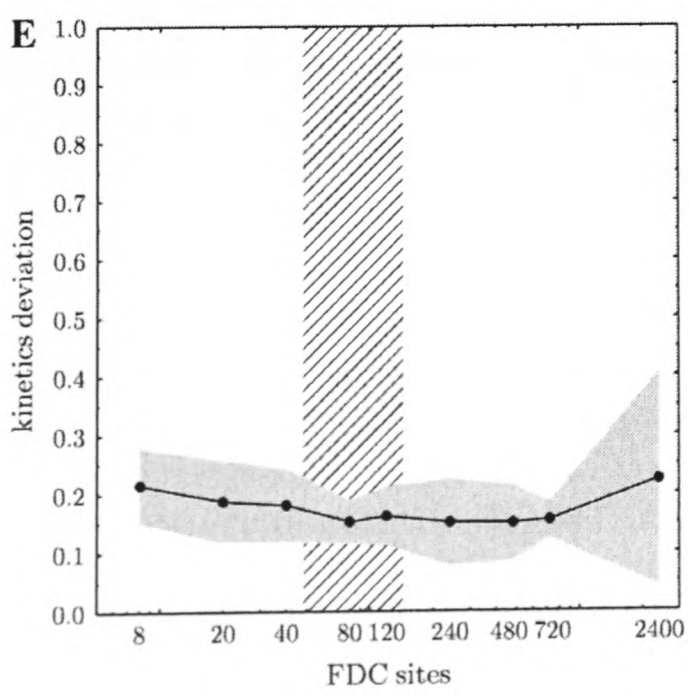
In one selection mechanism, antigen masking by antibodies is considered. Antibodies, b, are produced by output cells at some rate r_{ab}, diffuse on the lattice and locally bind to antigen, a, on FDCs to

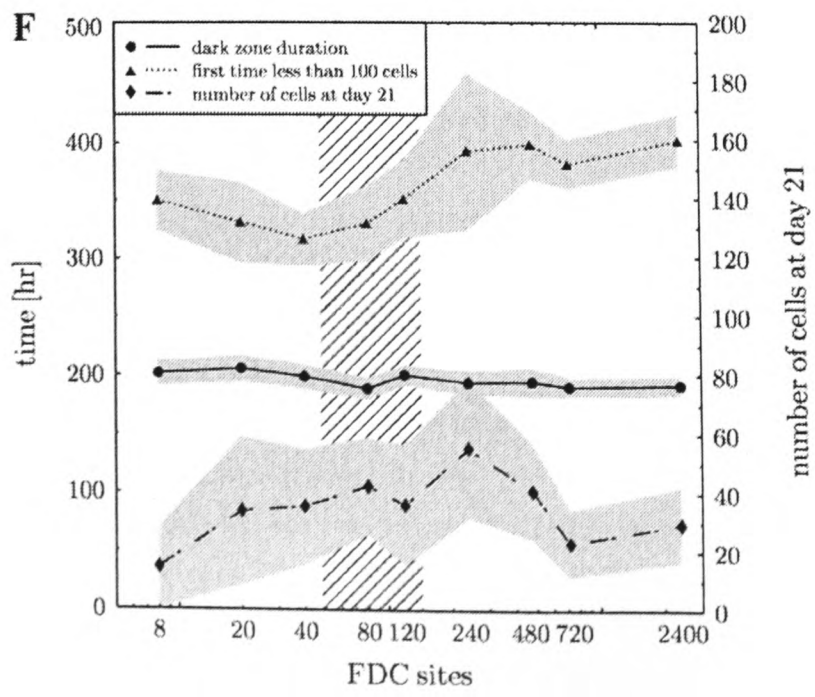

A
CB differentiation
signal production
duration of CB differentiation [hr]
signal production [quanta/(FDC hr)]
FDC sites


B
affinity maturation
average binding probability
number of output cells
average binding probability
number of output cells
FDC sites


C
CC to CB at day 12
ratio of output at day 12 to day 6
ratio of cell numbers
FDC sites


D
Liu et al.
Hollowood & Macartney
in silico average
standard deviation
GC volume [cells]
time [hr]


E
kinetics deviation
FDC sites


F
dark zone duration
first time less than 100 cells
number of cells at day 21
time [hr]
number of cells at day 21
FDC sites

form immune complexes, c, according to the rate equation

$$\frac{dc}{dt} = k_+ a(t) b(t) - k_- c(t). \tag{2}$$

While the affinity of the secreted antibodies will increase during the course of the immune response, we simplified the simulation by using binding rates characteristic of high-affinity antibodies, e.g. $k_+ = 10^6/(\mathrm{M\,s})$ and $k_- = 10^{-3}/\mathrm{s}$ (Batista & Neuberger, 1998; Fersht, 1998). This simplification is appropriate as we show that even under such conditions antibody production at a physiological rate does not sufficiently increase affinity maturation. The total amount of antigen and antibody is conserved in reaction (2), but these will nonetheless not remain constant since free antigen is consumed by CCs that bind to FDC, and antibodies are produced by output cells. This equation is solved using a simple Euler method at every node.

2.6 *Initial configuration*

The GC reaction is seeded by a small number of activated B cells that expand rapidly and fill the GC with about 10^4 B cells before somatic hypermutation starts (McHeyzer-Williams *et al.*, 1993; Toellner *et al.*, 2002) and enables the evolution of higher-affinity antibodies. In general, a small number of clones dominate the reaction after this expansion. We start the GC simulation after this expansion phase with 1100 CBs (which correspond to the 10^4 B cells in 3D) that stem from three different low-affinity clones (binding probability 0.04). The antibodies of these clones all have a distance of five mutations to the optimal clone in the shape space; i.e. they require a minimum of five mutations to gain the optimal affinity. However, most sequences of mutations will not follow such an optimal antibody affinity evolution path. In fact, we observe about nine mutations in most output cells, which is in agreement with experimental data (Kueppers *et al.*, 1993). The CBs are distributed randomly within the GC. We assume a polarised morphology of the GC in the sense that the FDCs are placed at arbitrary nodes on two-thirds of the total GC volume (Camacho *et al.*, 1998, Fig. 1C, D). If T cells are included, then they are distributed randomly within the GC. Note, however, that the bias of B cell-flow from dark to light zone induces an inhomogeneous T cell distribution which are then concentrated in the outer light zone as observed in experiment (Hardie *et al.*, 1993), without additional assumptions.

2.7 *Simulations and analysis of the results*

In order to achieve comparability between the different selection mechanisms, two parameters that affect CB to CC differentiation were varied within physiological limits, while all other parameters are kept constant throughout all simulations (see Table 1), such that the experimentally determined GC kinetics and dark zone duration were reproduced. These two GC characteristics were chosen since both are well established by experiments and variations of these strongly affect the output of the reaction (Meyer-Hermann, 2002a).

FIG. 1. Competition for FDC sites is too weak for affinity maturation. *In silico* GC experiments with different numbers of FDC sites. (A) Parameter adaptation: 'duration of CB differentiation' and differentiation 'signal production' rate per FDC (note that the jumps in the latter correspond to different numbers of FDCs), (B) extent of affinity maturation (measured as average binding probability and number of output cells), (C) CC/CB ratio at day 12 of the reaction, ratio q_6^{12} of number of output cells at day 12 to 6, (D) GC kinetics taken from 50 simulations with 80 FDC sites including one standard deviation compared to data read off from Liu *et al.* (1991); Hollowood & Macartney (1992), (E) deviation η (see (3)) from experimental GC kinetics and (F) end of dark zone, GC population drops below 100 cells for the first time, remaining cell number after 21 days. The hatched area in (A,B,C,E,F) indicate the physiological range. The shaded area denotes one standard deviation in 50 simulations.

We assume the differentiation of CB to CC to be initiated by an FDC-derived signal. A signal for CB to CC differentiation has not yet been identified experimentally. However, this mechanism—unlike other mechanisms—gives rise to the experimentally observed GC zoning (Meyer-Hermann & Maini, 2005b), and a realistic GC morphology is important for a realistic investigation of selection mechanisms. Beyond the effects stemming from the spatial organisation of the GC, this parameter does not affect B cell selection. The differentiation signal production rate per FDC, r_{signal}, widely determines the duration of the dark zone and is adjusted such that the dark zone vanishes between day 8 and 9 (~200 h—full line in Fig. 1F, and in panel C in Figs 2–11 in the Supplementary Information) after immunisation (Camacho *et al.*, 1998).

The second adjusted parameter, the duration of CB–CC differentiation, Δt_{diff}, governs the total population dynamics and is chosen such that GC kinetic data (Liu *et al.*, 1991; Hollowood & Macartney, 1992) are reproduced with sufficient accuracy (Fig. 1D). The deviation η from the data is calculated according to

$$\eta = \sum_{i=1}^{N} \frac{1}{N-1} \frac{(x_{\text{exp}}(t_i) - n(t_i)/n_{\text{max}})^2}{x_{\text{exp}}(t_i)^2}, \tag{3}$$

where N is the number of experimental values, t_i denotes the time in the reaction at which the value is taken, $n(t_i)$ is the corresponding volume in the simulation and n_{max} is the peak population averaged over all 50 simulations. We find acceptable GC kinetics when η is smaller than 0.3 (Fig. 1E and panel B of Figs 2–11 in the Supplementary Information). Note that Δt_{diff} must be less than 7 h since CBs are found in the light zone as CCs within 6–7 h (Liu *et al.*, 1991). A minimal value is not known.

The GC reaction is expected to end after 21 days. Given that the simulation was tuned to reproduce the GC kinetics, the cell number within the GC decreases below 100 cells after 300–400 h for all analysed selection mechanisms (Fig. 1F dotted line and panel C in Figs 2–11 in the Supplementary Information). The final cell numbers at day 21 vary for different selection regimes between almost zero and less than 100 (see the same figures, dashed dotted lines).

There are further characteristics of GC reactions to which the simulation was not fitted, but which had to be reproduced by the simulation in order to ensure the model's physiological relevance. Thus, the ratio of CCs to CBs at day 12 after immunisation needs to be larger than 2 in order to agree with the experimental observation that CCs greatly outnumber CBs during the GC reaction (MacLennan *et al.*, 1990) and the ratio q_6^{12} of produced output cells (i.e. pre-plasma and memory B cells) at day 12 to day 6 after immunisation should be the order of 6 (Han *et al.*, 1995a) (Fig. 1C, and panel D of Figs 2–11 in the Supplementary Information). The factor q_6^{12} can be interpreted as a measure for the steepness of the output production.

Unless stated otherwise, all simulations remain in agreement with the aforementioned experimental constraints (compare figures in the Supplementary Information where the full data sets are shown). The selection mechanisms that rescue CCs from apoptosis have to rely on some affinity-dependent competition between different CCs to achieve affinity maturation. Therefore, the success of a GC reaction is measured by the affinity of the output cells averaged over all cells produced during the reaction (panel B of Figs 1,2,4–6, and panel E of Figs 2–11 in the Supplementary Information). This quantity is an indicator of the entire GC reaction and is not restricted to arbitrary time points of the reaction. The total number of output cells produced is monitored since a stable population will need to be formed to enable robust antibody production. Note that the full data sets are shown only in the case of site competition. For all other scenarios, we show only the most important data and refer to the Supplementary Information for the full data sets.

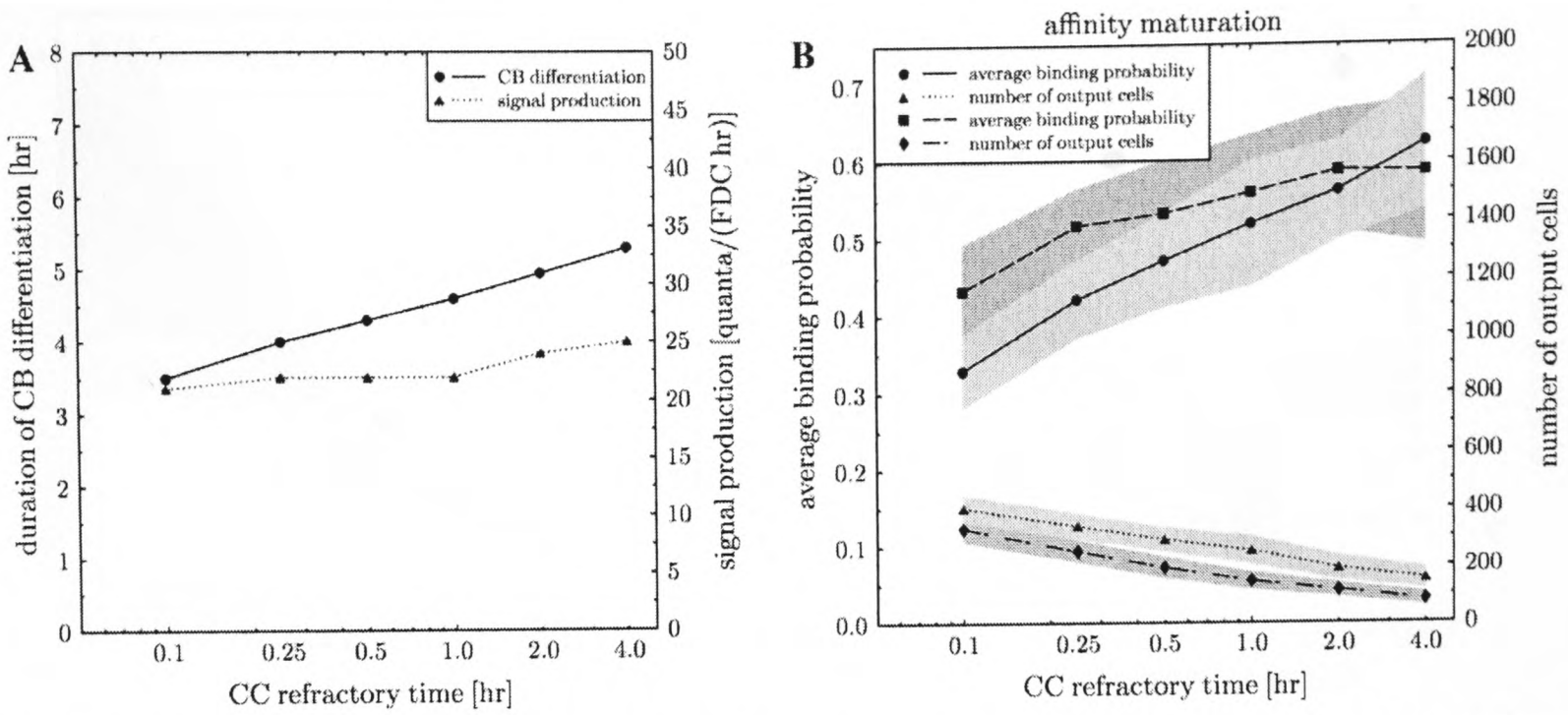


FIG. 2. A limitation of CC–FDC interaction allows for robust affinity maturation. *In silico* GC experiments with 10 FDC and 120 FDC sites, and for different refractory times of CC after FDC encounters (see Fig. 2 in the Supplementary Information for the full data set). (A) Parameter adaptation: 'duration of CB differentiation' and differentiation 'signal production' rate per FDC, (B) extent of affinity maturation (measured as average binding probability and number of output cells) with the probability of an optimal clone to bind an antigen presented on FDC of 1 (circles and triangles) and 0.5 (squares and diamonds, and Fig. 3 in the Supplementary Information).

3. Results

3.1 *Competition for binding sites on FDCs*

According to the simplest of all suggested models, B cells are selected only in a competition for access to antigen and/or survival factors that are provided by the FDCs; other potentially limiting factors are ignored (Fig. 1A in the Supplementary Information). Accordingly, the number of FDC sites X_{FDC} (see (1)) on which antigen is presented would be the limiting factor for which different clones would compete. As described in Section 2, we assume that CCs bind antigen held on FDC with a probability proportional to the affinity of the antibody. Given that no further limiting resources are considered in this very simple model, CCs that have been selected by FDCs (e.g. CC selected by FDC in the language of the model, see Section 2) do not need any further steps to be positively selected and can follow the differentiation paths of successfully selected CC.

By variation of the site number X_{FDC}, the simulation indeed reveals that affinity maturation is enforced when the number of FDC sites is low (Fig. 1B). Affinity maturation can be observed for a physiological number of FDC sites ($48 \leqslant X_{\mathrm{FDC}} \leqslant 144$—see (1)); the extent of the process (less than 50% high-affinity output cells) is however rather low compared to other selection mechanisms investigated here and not robust to changes in the number of accessible sites.

The GC characteristics are reproduced *in silico*. Thus, the CC to CB ratio at day 12, as well as the output ratio at day 12 to day 6, are in agreement with experimental data for the entire physiological range (Fig. 1C). The duration of CB–CC differentiation Δt_{diff}, which decreases from 7 to 1 h with increasing site numbers (Fig. 1A), remains within its expected range for the physiological FDC site numbers. Short CB to CC differentiation times had to be employed in order to reproduce the experimentally observed GC kinetics because the selection method is not stringent enough to reduce the volume of the GC reaction considerably.

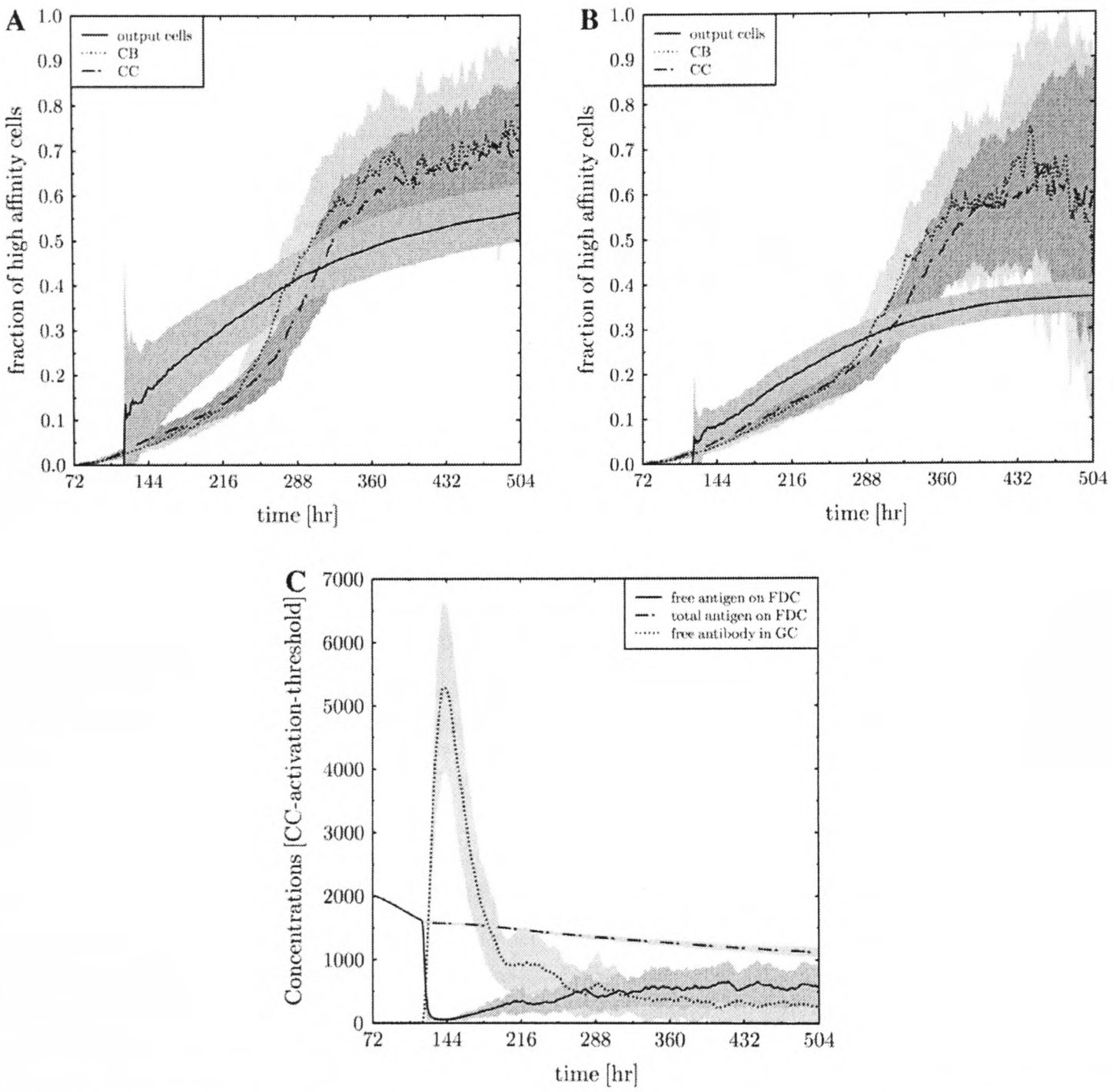


FIG. 3. The time course of affinity maturation. The fraction of high-affinity cells (defined as cells with antigen-binding probability of more than 0.3) is shown for CBs, CCs, and the accumulated sum of output cells, separately. In (A) selection is based on a refractory time for CC–FDC interaction of 2 h (taken from Fig. 2), while in (B) selection is based on competition for antigen with 40 antigen portions per FDC site (taken from Fig. 4). In (C) the time course of free and total antigen on FDC, and soluble antibody is shown for the same experiment as in (B) but including soluble antibody (taken from Fig. 5). Soluble antibody induces an early reduction of free antigen and thereby increases competition for antigen as compared to (B). The shaded area denotes one standard deviation in 50 simulations.

We conclude that while B cell competition for access to FDCs can give rise to the observed GC kinetics and properties, affinity maturation is relatively poor and not robust against small variations in the number of binding sites.

3.2 *Limiting the interactions with FDCs by introducing a refractory time*

If CCs can reinitiate binding to FDCs every 6 min (as assumed in our analysis of site competition), then the total number of encounters is considerable during a CC lifetime of 10 h. Any mechanism that limits the total number of encounters will lower the probability of a successful interaction within a CC lifetime

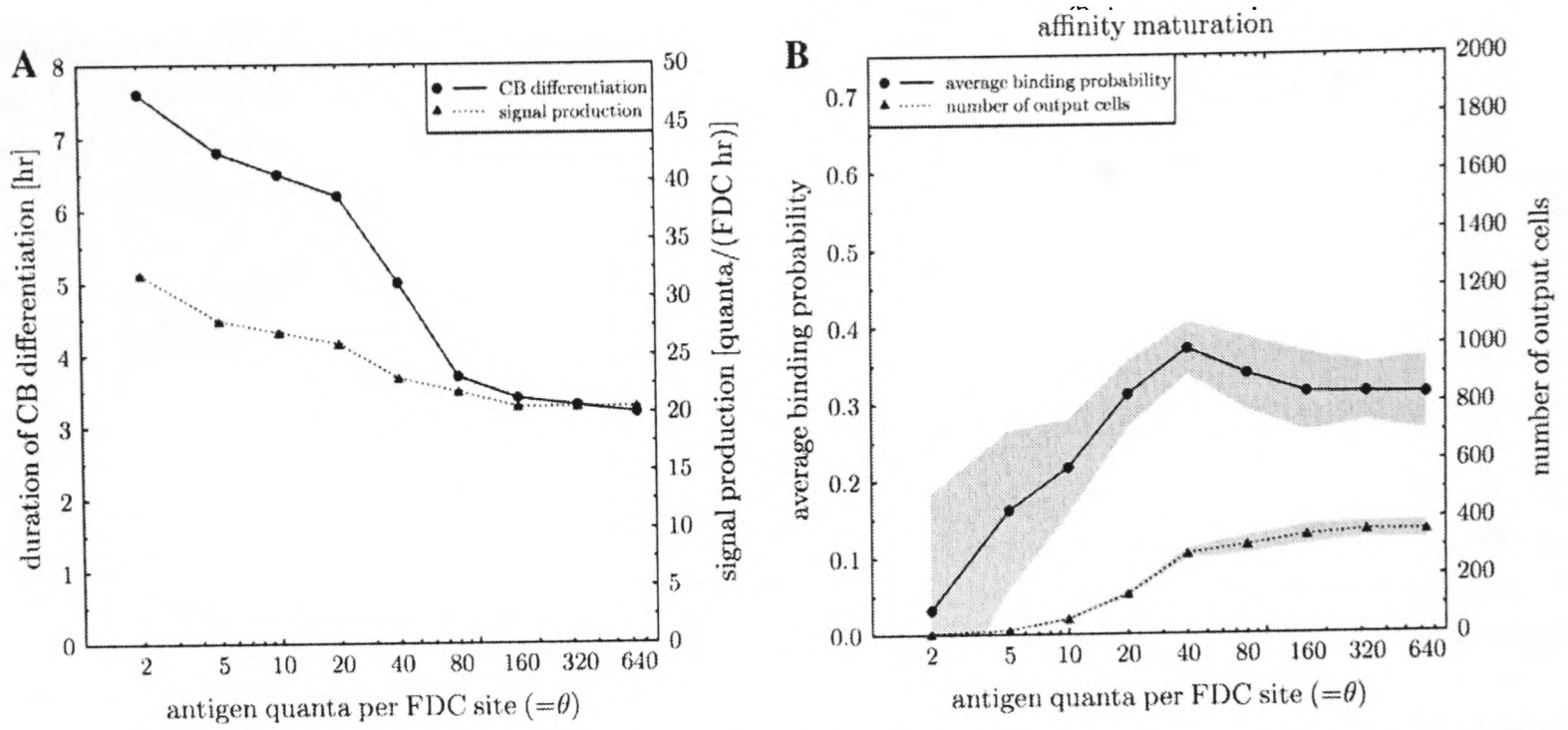


FIG. 4. Affinity maturation is not induced by competition for antigen. *In silico* GC experiments with 120 FDC sites. The antigen-binding probability of CCs is linearly reduced with the amount of remaining antigen on FDCs (see Fig. 4 in the Supplementary Information for the full data set). (A) Parameter adaptation: 'duration of CB differentiation' and differentiation 'signal production' rate per FDC, (B) extent of affinity maturation (measured as average binding probability and number of output cells).

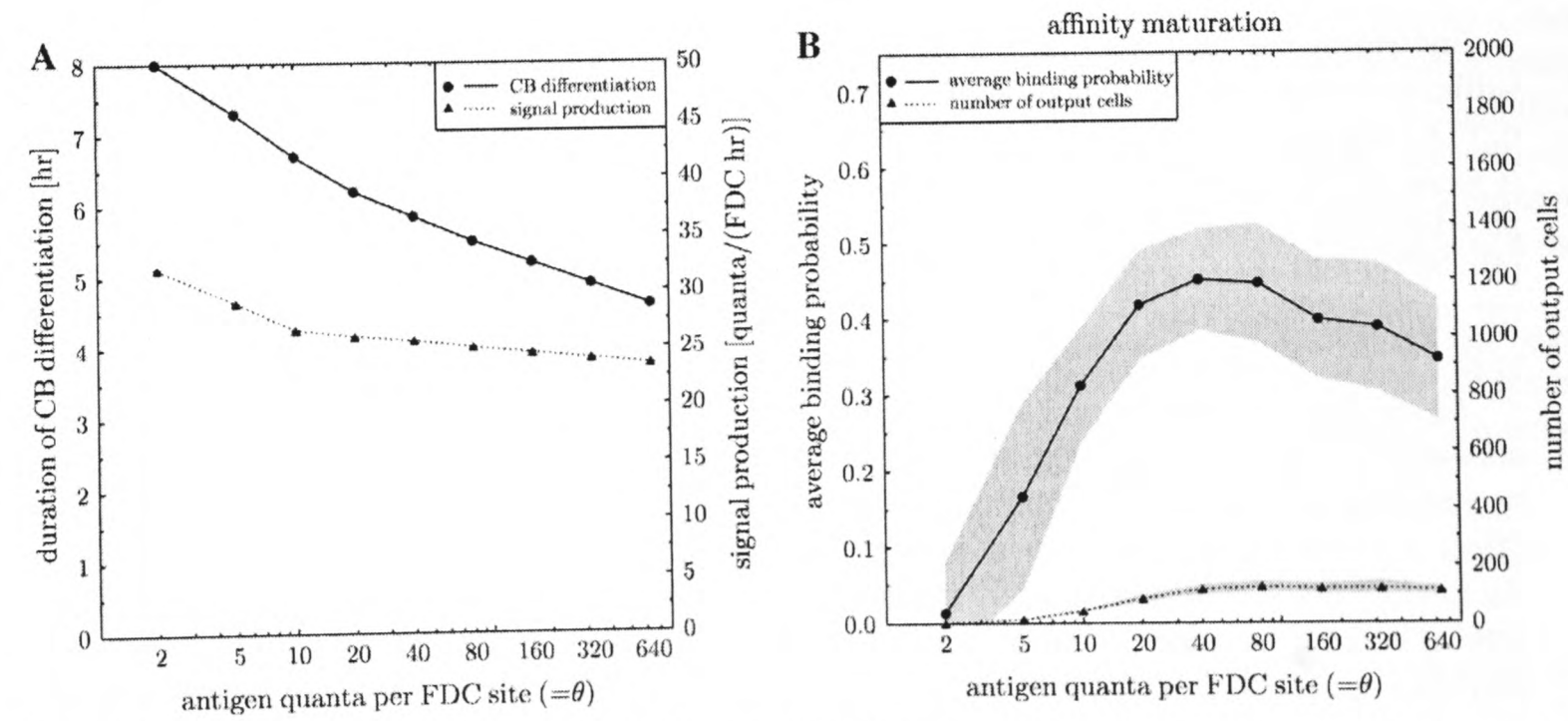


FIG. 5. Antigen masking by soluble antibodies increases competition for antigen in the early phase of GC reaction. *In silico* GC experiments as in Fig. 4 with antibody production of 10^2 antibodies per second and per plasma cell (see Fig. 7 in the Supplementary Information for the full data set). (A) Parameter adaptation: 'duration of CB differentiation' and differentiation 'signal production' rate per FDC, (B) extent of affinity maturation (measured as average binding probability and number of output cells).

and will favour higher-affinity clones because they have a higher chance of binding successfully in an early attempt. We therefore speculate that an increase in the refractory time (Δt_{delay}—the time during which B cells that failed to bind during a previous contact with a FDC are unable to bind again) will increase the selection pressure (see also Fig. 1B in the Supplementary Information).

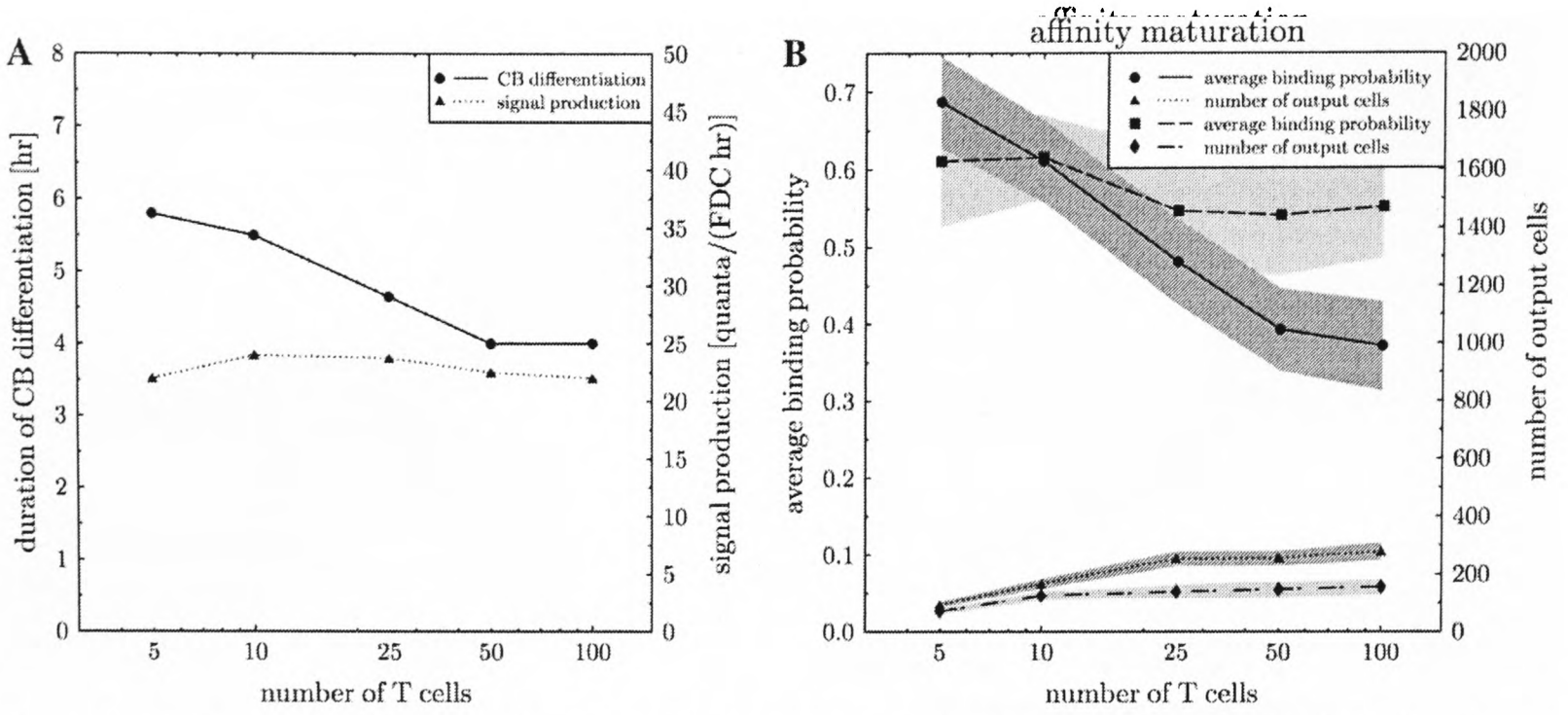


FIG. 6. Competition for T cell help allows for robust affinity maturation. *In silico* GC experiments with 120 FDC sites, abundant antigen, and T cells as indicated on the axis ($\Delta t_{\text{rescue}} = 2$ h and $\Delta t_{\text{apop}} = 2.1$ h) (see Fig. 8 in the Supplementary Information for the full data set). (A) Parameter adaptation: 'duration of CB differentiation' and differentiation 'signal production' rate per FDC, (B) extent of affinity maturation (measured as average binding probability and number of output cells. Combining competition for T cell help with a CC refractory time of 0.5 h and a reduction of the binding probability to 0.5 leads to more robust affinity maturation (squares and diamonds, and Fig. 11 in the Supplementary Information) than in the standard case (circles and triangles).

Increasing the refractory time from 6 min to 4 h, we find that a refractory time as low as 0.5 h is sufficient to induce affinity maturation of extent similar to that with site competition but for a wide range of FDC site numbers. Thus at $X_{\text{FDC}} = 120$ (Fig. 2), when competition for antigen-presenting FDC sites is weak, affinity maturation reaches a level previously only seen at low ($X_{\text{FDC}} = 40$) site numbers (compare full lines in Fig. 1B and 2B). A refractory time of 4 h leads to rather efficient affinity maturation (60–70% of all output cells are of high affinity) while allowing an even better reproduction of the other GC characteristics (kinetics, dark zone duration, ratio of CC to CB at day 12 and output ratio at day 12 to day 6 (Fig. 2 in the Supplementary Information)) than competition for FDC sites (Fig. 1).

Given that the binding probability depends on both the affinity-dependent binding probability per encounter as well as the number of encounters per CC lifetime, affinity maturation can also be fostered by reducing the binding probability per encounter by a certain factor for all affinities. However, the effect is smaller than in the case of an increased CC refractory time since such a general reduction in the binding probability also strongly reduces the selection probability for high-affinity clones. These are little affected by a reduction in the number of encounters since they will bind with high probability on their first or second trial. A combination of both effects can however reduce the refractory time required to gain good affinity maturation to more reasonable physiological values (Fig. 2B dashed line, and Fig. 3 in the Supplementary Information).

The agreement with general GC properties, the efficient affinity maturation, and the robustness to variations in the antigen-presenting FDC site number, make this a candidate mechanism for B cell selection *in vivo*.

3.3 *Competition for antigen presented on FDCs*

In the two previous scenarios, antigen is presented by FDCs on a limited number of sites where it is available in limitless supply. Instead, it has been proposed that antigen is widely spread but that the total

amount is limiting such that antigen consumption can drive affinity maturation (Sidman & Unanue, 1975). Using a sufficiently dense FDC network ($X_{FDC} = 120$) to avoid site competition, we can study this selection mechanism *in silico* by homogeneously distributing a number of antigen portions, N_{ag}, on all FDC sites and by removing one portion from each site on which CCs have successfully interacted with the FDC (see also Fig. 1C in the Supplementary Information). The binding probability is expected to decrease with decreasing amounts of antigen remaining on the FDC sites. As a simple approximation, we assume a linear decrease of the CC-binding probability for antigen amounts below some threshold Θ_{ag}. For larger antigen amounts, the binding probability is constant and solely determined by the antibody–antigen affinity. This assumption corresponds to a saturation of the binding probability when antigen is abundant.

While the selection pressure indeed increases over time as a result of this (Fig. 3B), the extent of affinity maturation is rather worse than for site competition alone (compare Fig. 1B for $X_{FDC} = 120$ and Fig. 4B). This is due to the initial abundance of antigen and the inferred low selection pressure which in turn results in the production of a large number of low-affinity output cells before antigen consumption can increase the selection pressure (compare Fig. 3A and B).

If the size of the removed antigen portions per CC–FDC interaction is constant, antigen consumption is insufficient to increase the selection pressure in the case of large initial antigen densities (more than 80 antigen portions per FDC site, compare Figs 1B and 4B); at lower antigen density, antigen is rapidly consumed and the GC reaction declines early, before high-affinity clones are found (Fig. 4, and Fig. 4 in the Supplementary Information). In the case of antigen consumption proportional to the level of presented antigen, a scenario comparable to antigen masking by antibodies arises (see Section 3.4).

Experiments have revealed a high robustness to variations in the initial antigen density (Vora *et al.*, 1997; Hannum *et al.*, 2000). If, in the simulation, the antigen threshold to the maximum binding probability Θ_{ag} is fixed and not scaled with the amount of initially deposited antigen ($\Theta_{ag} = N_{ag}$), then such robustness can be observed on a low level (see Figs 5 and 6 in the Supplementary Information). It should be noted that successful affinity maturation at lower antigen densities results from a reduced binding probability for all affinities (as discussed in Section 3.3) such that the observed robustness is the result of two different mechanisms acting in different antigen density ranges.

We conclude that *in silico* antigen consumption does not improve affinity maturation over site competition alone. At low antigen densities, the general properties of the GC reaction can no longer be reproduced. Affinity maturation is therefore unlikely to be driven by antigen consumption even when combined with site competition.

3.4 *The impact of antigen masking by competing antibodies*

Plasma cells outside the GC produce antibodies at rates of up to $r_{ab} = 2 \times 10^3$ antibody molecules per second (Randall *et al.*, 1992). These antibodies may mask antigen in the GCs and thereby increase the selection pressure on B cells and simultaneously provide a feedback mechanism that enables robustness towards alterations in the initial antigen density (Vora *et al.*, 1997; Tarlinton & Smith, 2000; Iber & Maini, 2002) (see also Fig. 1D in the Supplementary Information). Assuming that plasma cells produce high-affinity antibodies in the GC at a rate of $r_{ab} = 10^2$ per output cell (thus overestimating a realistic production of soluble antibody in GCs), we find that the above considerations do indeed hold true: A physiological GC kinetic can be obtained for antigen amounts between 20 and 200 antigen portions per FDC site (Fig. 7 in the Supplementary Information). A small improvement in affinity maturation is observed relative to site and antigen competition alone (Fig. 5). As before, affinity maturation approaches the site competition value for 120 sites when antigen is abundant (Fig. 5B and 1B).

The effect of strong antibody production is an early reduction in free antigen, and thus an early increase in the selection pressure (Fig. 3C). For example, in the case of 40 antigen portions per FDC site (i.e. for optimal affinity maturation), only 25% of the antigen is used during the GC reaction, but free antigen is kept in the limiting regime throughout the reaction (Fig. 3C). In that way the inefficient time course of affinity maturation found in the case of antigen consumption without soluble antibodies (Fig. 3B) is restored to some extent.

While antigen masking leads to the correct kinetics and a small improvement of affinity maturation, the number of produced output cells is rather small (Fig. 5B), as is the ratio of CC to CB, and $q_6^{12} \ll 6$ (Fig. 5B in the Supplementary Information). We conclude that antigen masking resolves some of the problems in the antigen competition scenario, but some major GC properties are still not reproduced. In addition, this mechanism is not robust to a substantial (10-fold) decrease in the antibody production rate, which is more realistic than the rate assumed in the present *in silico* experiment.

3.5 *Competition for T cell help*

Interactions between antigen-specific CCs and T cells are necessary for CC survival and differentiation (de Vinuesa *et al.*, 2000). Given that T cells only constitute 5–10% of the GC cell population (Kelsoe, 1996), this interaction may be competitive. While T cells can bind to several B cells simultaneously, they can only polarise to one (Kupfer *et al.*, 1994), which we assume to be the CC that has previously bound antigen with highest affinity (see also Fig. 1E in the Supplementary Information). In our simulation, polarisation has to be maintained for a minimum time (Δt_{rescue}) to rescue a B cell. Cells that bind to T cells for longer than $\Delta t_{\text{apop}} > \Delta t_{\text{rescue}}$ and do not receive rescue signals for at least Δt_{rescue} are doomed to apoptosis. Note that all CCs need to be selected by FDCs before they can compete for T cell help.

We find that the extent of affinity maturation is only slightly enhanced as compared to site competition alone ($X_{\text{FDC}} = 120$ sites), if 5–10% of all GC cells are antigen-specific T cells (50–100 T cells per GC in the 2D simulation) to which antigen-presenting CCs can bind (Fig. 6B full line). However, given that each antigen-specific T cell only recognises a certain antigen epitope and different CCs will process the antigen differently and therefore present different epitopes, only a small fraction of GC T cells will be reactive to a given CC. The simulation reveals that affinity maturation is strongest (60–70% of all output cells are of high affinity) when only about 0.5–1% of all GC cells (5–10 T cells per GC in the 2D simulation) can rescue a given antigen-presenting CC (Fig. 6B full line). The GC characteristics are reproduced (Fig. 6A, and Fig. 8 in the Supplementary Information). The mechanism is robust to large variations in antigen availability and may still work when antigen is encountered in soluble form since the simulations were performed in a regime where antigen acquisition and interactions with FDCs are uncompetitive.

The time span Δt_{apop} for which CCs can survive while binding to T cells without receiving rescue signals has a major impact on the level of affinity maturation. Thus a small increase in Δt_{apop} from 2.1 to 4 h already reduces affinity maturation to a level comparable to site competition (see Fig. 9 in the Supplementary Information). A combination of T cell competition with a general reduction of the binding probability to 50% of its value (see above) has no major effect on the result (see Fig. 10 in Supplementary Information). However, a combination of competition for T cell help with a longer CC refractory time makes affinity maturation more robust against changes in the T cell density (Fig. 6B dashed line).

4. Discussion

The simulation results presented here reveal current models of B cell selection (competition for access to FDCs or antigen) to be incompatible with available experimental information. We propose two novel mechanisms, a refractory time between CC–FDC engagements as well as competition for T cell help.

Both mechanisms enable strong affinity maturation *in silico* while reproducing all available experimental information on GC dynamics. In agreement with experiments (Vora *et al.*, 1997; Hannum *et al.*, 2000), the mechanisms are robust to variations in the amount of initially deposited antigen. As competition for antigen held on FDC is assumed to be non-limiting in both mechanisms, it is likely that these mechanisms also work with soluble antigen which would be in agreement with results from recent experiments that call into question the concept that antigen presentation by FDCs is essential (Hannum *et al.*, 2000; Haberman & Shlomchik, 2003). However, in the present simulations, an FDC-independent preselection of CCs with soluble antigen has not been tested. Note that this *in silico* simulation is not able to cover all possible cellular interactions that might serve as suitable mechanisms for affinity maturation. Thus, the two highlighted novel mechanisms have to be considered as propositions.

Competition for access to FDCs or antigen does not provide a sufficient selection pressure to enable a high level of affinity maturation in the simulation. While antigen consumption does lead to an increase in the selection pressure, this increase comes too late so that many low-affinity output cells have already been produced and the remaining cell numbers are insufficient for successful affinity maturation. Moreover, for low antigen densities, the GC reaction ends prematurely since antigen consumption then removes too much antigen. While antigen masking by emerging antibodies can, in principle, increase the selection pressure earlier, the antibody production rate would need to be unphysiologically high. Even then the available data on GCs could not be reproduced and, in addition, affinity maturation is not as strong as that produced by the alternative mechanism. Given that evolution tends to optimise performance, this latter limitation may also be interpreted as an argument against these mechanisms.

At first sight, less than 200 output cells (i.e. less than 8000 cells in 3D) may seem low. Given the efficient expansion of output cells, the success of an immune response can, however, be expected to primarily depend on the size of the high-affinity fraction; this is therefore a physiologically realistic result. Note that the level of affinity maturation that is achieved in the simulations (60–70% of all output cells are of high affinity) is in qualitative agreement with the experimentally observed domination of high-affinity clones (Smith *et al.*, 1997). We had to restrict ourselves to 2D simulations to generate the results with sufficient statistics, which prevent us from a quantitative comparison of this result.

To our knowledge, this theoretical investigation is the first systematic comparison of different B cell selection mechanisms in GC reactions as well as the first theoretical work to investigate a possible role of T cells in the selection process. Previous models have concentrated on single selection mechanisms (Iber & Maini, 2002; Meyer-Hermann, 2002a; Meyer-Hermann & Maini, 2005b; Oprea & Perelson, 1997; Oprea *et al.*, 2000; Beyer *et al.*, 2002; Kesmir & De Boer, 1999; Meyer-Hermann *et al.*, 2001) and have, in general, described them only phenomenologically, i.e. without including details of cell interactions. The impact of the spatial cell distribution has only been investigated in a few models (Kesmir & De Boer, 2003; Meyer-Hermann, 2002a; Meyer-Hermann & Maini, 2005b; Beyer *et al.*, 2002). The present model is based on available GC kinetics and cell motility data (see Section 2) and the parameters have been evaluated carefully using data from mice and rat lymph nodes (see Table 1). We did not find any experimentally uncertain parameter which would change our results qualitatively.

The only critical assumption is the shape space concept combined with a smooth affinity function. Changes of the width of the function for the affinity-dependent selection probability in the shape space has important consequences for GC development. For small variations of the width, all constraints from experiment can be respected by a corresponding adaption of other parameters. However, this becomes impossible when the width is strongly varied. This shows that our choice for the width is well-defined. While the suitability of the shape space concept for antigen–antibody affinity may be questioned, insufficient molecular information on antigen–antibody interaction is currently available to allow a more accurate model of mutation-dependent increases in antibody–antigen affinity.

Autoreactive B cells have not been considered in the present simulations because under normal circumstances, they are not positively selected by T cells and are therefore eliminated by apoptosis similar to other antigen-unspecific CCs. We therefore assumed autoreactive B cells to be part of the pool of low-affinity B cells that emerges from the seeder cells by disadvantageous mutations. This may shift the proportion of advantageous and disadvantageous mutations. However, we believe that this approximation remains within the error introduced by the shape space concept itself which most likely will inaccurately reproduce this proportion.

The CC refractory time and the competition for T cell help are equally attractive selection mechanisms to explain antibody affinity maturation in GCs and are both likely to play a role in B cell selection. The CC refractory time limits the number of selection trials per CC lifespan such that only high-affinity B cells which bind with high probability on the first or second trial are efficiently selected. The CC refractory time will be a consequence of IgM-independent interactions between CCs and FDCs. While the exact duration of such interactions still has to be determined in studies that employ CCs and FDCs, a refractory time between two CC–FDC encounters as long as 4 h appears to be unlikely. However, we have also shown that an additional general (i.e. affinity independent) reduction of the CC-FDC-binding probability to 0.5 may reduce the necessary refractory time to 15–30 min. One may speculate that integrin interactions may result in such a refractory time. LFA-1/ICAM-1 and VLA-4/VCAM-1 have been described to mediate adhesion of B cells to FDCs (Koopman *et al.*, 1991). Even though unspecific contacts are dissolved in the range of minutes (Gunzer *et al.*, 2004), experiments with lipid bilayers have also shown that especially at low- to medium-affinity, antigen binding may fail to induce the formation of an immunological synapse but can still result in a firm integrin-dependent attachment of B cells (Carrasco *et al.*, 2004). The speed at which these integrin-dependent contacts form and dissolve if B cells fail to establish an immunological synapse (which is generally believed to enable B cell activation and antigen extraction, Batista *et al.*, 2001) may determine the refractory time. A different possibility is a reduced CC motility after an unsuccessful binding event. This might reduce the subsequent interaction frequency of CCs with FDCs.[1]

An additional competition for T cell help further reduces the necessary CC refractory time. It has been shown *in vitro* that specific T cell help is essential for affinity maturation in the case of NP ((4-hydroxy-3-nitrophenyl)acetyl) (Aydar *et al.*, 2005), and more generally the role of T cells in the selection process has been highlighted (de Vinuesa *et al.*, 2000). While their is, as yet, no direct experimental evidence for competition for T cell help nor have antigen-specific T helper cells in the GC so far been suggested as a limiting factor for affinity maturation, what is known about B cell–T cell interactions strongly supports such a model. Thus, T cells have been observed to interact with several B cells at a time but to only activate the B cell towards which the microtubule organising centre (MTOC) (and the colocalised Golgi apparatus) is reorganised (Kupfer *et al.*, 1994, 1991; Poo *et al.*, 1988). Reorientation of the MTOC is dependent on and directed towards the site of T cell receptor signalling (Sedwick *et al.*, 1991), and, when interacting with several B cells, T cells polarise to the B cell with the highest density of specific major histocompatibility complex loaded with specific peptide (pMMC) (Depoil *et al.*, 2005). We propose that a higher affinity of interaction results in increased pMHC presentation such that only the highest affinity CC interacting with a T cell is rescued. Such a causal relationship is in agreement with the earlier observations that T cell responsiveness to B cells depends on both the antigen concentration and affinity (Batista & Neuberger, 1998) as well as on the (antigen availability dependent) number of MHC class II molecules loaded with antigenic peptide that are presented on the B cell surface (Harding & Unanue, 1990; Grakoui *et al.*, 1999). It is not an essential

[1] We thank the reviewer for this suggestion.

element of the present model but a plausible hypothesis is that apoptosis is induced in all other B cells to which the T cell does not sufficiently polarise. This negative selection by T helper cells could in principle be mediated by FasL–Fas as interactions which can be expected to form in all contact zones independent of T cell polarisation. Whether FasL is at all upregulated on GC T cells is, however, currently unclear since the spatial distribution of FasL in GCs from patients with lymphofollicular hyperplasia correlates with the FDC network rather than with the distribution of CD4-positive T cells (Verbeke *et al.*, 1999).

While simultaneous interactions of T cells with several B cells in a lymph node environment have been reported as transient (Okada *et al.*, 2005), all B cells and T cells used in that study were of the same specificity and T cells rather than B cells were abundant. It will be important to repeat these studies under conditions that are more representative of GC reactions and to access the affinity dependence of T cell–B cell interactions in far greater detail. Imaging of T cell interactions with B cells that have recognised antigen with different affinity should help to clarify whether the MTOC does indeed reorganise to the highest affinity B cell and whether Fas–FasL accumulate in the contact zones to induce apoptosis in the outcompeted CC. Moreover, it will be interesting to test whether an (artificial) expansion of antigen-specific GC T cell clones can hamper antibody affinity maturation.

B cell selection in competition for T cell help challenges the presently held view that FDCs play a pivotal role in B cell selection. In this novel mechanistic framework, FDCs only play a role in supporting fragile CCs with general survival and differentiation signals but do not drive affinity maturation by negatively selecting B cells.

A competition for T cell help and a long CC refractory time both enable affinity maturation under conditions when acquisition of FDC signals is uncompetitive such as for a wide range of antigen concentrations. Accordingly, these mechanisms are in agreement with experiments that show that a reduction of antigen densities on FDCs by at least 400-fold does not prevent antibody affinity maturation (Hannum *et al.*, 2000).

We conclude that within the selection mechanisms tested, thus using a restricted set of possible interaction mechanisms, a combination of T cell competition together with slow CC–FDC interactions and a suboptimal binding probability of high-affinity clones can drive B cell selection in GCs under the experimentally established conditions. Further insight into GC dynamics and affinity maturation should be gained by combining the powerful predictions of these agent-based simulations with the latest imaging techniques.

Supplementary data

Supplementary Figures 1–11 can be found at www.imammb.oxfordjournals.org.

Acknowledgements

MEM-H was supported by a Marie Curie Intra-European Fellowship within the Sixth EU Framework Program. DI is a Junior Research Fellow at St John's College, University of Oxford and is supported by a DTA EPSRC studentship. FIAS is supported by the ALTANA AG.

References

AYDAR, Y., SUKUMAR, S., SZAKAL, A. & TEW, J. (2005) The influence of immune complex-bearing follicular dendritic cells on the igm response, ig class switching, and production of high affinity igg. *J. Immunol.*, **174**, 5358–5366.

BATISTA, F., IBER, D. & NEUBERGER, M. (2001) B cells aquire antigen from target cells after synapse formation. *Nature*, **411**, 489–494.

BATISTA, F. & NEUBERGER, M. (1998) Affinity dependence of the B cell response to antigen: a threshold, a ceiling and the importance of off-rate. *Immunity*, **8**, 751–759.

BEREK, C. & MILSTEIN, C. (1987) Mutation drift and repertoire shift in the maturation of the immune response. *Immunol. Rev.*, **96**, 23–41.

BEYER, T., MEYER-HERMANN, M. & SOFF, G. (2002) A possible role of chemotaxis in germinal center formation. *Int. Immunol.*, **14**, 1369–1381.

CAMACHO, S., KOSCO-VILBOIS, M. & BEREK, C. (1998) The dynamic structure of the germinal center. *Immunol. Today*, **19**, 511–514.

CARRASCO, Y. R., FLEIRE, S. J., CAMERON, T., DUSTIN, M. L. & BATISTA, F. D. (2004) LFA-1/ICAM-1 interaction lowers the threshold of B cell activation by facilitating B cell adhesion and synapse formation. *Immunity*, **20**, 589–599.

DAL PORTO, J. M., HABERMAN, A. M., KELSOE, G. & SHLOMCHIK, M. J. (2002) Very low affinity B cells form germinal centers, become memory B cells, and participate in secondary immune responses when higher affinity competition is reduced. *J. Exp. Med.*, **195**, 1215–1221.

DEPOIL, D., ZARU, R., GUIRAUD, M., CHAUVEAU, A., HARRIAGUE, J., BISMUTH, G., UTZNY, C., MULLER, S. & VALITUTTI, S. (2005) Immunological synapses are versatile structures enabling selective T cell polarization. *Immunity*, **22**, 185–194.

DE VINUESA, C., COOK, M., BALL, J., DREW, M., SUNNERS, Y., CASCALHO, M., WABL, M., KLAUS, G. & MACLENNAN, I. (2000) Germinal centers without T cells. *J. Exp. Med.*, **191**, 485–493.

EISEN, H. & SISKIND, G. (1964) Variations in affinities of antibodies during the immune response. *Biochemistry*, **155**, 996–1008.

FERSHT, A. (1998) *Structure and Mechanism in Protein Science*. New York: W. H. Freeman and Company.

GRAKOUI, A., BROMLEY, S., SUMEN, C., DAVIS, M., SHAW, A., ALLEN, P. & DUSTIN, M. (1999) The immunological synapse: a molecular machine controlling T cell activation. *Science*, **285**, 221–227.

GUNZER, M., WEISHAUPT, C., HILLMER, A., BASOGLU, Y., FRIEDL, P., DITTMAR, K., KOLANUS, W., VARGA, G. & GRABBE, S. (2004) A spectrum of biophysical interaction modes between T cells and different antigen-presenting cells during priming in 3-D collagen and in vivo. *Blood*, **104**, 2801–2809.

HABERMAN, A. & SHLOMCHIK, M. (2003) Reassessing the function of immune-complex retention by follicular dendritic cells. *Nat. Rev. Immunol.*, **3**, 757–764.

HAN, S., HATHCOCK, K., ZHENG, B., KEPLER, T. B., HODES, R. & KELSOE, G. (1995a) Cellular interaction in germinal centers. Roles of CD40 ligand and B7-2 in established germinal centers. *J. Immunol.*, **155**, 556–567.

HAN, S., ZHENG, B., DALPORTO, J. & KELSOE, G. (1995b) In situ studies of the primary immune response to (4-hydroxy-3-nitrophenyl) acetyl. IV. Affinity-dependent, antigen-driven B cell apoptosis in germinal centers as a mechanism for maintaining self-tolerance. *J. Exp. Med.*, **182**, 1635–1644.

HANNUM, L., HABERMAN, A., ANDERSON, S. & SHLOMCHIK, M. (2000) Germinal center initiation, variable gene region hypermutation, and mutant B cell selection without detectable immune complexes on follicular dendritic cells. *J. Exp. Med.*, **192**, 931–942.

HARDIE, D., JOHNSON, G., KHAN, M. & MACLENNAN, I. (1993) Quantitative analysis of molecules which distinguish functional compartments within germinal centers. *Eur. J. Immunol.*, **23**, 997–1004.

HARDING, C. V. & UNANUE, E. R. (1990) Quantitation of antigen-presenting cell MHC class II/peptide complexes necessary for T-cell stimulation. *Nature*, **346**, 574–576.

HOLLOWOOD, K. & MACARTNEY, J. (1992) Cell kinetics of the germinal center reaction–a stathmokinetic study. *Eur. J. Immunol.*, **22**, 261–266.

HUPPA, J. B., GLEIMER, M., SUMEN, C. & DAVIS, M. M. (2003) Continuous T cell receptor signaling required for synapse maintenance and full effector potential. *Nat. Immunol.*, **4**, 749–755.

IBER, D. & MAINI, P. (2002) A mathematical model of germinal centre kinetics and affinity maturation. *J. Theor. Biol.*, **219**, 153–175.

JACOB, J., KASSIR, R. & KELSOE, G. (1991a) In situ studies of the primary immune response to (4-hydroxy-3-nitrophenyl) acetyl. I. The architecture and dynamics of responding cell populations. *J. Exp. Med.*, **173**, 1165–1175.

JACOB, J., KELSOE, G., RAJEWSKY, K. & WEISS, U. (1991b) Intraclonal generation of antibody mutants in germinal centres. *Nature*, **354**, 389–392.

JACOB, J., PRZYLEPA, J., MILLER, C. & KELSOE, G. (1993) In situ studies of the primary immune response to (4-hydroxy-3-nitrophenyl) acetyl. III. The kinetics of V region mutation and selection in germinal center B cells. *J. Exp. Med.*, **178**, 1293–1307.

JERNE, N. (1951) A study of avidity based on rabbit skin responses to diphteria toxin antitoxin mixtures. *Microbiol. Scand. Suppl.*, **87**, 1–183.

KELSOE, G. (1996) The germinal center: a crucible for lymphocyte selection. *Semin. Immunol.*, **8**, 179–184.

KESMIR, C. & DE BOER, R. J. (1999) A mathematical model on germinal center kinetics and termination. *J. Immunol.*, **163**, 2463–2469.

KESMIR, C. & DE BOER, R. J. (2003) A spatial model of germinal center reactions: cellular adhesion based sorting of B cells results in efficient affinity maturation. *J. Theor. Biol.*, **222**, 9–22.

KLEIN, U., TU, Y., STOLOVITZKY, G., KELLER, J., HADDAD, J., MILKOVIC, V., CATTORETTI, G., CALIFANO, A. & DALLA-FAVERA, R. (2003) Transcriptional analysis of the b cell germinal center reaction. *Proc. Natl. Acad. Sci. USA*, **100**, 2639–2644.

KOOPMAN, G., PARMENTIER, H., SCHUURMAN, H.-J., NEWMAN, W., MEIJER, C. & PALS, S. (1991) Adhesion of human b cells to follicular dendritic cells involves both the lymphocyte function-associated antigen 1/intercellular adheseion molecule 1 and very late antigen 4/vascular cell adhesion molecule 1 pathways. *J. Exp. Med.*, **173**, 1297–1304.

KOSCO-VILBOIS, M. H. (2003) Are follicular dendritic cells really good for nothing? *Nat. Rev. Immunol.*, **3**, 764–769.

KOUSKOFF, V., FAMIGLIETTI, S., LACAUD, G., LANG, P., RIDER, J. E., KAY, B. K., CAMBIER, J. C. & NEMAZEE, D. (1998) Antigens varying in affinity for the B cell receptor induce differential B lymphocyte responses. *J. Exp. Med.*, **188**, 1453–1464.

KROESE, F., WUBENA, A., SEIJEN, H. & NIEUWENHUIS, P. (1987) Germinal centers develop oligoclonally. *Eur. J. Immunol.*, **17**, 1069–1072.

KUEPPERS, R., ZHAO, M., HANSMANN, M.-L. & RAJEWSKY, K. (1993). Tracing B cell development in human germinal centres by molecular analysis of singel cells picked from histological sections. *EMBO J.*, **12**, 4955–4967.

KUPFER, A. & KUPFER, H. (2003) Imaging immune cell interactions and functions: SMACs and the immunological synapse. *Semin. Immunol.*, **15**, 295–300.

KUPFER, A., MOSMANN, T. R. & KUPFER, H. (1991) Polarized expression of cytokines in cell conjugates of helper T cells and splenic B cells. *Proc. Natl. Acad. Sci. USA*, **88**, 775–779.

KUPFER, H., MONKS, C. R. & KUPFER, A. (1994) Small splenic B cells that bind to antigen-specific T helper (Th) cells and face the site of cytokine production in the Th cells selectively proliferate: immunofluorescence microscopic studies of Th-B antigen-presenting cell interactions. *J. Exp. Med.*, **179**, 1507–1515.

LAPEDES, A. & FARBER, R. (2001) The geometry of shape space: application to influenza. *J. Theor. Biol.*, **212**, 57–69.

LINDHOUT, E., LAKEMAN, A. & DE GROOT, C. (1995) Follicular dendritic cells inhibit apoptosis in human B lymphocytes by a rapid and irreversible blockade of preexisting endonuclease. *J. Exp. Med.*, **181**, 1985–1995.

LIU, Y., ZHANG, J., CHAN, E. & MACLENNAN, I. (1991) Sites of specific B cell activation in primary and secondary responses to T-cell-dependent and T-cell-independent antigens. *Eur. J. Immunol.*, **21**, 2951–2962.

LIU, Y. J. & ARPIN, C. (1997) Germinal center development. *Immunol. Rev.*, **156**, 111–126.

LIU, Y.-J., BARTHELEMY, C. & DE BOUTEILLER, O. (1994) The differences in survival and phenotype between centroblasts and centrocytes. *In Vivo Immunology* (E. Heinen, M. P. Defresne, J. Boniver and V. Geenen, eds). New York: Plenum Press, pp. 213–218.

MACLENNAN, I. (1994) Germinal centers. *Annu. Rev. Immunol.*, **12**, 117–139.

MACLENNAN, I., DE VINUESA, C. G. & CASAMAYOR-PALLEJA, M. (2000) B-cell memory and the persistence of antibody responses. *Philos. Trans. R. Soc. Lond. B Biol. Sci.*, **355**, 345–350.

MACLENNAN, I., LIU, Y., OLDFIELD, S., ZHANG, J. & LANE, P. (1990) The evolution of B-cell clones. *Curr. Top. Microbiol. Immunol.*, **159**, 37–64.

MANSER, T. (2004) Textbook germinal centers? *J. Immunol.*, **172**, 3369–3375.

MCHEYZER-WILLIAMS, M., MCLEAN, M., LABOR, P. & NOSSAL, G. (1993) Antigen-driven b cell differentiation in vivo. *J. Exp. Med.*, **178**, 295–307.

MEYER-HERMANN, M. (2002a) A mathematical model for the germinal center morphology and affinity maturation. *J. Theor. Biol.*, **216**, 273–300.

MEYER-HERMANN, M. (2002b) Does recycling in germinal centres exist? *Immunol. Cell. Biol.*, **80**, 30–35.

MEYER-HERMANN, M. & BEYER, T. (2002) Conclusions from two model concepts on germinal center dynamics and morphology. *Dev. Immunol.*, **9**, 203–214.

MEYER-HERMANN, M. & BEYER, T. (2004) The type of seeder cells determines the efficiency of germinal center reactions. *Bull. Math. Biol.*, **66**, 125–141.

MEYER-HERMANN, M., DEUTSCH, A. & OR-GUIL, M. (2001) Recycling probability and dynamical properties of germinal center reactions. *J. Theor. Biol.*, **210**, 265–285.

MEYER-HERMANN, M. & MAINI, P. (2005a) Interpreting two-photon imaging data of lymphocyte motility. *Phys. Rev. E*, **71**, 061912.

MEYER-HERMANN, M. & MAINI, P. K. (2005b) Back to *one-way* germinal centers. *J. Immunol.*, **174**, 2489–2493.

MILLER, M., WEI, S., PARKER, I. & CAHALAN, M. (2002) Two-photon imaging of lymphocyte motility and antigen response in intact lymph node. *Science*, **296**, 1869–1873.

NOSSAL, G. J. (1992) The molecular and cellular basis of affinity maturation in the antibody response. *Cell*, **68**, 1–2.

OKADA, T., MILLER, M., PARKER, I., KRUMMEL, M., NEIGHBORS, M., HARTLEY, S., O'GARRA, A., CAHALAN, M. & CYSTER, J. (2005) Antigen-engaged B cells undergo chemotaxis toward the T zone and form motile conjugates with helper T cells. *PLOS Biol.*, **3**, 1–15.

OPREA, M. & PERELSON, A. (1997) Somatic mutation leads to efficient affinity maturation when centrocytes recycle back to centroblasts. *J. Immunol.*, **158**, 5155–5162.

OPREA, M., VAN NIMWEGEN, E. & PERELSON, A. (2000) Dynamics of one-pass germinal center models: implications for affinity maturation. *Bull. Math. Biol.*, **62**, 121–153.

PASCUAL, V., CHA, S., GERSHWIN, M. E., CAPRA, J. D. & LEUNG, P. S. (1994) Nucleotide sequence analysis of natural and combinatorial anti-PDC-E2 antibodies in patients with primary biliary cirrhosis. Recapitulating immune selection with molecular biology. *J. Immunol.*, **152**, 2577–2585.

PERELSON, A. S. & OSTER, G. F. (1979) Theoretical studies of clonal selection: minimal antibody repertoire size and reliability of self-non-self discrimination. *J. Theor. Biol.*, **81**, 645–670.

POO, W. J., CONRAD, L. & JANEWAY, C. A. J. (1988) Receptor-directed focusing of lymphokine release by helper T cells. *Nature*, **332**, 378–380.

RANDALL, T., PARKHOUSE, R. & CORLEY, R. (1992) J chain synthesis and secretion of hexameric igm is differentially regulated by lipopolysaccharide and interleukin 5. *Proc. Natl. Acad. Sci. USA*, **89**, 962–966.

SEDWICK, C., MORGAN, M., JUSINO, L., CANNON, J., MILLER, J. & BURKHARDT, J. (1991) Tcr, lfa-1 and cd28 play unique and complementary roles in signaling t cell cytoskeletal reorganization. *J. Immunol.*, **162**, 1367–1375.

SHIH, T.-A. Y., ROEDERER, M. & NUSSENZWEIG, M. C. (2002) Role of antigen receptor affinity in T cell-independent antibody responses in vivo. *Nat. Immunol.*, **3**, 399–406.

SIDMAN, C. & UNANUE, E. (1975) Receptor-mediated inactivation of early B lymphocytes. *Nature*, **257**, 149–151.

SISKIND, G. W. & BENACERRAF, B. (1969) Cell selection by antigen in the immune response. *Adv. Immunol.*, **10**, 1–50.

SMITH, K. G., LIGHT, A., NOSSAL, G. J. & TARLINTON, D. M. (1997) The extent of affinity maturation differs between the memory and antibody-forming cell compartments in the primary immune response. *EMBO J.*, **16**, 2996–3006.

TARLINTON, D. & SMITH, K. (2000) Dissecting affinity maturation: a model explaining selection of antibody-forming cells and memory B cells in the germinal centre. *Immunol. Today*, **9**, 436–441.

TOELLNER, K., JENKINSON, W., TAYLOR, D., KHAN, M., SZE, D., SANSOM, D., VINUESA, C. & MACLENNAN, I. (2002) Low-level hypermutation in T cell-independent germinal centers compared with high mutation rates associated with T cell-dependent germinal centers. *J. Exp. Med.*, **195**, 383–389.

VAN EIJK, M., DEFRANCE, T., HENNINO, A. & DE GROOT, C. (2001) Death-receptor contribution to the germinal-center reaction. *Trends Immunol.*, **22**, 677–682.

VERBEKE, C., WENTHE, U. & ZENTGRAF, H. (1999) Fas ligand expression in the germinal centre. *J. Pathol.*, **189**, 155–160.

VORA, K., RAVETCH, J. & MANSER, T. (1997) Amplified follicular immune complex deposition in mice lacking the Fc receptor γ-chain does not alter maturation of the B cell response. *J. Immunol.*, **159**, 2116–2124.

WEI, S. H., PARKER, I., MILLER, M. J. & CAHALAN, M. D. (2003) A stochastic view of lymphocyte motility and trafficking within the lymph node. *Immunol. Rev.*, **195**, 136–159.

11-4574-Caporale-10.qxd 9/9/2005 4:49 PM Page 177

10

Somatic Evolution of Antibody Genes

Rupert Beale and Dagmar Iber

Overview

Proteins evolve by the iterative alternation of mutation and selection over evolutionary time. Yet in a matter of days, the vertebrate immune system generates novel antibodies with high affinity for cognate antigens. This is accomplished by somatic mutation of the diverse pool of antibody genes generated from gene fragments as described in chapter 9, and clonal selection of high-affinity antibody producing B cells—a process of somatic rather than the familiar germline evolution. A spontaneously occurring process in DNA—deamination of deoxycytidine to deoxyuridine (C→U)—is catalyzed to produce mutations in antibody genes. A competitive environment is generated within the organism to select for mutations conferring high affinity—and to guard against self-reactivity. Thus the capability to produce high-affinity antibodies is an implicit property of the vertebrate genome.

The Biological Problem

Ehrlich's famous dictum, *corpora non agunt nisi fixata* ('a body will not work unless it is bound'),[1] poses a problem to the immune system: how can the germline genome encode the potential to bind to a vast array of distinct, rapidly evolving, infectious agents? Whereas the "innate" immune system attacks the problem by using receptors which bind to molecules substantially conserved amongst many different microorganisms,[2] the "adaptive" immune system attempts the more ambitious enterprise of evolving specific antibodies to recognize essentially any antigen that may be associated with a pathogen.

Antibodies consist of an amino-terminal antigen binding region called the V (variable) region and a carboxy-terminal C (constant) region, which mediates the effector properties of the antibody by directing other components of the immune system to eliminate the pathogen. The initial diversity generated by VDJ recombination is vast, but not so vast that high-affinity antibodies to every possible pathogen are created (see chapter 9). Fortunately, vertebrates have evolved a mechanism

11-4574-Caporale-10.qxd 9/9/2005 4:49 PM Page 178

capable of generating high-affinity antibodies from low-affinity antibodies. This process, known as affinity maturation, is achieved by means of multiple cycles of somatic hypermutation and clonal selection. Somatic hypermutation is characterized by point mutations in the V region at all four bases at a rate approaching 10^{-3} per nucleotide, many orders of magnitude above background. Most mutations do not improve affinity, but some give rise to increased affinity variants (and also to variants that are self-reactive). A clonal competition process therefore selects those B-cell clones that are capable of producing higher-affinity antibodies and also guards against the possibility of selecting high-affinity self-reactive clones, as these might pre-dispose to autoimmune diseases such as rheumatoid arthritis.

The mechanism of somatic mutation and the means by which selection is achieved have provided immunologists with a formidable series of interrelated problems in molecular, cellular, and mathematical biology. Recent data regarding how the balance of activity of multiple DNA repair proteins affects the spectrum of mutations observed in the immunoglobulin variable region has shed considerable light on the mutation mechanism. This chapter therefore presents a fair amount of detail regarding the steps from initial mutagenic insult to the observed mutation. After discussing the mutation mechanism we then summarize what is known about targeting of this mutation, and finally address the problem of how high-affinity B-cell clones are selected.

Somatic Hypermutation

Deamination as A Mutagenic Process

The mechanism of somatic hypermutation of the immunoglobulin genes has been a conundrum for many years. This important problem has been partially solved in an elegant manner, and we thus present the key experiments below in approximately chronological order. Whereas many puzzles still remain, it is now generally accepted that somatic hypermutation is initiated by the enzymatically catalyzed deamination of cytosine in DNA. Before describing the experimental basis for the conclusion that catalyzed deamination of cytosine initiates hypermutation, it is worth considering how DNA cytosine deamination might lead to mutation. When C is deaminated, it becomes U. This process occurs spontaneously, and usually triggers a nonmutagenic base excision repair response. Initially in this response, uracil is recognized by a DNA repair enzyme, uracil DNA glycosylase (UDG), which excises the uracil to leave an abasic site, and ordinarily this is subsequently repaired correctly (see chapter 2). However, if replication takes place either before uracil excision or over the abasic site, a mutation can occur. When uracil is present in DNA it is read as thymidine—hence a C→T transition mutation will result; and as incorporation of any base is possible at an abasic site a C→T, C→A, or C→G mutation can occur. Thus a C:G pair can be changed first to a U:G mismatch, then an abasic site:G mismatch and either subsequently fixed as T:A, A:T or G:C mutations or repaired to the original C:G. Clearly, deamination of C could be responsible for mutations at C and/or G, depending upon whether the deaminated C is on the coding or template strand. This idea provided the inspiration for the experiments that demonstrate that somatic hypermutation is initiated by catalyzed DNA cytosine deamination. Of course, the above scheme can only account for mutations

11-4574-Caporale-10.qxd 9/9/2005 4:49 PM Page 179

at C/G—the mechanism by which mutations at A/T occur is currently unknown. Mutations at C/G are called phase 1 mutations, and mutations at A/T are known as phase 2 mutations, for reasons discussed below.

Mutation, Recombination, or Conversion

Somatic mutation is the exclusive means by which mice and humans further diversify their antigen-binding repertoire after VDJ recombination. However, this does not represent the full extent of somatic modifications to antibody genes. Two other B-cell specific processes are mechanistically related to somatic hypermutation: antibody gene conversion and class-switch recombination. These apparently dissimilar processes arise as a result of differential repair of a common initiating lesion.

Antibody Gene Conversion

In contrast to mice and humans, some species (such as the chicken) utilize gene conversion templated on a number of pseudogenes downstream of the rearranged V gene to introduce additional diversity to the rearranged variable region (see also chapter 5 for a discussion of the use of pseudogenes to generate diversity). This appears especially important in the chicken since VDJ rearrangement generates little diversity in this species. Gene conversion is accompanied by somatic mutation and the relationship between the two has long been suspected to be intimate.

Class-switch Recombination

Class-switch recombination, which involves the deletion of some C-region genes, brings the V region next to constant regions with more appropriate properties for combating the infection at hand (see chapter 11; reviewed in reference 3). Thus the processes of antibody gene conversion and class-switch recombination give rise to very different final outcomes (see figure 10.1). However, both are initiated in the same way as somatic hypermutation, by the deamination of cytosine, and mutations occur during both processes. They are poorly understood at a mechanistic level after the initial events, and will be discussed here only in as much as they relate to somatic hypermutation.

The Importance of Editing

An important breakthrough occurred when a single gene called activation-induced deaminase (AID) with homology to an RNA editing enzyme called APOBEC1 was discovered to be necessary for both hypermutation and class switch recombination in both mice and humans.[4] Furthermore, the generation of V-region diversity by gene conversion in the chicken cell line DT40 also was shown to depend on AID.[5,6] As APOBEC1 was known to edit RNA, initial speculation centered on the possibility that distinct RNA targets would be edited and altered to generate the complex machinery hypothesized to be responsible for the apparently very different processes of point mutation and gene conversion. However, an alternative explanation was that AID's deaminating activity was focused directly on DNA encoding the V region, rather than on RNA.

11-4574-Caporale-10.qxd 9/9/2005 4:49 PM Page 180

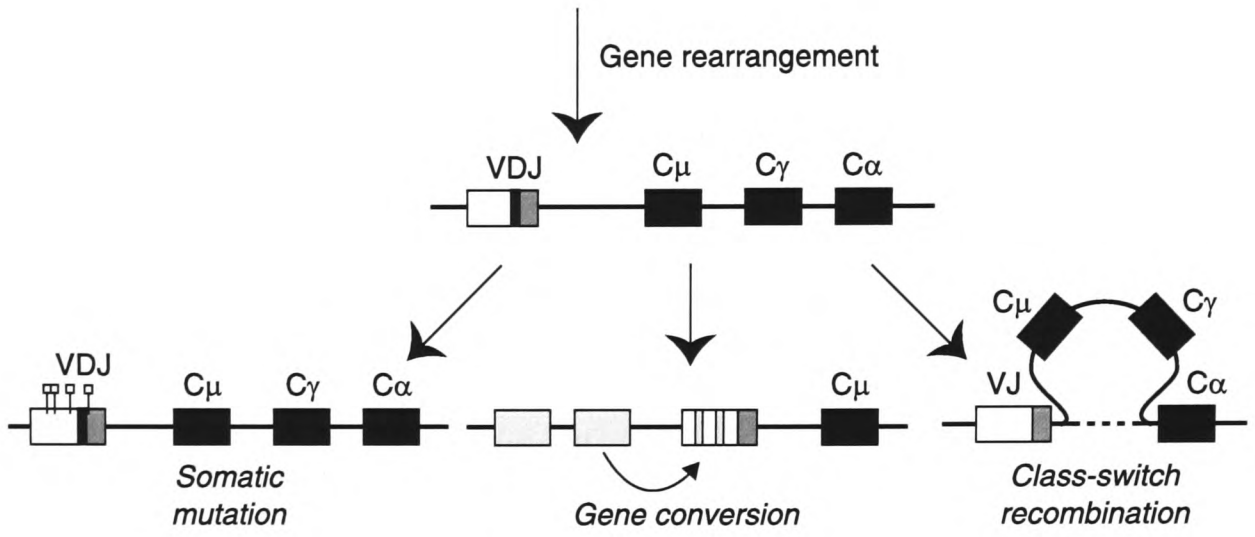


Figure 10.1. Somatic mutation, gene conversion, and hypermutaton occur after VDJ rearrangement. After antigen encounter in human and mouse, the VDJ rearranged genes in those B cells which express an antigen specific low affinity IgM antibody are subjected to a second wave of diversification, this time by hypermutation. In chickens and rabbits, V region diversification is achieved by using neighboring genes as templates. Short gene conversion tracts are observed. In CSR, the constant (C) region for IgM can be looped out and a different C region can be brought into proximity with the V region, and thus new antibodies with the same antigen specificity but different effector properties can be formed. (VDJ rearrangement is discussed in chapter 9, and class switch recombination in Chapter 11.)

DNA Suffers A C Change

AID is now known to be part of a DNA deaminase family of enzymes that act on retroviral DNA (see chapter 14). However, the prototypical family member APOBEC1 has an established physiological role as an RNA deaminase. The first strong evidence for AID acting directly on DNA, rather than on special RNAs expressed in lymphocytes about to undergo hypermutation, came when expression of AID in *Escherichia coli* gave rise to a mutator phenotype.[7] The mutator phenotype resulted from an increase in G/C to A/T point mutations (transition mutations at C/G). This is exactly as one would expect if the increase in mutation were due to deamination of C to U, as during replication A is inserted into the complementary strand opposite any U in DNA that is not repaired prior to replication. In *E. coli*, as in higher organisms, multiple mechanisms exist to repair G:U mismatches that arise from spontaneous deamination of C to U. In the base-excision repair pathway, uracil DNA glycosylase (UDG) recognizes U in DNA and excises it, leaving an abasic site. The abasic site triggers a repair response in which an AP-endonuclease nicks the DNA strand at the abasic site, an exonuclease chews back a patch of nucleotides thereby excising the abasic site, and a polymerase inserts the correct base using information retained in the undamaged complementary DNA strand (see figure 10.2). The mutator effect of AID was greatly enhanced in *E.coli* that, due to UDG deficiency, lack the ability to remove U prior to replication. This strongly suggested that AID is able to cause mutations by directly deaminating C in DNA. Subsequently, this was shown biochemically when human AID was shown to deaminate single-stranded DNA.[8]

11-4574-Caporale-10.qxd 9/9/2005 4:49 PM Page 181

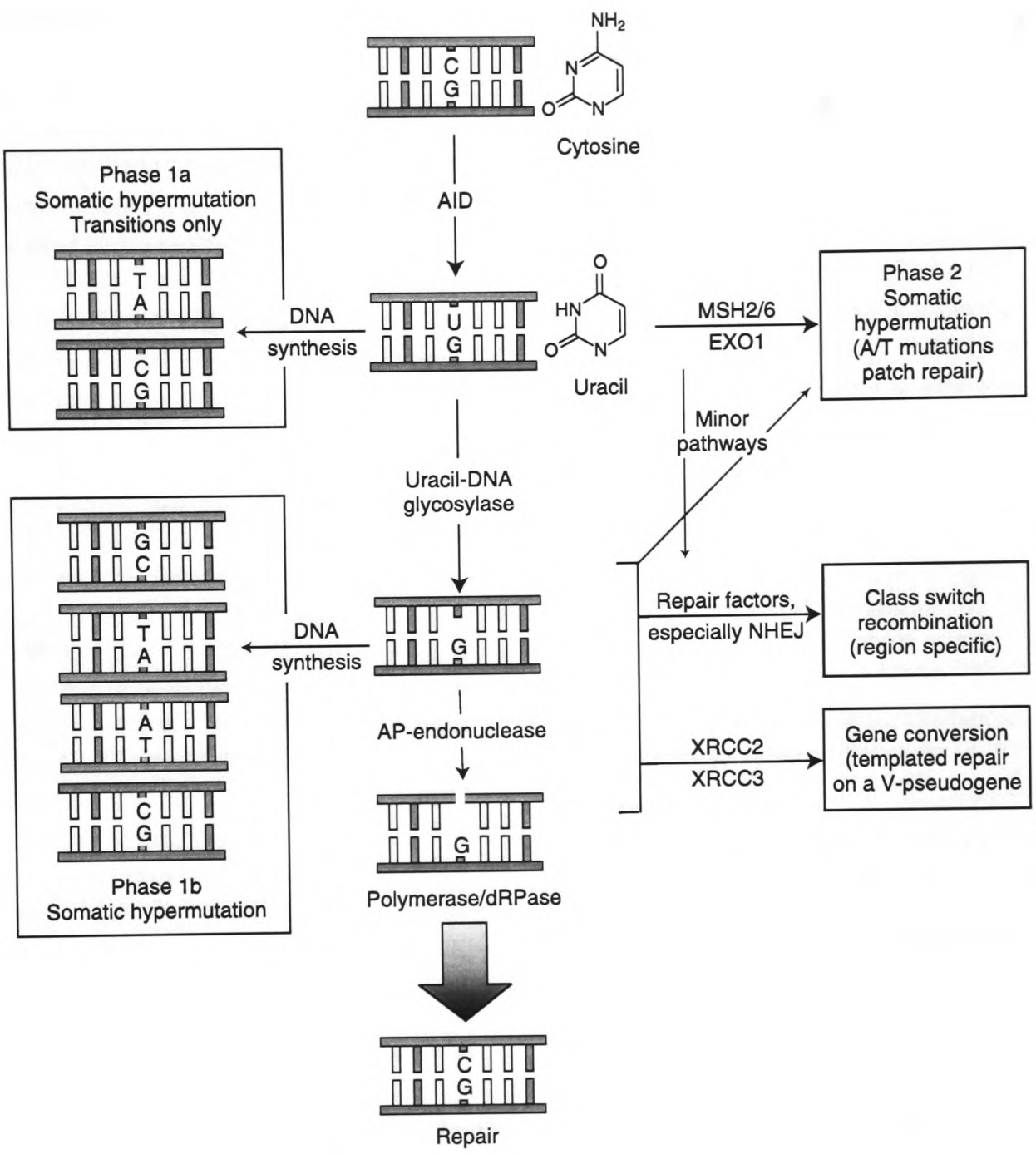


Figure 10.2. DNA deamination model of antibody diversification. AID deaminates C–U in DNA. Phase 1a mutation arises directly from deamination by reading of U as T by a replicative polymerase and results in C–T and G–A transition mutations only. Phase 1b arises as a result of replication over an abasic site, and thus can cause a C–N or G–N mutation. Phase II is dependent on MSH2/6, exonuclease I and polymerase Eta. It may arise from patch repair directed by MSH2/6 recognition of a G:U mismatch or a G:abasic site mismatch. It might also arise from AP-endonuclease dependent base excision repair. Gene conversion is predominantly triggered at a stage downstream of UDG, and is dependent on factors involved in homologous recombination such as XRCC2. CSR is partially dependent on MSH2/6 and exonuclease I, but shows a more pronounced dependence on UDG. It depends on nonhomologous end joining rather than homologous recombination. Finally, correct repair of the lesion may be achieved by base excision repair machinery. (AP endonuclease, apyrimidinic endonuclease; dRPase, 5′-deoxyribophosphodiesterase.)

11-4574-Caporale-10.qxd 9/9/2005 4:49 PM Page 182

Though provocative, the demonstration that AID had DNA cytidine deaminase activity did not prove that this was its physiological mechanism of action in lymphocytes. Independent evidence that AID deaminates V-region DNA came from testing the predictions of the model by examining of the effect of inhibiting, or genetically ablating, UDG on the observed pattern of V-region mutations. Whilst C→T (or G→A) transition mutations result from replication over unrepaired U (phase 1a mutations, see figure 10.2), as described above mutations from C to G or A (or from G to C or T) could be generated from the same initial lesion if U was removed by UDG, thus generating an abasic site, followed by the action of a polymerase capable of adding any nucleotide opposite an abasic site (phase 1b mutations, see figure 10.2).

As noted in chapter 2, the nucleotide insertion preference of the polymerases that replicate across the abasic site would influence the observed mutation spectrum. However, the spectrum of mutations observed will also be heavily influenced by the balance of different DNA repair pathways acting on a G:U mismatch. For example, if UDG activity were decreased, fewer abasic sites will be generated while more U remains in place, so mutation will be biased towards transition mutations (C to T or G to A) that result from insertion of an A opposite an unrepaired U on either the coding or complementary strand. A strong prediction would therefore be that if UDG were inhibited or knocked out, there would be a dramatic increase in the ratio of transitions to transversions at G/C (see figure 10. 2).

Of Mice and Men—and Chickens

As described above, chickens normally undergo gene conversion as well as point mutation in their V regions. The chicken cell line DT40 provided the first confirmation for the model presented in figure 10.2. This remarkable line exhibits constitutive AID-dependent antibody gene conversion, and its hyperrecombinogenic phenotype enables gene disruption by homologous recombination, facilitating experimentation. Both the gene conversion and hyperrecombinogenic phenotype are dependent on DNA repair enzymes which mediate homologous recombination, such as the Rad51 paralogues.[9] When DT40 cells are genetically deficient in either of two of these Rad51 paralogues (XRCC2 and XRCC3) the balance between point mutation and gene conversion is altered, greatly increasing the rate of point mutation at C/G.[10] However, unlike the human and mouse, in which mutations at C/G are predominantly transitions, as would be expected if much of the U was left unrepaired, mutations in the XRCC2 deficient DT40 are predominantly G/C→C/G transversions. This suggests that, in wild-type DT40, most Us are processed into abasic sites that then trigger gene conversion. In the XRCC2 deficient lines used in this experiment, translesion synthesis by a polymerase capable of adding nucleotides opposite the abasic site results in a high proportion of G/C→C/G transversion mutations (as discussed in chapter 2). If UDG were inhibited in the XRCC2 deficient DT40, one would expect a shift towards G/C→A/T transitions because the U that resulted from the deamination of C would remain in place and thus direct insertion of A on the new strand. In order to test this, the inhibitor of uracil DNA glycosylase (UGI) (found in bacteriophage which utilize U rather than T in their

11-4574-Caporale-10.qxd 9/9/2005 4:49 PM Page 183

genomes) was expressed in XRCC2-negative DT40 and the pattern of antibody hypermutation was examined. Indeed, G/C→A/T transitions now predominated,[11] exactly as one would expect according to the model in figure 10.2.

This model was further tested by targeted disruption of the UNG gene coding for UDG in mice. An examination of the sequence of the Immunoglobulin V regions of these mice lent support to the model.[12] As expected, if U is left unrepaired prior to DNA replication due to the absence of UDG, 95% of their mutations at G/C are transitions to A/T, as opposed to only about 50% in litter mate controls. Intriguingly, pointing to its dependence upon the same initiating event, these mice were also seriously defective in class switch recombination. Latterly, a group of patients have been identified with mutations in the gene for UDG who have a phenotype similar to that of the mice.[13]

Hypermutation Hotspots

It had long been observed that antibody hypermutation especially targets C and G in particular nucleotide contexts. These sequences correspond to the preferred DNA targets of AID in biochemical assays. Biochemical[14,15] and bacterial genetic[16] studies have shown that the local sequence specificity of AID and the local sequence context of mutations at G/C in the V region are congruent. These studies now identify WRC (A or T, purine, C) to be the preferred target of AID. WRC motifs are concentrated not just in the V regions, but are enriched in the parts of the V regions that encode antigen binding regions of the antibody. Thus the residues most critical to the generation of a broad range of combining site diversity are especially likely to mutate. Intriguingly, the hottest hotspots are invariably WGCW, a sequence formed from overlapping WRC motifs on opposite strands, suggesting AID may simultaneously engage both DNA strands.[16]

Phase 2—A/T Mutations

Whilst AID's ability to deaminate cytosine in DNA can, as described above, readily account for mutations at C/G pairs, A/T pairs also undergo hypermutation. The initial hypothesis put forward to explain somatic hypermutation was erratic replication by especially error-prone polymerases misincorporating opposite all four base pairs (Brenner and Milstein 1966).[17]

However, it now appears that mutation takes place in two discrete phases. Most of what we know about somatic hypermutation concerns phase 1—mutations at C/G as discussed above—since these are directly dependent on the deamination of C in a C/G pair. The mechanism by which AID triggers hypermutation at A/T pairs remains a mystery. Deficiency, in mice and humans, of components of mismatch repair recognition and the exonuclease and repair proteins that follow it, do give some clues as to how it might proceed. For example, mice deficient in either of the two components of the eukaryotic single-base mismatch recognition heterodimer mutS (i.e., MSH2 or MSH6) have C/G biased hypermutation—mutation appears to proceed normally at C/G but not at A/T (in addition, they have defective class-switch recombination, reviewed by Martin and Scharff).[18] This was perhaps the first

11-4574-Caporale-10.qxd 9/9/2005 4:49 PM Page 184

evidence in favor of two distinct phases of mutation, with all mutation initiated by AID and a second phase that involves mismatch repair.[19] In addition, mice deficient in exonuclease 1 exhibit a very similar phenotype to the mismatch repair-deficient mice. Exonuclease 1 is thought to excise a short patch of DNA adjacent to the mismatch recognized by the MSH2/6 heterodimer, which is replaced by the action of polymerases based on information in the complementary strand. Patients who are deficient in polymerase eta also have normal C/G mutations (and normal class-switch recombination), but reduced mutations at A/T. Thus genetic deficiencies in the mismatch repair pathway or DNA polymerase eta[18,20,21] all reduce phase 2 mutation but leave phase 1 intact. Furthermore, mice and humans deficient in UDG have normal mutations at A/T but all the C/G mutations are transitions (i.e., phase 1a, replication over U). The phenotype of mice deficient in both UDG and MSH2 is very instructive.[22] Whereas Msh2–/– mice show reduced mutations at A/T base pairs, these doubly deficient mice show a complete absence of mutation at A/T, and all the mutations at C/G are transitions—only phase 1a mutations (i.e., insertion of A opposite U) occur in these mice. These findings suggest that the G:U mismatch arising from a deaminated G:C pair is either recognized by UDG and the uracil is excised leading to a phase 1 mutation as discussed, or it is recognized as a mismatch by MSH2/6 and this leads to mutations at A/T mutations (i.e., phase 2 mutations).

The A/T specific nature of phase 2 mutations has prompted an intriguing suggestion that they arise as a result of misincorporation of U opposite A during MSH2/6-triggered repair in the region of a G–U mismatch.[22,23] According to this attractive but at present entirely speculative scheme, phase 1 mutation is triggered by deamination of C to form U, and phase 2 mutation is triggered by misincorporation of U. Both phases of mutation would then be dependent on excision of U and synthesis over the resultant abasic site to generate a full spectrum of mutations.

Targeting of Mutations

The very high levels of mutation seen in the V region could presumably not be tolerated genome-wide in lymphocytes. Early observations suggested that *cis*-acting elements were sufficient to direct hypermutation to any DNA sequence placed in the genomic context of the recombined V region.[24] On the other hand, some AID induced mutations are found outside the antibody locus, albeit at a much lower level (less than one tenth the level of somatic hypermutation in the V).

BCL-6 was the first such gene described as undergoing mutation *in vivo*, and it seems possible that many actively transcribed genes in mutating B cells may accumulate mutations with a WRC preference, suggesting AID dependence. Hypermutation is transcription linked, with the probability of acquiring a mutation increasing rapidly shortly after the promoter and then tailing off with further distance.[25] Biochemically AID acts on single-stranded DNA but not on double-stranded DNA. Since C and G seem equally likely to mutate, then both the transcribed and the nontranscribed strand must become accessible in the B cell. It has been suggested that supercoiling may possibly have the effect of promoting DNA deamination on both DNA strands.[26] There is some indirect evidence that increasing the single-strandedness of the DNA in the V region may be partly

11-4574-Caporale-10.qxd 9/9/2005 4:49 PM Page 185

responsible for targeting of mutations. A single-stranded DNA binding protein, replication protein A (RPA), has been identified as a binding partner of AID which stimulates the DNA deamination activity of AID on transcribed substrates in vitro.[27] It seems possible that a combination of transcription, supercoiling, and association with RPA could be sufficient to target mutations to the V region, but it is more likely that major components of the targeting mechanism are as yet undiscovered. There is no evidence at the time of writing for a V-region specific factor which recruits AID. Thus the mechanism by which targeting of mutations to the V region is achieved is currently unknown, and remains an important focus for research.

Selection

Targeting of mutations to the V region increases the fraction of effective mutations, that is of mutations that alter binding to the antigen at hand. However, in the immune system, much as in evolutionary biology, the great majority of all effective mutations are unfavorable. Such mutations may not only lead to loss of antigen specificity, but worse still may engender significant affinity to an autoantigen. Ongoing selection is therefore essential, both to eliminate self-reactivity and to select pathogen-specific antibodies that have acquired affinity-enhancing mutations.[28] While in the case of adaptive genome evolution selective forces derive from challenges from the external environment across generations, this cannot apply to a somatic evolution process. Rather, selective forces must originate from within the organism. The immune system thus had to evolve not only an elaborate mutation mechanism to generate variation in antibody genes but also an anatomic framework and a signaling infrastructure to enable selection of high-affinity variants.

The Basic Principles of Selection in the Immune System

The selective forces applied to the B cell are similar to those experienced at the whole organism level. For natural selection to drive genome evolution, entities must be able to produce similar offspring with variations in individual characteristics that affect the fitness of the offspring—that is its reproductive success. Likewise in the immune system, selection cannot act directly on antibodies (which cannot reproduce) but must act on B cells, which express the rearranged and possibly mutated antibody gene as B-cell receptor (BCR). B cells increase their proliferative rate upon stimulation by antigen via their BCRs, but low-affinity as well as self-reactive B cells are ultimately doomed to death by apoptosis. While apoptosis of autoreactive clones is crucial to guard against autoimmunity, apoptosis of low-affinity B cells increases the stringency of selection. The reproductive success of B-cell clones is thus represented by their ability both to proliferate and avoid apoptotic death.

In order to survive and proliferate, B cells need to pass a two-step selection process, during which they first acquire antigen and subsequently present fragments of this antigen to T helper cells.[29] The first step is dependent on BCR recognition of antigen, and thus serves to demonstrate binding capabilities of the BCR.

11-4574-Caporale-10.qxd 9/9/2005 4:49 PM Page 186

The second step of recruiting T cell help requires B cells to internalize BCR-bound antigen and target the antigen to specialized compartments (the MIIC) where the antigen is proteolytically processed into shortened peptides.

These peptides are subsequently loaded onto MHC class II molecules and transported to the B cell surface. Antigen specific T helper cells can recognize the peptide–MHC molecules (pMHC) and rescue the pMHC-presenting B cells from apoptosis. While antigen presentation by "professional" cells (cells that also provide co-stimulation) is likely to reduce the risk for B cells to acquire self-reactivity, it seems to be the requirement for B cell–T cell interaction that mainly helps guard against autoimmunity. This is because self-reactive T cells are eliminated during their development in the thymus[30] and should thus not be available in the periphery.

A Place to Meet

Antibody affinity maturation requires multiple interactions between antigen, B cells, and T cells. Usually antigen and antigen-specific B and T lymphocytes are all scarce at the onset of an infection and thus it is insufficient to rely on chance encounters. The immune system solves this problem of first contact by concentrating antigen in local lymph nodes through which lymphocytes pass.

After a proliferative burst in primary foci, a small number of B cells and T cells enter primary follicles and seed germinal centers. These germinal centers are microenvironments for antibody affinity maturation and greatly facilitate B cell selection and survival by increasing the number of B cell–antigen and B cell–T cell encounters. It should be noted that affinity maturation can, however, also be observed in the absence of germinal center reactions, though not with the same efficiency.[31]

The germinal center reaction is complex, as shown by figure 10.3, and fully reviewed by MacLennan.[29] Briefly, once the primary follicles are filled with proliferating B cells, the B cell blasts differentiate into so-called centroblasts.[32] Centroblasts are the cells that are thought to express AID and thus to hypermutate their antibody genes. Centroblasts differentiate into centrocytes, increase the expression of surface immunoglobulin, and are selected upon their BCR's affinity for antigen. Centrocytes are prone to apoptosis and will die rapidly unless they are rescued by follicular dendritic cells (FDCs), which retain the antigen in form of immune complexes (composed of antigen, antibodies, and complement)[29] and which provide temporary survival signals to antigen-specific centrocytes.[33,34] While germinal centers formed in the absence of FDCs fail to support affinity maturation and rapidly regress,[35] FDCs are not sufficient for long-term B-cell selection and survival. T cells need to finally rescue and select antigen presenting B cells.[32,36] Nonselected centrocytes undergo apoptosis and are quickly engulfed by macrophages; selected centrocytes may leave the germinal center reaction to become memory or plasma cells.[37] Back-differentiation of selected centrocytes into centroblasts enables a B-cell clone to go through multiple rounds of mutation and selection.[28,38]

11-4574-Caporale-10.qxd 9/9/2005 4:49 PM Page 187

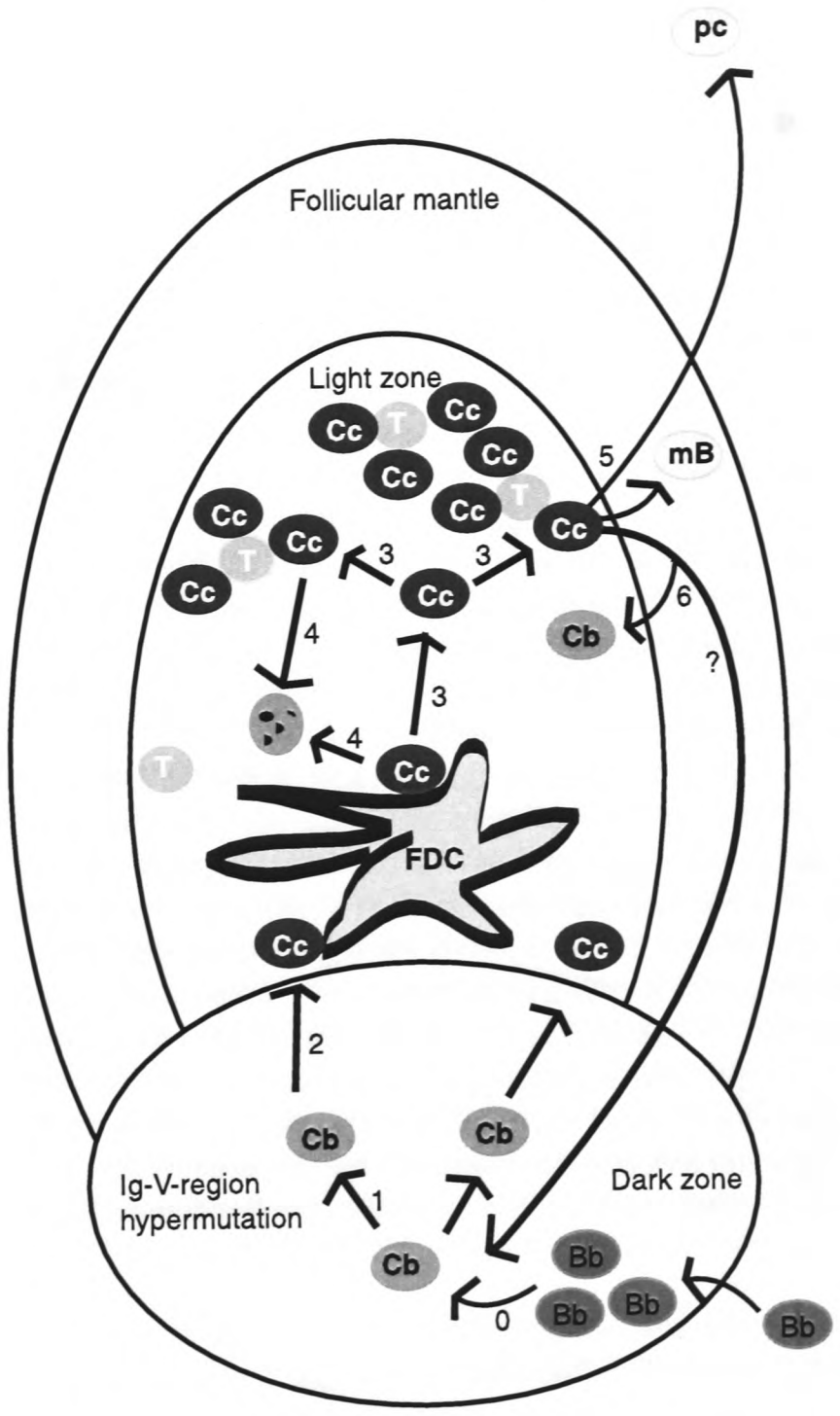


Figure 10.3. A simple model of the GC reaction. A small number of B blasts (Bb) initially seed the germinal centre reaction and exponentially expands before differentiating into centroblasts (Cb). Centroblasts (Cb) continue to strongly proliferate (1), start hypermutating their antibody genes and eventually differentiate (2) into centrocytes (Cc). Centrocytes re-express IgM and are selected according to their affinity for antigen. Selection involves antigen acquisition from follicular dendritic cells (FDCs) and subsequent presentation to T cells (3). Failure to either acquire antigen or to find T-cell help results in apoptosis of B cells (4). Selected B cells, on the other hand, either leave the germinal centre reaction to become memory cells or plasma cells (5), or back-differentiate into centroblasts, thus enabling several rounds of mutation and selection (6). It is currently unclear whether these back-differentiated centroblasts migrate back to the initial pool of centroblasts which in some (but not all) germinal centre reactions segregate into a so-called dark zone, while centrocytes and FDCs are found in a so-called light zone.

The Mechanism of B-cell Selection

For affinity to increase during the course of the germinal center reaction, the affinity threshold for selection needs to increase (i.e., a higher affinity must be required for survival as selection proceeds over time). The extent of increase required for survival appears to be determined by clonal competition within the B-cell population. Accordingly, low-affinity B-cell clones can persist when competition with high-affinity B-cell clones is reduced. Experimentally, this is achieved in germinal centers of transgenic mice that bear a prerecombined antigen-specific (low-affinity) V_HDJ_H transgene, which is also not well-targeted by somatic hypermutation.[39,40]

Principally, B-cell clones might compete for antigen or for T-cell help—or both. Older models have particularly stressed the role of B-cell competition for scarce antigen[41] and suggest that antigen removal during the immune response as well as emerging serum antibodies would lead to a gradual increase of the affinity threshold.[42,43] However, affinity maturation is hardly compromised by alterations in the initial amount of antigen deposited on FDCs[44,45] or by lack of secreted antibodies.[46] Competition for antigen thus appears inadequate to explain B-cell selection for all the conditions under which it occurs.

In contrast, recent experiments suggest that B cells can discriminate between different affinities of binding on an individual basis and signal accordingly.[47]

Given that T-cell responsiveness to antigen-challenged B cells correlates with binding affinity,[48] it is conceivable that the BCR binding affinity is translated into a cellular signal that affects the ability of B cells to recruit T-cell help. One way that the signaling strength of B cells may affect T-cell responsiveness is an enhanced presentation of pMHC,[49,50] which may be enabled by an improved targeting of antigen to the processing compartments. Targeting to and accession of the processing compartments requires signaling through Igα and Syk (as well as downstream effectors).[51] The degree of Igα and Syk phosphorylation is affinity dependent[47] thus suggesting a link between BCR affinity and the level of pMHC presentation on the B-cell surface.

The Basis for the Efficiency of the Somatic Evolution of Antibodies

Starting with weak binders, the immune system is capable of generating high-affinity antibodies with remarkably few mutation and selection steps. Key to this efficiency are both the evolved antibody structure, which permits large (targeted) mutation rates, and the stringency of the selection mechanism.

Antibodies Evolved to Evolve

Increased mutation rates are in general harmful as most mutations are detrimental (as discussed in chapter 4). In the case of antibodies, mutations are targeted to the V region, and in particular to the complementarity-determining regions (CDRs). The CDRs form loops that mediate contact with the antigen (chapter 9). Targeting of mutations to the CDRs increases the fraction of mutations which alter affinity and limits the number of mutations that may disrupt other essential structural elements

of the antibody—a cause for a large proportion of detrimental mutations in other proteins.[52] The affinity of antibody binding is increased both by direct changes in the binding site as well as by mutations that lie more distant and alter the conformation of the binding site. While some single mutations can increase an antibody's affinity by tenfold, affinity maturation is the result of several additive changes; high-affinity antibodies harbor on average six to eight mutations.[53] Considering that in protein engineering approximately six to eight appropriately targeted mutations are required to alter binding specificity,[54] the optimized character of antibody affinity maturation becomes clear.

Efficient Selection

Another evolved feature of the immune system is its effective selection strategy. There are several key features. First of all, and most importantly, the multiple rounds of mutation and selection enable a stepwise affinity maturation process, which strongly facilitates the generation of high-affinity antibodies.[38] Analysis of fitness landscapes in evolutionary biology suggests that a potential danger of such stepwise evolution process is the trapping in local optima.[55] However, the parallel but spatially separate evolution of many germinal center reactions in the follicle (each seeded by few B blasts) avoids trapping all lineages of B cells in what may prove to be an unfavourable local optimum that lacks paths to high-affinity antibodies.

But B cells must not only be selected for their ability to produce high-affinity antibodies. There also must be a mechanism that guards against emerging autoreactivity. This challenge is met by the second key feature of the selection strategy, that B-cell selection depends not only on the acquisition of antigen but also on T-cell help. The requirement for T-cell help may also enable the large robustness of affinity maturation to variations in the initial amount of available antigen since competition for interaction with T cells (which only make up 5–10% of all germinal center cells) may drive affinity maturation over a wide range of antigen concentrations.

The third feature is the short lifespan of centrocytes, and the ability of T cells to confer both death and survival signals increases the efficiency of B-cell selection. In mice in which apoptosis is impaired either by decreased ability to generate an apoptotic signal (mice that lack Fas) or by increased suppression of apoptosis (mice that overexpress Bcl-x), low-affinity B cells persist in the germinal centre reaction and the selection of high-affinity B cells is impaired.[56,57]

Conclusions

The vertebrate immune system must adapt to pathogens that are both rapidly reproducing and evolving. Adaptation on the time scale of host generations is not sufficient. What has evolved, on the time scale of host generations, is an immune system that is organized to generate the diversity required to adapt to pathogens rapidly within the lifetime of an individual. Rapid adaptation can be enabled by a situation-dependent increase in the local mutation rate, which generates functional variation.

11-4574-Caporale-10.qxd 9/9/2005 4:49 PM Page 190

As a result of targeted mutation and an efficient somatic selection mechanism, antibodies somatically evolve that will bind with high affinity to any attacking pathogen, including one never before encountered in the evolutionary history of the host.

Whilst an organism inherits a single genome, it can generate B cells with varied genomes. This is achieved by VDJ recombination as described in chapter 9 and a subsequent targeted mutation mechanism that exploits fundamental properties of DNA mutability and repair, and which acts on an easy-evolvable antibody structure. The selection mechanism is fine-tuned to avoid autoreactivity and promote rapid generation of high-affinity antibodies. Although our current understanding of these processes appears to be sufficient to generate and select high-affinity antibodies to a desired specificity in vitro, this requires a much longer time span and far more cumbersome selection methods than employed by the immune system.[58] The elegance of the biological process thus belies its bewildering complexity.

The extracted article "The Mechanistic Basis of Compartmentalized Gene Expression in *Bacillus subtilis*" can be found at http://dx.doi.org/10.1007/s11047-005-3670-y